CLAS12 Technical Design Report

Version 5.1

July 15, 2008

Participating Institutions:

Arizona State University, Tempe, AZ

Argonne National Laboratory, Argonne, IL

California State University, Dominguez Hills, CA

Catholic University of America, Washington, DC

CEA-Saclay, Gif-sur-Yvette, France

University of Connecticut, Storrs, CT

Edinburgh University, Edinburgh, UK

Fairfield University, Fairfield, CT

Florida International University, Miami, FL

University of Glasgow, Glasgow, UK

Hampton, University, Hampton, VA

Idaho State University, Pocatello, Idaho

INFN, Laboratori Nazionali di Frascati, Fascati, Italy

INFN, Sezione di Genova, Genova, Italy

Institute of Theoretical and Experimental Physics (ITEP), Moscow, Russia

James Madison University, Harrisonburg, VA

Kyungpook University, Daegu, South Korea

Los Alamos National Laboratory, Los Alamos, NM

Moscow State University, Moscow, Russia

University of New Hampshire, Durham, NH

Norfolk State University, Norfolk, VA

Ohio University, Athens, OH

Old Dominion University, Norfolk, VA

Institut de Physique Nucleaire, Orsay, France

Rensselaer Polytechnic Institute, Troy, NY

Rice University, Houston, TX

University of Richmond, Richmond, VA

University of South Carolina, Columbia, SC

Temple University, Philadelphia, PA

Thomas Jefferson National Accelerator Facility, Newport News, VA

Virginia Polytechnic Institute and State University, Blacksburg, VA
University of Virginia, Charlottesville, VA
College of William and Mary, Williamsburg, VA
Yerevan Institute of Physics, Yerevan, Armenia

Contents

Part I

Physics

Chapter 1

Executive Summary

In the past five decades many important discoveries have been made in electron-proton scattering experiments. The finite size of the proton was measured in Hofstadter's pioneering experiment in which electrons of 188 MeV energy were elastically scattered off a hydrogen target [1]. It demonstrated conclusively that the proton is not a Dirac particle but has a finite size. Hofstadter was awarded the Nobel prize in 1961 for this discovery. The energy of Hofstadter's accelerator was not high enough to resolve the internal structure of the proton but it laid the groundwork for a vigorous research program of inclusive electron scattering. It took another decade, and the construction of the powerful electron accelerator and the large magnetic spectrometers at the Stanford Linear Accelerator Center (SLAC), to "see" deep into the proton's interior. At energies of 20 GeV, experimental groups led by Jerome Friedman, Henry Kendall, and Richard Taylor discovered "scaling", i.e. the independence of deeply inelastic structure functions of the proton on the virtuality of the electromagnetic probe [2, 3]. These results could only be interpreted in terms of electron scattering off point-like "partons" inside the proton. They were also a triumph for the quarks postulated earlier by theorists Murray Gell-Mann [4] and George Zweig [5] as the fundamental building blocks for hadrons. Gell-Mann received the Nobel prize in 1969. For the experimental discovery of the proton's quark structure Friedman, Kendall, and Taylor shared the Nobel prize in 1990. The small but significant deviations from scaling that were observed in the SLAC experiments also had significant impact on the development of the theory of Quantum Chromodynamics (QCD), and are fully explained by the emission of gluons from the struck quarks.

Deeply Inelastic Scattering (DIS) experiments, where only the scattered electron is de-

tected, have been carried out up to the highest energies at CERN and at DESY. The longitudinal momentum and spin densities of the quarks have been mapped out in detail. We have also learned that the quarks are not the only tenants of the proton, but that more than 50% of the momentum of the proton is carried by the glue needed to bind the quarks together. More recently, inclusive polarized electron scattering off polarized protons led to the "spin puzzle", the finding that the quark spin contributes less than 25% of the total spin of the proton, leaving much to be understood about the origin of spin [6]. DIS experiments will continue to play an important role in further unraveling the valence quark structure, especially under extreme conditions, e.g. when one quark carries nearly the full proton momentum.

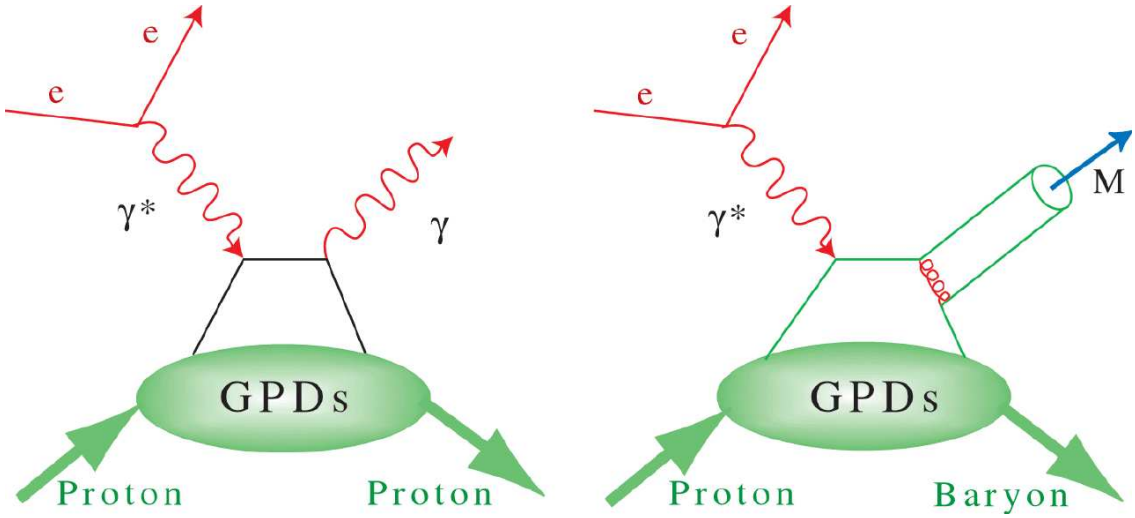

Figure 1.1: The "handbag" diagrams for deeply virtual Compton scattering (a), and for deeply virtual meson production (b). Four GPDs describe the "soft" proton structure part. They depend not only on x, but on two more variables: the momentum imbalance of the quark before and after the interaction, ξ, and the momentum transfer to the proton, t.

A glorious past and present is a good basis but not a guarantee for a successful future. So, what is the new physics that we are confident will shape the future of nuclear physics with electromagnetic probes for the coming decades? While the major discoveries in electromagnetic physics have so far come from electron scattering experiments where only the scattered electron is measured in magnetic spectrometers, in particular measurement of elastic form factors and longitudinal parton densities, they are not sufficient to unravel the full structure and internal dynamics of the proton. Semi-exclusive measurements, in which one hadron is

observed in addition to the scattered electron, are needed to study its flavor structure, and only fully exclusive processes in which all final products are reconstructed can unravel the complete internal dynamics of the proton. The experimental and theoretical tools for such an endeavor are now on the horizon: electron machines such as CEBAF at 12 GeV, with its CW beams and large acceptance detectors operating at high luminosities, are needed for the experimental part of such a program, while the new formalism of Generalized Parton Distributions (GPDs) provides the theoretical framework for the interpretation of the new experiments [7, 8, 9, 10, 11]. The basis for this approach are the "handbag" diagrams shown in Fig. 1.1. Here the electron knocks a quark out of the proton by exchanging a deeply virtual (massive) photon. The quark then emits a high energy photon (a) and is put back into the proton. Alternatively, a $q\bar{q}$ pair (meson) is created, and one of the quarks is returned into the proton (b). At sufficiently high energies and high virtuality of the exchanged photon ("Bjorken regime") these processes are controlled by perturbative QCD, and the results can be interpreted in terms of "soft" correlation functions, the GPDs. They describe the full complexity of the proton's structure and dynamics.

What can these experiments tell us about the proton beyond what previous experiments have? Elastic scattering and deeply inelastic scattering give us two orthogonal one-dimensional projections of the proton: The quarks in the proton are subject to quantum fluctuations, resulting in variations of the proton size at a time scale of $< 10^{-23}$ seconds. Elastic scattering measures the probability of finding a proton with a transverse size $b_\perp$ matching the resolution of the probe given by the momentum transfer t: $b_\perp \approx 1/\sqrt{|t|}$. The expression relates the momentum transfer to the transverse size of the proton probed in the interaction. Deeply inelastic scattering probes the longitudinal momentum distribution of the quarks, but has no sensitivity to the transverse dimension. These two aspects are illustrated in the first two panels of Fig. 1.2 [13]. The information resulting from these two types of experiments is disconnected, and does not allow us to construct the image of a real 3-dimensional proton.

Deeply exclusive scattering processes connect both transverse and longitudinal information including their correlations as described by GPDs. This is shown in the third panel of Fig. 1.2. The GPDs now depend on 3 dimensions (x, ξ, t). Once the GPDs are measured they allow the construction of a 3-dimensional image (two in transverse space and one in longitudinal momentum) of the proton in what has been called "nucleon-tomography" [12]. GPDs will allow the study of the mass and angular momentum distributions of quarks, and the forces

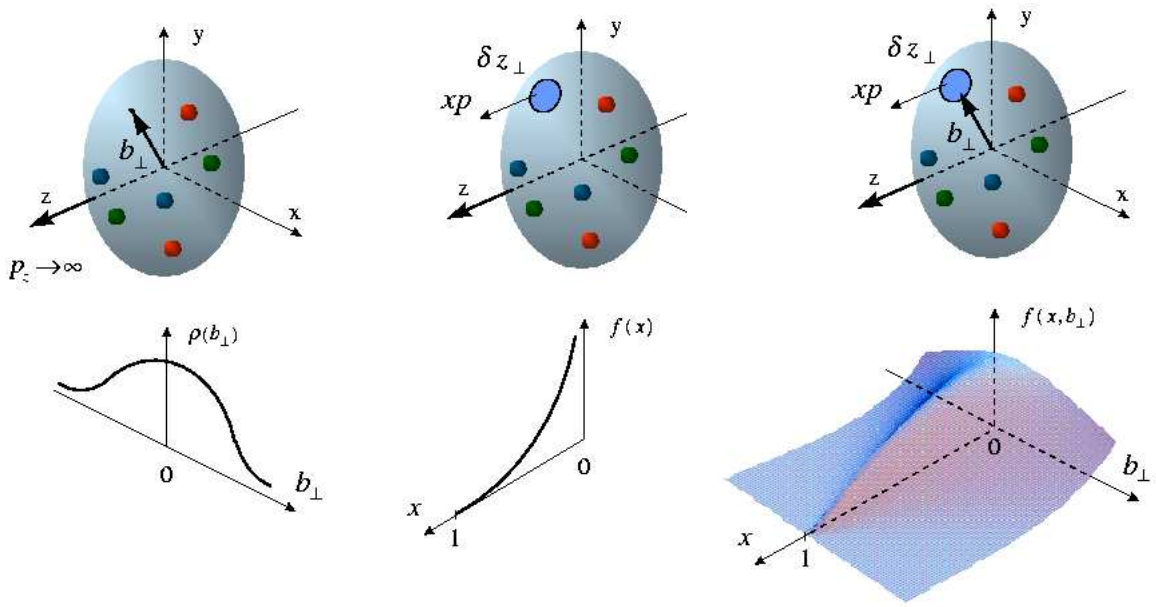

Figure 1.2: Representations of the proton properties probed in elastic scattering (left), deeply inelastic scattering (center), and deeply exclusive scattering processes (right). Elastic scattering measures the charge density $\rho(b_\perp)$ as a function of the impact parameter $b_\perp$. DIS measures the longitudinal parton momentum fraction density $f(x)$. GPDs measure the full correlation function $f(x, b_\perp, \xi)$ where ξ represents the longitudinal momentum imbalance of the struck quark before and after the interaction. The graph shows the correlation function at $\xi = 0$.

and pressure distributions in the proton.

On very general grounds we expect a correlation between the transverse and longitudinal variables that, for example at $\xi = 0$, could be of the form [12]:

$$H_f(x, 0, t) \approx q_f(x) \exp^{-a|t|(1-x)\ln\frac{1}{x}}, \tag{1.1}$$

where $q_f(x)$ is the forward parton distribution of flavor f and a is a scale parameter characterizing the transverse size. While the exact shape of this function needs to be determined experimentally, it must qualitatively contain the correlation between these parameters. Fig. 1.3 illustrates the physical significance of Eq.(1.1) [12]. The graphs show the strong correlation between the t-dependence (transverse size $b_\perp$) and the x-dependence (longitudinal momentum). For the spin-independent GPD $H(x, \xi, t)$ the left panels show the dramatic change in transverse profile as a function of longitudinal momentum x, while the image remains isotropic. A spatial anisotropy in the proton is observed for the spin-dependent GPD $E(x, \xi, t)$ shown in

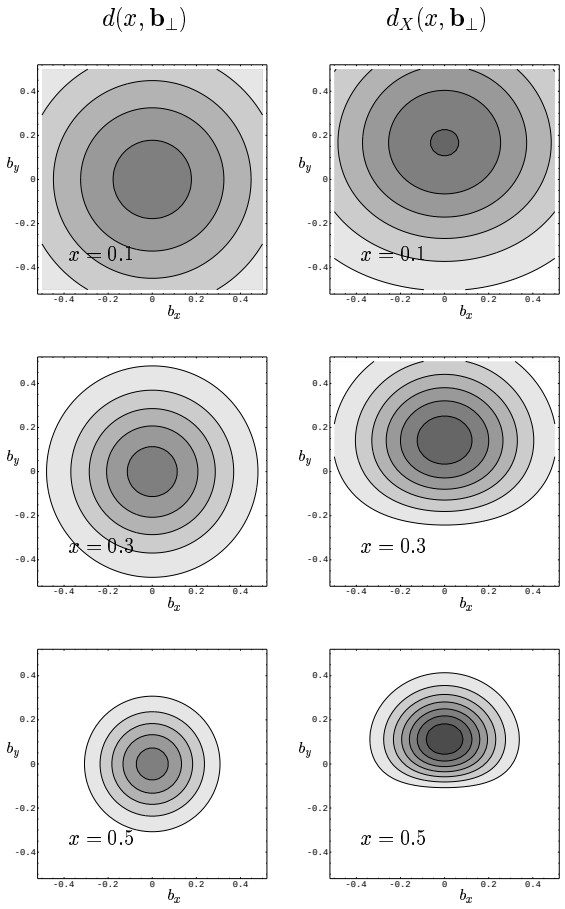

Figure 1.3: Simulated proton tomography images for the d-quarks, showing the strong correlation between the transverse size and the longitudinal momentum[12]. For small quark momentum x, the proton has a large transverse size, and it becomes very dense at large x. Left column: unpolarized proton, right column: transversely polarized proton.

the right panels.

Electron scattering is the fundamental tool to determine the structure of atoms, nuclei, protons, and hadrons. This program must remain the flagship of an electromagnetic laboratory aimed at making fundamental contributions at the frontier of hadronic physics. This continues to be true for measurements of form factors and inclusive processes at high x. The new physics contained in the GPDs will be the climax of electron scattering and revolutionize nucleon structure physics. With the 12 GeV upgrade, JLab will be in the unique position to carry out a major part of the program using its powerful electron accelerator and its versatile instrumentation. The upgraded `CLAS12` detector will make major contributions in many areas of hadron physics. In particular, `CLAS12` will have design features that are essential for probing the new physics of the GPDs.

Chapter 2

GPDs and Quark Distributions in Transverse Space

2.1 Introduction

The challenge of understanding nucleon electromagnetic structure still continues after five decades of experimental scrutiny. From the initial measurements of elastic form factors to the accurate determination of parton distributions through deep inelastic scattering (DIS), the experiments have increased in statistical and systematic accuracy. Only recently it was realized that in fact the parton distribution functions represent special cases of a more general, much more powerful, way to characterize the structure of the nucleon, the generalized parton distributions (GPDs) [14, 15, 10, 11]. The GPDs are the Wigner quantum phase space distribution of quarks in the nucleon – functions describing the simultaneous distribution of particles with respect to both position and momentum in a quantum-mechanical system, representing the closest analogue to a classical phase space density allowed by the uncertainty principle. In addition to the information about the spatial density (form factors) and momentum density (parton distribution), these functions reveal the correlation of the spatial and momentum distributions, *i.e.* how the spatial shape of the nucleon changes when probing quarks and gluons of different wavelengths.

The concept of GPDs has led to completely new methods of "spatial imaging" of the nucleon, either in the form of two-dimensional tomographic images (analogous to CT scans in medical imaging), or in the form of genuine three-dimensional images (Wigner distributions).

GPDs also allow us to quantify how the orbital motion of quarks in the nucleon contributes to the nucleon spin – a question of crucial importance for our understanding of the "mechanics" underlying nucleon structure. The spatial view of the nucleon enabled by the GPDs provides us with new ways to test dynamical models of nucleon structure.

The mapping of the nucleon GPDs, and a detailed understanding of the spatial quark and gluon structure of the nucleon, have been widely recognized as the key objectives of nuclear physics of the next decade. This requires a comprehensive program, combining results of measurements of a variety of processes in electron–nucleon scattering with structural information obtained from theoretical studies, as well as with expected results from future lattice QCD simulations.

GPDs, in basic terms, describe the structure of the nucleon probed in reactions in which a high-energy, short-distance probe interacts with a *single quark* in the nucleon. Mathematically, this is the quantum-mechanical amplitude for "taking out" a quark from the wave function of a fast-moving nucleon and "putting it back" with different momentum, thereby imparting a certain momentum transfer to the nucleon. It depends on the fractions of the nucleon momentum carried by the quark before and after the process, $x + \xi$ and $x - \xi$ (ξ defines the longitudinal momentum transfer to the nucleon), as well as on the transverse momentum transfer to the nucleon, $\boldsymbol{\Delta}_\perp$. In the special case of zero momentum transfer, $\xi = 0$ and $\boldsymbol{\Delta}_\perp = 0$, this amplitude reduces to the usual parton density of quarks in the nucleon, measured in inclusive deep-inelastic eN scattering. Similarly, in the case of non-zero transverse momentum transfer, $\boldsymbol{\Delta}_\perp \neq 0$, the integral of the GPD over x reduces to the nucleon form factor at invariant momentum transfer $t = -\boldsymbol{\Delta}_\perp^2$, measured in elastic eN scattering. Thus, the GPDs combine the traditional concepts of parton density and elastic form factor within a single structure. The presence of spin – both of the nucleon and the quark – as well as quark flavors (u, d, s) leads to the appearance of various independent spin/flavor components of the GPDs. Together, they provide a comprehensive description of the quark structure of the nucleon.

The GPDs, however, contain much more information than the parton densities and elastic form factors alone. They describe the correlation of the quark longitudinal momenta ($x+\xi, x-\xi$) with the transverse momentum transfer to the nucleon ($\boldsymbol{\Delta}_\perp$). This information permits a simple interpretation in terms of a spatial distribution of quarks in the nucleon. For $\xi = 0$, the two-dimensional Fourier transform of the GPD with respect to $\boldsymbol{\Delta}_\perp$ describes the distribution of quarks with longitudinal momentum fraction x over the transverse distance, $\boldsymbol{b}$, from the center

of the nucleon (impact parameter). The integral of this spatial distribution over $\boldsymbol{b}$ gives the total parton density at a longitudinal momentum fraction x. This 1+2-dimensional "mixed" momentum and coordinate representation corresponds to a set of "tomographic images" of the quark distribution in the nucleon at fixed longitudinal momentum, x.

A fully 3–dimensional spatial image of the nucleon is obtained when taking the Fourier transform of the GPD also with respect to the longitudinal momentum transfer to the nucleon, ξ, thus localizing the nucleon also in longitudinal space. In this case the GPD turns into the Wigner phase space distribution of quarks in the nucleon, describing their simultaneous distribution with respect to longitudinal momentum x and the conjugate coordinate. A quantum phase space distribution describes the distribution of particles over both coordinate and momentum (or, more generally, pairs of conjugate variables) in a quantum mechanical system and represents the closest analogue to a classical phase space density allowed by the uncertainty principle. Fig. 2.1 shows the spatial shape of the nucleon (contours of equal density) for quarks of different longitudinal momentum fraction, x, as obtained from a model GPD consistent with present parton density and form factor data. One sees that the effective shape of the nucleon changes with the quark momentum fraction probed in a certain reaction. This new 3D representation offers unprecedented possibilities not only for visualizing the nucleon as an extended object in space, but also for understanding the space-time evolution of scattering processes probing the quark and gluon structure of the nucleon.

Further motivation for the study of GPDs comes from the fact that certain moments of the GPDs – integrals over the quark momentum fractions – are related to fundamental static properties of the nucleon that cannot directly be accessed experimentally otherwise. In particular, the second moment of the GPDs gives the fraction of the nucleon spin carried by the quarks, including their spin and orbital angular momentum. Starting with the historic measurements by the EMC collaboration 20 years ago, determining how the spin of the nucleon is composed from the spins of the quarks and gluons and their orbital motion has been the central goal of polarized deep-inelastic scattering experiments. Measurements of the GPDs would give access to the quark orbital angular momentum, thus providing information about another crucial piece of the nucleon "spin puzzle".

The momentum transfer, Q^2, in eN scattering defines the spatial resolution of the probe. The description of hard exclusive processes in terms of GPDs applies to the limit of large Q^2, where the reaction is dominated by the scattering from a single, quasi-free quark ("leading–

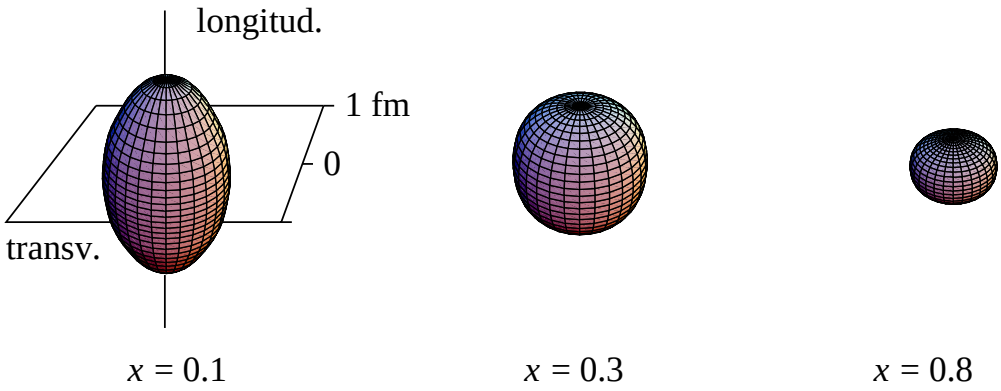

Figure 2.1: "3D images" of the nucleon as obtained from a model phase space distribution incorporating phenomenological information about GPDs. Shown are constant-density surfaces of the spatial distribution of u-quarks, for three values of the momentum fraction x. In the valence quark region ($x \geq 0.1$) the nucleon has a spherical shape. At large x the size shrinks and the shape becomes oblate (disk-like). At small x, the quarks spread out in the longitudinal direction, and the shape becomes prolate (cigar-like).

twist approximation"). At lower Q^2, effects related to the interaction of quarks during the hard scattering process, or coherent scattering involving more than one quark, become important ("higher–twist effects"). The minimum value of Q^2 required for the GPD description to be applicable in practice depends on the final state, and can ultimately only be determined experimentally. For DVCS (see Fig. 2.2), the experience with inclusive DIS and other two-photon processes such as $\gamma^*\gamma \to \pi^0$ (measured in e^+e^- annihilation) suggest that the leading-twist approximation should be reliable already at $Q^2 \sim$ few GeV^2. Thus, DVCS can be used to extract information about GPDs at the momentum transfers accessible in fixed-target experiments. For meson production, the experience with the pion form factor at high Q^2 and available meson electroproduction data suggest that higher-twist effects are significant up to momentum transfers of $Q^2 \sim$ 10-20 GeV^2. While such effects can be reduced by forming ratios of observables, or can be accounted for in phenomenological models, it seems likely that the use of meson production data for a quantitative extraction of GPDs requires measurements at significantly higher momentum transfers than in DVCS.

In the $eN \to eN\gamma$ cross section, the DVCS amplitude interferes with the known amplitude of the Bethe-Heitler (BH) process, in which the final-state photon is emitted from the electron (see Fig. 2.3). The total cross section is given by [16]:

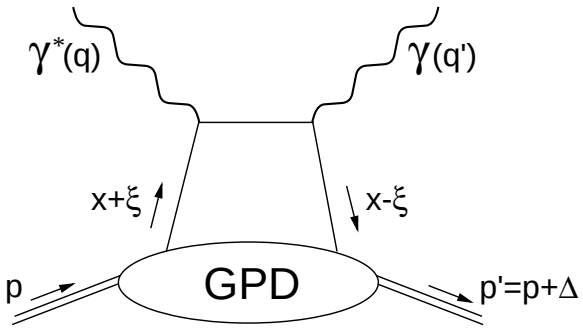

Figure 2.2: Reactions in eN scattering probing the generalized parton distributions. Deeply-virtual Compton scattering and meson production probe the GPDs at non-zero longitudinal and transverse momentum transfer, $\xi \neq 0, \boldsymbol{\Delta}_\perp = 0$. Different mesons (ρ, π, K) select different spin-flavor components of the GPDs.

$$\frac{d\sigma^{ep\to ep\gamma}}{dx_B dy d\Delta^2 d\varphi} = \frac{\alpha^3 x_B y}{16\pi^2 Q^2 \sqrt{1+\epsilon^2}} \left| \frac{\mathcal{T}}{e^3} \right|^2 , \tag{2.1}$$

where $\epsilon = 2x_B M/Q$, y is the fraction of the electron energy lost in the nucleon rest frame and φ is the angle between the leptonic plane (e, e') and the photonic plane (γ^*, γ).

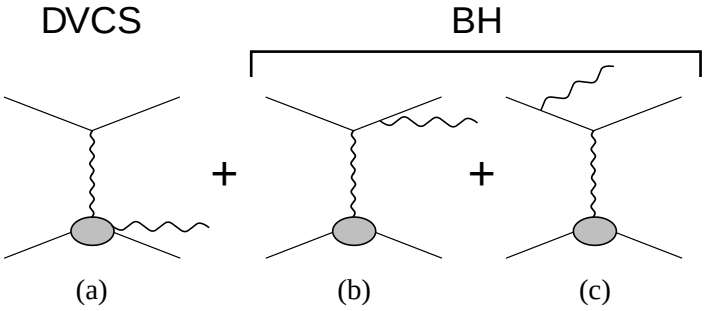

Figure 2.3: Diagrams contributing to the electroproduction of a real photon. The DVCS process (a) is shown along with the interfering Bethe-Heitler diagrams (b) and (c).

The total amplitude $\mathcal{T}$ is the superposition of the BH and DVCS amplitudes:

$$|\mathcal{T}|^2 = |\mathcal{T}_{BH}|^2 + |\mathcal{T}_{DVCS}|^2 + \mathcal{I} \tag{2.2}$$

$$\mathcal{I} = \mathcal{T}^*_{DVCS}\mathcal{T}_{BH} + \mathcal{T}_{DVCS}\mathcal{T}^*_{BH} , \tag{2.3}$$

where $\mathcal{T}_{DVCS}$ and $\mathcal{T}_{BH}$ are the amplitudes for the DVCS and Bethe-Heitler processes, and $\mathcal{I}$

denotes the interference between these amplitudes. The individual contributions to the total $ep \to ep\gamma$ cross section can be written as (up to twist-3 contributions) [16] as:

$$|\mathcal{T}_{BH}|^2 = \frac{\Gamma_{BH}(x_B, Q^2, t)}{\mathcal{P}_1(\varphi)P_2(\varphi)} \left\{ c_0^{BH} + \sum_{n=1}^{2} c_n^{BH} \cos(n\varphi) + s_1^{BH} \sin\varphi \right\}, \quad (2.4)$$

$$|\mathcal{T}_{DVCS}|^2 = \Gamma_{DVCS}(x_B, Q^2, t) \left\{ c_0^{DVCS} + \sum_{n=1}^{2} [c_n^{DVCS} \cos(n\varphi) + s_n^{DVCS} \sin(n\varphi)] \right\}, \quad (2.5)$$

$$\mathcal{I} = \frac{\Gamma_I(x_B, Q^2, t)}{\mathcal{P}_1(\varphi)P_2(\varphi)}] \left\{ c_0^I + \sum_{n=1}^{3} [c_n^I \cos(n\varphi) + s_n^I \sin(n\varphi)] \right\}, \quad (2.6)$$

where $\mathcal{P}_1(\varphi)$ and $\mathcal{P}_2(\varphi)$ are the BH electron propagators and c_i, s_i are azimuthal moments in the corresponding cross section contributions.

Depending on whether the beam helicity or target spin is flipped, different GPD contributions enter the cross section azimuthal moments (σ_{LU}, σ_{UL}). In practice, cross section asymmetries are experimentally easier to determine:

$$A = \frac{d\sigma^{\leftarrow} - d\sigma^{\rightarrow}}{d\sigma^{\leftarrow} + d\sigma^{\rightarrow}} \simeq \Gamma_A(x_B, Q^2, t) \frac{s_1^I \sin\varphi + s_2^I \sin 2\varphi}{c_0^{BH} + c_0^I + \Gamma_D c_0^{DVCS} + (c_1^{BH} + c_1^I + \Gamma_D c_0^{DVCS}) \cos\varphi}, \quad (2.7)$$

where Γ_A, Γ_D are known kinematical prefactors.

DVCS measurements thus allow one to separate the imaginary and real parts of the DVCS amplitude (*cf.* Fig. 2.2) by measuring combinations of cross sections and asymmetries with respect to the beam spin (helicity), beam charge (e^+/e^-), and/or target or recoil polarization. The imaginary part of the amplitude probes the GPDs at $x = \xi = x_B/2$, the real part probes a certain integral over the quark momentum fractions.

The different nucleon spin components of the GPDs can be extracted by measuring target spin asymmetries. Measurements of the t ($\Delta_\perp$) dependence provide the information necessary for transverse nucleon imaging. Information about the flavor decomposition requires measurements with both protons and neutrons. Additional information about the spin/flavor separation can come from meson production data. Studies of DVCS and meson production processes will require a combination of high energy and high beam intensity, and are generally much more challenging than traditional inclusive scattering experiments.

The `CLAS12` setup will provide unprecedented capabilities for exploring nucleon structure in the valence quark region. In particular, it will provide the combination of high beam intensity

(luminosity), high energy, high beam polarization, and advanced detection capabilities to provide a unique opportunity for studying nucleon GPDs in exclusive processes in the valence region.

2.2 Present Experimental Results on Hard Exclusive Processes

Measurements of exclusive processes at large momentum transfers have been carried out in eN scattering experiments with existing fixed–target facilities (HERMES at DESY, JLab with 6 GeV beam energy) and the HERA collider. These studies have demonstrated the basic feasibility of such measurements, and have provided crucial evidence for the applicability of a GPD–based description of such processes. They are also providing the first useful constraints for GPD phenomenology.

Experiments at fixed–target facilities aim to extract the interference terms between the DVCS and the Bethe–Heitler (BH) amplitudes in the $eN \to e'N\gamma$ cross section. The interference terms are experimentally accessible from combinations of measurements of the spin–dependent and independent cross sections and relative asymmetries, as well as from measurements of the beam charge dependence (e^+/e^-) of the cross section. In kinematic regions where the BH amplitude is much larger than the DVCS amplitude, the interference with the BH amplitude acts as a natural "amplifier and filter" for the DVCS amplitude, boosting it to comfortably measurable levels.

Measurements of the beam spin asymmetry in $eN \to e'N\gamma$ have been performed by HERMES ($0.02 < x_B < 0.3$) [17], CLAS [18, 19] and Hall A ($0.15 < x_B < 0.55$) [20]. Fig. 2.4 shows the kinematic coverage of the CLAS detector at 5.7 GeV, as well as the results for the asymmetry in a typical (x_B, Q^2) bin. A new inner calorimeter was used to detect photons at small scattering angles. The azimuthal angle dependence of the asymmetry clearly exhibits the $\sin\phi$ behavior characteristic of the BH–DVCS interference. This asymmetry can be related to a linear combination of GPDs at $x = \xi$; the experimental results are consistent with the predictions of present GPD models. An important point is that with the CLAS detector data in all (x_B, Q^2, t) bins are taken simultaneously, making it possible to extract information about the GPDs over a wide kinematic range.

While the unpolarized GPD $\mathcal{H}$ dominates the beam spin asymmetry at small t [16], $\sigma_{LU} \sim F_1\mathcal{H} - \xi F_2\widetilde{\mathcal{H}}$, the target single spin asymmetry at small t has a significant contribution from the polarized GPD $\widetilde{\mathcal{H}}$ [16]: $\sigma_{UL} \sim F_1\widetilde{\mathcal{H}} - \xi F_2\mathcal{H}$. Therefore, a combined analysis of the beam and target single spin asymmetries will allow for separation of $\mathcal{H}$ and $\widetilde{\mathcal{H}}$.

Recently published results by the CLAS collaboration on the first measurements of the target spin asymmetry [21] confirmed again that the factorization is likely to be applicable at Q^2 values as low as 2 GeV^2. These measurements eventually will allow one to separate the contributions from unpolarized and polarized nucleon GPDs. An order of magnitude more data are expected from JLab during the next two years, which would allow for more accurate extraction of GPD parameters.

The measurements of the DVCS cross sections and beam spin asymmetries carried out by JLab with 6 GeV beam energy support the theoretical expectation of dominance of the single-quark reaction mechanism (leading-twist approximation) for DVCS for momentum transfers Q^2 of a few GeV^2, essential for the GPD interpretation of the $eN \to e'N\gamma$ data. They also demonstrate the feasibility of accurate differential measurements of the t-dependence of the cross sections needed for the GPD-based reconstruction of the spatial images of the nucleon.

The HERMES collaboration measured for the first time the beam charge asymmetry of the cross section, which probes a dispersive integral of the GPDs over the quark momentum fractions [22]. DVCS cross sections at high Q^2 were measured at HERA [23, 24], including its t-dependence; the results are well described by leading-order (LO) and next-to-leading order (NLO) QCD calculations incorporating QCD evolution of the GPDs, thus fully confirming the applicability of QCD factorization to exclusive processes at high energies.

2.2.1 GPD Measurements with Jefferson Laboratory at 12 GeV

CLAS12 will provide a unique combination of high beam intensity (luminosity), high energy, and large–acceptance detectors, which will enable studies of exclusive processes such as DVCS and meson production in the valence quark region.

Detection of the photon in the CLAS inner calorimeter, in addition to the recoil proton and scattered electron, provides the exclusivity condition crucial for complete control over different background processes. Using the epX sample has its own advantages with regard to background suppression (π^0) and azimuthal angle coverage. The two samples probe $ep \to e'\gamma p$ in regions of different relative magnitudes of the DVCS and Bethe-Heitler amplitudes. In this

way, GPDs can be extracted using both absolute cross section and polarization asymmetry data. The possibility to use both methods in experiments at a single facility represents a crucial advantage of CLAS12.

To separate the different spin components of the GPDs, measurements of a variety of polarization observables (beam and target spin) will be performed. The longitudinal beam single spin asymmetry, A_{LU} (see Fig. 2.5), will access mainly the unpolarized Dirac GPD, $\mathcal{H}$. Combined analysis of the DVCS data on a longitudinally polarized target single spin asymmetry (see Fig. 2.6) with the beam single spin asymmetry will provide separation of contributions from unpolarized and polarized GPDs. The double spin asymmetry for longitudinal target polarization, A_{LL}, provides information on the real part of the corresponding GPDs, complementary to beam charge asymmetries.

The results of these measurements can directly be translated into transverse spatial images of the nucleon. As an example, Fig. 2.7 shows the projected results for the Dirac GPD, $\mathcal{H}$, as a function of x and t, and its corresponding transverse spatial representation. Complementary information can be obtained about integrals of the GPDs over the quark momentum fraction. With the help of GPD parameterizations, this information can be used to construct 2-dimensional tomographic images of the nucleon.

Additional information about the flavor structure of GPDs will come from ratios of meson production cross sections in channels with the same spin/parity quantum numbers, such as η/π^0 and K^*/ρ^+. These channels will be measured simultaneously with DVCS, not requiring any extra beam time.

Measurements of exclusive meson production in non-diffractive channels in CLAS12 would allow for detailed studies of the spin, flavor, and spatial distributions of quarks in the nucleon in the valence region, complementing the information from DVCS measurements. Very interesting information can already be gained by comparing observables for different mesonic channels, without detailed modeling of the GPDs. For example, a comparison of π^0 and η provides model-independent information about the ratio of the quark spin distributions Δu and Δd and their spatial distributions. Comparison between π^+ and K^+ production, as well as between ρ^+ and K^{*+}, allows one to study $SU(3)$ flavor symmetry breaking in the nucleon's quark distributions in different spin/parity channels. More information about the spatial distribution of quarks can be obtained from the GPD analysis of absolute cross sections (σ_L) in these channels. Separation of the various response functions (L, T, etc.) would provide a

crucial test of the dominance of the single-quark reaction mechanism at large Q^2.

Another interesting class of processes that could be studied are exclusive reactions with $N \to N^*$ transitions. Such processes probe the "transition GPDs" – the probability amplitude for the nucleon to undergo a transition to an excited state when "taking out" a quark and "putting it back" with different momentum. In these reactions the hard scattering process can be regarded as an operator inducing an $N \to N^*$ transition. CLAS12 is capable of performing such measurements requiring detection of decay products of the recoiling nucleon resonances.

2.3 GPD Studies with a Transversely Polarized Target

Asymmetries in the exclusive production of photons and vector mesons with a transversely polarized target were identified as the most sensitive observables providing access to the total orbital angular momentum. Eight observables, namely the first harmonics $\cos\phi$ and $\sin\phi$ of the interference term, are accessible in polarized beam and target experiments [16]. Thus, experiments with both longitudinally and transversely polarized targets can measure all eight Fourier coefficients $c^{\mathcal{I}}_{1,\Lambda}$ and $s^{\mathcal{I}}_{1,\Lambda}$ and with $\Lambda = \{\mathrm{unp}, \mathrm{LP}, \mathrm{TP}_x, \mathrm{TP}_y\}$.

The DVCS single spin asymmetry (SSA) for a transversely polarized target is the most sensitive observable to the elusive GPD $\mathcal{E}$, providing access to the orbital angular momentum. First results on DVCS single spin asymmetries from the HERMES Collaboration for transverse target polarizations [26] indeed indicate great sensitivity of target single spin asymmetries to the contribution of u-quarks to the total angular momentum. The most sensitive to the GPD-$\mathcal{E}$ asymmetry appeared to be the $\cos\phi$ moment of the spin-dependent contribution σ_{UT} [16],

$$\sigma_{UT} \sim \frac{1-x}{2-x}\frac{t}{M^2}F_2\mathcal{H} + \frac{t}{4M^2}(2-x)F_1\mathcal{E}. \tag{2.8}$$

Transverse target DVCS SSA measurements in addition to unpolarized SSA and longitudinally polarized SSA measurements will provide the full set of data needed for the extraction of Compton form factors and corresponding GPDs. A_{UT} is especially sensitive to the GPD $\mathcal{E}$, and as such will constrain any extraction of the angular momentum J.

The projection curves for CLAS12 running with a transversely polarized target have been calculated assuming a luminosity of 5×10^{34} cm^{-2}s^{-1}, with an NH_3 target polarization of 85% and a dilution factor 0.14, with 2000 hours of data taking and an overall efficiency 50% (see Fig. 2.8).

The theoretical uncertainty in the factorization procedure on the amplitude level for the meson sector is translated into large variations of the physical cross section. However, in the single-spin asymmetry, given by the ratio of the Fourier coefficients of the cross section, the ambiguities approximately cancel [28]. Thus, the perturbative predictions for this quantity are rather stable. The NLO effects result in $^{+7\%}_{-18\%}$ corrections to the LO prediction for $0.1 < x_B < 0.5$.

The GPD-based calculations were performed for the case when the incoming virtual photon is longitudinally polarized. The cross section for the transversely polarized photons is suppressed by a power of Q [29], but at CLAS energies it may still be significant. Insensitivity to the higher-order corrections make single spin asymmetries appropriate quantities for experimental study at JLab, and will provide an important test of the applicability of GPD-based predictions at JLab energies.

Even though the power corrections for the absolute cross section of exclusive meson electroproduction analyzed in terms of generalized parton distributions are expected to be large, there are indications of a *precocious scaling* in the ratios of observables [28]. The measurement of spin asymmetries could therefore become a major tool for studying GPDs in the Q^2 domain of a few GeV^2. Projections for CLAS12 for measurements of transverse asymmetries for vector mesons are shown in Fig. 2.8. The transverse asymmetries for ρ mesons (neutral and charged) are widely accepted as an important source of independent information on the GPD $\mathcal{E}$. SSA measurements in hard exclusive processes will allow mapping of the underlying GPDs and will provide access to the orbital angular momentum of quarks.

The quark angular momentum in the nucleon, J_q, can be estimated if one uses the results of measurements of DVCS and meson production observables to constrain GPD parameterizations, which incorporate information about GPDs obtained from other processes (inclusive DIS, form factors). These parameterizations allow one to estimate the second moment of the GPDs, based on the information about the GPDs at $x_1 = x_2$ and the momentum fraction integrals probed in the observables. Fig 2.8 shows the constraints on J_u and J_d from DVCS and ρ asymmetries, which is particularly sensitive to the Pauli form factor-type GPD, $\mathcal{E}$. One sees that accurate measurements of the asymmetries will be able to constrain J_q in this way. While not fully model–independent, this method of extracting J_q will become more and more accurate as amplitude calculations and GPD parameterizations become more refined as a result of measurements of a variety of other DVCS and meson production observables. High

statistics data will allow us to constrain the quark angular momentum in the proton.

The data from CLAS with a transversely polarized target focussing on hard exclusive photon and meson production, combined with data from unpolarized and longitudinally polarized targets, will provide a complete set of measurements required for the separation of all four leading-twist, chiral-even GPDs, and in particular, will provide a constraint on the quark orbital angular momentum.

2.4 Summary

GPDs unify the momentum-space parton densities measured in inclusive deep-inelastic eN scattering with the spatial densities (form factors) measured in elastic scattering. They describe correlations between the momentum and spatial distributions of quarks, which are revealed in exclusive processes in eN scattering at large momentum transfer (deeply virtual Compton scattering, meson production).

A full program to extract GPDs from measurements requires coverage of a large kinematic range in ξ, t, and Q^2, along with measurements of several final states together with the use of polarized beam and polarized targets (both longitudinal and transverse polarization). The 12-GeV upgrade of the electron accelerator and of the equipment required for the GPD program will provide the kinematic coverage needed for a broad program of DVCS and meson production measurements. The JLab 12-GeV upgrade will allow us to map the nucleon GPDs in the valence quark region at large x, exploring its quark structure in unprecedented detail.

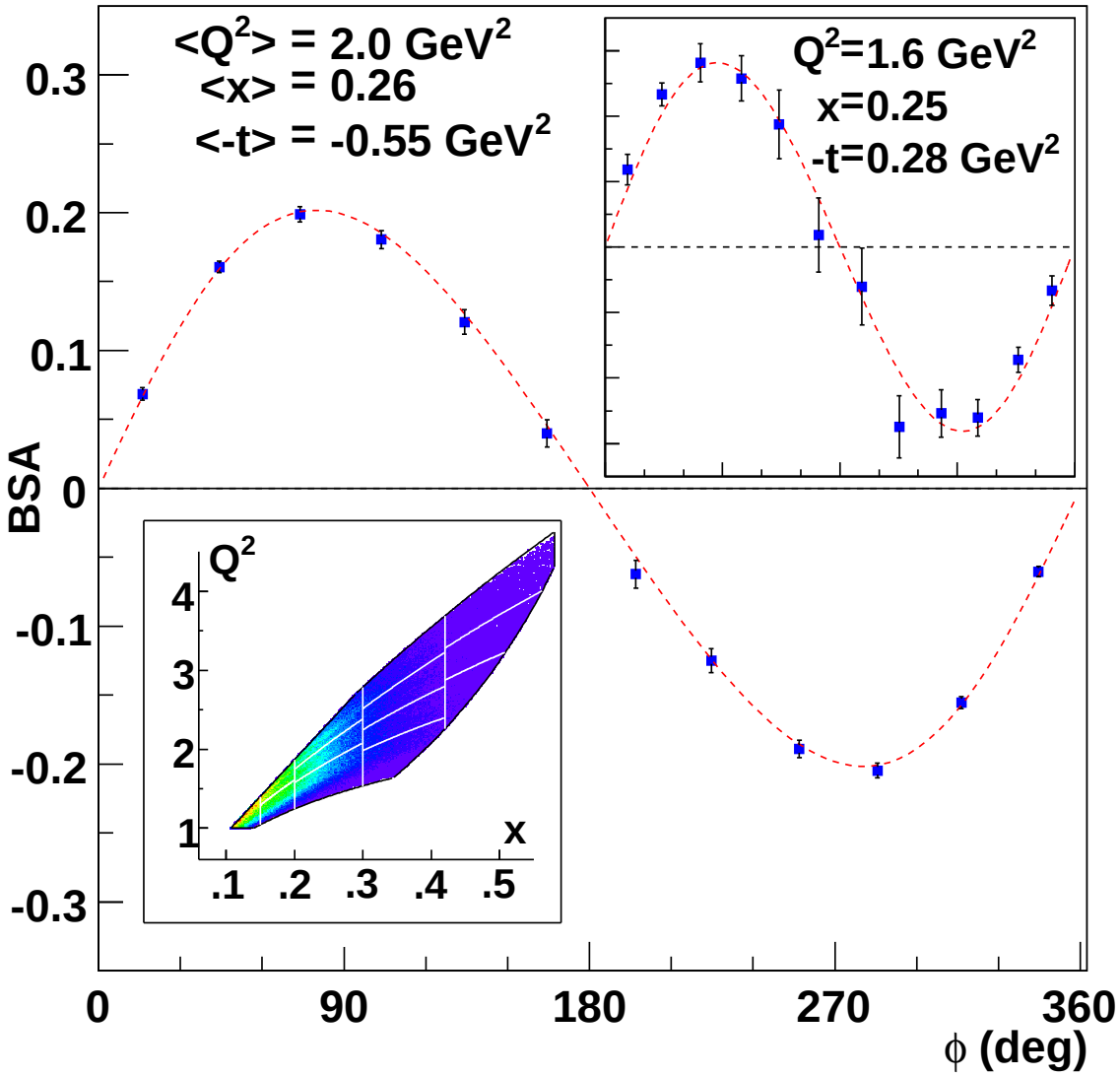

Figure 2.4: Measurements of the beam spin asymmetry, A_{LU}, of the $eN \to e'N\gamma$ cross section from CLAS at 6 GeV. The plot in the lower left corner shows the kinematic coverage in x_B and Q^2. The main plot shows the beam spin asymmetry vs. ϕ integrated over all kinematics (the average values are shown in the upper left of the plot. In the upper right of the plot, the beam spin asymmetry is shown for one of our many kinematic points as an illustration. The $\sin\phi$ dependence is characteristic of the BH-DVCS interference cross section. The magnitude of the asymmetry can be related to a linear combination of the GPDs at $x = \xi$.

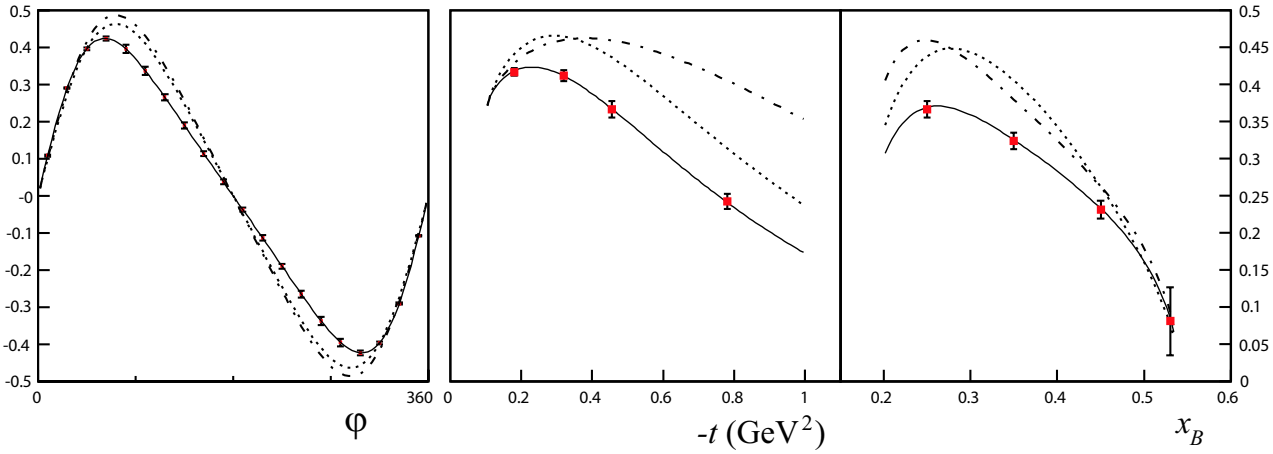

Figure 2.5: On all figures: points in red represent data with statistical error bars. Lines are models with different input parameters, none of which includes twist-3 contributions: The full line is a model with a Regge-type t-dependence and D-term. The dotted line includes the Regge-type t-dependence but has no D-term. The dash-dotted line has the D-term but the t dependence only comes from form factors. Left figure: Beam spin asymmetry (BSA) as a function of φ for $< x_B >= 0.2$, $< Q^2 >= 3.3$ GeV^2, and $< -t >= 0.45$ GeV^2. Middle figure: BSA as a function of $-t$ for $< x_B >= 0.2$, $< Q^2 >= 3.3$ GeV^2, and $\varphi = 90°$. Right figure: BSA as a function of x_B for $t = 0.45$ GeV^2, $< Q^2 >= 3.3$ GeV^2 and $\varphi = 90°$.

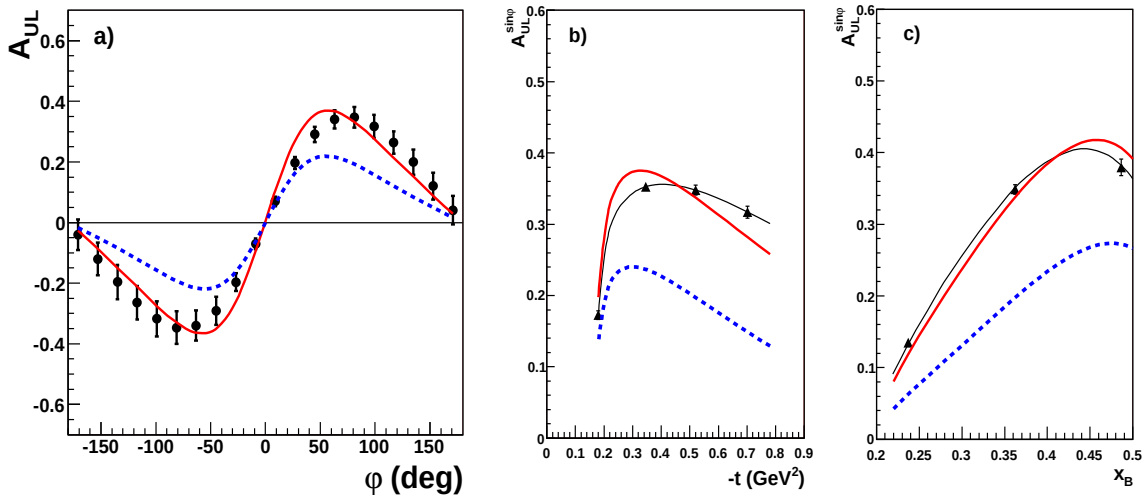

Figure 2.6: (a). Target spin asymmetry versus φ for Q^2=4.1 GeV^2, x_B=0.36, and $-t$=0.52 GeV^2. The black points show the values from Ref. [25] using CTEQ6 PDFs with the estimated errors from the proposed measurement. The red solid curve is using MRST02 PDFs with $E = \widetilde{E}$=0, and for the blue dashed curve is $\widetilde{H}$ is also set to zero. (b). $\sin\varphi$ moments of the target spin asymmetry versus $-t$ at Q^2=4.1 GeV^2 and x_B=0.36, and (c). versus x_B at Q^2=4.1 GeV^2 and $-t$=0.52 GeV^2. The projected error bars represent the statistical uncertainties only.

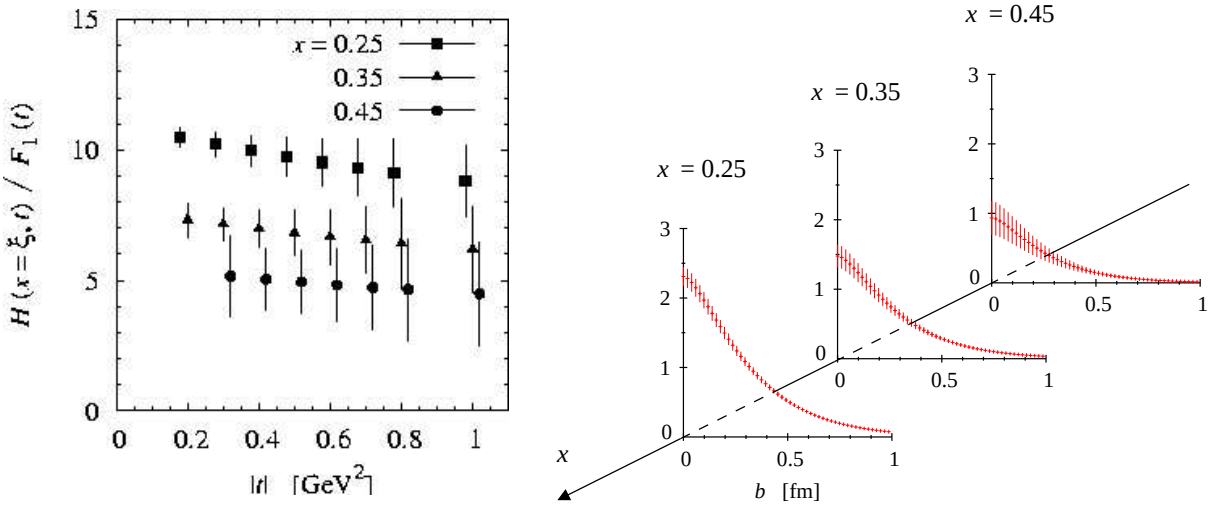

Figure 2.7: Left: Projected results for the Dirac GPD of the proton, $\mathcal{H}(x = \xi, t)$, as a function of x and t, as extracted from the DVCS beam spin asymmetry, A_{LU}, measured at JLab at 12 GeV. Shown is the ratio of the GPD to the the proton's Dirac form, $F_1(t)$. Right: Transverse spatial image of the proton obtained by Fourier-transforming the measured GPD. The errors were estimated assuming a dipole-like t-dependence.

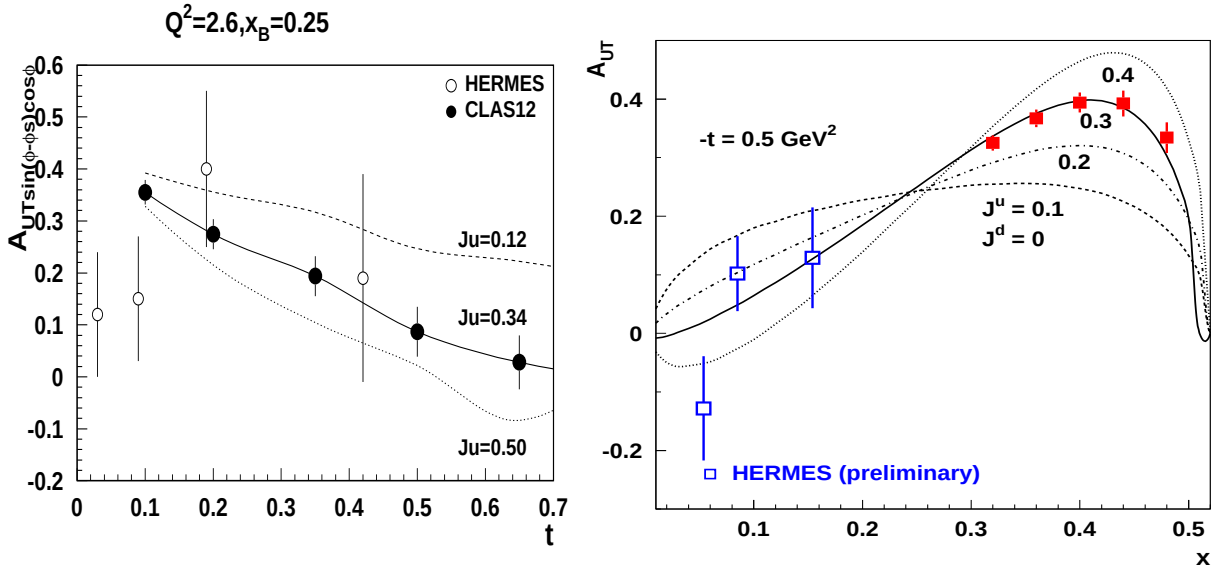

Figure 2.8: Projected transverse spin asymmetry ($A_{UT}^{\sin\phi}$) in exclusive photon production at 11 GeV. All points correspond to different values of J_u calculated for the bin with $< Q^2 >$=2.6 GeV^2 and $< x >= 0.25$ (left). Projections for the transverse target asymmetry for exclusive ρ^0 production from a hydrogen target (filled squares) using `CLAS12` are shown compared to preliminary HERMES data [27].

Chapter 3

Parton Distributions at Large x

3.1 Parton Distributions

Knowledge of parton distributions forms the basis of our understanding of hadronic matter in terms of its fundamental constituents. However, extracting parton distributions in the large x domain is notoriously difficult. One difficulty comes from the requirement to stay away from the region where partonic initial and final state interactions play important roles. This imposes a minimum Q^2 threshold of at least a few GeV^2 and W greater than a few GeV in addition to the large x constraint. For polarized parton distributions, an additional problem stems from the lower luminosity available with polarized targets. In the unpolarized case, luminosities are adequate and free proton targets exist, so proton data are satisfactory. For the neutron no such targets exist and deuteron is used. The difficulty is to control sufficiently well nuclear final state interactions (FSI) and binding effects to allow for a systematically accurate extraction of the neutron information.

The consequences of these difficulties can be readily seen in Fig. 3.1. The lack of experimental constraints allows for a variety of predictions that needs to be sorted out to establish the proper phenomenology. Studies of parton distributions have already been undertaken at JLab, with $x \leq 0.6$. The BONUS experiment [30] gathered neutron data from quasi-free neutrons within unpolarized deuterons. The FSI and binding effects were minimized by measuring recoiling protons and selecting events for which the two nucleons were not interacting. On the polarized data front, data were collected up to $x \sim 0.6$ in Halls A and B [31, 32]. An exciting outcome is the apparent failure of leading order (LO) pQCD to describe the data, hinting

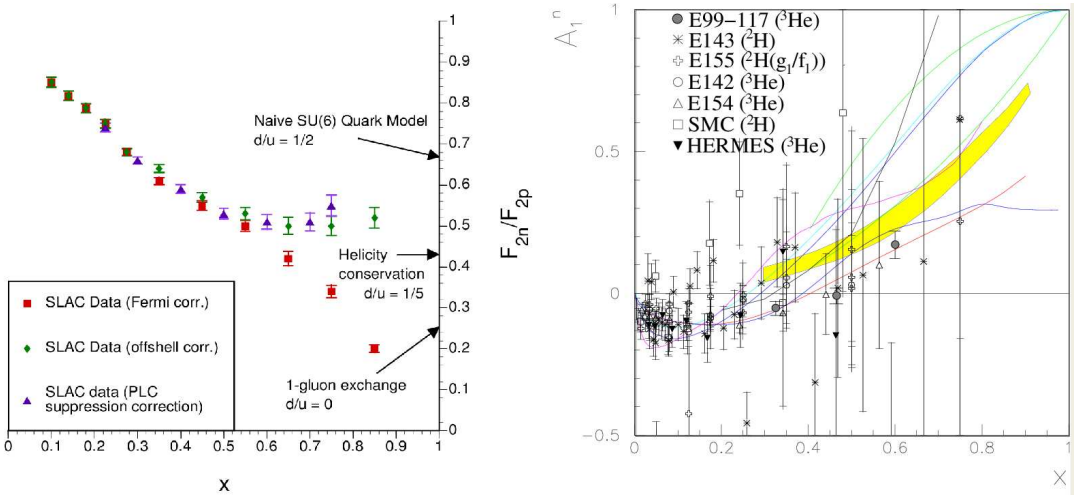

Figure 3.1: World data on the d/u parton distribution ratio from unpolarized measurements of F_2^n/F_2^p (left) and on the photon asymmetry A_1^n from polarized data (right). The substantial systematic (left) or statistical (right) errors at large x do not permit constraints of the various predictions.

that the validity domain of LO pQCD is not reached yet or that quark orbital momentum (an important but experimentally elusive contribution to the nucleon spin) may be sizable. In particular, LO pQCD predicts that the d-quark polarization (lower panel Fig. 3.2) should become positive and approach $+1$ at large x, which is in contradiction to the data.

An 11-GeV beam will allow us to reach $x \sim 0.8$. The luminosity expected with an unpolarized deuterium gas target needed for the recoil proton tagging method is 2×10^{34} cm^{-2}s^{-1}. It will be about 10^{35} cm^{-2}s^{-1} for the polarized target currently under design. Those luminosities and the large solid angle of `CLAS12` makes it a superior choice to measure parton distributions at large x, sort out mechanisms of SU(6) symmetry breaking and of quark-hadron duality, and explore the role of quark orbital momentum. In addition to their intrinsic interest, quark distributions at large x are crucial for studying physics beyond the Standard Model at high energy colliders [33]. To extend the BONUS results to higher x, a proposal [34] for 35 days of running on gaseous deuterium and 5 days on gaseous hydrogen at 11 GeV was submitted to JLab PAC30 and conditionally approved. The experiment will use the standard `CLAS12` equipment with the additional recoil detector already used in E03-012 [30]. The anticipated results can be seen in Fig. 3.3 for F_2^n/F_2^p (left) and u/d (right). Clearly the F_2^n/F_2^p data obtained using the new method will allow us to differentiate unambiguously between different expectations for this ratio.

JLab PAC30 also approved E12-06-109 [35] which will, in particular, study polarized parton

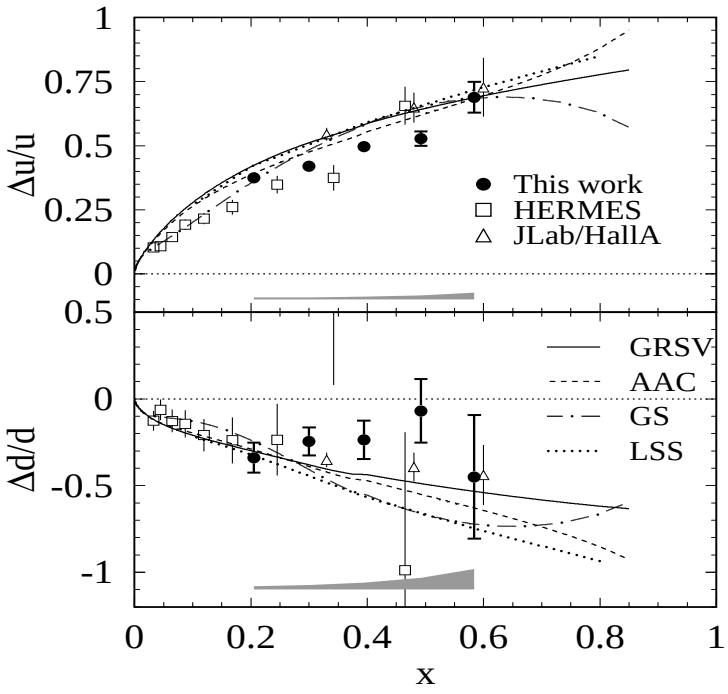

Figure 3.2: Quark polarizations $(\Delta u + \Delta\bar{u})/(u + \bar{u})$ and $(\Delta d + \Delta\bar{d})/(d + \bar{d})$ as extracted from A_1^n, A_1^p, and A_1^d [31, 32]. Several NLO fits to previous measurements are shown, while the leading-order pQCD predictions require both polarizations to tend to +1 as $x \to 1$.

distributions at large x. Using standard detection equipment, a redesigned polarized target adapted to CLAS12 and 30 (50) days of running on a longitudinally polarized NH_3 (ND_3) target, high precision measurements can be achieved as shown in Fig. 3.4. These data will disentangle models in the large-x region. While the results shown in Fig. 3.4 are with a $W > 2$ GeV constraint, hadron-parton duality studies (see page 47) will tell us by how much this constraint can be relaxed, possibly increasing the x range up to 0.9. The expected accuracy for $(\Delta d + \Delta\bar{d})/(d + \bar{d})$ is shown in Fig. 3.5.

3.2 Global Fit of Polarized Parton Distributions

The large window opened by the 12-GeV upgrade over the DIS domain will permit constraints of global fits of the parton distributions. The unique impact at large x has just been discussed. The improvement from the 12-GeV upgrade is also significant at low and moderate x, noticeably for the polarized gluon distribution ΔG. For a more complete picture of the precision achievable with the expected CLAS12 data, we have plotted in Fig. 3.6 an analysis of the

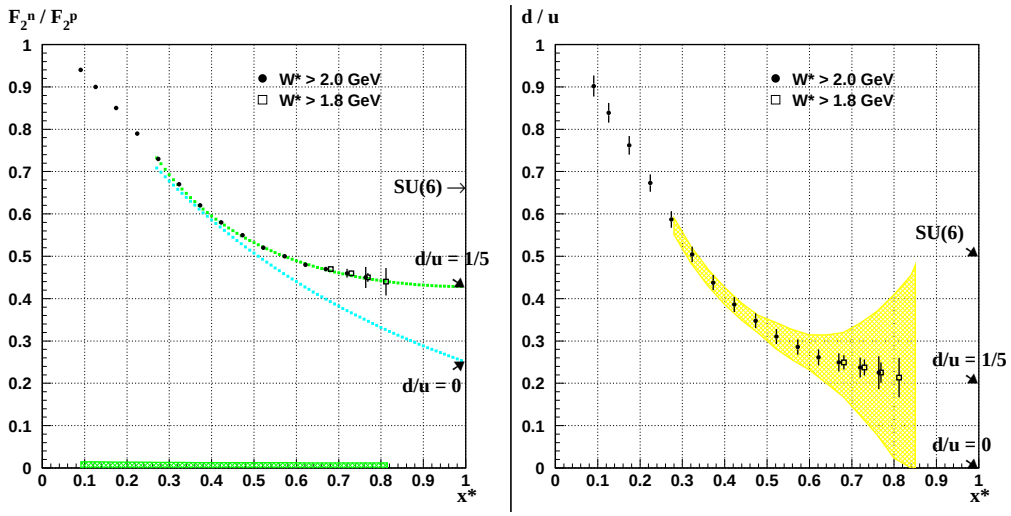

Figure 3.3: Anticipated results on F_2^n/F_2^p (left) and the extracted u/d ratio (right) for 40 days of data taking at 11 GeV with CLAS12. The arrows along the ordinate indicate model predictions. The error bars pertaining to filled circles are statistical with a $W > 2$ GeV constraint. The smaller errors (with open squares) are for $W > 1.8$ GeV. The systematic error is indicated by the band along the abscissa on the left plot. The two curves on the left plot represent hadron-parton duality based predictions with two different mechanisms for SU(6) symmetry breaking. The shaded band on the right plot indicates our present knowledge on the d/u ratio.

impact on NLO analyses. A dramatic improvement can be achieved with the expected data from the CLAS12 proposal E12-06-109 [35]. We emphasize that the data will not only reduce the error band on ΔG, but will likely allow a more detailed modeling of its x-dependence.

3.3 Moments of Structure Functions

Moments of structure functions provide powerful insight into nucleon structure. Inclusive data at JLab have permitted evaluation of the moments at low and intermediate Q^2 [37, 38, 39]. With a maximum beam energy of 6 GeV, however, the measured strength of the moments becomes rather limited for Q^2 greater than a few GeV^2. The 12-GeV upgrade removes this problem and allows for measurements to higher Q^2.

Moments of structure functions can be related to the nucleon static properties by sum rules. At large Q^2 the Bjorken sum rule relates $\int g_1^{p-n} dx$ to the nucleon axial charge [40]. At the other end of the spectrum, $Q^2 = 0$, the Gerasimov-Drell-Hearn (GDH) sum rule links the

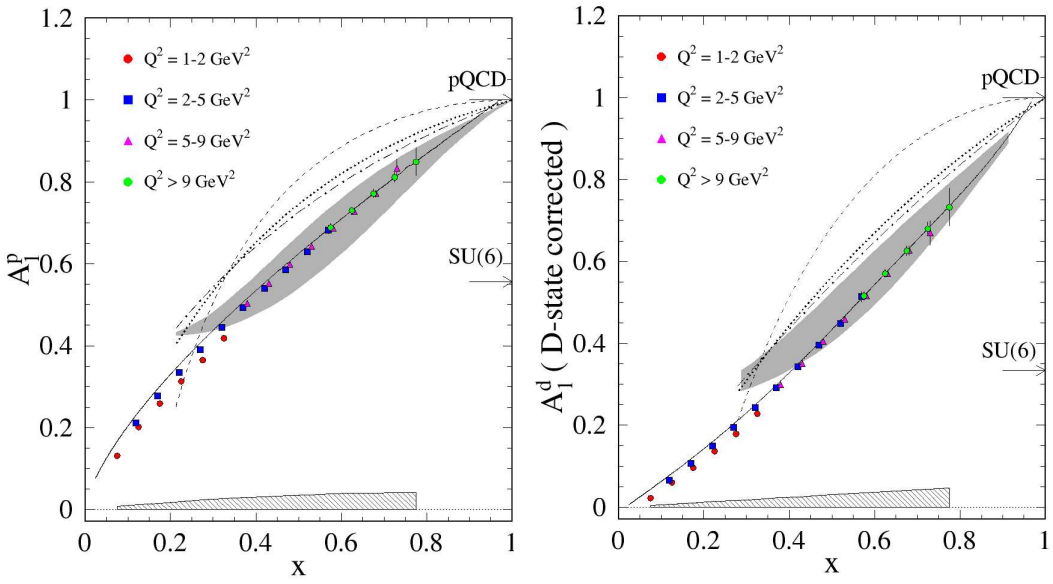

Figure 3.4: Anticipated results on A_1^p (left) and A_1^d (right). The four different symbols represent four different Q^2 ranges. The statistical uncertainty is given by the error bars while the systematic uncertainty is given by the shaded band.

difference of spin dependent cross sections, integrated over photon energy, to the anomalous magnetic moment of the nucleon [41, 42]. The two sum rules are aspects of a general one derived recently by Ji and Osborne [43] that is valid at any Q^2 and links the first moments of spin structure functions to spin-dependent Compton amplitudes. Low Q^2 is a testing ground for chiral perturbation theory, while large Q^2 data can be compared to higher-twist series derived within the operator product expansion (OPE) method. Lattice QCD can calculate higher-twist terms, thus extending the validity domain of OPE to lower Q^2. However OPE is unusable at low Q^2. To bridge the gap, lattice QCD can be used to compute Compton amplitudes at any Q^2. Hence, the Ji and Osborne sum rule can be computed and compared to experiments at any Q^2, making it a unique tool to study the transition from partonic to hadronic degrees of freedom.

The left plot in Fig. 3.7 shows the expected precision on the measured part of Γ_1^p. The inner error bar is statistical while the outer one is the statistics and systematics added in quadrature. Published results and preliminary results from EG1b are also displayed for comparison. Like the CLAS12 data, the EG1 data do not include the unmeasured DIS contribution. The hatched blue band corresponds to the systematic uncertainty on the EG1b data points. The red band indicates the estimated systematic uncertainty from CLAS12. The right plot in Fig. 3.7 shows

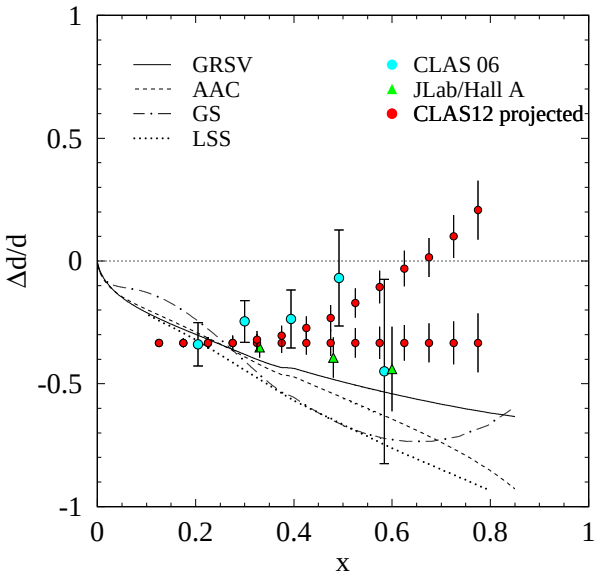

Figure 3.5: Expected results for $(\Delta d + \Delta\bar{d})/(d + \bar{d})$. The central values of the data are following two arbitrary curves to demonstrate how the two categories of predictions, namely the ones that predict $\Delta d/d$ stays negative (LO and NLO analyses of polarized DIS data: GRSV, LSS, AAC, GS, statistical model, and a quark-hadron duality scenario) and the ones predicting $\Delta d/d \to 1$ when $x \to 1$ (leading order pQCD and a quark-hadron duality scenario).

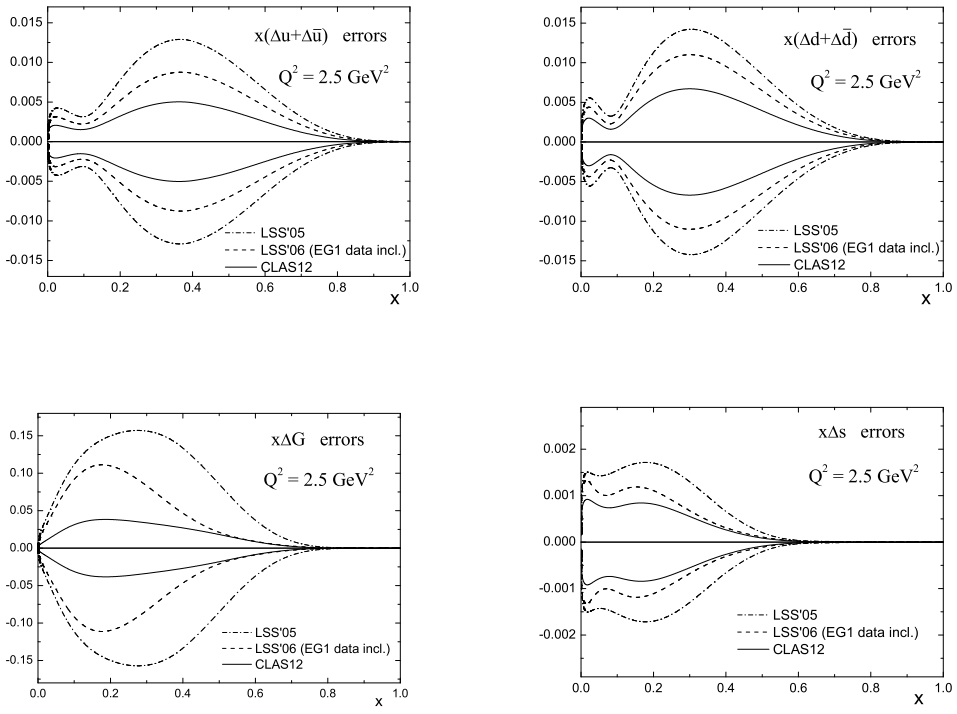

Figure 3.6: Expected uncertainties for Δu, Δd, ΔG, and Δs from an NLO analysis of all world data. The outermost line shows the result from the analysis by Leader, Sidorov, and Stamenov [36]. The second line is the updated result after inclusion of the new EG1b data from CLAS at 5.7 GeV [32]. The innermost line shows the expected uncertainty after including the data set to be collected with CLAS12, including statistical and systematic errors.

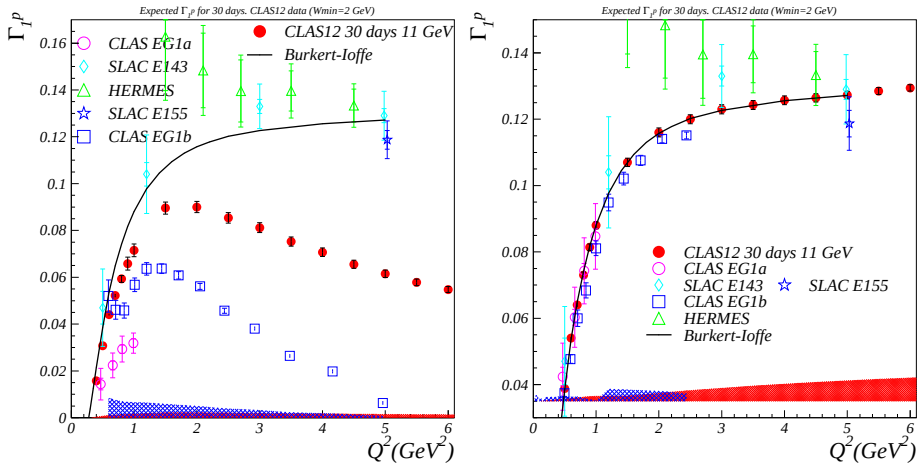

Figure 3.7: Left plot: expected precision on Γ_1^p for CLAS12 and 30 days of running. CLAS EG1a [37, 38] data and preliminary results from EG1b are shown for comparison. The data and systematic uncertainties do not include estimates of the unmeasured DIS contribution. HERMES [44] data, and E143 [45] and E155 data [46] from SLAC are also shown (including DIS contribution estimates). The model is from Burkert and Ioffe [47, 48]. Right plot: same as the left but including an estimate of the DIS contribution.

the results on Γ_1^p and Γ_1^d including an estimate of the unmeasured DIS contribution. The systematic uncertainties for EG1 and CLAS12 here include the estimated uncertainty on the unmeasured DIS part estimated using the model from Bianchi and Thomas [49]. As can be seen, moments can be measured up to Q^2=6 GeV^2 with a statistical accuracy improved several fold over that of the existing world data.

Higher moments are also of interest: generalized spin polarizabilities are linked to higher moments of spin structure functions by sum rules based on similar grounds as the GDH sum rule. Higher moments are less sensitive to the unmeasured low-x part, so measurements are possible up to higher Q^2 compared to first moments. Just like the GDH/Bjorken sum rules, measurements of the Q^2-evolution allow us to study the parton-hadron transition since theoretical predictions exist at low and large Q^2 [39]. In addition, spin polarizabilities are also fundamental observables characterizing the nucleon structure and the only practical way known to measure them is through measurement of moments and application of the corresponding sum rules.

Finally, moments in the low ($\simeq$ 0.5 GeV^2) to moderate ($\simeq$4 GeV^2) Q^2 range enable us to extract higher-twist parameters, which represent correlations between quarks in the nucleon.

This extraction can be done by studying the Q^2 evolution of first moments [39]. Higher twists have been consistently found to have, overall, a surprisingly smaller effect than expected. Going to lower Q^2 enhances the higher-twist effects but makes it harder to disentangle a high twist from the yet higher ones. Furthermore, the uncertainty on α_s becomes prohibitive at low Q^2. Hence, higher twists turn out to be hard to measure, even at the present JLab energies. Adding higher Q^2 to the present JLab data set removes the issues of disentangling higher twists from each other and of the α_s uncertainty. The smallness of higher twists, however, requires statistically precise measurements with small point-to-point correlated systematic uncertainties. Such precision at moderate Q^2 has not been achieved by the experiments done at high energy accelerators, while JLab at 12 GeV presents the opportunity to reach it considering the expected statistical and systematic uncertainties of E12-06-109. The total point-to-point uncorrelated uncertainty on the twist-4 term for the Bjorken sum, f_2^{p-n}, decreases by a factor of 5.6 compared to results obtained in Ref. [50].

3.3.1 The GDH Sum Rule

Despite its fundamental nature, the GDH sum rule has not yet been fully verified experimentally. Combined results from MAMI and ELSA [51] are about 10% above the expected value. This is for an upper integration limit in photon energy of about 2.8 GeV. With the cancellation of the fixed target program at SLAC and consequently of experiment E159 [52] that would have investigated the GDH strength at large ν, JLab is now the best place to test the convergence of the GDH sum. Using real photons or near real photons, we can measure the contribution to the GDH sum rule up to 10.5 GeV, about 4 times the maximum energy reached at ELSA (see Fig. 3.8). A non-convergence of the sum rule would be intriguing and may signal physics beyond the Standard Model. In any case it will provide important insight on soft Regge physics.

3.3.2 Moments of F_2 and the Precise Determination of $\alpha_s(M_Z)$

Simulated results for the moments $\int x^n F_2 dx$ with $n \leq 8$ are shown in Fig. 3.9. It reveals that `CLAS12` will provide a unique tool to extract moments of F_2 up to Q^2 values of 10 - 14 GeV^2. These can be used to extract the strong coupling constant $\alpha_s(M_z)$. The extraction of $\alpha_s(M_Z)$ from the scaling violations of the proton structure function F_2 is one of the most

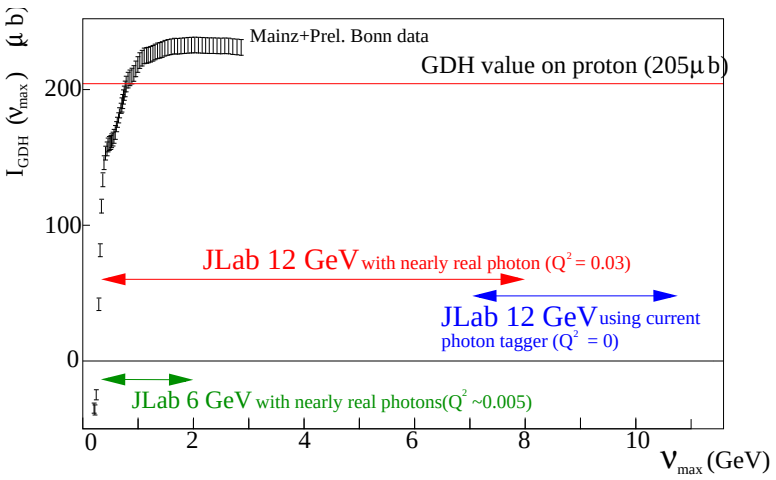

Figure 3.8: Coverage of the GDH sum rule for low-Q^2 experiments with CLAS and CLAS12. The data points are the GDH running sum from MAMI and ELSA at $Q^2 = 0$.

precise methods available up to now (see Fig. 3.10). Simulation shows that a new procedure for the extraction of $\alpha_s(M_Z)$ [53] together with the CLAS12 data can allow an unprecedentedly accurate determination of $\alpha_s(M_Z)$ with a statistical uncertainty of 0.0008 and a systematic uncertainty of about 0.0007.

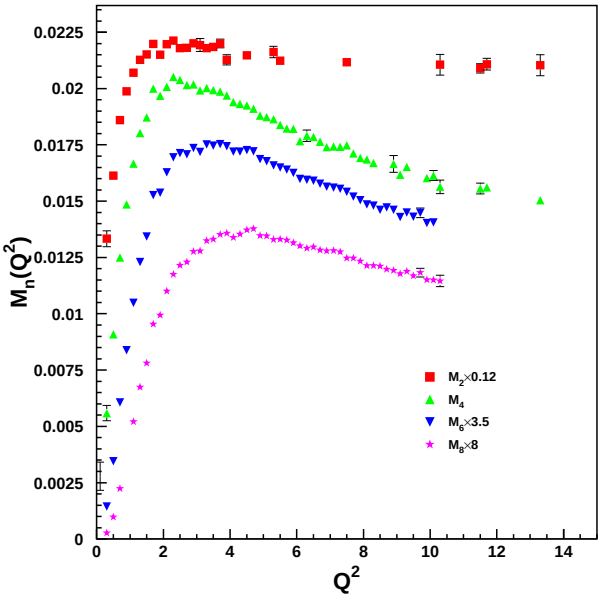

Figure 3.9: Expected moments of the proton structure function F_2 obtained with the CLAS12 detector simulations for a few days of running. The meaning of the markers and the scale factors for each moment are indicated in the inset.

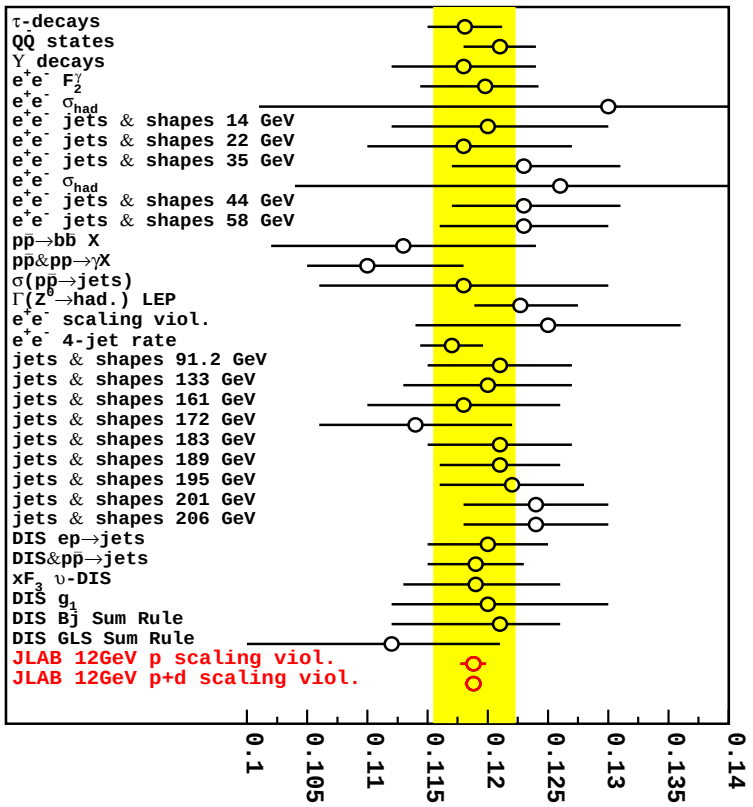

Figure 3.10: Existing determinations of the QCD coupling constant $\alpha_S(M_Z)$ [54].

3.3.3 Quark-Hadron Duality

The phenomenon of quark-hadron duality relates the physics of nucleon resonances to the dynamics of single quark scattering that governs the scaling structure functions at high energy. JLab measurements of the unpolarized proton structure functions in the resonance region [55, 56] have sparked considerable interest in quark-hadron duality [57, 58, 59, 60]. While quark-hadron duality has been observed in the spin-independent F_2 structure function [57, 58, 55], it has not yet been firmly established for spin-dependent structure functions. Because the g_1 structure function is given by a difference of cross sections, which need not be positive, the workings of duality will necessarily be more intricate for g_1 than for the spin-averaged F_2 structure function. The first results from the spin structure function measurements in Hall A [61, 62] and with CLAS [63] indicate that, if one averages over the entire resonance region, duality roughly holds for Q^2 above 1.5 GeV^2. To achieve a more precise understanding of the mechanism of duality, it is necessary to determine the conditions under which duality occurs in both polarized and unpolarized structure functions. An upgraded CLAS12 would permit measurements of the structure functions in the DIS region with high precision. For

unpolarized parton distributions, the tagging technique used by the BONUS experiment [30] (see Section 3.1) can also be applied to the neutron resonance region, where at present there are essentially no data.

Chapter 4

SIDIS and the Transverse Structure of the Nucleon

4.1 Introduction

The spin structure of the nucleon has been of particular interest since the EMC [64] measurements implied that the helicity of the constituent quarks account for only a fraction of the nucleon spin. The so-called "spin crisis" was subsequently confirmed by a number of other experiments at CERN [65], SLAC [45, 66], HERA [67, 68], and JLab [37]. Possible interpretations of this result include the contribution of the orbital momentum of quarks and significant polarization of either the strange sea (negatively polarized) or gluons (positively polarized). The contributions to the sum rule for the total helicity of the nucleon include the following:

$$\frac{1}{2} = \frac{1}{2}\sum_{q} \Delta q^{val} + \Delta q^{sea} + L_z^{val} + L_z^{sea} + L_z^{glue} + \Delta G, \tag{4.1}$$

where Δq, L_z, and ΔG are respectively the quark helicity, the orbital angular momentum of all partons, and the gluon helicity.

Present knowledge about the spin structure of the nucleon comes mainly from polarized deep inelastic scattering (DIS). The polarization of the individual flavors and anti-flavors were mainly studied using fits to the inclusive data. Inclusive DIS is sensitive to only the squared charges of the partons, and requires additional assumptions (*e.g.* an SU(3) symmetric sea), which leads to certain ambiguities. Semi-inclusive deep inelastic scattering (SIDIS) studies, when a hadron is detected in coincidence with the scattered lepton that allows so-called "flavor

tagging", provide more direct access to contributions from various quarks. In addition, they give access to the transverse momentum distributions of quarks, not accessible in inclusive scattering. Azimuthal distributions of final state particles in semi-inclusive deep inelastic scattering provide access to the orbital motion of quarks and play an important role in the study of transverse momentum distributions of quarks in the nucleon.

Significant progress has been made recently in understanding the role of partonic initial and final state interactions [69, 70, 71]. The interaction between the active parton in the hadron and the spectators leads to gauge-invariant transverse momentum dependent (TMD) parton distributions [69, 70, 71, 72, 73]. Furthermore, QCD factorization for semi-inclusive deep inelastic scattering at low transverse momentum in the current-fragmentation region has been established in Refs. [74, 75]. This new framework provides a rigorous basis to study the TMD parton distributions from SIDIS data using different spin-dependent and independent observables. TMD distributions (see Table 4.1) describe transitions of a nucleon with one polarization in the initial state to a quark with another polarization in the final state.

The diagonal elements of the table are the momentum, longitudinal and transverse spin distributions of partons, and represent well-known parton distribution functions related to the square of the leading-twist, light-cone wave functions. Off-diagonal elements require non-zero orbital angular momentum and are related to the wave function overlap of L=0 and L=1 Fock states of the nucleon [76]. The chiral-even distributions $f_{1T}^{\perp}$ and g_{1T} are the imaginary parts of the corresponding interference terms, and the chiral-odd $h_1^{\perp}$ and h_{1L} are the real parts. The TMDs $f_{1T}^{\perp}$ and $h_1^{\perp}$, which are related to the imaginary part of the interference of wave functions for different orbital momentum states and are known as the Sivers and Boer-Mulders functions [77, 78, 79, 70, 71, 72], describe unpolarized quarks in the transversely polarized nucleon and transversely polarized quarks in the unpolarized nucleon respectively. They vanish at tree-level in a T-reversal invariant model (T-odd) and can only be non-zero when initial or final state interactions cause an interference between different helicity states. This function parameterizes the correlation between the transverse momentum of quarks and the spin of a transversely polarized target or the transverse spin of the quark, respectively. They require both orbital angular momentum, as well as non-trivial phases from the final state interaction, that survive in the Bjorken limit. Experimental results on the Sivers functions for up and down quarks so far are consistent with a heuristic model of up and down quarks orbiting the nucleon in opposite directions. The most simple mechanism that can lead to a

N/q	U	L	T
U	$\mathbf{f_1}$		$h_1^\perp$
L		$\mathbf{g_1}$	$h_{1L}^\perp$
T	$f_{1T}^\perp$	g_{1T}	$\mathbf{h_1}$ $h_{1T}^\perp$

Table 4.1: Leading-twist transverse momentum-dependent distribution functions. U, L, and T stand for transitions of unpolarized, longitudinally polarized, and transversely polarized nucleons (rows) to corresponding quarks (columns).

Boer-Mulders function is a correlation between the spin of the quarks and their orbital angular momentum. In combination with a final state interaction that is on average attractive, already a measurement of the sign of the Boer-Mulders function, would thus reveal the correlation between orbital angular momentum and spin of the quarks.

The impact parameter space displacement of transversely polarized quark distributions in an unpolarized target is described by a chirally odd GPD [80], and has recently been calculated for the first time in lattice QCD [81, 82]. The resulting transverse flavor dipole moment for transversely polarized quarks in an unpolarized nucleon suggests that the Boer-Mulders functions are significantly larger than the Sivers functions. Moreover, consistent with large N_C predictions, the displacement of transversely polarized u and d quarks was found to be in the same direction, indicating the same sign for the Boer-Mulders functions for u and d quarks, and suggesting a further enhancement of the SIDIS asymmetry from the d quark contribution.

Similar quantities arise in the hadronization process. One particular case is the Collins T-odd fragmentation function $H_1^\perp$ [83] describing fragmentation of transversely polarized quarks into unpolarized hadrons. Parton model analyses [84, 85, 86, 87] of sub-leading single-spin asymmetries observed at HERMES [88, 89] and `CLAS` [90] lead to the introduction of new twist-3 T-odd distribution functions [75, 73].

The off-diagonal TMD distributions arise from interference between amplitudes with left- and right-handed polarization states, and only exist because of chiral symmetry breaking in the nucleon wave function in QCD. Their study therefore provides a new avenue for probing the chiral nature of the partonic structure of hadrons. The universality of the TMD correlation functions has been proven, resulting in a sign change for two T-odd TMD distributions

between Drell-Yan and DIS [70, 75], an exciting prediction that has to be confirmed by future experiments.

The JLab 12-GeV upgrade will provide the unique combination of wide kinematic coverage, high beam intensity (luminosity), high energy, high polarization, and advanced detection capabilities necessary to study the transverse momentum and spin correlations allowing studies of semi-inclusive processes both in the target and current fragmentation regions. The study of the quark distributions in the valence quark region is one of the key objectives of the upgrade project [91].

4.2 Present Experimental Results on Spin-Azimuthal Asymmetries

In recent years, semi-inclusive deep inelastic scattering (SIDIS) has emerged as a powerful tool to probe nucleon structure through transverse single spin asymmetries (SSAs) [88, 92, 93]. In contrast to inclusive deep inelastic lepton-nucleon scattering where transverse momentum is integrated out, these processes are sensitive to transverse momentum scales on the order of the intrinsic quark momentum $P_T \sim k_\perp$. Measurements of SSAs in SIDIS provide access to a list of novel physics observables including transversity (h_1) [94, 95], and the time-reversal odd Sivers distribution function ($f_{1T}^\perp$) [77, 78, 69, 70, 71].

For transversely polarized targets, several azimuthal asymmetries already arise at leading order. Four contributions related to the corresponding distribution functions were investigated in Refs. [83, 96, 97, 69, 71, 98]:

$$\sigma_{LT}^{\cos\phi} \propto \lambda_e S_T y(1-y/2)\cos(\phi-\phi_S)\sum_{q,\bar{q}} e_q^2 x g_{1T}^q(x) D_1^q(z), \tag{4.2}$$

$$\begin{aligned}\sigma_{UT}^{\sin\phi} &\propto S_T(1-y)\sin(\phi+\phi_S)\sum_{q,\bar{q}} e_q^2 x h_1(x) H_1^{\perp q}(z) \\ &+ S_T(1-y+y^2/2)\sin(\phi-\phi_S)\sum_{q,\bar{q}} e_q^2 x f_{1T}^{\perp q}(x) D_1^q(z) \\ &+ S_T(1-y)\sin(3\phi-\phi_S)\sum_{q,\bar{q}} e_q^2 x h_{1T}^{\perp q}(x) H_1^{\perp q}(z),\end{aligned} \tag{4.3}$$

where ϕ and ϕ_S are the azimuthal angles of the hadron and transverse spin in the photon frame, x, y, z define the fractions of the proton momentum carried by the struck quark, electron

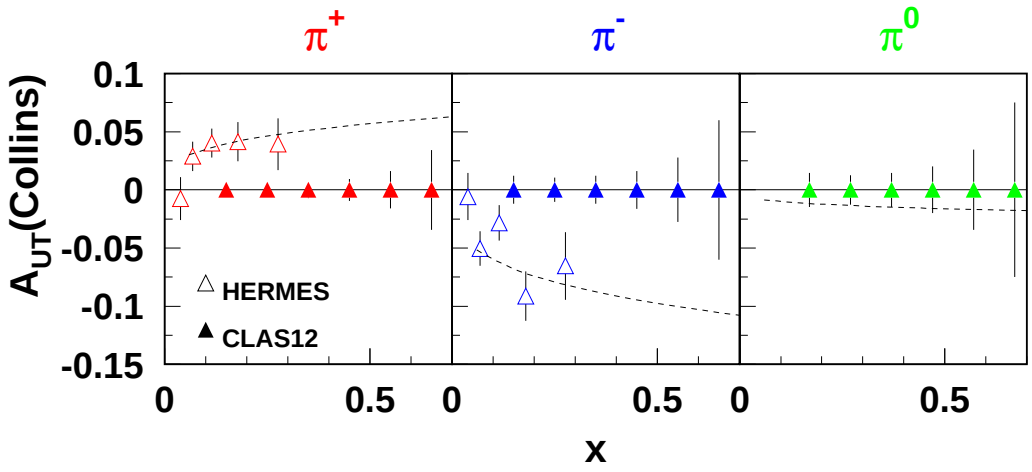

Figure 4.1: Projected transverse spin asymmetry from the Collins effect ($A_{UT}^{\sin(\phi+\phi_S)}$) in single π production with CLAS at 11 GeV.

momentum carried by the virtual photon. and the virtual photon momentum carried by the final state hadron, respectively. $D_1^q(z)$ and $H_1^{\perp q}(z)$ are the spin-independent and spin-dependent fragmentation functions.

The leading-twist transversity distribution h_1 [94, 95] and its first moment, the tensor charge, are as fundamental for understanding of the spin structure of the nucleon as are the helicity distribution g_1 and the axial vector charge. The transversity distribution h_1 is charge conjugation odd. It does not mix with gluons and for non-relativistic quarks it is equal to the helicity distribution g_1. Thus, it probes the relativistic nature of quarks and it has a very different Q^2 evolution than g_1. The tensor charge is reliably calculable in lattice QCD with $\delta\Sigma = \sum_f \int_0^1 dx(h_1^f - \bar{h_1^f}) = 0.562 \pm 0.088$ at Q^2=2 GeV^2, which is twice as large as the value of proton axial charge [99]. A similar quantity ($\delta\Sigma \approx 0.6$) was obtained in the effective chiral quark soliton model [100].

A detailed study of the Q^2 and x_B dependencies as a function of the azimuthal angle ϕ will allow the separation of contributions from different mechanisms. During the last few years, first results on transverse SSAs have become available [92, 93]. HERMES measurements for the first time directly indicated significant azimuthal moments generated both by Collins

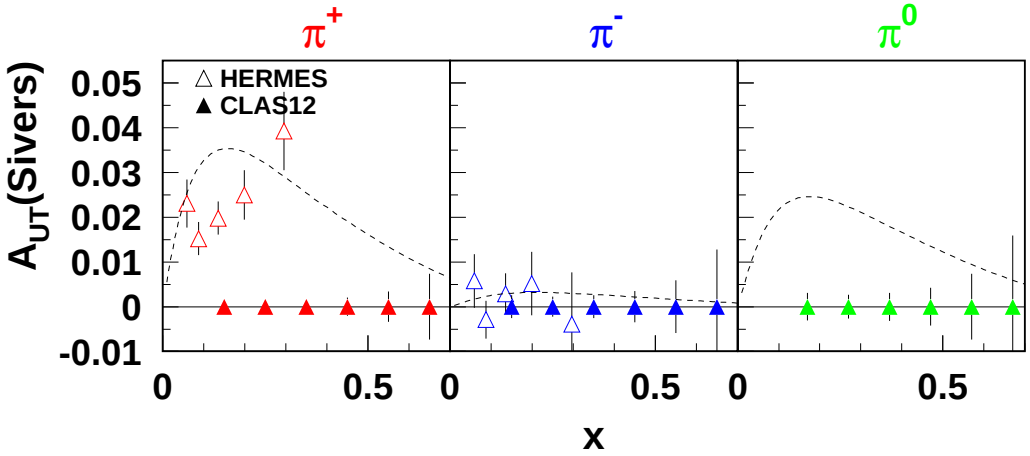

Figure 4.2: Projected transverse spin asymmetry from the Sivers effect ($A_{UT}^{\sin(\phi-\phi_S)}$) in single π production with CLAS12 at 11 GeV.

(Fig. 4.1) and Sivers (Fig. 4.2) effects.

Spin-orbit correlations are also accessible in SIDIS with longitudinally a polarized target, where they give rise to the Mulders leading-twist distribution function $h_{1L}^{\perp}$. It is related to the real part of the interference of wave functions for different orbital momentum states, and describes transversely polarized quarks in the longitudinally polarized nucleon. For a longitudinally polarized target the only azimuthal asymmetry arising in leading order is the $\sin 2\phi$ moment,

$$\sigma_{UL}^{\sin 2\phi} \propto S_L 2(1-y) \sin 2\phi \sum_{q,\bar{q}} e_q^2 x h_{1L}^{\perp q}(x) H_1^{\perp q}(z). \tag{4.4}$$

The physics of σ_{UL}, which involves the Collins fragmentation function $H_1^{\perp}$ and Mulders distribution function $h_{1L}^{\perp}$, was first discussed by Kotzinian and Mulders in 1996 [96, 97, 98]. The same distribution function is accessible in double polarized Drell-Yan, where it gives rise to the $\cos 2\phi$ azimuthal moment in the cross section [101].

Measurements of the $\sin 2\phi$ SSA [98], thus allow the study of the Collins effect with no contamination from other mechanisms. A recent measurement of the $\sin 2\phi$ moment of σ_{UL} by HERMES [88] is consistent with zero. A measurably large asymmetry has been predicted

only at large x ($x > 0.2$), a region well-covered by JLab [84].

The kinematic dependence of the SSA for π^+, measured from the CLAS EG1 data set at 6 GeV is consistent with predictions [84]. The π^+ SSA is dominated by the u-quarks; therefore with some assumption about the ratio of unfavored to favored Collins fragmentation functions, it can provide a first glimpse of the twist-2 Mulders TMD function. The distribution function $h_{1L}^{\perp}$ was extracted using the π^+ target SSA [102], which is less sensitive to the unknown ratio of unfavored (d-quark fragmenting to π^+) to favored (u-quark fragmenting to π^+) polarized fragmentation functions (see Fig. 4.5). The curve is the result of the calculation by Efremov *et al.* [84], using $h_{1L}^{\perp}$ from the chiral quark soliton model evolved to Q^2=1.5 GeV^2. The extraction, however, suffers from low statistics and has a significant systematic error from the unknown ratio of the Collins favored and unfavored fragmentation functions, the unknown ratio of h_{1L}^d/h_{1L}^u, as well as from background from exclusive vector mesons. Current statistical errors for π^-, and in particular π^0, which is relatively free of possible higher twist contributions [103], are large and do not allow strong conclusions from the measured SSAs. More data are required for a statistically significant measurement of the $\sin 2\phi$ moment.

The only leading-twist contribution to the unpolarized target cross section depending on the azimuthal angle has a term with the Boer-Mulders function coupling to the Collins function [83]:

$$\sigma_{UU}^{\cos 2\phi} \propto 2(1-y)\cos 2\phi \sum_{q,\bar{q}} e_q^2 x h_1^{\perp q}(x) H_1^{\perp q}(z). \tag{4.5}$$

The physics of $\sigma_{UU}^{\cos 2\phi}$, which involves the Collins fragmentation function $H_1^{\perp}$ and the Boer-Mulders distribution function $h_1^{\perp}$, was first discussed by Boer and Mulders in 1998 [104]. In recent years, the $\cos 2\phi$ asymmetry in leptoproduction was phenomenologically studied using different approximations for the Boer-Mulders function [105, 106, 107].

Independent information on the Boer-Mulders function $h_1^{\perp}(x, \mathbf{k}_T^2)$ can be obtained from the study of the $\cos 2\phi$ azimuthal asymmetry in unpolarized Drell-Yan processes, which has been measured in πN collisions [108, 109]. In Refs. [110, 111] this asymmetry was estimated by computing the $h_1^{\perp}$ distribution of the pion and of the nucleon in a quark spectator model [112, 113]. The $\cos 2\phi$ azimuthal asymmetry in SIDIS was computed assuming that the π^+ production is dominated by u quarks and using the same distributions $h_1^{\perp}(x, \mathbf{k}_T^2)$ and $f_1(x, \mathbf{k}_T^2)$ used in Ref. [111].

The calculation of the $\cos 2\phi$ asymmetry appeared to be in rather good agreement for low values of P_T (up to 0.5 GeV) with SIDIS data coming from the ZEUS experiment [114] at large Q^2 values ($0.01 < x < 0.1$, $0.2 < y < 0.8$, $0.2 < z < 1$, $Q^2 > 180$ GeV^2) where the higher-twist contributions are not expected to be relevant.

It is important to note that both π^+ and π^- azimuthal moments may have significant contributions from exclusive vector meson production. The fraction of π^+ in the single pion sample, coming from exclusive ρ^0 decays, is somewhat less but still significant at large z and in particular for small x. The two pion data from `CLAS12` would allow us to extract exclusive two pion asymmetries and estimate their contribution to the single pion SSA.

4.3 TMD Measurements with JLab at 12 GeV

Projections for target single-spin asymmetry measurements with `CLAS12` at 11 GeV are plotted in Figs. 4.1-4.2. The projected error bars have been calculated assuming a luminosity of 5×10^{34} cm^{-2}s^{-1}, with an NH_3 target polarization of 85% and a dilution factor of 0.14, with 2000 hours of data taking. The asymmetry is integrated over all hadron transverse momenta.

The target single-spin asymmetry from polarized quark fragmentation extracted for `CLAS12` kinematics at 11 GeV is plotted in Fig. 4.1. The estimate was done assuming $h_1 \approx g_1$ and an approximation for the Collins fragmentation function from Ref. [84]. Additional cuts were applied on z ($z > 0.5$) and the missing mass of the $e'\pi^+$ system ($M_X(\pi^+) > 1.3$ GeV).

The extraction of the transversity from $A_{UT}^{\sin\phi}$ could be performed using parameterizations for the unpolarized distribution functions $u(x)$ and $\bar{d}(x)$ and certain approximations for the polarized Collins fragmentation function $H_1^\perp$. The measurement of transversity is complicated by the presence of an essentially unknown Collins function. Recently, the Collins function for pions was calculated in a chiral invariant approach at a low scale [115] and it was shown that at large z the function rises much faster than previously predicted [84, 116] in the analysis using the HERMES data on target SSA. It was also pointed out that the ratio of polarized and unpolarized fragmentation is almost scale independent [115]. Significant asymmetry was measured by Belle [117] indicating that the Collins function is indeed large. The transverse asymmetry measurements were performed at HERMES [118] and COMPASS [93]. The first extraction of the transversity distribution has been carried out recently [119] combining e^+e^- and semi-inclusive DIS data [92]. The statistics, however, are not enough to make statistically

significant predictions in the valence region, where the effects are large.

Significantly higher statistics from CLAS12 data, especially in the large x_B region, will enable the extraction of the x_B and Q^2 dependencies for different azimuthal moments in a wide kinematic range allowing the source of the observed SSA to be revealed and will allow extraction of the underlying distribution functions.

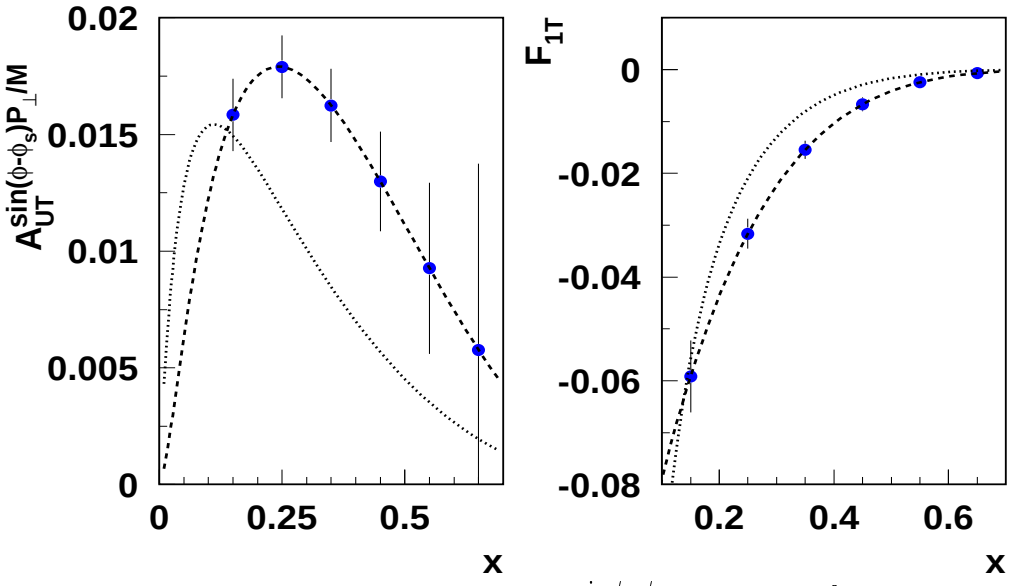

Figure 4.3: Projected transverse spin asymmetry ($A_{UT}^{\sin\phi-\phi_S}$) in single π^0 production with CLAS12 at 11 GeV. The curves are calculated using models for the Sivers function from Efremov *et al.* [120], $F_{1T} = \sum_q^{u,d} e_q^2 f_{1T}^{\perp q}$.

The measurement of the transverse asymmetry from the Sivers effect (see Fig. 4.3) with π^0 will provide a model-independent extraction of the Sivers function. Furthermore, measurements with proton and neutron targets will provide model-independent information on flavor partners of the Sivers function.

The transversely polarized target measurements also provide access to the leading-twist TMD $g_{1T}^q(x)$ appearing in convolution with the unpolarized fragmentation function $D_1^q(z)$ in a $\cos\phi$ moment of the cross section. Significant asymmetries were predicted recently for CLAS12 [121] providing access also to $g_{1T}^q(x)$, describing longitudinally polarized quarks in the transversely polarized nucleon. Measurements of transverse momenta of final state hadrons in SIDIS with longitudinally polarized targets will provide complementary to transverse target information, probing the longitudinal nucleon structure beyond the collinear approximation. The $P_\perp$-dependence of the double-spin asymmetry, measured for different bins in z and x will provide a test of the factorization hypothesis and probe the transition from the non-

perturbative to perturbative description. At large P_T ($\Lambda_{QCD} << P_T << Q$) the asymmetry is expected to be independent of $P_\perp$ [74]. There are indications that the double-spin asymmetry (see Fig. 4.4) at small P_T tends to increase for π^- and decrease for π^+. A possible interpretation of the P_T-dependence of the double spin asymmetry may involve different widths of transverse momentum distributions of quarks with different flavor and polarization [122] resulting from a different orbital structure of quarks polarized in the direction of the proton spin and opposite to it [123, 124]. This interpretation may demand a different width for d-quarks than for u-quarks, consistent with observation from lattice QCD studies of a different spread in transverse distances for d-quarks compared to u-quarks [81]. The same effect may be responsible for the relatively large $\cos\phi$ moment of the double spin asymmetry (see Fig.4.4, right panel).

Detailed measurements of A_{LL} and its $\cos\phi$ moment as a function of P_T in different bins in x, z, Q^2 combined with measurements of azimuthal moments of the unpolarized cross section proposed for `CLAS12` will allow study of the flavor dependence of transverse momentum distributions.

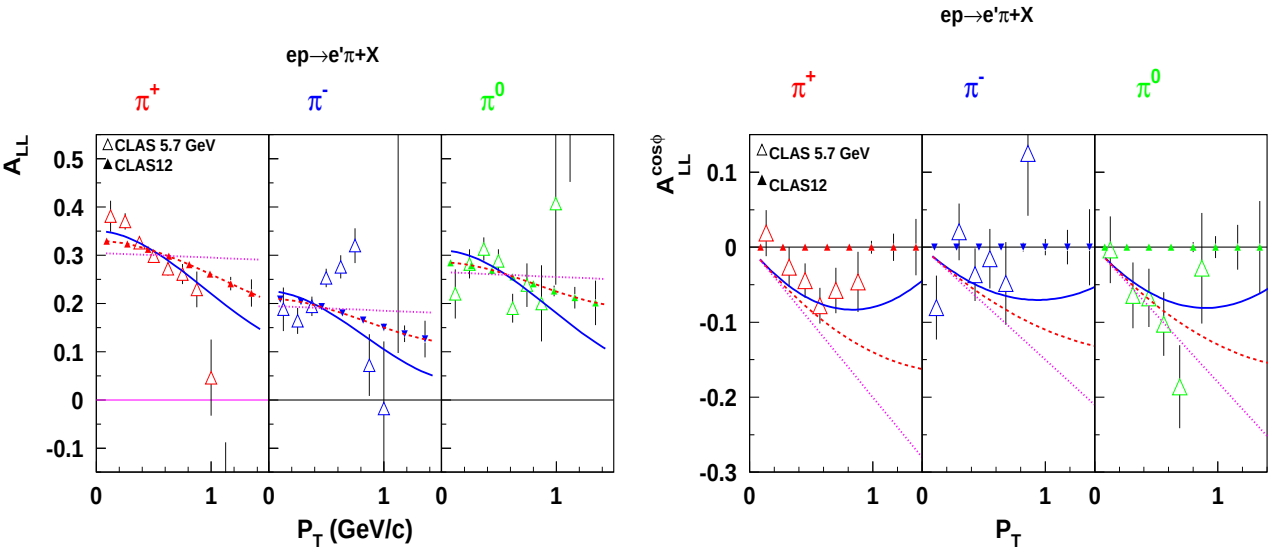

Figure 4.4: The double spin asymmetry A_{LL} (left) and its $\cos\phi$ moment (right) as a function of the transverse momentum of hadrons, P_T, averaged in the $0.4 < z < 0.7$ range.

Projections for the resulting kinematic dependence of the leading-twist SSA are shown in Fig. 4.5. Calculations were done using $h_{1L}^\perp$ from the chiral quark soliton model evolved to Q^2=1.5 GeV^2 [84], f_1 from GRV95 [125], and D_1 from Kretzer, Leader, and Christova [126]. Three different curves correspond to $H_1^{\perp u\to\pi^+}/H_1^{\perp u\to\pi^-} = 0, -1.2, -5$ [127]. Corresponding projected error bars for the Mulders TMD parton distribution are shown in Fig. 4.5. An im-

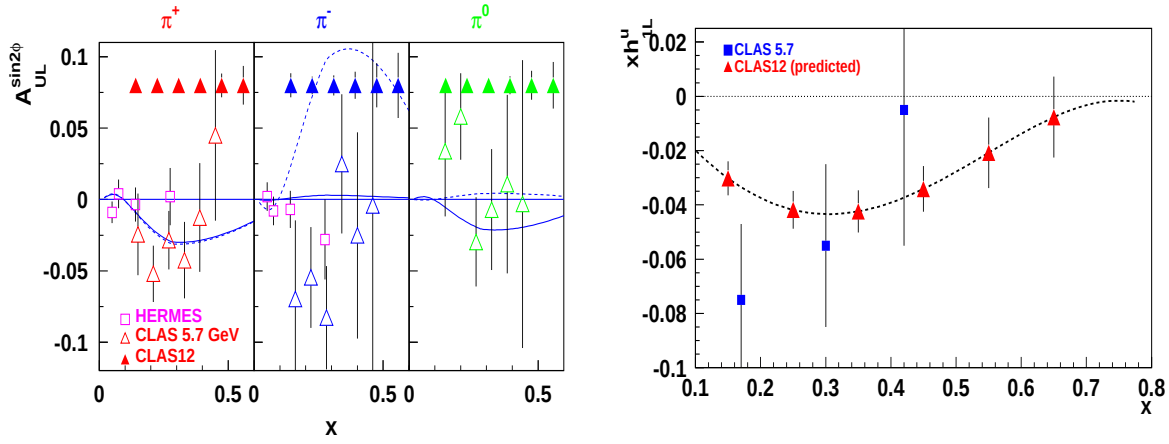

(a) (b)

Figure 4.5: (Left) The projected x-dependence of the target SSA at 11 GeV. The triangles illustrate the expected statistical accuracy. The open squares and triangles show the existing measurement of the Mulders TMD from HERMES and the CLAS 5.7 GeV EG1 data sets, respectively. The curves are calculated using Ref. [127]. (Right) Projection for the Mulders distribution function for the u-quark from the π^+ SSA from CLAS12 (predicted) compared with the CLAS EG1 data set at 5.7 GeV.

portant ingredient for the estimates are so-called "Lorentz-invariance relations" that connect $h_{1L}^{\perp}$ with h_1 [96]. Meanwhile these relations are known not to be valid exactly [128, 129]. It is of importance to find out experimentally to which extent such relations can provide useful approximations, or whether they are badly violated, since there is little theoretical intuition on that point.

Proposed measurements of SSAs in SIDIS will pin down the corresponding TMD distribution and will constrain the ratio of favored to unfavored polarized fragmentation functions. The new data will also allow a more precise test of the factorization ansatz and the investigation of the Q^2 dependence of $\sin 2\phi$, $\sin\phi$, and $\cos\phi$ asymmetries. This will enable us to study the leading-twist and higher-twist nature of the corresponding observables [130, 95, 116, 85, 86, 87, 75].

The Boer-Mulders contribution, being leading twist, is expected to survive at higher Q^2 and that can be tested at the large Q^2 accessible with CLAS12. At large transverse momentum, *i.e.* $P_{h\perp} \gg \Lambda_{\rm QCD}$, the transverse-momentum dependence of the various factors in the factorization formula [74] may be calculated from perturbative QCD. Following the similar arguments in

Ji-Qiu-Vogelsang-Yuan [131], the $\cos 2\phi$ azimuthal asymmetry has the following behavior at $\Lambda_{\rm QCD} \ll P_{h\perp} \ll Q$,

$$\langle \cos 2\phi \rangle |_{P_{h\perp} \gg \Lambda_{\rm QCD}} \propto \frac{1}{P_{h\perp}^2} \ . \tag{4.6}$$

When the transverse momentum is compatible with the large-scale Q, the above results will be modified, because the gluon radiation from the pQCD diagram will dominate, and contribute to the azimuthal asymmetry not being suppressed by any hard scale. At Q^2 values accessible at JLab ($1.0 < Q^2 < 10$ GeV^2), however, the reduction of the Boer-Mulders asymmetry due to Sudakov form factors arising from soft gluon contributions [132] is not expected to be significant.

Measurement of the P_T dependence of the Boer-Mulders-asymmetry (see Fig. 4.6) will allow for checking of the predictions of a unified description of SSA by Ji and collaborators [74, 131] and for study of the transition from a non-perturbative to a perturbative description. The $\cos 2\phi$ asymmetry for semi-inclusive deep inelastic scattering in the kinematic regions of CLAS12 is predicted to be significant (a few percent on average) and tends to be larger in the small-x and large-z region. The preliminary data from CLAS at 6 GeV indeed indicate large azimuthal moments both for $\cos\phi$ and $\cos 2\phi$.

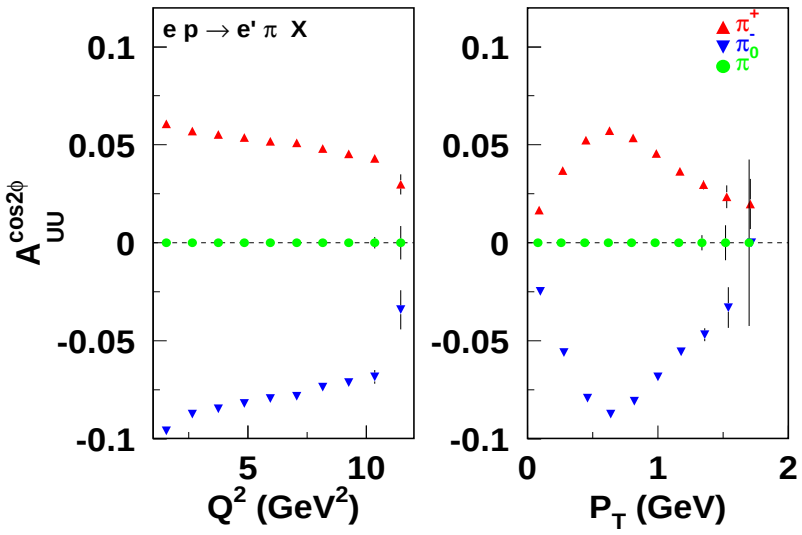

Figure 4.6: The $\cos 2\phi$ moment (Boer-Mulders asymmetry) for pions as a function of x and P_T for $Q^2 > 2$ GeV^2 (right) with CLAS12 at 11 GeV from 2000 hours of running. Values are calculated assuming $H_1^{\perp u \to \pi^+} = -H_1^{\perp u \to \pi^-}$.

The combined analysis of the future CLAS12 data on $\langle \cos 2\phi \rangle$ and of the previous ZEUS

measurements in the high-Q^2 domain (where higher-twist effects are negligible) will provide information on the Boer-Mulders function, shedding light on the correlations between transverse spin and transverse momenta of quarks. Significantly increasing the kinematic coverage at large Q^2 and P_T, CLAS12 (see Fig. 4.6) will map the quark TMDs in the valence region allowing study of the transition from a non-perturbative description at small P_T to a perturbative description at large P_T.

Measured single and double spin asymmetries for all pions in a large range of kinematic variables (x_B, Q^2, z, $P_\perp$, and ϕ) combined with measurements with unpolarized targets will provide detailed information on the flavor and polarization dependence of the transverse momentum distributions of quarks in the valence region, and in particular, on the x_B, z, and $P_\perp$ dependence of the leading TMD parton distribution functions of u and d quarks. Such measurements across a wide range of x, Q^2, and P_T would allow for detailed tests of QCD dynamics in the valence region complementing the information obtained from inclusive DIS. They would also serve as novel tools for exploring nuclear structure in terms of the quark and gluon degrees of freedom of QCD.

4.4 Summary

In summary, with upgraded energy and luminosity, CLAS12 can study single- and double-spin asymmetries, involving essentially unexplored chiral-odd and time-odd distributions functions, including transversity [94, 95], Sivers [77, 69, 70, 71], Boer-Mulers [104], and Collins [83] functions, providing detailed information on the quark transverse momentum and spin correlations [83, 97, 96, 79, 133].

Measurements of semi-inclusive processes combined with inclusive and exclusive measurements with an upgraded JLab will allow us to study the quark structure of the nucleon with unprecedented detail. Understanding of spin-orbit correlations, together with independent measurements related to the spin and orbital angular momentum of the quarks, will help to construct a more complete picture of the nucleon in terms of elementary quarks and gluons going beyond the simple collinear partonic representation.

Chapter 5

Properties of QCD from the Nuclear Medium

5.1 Introduction

While the strong interaction seems to be well described by QCD at high energies, in the non-perturbative domain it remains largely unsolved and untested. Further, little is known from experiment about the space-time characteristics of QCD at any energy scale. Exploration of the QCD phase diagram for hot, dense matter is a large effort in QCD physics, and these studies can take advantage of pQCD, however, a QCD-based description of cold, dense matter still represents a formidable challenge. Lattice QCD, in combination with chiral effective theory, will partly address the non-perturbative physics and the hot, dense matter, but space-time processes and non-zero baryon density are still inaccessible via lattice techniques.

New experimental access to a number of properties and consequences of QCD will become available at 12 GeV. Properties of deconfined quarks, such as their lifetimes and energy loss, can be extracted. The time evolution of $q\bar{q}$ pairs can be deduced from studies of color transparency. The process in which hadrons are formed out of energetic quarks can be characterized, both in terms of formation times and formation mechanisms. The properties of strongly interacting nucleons and their connections to cold, dense matter can be accessed with precision over a broad kinematic range, potentially connecting to astrophysical systems such as neutron stars. These are exciting prospects that will provide profound new insights into the space-time characteristics of fundamental QCD processes and the nature of cold QCD

matter.

5.1.1 p_T Broadening and the Lifetime of Deconfined Quarks

The confinement of quarks into hadrons is the most important manifestation of the non-Abelian character of QCD. Achieving a quantitative understanding of confinement is one of the highest priority endeavors of nuclear and hadronic physics, and ranks as one of the great quests of modern science. The effort to understand confinement is multi-pronged, typically involving hadron spectroscopy interpreted through the use of models and lattice calculations, which aim to characterize the effective potential between quarks. In addition to the effective potential, another important piece of confinement is the process of color neutralization, wherein a deconfined colored quark finds colored partners, such that the resulting system is a color singlet. Experimental access to the characteristics of the deconfined quark can be obtained using semi-inclusive deep inelastic scattering on nuclei in specific kinematic regions.

In deep inelastic scattering (DIS) kinematics with $x > 0.1$, quark-pair production by the virtual photon is suppressed [134] and the target quark absorbs all of its energy and momentum. Thus, neglecting the intrinsic quark momentum, the initial quark energy is ν and its direction is given by the direction of the virtual photon. The quark propagates for some distance until its color is neutralized, at which point it is contained in a "pre-hadron" that subsequently evolves into a fully formed hadron [135]. In the event that the neutralization takes place outside of a nuclear target, the interactions of the struck quark with the nuclear medium are limited to partonic-level multiple scattering, primarily due to the emission of medium-stimulated gluons [136]. This multiple scattering broadens the distribution of momentum transverse to the virtual photon direction, which is observable by measurement of the final state hadron's p_T^2 distribution. Subtracting the intrinsic quark p_T^2 distribution as measured in deuterium yields the basic observable of p_T broadening:

$$\Delta p_T^2 = p_T^2(A) - p_T^2(^2H). \tag{5.1}$$

One property of the deconfined quark that can be accessed is its lifetime, known as the production time τ_p [137]. This is accessed by studying the dependence of p_T^2 on ν for several nuclei. Since τ_p is time dilated in proportion to ν, the ν dependence of p_T^2 for a series of nuclei of known dimensions can be deconvoluted to reliably yield an estimate of τ_p. While measurements

with a 5-GeV electron beam have demonstrated the feasibility of the method [138, 139], with an 11-GeV beam a much wider range in ν will be accessible. An example of a measurement of this type is shown in Fig. 5.1, where Δp_T^2 is shown for three nuclei in a range of ν from 2 to 9 GeV.

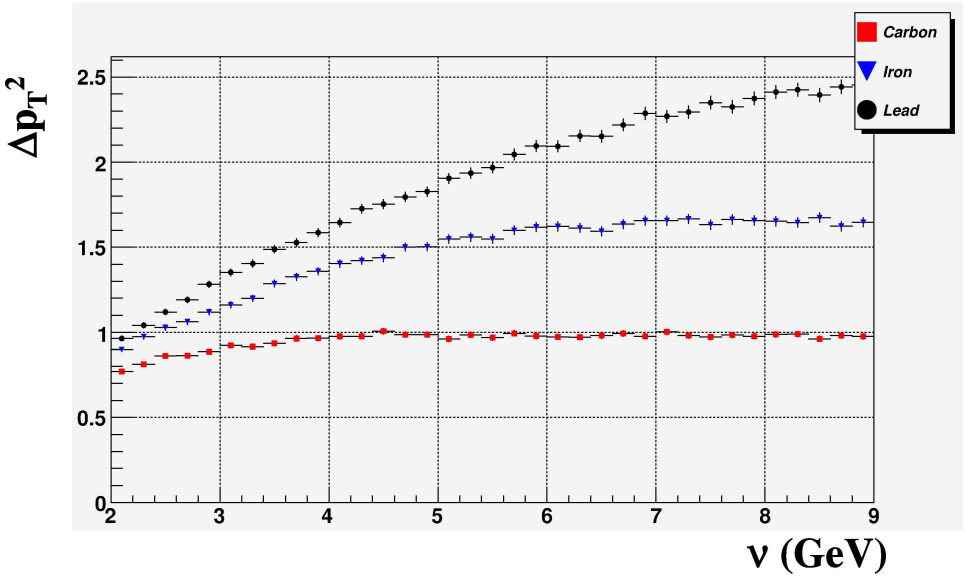

Figure 5.1: A plot of Δp_T^2 vs. ν for three different nuclei. Plateaus are observed in the carbon and iron targets for larger values of ν, indicating the production length τ_p is longer than the full thickness of either nucleus, but still less than that of the lead nucleus.

A second property of the deconfined quark is the rate of its loss of energy due to gluon emission. This partonic energy loss has a simple relationship to Δp_T^2 under certain simplifying assumptions. This energy loss can be written as:

$$\frac{dE}{dx} \approx \frac{3}{4}\alpha_s \Delta p_T^2. \tag{5.2}$$

This energy loss has been estimated previously using the Drell-Yan reaction [140, 141], although theoretical ambiguities have hampered the extraction. In addition, energy loss by gluon radiation is the primary evidence for the quark-gluon liquid discovered at RHIC [142] through the phenomenon known as jet suppression or mono-jet production [143]. Thus these measurements have important interdisciplinary connections. In a simple picture, the energy loss can be estimated simply from data such as that shown in Fig. 5.1 from the functional form and the known properties of the nucleus. A picture such as that shown in Fig. 5.1 implies the observation of the novel result that the total energy loss is proportional to the square of the

distance traveled through the medium, a result long predicted [144]. This implies a coherence behavior in QCD analogous to the QED effect known as the Landau-Pomeranchuk-Migdal (LPM) effect, in which electron bremsstrahlung is suppressed by coherent scattering from multiple scattering centers [145, 146, 147].

Models for the energy loss of quarks typically contain a parameter called the transport coefficient or jet quenching parameter, $\hat{q}$. While difficult to calculate in lattice QCD, this parameter can be calculated for a hot medium [148] using the AdS/CFT correspondence that connects nonperturbative phenomena in hot, strongly coupled gauge theories onto calculable problems in a dual gravity theory [149, 150, 151]. While this technique cannot be applied to a cold medium, an extrapolation procedure such as that employed by Baier *et al.* [152, 153] could potentially extrapolate from hot to cold media.

5.1.2 Color Transparency and the Time Evolution of $q\bar{q}$ Pairs

The color transparency (CT) phenomenon illustrates the power of exclusive reactions to isolate simple elementary quark configurations. For a hard exclusive reaction, such as vector meson electroproduction on the nucleon, the scattering amplitude at large momentum transfer is suppressed by powers of Q^2 if the hadron contains more than the minimal number of constituents. This is derived from the QCD-based quark counting rules. Therefore, the hadron containing valence quarks only, participates in the scattering. Moreover, each quark, connected to another one by hard gluon exchange carrying momentum of order Q, should be found within a distance of order $1/Q$. Therefore, at large Q^2 one selects a very special configuration of the hadron wave function where all connected quarks are close together, forming a small size color neutral configuration called a Point Like Configuration (PLC). Such an object is unable to emit or absorb soft gluons. Therefore, its strong interaction with the other nucleons becomes significantly reduced, and then the nuclear medium becomes more transparent. The nucleus offers a unique laboratory to study quark dynamics. Indeed, the nucleus can be used as a revealing medium of the evolution in time of elementary configurations in the hadron wave function. The time necessary for a quark to cross distances typical of the confined systems is of the order of 1 fm. By taking into account the relativistic time dilation factor, the characteristic time scale corresponds to length scales on the order of a few fm. The only medium available at this scale is the nucleus, offering to us a new generation of experiments where the nucleus functions as bubble chamber!

Experimentally, we would like to understand this spectacular phenomenon by studying the hadron attenuation as it propagates through the nuclear medium. These measurements will allow us to not only access the special configuration of the hadron wave function, but also to study how this configuration dresses with time to form the fully complex asymptotic wave function of the hadron. This puts us in the heart of the dynamics of confinement. Furthermore, the onset of CT is related to the onset of factorization, which is an important requirement for accessing Generalized Parton Distributions (GPDs) in deep exclusive meson production. The ρ^0 meson is our hadron of choice because it offers many advantages. It is believed that the onset of CT is expected at lower Q^2 in the $(q\bar{q})$ system than in the (qqq) system, as it is much more probable to produce a small-size system of two quarks than one of three quarks [154]. In addition, the ρ^0 is a vector meson similar to the virtual photon. Therefore its production mechanism is fairly well understood because the virtual photon fluctuates into a $(q\bar{q})$ pair which then materializes into the ρ^0 meson. The size of the produced $(q\bar{q})$ can be directly connected to the virtuality of the photon. Therefore, smaller sizes can be reached at larger Q^2.

More than two decades of experimental investigations have lead to only one clear signal of CT at high energies. It was observed in experiment E791 [155] at Fermilab. The A-dependence of the diffractive dissociation into di-jets of 500 GeV pions scattering coherently from carbon and platinum targets was measured. It was found that the cross section can be parameterized as $\sigma = \sigma_0 A^\alpha$, with $\alpha = 1.6$. This result is quite consistent with theoretical calculations [156, 157, 158] including CT and obviously inconsistent with a cross section proportional to $A^{2/3}$, which is typical of inclusive pion-nucleus interactions. At moderate energies, the situation is more complicated. No evidence of CT was found in quasi-free $A(e, e'p)$ reactions [159, 160, 161, 162] even for Q^2 values as large as 8 GeV^2. While the outcome of quasielastic $(p, 2p)$ scattering from nuclei [163, 164, 165] was very controversial due to the fact that the results do not support a monotonic increase in transparency with Q^2 as predicted by CT, the transparency increases for Q^2 from 3 to 8 GeV^2, but then decreases for higher Q^2, up to 11 GeV^2. This subsequent decrease was explained as a consequence of soft processes that interfere with perturbative QCD in free pp scattering but which are suppressed in the nuclear medium [166]. Other measurements studied the attenuation of the ρ^0 vector meson in the nuclear medium via exclusive ρ^0 lepto-production off nuclei. The results from the two measurements [167, 168] are very suggestive of a CT signal, but they are statistically limited.

The exclusive, diffractive, incoherent electroproduction of vector mesons off nuclei has been suggested [169] as a sensitive way to detect CT. In the laboratory frame, the photon fluctuation can propagate over a distance l_c known as the coherence length. The coherence length can be estimated relying on the uncertainty principle and Lorentz time dilation as $l_c = 2\nu/(Q^2+M^2_{q\bar{q}})$, where ν is the energy of the virtual photon in the laboratory frame, (-Q^2) is its squared mass, and $M_{q\bar{q}}$ is the mass of the $(q\bar{q})$ pair. In the case of exclusive ρ^0 electroproduction, the mass of the $(q\bar{q})$ is dominated by the ρ^0 mass. The produced small-size, colorless hadronic system will then propagate through the nuclear medium with reduced attenuation because its cross section is proportional to its size. The effect of the nuclear medium on the particles in the initial and final states can be characterized by the nuclear transparency T_A. T_A is defined as the ratio of the measured exclusive cross section to the cross section in the absence of initial and final state interactions. It can be measured by taking the ratio of the nuclear per-nucleon (σ_A/A) to free nucleon (σ_N) cross sections:

$$T_A = \frac{\sigma_A}{A\sigma_N}. \tag{5.3}$$

The signal of CT would be an increase of the nuclear transparency as Q^2 increases. It was shown by the HERMES collaboration [170] that the nuclear transparency increases when l_c varies from long to short compared to the size of the nucleus. This is due to the fact that the nuclear medium seen by the $(q\bar{q})$ fluctuation becomes shorter. Thus the $(q\bar{q})$ pair interacts less. This situation occurs when Q^2 increases at fixed ν. This so-called coherence length effect (CL) can mimic the CT signal. Therefore one should keep l_c fixed while measuring the Q^2 dependence of the nuclear transparency.

`CLAS12` is the ideal detector for such measurements. It offers large acceptance, good particle identification, and high luminosity. Using an 11-GeV electron beam, one can extend the Q^2 region up to 5.5 GeV^2. An indication of the quality of the data that can be obtained is shown in Fig. 5.2. The nuclear transparency for several targets (C, Fe, and Sn) could be measured. This is important in order to study the formation time of the hadron as it propagates through different nuclear sizes. These measurements would also be a natural extension of a previous `CLAS` experiment [171], where the preliminary results indicate a clear evidence of a CT signal despite the limited Q^2 range to 2 GeV^2.

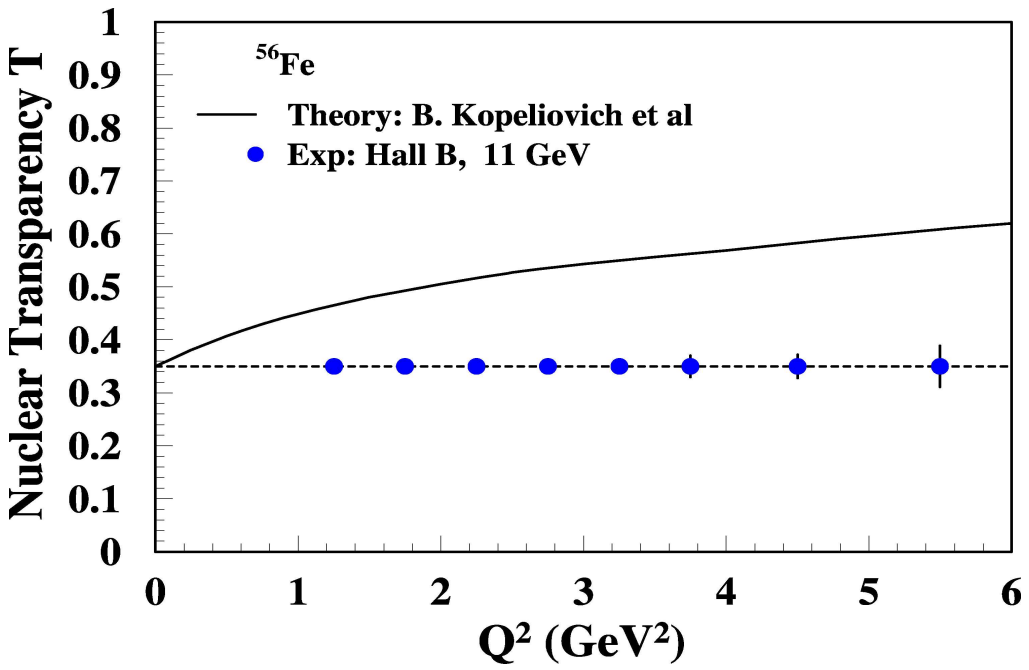

Figure 5.2: A plot indicating the expected error bars for the 11-GeV measurements of nuclear transparency for ρ_0 production on Fe from incoherent ρ electroproduction (12 days of beam time), and the predictions of Ref. [169].

5.2 Hadron Attenuation and the Formation Time of Color Fields

In the preceding discussion, the focus was on the kinematics in which the color of the quark is neutralized outside the nucleus. In those kinematics one learns about the properties of the propagating quark through its partonic-level multiple scattering in the medium. In this section the focus is on the case when the color neutralization happens within the nuclear medium, creating a color singlet object referred to as a pre-hadron. The pre-hadron evolves to a full hadron over a period of time τ_f, the formation time. The pre-hadron and the final hadron can both interact with the nuclear medium and the most probable interaction is a highly inelastic reaction. Relative to the same kinematics on deuterium, in a heavy nucleus these interactions move hadron flux at high energies to lower energies (or lower z) and higher multiplicities. This is referred to as hadron attenuation. It is quantitatively measured by the hadronic multiplicity ratio R_M^h:

$$R_M^h = \frac{(N_h^{DIS,A})/(N_e^{DIS,A})}{(N_h^{DIS,^2H})/(N_e^{DIS,^2H})}, \tag{5.4}$$

where $N_h^{DIS,A}$ is the number of hadrons of species h produced in DIS kinematics on nucleus A, $N_e^{DIS,A}$ is the number of DIS electrons from nucleus A, and the denominator refers to the same quantities for deuterium ^2H [172]. R_M^h may in principle depend on a number of kinematic variables such as Q^2, ν, z, p_T, and ϕ. Isolating the multi-variable dependence of R_M^h is a powerful discriminator between models based on different physical pictures. At the current time, two different physical pictures dominate model descriptions. The first [173, 174] assumes that hadronization takes place outside the nucleus. The second [135, 175] assumes that hadronization can take place inside the nucleus, and cite the interaction of the pre-hadron as the main cause of the attenuation. Both approaches provide adequate descriptions of the HERMES data, which is statistics limited to one or at most two dimensional analyses. A full multi-dimensional analysis spanning a wide kinematic range is feasible with CLAS12, and such an analysis will be certain to strongly constrain theoretical descriptions. In addition to spanning a range of kinematic variables, it is feasible to measure a wide range of hadron masses with varied flavor content, as may be seen in Table 5.1, which lists hadrons with $c\tau$ greater than nuclear dimensions for which measurements with CLAS12 are feasible. With a dataset of this quality and breadth, a comprehensive program to extract hadron formation lengths is practical to carry out. Such a program will yield insights into the systematic behavior of how hadrons form, a heretofore unknown sector of nonperturbative QCD in the spacetime domain.

5.2.1 $D(e, e'p_s)$ and the Quark Structure of Neutrons in a Cold Dense Medium

For a complete understanding of QCD at hadronic scales, we need to learn more about the interplay between the internal (quark) structure of nucleons and the interaction between two nucleons. In particular, it is of high interest whether nucleons in close proximity to each other (effectively at non-equilibrium high density) change their internal structure or perhaps even lose their separate identity to fuse into a "six quark cluster" [176]. Some less dramatic modifications of the nucleon structure that have been proposed include off-shell effects [177], Q^2 rescaling effects, and the suppression of small-size configurations (PLCs) in the nucleon wave function [178, 179]. Deuterium is the optimal system to study such "tightly bound

hadron	$c\tau$	mass (GeV)	flavor content	detection channel	Production rate per 1k DIS events
π^0	25 nm	0.13	$u\bar{u}d\bar{d}$	$\gamma\gamma$	1100
π^+	7.8 m	0.14	$u\bar{d}$	direct	1000
π^-	7.8 m	0.14	$d\bar{u}$	direct	1000
η	0.17 nm	0.55	$u\bar{u}d\bar{d}s\bar{s}$	$\gamma\gamma$	120
ω	23 fm	0.78	$u\bar{u}d\bar{d}s\bar{s}$	$\pi^+\pi^-\pi^0$	170
η'	0.98 pm	0.96	$u\bar{u}d\bar{d}s\bar{s}$	$\pi^+\pi^-\eta$	27
ϕ	44 fm	1.0	$u\bar{u}d\bar{d}s\bar{s}$	K^+K^-	0.8
$f1$	8 fm	1.3	$u\bar{u}d\bar{d}s\bar{s}$	$\pi\pi\pi\pi$	-
K^+	3.7 m	0.49	$u\bar{s}$	direct	75
K^-	3.7 m	0.49	$\bar{u}s$	direct	25
K^0	27 mm	0.50	$d\bar{s}$	$\pi^+\pi^-$	42
p	stable	0.94	ud	direct	530
$\bar{p}$	stable	0.94	$\bar{u}\bar{d}$	direct	3
Λ	79 mm	1.1	uds	$p\pi^-$	72
$\Lambda(1520)$	13 fm	1.5	uds	$p\pi^-$	-
Σ^+	24 mm	1.2	us	$p\pi^0$	6
Σ^0	22 pm	1.2	uds	$\Lambda\gamma$	11
Ξ^0	87 mm	1.3	us	$\Lambda\pi^0$	0.6
Ξ^-	49 mm	1.3	ds	$\Lambda\pi^-$	0.9

Table 5.1: Final-state hadrons potentially accessible for formation length and transverse momentum broadening studies in CLAS12. The rate estimates were obtained from the LEPTO event generator for an 11-GeV incident electron beam. (The criteria for selection of these particles was that $c\tau$ should be larger than the nuclear dimensions, and their decay channels should be measurable by CLAS12.)

pairs", since there are no additional nucleons interacting with the pair under study and the pair is at rest in the lab, with completely defined kinematics. While the probability for a small inter-nucleon distance configuration in deuterium is rather small compared to heavier nuclei, such configurations can be "tagged" by the emission of a fast proton in the backward hemisphere relative to the momentum transfer vector. We therefore propose to measure the reaction $D(e,e'p_b)X$ with coincident detection of the scattered electron in the forward part of CLAS12 and the fast (above 300 MeV) backwards proton in the central detector.

In the simple spectator picture, the backwards-moving proton does not participate in the scattering process and can serve as a tag of the initial state momenta of both nucleons. By measuring the momentum of this backward proton, we can correct the observed electron kinematics for the initial motion of the unobserved struck neutron and extract the modified neutron structure function $F_2^{n(eff)}(x,Q^2,p^2)$. The emphasis here is not on nearly on–shell neutrons, but rather on the opposite kinematic extreme of fast–moving neutrons, where off-shell effects and other internal structure changes are much more pronounced. We can extract the dependence of the structure function $F_2^{n(eff)}(x,Q^2,p^2)$ at fixed x and Q^2 on the spectator momentum p in the range from about 70 MeV to 700 MeV. We will simultaneously cover a large range in x and Q^2, allowing us to make detailed comparisons with the different models mentioned above, including the rather striking change in the shape of the structure function F_2 predicted for a non-trivial six quark configuration [176].

For the proposed experiment, we will use CLAS12 in the standard configuration, with a liquid-deuterium target and the fully instrumented central detector to tag the backward proton. We estimated the expected number of counts for a 20-day run with full luminosity (10^{35} cm^{-2}s^{-1}). The results are shown in Fig. 5.3 as a function of the "ordinary" Bjorken variable $x = Q^2/2m\nu$ in the lab and for several bins in the light cone fraction α of the backward proton. One can clearly see the kinematic shift due to the motion of the struck neutron, which we can fully correct using the proton kinematics. We clearly will have good statistics for a large range in x and in α (the highest bin corresponds to more than 600 MeV momentum opposite to the direction of the q vector), drastically extending the kinematic coverage and statistical precision of the existing data from the analog experiment at 6 GeV (E94-102) [180].

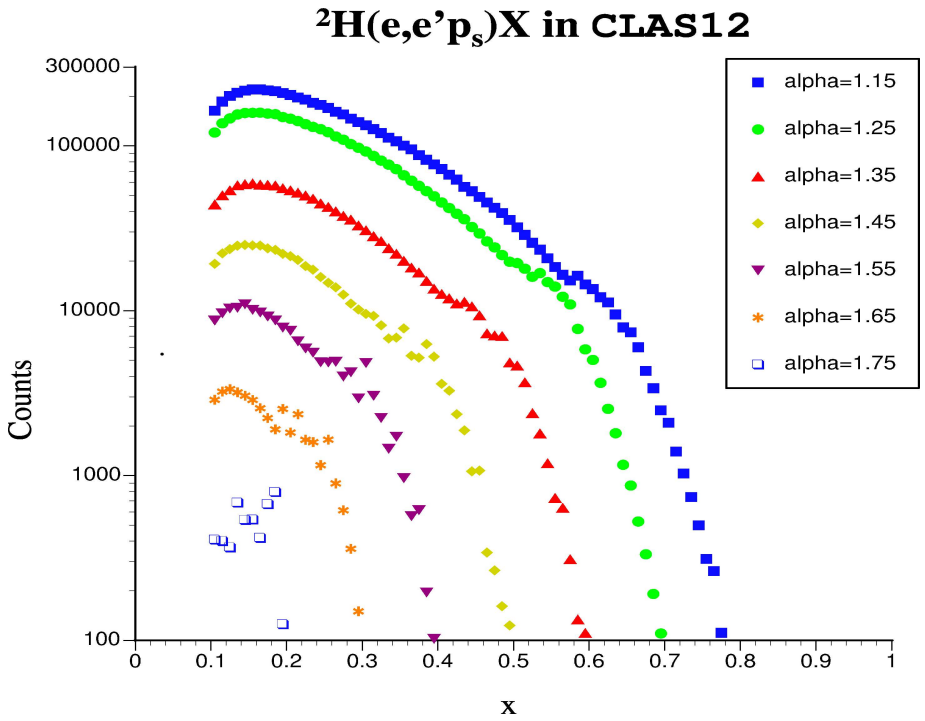

Figure 5.3: Kinematic coverage in Bjorken–x and proton light-cone fraction α_S for the proposed experiment. The count rates have been estimated for a 20-day run with the standard CLAS12 configuration.

5.3 $x > 1$ and the Properties of Cold Dense Matter

Measurements with $x > 1$ have been demonstrated to provide insight into the properties of nucleon-nucleon correlations [181, 182]. With CLAS12, the combination of increased luminosity and large acceptance promises to permit investigation of the hadronic final states associated with $x >> 1$, which means that the properties of cold nuclear matter fluctuating ephemerally to conditions of high density can be accessed experimentally. Together with theoretical extrapolations to equilibrium conditions, one can hope to explore such exotica as stable strange matter as an equilibrium component of neutron stars. A possible experimental avenue to explore these ideas is to measure strangeness production on a series of nuclei in $x > 1$ kinematics. A significant enhancement in kaon production increasing with x may be a signature that can be connected to equilibrium conditions at high nuclear density which have a persistent strangeness component. These studies complement investigations in heavy-ion reactions [183] where kaon yields have recently been shown to be consistent with thermal production in high-density nuclear matter. These exclusive or semi-inclusive studies with $x > 1$ are the natural next step following the inclusive experiments to date.

5.3.1 The Polarized EMC Effect and the Quark Structure of Nuclei

The well known "EMC effect", which shows a modification of the F_2 structure function in nuclei relative to the proton, has been a puzzle for over two decades. Nearly 1000 papers have been written on the subject to try to explain the EMC effect and its associated phenomena. The best models generally use a modification of the nucleon structure within the nuclear medium to explain the effect. It is known from lattice QCD that the region surrounding a baryon or a meson has a suppressed chiral condensate, and it is reasonable to infer that the nuclear medium continues this pattern. In a quantum field theory picture of the nucleus, the structure of bound baryons is dominantly affected by the scalar field of the nucleus, which essentially polarizes the nucleon and modifies its structure, particularly that of the lower component of the relativistic wave function. Calculations of the polarized EMC effect indicate it is approximately twice as big as the unpolarized effect [184]. A plot indicating the achievable uncertainties is shown in Fig. 5.4.

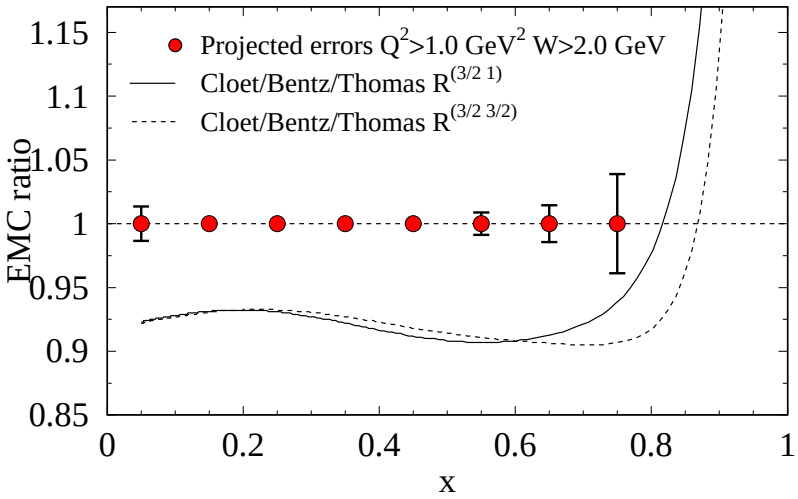

Figure 5.4: A plot of the polarized EMC effect for an 11-GeV beam, 40% target polarization, 80% beam polarization, and 70 PAC days measured in CLAS12. The two curves are for the two dominant structure function multipoles for this ($J^\pi = 3/2^-$) nucleus; the solid line is for $K = 1$ and the dashed line is for $M = J$.

Chapter 6

Spectroscopy

6.1 Introduction

Spectroscopy of hadrons (mesons and baryons) is one of the key tools for studying the theory of strong interactions, Quantum Chromodynamics (QCD), in the non-perturbative (*i.e.* confinement) regime. Hadron spectroscopy has been an essential component of the physics program with CLAS [185, 186, 187, 188, 189, 190, 191, 192]. To date, a large amount of experimental data on electromagnetic production of hadrons has been collected by CLAS. However, more data will be necessary to guide improvements in hadronic phenomenology and to compare with lattice QCD calculations.

The majority of the data obtained so far with CLAS is restricted to the lowest mass states formed with the lightest quarks, up, down, and strange. A complete picture of QCD in the strong-coupling (non-perturbative) regime requires extension of hadron spectroscopy studies to higher masses and/or higher transferred momenta. Fulfillment of this task requires upgrading the electron beam energy to about 12 GeV, along with the necessary upgrade of the detector package, with a large-acceptance spectrometer being an obvious choice for studies of multi-particle final states.

The key experiments in hadron spectroscopy that we plan for the upgraded CLAS detector (CLAS12) will study reactions produced by both quasi-real and virtual photons. They include:

- Studies of high-mass mesonic states (consisting of ordinary mesons, hybrids, and mesons with exotic J^{PC}) using H_2 and light nuclear targets;
- Higher mass baryon production, *e.g.* Σ and Ξ baryons;

Along with traditional bremsstrahlung photon beams, we are planning to use quasi-real photons produced when electrons are scattered at very forward angles (*i.e.* scattering angles $<1.5^{\circ}$). We plan to use a small-angle forward electron tagger in coincidence with the detection of multi-particle final states with the CLAS12 detector to study electroproduction at Q^2 values of $< 10^{-2}$ GeV^2. *Electroproduction at these very small values of Q^2 using unpolarized electrons is equivalent to photoproduction using partially linearly polarized photons* [193].

The physics program using the very small-angle electron scattering facility will take advantage of polarized photons and relatively high photon fluxes. The use of high precision, high intensity electron beams will allow us to achieve the required luminosities on very thin targets (*i.e.* gas targets) without jeopardizing the signal to accidental ratio. In turn, this will allow detection of low-energy recoils (*e.g.* coherent scattering experiments) and spectators (*e.g.* scattering off of the neutron in the deuteron). High-flux, linearly polarized photon beams, together with the use of the nearly 4π coverage for hadronic final states of CLAS12, will allow the study of hadron spectroscopy in a competitive and complementary experimental environment to the already planned GlueX coherent bremsstrahlung production experiment in Hall D.

6.2 Physics Motivation

Perhaps the most fundamental question of interest to hadron physicists is that of understanding the mechanism of confinement. It has been more than thirty years since QCD was postulated as the theory of strong interactions. While much progress has been made in understanding perturbative phenomena, the non-perturbative regime, the regime of hadrons, their excitations, and their couplings, has remained largely impervious to our varied assaults. Only recently, with improvements to calculations of lattice QCD, has it become possible to make predictions of the spectrum of hadrons [194, 195] directly from QCD, based on very few parameters (such as the bare quark masses). New experimental efforts to determine the hadron spectra are timely and are important for theoretical progress in non-perturbative QCD.

In order for this lattice effort to make significant progress in addressing confinement, and in order for this investment to pay off, lattice calculations for the masses and couplings of baryons and mesons must be compared with information extracted from precision experiments. Lattice QCD is not only capable of studying masses of bound systems of quarks and gluons, but it

can also give insight into a space-time picture of electromagnetic interactions of these systems through studying the Q^2 dependence of electro-excitation form factors. We can have confidence that lattice calculations are indeed simulating QCD only when it successfully reproduces a wide range of hadron properties. Some of the precision experiments needed have been, and are being, carried out at Jefferson Lab, and at other facilities around the world.

While mesons and baryons may be viewed differently, their phenomenology reflects common aspects of strong interaction dynamics. Searching for mesons with exotic quantum numbers gives us an opportunity to capture gluons as constituent particles that have their own identity, along with quarks, in forming hadronic bound states. On the other hand, considering interactions between three quarks in a baryon, one finds that the presence of meson-type quark correlations may be crucial in describing baryon properties, reflecting fundamental features of the QCD vacuum. In addition, multi-quark configurations in baryons are possible.

A number of legitimate questions about why this research is important might be asked. For instance, some may question the need for more experiments in hadron spectroscopy, since many experiments have already addressed some of the issues discussed here. However, the experimental coverage is incomplete. Many individual experiments have been carried out with the aim of addressing single aspects of hadron phenomenology. Like a map drawn by many hands, the picture of hadrons that has emerged is incomplete in some areas, and inconsistent in others. The goal of further experimentation in this area is compelling: to continue our efforts to arrive, as far as possible, at a clear, complete, and consistent description of hadrons and their properties.

In order to understand the dynamics of QCD in the confinement region, a systematic study of many states, including their couplings to other states, is needed. Many of the current experiments at JLab, in combination with a systematic analysis effort, will have (in principle) information primarily on non-strange baryons, the nucleons and the Deltas. This information is not sufficient for us to arrive at a complete and consistent picture of the dynamics of QCD in the confinement region. Information on hyperons is a crucial element needed for constructing such a picture. For instance, the SU(3) singlet Λs play key roles in identifying the states of the 70-plets and the 20-plets. At present, only one paper from `CLAS` on the excited Λ^*s [196] has been published, and this study was statistically limited by the low production cross sections at the currently available beam energies. Other studies of the excited hyperon states are in progress at `CLAS` and further work can be done with the availability of higher energies.

Some information on hyperons can be extracted from ongoing experiments, but the kinematic reach of the current JLab accelerator at present does not allow the kind of systematic study that is essential. The higher energies provided by the upgraded facility will allow for more detailed analysis of the spectrum and interactions of the hyperons, through processes like $\gamma N \to K\bar{K}N$ and $\gamma N \to KK\Xi$.

The proposed CLAS12 experimental program is in step with current developments in hadronic phenomenology and lattice QCD, where the main thrust is a comprehensive study of the spectrum of conventional hadrons, along with hybrid and exotic mesons and baryons.

6.3 Meson Spectroscopy

A complete mapping of meson resonances in the mass region of 1 to 3 GeV will be particularly important for a better understanding of the QCD confinement mechanism. QCD predicts the existence of several new types of states beyond the naive quark model, *e.g.*: glueballs, hybrids, and multi-quark $q\bar{q}q\bar{q}$ states [197, 198]. Gluons play a central role in strongly interacting matter – quark confinement is due to gluonic forces. The clearest most fundamental experimental signature for the presence of dynamics of gluon degrees of freedom is the spectrum of gluonic excitations of hadrons. Gluonic excitations of mesons with "exotic" quantum numbers, *i.e.* quantum numbers not accessible to the $q\bar{q}$ system, would be the most direct evidence for these states. Determining the properties of such states would shed light on the underlying dynamics of quark confinement.

The identification of these states has been difficult, as high-mass resonances are generally broad and overlapping, and often have similar quantum numbers (mixing). Photoproduction cross sections are small, so statistics have been limited. Ideally, for a complete mapping of the mesons in this mass region, we will need to study each resonance through as many decay channels and production mechanisms as possible in order to disentangle mixing. To determine meson quantum numbers, we use partial wave analysis (PWA) (in a broad sense, fits to the angular distributions of final states). A complete PWA requires high event statistics, as well as high resolution and geometrical acceptance of the detector. Meson spectroscopy at CLAS12, using the low-Q^2 tagger, will fulfill many of these stipulations.

6.3.1 Coherent Photoproduction on Light Nuclei

In the electromagnetic production of t-channel meson resonances at moderate energies, the main physics background arises from associated production of baryon resonances that decay into the same final state particles. Often these particles in both production reactions occupy the same phase space, and therefore, it becomes impossible to separate them using kinematic cuts. The contribution of baryon resonances to the final state makes PWA analysis rather complicated. The production of meson resonances coherently on nuclear targets, when the recoiling nucleus remains intact, is a *clean* way to eliminate baryon resonances. A particular case of such processes is coherent production off of light nuclei, *e.g.* ^{3}H, ^{3}He, and ^{4}He. For these reactions, the recoiling nuclei can be detected in order to ensure that they remain intact.

We propose a program to study charged and neutral meson resonances in the coherent production reactions on light nuclei, $\gamma^* {}^3\mathrm{H} \rightarrow {}^3\mathrm{He}\, M^-$, $\gamma^* {}^3\mathrm{He} \rightarrow {}^3\mathrm{H}\, M^+$, and $\gamma^* {}^4\mathrm{He} \rightarrow {}^4\mathrm{He}\, M^0$, using the `CLAS12` detector and the 12-GeV electron beam. *The key feature of these measurements is the detection of the recoiling nuclei.*

For meson masses from 1 to 3 GeV, the minimum transferred momentum, t_{min}, at beam energies up to 10 GeV, ranges from 0.02 to 0.2 GeV^2. At these transferred momenta, reduction of yields due to the nuclear form factor is expected to be only a factor of a few, while the energy obtained by the recoiling nucleus, 5 to 30 MeV for ^{3}H, ^{3}He, and ^{4}He, will be enough to detect them using thin gas targets. Such experiments can only be conducted with high-intensity electron beams, where the low density of the target can be compensated for by a high flux of quasi-real photons. High precision electron beams, with sub-millimeter cross sections, will allow us to use a small diameter target cell, consequently to have thin windows at high pressure, a critical component for the detection of low-energy recoiling particles. *Electron scattering at very small angles is a unique technique for experiments on thin targets.*

Besides the elimination of baryon resonances, coherent production on nuclei has other advantages as well. In many cases it imposes constraints on the allowed helicity states of the produced meson, and on the possible exchange particles. These will significantly aid the PWA.

Examples of such reactions include coherent production of $\pi\eta$ and $\pi\eta'$ final states on ^{4}He [199]. The attractive feature of these final states is that in the P-wave they have exotic quantum numbers, $J^{PC} = 1^{-+}$. Photoproduction of $\pi\eta$ and $\pi\eta'$ on the nucleon proceeds only via C-odd ρ or ω exchanges. Since ^{4}He has isospin 0, only ω exchange is allowed, and as ^{4}He

has spin 0, the helicity of the final state (at small angles) should be equal to the helicity of the incoming photon (SCHC).

6.3.2 Electroproduction on the Proton at Very Small Q^2

The general idea of PWA is to parameterize the intensity distribution in the space of quantum numbers available to the observed final states. The intensity distribution is written as a sum of interfering and non-interfering amplitudes (partial waves). A maximum likelihood fit is done to the intensity distribution by a set of given partial waves and reasonable assumptions of the production mechanism. The goodness of the fit is related to the statistics (number of events per binned data), the rank of the production matrix, and the number of parameters to be fitted. The fit could then be improved by using higher statistics or (equivalently) by reducing the rank of the fit by having more information about the production mechanism.

The knowledge of photon polarization simplifies the PWA by giving direct information on the production mechanism, and therefore, reducing the rank of the fit. In electroproduction at very low Q^2, we will be able to measure, on an event-by-event basis, the linear polarization of the photons.

Spectroscopy studies of mesons have started with `CLAS` at lower energies [200]. Preliminary results of these experiments show the viability of such studies using the current `CLAS` configuration, where PWA of simple final states ($\pi\pi\pi$) has already been carried out successfully. However, with the limited acceptance of the present `CLAS` and only circular polarization of the electron beam, there are many analysis ambiguities created by the assumptions on the production mechanism and the baryon backgrounds. These ambiguities will be mostly resolved when using linearly polarized, high-energy (greater than 8 GeV) photons, and larger acceptances. At higher energies we will be able to map out the mesons in the interesting 1 to 3 GeV mass range and, most importantly, to better kinematically differentiate mesons from baryons. More specifically, we plan to study mesons decaying into multiple final states (*e.g.* $\rho\pi$, $\eta\pi$, $\phi\eta$, $b_1\pi$, KK^*, $\cdots$).

6.4 Baryon Spectroscopy and Structure

Ground and excited baryon states provide a wealth of information on non-perturbative QCD in addition to that available using mesons. First, baryons are the simplest systems that

manifest the non-abelian nature of QCD. This results in a complex internal structure whose degrees of freedom and dynamics may depend on the distance scale probed. Second, the predicted mass spectrum involves many transitions to a variety of spin-flavor multiplets (56, 70 and 20-plets) which partially overlap in excitation energy. Some of these states have not yet been seen. Understanding and unraveling this rich structure requires experimental data of high precision using a variety of exclusive channels, final hadronic state invariant masses and photon virtualities. The enhanced kinematic range available at 12 GeV will make feasible a study of the evolution of baryon structure and quark binding mechanisms in the transition between QCD strong coupling and asymptotic freedom.

Recent experimental measurements of transition form factors [201, 202] have provided a better understanding of the role played by the nucleon's meson cloud in baryon excitation at low to moderate Q^2. For the $N \rightarrow \Delta(1232)$ transition, there is evidence of strong longitudinal photocouplings and helicity non-conservation out to Q^2=6 GeV^2, which is consistent with significant meson cloud contributions. There is also substantial evidence that meson-baryon interactions may dominate quark-gluon dynamics for $Q^2 < 1$ GeV^2 in the $P_{11}(1440)$ (Roper) and $D_{13}(1520)$ transitions. This interpretation has been substantiated by dynamical meson-baryon calculations [203] and chiral quark models. On the other hand, for the $S_{11}(1535)$ transition, the pion cloud plays a lesser role, and the transition form factor scales with Q^2 as expected from scattering off bare quarks.

Computations using the Dyson-Schwinger equation [204], as well as explicit lattice QCD calculations [205], show a dynamical dressing of bare quarks which persists down to distances equivalent to Q^2=4 GeV^2. Baryon structure physics at 6 GeV is thus limited to the regime where the meson cloud obscures the direct view of the quark and gluon structure in baryons. A recent lattice calculation [206] of the QCD action clearly shows a compact Y-shaped structure binding the 3 valence quarks in the nucleon. To access the genuine gluon dominated QCD interaction thus requires a short distance probe, either high Q^2 for light quark systems, or the photoproduction of heavy quark baryons.

6.4.1 Cascades

The double-strangeness cascades have several advantages when it comes to baryon spectroscopy. First, two of the three valence quarks are heavier ($m_s \simeq 100$ MeV) than light quarks, which reduces the uncertainties in extrapolations of lattice gauge calculations for the

cascade mass. Second, the width of the cascades are typically about a factor of ten smaller than their N^* counterparts. Third, the detached decay vertices for many cascades allows experiments to more easily separate cascades from various backgrounds. These advantages can only be utilized if there is a sufficient beam energy to produce the Ξs in reasonable quantities.

Recently, experiments with the CLAS detector have shown that the ground state Ξ and the first excited Ξ^* can be clearly seen [190] in photoproduction from the proton. The Particle Data Group [207] shows that there are many excited Ξ^*s with fairly narrow widths based on older bubble-chamber or hadronic-beam experiments. However, in some cases, the data for Ξ^*s is not very consistent (some experiments that have reported a Ξ^* should have seen other Ξ^*s in their mass window, but did not). In addition, of the 22 Ξ candidates expected in the SU(3) multiplets, only six are well-established.

Lattice gauge theory will be a useful theoretical tool to tell us the relative masses of the Ξ^* states [208, 209, 210]. An important goal of lattice QCD is to correctly identify the quantum numbers of states, and especially to separate high-spin excitations, which is a particularly delicate problem in the baryon sector. It has been realized, for instance, by the LHP (lattice QCD) Collaboration, that studying the hadronic spectrum around the strange quark mass, instead of attempting to attain the lightest possible quark masses in the computations, allows one to reach the above goal in shorter times. In addition it can take advantage of a more straightforward, and tractable, behavior of the states such as cascade baryons in quenched chiral perturbation theory. Unfortunately, experimental information about these states is incomplete, and our proposal aims at filling this gap.

Because the Ξ^* states are expected to have narrow widths, the experimental determination of their masses should be rather simple. However, the cross section for cascade production decreases dramatically as the beam energy goes down [211], and a systematic study of cascades is only possible with beams of 6 GeV or higher. Data on Ξ^*s, which can be compared with the spectrum calculated from lattice QCD, will be greatly enhanced by the energy upgrade. Furthermore, measurements of the various decay branches of the Ξ^*s will be useful to compare with theoretical models. There is a richness of physics here that cannot be passed up.

6.5 Summary

The simultaneous study of both mesons and baryons using the upgraded CLAS12 detector with 12-GeV electron beams is our goal. By using a small-angle forward electron tagger, a high flux of polarized photons is obtained. This allows thin gas targets to be used, making possible detection of low-energy recoils and spectators.

The physics to be learned is motivated by a combination of lattice QCD and phenomenology. Lattice calculations are useful for understanding of the non-perturbative structure of QCD vacuum, spectroscopy, and dynamics of bound systems of quarks and gluons. At the same time, a consistent experimental program aimed at describing hadron properties requires a broad systematic approach (not limited only to quantities the lattice can presently calculate). In order to understand the dynamics of confinement, many states and their decays must be studied. Furthermore, a proper partial wave analysis should include both baryon and meson amplitudes applied to high statistics data over a wide range of kinematic phase space. This program is limited at the current beam energies, but will be hugely improved with the linearly polarized, quasi-real photons at CLAS12, along with the energy upgrade. Using a combination of lattice QCD and systematics, the physics of mass spectroscopy and possible exotic mesons and baryons can be investigated. Individual experiments have been (are being) designed (and will be presented to the PAC) to show specifically how this program will be carried out and how the measurements are connected with the physics of confinement.

Chapter 7

Baryon Form Factors

7.1 Introduction

The structure of the nucleon is a defining problem for nuclear physics. The most basic observables that reflect the composite nature of the nucleon are its EM form factors (FFs). Indeed, historically the first direct indication that the nucleon is not elementary came from measurements of these quantities in elastic *ep* scattering [212]. The elastic electric and magnetic FFs characterize the distributions of charge and magnetization in the nucleon as a function of spatial resolving power. The transition FFs reveal the nature of the excited states of the nucleon. Further, these quantities can be described and related to other observables through the use of generalized parton distributions (GPDs). Therefore, this topic connects strongly to other thrusts of the 12-GeV program and is central to answering one of the questions in the DOE Nuclear Physics Long Range Plan, 'What is the structure of the nucleon?' [213].

7.2 Context and Motivation

The nucleon elastic FFs are defined via matrix elements of the EM current, $J_\mu = \overline{\psi}\gamma_\mu\psi$, as:

$$\langle N(P')|J_\mu(0)|N(P)\rangle = \overline{u}(P')\left(\gamma_\mu F_1(Q^2) + \frac{i\sigma_{\mu\nu}q^\nu}{2M}F_2(Q^2)\right)u(P), \tag{7.1}$$

where P and P' are the initial and final nucleon momenta, and $q = P - P'$ is the 4-momentum transferred to the nucleon, with $Q^2 = -q^2$. The Sachs electric and magnetic FFs are defined in terms of F_1 and F_2 as:

$$G_E(Q^2) = F_1(Q^2) - (Q^2/4M^2)\ F_2(Q^2), \quad (7.2)$$

$$G_M(Q^2) = F_1(Q^2) + F_2(Q^2)\ . \quad (7.3)$$

EM transition FFs may be similarly defined. In this case the final state is no longer a nucleon, but rather may be a resonance state: $\langle R(P')|J_\mu(0)|N(P)\rangle$.

The elastic FFs at low Q^2 approximately follow a dipole form, $G_D(Q^2) \propto 1/(1+Q^2/Q_0^2)^2$, with $Q_0^2 \approx 0.71$ GeV^2. This behavior can be qualitatively understood in a VMD picture where the virtual photon interacts with the nucleon after fluctuation into a virtual vector meson. Deviations from this form have been observed (see Fig 7.1), and it is important to understand their nature. At asymptotically large Q^2, the elastic FFs can be described in terms of perturbative QCD [214]. Here the short wavelength of the highly virtual photon enables the quark substructure of the nucleon to be cleanly resolved.

Just where the perturbative behavior sets in is still an open question. Evidence from recent experiments at JLab and elsewhere suggests that non-perturbative effects still dominate the FFs for $Q^2 < 10$ GeV^2. The Q^2 dependence of G_E and G_M, which is expected to be the same in perturbative QCD, is observed to be rather strong in the G_E/G_M ratio for the proton out to $Q^2 \approx 6$ GeV^2 [215, 216].

Understanding the transition from the low to high Q^2 regions is vital not just for determining the onset of perturbative behavior. FFs in the transition region are very sensitive to mechanisms of spin-flavor symmetry breaking, which cannot be described *in principle* within perturbation theory. A classic example is the electric FF of the neutron, G_E^n [217], which is identically zero in a simple valence quark picture, and whose non-zero value can only be understood in terms of non-perturbative mechanisms, such as the hyperfine interaction between quarks [218] or a pion cloud [219].

Theoretical guidance on the FFs in the transition region can be obtained from lattice QCD. These calculations will have achieved a high degree of accuracy by the time `CLAS12` is taking data [220] and challenging these fundamental calculations with high-precision data for both the proton and the neutron out to high Q^2 will be an important test.

The Q^2 dependence of the nucleon elastic FFs reflects the dynamics of the quark constituents in a region where confinement plays an important role. Because the EM current couples to the charged quark constituents, one can decompose the FFs into a sum over the quark contributions $G_{E,M}(Q^2) = \sum e_q\ G_{E,M}^{(q)}(Q^2)$, where e_q is the quark charge and the sum

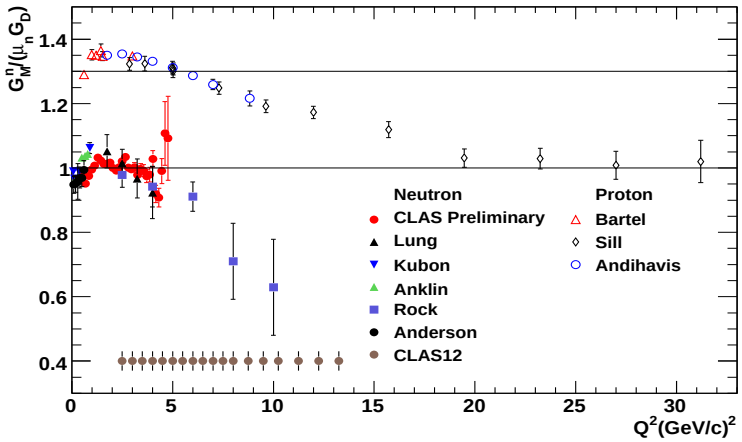

Figure 7.1: The normalized elastic proton and neutron magnetic form factors ($G_{Mn}/G_D\mu_n$, $G_{Mp}/G_D\mu_p$) [221, 222]. The proton data have been shifted upward by 0.3 for clarity. Note the lack of high-quality data for the neutron at large Q^2. The red circles are preliminary results from the CLAS E5 data set. The dark green circles are anticipated results for a 45-day CLAS12 measurement.

is over the valence quarks. To determine $G_{E,M}^{(q)}$ from each individual quark flavor requires measurement of the FFs of both the proton and neutron. However, at present, precision data at high Q^2 exists only for the proton (see Fig. 7.1), which extends beyond 30 GeV^2.

Recent work on GPDs has provided a unifying framework within which both FFs and structure functions can be simultaneously embedded [223, 11]. GPDs hold the promise of providing a 3D image of the nucleon (two spatial, one momentum), but require a variety of measurements. The elastic and transition FFs can be related to each other in dynamical quark models of the nucleon, and more rigorously, in the large N_C limit of QCD. Therefore, within this new framework, they measure different combinations of the same set of GPDs and provide an essential constraint on theory. In particular, the elastic FFs are related to the 0^{th} moments of the GPDs, *e.g.* $H^q(x,\xi,t)$ is given by [223]:

$$\int_{-1}^{1} \sum_q H^q(x,\xi;t)dx = F_1(t), \tag{7.4}$$

where t is the momentum transfer, x is the longitudinal momentum fraction, ξ is the skewness, and the sum is over the valence quarks. The various FF measurements accessible in CLAS12 are therefore interrelated and can be interpreted within a unified analysis. They complement and support other deeply virtual exclusive reactions that are part of the JLab 12-GeV program.

From another perspective, the interplay between FFs and structure functions is central to the phenomenon of quark-hadron duality [224, 55, 225, 226, 227], and the transition from

quark to hadron degrees of freedom in QCD. FFs obtained in exclusive reactions can be related through local quark-hadron duality to deep-inelastic structure functions measured in inclusive processes. For elastic scattering, the FFs can be used to predict the behavior of structure functions in the limit $x \to 1$ [224, 228, 229, 230], which is a difficult region to access experimentally. For example, the F_1 structure function of the nucleon at large Q^2 [224, 230] is proportional to $dG_M^2(Q^2)/dQ^2$. Conversely, from data on structure functions at very large x, one can extract the elastic FFs as a function of Q^2 and compare them directly with data [55, 225]. One can similarly use quark-hadron duality to study not just the elastic case, but the entire spectrum of excited final states, and more generally, the transition from resonance production to scaling in deep-inelastic scattering [231].

Nucleon ground and excited states represent different eigenstates of the Hamiltonian, therefore to understand the interactions behind nucleon formation from the fundamental constituents, the structure of both the ground and excited states should be studied. Nucleon resonances are clearly seen in inelastic inclusive structure functions off nucleons. Moreover, the Q^2 evolution of the non-resonant parts of the inclusive structure functions may be described reasonably well by QCD-based approaches [232], while the evolution of the N^* excitation strength with Q^2 strongly depends on the quantum numbers of the excited state [201]. Therefore, N^* states contain important information on binding interactions, which is complementary to that obtained from the studies of the ground state.

Obviously the data on the Q^2-evolution of N^* electrocouplings offer just phenomenological information. Lattice simulations represent the most straightforward way to relate this phenomenology to fundamental QCD. Lattice studies of N^* states are making steady progress [233, 234, 235, 236, 237], and on the time scale for the 12-GeV upgrade, we may expect lattice predictions for the Q^2-evolution of the electrocouplings of the lightest N^*s in each partial wave. This is an important goal in the current activity of the Theory Center at JLab.

Recent QCD calculations on the lattice [238] show evidence for a "Y-shape" color-flux tube, indicating a genuine 3-body force for baryons with stationary quarks as shown in Fig. 7.2. This 3-body force is a unique feature of a 3-quark baryon system in QCD. Lattice simulations [239] also relate the fundamental QCD Lagrangian to quark confinement potentials, which are responsible for the formation of the ground state and a variety of excited nucleon states, and determine the behavior of the N^* EM FFs as a function of Q^2. These FFs may be estimated in various models [240, 241, 242, 243, 244], which are potentially capable of relating them to

the binding potential and quark-quark interactions at various distance scales.

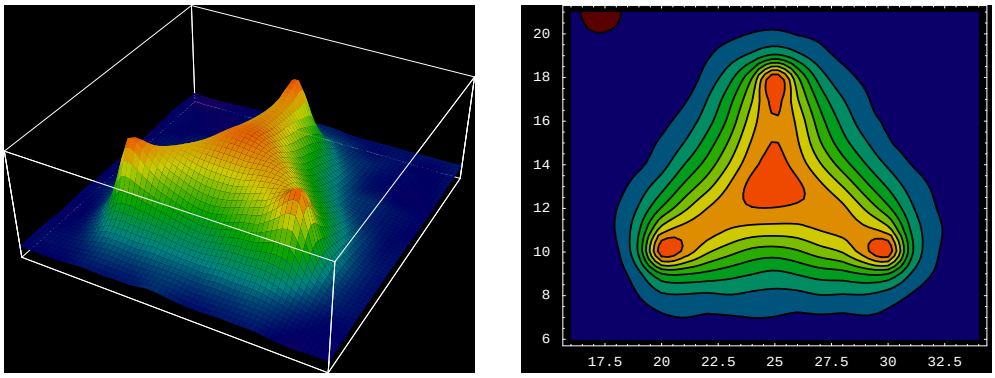

Figure 7.2: Lattice QCD calculation of the 3D color-flux distribution for a baryon. The calculation was carried out to study the abelian color-flux distribution in a static 3-quark system. The "Y-shape" configuration is evident, indicating the presence of a genuine 3-body force. The graph shows high density at the quark locations and in the center. The Δ-shaped flux configuration, characteristic of 2-body forces, would have a depletion in the center.

The CLAS N^* program with energies up to 6 GeV has already provided valuable data on resonance electrocouplings [201, 245]. Further extension of this research with CLAS12 in the Q^2 region up to 10 GeV^2 will open new opportunities to study N^* states at still unexplored distance scales, where considerable contributions from the bare quark core are expected.

Studies of CLAS data on nucleon resonance transitions at increasingly short distances have resulted in strong empirical evidence of large meson-baryon dressing contributions to the resonance excitations at large and medium distances. This is particularly evident in the region of the $\gamma^* N\Delta$ transition where constituent quark models using point-like γ^*-q couplings are unable to explain the much larger strength of the magnetic dipole transition from what is predicted from quark contributions alone [201].

The JLab Excited Baryon Analysis Center (EBAC) is developing an approach capable of evaluating contributions of meson-baryon dressings to N^* electrocouplings based on coupled-channels analyses of the world data [246]. Isolating hadronic dressing effects, we eventually get information on bare quark core contributions. Preliminary studies have shown that these contributions become increasingly important as Q^2 increases.

In Fig. 7.3 we show recent results from CLAS data on $\vec{e}p \to en\pi^+$ in terms of the leading, helicity-conserving $A_{1/2}$ amplitudes to the excitation of the $P_{11}(1440)$, $D_{13}(1520)$, $S_{11}(1535)$, and $F_{15}(1680)$. The amplitudes are multiplied by Q^3, the expected dependence for point-

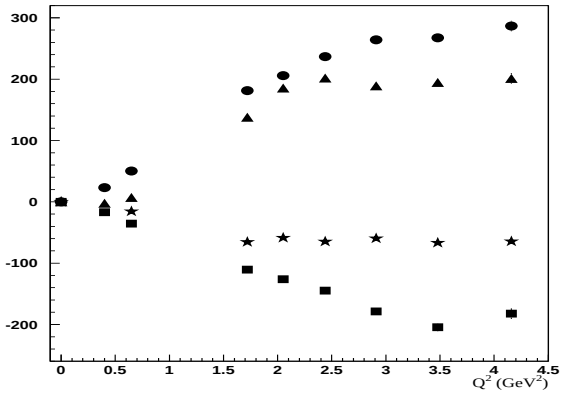

Figure 7.3: Helicity amplitudes $A_{1/2}(Q^2)$ scaled by Q^3 for the Roper $P_{11}(1440)$ (triangles), $S_{11}(1535)$ (circles), $D_{13}(1520)$ (squares), and $F_{15}(1680)$ (stars). At the highest Q^2 the dependence is consistent with a flat behavior.

like coupling to the quarks. The quantity $Q^3 \cdot A_{1/2}(Q^2)$ is consistent with a constant for all resonances above Q^2=3 GeV^2, an encouraging sign that a considerable contribution from the bare quark core may be reached with the energy upgrade.

This regime in N^* excitations is governed by light front wave functions (LFWFs) [247]. The data on N^* electrocouplings at high Q^2 enable us for the first time to access LFWFs for excited nucleon states. Substantial progress has been made in calculations of LFWFs from first principles in QCD, including lattice gauge theory [248], transverse lattice [249], and discretized light front quantization [250]. All of these developments offer promising avenues to relate data on N^* electrocouplings at high Q^2 to fundamental QCD.

The studies of N^* electrocouplings at high Q^2 are of considerable interest for various 12-GeV upgrade research programs. Data on N^* electrocouplings are needed in the studies of inclusive structure functions at large x_b for reliable treatment of resonant contributions. Credible estimates of the resonant parts in various meson electroproduction amplitudes at high Q^2 may allow us to extend GPD studies toward the N^*-excitation region.

7.3 Form Factor Measurements

The program we describe here is part of a broad assault on the nucleon elastic and transition FFs at JLab [222, 215, 216]. All four elastic FFs are needed to untangle the physics including the different quark contributions. In the upgraded `CLAS12` we have proposed measuring G_M^n out to Q^2=13 GeV^2 using a ratio method described below. A proposal (PR12-07-104) for this

experiment was approved by the JLab PAC in 2007 [251]. Another proposal to measure the ratio G_E^p/G_M^p in the upgraded Hall A (PR12-07-109) was also approved to push our knowledge of G_E^p out to Q^2=13 GeV^2 [251]. There are plans to measure G_E^n in the upgraded Hall A out to Q^2=7.2 GeV^2 and to explore the baryon transition FFs with CLAS12 and in Hall C. The N^* program in CLAS12 will measure the electrocouplings of almost all the known N^* states up to Q^2=10 GeV^2. The CLAS12 detector, coupled with the unprecedented quality of the upgraded CEBAF beam, will be the only facility worldwide capable of accessing the N^* transition EM FFs in the unexplored domain of high Q^2, from 5 to 10 GeV^2.

7.3.1 Nucleon Elastic Form Factors

The FF G_M^n will be accessible out to $Q^2 \approx 13$ GeV^2 (see Fig. 7.1) by extending the method used in JLab experiment E94-017 [252]. An unpolarized cryogenic liquid-deuterium target is employed as a "neutron target", and the ratio of e-n events to e-p events off deuterium is measured. A cut on W selects quasi-elastic (QE) kinematics, and in the conceptual limit where the n and p are considered as free in the deuteron, the e-n/e-p ratio can be directly related to the free FFs of the nucleons. Using the more accurately determined proton FFs and an estimate of G_E^n, one extracts G_M^n from the deuteron QE cross section.

There are a number of factors that affect the accuracy of the measured G_M^n. While these are the same for low and high Q^2, their relative importance changes. As long as G_M^n is much larger than G_E^n, uncertainty of the latter does not contribute significantly to the uncertainty in G_M^n. The proton FFs must be well known. In QE kinematics, corrections to the ratio due to the binding of the nucleons within the deuteron will become increasingly smaller at high Q^2. At $Q^2 \approx 4$ GeV^2 the correction was found to be $\sim$0.2% [253, 254, 255].

The neutron detection efficiency, which must be known accurately in this method, will be more stable at high Q^2. The intrinsic detection efficiency in the calorimeter reaches a nearly constant value for neutron momenta above $\sim$1.75 GeV [255]. The detection efficiency was continuously monitored in E94-017 using a novel dual-cell deuterium-hydrogen target which allowed two target cells to be simultaneously in the beam. The neutron detection efficiency was thereby continuously measured using the exclusive reaction $p(e,e'\pi^+)n$ from the proton target. Our preliminary studies of this method in CLAS12 are promising.

Two factors are expected to become more important at high Q^2. The first is the QE scattering rate becomes small relative to inelastic processes nearby in the W spectrum. The

tails of these processes become an important contamination beneath the region of QE scattering. The second effect is the kinematic broadening of the W peak. Taking these two effects together will reduce the QE peak in the W spectrum for $Q^2 > 8$ GeV^2, independent of experimental resolution. Previous measurements of G_M^n at high Q^2, using inclusive electron scattering, encountered this limitation [256]. These difficulties can be overcome in CLAS12 using two types of cuts that do not introduce bias into the ratio measurement. First, the angle between the virtual photon and the detected nucleon is very small for QE kinematics. Eliminating angles that are not consistent with the QE process removes much of the inelastic background. Second, the hermiticity of CLAS12, and its increased capability for detection of neutrals, means that events with in-time charged particles that are inconsistent with QE scattering can be vetoed with high efficiency, as can neutral hit pairs reconstructing to the π^0 mass. The events of interest can be separated from inelastic events. The expected quality of the measurements feasible is seen in Fig. 7.1. The errors are dominated by systematics even at the highest Q^2 as a result of the increased luminosity limit from the upgraded detectors.

7.3.2 Electromagnetic Transition Form Factors

As the first step in the CLAS12 N^* program, we plan to determine in combined analysis of the single and double pion electroproduction, the electrocouplings for almost all well established N^* states at high Q^2 from 5 to 10 GeV^2. Together, 1π and 2π processes account for a major part of the total meson electroproduction cross section in the N^* excitation region. Moreover, they are strongly coupled due to hadronic FSI [257]. Therefore, data on 1π and 2π production amplitudes are needed for credible evaluation of N^* electrocouplings in any meson electroproduction channel. Phenomenological studies have clearly shown that in both of these major channels, the resonant/non-resonant amplitude ratio increases with Q^2 [258].

The CLAS Collaboration has already produced the most extensive, high quality data available for 1π and 2π electroproduction [201, 245]. Two phenomenological approaches [259, 260] were developed for extraction of the N^* electrocouplings from the single pion data. In Ref. [259] the electrocouplings were determined based on almost model-independent dispersion relations. The Unitary Isobar Model [260] enables a good description of all multipoles with $l < 4$ up to W=2.0 GeV. In Fig. 7.4 we present the $P_{11}(1440)$ and $D_{13}(1520)$ electrocouplings for the first time determined from CLAS data on single pion electroproduction. It was shown in Ref. [258], that the approaches of Refs. [259, 260] may be extended for analysis of the data

at high Q^2 available with an 11 GeV beam.

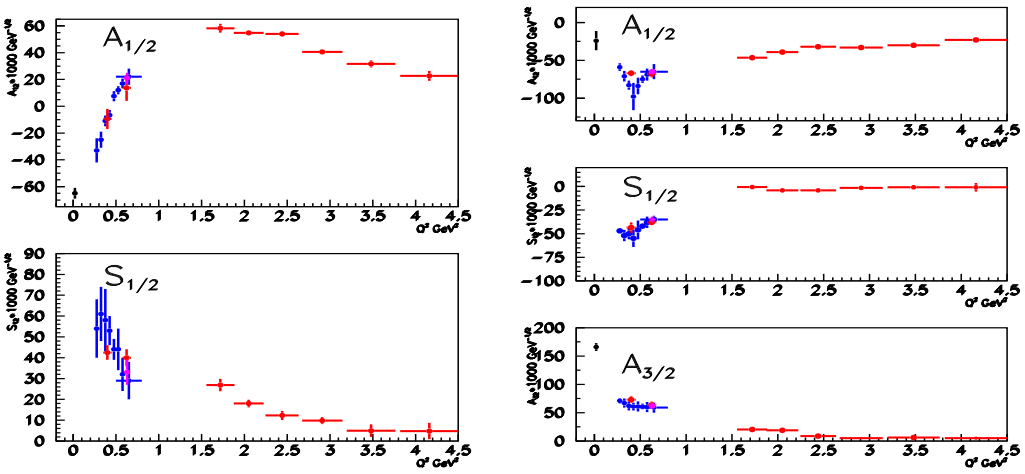

Figure 7.4: Helicity amplitudes for the $P_{11}(1440)$ (left) and $D_{13}(1520)$ (right) states from analysis of CLAS 1π (red points) and 2π (blue points) data. Also shown are the combined $1\pi/2\pi$ data at Q^2=0.65 GeV^2 (magenta points). The PDG photocouplings are in black.

The measurements of the $\pi^+\pi^- p$ exclusive channel with CLAS provided for the first time an entire set of unpolarized single-differential cross sections, and consisted of 9 single-differential cross sections in each (W,Q^2) bin [257, 185]. The JLab-MSU collaboration has developed [257, 261] a phenomenological model (JM06) with tree-diagram mechanisms and additional phenomenological terms to analyze $\pi^+\pi^- p$ electroproduction data sets from the available world data. Several new mechanisms were established for the first time. A reasonable description of the CLAS and world data was achieved. $P_{11}(1440)$ and $D_{13}(1520)$ electrocouplings determined from analysis of recent CLAS 2π data are shown in Fig. 7.4. They are consistent with those extracted from the 1π data, as well as with those obtained in combined $1\pi/2\pi$ analysis [262]. Analysis of the data on 2π electroproduction allowed us for the first time to obtain accurate information on electrocouplings for several high-lying states, which decay preferably with 2π emission. The JM06 approach may be used for the evaluation of N^* electrocouplings in still unexplored areas of high Q^2.

A combined fit of all observables in $1\pi/2\pi$ exclusive channels within the framework of a coupled-channels formalism would enable us to determine the most reliable data on N^* electrocouplings. We are going to carry out a coupled-channels analysis within the framework of the most advanced approach [246], for the first time fully accounting for FSI complexity both in the 2-body and 3-body final states.

Extensive simulation of 1π and 2π electroproduction measurements with CLAS12 were

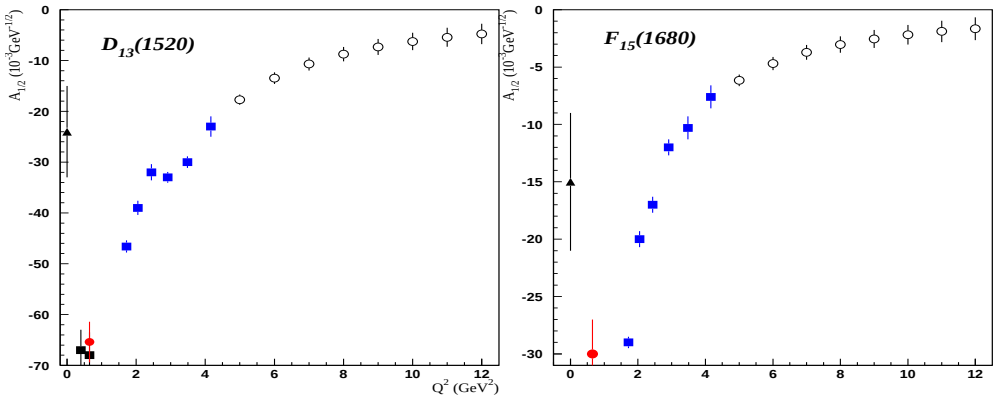

Figure 7.5: Projected $A_{1/2}$ electrocouplings for the $D_{13}(1520)$ and $F_{15}(1685)$ states (open circles) expected from CLAS12 $1\pi/2\pi$ data. Preliminary results from CLAS 1π data (blue) and combined $1\pi/2\pi$ analysis at Q^2=0.65 GeV^2 [262] (red) are shown. Previous world data are shown in black.

carried out in Ref. [258]. It was found that a 60-day measurement would provide observables of the same or better quality than those measured with the CLAS detector at lower photon virtuality. The expected $A_{1/2}$ electrocouplings for the $D_{13}(1520)$ and $F_{15}(1685)$ states are shown in Fig. 7.5.

Chapter 8

PAC Reviewed 12-GeV Proposal Overview

The Jefferson Laboratory Program Advisory Committee (PAC) held meetings on August 21-26, 2006 (PAC30) and August 6-8, 2007 (PAC32). These were the first two PACs to consider experimental proposals to use the base equipment currently planned for the 12-GeV upgrade. In Hall B, 11 proposals and 6 letters-of-intent were presented for the new facility utilizing the `CLAS12` detector system (note that two of the letters-of-intent presented to PAC30 were defended as full proposals to PAC32).

PAC reviewed the physics and equipment with respect to their appropriateness for data taking with the base equipment of `CLAS12` during the first five-year running period with the 12-GeV beam. The presentations covered a broad physics program that reflected almost a decade of discussions and preparations focussed on the physics possibilities opened up by the availability of 11 to 12 GeV electron beams at JLab and the planned experimental equipment. The physics proposals presented reflect the main topics that provided the physics case for the 12-GeV upgrade, which were extensively discussed during the PAC18, PAC23, and PAC27 meetings.

The core of the first five-year running period with `CLAS12` consists of experiments in the following areas:

- Generalized parton distributions and hard exclusive processes;
- Semi-inclusive deep inelastic scattering and single-spin asymmetries;

- Deep inelastic structure functions of the nucleon;
- Elastic and transition form factors of the nucleon;
- Experiments using the nucleus as a laboratory;
- Hadron spectroscopy.

Each of these areas was represented by proposals and letters-of-intent at PAC30 and PAC32. The experiments that were presented in each of these areas are discussed briefly below. The proposals and letters of intent are listed in Tables 8.1 and 8.2, respectively. Fig. 8.1 shows the current allocation of approved beam time in each experimental Hall for the 12-GeV upgrade as a function of beam energy.

◇ Generalized Parton Distributions and Exclusive Processes

1). **PR12-06-108**: *Hard Exclusive Electroproduction of π^0 and η with CLAS12*

Spokespersons: K. Joo, V. Kubarovsky, P. Stoler, M. Ungaro, C. Weiss

This experiment will provide π^0 and η electroproduction cross sections from the proton over a broad range of Q^2, W, and t. The data will have an important impact on the GPD program and will provide a means to constrain the axial GPD of the proton. Both pseudoscalar meson channels are interesting because they provide information on the quark flavor components of the axial GPD.

2). **PR12-06-119**: *Deeply Virtual Compton Scattering with CLAS at 11 GeV*

Spokespersons: A. Biselli, H. Egiyan, L. Elouadrhiri, D. Ireland, M. Holtrop, W. Kim, F. Sabatie

GPDs are physical observables that can provide deep insight into the internal structure of nucleons. DVCS is one of the cleanest processes to measure these functions. This experiment extends the current DVCS program at `CLAS` to higher energy, expanding the kinematic coverage in x and Q^2, and allowing the structure of the nucleon to be probed at much smaller distance scales.

◇ Semi-Inclusive Deep Inelastic Scattering

1). **PR12-06-112**: *Probing the Proton's Quark Dynamics in Semi-Inclusive Pion Production*

Spokespersons: H. Avakian, K. Joo, Z.E. Meziani, B. Seitz

This experiment will perform an extensive study of the transverse momentum proton structure functions and fragmentation functions, which arise from parton transverse momentum and its cou-

pling to spin within the nucleon. Due to immense theoretical progress in recent years in this area and that of GPDs, the true three-dimensional nature of the proton is beginning to be explored.

2). **LOI12-06-108**: *Transverse Polarization Effects in Hard Scattering at CLAS12*

Spokesperson: H. Avakian

This experiment is designed to perform a program of measurements of semi-inclusive deep inelastic scattering and of hard exclusive processes using a transversely polarized proton target. The use of a transversely polarized target has been revealed in recent years to be the ideal test bed for the exploration of quark orbital angular momentum and its correlation with transverse spin, both within the nucleon and in the fragmentation process.

3). **PR12-07-107**: *Studies of Spin-Orbit Correlations with a Longitudinally Polarized Target*

Spokesperson: H. Avakian

This experiment will perform semi-inclusive measurements with a longitudinally polarized proton target to measure single and double-spin asymmetries for charged and neutral pion production. These data are sensitive to the helicity distributions and the transverse momentum and polarization distributions of the different quark flavors in the proton.

4). **LOI12-07-101**: *Lambda Polarization in the Target Fragmentation Region*

Spokespersons: H. Avakian, D.S. Carman

This experiment will measure the beam-recoil polarization transfer to the Λ hyperon in semi-inclusive and exclusive processes at large momentum transfer in the target fragmentation region. These measurements are expected to provide information on the strange sea in the nucleon and may shed light on the proton spin puzzle. They will significantly improve the accuracy of previous measurements and allow for decisive tests of models of the reaction mechanism.

5). **LOI12-07-103**: *A Detailed Study of Semi-Inclusive Deep Inelastic Pion Production on Unpolarized Proton and Deuteron Targets with the CLAS12 Detector*

Spokesperson: X. Jiang

This experiment involves a detailed study of hadron multiplicities, their relative ratios, as well as studies of the azimuthal and transverse momentum dependencies of semi-inclusive deep-inelastic production. Data from electron beam energies of 6.6, 8.8, and 11 GeV will be used to study single pion production from unpolarized proton and deuterium targets. The goal of this work is to firmly establish the kinematic region over which semi-inclusive deep-inelastic scattering pion production can

be reliably interpreted to NLO QCD in terms of parton distributions and fragmentation functions.

◇ Deep Inelastic Structure Functions of the Nucleon

1). **PR12-06-109**: *The Longitudinal Spin Structure of the Nucleon*

Spokespersons: D. Crabb, A. Deur, V. Dharmawardane, T. Forest, K. Griffieon, M. Holtrop, S. Kuhn, Y. Prok

This experiment will measure with high accuracy the g_1 spin structure functions of the proton and deuteron for higher x, where the valence quark structure is dominant. This determination of g_1 will test quark model predictions at large x and constrain Δg using NLO-based global parton analyses. Measurements from the resonance region will be used to determine the lowest moments of g_1 over a broad range in Q^2.

2). **PR12-06-113**: *The Structure Function of the Free Neutron at Large x*

Spokespersons: S. Bueltmann, S. Kuhn, H. Fenker, W. Melnitchouk, M. Christy, C. Keppel, V. Tvaskis, K. Griffioen

The ratio of the proton to neutron spin-independent structure functions F_{2n}/F_{2p} in deep-inelastic scattering is poorly known at large x due to theoretical uncertainty in the free neutron structure function. This experiment will minimize the effect of the nuclear corrections by insuring that the scattering occurs on an almost on-shell neutron by tagging the spectator proton.

3). **LOI12-07-102**: *Tagged Neutron Structure Function in Deuterium with CLAS12*

Spokesperson: S. Bueltmann, K. Griffioen, S. Kuhn

This experiment represents an extension of PR-12-06-113 to extract the neutron structure function by tagged deep inelastic scattering of deuterium. Here higher-momentum backward-going protons in the range from 0.2 to 0.7 GeV will be selected as a way of identifying the off-shell neutrons in a regime where final state interactions are minimized. The data are expected to provide important insights into the EMC effect and to discriminate between different models.

◇ Elastic and Transition Form Factors of the Nucleon

1). **PR12-07-104**: *Measurement of G_M^n at High Q^2 with the Ratio Method on Deuterium*

Spokesperson: G. Gilfoyle

This experiment will measure the ratio of quasi-elastic *en/ep* scattering on the deuteron to

determine the ratio of the neutron to proton magnetic form factors in the range of Q^2 from 2 to 14 GeV^2. With the well measured proton magnetic form factor, this experiment will enable the extraction of the much more poorly measured neutron magnetic form factor. Its measurement is part of a broad effort to understand how nucleons are constructed from the quarks and gluons of QCD. This form factor, along with the other elastic nucleon form factors G_E^n, G_M^p, and G_E^p, are provide key constraints on the generalized parton distribution functions.

◇ Experiments Using the Nucleus as a Laboratory

1). **PR12-06-106**: *Study of Color Transparency in Exclusive Vector Meson Electroproduction off Nuclei*

Spokespersons: K. Hafidi, B. Mustapha, L. El Fassi, M. Holtrop

In QCD color transparency would manifest itself by a reduced attenuation of hadron transmission in nuclear matter when it is in a point-like configuration. Studies of this effect with vector mesons will provide strong control of the initial state. In this experiment the coherence length related to the production time will be fixed, shifting the focus solely on the transparency phenomenon.

2). **PR12-06-115**: *Study of the Short Range Properties of Nucleons at $Q^2 < 12$ GeV^2 Using $d(e,e'p)n$ Reactions with CLAS12*

Spokespersons: K. Egiyan, N. Grigoryan, L. Weinstein

This experiment will search for the possible modification of the properties of deeply bound nucleons and search for point-like configurations of the nucleon. These new data could help in testing our knowledge of nuclear models and nucleon modification over a broad kinematic range. This experiment was deferred by PAC30.

3). **PR12-06-117**: *Quark Propagation and Hadron Formation*

Spokespersons: W. Brooks, K. Hafidi, K. Joo, G. Niculescu, I. Niculescu, M. Holtrop, K. Hicks, L. Weinstein, M. Wood, G. Gilfoyle, H. Hakobyan

The goal of this experiment is to characterize the hadronization process during the time the struck quark travels unconfined through the nuclear medium carrying a net color charge, and during the time when it travels as a pre-hadron through the nuclear medium. This experimental program will study a variety of hadrons to characterize important and subtle aspects of hadron formation.

◇ Hadron Spectroscopy

1). **PR12-06-116**: *Nucleon Resonance Studies with CLAS12 in the Transition from Soft to Partonic Physics*

Spokespersons: V. Burkert, R. Gothe, K. Joo, V. Mokeev, P. Stoler

This experiment will study the excited baryon spectrum by measuring photocouplings of established baryon resonances as a function of Q^2, where it is expected that resonant signals rise relative to the backgrounds as Q^2 increases. Photocouplings of these baryons will provide information on the confining mechanism for three-quark hadrons and will provide valuable input to ongoing coupled-channels analyses. This experiment was deferred by PAC30.

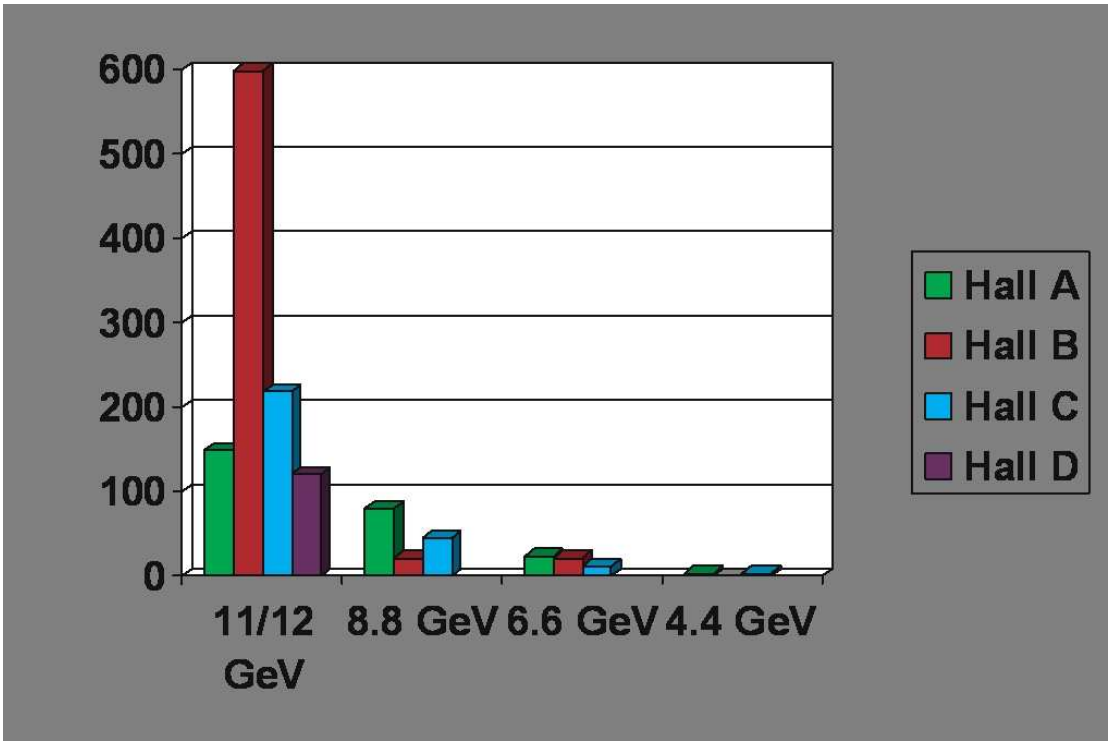

Figure 8.1: Current PAC approved experiment allocation (PAC days) for each of the experimental Halls for the upgrade as a function of beam energy.

Experiment	Status	Beam Request
PR12-06-106: Study of Color Transparency in Exclusive Vector Meson Electroproduction off Nuclei	Approved	40 days
PR12-06-108: Hard Exclusive Electroproduction of π^0 and η with CLAS12	Approved	120 days
PR12-06-109: The Longitudinal Spin Structure of the Nucleon	Approved	80 days
PR12-06-112: Probing the Proton's Quark Dynamics in Semi-Inclusive Pion Production	Approved	60 days
PR12-06-113: The Structure of the Free Neutron at Large x	Conditionally Approved	40 days
PR12-06-115: Study of the Short Range Properties of Nucleons at $Q^2 < 12$ GeV^2 Using $d(e, e'p)n$ Reactions with CLAS12	Deferred	32 days
PR12-06-116: Nucleon Resonance Studies with CLAS12 in the Transition from Soft to Partonic Physics	Deferred	60 days
PR12-06-117: Quark Propagation and Hadron Formation	Approved	60 days
PR12-06-119: Deeply Virtual Compton Scattering with CLAS at 11 GeV	Approved	200 days
PR12-07-104: Measurement of G_M^n at High Q^2 with the Ratio Method on Deuterium	Approved	56 days
PR12-07-107: Studies of Spin-Orbit Correlations with a Longitudinally Polarized Target	Approved	103 days

Table 8.1: Summary of experiments presented to JLab PAC30 and PAC32 focussing on 12-GeV experiments and the base equipment that will be part of `CLAS12`.

Experiment	Status	Beam Request
LOI12-06-108: Transverse Polarization Effects in Hard Scattering at CLAS12	**	—
LOI12-07-101: Lambda Polarization in the Target Fragmentation Region	**	—
LOI12-07-102: Tagged Neutron Structure Function in Deuterium with CLAS12	**	—
LOI12-07-103: A Detailed Study of Semi-Inclusive Deep Inelastic Pion Production on Unpolarized Proton and Deuteron Targets with the CLAS12 Detector	**	—

Table 8.2: Summary of letters-of-intent presented to JLab PAC30 and PAC32 focussing on 12-GeV experiments and the base equipment that will be part of `CLAS12`. For all LOIs, PAC strongly encouraged submission of a full proposal for review.

Part II

Detector

Chapter 1

Design Overview

1.1 System Description

The 12-GeV Upgrade project scope is divided into three major systems: 1) Accelerator System, 2) Physics System, and 3) Civil Construction System. The Physics System is further divided into four systems: 1) Hall A Upgrade, 2) Hall B Upgrade, 3) Hall C Upgrade, and 4) Hall D.

The Physics System equipment planned for the Upgrade project takes full advantage of the apparatus developed for the present program. In HallB, the CEBAF Large Acceptance Spectrometer (`CLAS`), which was designed to study multi-particle, exclusive reactions with its combination of large acceptance and moderate momentum resolution, will be upgraded to `CLAS12` and optimized for studying exclusive and semi-inclusive reactions (emphasizing the investigation of so-called Generalized Parton Distributions and Transverse Momentum Dependent Parton Distributions) at high energy. It will also be used for selected valence quark structure studies involving neutron "tagging" or polarized targets capable of supporting only very low beam current. Most importantly, the maximum luminosity will be upgraded from 10^{34} $cm^{-2}s^{-1}$ to more than 10^{35} $cm^{-2}s^{-1}$. The present time-of-flight counters, Čerenkov detectors, and electromagnetic calorimeters will be retained, but the tracking system and other details of the central region of the detector will be changed to match the new physics goals.

1.2 Upgrade Hall B System Requirements

The Hall B System shall meet the following requirements:

- 11 GeV polarized electrons beam,
- Capability to run at luminosities of 10^{35} $cm^{-2}s^{-1}$,
- Operation of a longitudinally polarized target,
- Capability to detect forward-going, high momentum particles from 5 - 35°,
- Capability to detect recoil baryons at angles >35°,
- Large momentum range for the separation of electrons, pions, kaons, and protons.

The safety of personnel and equipment must be implemented in all phases of the CLAS12 detector upgrade, including R&D, design, construction, and commissioning.

1.3 Technical Approach to Meet the Upgrade Hall B System Requirements

1.3.1 Introduction

The Hall B Upgrade System, also termed the CLAS12 detector, has evolved from the CEBAF Large-Acceptance Spectrometer, or CLAS, to meet the basic requirements for the study of the structure of nucleons and nuclei with the CEBAF 12-GeV Upgrade. A major focus of CLAS12 will be to determine the Generalized Parton Distributions (GPDs). CLAS12 will be able to carry out the core program for the study of the internal dynamics and 3D imaging of the nucleon, and quark hadronization processes. Both of these programs impose broad requirements for measuring multiple uncorrelated particles over a wide kinematic range with good resolution in momentum and angles. These studies are carried out by measuring exclusive and semi-inclusive processes from hydrogen and nuclear polarized and unpolarized targets. The access to GPDs at high photon virtuality requires use of large acceptance detectors capable of operating at high luminosity. Moreover, a program to access GPDs requires use of

polarized solid state targets that can only operate at a limited luminosity. CLAS12 will provide the large acceptance to measure these processes well.

CLAS12 makes use of many existing detector components. Major new components include the superconducting torus coils that cover only the forward angle range, a new gas Čerenkov counter for electron/pion separation, additions to the electromagnetic calorimeters, and the central detector. In the following the modifications and new components are briefly described.

Forward detector: The forward detector system will use several of the existing components: the low threshold gas Čerenkov counters, all electromagnetic calorimeters, and the time-of-flight scintillators. New components include the high threshold Čerenkov counter, the torus magnet, and the forward drift chambers, which will cover an angle range from 5 to 40°. The large drift chambers in CLAS will be replaced by new detectors that will cover the 5 to 40° angle range. Two of the existing detector systems, the time-of-flight system and the electromagnetic calorimeter system, need some upgrading to allow measurement of high momentum forward-going particles. A pre-shower detector will be inserted in front of the existing CLAS electromagnetic calorimeters to allow high energy photon detection and separation of single photons from neutral pion events. Improved particle identification will be accomplished by several means: the timing resolution of the scintillation counters will be improved by adding an additional layer of scintillators with 40% the widths of the existing layer and by using PMTs with better timing characteristics.

Central detector (CD): A main component is a compact superconducting solenoid magnet, which has a triple function: it provides magnetic shielding of all tracking detectors from charged electromagnetic background, mostly Møller electrons and particles from secondary interactions. It provides the magnetic field for the momentum analysis of charged particles at large angles, and it provides the uniform 5-T field needed for the operation of a dynamically polarized solid state target. The CD will detect charged particles from 35 to 125°. Several layers of silicon strip sensors will provide momentum analysis. Particle identification is achieved by the combination of momentum analysis and time-of-flight measurements in the scintillation counters.

Beamline and targets: Most of the existing beamline components will be re-used without changes. This includes the photon tagger and pair spectrometer, the polarized photon instrumentation, a polarized target for photon experiments, and beam position and current monitors.

1.3.2 Design Solutions to Fulfill the Requirements

Requirement 1 (11-GeV beam capability) is satisfied by upgrading the 11-GeV Hall B beamline transporting electrons from the extraction region into the hall. This scope resides within the Accelerating Systems Beam Transport WBS 1.3.4 and the Hall B Upgrade Beamline WBS 1.4.2.5.

Requirement 2 (luminosity capability) requires a factor of 10 increase over the existing CLAS luminosity. This requirement drives two parts of the Hall B upgrade: the development of improved Møller electron shielding and changes in the drift chamber geometries.

Improved Møller Electron Shielding

The present luminosity limit for electron scattering experiments comes from Møller electrons produced in the target that interact either directly (first region of drift chambers) or through primary photons and the production of secondary particles in the support structures and torus coils with all three regions of drift chambers. A large fraction of the Møller electrons affecting the first region are already shielded using a small toroidal magnet that does not block higher-energy charged particles from reaching the drift chambers, but which deflects the Møller electrons into the outer surface of massive shielding where they are absorbed. This method allows CLAS to operate at a luminosity of 10^{34} cm^{-2}s^{-1}. In the course of CLAS operation of polarized targets using Helmholtz coils, it was determined that solenoidal shielding would be more effective at suppressing Møller electrons, because these electrons are 'trapped' starting at their point of origin and they can be transported and dumped on the interior of a conical pipe, rather than on an exterior surface. Subsequent simulations have validated this conclusion, and in addition showed that a strong solenoidal field with a large $\int Bdl$ gains another factor of $\sim$1.5 in luminosity increase, showing the luminosity increase is expected to be a factor of $\sim$3 in this approach. However, use of solenoidal shielding is not practical in the current CLAS except for experiments where the particles of interest are confined to small angles, since a solenoid magnet will block larger-angle particles that are needed for many experiments. The technical solution for CLAS12 is to use solenoidal shielding where detector elements within the magnet bore cover the angles that would otherwise be blocked. The discussion of Requirement 5 will elaborate further on this solution. Requirement 4 (forward-angle range from 5 to 35°), which specifies a minimum angle of 5° at 50% acceptance in azimuthal angle for measured particles,

means that the cone of Møller electrons must be confined to a significantly smaller angle so as to not flood the active detector volumes with low-energy tracks. This requires that the $\int Bdl$ provided by the solenoid magnet downstream of the target must be sufficiently high to confine the Møller electrons into a small forward cone where they can be safely absorbed. In detailed simulations of the field needed for this it was determined that a 5-T field was required with $\int Bdl$ =2.5 Tm downstream of the target, thus fixing the maximum solenoid field specification and its length. The other limit of Requirement 4, a maximum angle of 35°, constrains the geometry of the massive components of the magnet. This requirement means that the downstream end of the solenoid needs to be a conical aperture allowing 35° particles from the cryo-target to pass through, thus fixing the downstream geometrical specification of the solenoid magnet.

Drift Chamber Geometry

Since improving the Møller shielding yields a factor of ∼3 increase in the luminosity limit, a remaining factor of 3-4 needs to be obtained relative to the existing drift chambers by reducing the solid angle of the drift chamber cell sizes in order to achieve Requirement 2. The rate due to charged particles is approximately proportional to the drift chamber cell radius for a fixed distance between the target and the chamber. The new Region 1 forward chamber will be at a 2.5 times larger distance from the target than the existing chamber (200 cm vs. 80 cm), which by itself will provide a luminosity limit increase of approximately a factor of 2.5. Further rate reduction (factor ∼2) is obtained by using a reduced time window due to the use of a higher field gradient, a slightly reduced wire spacing, and an additional reduction due to the better shielding of the large $\int Bdl$ of the solenoid field. The 5-35° angle coverage in Requirement 4, together with the design choice of six-layer superlayers (to maintain the existing level of redundancy) and the wire spacing reduction, determines the forward drift chamber channel counts. All three regions have 112 channels/layer/sector, and there are 12 layers per region, which for six sectors yields a total channel count of $112\times12\times3\times6 = 24{,}192$ drift chamber cells. Region 2 and Region 3 also need significantly lower rates, which are achieved by a combination of reduced production of secondary background particles and the reduced solid angle coverage due to the larger distance from the target, although this effect is smaller for the Region 2 (factor ∼1.7) and the Region 3 (factor ∼1.3) than for Region 1 (factor 2.5). The combined increase in luminosity due to improved Møller electron shielding and the reduced sensitivity of

the drift chamber cells was obtained in a detailed simulation and event reconstruction analysis with realistic physics background that resulted in comparable occupancies and reconstruction efficiencies for the CLAS12 and CLAS configurations at 10 times higher luminosity for CLAS12.

Requirement 3 (longitudinally polarized target) is satisfied by adapting the design of the existing polarized target to the geometry and conditions resulting from addressing Requirement 2 as discussed above. Specifically, the polarized target cell operates in magnetic fields of high intensity, typically 3 to 5 T, and high uniformity, and that is oriented along the beam axis. The 5-T solenoid field required to satisfy Requirement 2 can be used for this purpose, as long as the field uniformity required can be achieved. The field uniformity required is 10^{-4} within a cylindrical volume 3 cm in diameter and 10 cm in length. This requirement sets the field uniformity specification for the solenoid magnet.

It should be noted that there are a number of differences between the existing polarized target and the CLAS12 polarized target. The most important one is that the CLAS12 polarized target is fully contained in a cylindrical cryostat of 10-cm diameter and uses the 5-T field of the solenoid as the polarizing field. It can thus be used in conjunction with the tracking detectors in the CLAS12 central detector. The existing polarized target has its own large 5-T magnet coils integrated into the same vacuum system, and cannot be used together with the CLAS12 central tracking detectors and the solenoid magnet. Also, the target mounting mechanism must be of a different geometry than the existing design. All of these considerations are being taken into account.

Requirement 4 (capability to detect high-momentum particles from 5 to 35°) has been partially discussed under Requirement 2 above. High-momentum charged particles are detected by the combination of the forward part of the silicon vertex tracker, the drift chambers, the magnetic field from the torus magnet, and the time-of-flight scintillators. The silicon vertex tracker is addressed in the discussion of Requirements 5 and 6. The design solution for the drift chambers that satisfies Requirement 2 as discussed above is adequate to satisfy Requirement 4 as well. The resolutions achievable with the wire spacing given and the planned drift chamber gas are consistent with the missing mass resolution needed to reconstruct missing particles. The timing information from the time-of-flight counters is needed to perform the time-based tracking needed for the drift chamber analysis. The magnetic field needed to momentum-analyze the detected charged particles is determined by the energy ranges of the particles and the geometries of the detectors and magnets. The maximum field value and

the profile of its intensity have been determined and specified by these considerations. The azimuthal angle coverage extends down to polar angles of 5° where it is 50% of 2π. The minimum angle coverage in the CLAS standard configuration is limited to about 10° and covers a smaller range in azimuthal angle. The fall-off in integrated field strength is also significantly different from the existing torus, and is well-matched to the momentum spectra of the charged particles anticipated.

Neutral particles at high energies will be detected using the forward calorimeters. Because of the increased beam energies, neutral pions at high momentum are no longer able to be detected with the existing CLAS forward calorimeter, necessitating the addition of the pre-shower calorimeter that has a finer-grained readout that can resolve the two photons from neutral pion decay. The parameters of the pre-shower calorimeter have been optimized for this purpose, determining the specifications for the device. Neutrons will be detected in the pre-shower calorimeter, as well as the existing calorimeter, increasing the overall efficiency of neutron detection. The increase in granularity also translates into an improved angular resolution for neutrons detected in the pre-shower calorimeter. While the design was optimized for neutral pions, as driven by Requirement 4, the improvement in neutron detection is an important additional benefit.

It should be noted that the fulfillment of Requirement 4 is supported in an important way by Requirement 6 (particle identification over a wide momentum range), since 'detecting' a particle generally requires a determination of the particle type.

Requirement 5 (detecting recoil baryons at large angles) is addressed by the central detector package. This detector set is mounted inside the solenoid magnet. It includes the barrel portion of the silicon vertex tracker, a time-of-flight array, and the provision of space for a compact detector for neutral particle detection. Determination of the charged particle momentum is performed by recording the hit positions of the helical trajectories in the silicon vertex tracker in the solenoid magnetic field. Identification of the particle type is performed by combining the momentum information with the time as measured by the time-of-flight system. The parameters of the barrel portion of the SVT, such as strip pitch, level of redundancy, and thickness of materials are chosen to optimize detection of recoil particles.

Requirement 6 (particle identification over a large range in momentum) has been addressed by a number of design choices. A second gas Čerenkov counter that has a higher pion detection threshold was added to increase the range of electron-pion separation to approximately 5 GeV.

This high threshold Čerenkov counter (HTCC), which is located in front of the Region 1 drift chamber, is designed to have minimal mass to reduce its impact on the tracking information. To further reduce the impact of this added mass, the forward part of the Silicon Vertex Tracker (SVT) was added, which samples tracking information before the particles arrive at the HTCC and provides a track vector to match to the forward drift chambers.

The location of the HTCC just downstream of the target and before the torus magnet and the drift chamber system is a natural choice that does not add much length along the beam line to the overall length of CLAS12. The relative positioning of the solenoid and the torus magnet is largely determined by the out-of-plane forces the transverse magnetic field of the solenoid exerts on the current in the torus coils. The transverse magnetic field must be limited to <50 G to limit distortions of the torus coil panels to acceptable levels, which requires a distance of at least 220 cm from the solenoid center (target center) to the torus coils. This space is ideally suited for inserting the HTCC detector, which requires an overall length of approximately 150 cm beginning 30 cm downstream of the target center.

A second component of the particle identification scheme is to use the existing panels of time-of-flight scintillators in the forward region and to add a second layer with smaller scintillator widths and new photomultiplier tubes to construct new time-of-flight detectors with better timing resolution. This requirement is the basis for the specifications for their performance. A third component is the time-of-flight counters within the solenoid magnet, part of the central detector, which was mentioned in the discussion of Requirement 5. Identification of the particles in this lower-momentum region is important and it drives the performance requirements for these detectors.

Finally, as already discussed for Requirement 4, the pre-shower calorimeter is required to identify neutral pions at the highest energies. While it has been optimized for this purpose, it will also improve the identification of electrons, pions, and neutrons.

1.4 Superconducting Torus and Solenoid Magnets

The CLAS12 spectrometer system (see Fig. 1.1) contains two superconducting magnets, a 5-T solenoid magnet and a toroid magnet with a maximum field of 2.5 T. The two magnets provide magnetic analysis of charged particles in the large-angle range and the forward-angle range, respectively. The magnets are separated in space by a distance of about 1.5 m and

their respective fields are partially overlapping. Owing to its symmetry properties, the toroid field drops rapidly with distance and has virtually no impact on the solenoid magnet. In particular, since its field is zero on the beam axis, it does not affect the homogeneity of the solenoid magnet in the critical target region. The solenoid field drops more slowly with distance and exerts a measurable force on the coils of the toroid magnet that must be taken into account in the mechanical design of the toroid magnet. At the closest distance between the solenoid and toroid magnets, the coil deflection is about 1.3 mm. Since the solenoid field is cylindrically symmetric, it affects all six toroid coils in the same way.

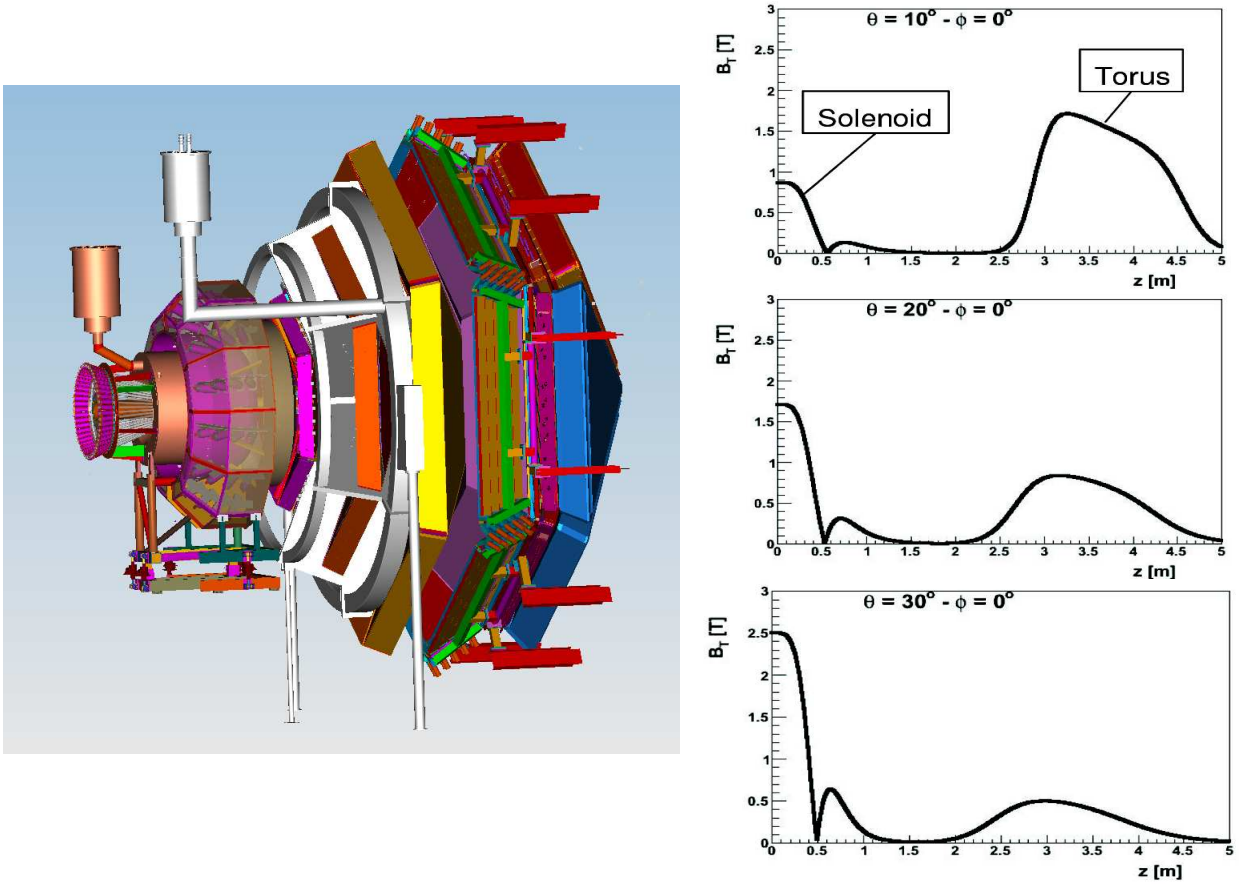

Figure 1.1: (Left) `CLAS12` showing the solenoid (brown) on the left and the torus (gray) between the drift chambers. (Right) `CLAS12` transverse magnetic field as a function of z for polar angles of 10°, 20°, and 30° at ϕ=0°. The torus transverse field becomes weaker with increasing angle, while the solenoid transverse field increases in strength.

1.4.1 The CLAS12 Toroid

CLAS12 is a magnetic spectrometer based on six super-conducting coils arranged around the beam line to produce a field primarily in the ϕ direction (see Fig. 1.2). The choice of this configuration leads to an approximate toroidal field distribution around the beam axis. It has been driven by the necessity of satisfying the precise requirements determined by the physics program of:

- uniform coverage of a large angular and momentum range for charged and neutral particles;
- good momentum and angular resolution; due to the Lorentz boost, the average momentum increases with decreasing emission angle from the target and the relative momentum resolution ($\Delta p/p$) has to improve in the forward direction to maintain a constant absolute resolution;
- good particle identification; the open structure of the toroid allows for long path lengths for charged and neutral particles for good particle identification through time-of-flight measurements, high luminosity, and counting rate capability: expected operating luminosity is 1×10^{35} cm^{-2}s^{-1}.
- low background from electromagnetic processes (Møller electrons; e^+e^- pairs, etc.);
- symmetry around the beam axis;
- compatibility with the operation of a polarized target; the field symmetry of a toroid provides full field compensation on the magnetic symmetry axis and allows operation of polarized targets near the beam axis with their own magnetic holding fields.

The toroid configuration offers a field-free region around the target and a magnetic field that is always transverse to the particle trajectory. The first characteristic allows the installation of a polarized target with no interference between the target and detector magnetic fields. In addition, since the ϕ pattern of the event is preserved in the toroidal magnetic field, the determination of the azimuthal angle ϕ is decoupled from the measurement of the polar angle θ and momentum p.

The six coils have been shaped to give the desired $\int Bdl$, and therefore, the requested resolution as a function of θ. The coil-operating temperature of 4.5 K is maintained by a

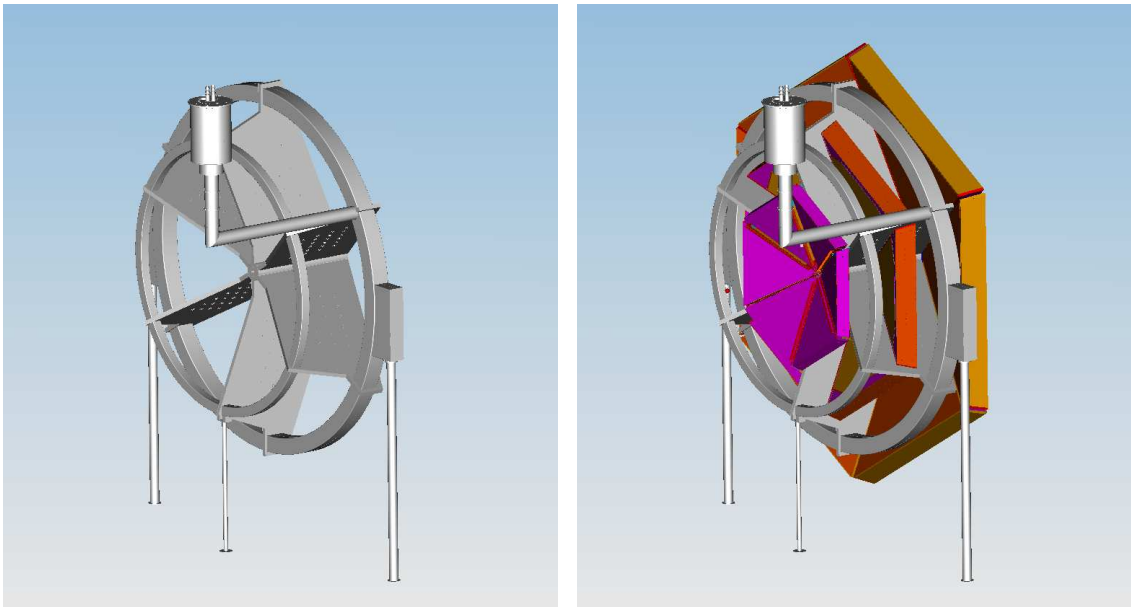

Figure 1.2: The CLAS12 toroid magnet. The left panel shows the toroid model by itself and the right panel shows the toroid with the full set of drift chambers attached.

forced flow of super-critical liquid helium supplied by the Central Helium Liquefier (CHL). The total stored electromagnetic energy at the nominal operating current is 16 MJ. Table 1.1 shows the main parameters of the toroid coils.

1.4.2 The CLAS12 Solenoid

Solenoid magnets provide an ideal field distribution for the analysis of particle trajectories in the central region, where the bending power of the solenoid field is at a maximum. In CLAS12 the choice of a 5-T strong solenoid field has been driven by the necessity of satisfying precise requirements determined by the physics program of:

- large opening for charged and neutral particles in the forward hemisphere; high momentum forward-going particles will not experience high enough transverse field components from the solenoid field and must be momentum-analyzed in the toroidal field located downstream of the solenoid magnet. An opening in θ up to $\pm 40^\circ$ is required;
- good charged particle momentum resolution in a limited radial space for polar angles θ from 35° to 125° and momentum range from 0.3 to 1.3 GeV;
- operation of a dynamically polarized target; requires a high magnetic field with field non-uniformity over the target volume of $\Delta B/B < 10^{-4}$;

Conductor	NbTi
Configuration, overall dimensions	Six trapezoidal sections
Radial thickness	294 mm
No. of double pancakes in section	1
No. of turns in double pancake	2×140 = 280
Conductor length (one section)	2.43 km
Conductor length (torus)	14.56 km
Torus inductance	3.12 H
Conductor current	3150 A
Amp-turns (one section)	0.882 mA
Amp-turns (torus)	5.3 mA
Stored energy (torus)	15.5 MJ
Max. field (at the winding)	4.6 T
$\int Bdl$ (θ=40°)	0.517 Tm
$\int Bdl$ (θ=5°)	3.32 Tm
$\int Bdl$ (θ=20°)	1.43 Tm

Table 1.1: Parameters of the torus reference winding.

- high luminosity operation; the solenoid field offers an effective shield of the sensitive tracking detectors against the very high background of Møller electrons. The longitudinal field keeps low-energy electrons (and positrons) away from the sensitive tracking detectors and guides them into areas where they can dump their energy in specially designed heavy metal (lead or tungsten) absorbers;

- compensation of the solenoid magnetic stray field; the CLAS12 detector setup requires locating magnetic sensitive photon detectors in areas surrounding the solenoid magnet. The magnetic field drops only slowly with radial distance, and must be shielded with additional superconducting compensation coils built directly into the same cryostat as the solenoid coils and powered in series with the main coils. The field in the sensitive regions can be compensated to values below 25 G.

The solenoid magnet provides a strong effective field needed for a dynamically polarized solid-state target. At the same time, the solenoid field is used for particle tracking and momentum analysis by measuring the trajectory of charged particle in the field with a high-resolution tracking detector. Fig. 1.3 shows the magnetic field distribution associated with the solenoid design.

The total $\int Bdl$ on the magnetic axis is 6.0 Tm and the stored energy at the 5 T central field is 25 MJ. The main parameters are given in the Table 1.2.

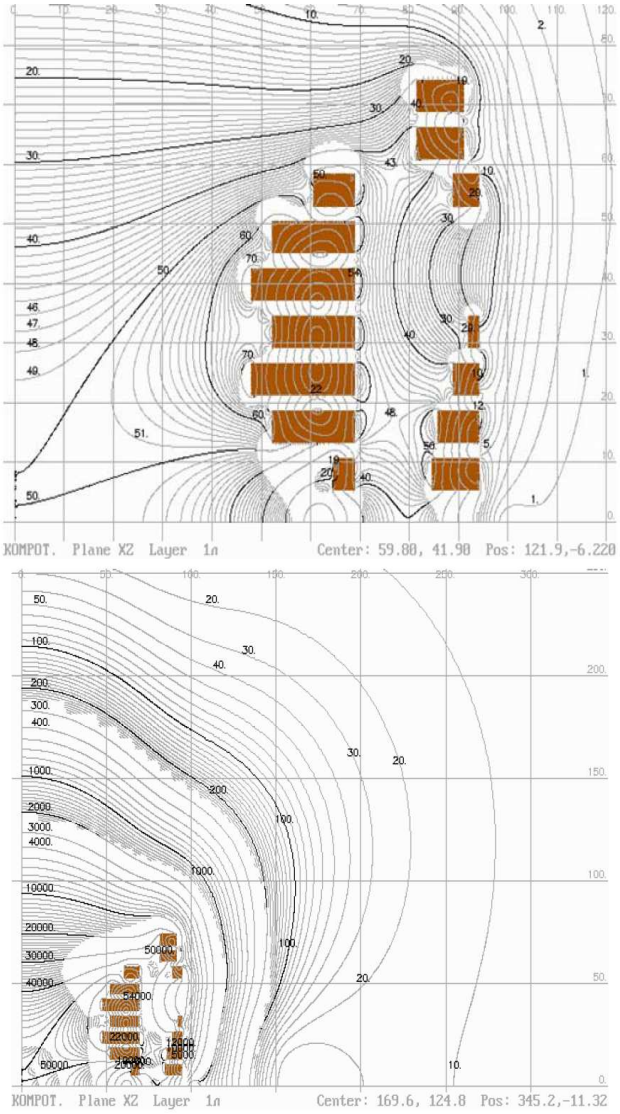

Figure 1.3: (Top) One "quadrant" of the 5-T superconducting solenoid coil system. Shown is the inner main coil and the outer compensation coil. Also shown are lines of constant field. (Bottom) The large distance field distribution, showing the effect of the compensation coil. At a 1.5 m radial distance at z=0 from the symmetry axis, the field strength is below 15 G. (Coordinates given in cm.)

Main winding	
Inner diameter	943 mm
Aperture	780 mm
Max. outer diameter	1300 mm
Length	1225.6 mm
Number of turns	4000
Shielding winding	
Min. inner diameter	1636 mm
Outer diameter	1804 mm
Length	1685.2 mm
Number of turns	1800
General	
Inhomogeneity in working area	5 ppm
Field in center	4.5 – 5.0 T
Field at PMTs	<18 G
Max. field at the winding	6.8 – 7.5 T
Nominal operating current	2399 – 2665 A
Inductance	6.95 H
Stored energy	19.99 – 24.68 MJ

Table 1.2: Parameters of the solenoid reference winding.

Chapter 2

Tracking Systems – Drift Chambers & Vertex Tracker

2.1 Physics Requirements for CLAS12 Tracking

The CLAS detector in Hall B is being upgraded to take advantage of the increase of the CEBAF beam energy from 6 to 12 GeV, thus the new name, CLAS12. There are several broad areas of physics enquiry that drive these changes: spectroscopic studies of excited baryons, investigations of the influence of nuclear matter on propagating quarks, studies of polarized and unpolarized quark distributions, and a comprehensive measurement of generalized parton distributions (GPDs). Many of the reactions of interest are electroproduction of exclusive and semi-inclusive final states. The cross sections for these processes are small, necessitating high-luminosity experiments. A variety of simulated experiments rely on luminosities of 10^{35} cm^{-2}s^{-1} to achieve the desired statistical accuracy in runs of a few months duration. The new kinematic range to be explored is characterized not only by smaller cross sections, but also by more outgoing particles per event, with those particles being emitted with higher values of momentum and at smaller laboratory angles. These basic physics criteria drive the design.

The deep exclusive reactions, in which an electron scattering at moderate to high values of Q^2 results in a meson-baryon final state, provide the most stringent requirements for the CLAS12 tracking system. A final state of a few high-momentum, forward-going particles (the electron as well as one or more mesons), combined with a moderate-momentum baryon emitted

at large angles, is the typical event type that determines the specifications of the tracking system.

The higher momentum and more forward angles of most hadrons leads us to split the design into a "forward" detector, which covers lab angles between 5° and 40°, and a "central" detector for hadrons with angles greater than 35°. The higher luminosity goal necessitates the use of a solenoidal magnet to shield the detector from Møller electrons. To reduce interactions between this solenoidal field and the main CLAS12 toroidal field, and to facilitate construction and installation of new detector elements, the torus has been re-designed. It is more compact than the present CLAS torus, while providing equivalent bending power. This smaller torus design provides several advantages in the overall detector design: it decouples the design of the central solenoid and detector from that of the torus and forward tracking system, and it makes detector installation and removal easier.

In broad strokes, the detector must provide tracking for laboratory angles as small as 5° and as large as 125° in order to cover as much of the hadronic center-of-mass region as possible. We require very good momentum and angular resolution for the scattered electron in order to determine the virtual photon flux factor, Γ_v, to an accuracy of a few percent. Because the average particle momenta will be higher, the resolution of the tracking system must be better than the current CLAS values; the goal for the fractional momentum resolution is 0.5% to 1% at a track momentum of 5 GeV. Angular resolutions of about 1 mrad are required for the electron in order to know the virtual photon flux factor, and hence, the cross section, to a few percent. Finally, good vertex resolution will allow detection of secondary decay vertices and serve as a good marker for strangeness production.

Because only about 20% of the total charged particle momenta is carried by tracks in the central region, the fractional momentum resolution requirement for the central tracking system at a momentum of 1 GeV is 5% in order to match the absolute momentum resolution of the forward tracking system. This momentum resolution of about 50 MeV is necessary in order to positively identify a missing pion in these exclusive reactions. Similarly, to keep our knowledge of the individual vector components of the momentum at the 25 MeV level, the central trackers angular resolution should be of the order of 1.5°. Our present design has an expected performance about a factor of two better than these simple limits.

A tracking system capable of achieving these standards was described in the PCDR [263] and quantitatively parameterized in a "fast" Monte Carlo program [264]. A number of CLAS

collaborators used the model of the detector as described in FASTMC in proposals presented at JLab PAC30 and PAC32 [265, 251].

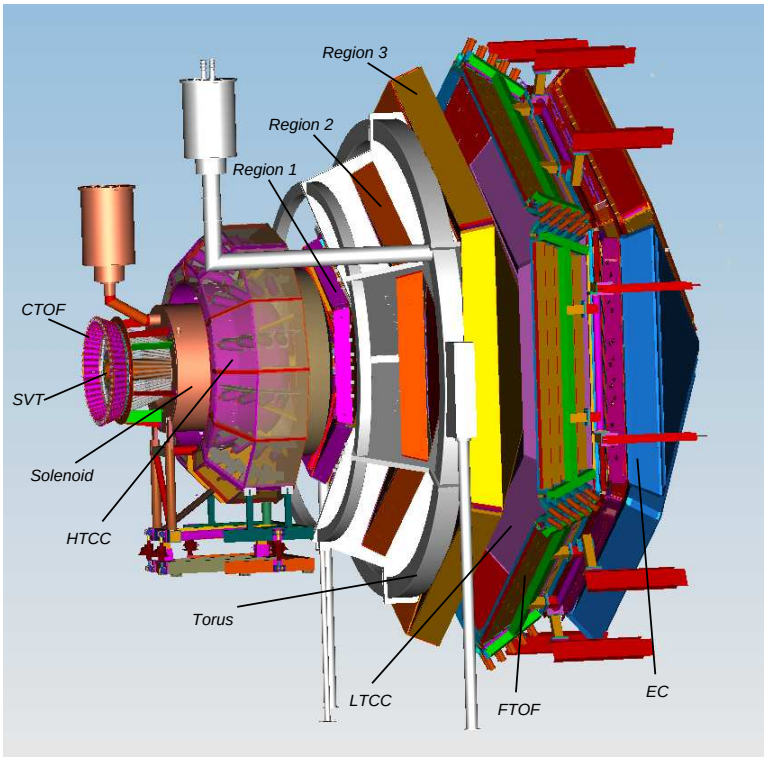

Figure 2.1: A three-dimensional view of the proposed CLAS12 detector highlighting the various subsystems.

2.2 Tracking System Design

As noted above, the CLAS12 detector is divided into a forward and a central detector. Fig 2.1 shows a perspective view of the CLAS12 detector. A solenoid magnet surrounds the target, followed by a Møller absorber on the beam-line and a high-threshold Čerenkov counter for electron identification. Besides curling background Møller electrons into the absorber, the solenoid provides a nearly constant magnetic field that allows charged particle momentum determination by a set of "central tracking chambers" consisting of 8 layers of silicon strip sensors. This central tracking region covers polar angles from 35° to 125°. Just downstream of the cylindrical central tracker are the "forward vertex chambers": 6 layers of silicon strip chambers. Downstream of the high-threshold Čerenkov counter is the torus magnet that supports three "regions" of "forward drift chambers", designated as Regions 1, 2, and 3. Surrounding

and downstream of the torus/drift chamber assembly are the forward time-of-flight counters, a low-threshold Čerenkov counter for hadron identification, and two sets of electromagnetic shower counters. This document describes each of the elements of the CLAS12 tracking system, the central tracker, the forward vertex tracker, and the forward drift chambers.

We have designed the tracking detectors with these external constraints: a solenoid of 5 T central field value and a radius available for tracking detectors of 25 cm, a new torus with a different aspect ratio but with the same number of amp-turns as the present CLAS torus, an expected background rate consistent with a luminosity of 10^{35} cm^{-2}s^{-1}, and a separation between the "forward" and "central" regions defined to be at about 40°; specifically the forward tracking chambers are designed to cover scattering angles between 5° and 40° and the central tracker will cover 35° to 125°. Although the torus cryostat will limit the azimuthal coverage to about 50% at 5°, our goal is that the inactive portion of the drift chambers not further intrude into the active volume; i.e. the dead areas of the drift chambers (endplates, electronics, etc.) will be located in the "shadow" of the coil as viewed from the target. For Region 2, this is not possible; but we shall try to minimize this dead area. To summarize, we are designing the CLAS12 tracking system with the requirements shown in Table 2.1.

	Fwd. Tracker	**Central Tracker**
Angular coverage	5° - 40°	35° - 125°
Momentum resolution	$dp/p < 1\%$	$dp/p < 5\%$
θ resolution	1 mrad	1 mrad
θ resolution	1 mrad	5 - 10 mrad
ϕ resolution	1 mrad/sin θ	5 mrad/sin θ
Luminosity	10^{35} cm^{-2}s^{-1}	10^{35} cm^{-2}s^{-1}

Table 2.1: General specifications for CLAS12 tracking.

2.2.1 Forward Tracking Design

The higher beam energies available to CLAS12 mean that tracks will go more forward and have higher momenta than for the present CLAS experiments. We thus require better resolution from the forward drift chambers. Our design should give better spatial resolution than the

present CLAS chambers for several reasons: the use of thicker (30-μm diameter) sense wires will result in a more linear drift velocity, all cells in a superlayer will be identical, easing the calibration, and the simpler mechanical structure should make these chambers easier to survey. The other feature of higher energy and associated smaller cross sections, requires the use of higher intensity beams. The resultant higher backgrounds represent the primary motivation for the central solenoidal magnet and Møller absorber. The higher background can also be mitigated by cells that cover a smaller angular range and have a smaller active time window.

Forward tracks (angles between 5° and 40°) will be momentum-analyzed by passing through the magnetic field of the torus. The magnet provides an integral Bdl of almost 3 T-m at 10°, falling to about 1 T-m at 30° (see Fig. 2.2).

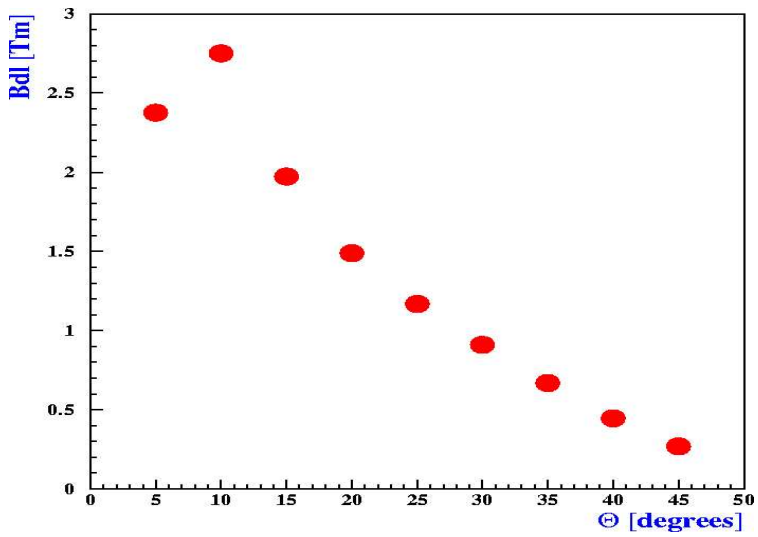

Figure 2.2: The integral of the B field times path length along rays from the target at various angles.

Such forward tracks will first pass through six layers of the forward silicon vertex tracker (FST); a silicon strip tracker with a strip pitch of 150 μm arranged with alternating V-W stereo layers with a stereo angle of $\pm 12°$, located about 27 cm from the target. These tracks will then traverse the high-threshold Čerenkov counter (HTCC) before entering the Region 1 drift chamber at a distance of 2.1 m from the target. The track continues through the magnetic field region and its trajectory is measured in two more drift chambers, denoted Regions 2 and 3, respectively. The Region 2 and 3 chambers are located at 3.3 and 4.5 m from the target, respectively. The FST should localize hits with an estimated accuracy of about 50 μm perpendicular to the strip direction, while the three regions of drift chambers are expected to

have spatial resolutions of about 250 μm per layer. The expected momentum resolution from such an assembly is a function of angle, ranging from about 0.3% at 5° to about 1.0% at 30°, and nearly constant as a function of momentum. The angular resolution falls rapidly with increasing momentum, but should be better than 2 mrad at a momentum of 1 GeV.

2.2.2 Central Tracking Design

The momentum and angular resolution goals for the central tracker are set by the requirement that we be able to positively identify a single missing pion; roughly a 50 MeV momentum resolution is needed, i.e. a fractional momentum resolution of 5% or better at a track momentum of 1 GeV. Our design consists of 8 layers of silicon strips with alternating plus and minus stereo angle strips. Each detector plane is formed as a polygonal shell with the silicon strips running along the z-direction. Each single-sided layer is comprised of 300-μm thick silicon. This detector has good intrinsic resolution in the r-ϕ coordinate due to the small strip pitch (150 μm readout and 75 μm implant pitch). It relies on a small stereo angle to determine the r-z position of tracks.

A solenoidal magnet contains the target, the silicon vertex tracker, the central time-of-flight system (CTOF), and the Møller absorber. Charged particles with emission angles greater than 35° follow helical paths through the 8 layers of the BST, which are arranged into four V-W modules with "V" and "W" referring to strip orientations. The time resolution of the CTOF (∼60 ps) will enable particle identification of the charged tracks, as well as allowing for a very efficient rejection of out-of-time accidentals.

2.3 Silicon Vertex Tracker for CLAS12

2.3.1 Overview

The Silicon Vertex Tracker (SVT), anticipated to have ∼65,000 channels, will consist of a forward silicon tracker (FST) and a barrel silicon tracker (BST). The θ-coverage of the forward part is from 5° to 35° and that of the barrel part is from 35° to 125°. Conceptual design studies started in 2004 [266]. For both the forward and barrel parts, the ϕ coverage is nearly 2π. The SVT will be centered inside the 1800-mm long solenoid, that has an outer and inner diameter of 2040 mm and 780 mm, respectively .

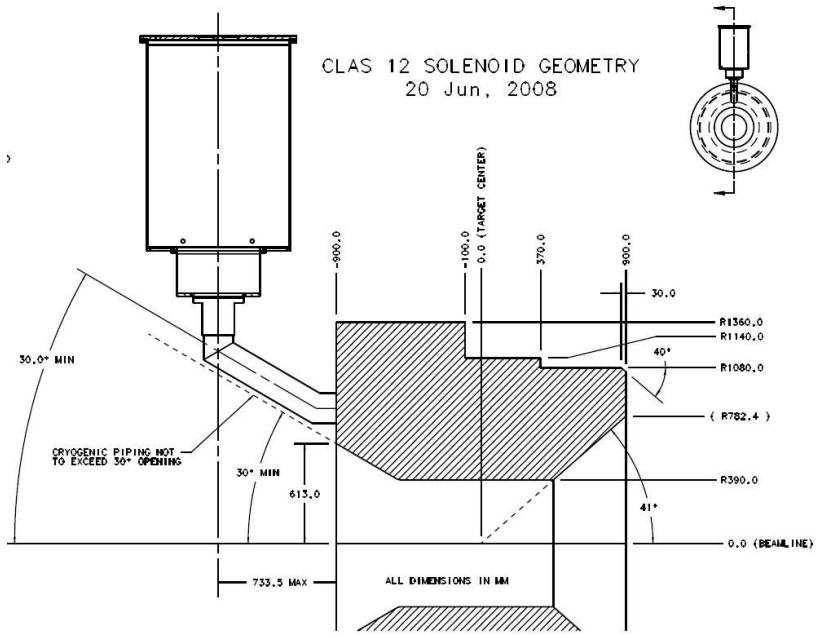

Figure 2.3: Side view of the solenoid magnet (units in inches – with mm in parentheses).

2.3.2 Configuration

Several configurations of the BST and the FST were studied [267] with the aim to optimize the layout with respect to operability, performance and cost. The BST is designed to have four regions and the FST is designed to have three regions. The BST and FST form two independent detectors (see Fig. 2.4), providing operational flexibility in that either or both detectors could be used in a given experiment. There are only three FST regions because the FST will be used in conjunction with the three drift chambers in the forward region.

2.3.3 Rate Estimates

Event and background rates were estimated using a GEANT simulation [268, 269]. These studies indicate that the maximum rate, including electromagnetic background for a full-field setting of the solenoid (5 T) is ∼40 MHz in the FST and ∼60 MHz in the BST. In Fig. 2.4, the green and red curve (full and half-field settings of the solenoid) along the beam axis is the Møller electron envelope, on the surface of which the rate is ∼1 MHz. The rate drops rapidly with increasing scattering angle [269].

To keep Møller electron rates on the FST sensors less than 1 MHz, the first region of the FST is placed at z=256.405 mm (see Figs. 2.4 and 2.5), past the intersection of the Møller

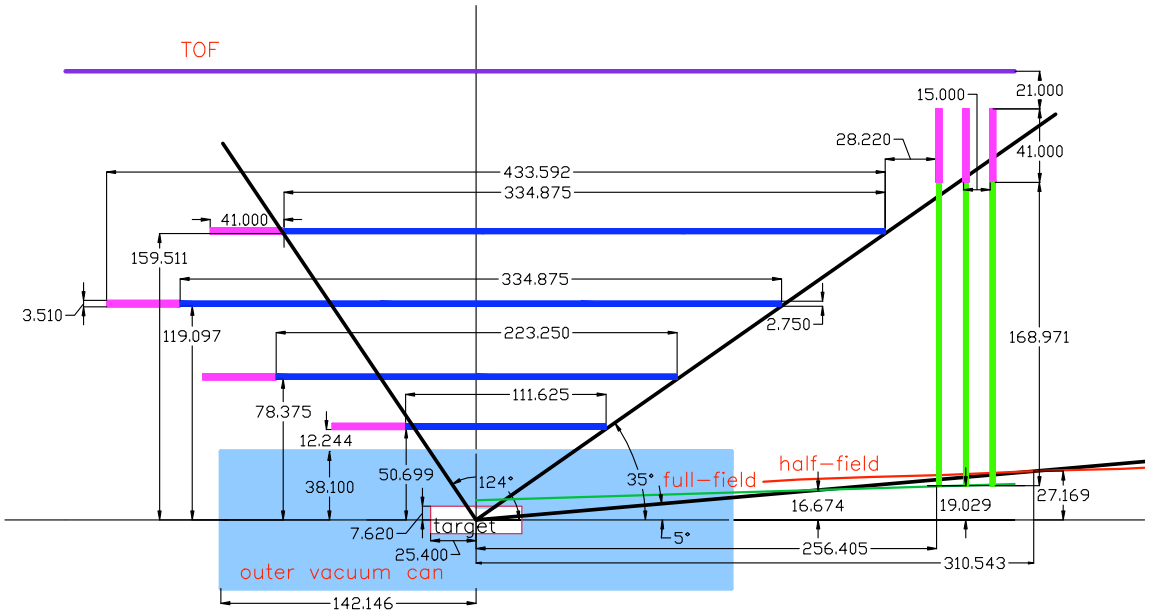

Figure 2.4: Side view of the SVT showing the layout of the barrel and forward regions (all dimensions in mm).

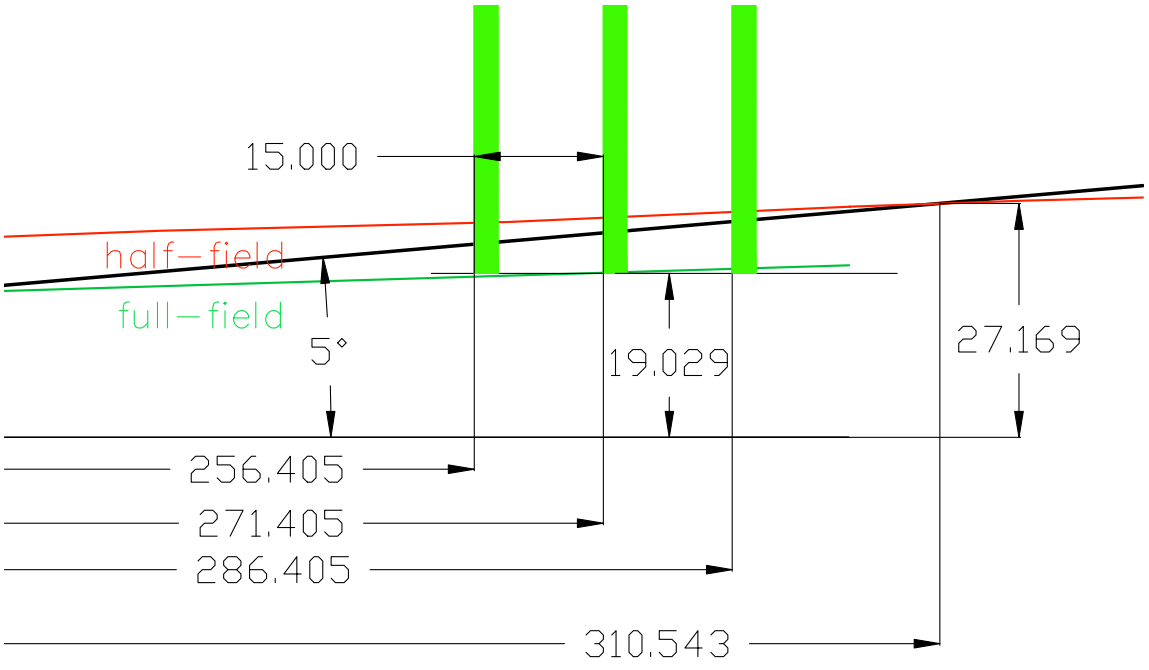

Figure 2.5: Close up view of the three forward SVT regions near the beam line and the Møller absorber.

electron envelope for the full-field setting with the keep-out zone, defined to be a cone with a half opening angle of 5°. The second and third regions of the FST are at z=271.405 mm and z=286.405 mm, respectively.

2.3.4 Forward Silicon Tracker (FST)

The trapezoidal sensors of the FST are designed to be identical. Such a design requires that the regions be parallel to the beam axis, rather than ride the 5° keep-out cone. In ϕ, each FST region consists of 15 sectors as shown in Fig. 2.6.

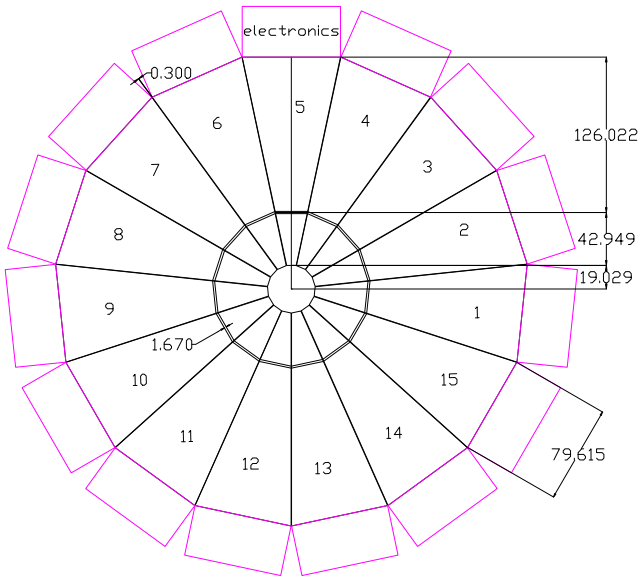

Figure 2.6: Front view of the first region of the FST showing the layout and positioning of the trapezoidal sensors.

In the critical region around the beam axis at r ~19 mm, because the sensors are trapezoidal, the V and the W layers of a region each have ~40 strips per sector, distributed over 2π, a total of ~600 strips per layer. The rate near the beam axis has to be handled by these 600 strips. Though 600 strips per layer around the beam axis appears to be a small number, the readout electronics associated with these strips will on average have a rate-load of ~10 kHz that can be handled by the readout electronics.

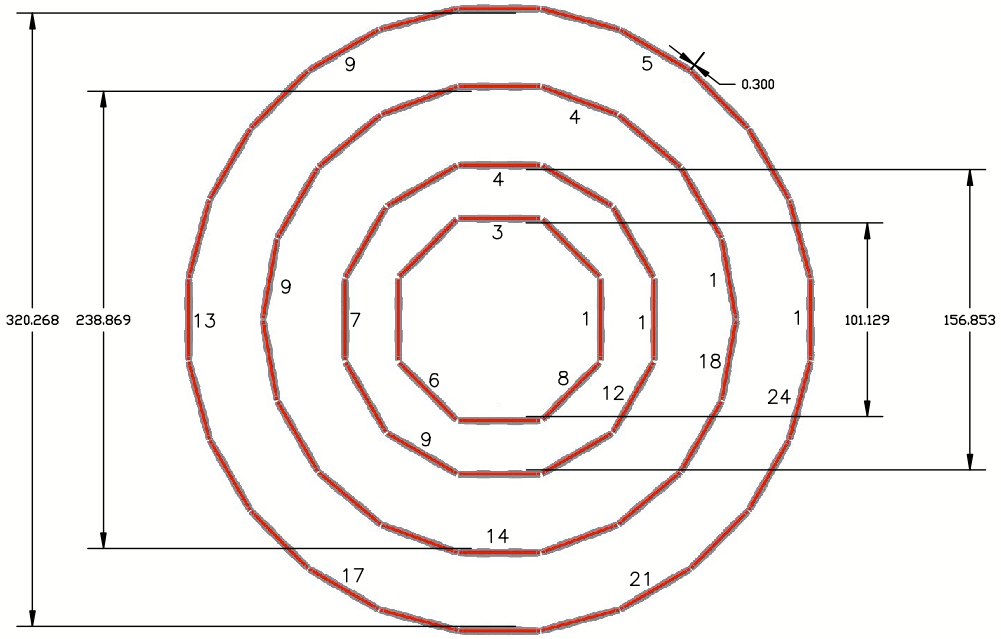

Figure 2.7: Rear view of the barrel section of the SVT showing the sensor partitioning in each region.

2.3.5 Barrel Silicon Tracker (BST)

The four BST regions have ∼240 mm of radial space available for tracking. Having four regions instead of the minimum three needed for track reconstruction provides a redundant tracking region that mitigates the risk of tracking inefficiencies due to layer problems such as malfunctioning strips, electronics, or noise. Further, tracking simulations indicate that with four regions instead of three, the probability of reconstructing fake tracks for a given number of correlated background hits per region (that are randomly distributed over the four BST regions) is reduced by a factor of three. Our simulations indicate that four regions should be able to handle about forty background hits in the time window. The first BST region has a diameter of ∼101 mm. The second, third, and fourth BST regions have diameters of ∼157 mm, ∼239 mm, and ∼320 mm, respectively. The radial distance, Δr, between region four and region one of the BST has been chosen to maximize momentum resolution, which has an inverse square dependence on Δr. In ϕ, the BST regions, from the innermost to the outermost, are partitioned in 8, 12, 18, and 24 sectors, as shown in Fig. 2.7. Studies indicate that track loss due to the cracks between adjacent sectors in the BST is less than 5% for a half-field setting of the solenoid, as long as the cracks are no wider than 2 mm.

2.3.6 Dicing Layout

The dicing layout for a trapezoidal sensor from a 6-in diameter wafer is shown in Fig. 2.8. The dicing process demands a keep-out zone of 0.25 in around the edge of the wafer.

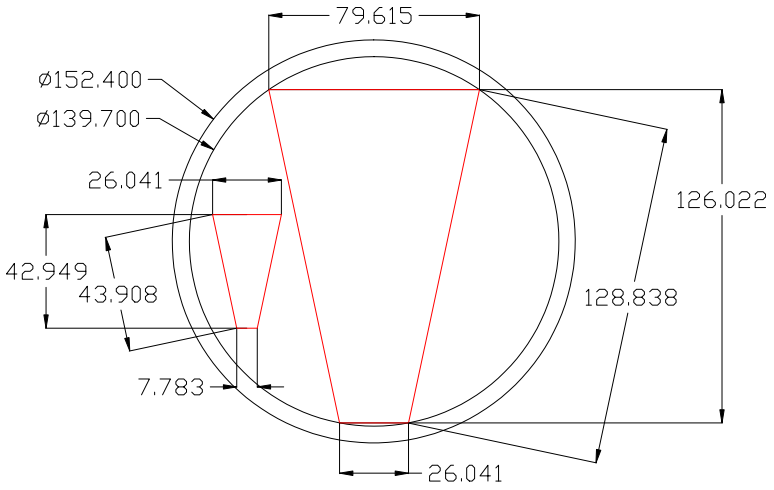

Figure 2.8: Trapezoidal sensor dicing from a standard 6-in wafer. All units in mm.

The BST dicing layout of a 6-in wafer, as shown in Fig. 2.9, is such that it provides the longest sensors possible. Such a layout reduces the number of sensors needed for the BST modules. Further, cost is reduced by maximizing the yield of sensors from a single wafer – minimizing the total number of wafers required for the BST. All BST regions use sensors with a cut size of 111.62 mm × 42.00 mm × 0.300 mm.

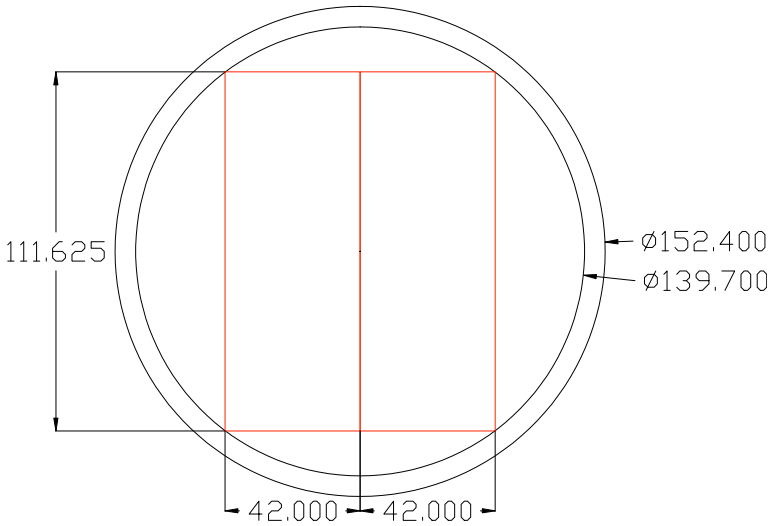

Figure 2.9: Barrel sensor dicing from a standard 6-in wafer. All units in mm.

2.3.7 Module and Strip Layout

Fig. 2.10 shows the cross sectional view of the sensor. The lengths of the readout strips of the SVT vary from 0.5 cm to 33 cm. The strip width is ∼8 μm and the implant depth ∼1.2 μm.

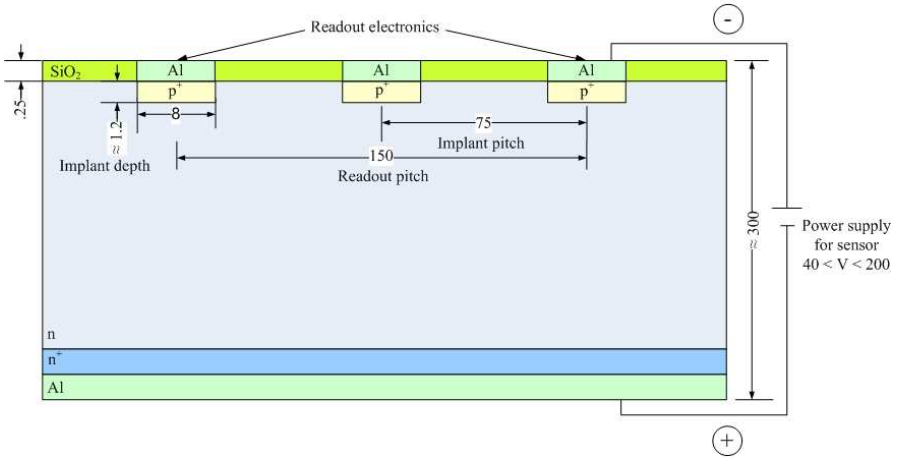

Figure 2.10: Cross sectional view of a sensor showing the different layers and the spacing of the strips (all units in μm).

A completed module in the BST has 256 readout channels per layer – 512 channels in all per module. The modules of the FST have 512 channels per layer – 1024 channels total per module. Each FST sector consists of a module – a single trapezoidal unit as shown in Fig. 2.8 that consists of a V and a W silicon layer that sandwich a 2-mm-thick Rohacell 71 carbon fiber composite.

To reduce costs, the V and W layers for the modules of the different BST regions are made of one or more fundamental rectangular sensors. If more than one sensor is needed for a module, the sensors are wire-bonded together. Modules of the BST Regions 1, 2, 3, and 4 have 1, 2, 3, and 3 sensors, respectively (see Fig. 2.4). Fig. 2.11 shows 3D renderings of how the complete SVT system is expected to look.

Table 2.2 gives the radiation length of the materials used for the sensor structure. Because of the large variety of commercial graphite fibers available for GFRP (glass fiber reinforced polymer) composites, they have an added bonus of being easily obtainable at an acceptable cost. The preferred structural materials are GFRP and Rohacell. The total anticipated radiation length for the BST is ∼3.5% and for the FST ∼2.7%.

The readout pitch for the strips, which is twice the implant pitch, is determined by the minimization, as far as affordable, of spatial resolution. Based on this criterion, the strips

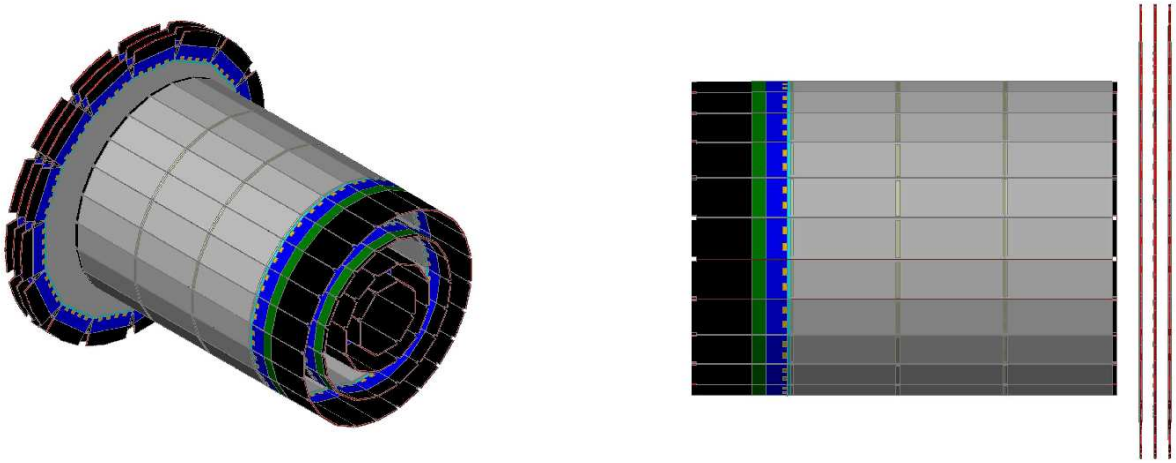

Figure 2.11: Overall conceptual renderings for the SVT showing a rear view (left) and a side view (right).

Material	Radiation Length (mm)	Thickness (mm)	Radiation Length [%X0]
Silicon	93.7	0.300	0.320
Epoxy	443.7	0.025	0.007
GFRP	250.0	0.250	0.100
Rohacell71	5450.0	2.000	0.040
GFRP	250.0	0.250	0.100
Epoxy	443.7	0.025	0.007
Silicon	93.7	0.300	0.320

Table 2.2: Material thickness with radiation lengths for the different layers that make up the sensors of the BST and FST.

are designed to have an implant pitch of 0.075 mm and a readout pitch of 0.150 mm. The expected spatial resolution for this pitch spacing is about 0.050 mm and the occupancy in a layer of an FST region, for half-field operation of the solenoid, is less than ∼1.5%. The V and W layer strips for the FST sensors run parallel to the edges of the trapezoid (see Fig. 2.12), with the strips intersecting at an angle of 12°.

For the BST, the 42-mm width of the sensor accommodates 256 input channels, at a readout strip pitch of 0.150 mm, to the two SVX4 ASICs, and the required keep-out zones around the sensor (see Fig. 2.13). The V and W strips are designed such that strip 1 is at an angle of 0° with respect to the length axis of the rectangular BST sensors and strip 256 is at an angle of 3°. This was done to minimize sensor dead area. Details are shown in Fig. 2.13.

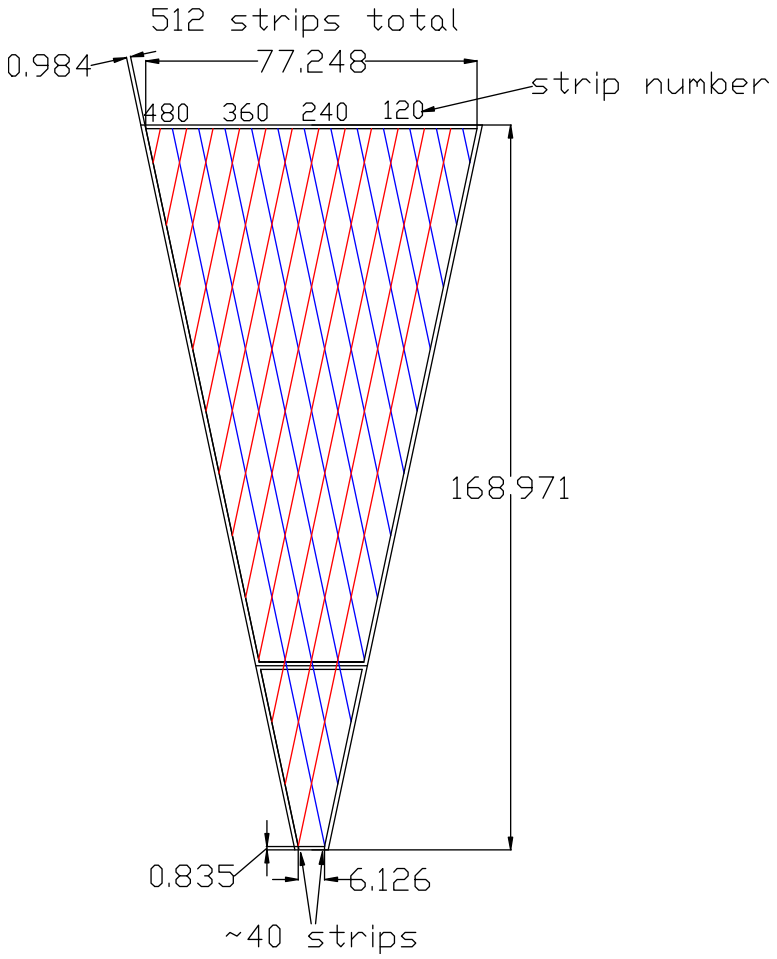

Figure 2.12: Strip layout for the trapezoidal sensors. All units in mm.

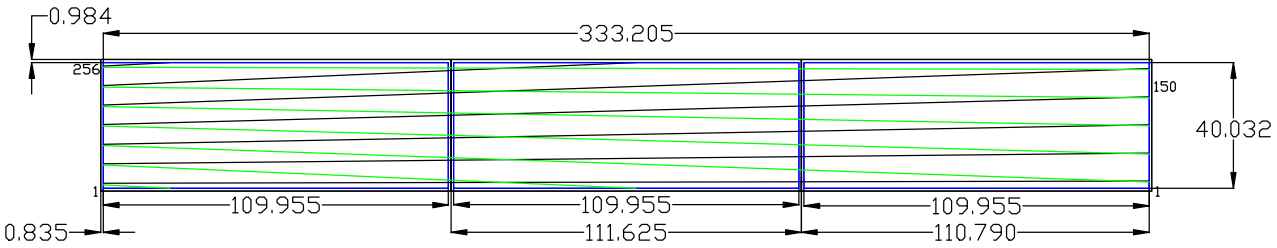

Figure 2.13: A standard BST module showing the V and W strips. All units in mm.

2.4 Mechanical

2.4.1 Support Structure

Fig. 2.14 shows a view of the complete SVT, including its support structure. A large stainless-steel tube is used to support the BST, and the FST is supported off of the BST. The size and stiffness of the support tube seems extreme, but it is a simple system that has been used to support other detectors in high magnetic fields in CLAS experiments, such as the light-weight BONUS detector. It is expected that the total weight of the SVT is less than 10 kg. The calculated deflection of the support pipe is 0.033 mm.

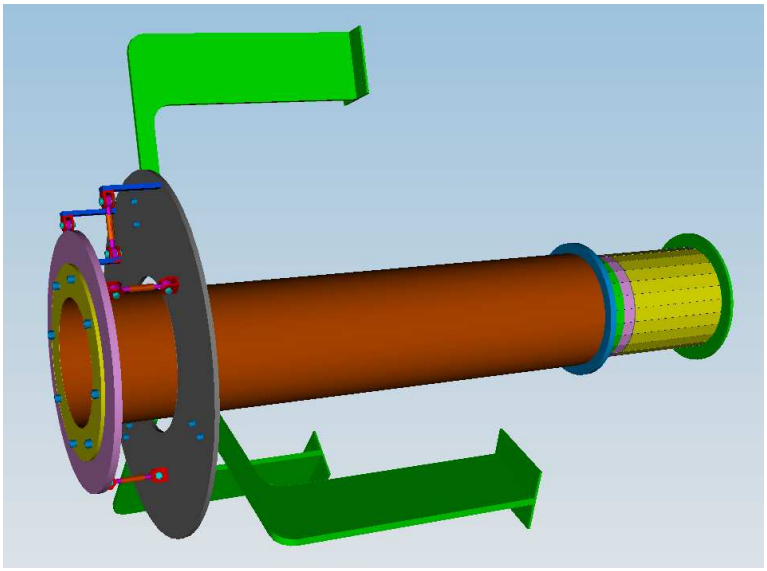

Figure 2.14: SVT on support arm with mounting/alignment hardware to CLAS12 solenoid.

The relative mass of the support structure is more than 5 times the mass of the detector, and it is mounted to the solenoid, which has a mass on the order of 20 metric tons, thus vibration will not be an issue.

2.4.2 Detector Element Deflection

Individual staves of the barrel section have been analyzed using ANSYS finite element modeling software. The worst case is Region 1, where its deflection is shown in Fig. 2.15. In this modeling, all elements of the stave were given both density and stiffness properties, as well as the dead weight of the electronics (10 g). Deflection of the wafer material can be seen to be less than 0.03 mm, which is much less than the required 0.1 mm that can cause self induced noise.

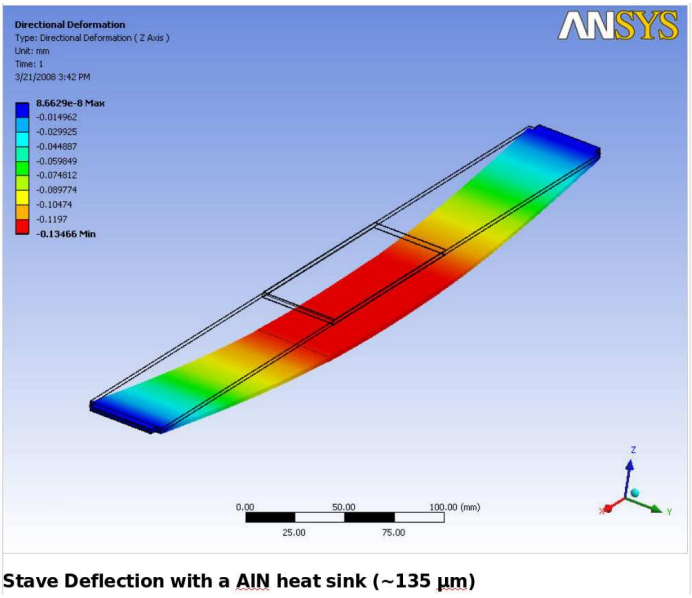

Figure 2.15: BST Region 1 stave deflection analysis results (units in mm).

2.4.3 Detector Element Heat Removal

Heat removal from the SVT is a significant design issue. The design heat load for the SVT is to remove all the on-board electronics heat using chilled-water cooling. The total power to be removed is shown in Table 2.3.

The primary mode of heat transfer will be conduction heat transfer to a water-cooled heat sink. We have chosen aluminum nitride because it is a non-magnetic and electrically non-conductive ceramic material with good thermal conductivity. Two millimeter thick aluminum nitride has been put into the core of the staves, replacing the Rohacell core material where its mass is not in the acceptance. Finite element analysis of a Region 4 module shows that

Heat Load for SVX4		
Item	Barrel	Disk
No. of modules	62	45
Chips/module	4	8
Total chips	248	360
Idle power (W)	47.6	69.1
Max power/ch (mW/ch)	3	3
Max power (W)	95.2	138.2
Transceiver power (W)	0.5	0.5
No. of transceivers/module	4	4
Total transceiver power (W)	124.0	90
Total idle power (W) (with transceiver)	171.6	159.1
Total max. power (W) (with transceiver)	219.2	228.2

Table 2.3: Heat load on the SVT,

most of the heat can be conducted away, keeping the electronics maximum temperature to approximately 40°C with the heat sink temperature at 15°C. A very small amount of heat (much less than 1 W) must be removed from the surface of the wafers to keep them from warming to the maximum temperature of the chips. This can easily be done by flushing the detector with a small purge of dry nitrogen. The temperature distribution of a stave in Region 4 is shown in Fig. 2.16.

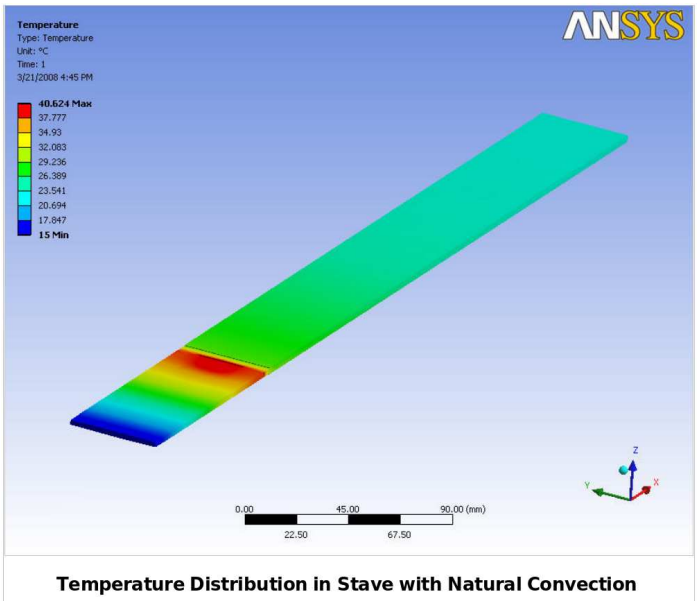

Figure 2.16: BST Region 4 stave heat transfer analysis results (units in °C).

Notice that the temperature along the wafer portion of the stave is around 23°C. This is because the dry nitrogen that will be purging the detector is assumed to be 22°C. Region 1 has a longer conduction length, and therefore, higher temperatures are expected. Two potential solutions are being considered. The first is to use a material with higher thermal conductivity (such as a high thermally conductive carbon composite). The second is to locate the electronics on Region 1 closer to the cooling plate.

2.5 Electronics

2.5.1 Readout

Both the BST and FST will be made of single-sided sensors, as single-sided sensors avoid manufacturing problems and the higher costs associated with double-sided sensors. Further, the

SVX4 ASIC, a candidate for the readout electronics, supports single-sided sensors only. The single-sided sensors to be used are n-type, AC-coupled, and poly-biased. After an evaluation of the readout ASICs that are available (see Table 2.4), the 128-channel SVX4 ASIC that is fabricated on standard 0.25-μm CMOS technology, is considered to be a potential candidate. SVX4 implements a complete readout system and is a low-power device (at 3 mW/channel). Further, the SVX4 ASIC has a good track record and is presently the readout system of choice for several single-sided micro-strip detectors.

Institution	Experiment	Chip	Manufacturer	Process
CERN	ALICE	HAL25	IBM	0.25
CERN	ATLAS	ABCD	Honeywell	0.8
CERN	CMS	APV25	IBM	0.25
CERN	LHCb	BEETLE	IBM	0.25
FNAL	CDF	SVX4	TSMC	0.25
FNAL	D0,CDF	SVX3D	Honeywell	0.8
KEK	Belle	VA1TA	IDEAS	0.35
SLAC	BaBar	AToM	Honeywell	0.8

Table 2.4: Available ASICs that were evaluated for use in `CLAS12`.

As an example of the on-board electronics, a photo-composite of a BST Region 2 module is shown in Fig. 2.17. This assembly is called a stave. Table 2.5 lists the significant components of the on-detector electronics. The operating bias voltage is expected to be $\sim$200 V. For low thermal noise and production uniformity, the poly-silicon bias resistor is required to be $\sim$2.5 MΩ. The inter-strip resistance is expected to be $\sim$1 GΩ. To minimize signal dispersion, a strip resistance of less than 30 Ω/cm is desirable.

The SVX4 design handles sensor capacitances from 10 pF to 35 pF. For the FST and the BST, the total inter-strip capacitance is expected to be $\leq$1.2 pF/cm and the coupling capacitance is expected to be $\geq$10 pF/cm for AC-coupled strips. The equivalent noise charge (ENC) in a channel is given by ENC = $400e^- + 42e^-/$ pF. For a capacitance of 30 pF, the typical capacitance of a long strip, plus some additional stray capacitance due to the wire-bonds connecting the sensor and the chip, ENC is estimated to be $1800e^-$. This noise level is about a tenth of the signal level generated by a minimum ionizing particle.

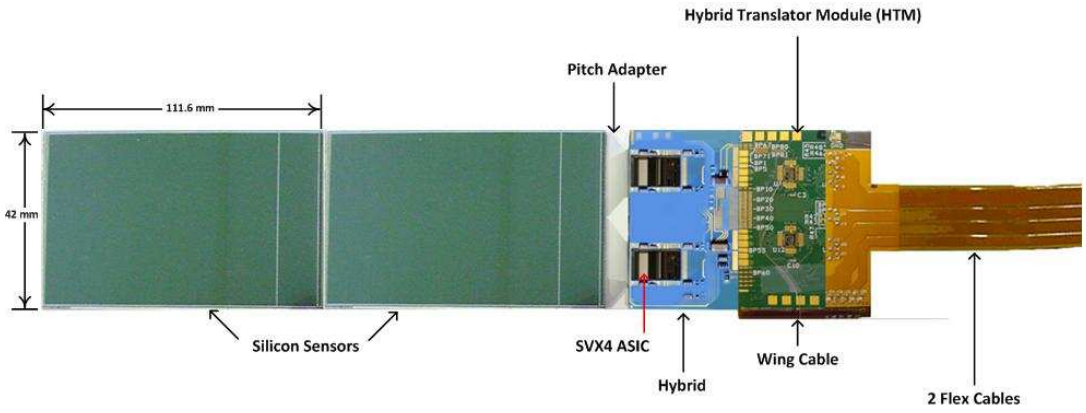

Figure 2.17: Photo-composite of a Region 2 barrel module stave assembly.

Component	Basic Specifications	Function
Silicon sensors	Single sided, 300-μm thick, 42 mm×111.62 mm (cut), 75 μm implant pitch, 150 μm readout pitch, V/W layers $\pm 1.5°$, n-type, 2 sensors from a 6-in wafer	Charge collection
Pitch adapters	Adapts SVX4 48-μm pitch to sensor 150-μm readout pitch	Hybrid to sensor Connection
Hybrids	BeO substrate, ~38 mm×20 mm, bonding pads for 2 SVX4 ASICs	SVX4 ASIC mounting
Hybrid Translator Module (HTM)	LVDS signal transceivers, ~40 mm×40 mm (smaller if possible)	Translates and repeats module control and data signals
Wing cable	Flex cable extension of HTM circuit board, wire-bond pads for bottom hybrid	Connects signals from top to bottom HTM

Table 2.5: Significant components of the on-board electronics.

Fig. 2.18 shows a block diagram of a single SVX4 channel. The detector signals are integrated, correlated double samples, the difference of which is stored in the analog pipeline. Up to 42 measurements can be stored in the pipeline. Digitization is by means of a Wilkinson-type ADC and an 8-bit counter. Timing control signals govern, among other functions, the operation of each channel's preamp reset, the double-correlated sampling, and the ADC. These timing control signals must be generated by a trigger generated by other detectors in CLAS12. Once a pipeline cell is marked by the Level-1 accept (L1A) trigger, the counter value is stored in a FIFO buffer. An 8-bit output bus transmits the data in a sequence of bytes identifying the chip, pipeline cell, the channel number, and the content.

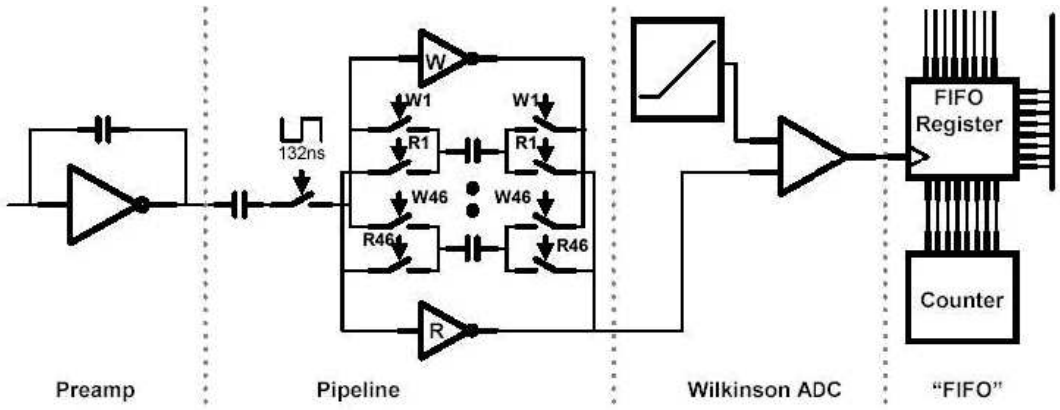

Figure 2.18: Schematic of an SVX4 chip showing the layout for the preamp, through the pipeline and ADC to the FIFO buffer.

Fig. 2.19 shows the floor plan of the SVX4 ASIC. The thickness of the chip is 0.25 mm. The diced area of the chip is 6.40 mm × 9.11 mm. The channel input pads are 0.096 mm apart, center-to-center, and the pad widths are 0.048 mm. There are two rows of input pads to which the outputs of the silicon sensors have to be wire-bonded. Pitch adapters connect the sensor and the hybrid. Wire-bond pads are located on both ends of the pitch adapter for connections to the SVX4 ASICs and to the sensor. The wire-bonding pads will be compatible with the aluminum-wire ultrasonic wedge-bonding method. A separate ceramic pitch adapter will be glued onto the module support assembly. Fig. 2.20 shows the pitch adapter connections to the sensor and SVX4 ASICs. Fiducial marks will be made on the pitch adapter for assembly and alignment. In addition to routing the sensor signals and the guard ground, the high voltage will be routed across the pitch adapter from the hybrid to the sensor bias ring. Adequate spacing between the pitch adapter, high voltage trace, sensor guard, and ground will be provided.

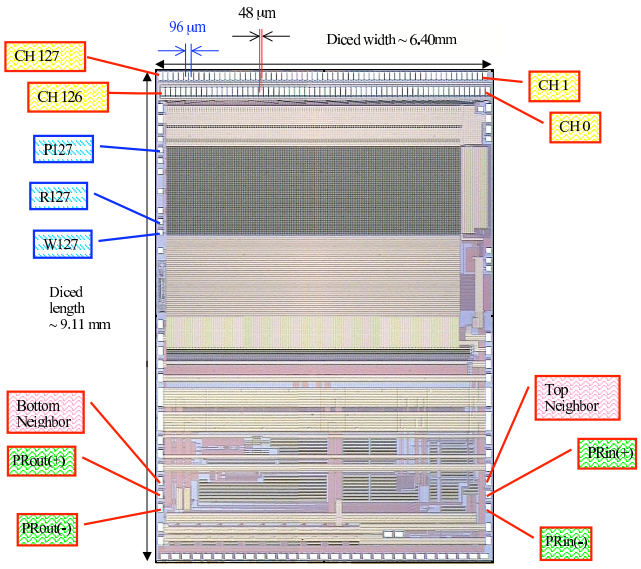

Figure 2.19: SVX4 ASIC floor plan.

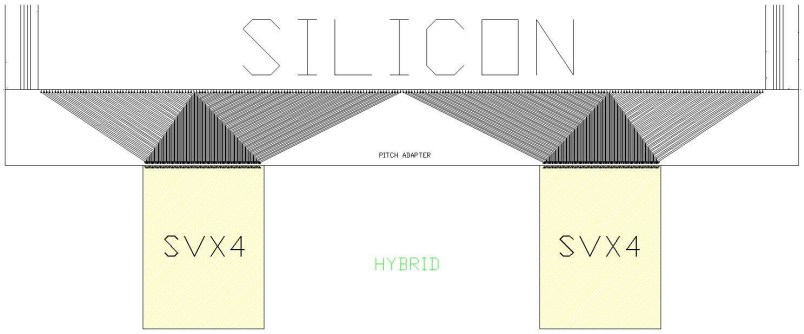

Figure 2.20: Pitch adapter connections to the sensor.

Fig. 2.21 shows a photo-composite of the proposed hybrid for mounting the SVX4 chips. The hybrid will be outside of the active area, not on the sensor, and glued directly onto the support structure. The proposed hybrid with approximate dimensions of 38 mm × 20 mm will be used to mount the two SVX4 readout ASICs. The hybrid substrate uses beryllium oxide, which is a good heat conductor and has a long radiation length. The gold bond pads of the hybrid will be aluminum-wedge bondable to be compatible with the other components. The high voltage for the sensors will be routed across the hybrid with an adequate wire-bonding surface for connections to the pitch adapter and the hybrid translator module (HTM). An RTD (resistance temperature detector) will be mounted on the hybrid for temperature measurements.

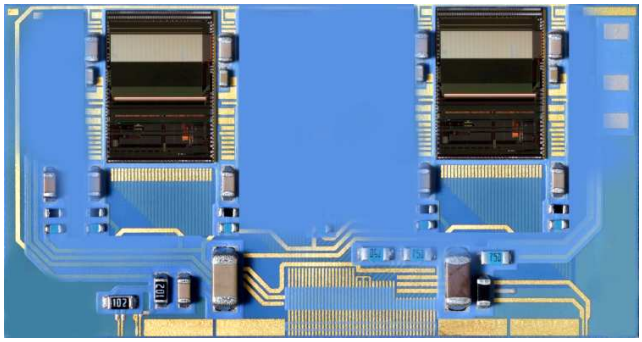

Figure 2.21: Photo-composite of the hybrid board for mounting of the SVX4 chips.

Separate power supplies and grounds for the analog and digital sections will be used. The dielectric strength of the circuit board will be ≥650 V/mil. SVX4 diagnostic signals have external pull-up resistors and will be routed to the hybrid test points. Fig. 2.22 shows a conceptual schematic of the hybrid based on the FNAL CDF design.

The connections for the priority in - priority out SVX4 readout chain allow for reading the top side and then the bottom side of the module. The input and output for the readout chain are then routed to HTM transceivers and then to the external connectors. The HTM translates and repeats control and data signals from the two hybrids on a module to the DAQ. The HTM also routes the low voltage and high voltage supply lines from the flex cables to the hybrid. Fig. 2.23 shows a conceptual block diagram of the SVX4 readout chain. Fig. 2.24 (top) shows a FNAL HTM that has the dimensions of 39 mm × 50 mm; at JLab a smaller module (∼40 mm × 30 mm or less) is being developed for `CLAS12`. Fig. 2.24 (bottom) shows a block diagram of the HTM board. The FNAL 10-bit low voltage differential signal ASIC

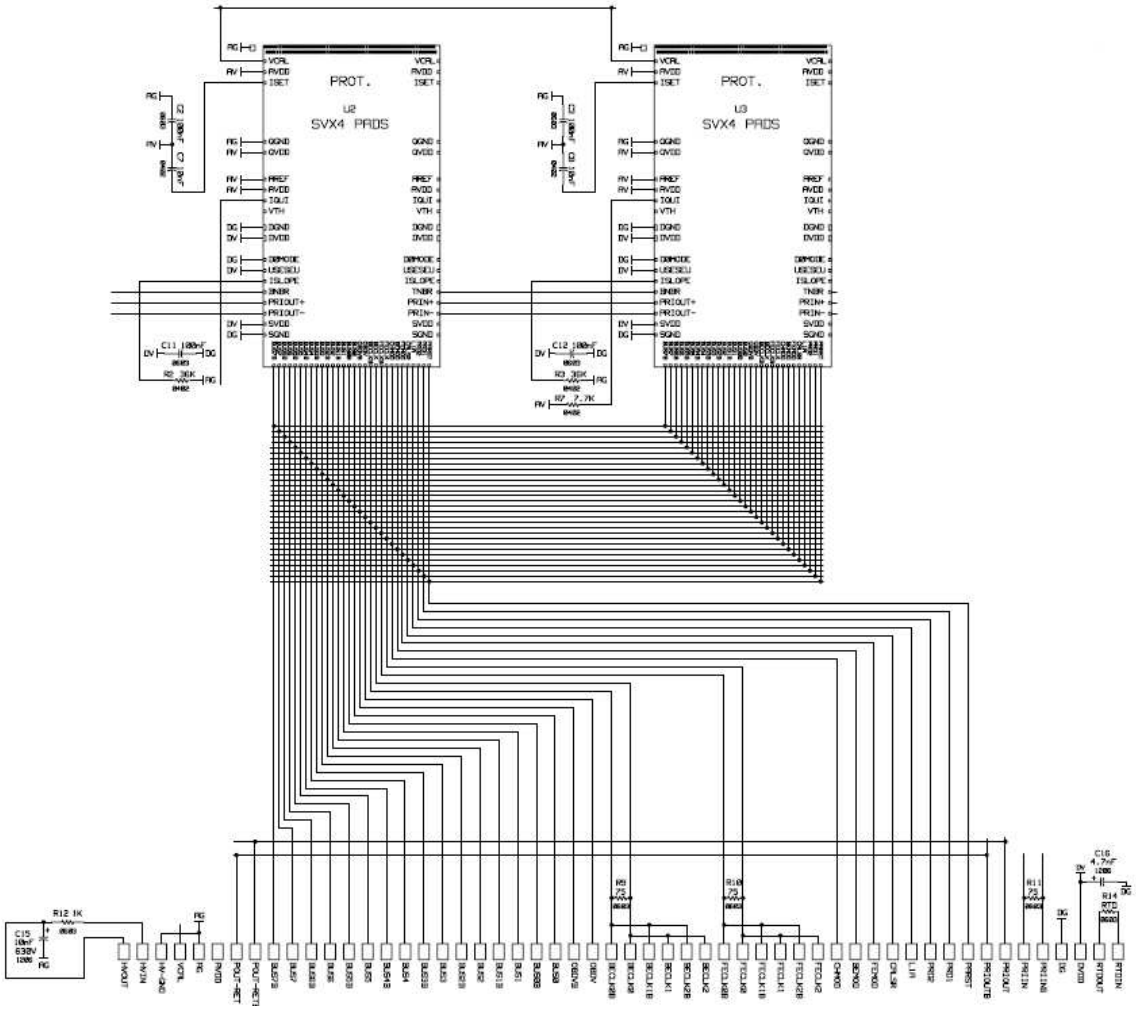

Figure 2.22: Conceptual schematic of the hybrid board layout of the SVT.

transceiver will be used because of its high density and its good track record with silicon-strip detectors. The transceiver comes in die form and is wire-bonded to the HTM board.

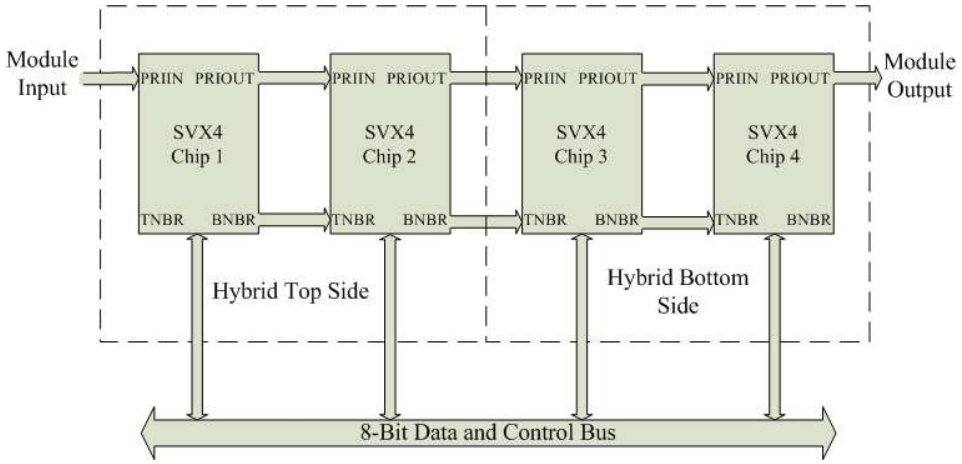

Figure 2.23: SVX4 readout chain configuration.

The "wing" cable connects the bottom-side hybrid to the transceiver on the HTM board. The wing cable and the HTM will be combined together into a single polyimide rigid (HTM) and flex (wing cable) assembly. In addition to the wing cable, the two flex cables with the data, low voltage, and high voltage connectors will be attached to the HTM board. Fig. 2.25 shows the wing cable on bottom side of the module. Fig. 2.26 shows the HTM board and wing cable before folding. Fig. 2.27 shows the flex cable assembly. The length of the cable is limited to ∼30 cm. Fig. 2.28 shows the flow of the cables. All cables will be routed to the electronic racks located at the rear of the detector.

2.5.2 High and Low Voltage

The system is designed with the highest low voltage and high voltage segmentation affordable, without compromising performance and operability. Each side of the module has its own high voltage channel, two high voltage channels per module. The five channels of low voltage for the module consist of a hybrid analog and a hybrid digital channel for the top and for the bottom sides of the sensor module and a digital channel for the HTM. All of these channels operate at 2.5 V. In addition to the low voltage and high voltage, a calibration voltage for each of the two hybrids connects to the flex cable low voltage connector.

The low voltage system consists of ∼625 channels in four groups. The high voltage system has ∼240 channels. Fig. 2.29 shows the distribution of voltage and monitoring channels for the

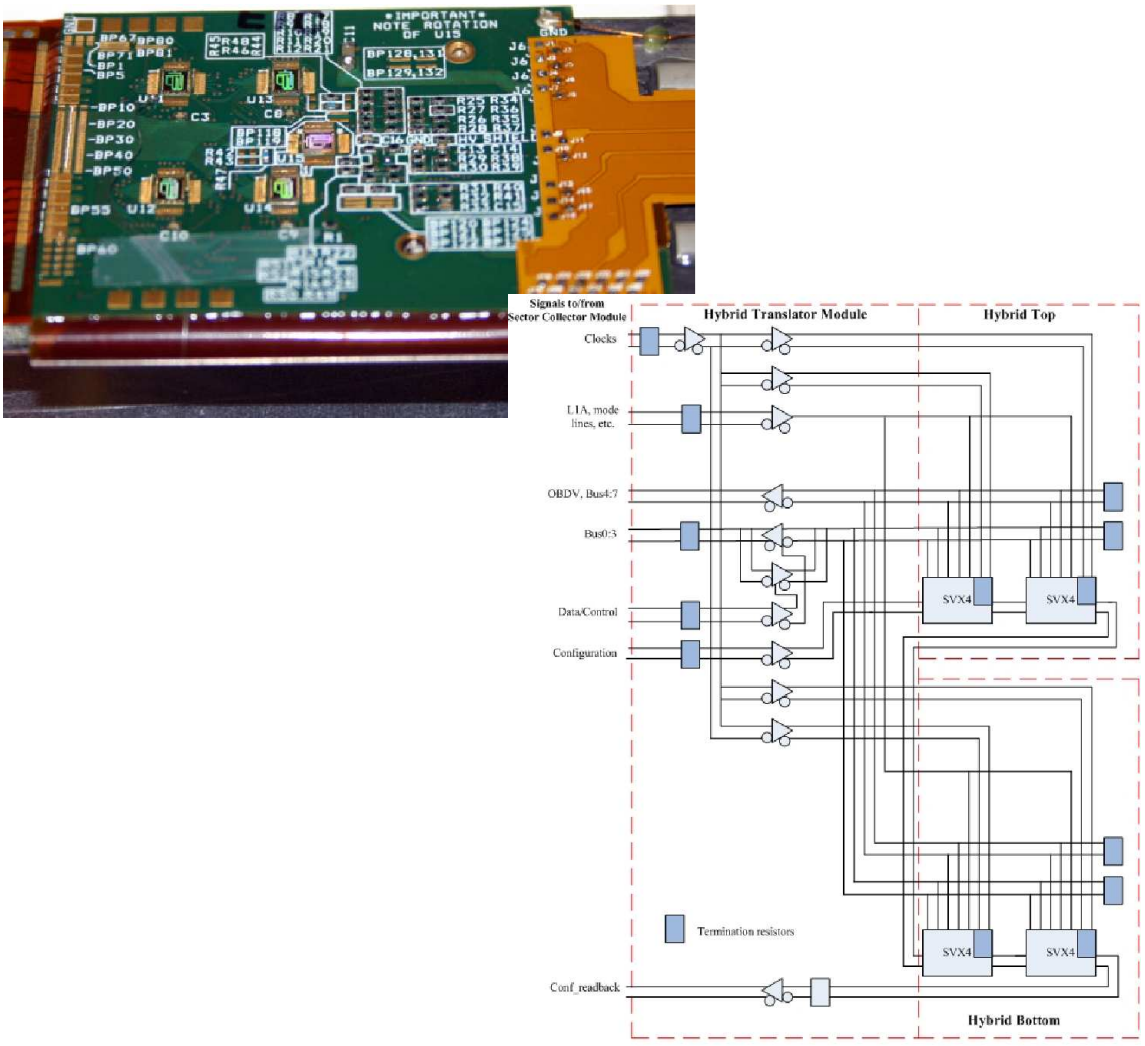

Figure 2.24: (Top) Top side view of the hybrid translator module (HTM). (Bottom) Corresponding block diagram for the HTM board.

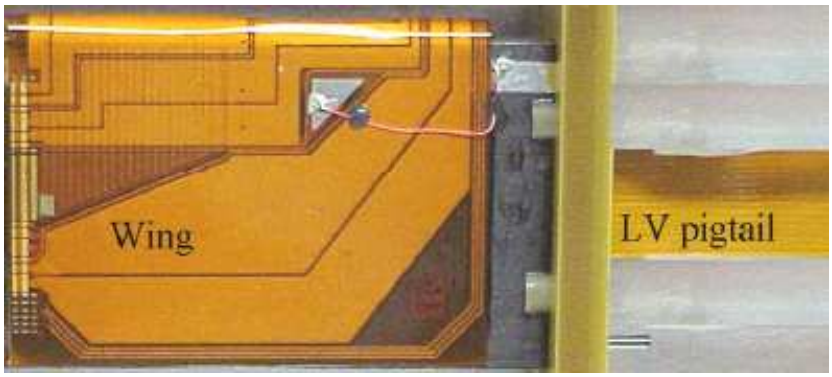

Figure 2.25: Wing cable on the bottom of the HTM board.

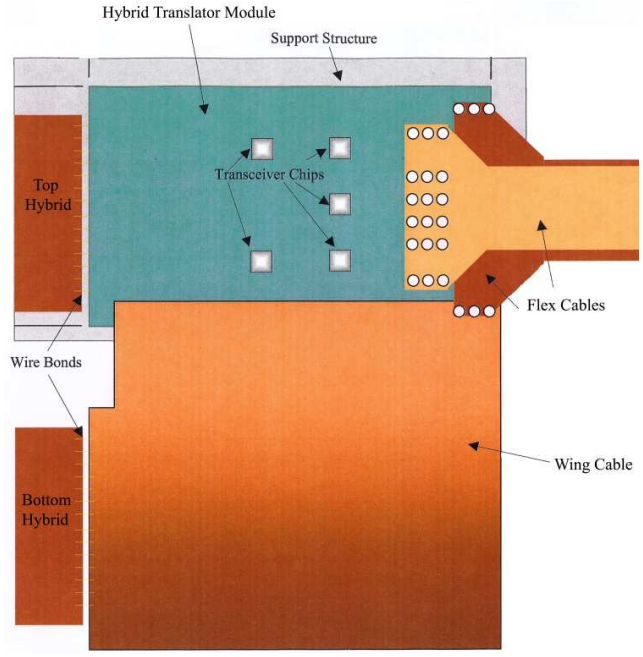

Figure 2.26: HTM assembly showing the wing cable to connect the top and bottom side boards and the readout flex cable.

Figure 2.27: Photograph of the flex cable assembly.

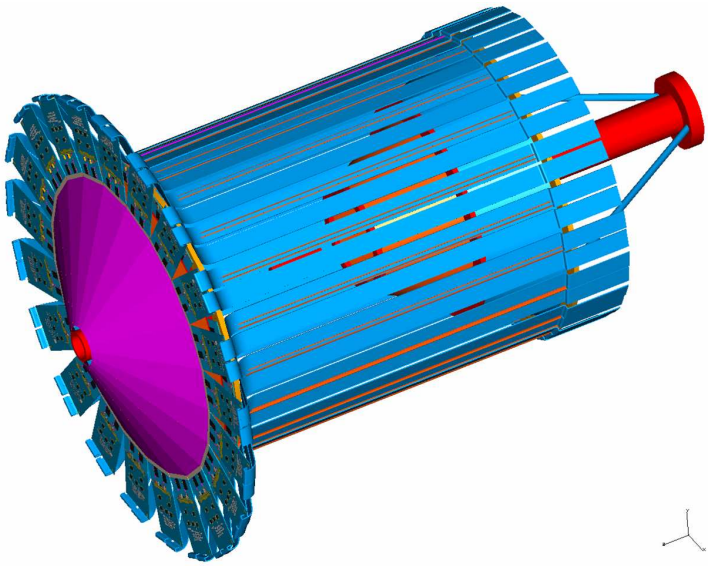

Figure 2.28: Cable routing diagram for the SVT detector.

SVT. The low voltage and high voltage supplies for the SVT will be modular with individual channels provided by a module within a main supply crate. Sensors will have a controllable and monitorable high voltage channel with over-current and over-voltage trip protection. A calibration signal and a temperature sensor on each hybrid will be instrumented on the detector modules. Table 2.6 shows the distribution of low and high voltage channels needed for the sensors, the HTMs, and the sector collector modules (SCM).

The CAEN crate-based high voltage systems, including the 1527 and 1527LC, and the WIENER universal multi-channel modular system for both low voltage and high voltage supply are being considered. The WIENER modular system has the advantage of a common crate that will support both high voltage and low voltage modules. Fig. 2.29 shows an overview of the connections of the system.

2.5.3 Slow Controls

Calibration and testing of the detector modules and readout chain is accomplished by a calibration input signal (VCAL). This external input on each SVX4 ASIC has the capability of injecting a small charge via a charge injection capacitor (25 fF). This capacitor can be switched in from each preamp input to a common bus line. A 128-bit programmable channel register, downloaded in the initialize mode, can function as a mask register and determine

Specification	Region 1	Region 2	Region 3	Region 4	Total
Hybrid 2.5 V digital channels (barrel)	14	24	34	44	116
Hybrid 2.5 V digital channels (nose cone)	40	42	42	0	124
Hybrid 2.5 V analog channels (barrel)	14	24	34	44	116
Hybrid 2.5 V analog channels (nose cone)	40	42	42	0	124
HTM LV channels (barrel)	7	12	17	22	58
HTM LV channels (nose cone)	20	21	21	0	62
SCM LV channels (barrel)	2	3	4	4	13
SCM LV channels (nose cone)	4	5	5	0	14
HV channels (barrel)	14	24	34	44	116
HV channels (nose cone)	40	42	42	0	124

Table 2.6: High and low voltage channel distribution for the SVT.

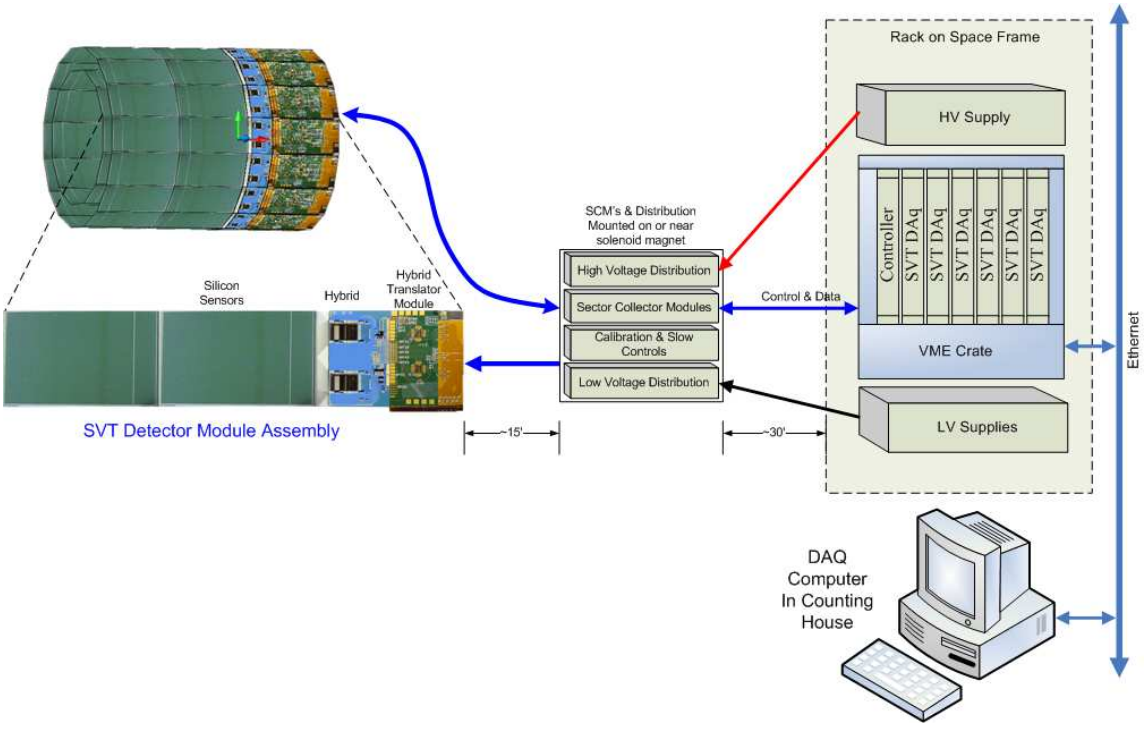

Figure 2.29: System connections overview for the SVT.

whether or not the injection capacitor is switched on for each channel. Fig. 2.30 (left) shows the preamp stage of the SVX4 ASIC and the VCAL calibration input.

The slow controls system (SCS) will be responsible for controlling all essential run-time parameters of the experiment and for monitoring the status of various hardware components. The primary goals are to enhance safety by providing early warnings about malfunctioning equipment and check the health of the experiment and the integrity of data. The system will also transmit important parameters to the DAQ for insertion in the `CLAS12` data stream. The SCS will have the ability to trigger alarms to notify personnel when parameters are detected to be outside pre-defined limits and will have the option of automatically disabling DAQ in case of a severe malfunction of the equipment. The implementation of the SCS will need a VME crate with an IOC and input/output boards. Some of the hardware will be connected directly to the Ethernet network. The settings of all critical operating parameters will be protected against computer failure. The failure of the computer in the system will only result in the loss of monitoring. When a computer reboots, parameters will not reset to previous or default values but remain at currently set values.

The SVT computers and vital support hardware will be protected by Uninterruptible Power Supplies (UPS) with battery backup and software to signal an alarm and notify the operators when external power is lost. The UPS will have surge protection and line filtering. Monitoring and control of the system will be implemented through the use of a Motorola single board computer embedded in a VME crate running VXworks real-time operating system. Sun or Hewlett-Packard workstations will support the user interfaces and controls. The control software will be built using the toolkit provided by the Experimental Physics and Industrial Control System (EPICS), which is based on the client-server model.

2.5.4 Data Acquisition

Each channel of the SVX4 ASIC has a 42-cell deep analog pipeline. Fig. 2.30 shows the block diagram of the ASIC. The front-end of the ASIC contains the integrator and storage pipeline, which at a front end clock rate (FEClk) of 132 ns, allows a trigger latency of $\sim$4 μs. The back-end of the ASIC has an ADC for digitization and the readout and driver logic.

The Level-1 accept (L1A) signal to the ASIC is used to remove a "hit" cell from the pipeline. The hit is temporarily stored in a FIFO buffer that can store up to four cells, corresponding to four L1As. These hits are queued for readout to the back-end. Once four

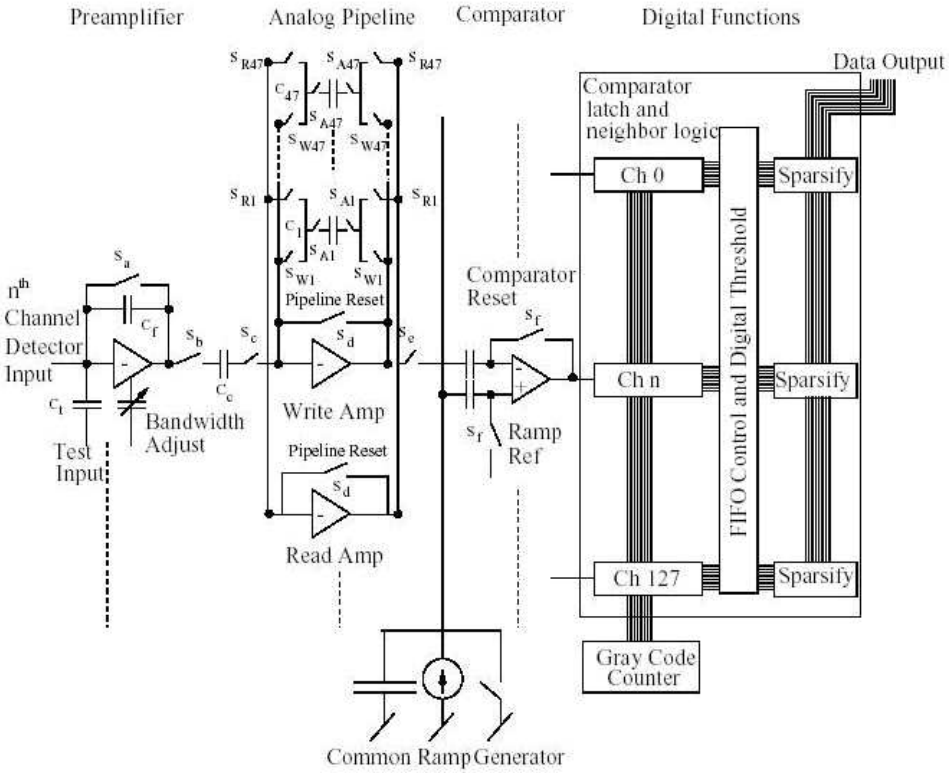

Figure 2.30: Block diagram of the SVX4.

cells are stored in the FIFO, additional L1As are ignored. The trigger latency is programmed in the shift register during the initialize mode so that the right pipeline cell is read out. L1A is normally high during acquisition and pulsed low to store a cell. L1A must go low and return high between front-end clocks.

The pedestal pipeline cell is reserved for acquiring only pedestal data. This cell is used during readout along with a stored cell. The back-end digitizes the difference between the hit cell and the pedestal cell. The pedestal cell is not part of the round robin ensemble of acquisition cells, hence the pedestal cell must be refreshed periodically. Because of the continuous electron beam, L1A arrivals are not synchronized to the front-end clock, which implies that the associated detector signals are Poisson-distributed with respect to this clock.

SVX4 data acquisition rates at a luminosity of 1×10^{35} $cm^{-2}s^{-1}$ were simulated to check their performance in a continuous electron beam environment. The first aspect of the SVX4 that was simulated was the L1A acceptance rate [270]. The triggers generated were Poisson-distributed with respect to the SVX4s FEClk. The simulation estimated the number of triggers that had an early arrival time and also estimated the number of triggers that were missed. The results of the simulation showed that for half-field operation of the solenoid, 2.5 T, with an L1A rate of 10 kHz, $\sim$0.1% of the triggers arrived early. No triggers were missed. The simulation was run for an L1A rate of 100 kHz as well, over ten times the expected trigger rate. For these conditions only $\sim$1.3% of the triggers arrived early and $\sim$0.3% triggers were missed.

Another simulation checked the effect of issuing a reset and the associated restore operation when the pre-amplifiers on the chip saturate [271]. In operating the SVX4, charge is accumulated on the pre-amplifier and this charge needs to be periodically reset when it reaches $\sim$200 fC. The results of these simulations show that at half-field of the solenoid, a $\sim$1% deadtime can be expected; at full-field operation the deadtime is $\sim$0.4%.

SVX4 is designed for daisy-chained operation. Daisy-chaining minimizes the number of bus and control lines required to operate the device. Fewer control lines means less space on the high density interconnect and less mass in the system. All the chips share a common communication bus and a common differential and back-end clock. Each chip has two pads that are used for communication between adjoining chips. After powering up the SVX4, the chip parameters must be downloaded before operation of the readout chips can begin. For each SVX4 chip, 198 bits must be downloaded into the internal registers.

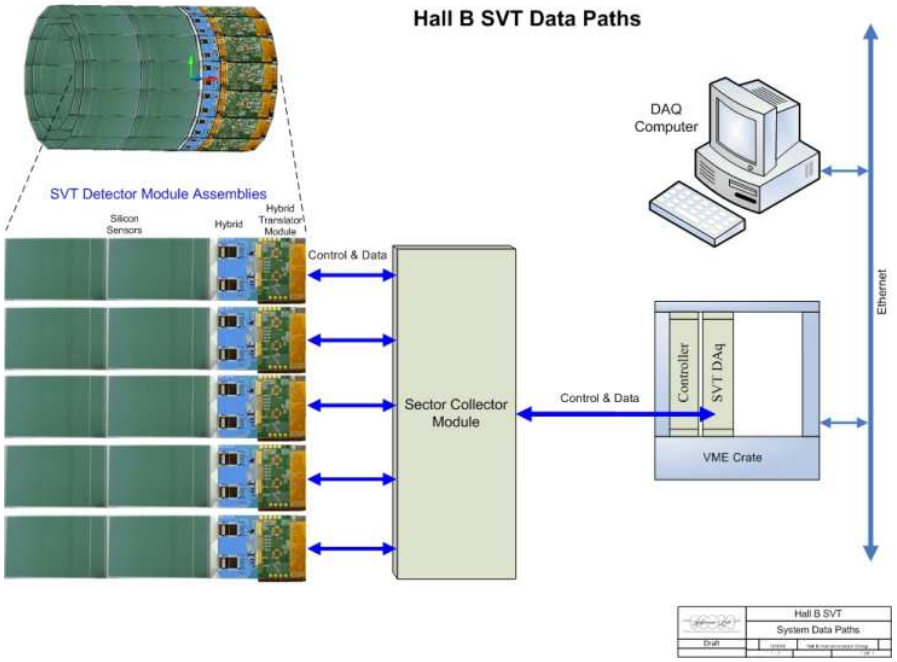

Figure 2.31: SVT system data paths.

Fig. 2.31 shows the data path for the Hall B SVT system. Signals are digitized in the SVX4 ASICs on the hybrids. The control signals and data bus for a module are connected to a sector collector module (SCM). Up to five modules are connected to an SCM that buffers and passes the data and control signals to the DAQ system. SCMs may also be daisy-chained together to form a longer readout chain. The readout chain requires only one detector module buffered by a single SCM to form a valid control and data path. Unused SCM inputs are bypassed. Increasing the number of SCMs connected together increases the daisy-chain length and the DAQ readout time. The fastest readout is accomplished by a single silicon detector module, SCM, and SVT DAQ module chain. Fig. 2.32 shows the daisy chain connections through an SCM.

For the `CLAS` upgrade, VME systems will be used for both DAQ and slow controls. Currently, `CLAS` uses about 30 VME crates and several types of modules. As a standard DAQ framework at JLab, 6U VME single board computers (SBCs) running VxWorks RTOS are used. The Harvard-designed Silicon Readout Controller (SRC) used in FNAL-CDF was studied for possible implementation in our system. This controller was originally designed for SVX3 readout. The CDF-SRC printed circuit board is in 9U VME format. This format is incompatible with our 6U-sized systems. The board has nine FPGAs and only controls the

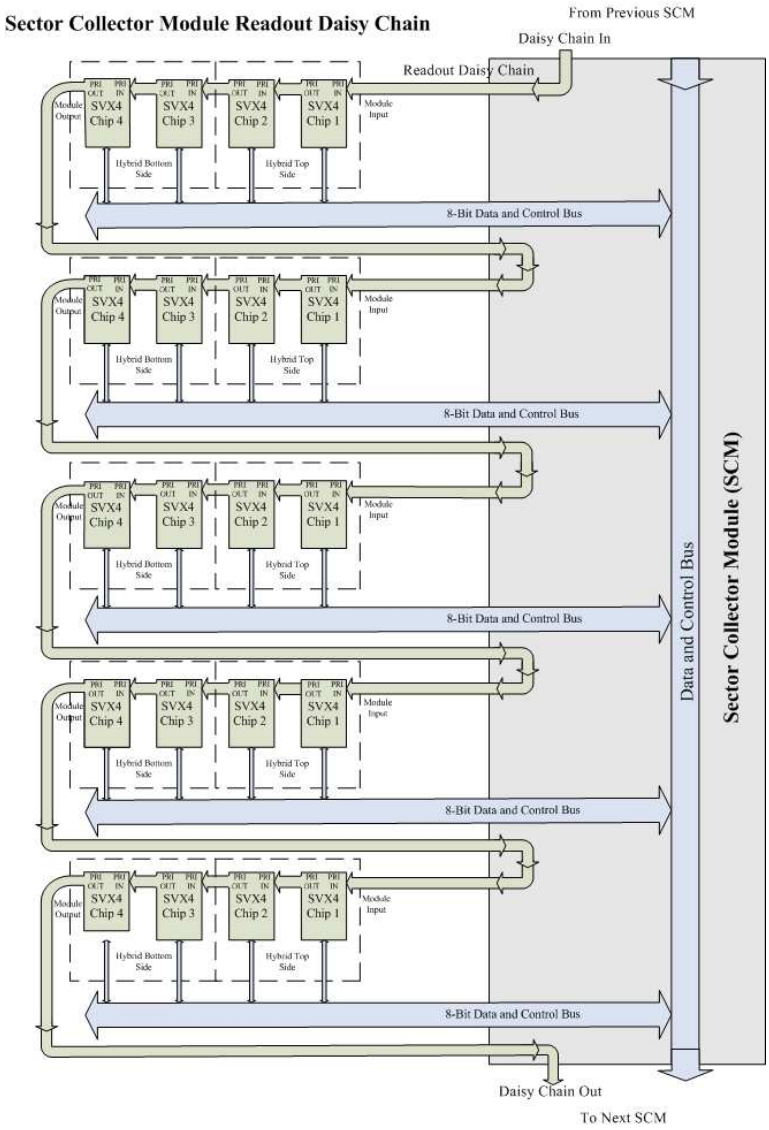

Figure 2.32: Sector collector module daisy-chain readout.

SVX3 ASIC. Separate VME hardware is needed to handle and store the data received from the silicon sensors. In addition, this SRC is application specific for the pulsed accelerator at FNAL and designed around the triggering system used at CDF.

For control and data acquisition for the SVT, a 6U VME board compatible with the `CLAS` data stream format is being developed [272]. This modular SRC will control and integrate the data received from the SVT readout chain into the DAQ system. Fig. 2.33 shows the block diagram of the prototype SRC. The heart of the SRC design is Field-Programmable Gate Arrays (FPGAs). The advantage of FPGA technology is that it combines the ease of software with the speed of hardware with permanent upgrade capabilities via downloaded updates. FPGAs have already provided the lab with versatile VME bus data acquisition and control interfaces. Current JLab FPGA designs provide control and monitoring for numerous systems by interfacing sensors and instrumentation with ADCs and TDCs. As shown in Fig. 2.33, data and control signals from the readout chain connect to the SVX4 controller FPGA logic for processing. Interface I/O signals are provided by the FPGA for external triggering, clock, and phase lock interfaces among others. The FPGA has a memory management unit and PCI interface that connects to the VME interface. On-board memory stores the events to be read out. The VME slave interface completes the data and control path to the VME backplane through bus transceivers.

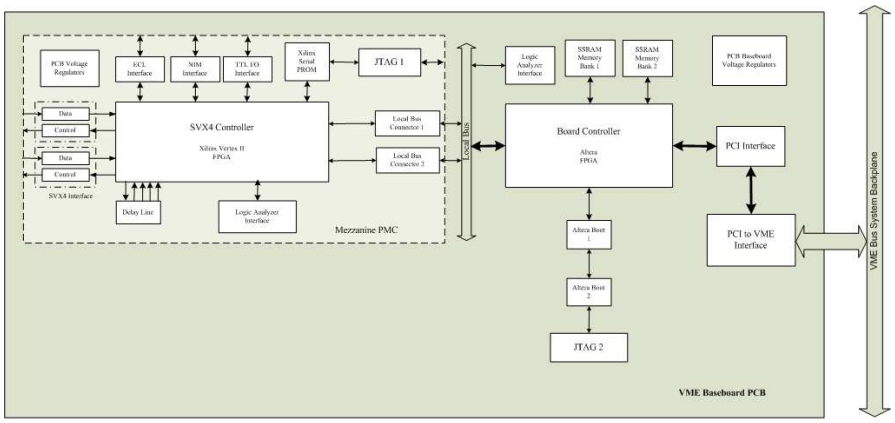

Figure 2.33: SRC prototype block diagram.

The SRC generates initialize, acquisition, digitization, and readout timing sequences for the SVX4 ASIC. The initialization cycle is typically performed once, followed by repetitive data acquisition, digitization, and readout sequences. Since we will be operating the SVX4 ASIC in continuous data format mode, the acquisition cycle occurs simultaneously with the

digitize and readout sequences. After the hit cell has been digitized in the SVX4, the SRC starts a readout cycle and the event data is stored locally. The event data will be continuously stored until the SRC is instructed to read out the data by the VME system controller or until the local memory is full. The VME slave interface on the SRC accepts instructions from the VME SBC. These instructions control the SVX4 sequences and read out the stored events. The SRC status register reports on the operating condition of the board including memory overflow.

The SRC design includes a Joint Test Action Group (JTAG) interface that provides In System Programming (ISP) capability. The ability to reprogram the on-board components provides a permanent upgrade path via software updates. It also provides a way to implement new features (even remotely) into an existing system after fabrication and installation. In addition, JTAG technology can be used for board level interconnection and functionality testing.

Based on the GEANT3 simulation, approximately 16 particles will be generated per trigger in the cone part of the SVT when the solenoid is operating at half-field. The forward cone is split into four groups, three of which have six modules and the last group has four modules. The four group partition results in four tracks per group per trigger. Six modules have 24 ASICs in all. For each chip, the pipeline cell and ID has to be read; this contributes 96 bytes, whether or not there is data. Four tracks in a group give rise to 6 hits, each of which requires a byte for cell ID and a byte for content, contributing 12 bytes per track. Therefore there are 48 bytes per track from hits alone. Therefore, there are 144 bytes per trigger. Since the groups are independently read out, this data rate translates to 1.44 MB/s for a trigger rate of 10 kHz, well below the 56 MB/s readout rate capable by the ASIC. Our expectations for the time taken for digitization and readout as a function of the number of hits in a sector of the FST have been computed and are shown in Fig. 2.34. Each sector can handle up to 2500 hits in 105 ns (25 MHz). A higher rate implies that before the digitization process can be completed a new L1A arrives, eventually filling up the FIFO and leading to a loss of triggers.

2.6 Research & Development

R&D for the SVT system started in FY2004 [273]. The R&D goals are to evaluate silicon strip detector systems, assess compatibility of SVX4 performance with `CLAS12` requirements, study

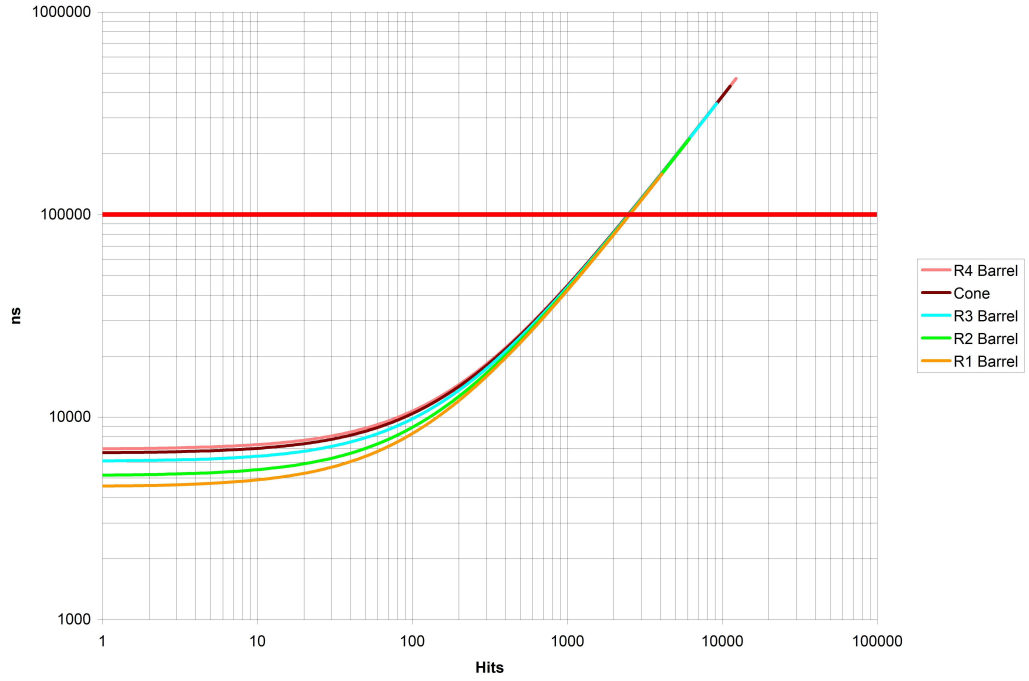

Figure 2.34: Readout time as a function of the number of hits in a given layer or portion of the SVT.

the features of the FNAL stave design that could be useful for CLAS12, and gain experience and know-how about developing support fixtures, installation, and DAQ by conducting lab tests and installing a test stave in Hall B for in-beam tests [266].

The initial R&D effort [274, 275] focused on the DAQ system of the stave received from FNAL. The Hall B Instrumentation Group modified the DAQ hardware and software to run lab and beam tests. Some of the significant modifications that were made were the addition of plots to show the number of hits in each strip, the archiving of selected real-time strip plots, the storage of output data for off-line analysis, the ability to change the clock-base, and the addition of the external trigger mode. For the operation of the stave, low and high voltage control programs were researched, developed, and implemented [276, 277].

R&D activities during FY2004 culminated with the conduction of beam tests [278]. To perform these tests, specialty cables, data buffers, data repeaters, controls and monitoring programs for low and high voltages, DAQ software, off-line analysis software, support structures, and finite element analyses were designed, developed, debugged, and implemented. The significant result of the FY2004 R&D effort was that it provided hands-on experience with several facets of the endeavor to build a reliable state-of-the-art silicon vertex tracker tailored

to meet CLAS12 requirements. For FY2005 the R&D plan was to develop a laser test stand and a PCI-based DAQ board [279]. However, due to budgetary considerations, work was done only on the laser test stand. Additionally, the prototype FPGA-based, PCI-bus-compatible, printed circuit carrier board for the DAQ controller of the SVT was successfully built and tested [280] (see Fig. 2.35).

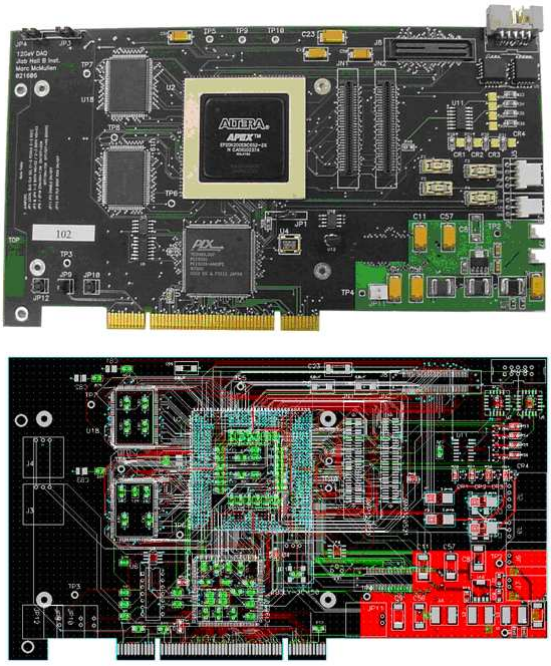

Figure 2.35: New PCI-based CLAS12 DAQ base board.

R&D for FY2006 focused on the design of the DAQ mezzanine circuit board (shown in Fig. 2.36) that will be compatible with a VME board. The block diagram for the circuit board is shown in Fig. 2.37. The FPGA design of the SVT DAQ/controller board is flexible and permits use of different silicon sensor readout ASICs.

R&D on the advanced conceptual design for the SVT is continuing. Support structures and instrumentation strategies are being developed, and detector installation procedures are being studied. Safety issues for each step of the detector construction and installation are being analyzed.

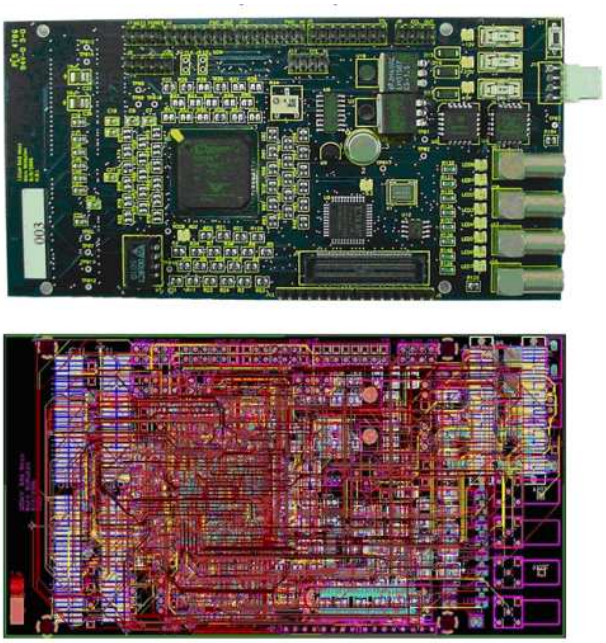

Figure 2.36: SVX4-based PMC controller card.

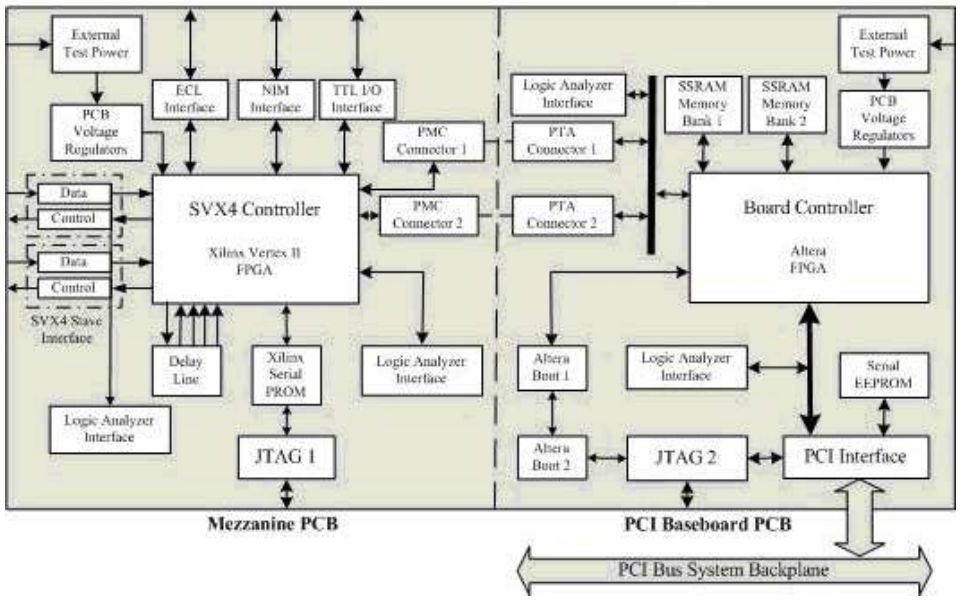

Figure 2.37: Prototype DAQ circuit board diagram.

2.7 SVT Commissioning and Operation

The objective of the SVT commissioning plan is to debug, fix, and calibrate system components. Over the last several decades, much experience in this area has been gathered by experiments at other facilities. The SVT commissioning program will draw on these experiences. The commissioning plan includes studies without and with beam.

After installation of the SVT in the solenoid, a complete set of system checks will be performed. First, a visual inspection of cables and electronics will be carried out. Control, data, low voltage (LV), high voltage (HV), and monitoring cables will be checked for proper strain relief, sheathing, insulation integrity, and connections.

The detector will be monitored continuously by the `CLAS12` slow controls system. The slow controls procedures to adjust critical parameters of the equipment will be checked. Power will not be turned on until all alarms and fail-safe systems have been verified. Power-up tests will be conducted first on dummy loads. This checkout will include all systems controlled by EPICS as well.

Temperature and humidity conditions in and around the SVT will be monitored continuously. Also, light sensors inside the SVT will monitor the level of light infiltration.

The LV system, including LV distributions, will be checked with dummy loads. Correlations between demand, monitored, and measured voltages will be logged. Once it is ascertained that the LV system is functional, it will be connected to the SVT. The HV system will be checked in a similar fashion.

Once both the LV and HV systems have been checked, the SVT will be powered up; the power-up sequence will be, first the LV system, and then the HV system. The powering up of both the systems will be done in appropriate steps. Current draw by both the systems will be automatically recorded.

Read/write tests on the ASIC registers will check whether all ASICs are able to be programmed and whether they can be read back. Calibration of the detector modules and testing of the readout chain will be accomplished by inputting an external signal. This external input on each SVX4 ASIC has the capability of injecting a small charge via a small charge injection capacitor (25 fF). Calibration will be done with different inject masks. The acquired ADC spectra will be used to calibrate the ASICs. The performance of the system, including that of the front-end electronics, will be checked at the channel level by inspecting the occupancy

plots.

Hit/no hit data will indicate noisy or dead channels. An effort will be made to fix channels with problems by appropriate measures, such as varying the threshold, low, and high voltage values.

Once these basic tests have been completed, efficiency and tracking accuracy tests will be performed using cosmic rays. Cosmic triggers generated by the CTOF will be used to measure the efficiency and the track reconstruction accuracy in the Barrel Silicon Tracker. These tests will be done for zero, half, and full fields of the solenoid. Tracks will be reconstructed in the eight SVT layers in the upper hemisphere and the projected track hits will be checked against the registered hits in the eight layers of the opposite hemisphere. These tests will be repeated with test beam.

2.8 CLAS12 Drift Chambers

2.8.1 Overview

The overall tracking requirements (0.5 - 1% fractional momentum resolution at 5 GeV and efficient tracking at a luminosity of 10^{35} cm^{-2}s^{-1}) are the main drivers for drift chamber design. Because the CLAS drift chamber system [281] has operated successfully for 8 years, we plan to re-use many of the design concepts and most of the utility infrastructure. In particular, we plan to re-use the present gas mixing and handling system, the high-voltage and low-voltage systems, the FASTBUS TDC system, and the post-amplifier/multiplexer systems. The construction project thus consists of new chambers, on-board electronics, and on-board jumper cables.

The forward tracking system consists of three regions divided into six sectors as shown in Fig. 2.38; located just before, inside, and just outside the torus field volume, and referred to as Regions 1, 2, and 3. Each chamber will have its wires arranged in two superlayers of six layers each, with the wires in the two superlayers strung with $\pm 6^\circ$ stereo angles, respectively. The cell structure will be hexagonal, that is, each sense wire is surrounded by six field wires. This arrangement is similar to the present CLAS design and offers good resolution with very good pattern recognition properties. Refer to our article on the overall CLAS detector [282] and our article on the drift chambers themselves [281] for details of the present detector and

chambers. The groups responsible for the CLAS12 drift chamber construction include Old Dominion University, Idaho State University, and Jefferson Laboratory.

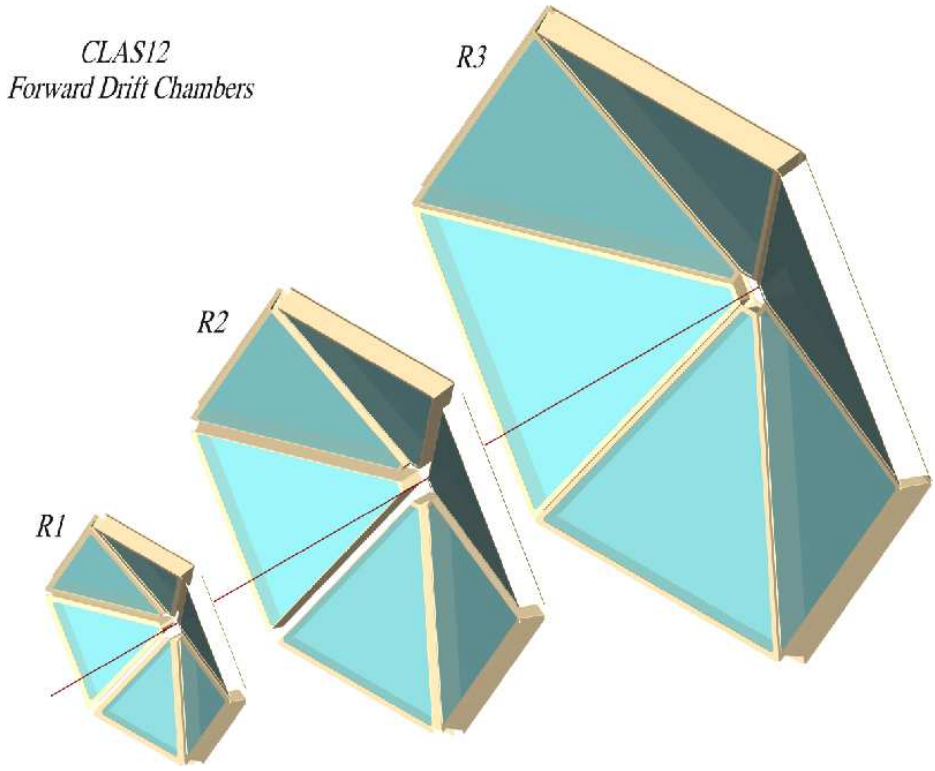

Figure 2.38: Schematic layout of the CLAS12 Forward Drift Chambers: Regions 1, 2, and 3.

The major difference in the drift chambers for CLAS12 is that the cells cover a smaller solid angle than those in the present CLAS chambers, allowing efficient tracking at higher luminosities because the accidental occupancy from particles not associated with the event is smaller. Table 2.7 lists the main design parameters for each region of the CLAS12 drift chambers. For the purposes of simulating track resolutions, we assumed that the position resolution of the individual drift cells would be 250 μm.

There are also other differences in the design of the CLAS12 chambers compared to the current CLAS chambers. ways. Successive superlayers have their wires arranged with a $\pm 6^\circ$ stereo angle; the present arrangement has an axial layer and a 6° stereo layer. For the present CLAS detector, the ϕ resolution times $\sin\theta$ is about two times larger than the θ resolution. To have more equal resolution in the two angles, we doubled our stereo angle from 0 and 6° to $\pm 6^\circ$. Unlike the present chambers, all of the wires in one of the superlayers are strictly parallel, and in a plane perpendicular to the wire direction, form perfect hexagons. This should allow a

	Region 1	Region 2	Region 3
Distance from target	2.3 m	3.5 m	4.7 m
Num. of superlayers	2	2	2
Layers/superlayer	6	6	6
Wires/layer	112	112	112
Cell size	0.75 cm	1.18 cm	2.07 cm
Active time window	150 ns	250 - 500 ns	500 ns
Resolution per wire	0.020 cm	0.025 cm	0.030 cm

Table 2.7: Design parameters for the CLAS12 drift chambers.

more accurate drift velocity calibration than the current design with its layer-to-layer increase in cell size. The choice of gas; a 92:08 Argon:CO_2 mixture is a small departure from our present 90:10 mixture and should result in a higher and more constant drift velocity. We plan to run with a gas gain of 5×10^4.

Another departure from the present design is to design every chamber (in all three regions) to be self-supporting in order to ensure that they are easy to install and remove for maintenance. In the present CLAS, the Region 1 chambers are all bound together into a single unit in order to maintain the wire tension without excessively thick endplates, and the Region 2 chambers are actually mounted onto the magnet cryostat, with the cryostat itself maintaining the internal wire tensions. None of the present Region 1 or 2 chambers can be accessed individually without a lengthy "tension-transfer" process. To avoid this, we are designing the Region 1 and Region 2 chambers to be self-supporting like our present Region 3 chambers. To keep a very thin endplate (to minimize dead area), some of the wire tension in the Region 2 chambers may be borne by springs mounted to the torus cryostat, but many fewer springs than in the present detector. The key to these improvements will be ultra-stiff endplate assemblies that obtain their stiffness by a flanged design.

A third design change is to use 30-μm diameter sense wire rather than the presently-used 20 μm wire. Our choice of wire is 30-μm diameter, gold-plated tungsten for the sense wires, 140-μm diameter, gold-plated aluminum for the field wires, and 140-μm diameter, stainless steel for the guard wires. This should make the chamber more robust to wire breakages. Higher voltages will be required to achieve the same gas gain, and the resulting higher electric

field in the drift cells will result in a more nearly constant drift velocity that should be easier to calibrate. Prototypes are being built to study possible negative side-effects of the higher voltage operation, such as leakage currents on the circuit boards and/or higher rates of cathode emission from the field wire surfaces.

Fig. 2.39 shows GARFIELD calculations for a Region 3 drift cell with both a 20-μm and a 30-μm diameter sense wire. Here the cells with the thicker sense wire will have a significantly higher drift velocity, which is desirable to reduce the time window, and hence the chamber occupancy.

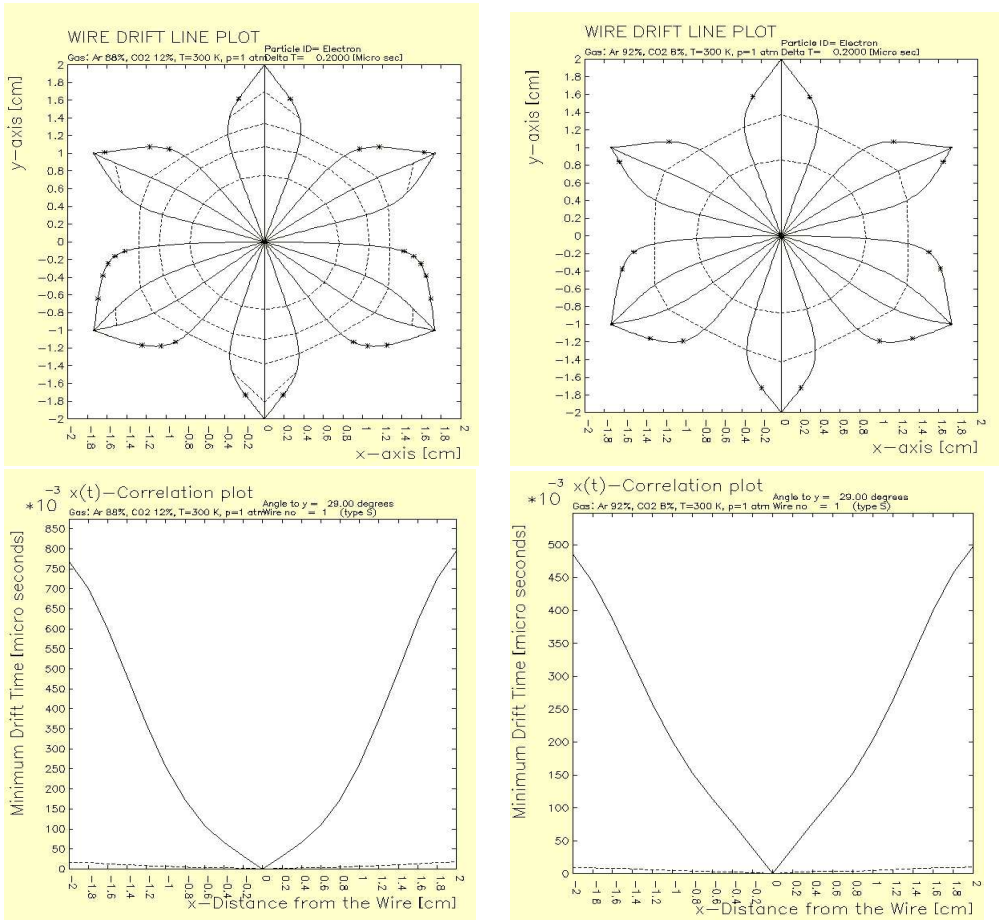

Figure 2.39: GARFIELD calculations of the electric field lines (top) and drift time vs. drift distance (bottom) for a Region 3 drift cell. The left plots show the configuration with a 20-μm diameter sense wire and the right plots show the configuration with a 30-μm diameter sense wire. The high voltages were set to provide the same gas gain for each configuration.

2.8.2 Mechanical Design

The chambers are designed to position the wires with an accuracy of 100 μm and to be robust and easily serviceable. The chambers are being designed with in-position surveying in mind. In order to cover angles down to 5°, the dead areas of each chamber (endplates, printed circuit boards, etc.) must be made as small as possible. The chambers in the high-field region (Region 2) must not be susceptible to eddy-current forces that might arise in the event of a quench of the superconducting torus.

We have arrived at different solutions for the three regions, but they share some characteristics:

- a very accurately drilled, flat endplate is affixed to a much stiffer frame;
- the flanges of the frame extend beyond the endplate thickness but do not further increase the dead area of the chamber;
- the chambers can be supported from two points only, at two ends of the outer "backplate";
- the Region 1 and Region 3 chambers are fully self-supporting in any orientation relative to gravity by the aforementioned two-point attachment;
- to further minimize dead area, the Region 2 chambers may have a portion of the wire tension borne by springs attached to the torus cryostats;
- when out of position, the Region 2 chamber may have temporary posts in compression taking the wire tension;
- signal translator boards (STB) will be mounted on the chamber and provide a connection between the wire crimp pins and the on-board preamplifier hybrid units;
- similarly, on-board high-voltage translator boards (HVTB) provide a connection to the high-voltage for each group of wires;
- on-board cables will run from the STBs and HVTBs to a connector box on the backplate.

Wire Layout: Cells, Layers, Superlayers

The wires are laid out in a "brick-wall" pattern with a guard wire layer followed by two layers of field wires and one layer of sense wires in a repeating pattern. Six layers of sense wires and their corresponding field and guard layers constitute a single superlayer. All of the wires in one superlayer are parallel. As we progress through the three regions, the superlayers are alternately U, V, U, V, U, V, with "U" representing wires with a +6° stereo angle and "V", -6°. The present `CLAS` detector has a similar wire layout structure and we have had very robust track-finding ability, even in the presence of modest backgrounds (up to 4% occupancy levels). Even in the presence of malfunctioning areas of the chambers, tracking is still efficient even with only 5 superlayers active.

The proposed chambers are planar; all wires in a given layer lie within a plane, as opposed to the present `CLAS` design where wires in a given layer lie on a cylindrical surface. This has the advantage that all cells within a given layer are equal-sized, facilitating calibration.

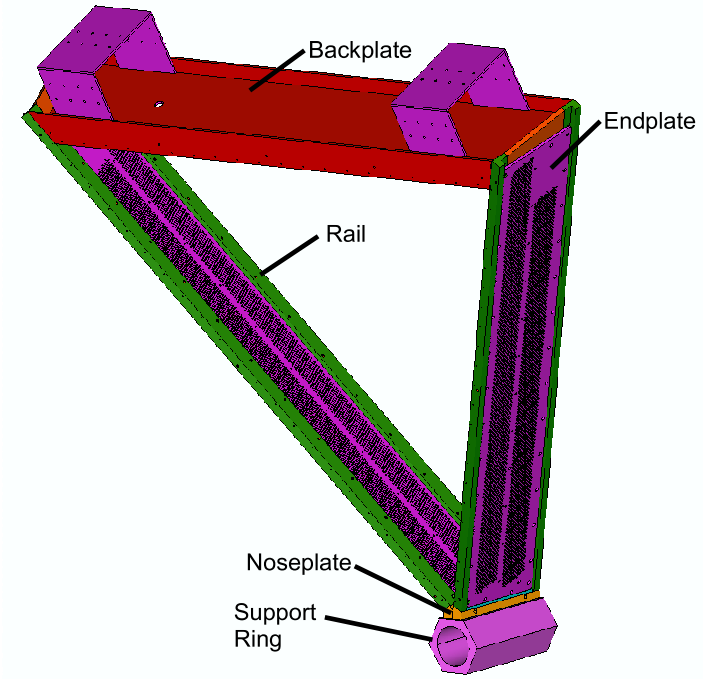

Figure 2.40: Assembly drawing showing the key elements of the drift chamber box. Gas window, electronic boards, and cables not shown.

Endplates and Box Assembly

The chamber body consists of a precisely drilled flat endplate fitted into a stiff, machined frame. We have already completed the design of a full-sized Region 1 prototype chamber. Fig. 2.40 shows the essential elements of the drift chamber: the endplates, the "backplate", the stiffening "rails" into which the endplates fit, and the "noseplate" that fits into a common hexagonal support ring. Fig. 2.41 shows design details for the endplate itself and Fig. 2.42 shows how the endplates fit into the associated box frame. Table 2.8 lists the design parameters for the Region 1 prototype chamber. Fig. 2.43 shows expected deflections of the endplate assembly after stringing (relative to unstrung).

Parameter	**Value**
Total weight	160 kg
Total wires	4928
Diameter,tension sense wires	30 μm, 20 g
Diameter,tension field wires	140 μm, 63 g
Diameter,tension guard wires	140 μm, 285 g
Total wire tension	352 kg
Endplate span	1.75 m
Backplate span	1.75 m
Max. endplate deflection	1.6 mm
Max. gravitational wire sag	250 μm

Table 2.8: Design parameters for the single-sector Region 1 drift chamber prototype.

Wires, Feedthroughs, Crimp Pins

Table 2.9 lists the materials and specifications for our wires, feedthroughs, and crimp pins. Our endplates are not parallel to each other, but instead are oriented with respect to each other at an angle of 60°. For this reason, the wire position is fixed not by the location of the crimp, but by the position at which the wire leaves the end of the feedthrough. This concept was tested before the present CLAS construction. The nominal wire-stringing tension was enough to force the wire to the "bottom" of the feedthrough mouth, establishing the position

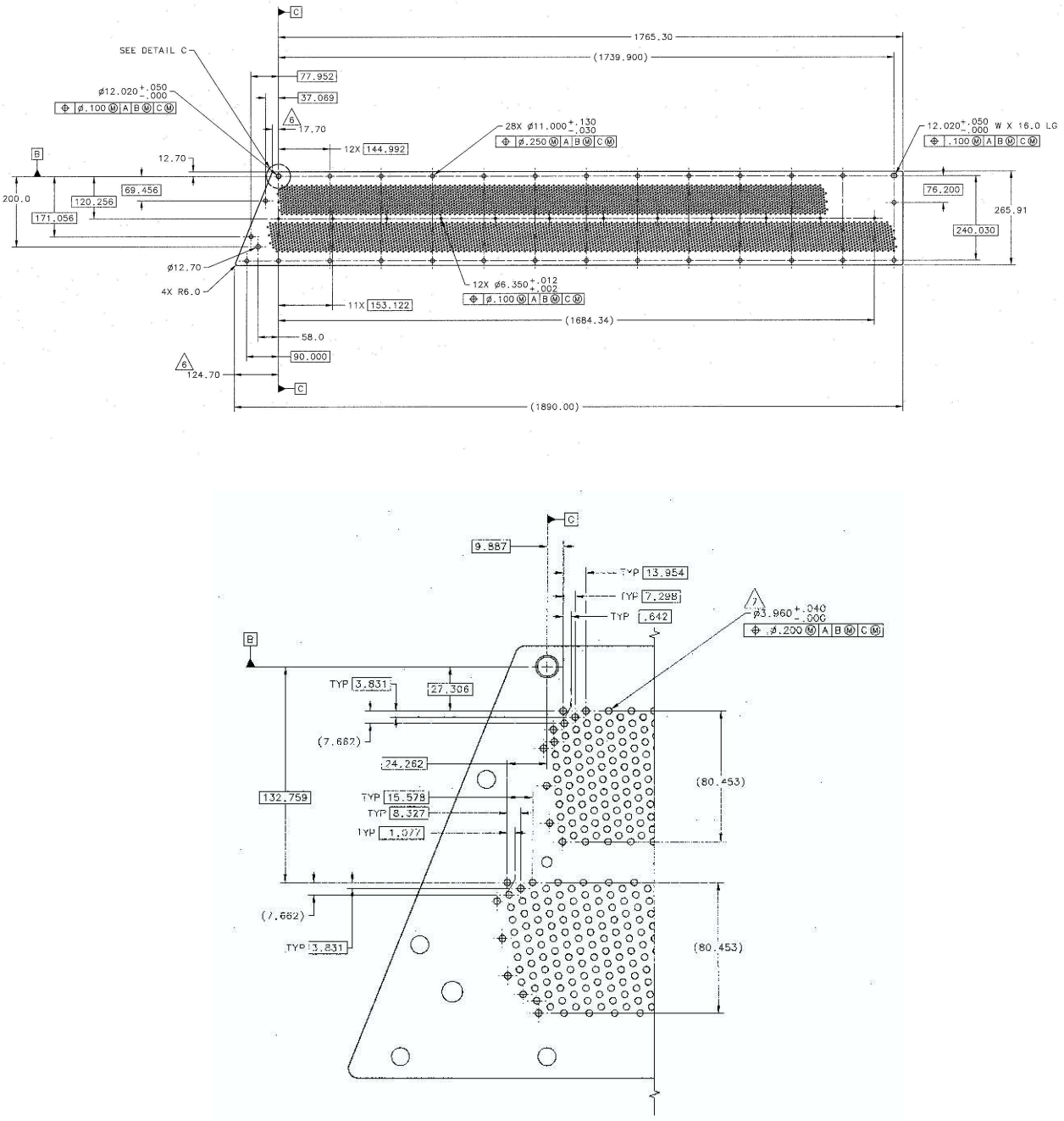

Figure 2.41: Design drawings of a Region 1 endplate showing the dimensions, hole locations, and tolerances.

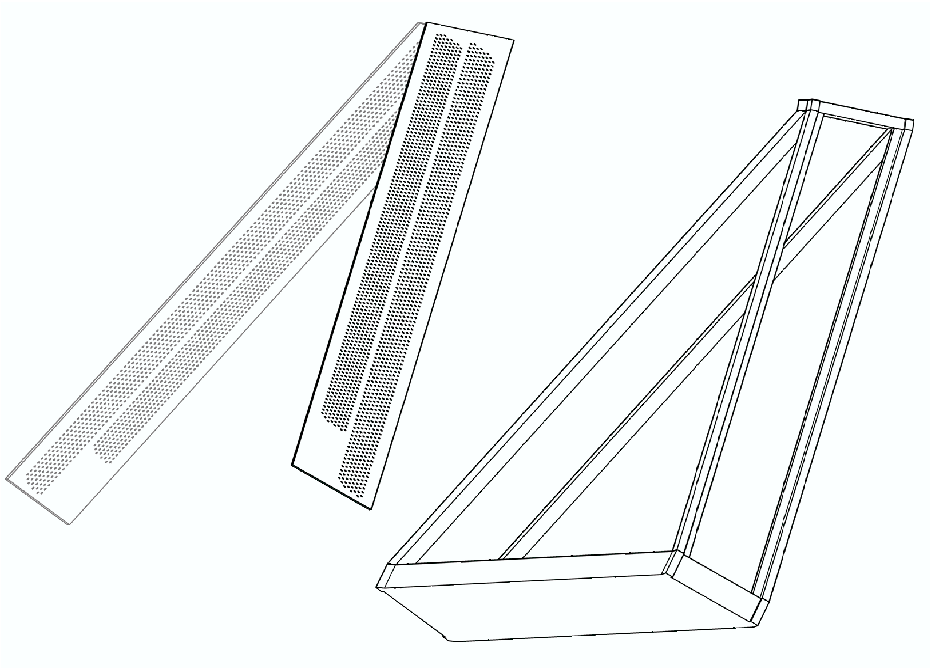

Figure 2.42: Drawing to show how a Region 1 endplate fits into its associated frame.

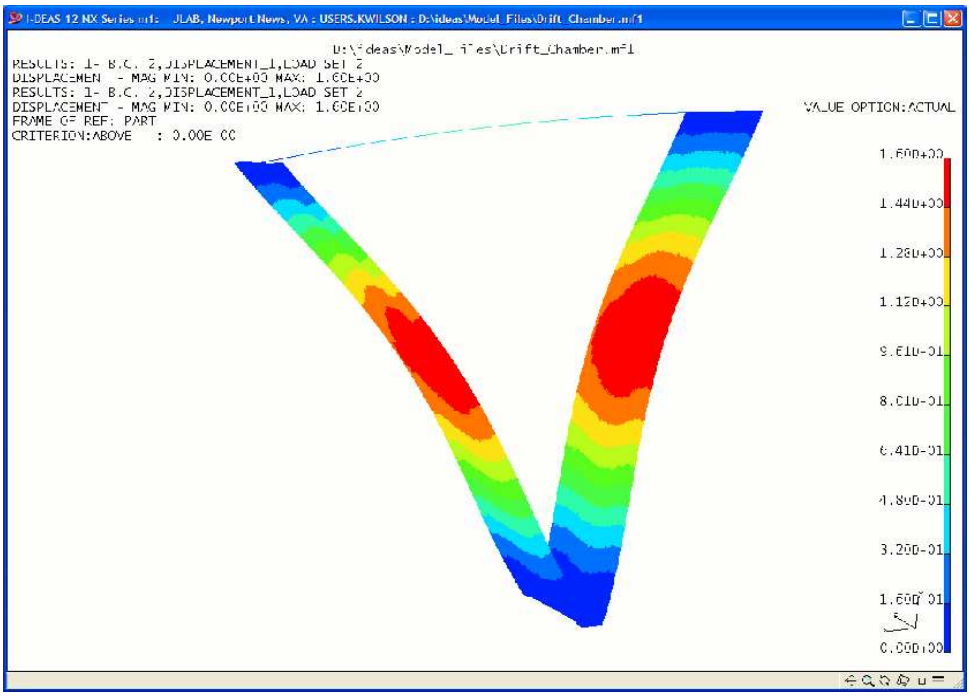

Figure 2.43: Finite-element analysis of the Region 1 prototype endplate showing expected deflections due to wire tension. Note that the red areas correspond to the maximum deflections of about 1.6 mm.

within an accuracy of 25 μm. Fig. 2.44 shows the details of a feedthrough penetration.

Parameter	Value
end-plate material	Aluminum, Stesalit
frame material	stainless steel
gas-bag material	aluminized Mylar
sense wire material	gold-plated tungsten
field wire material	gold-plated aluminum
guard wire material	stainless steel
feedthrough material	Noryl
crimp pin material	gold-plated copper (OFHC)

Table 2.9: Material choices for the wires, feedthroughs, and crimp pins.

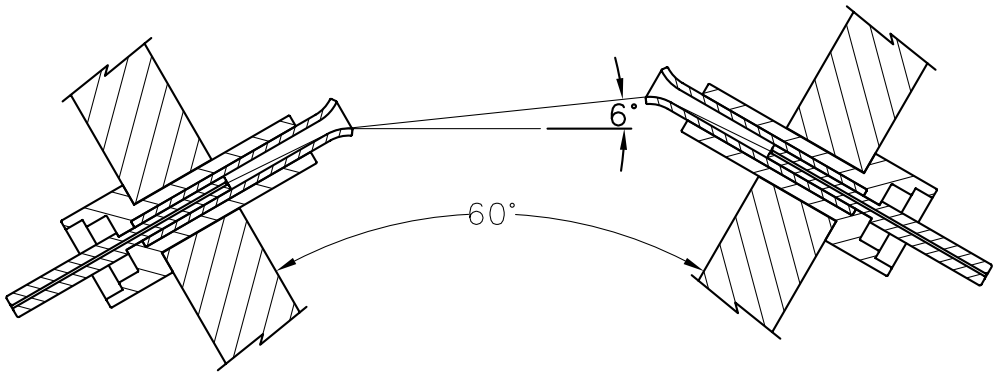

Figure 2.44: Illustration of two neighboring endplates showing the feedthrough penetration on each and the wire strung between the two feedthroughs.

Attachment Points

The chambers are being designed to be supported from two points on the backplate without imposing a large change of stress on the wires. This will facilitate installation. Fig. 2.40 shows a sketch of the attachments on the backplate of the chamber.

Survey, Alignment, and Magnetic Field Mapping

The chambers are being designed with survey and alignment in mind. For accurate tracking, the chamber locations must be well-known in space, especially with respect to the magnetic field. Survey points will be located on accessible faces of the chamber frame. Internal surveys (see Section 2.8.5) will transfer our knowledge of the location of the wire holes to these faces.

The magnetic field mapping strategy has not been worked out pending a final design of the torus magnet, but the concept will be to use hall probes to locate the positions of the energized conductors within the cryostats to sub-millimeter accuracy, and then to calculate the fields. We will take advantage of the very precise magnetic probe technology now available, and also of sophisticated software packages to calculate fields. This allows us to design small, precise instruments that can abut the cryostats themselves and be surveyed accurately.

2.8.3 Electronic Readout

The signal connections to the wires are made through printed-circuit boards mounted along one side of each chamber, called Signal Translator Boards (STBs). These boards are responsible for signal routing and preamplification. On the opposite side of each sector, another set of circuit boards called the High Voltage Translator Boards (HVTBs) is used to make the high-voltage connections to the wires.

On-Chamber PCBs and Cables

The `CLAS12` wire chamber geometry changes significantly from `CLAS`, so the circuit boards that interface the high voltages for the field, sense, and guard wires are new designs. The circuit boards that interface the sense wires to the preamplifiers (STBs) are also new designs. These interface circuit boards, both for the high voltage and the preamplifiers, will be designed on a 96-channel format. This format will allow for only seven circuit boards for each superlayer. Each sector in a particular region will use these seven circuit board formats for either high voltage or preamplification of the sense wire signal. Table 2.10 gives a channel count of the system. Fig. 2.45 shows the traces routed from the signal pick-up at the plated-through holes to the signal inputs of the preamplifier.

Fortunately the preamplifier used for the `CLAS` drift chambers can still be manufactured and the components are readily available. A large order for the `CLAS` preamplifier, CP01,

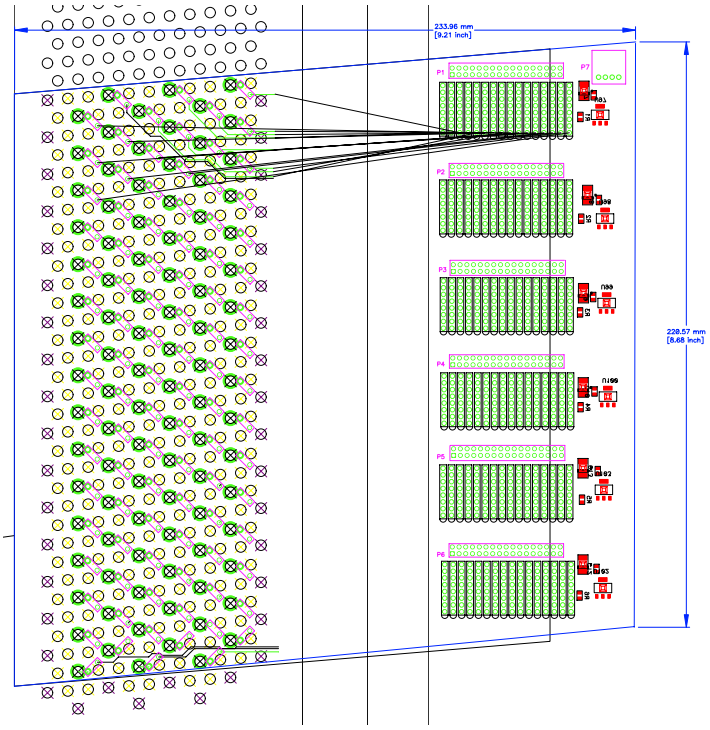

Figure 2.45: Trace routing shown on one of the Region 1 STBs being designed.

was ordered less than two years ago, as replacements for the original 1994 design. The new order included an epoxy resin encapsulation of the components on the preamplifier single in-line package or SIP. The encapsulation of the components on the hybrid SIP preamplifier is present to prevent component corrosion.

The CP01 preamplifier specifications are suitable for the CLAS12 wire chamber signal levels, and provide the gain, dynamic range, rise time, low noise, and low power for the upgrade performance requirements. These preamplifiers were designed in unison with the Amplifier Discriminator Boards (ADBs), that provide another level of amplification and a monostable discriminator pulse with the threshold setting optimized for the best resolution or sensitivity to a minimum ionizing signal. The monostable discriminated pulse widths are then multiplexed into a single channel of a pipeline TDC, with a least significant count of 500 ps and 8 μs of pipeline memory depth.

The low voltage power supplies used for CLAS will be used for CLAS12. These units are robust and manufactured by Hewlett Packard. The supplies are remotely programmable and monitored, and will provide more than enough power for the new wire chamber preamplifier requirements. We will use the same successful method of isolating the low voltage from

ground loops, using local voltage regulators on the preamplifier interface boards (STBs). The segmentation of the low voltage distribution cables is based on 32 preamplifier channels per supply cable. Each of these supply cables is fused with an appropriate type of fuse rated for over-current protection based on 32 preamplifier loads. We plan to re-use our CAEN system 527 high voltage supplies with somewhat finer segmentation than our current system, consistent with our total channel count dropping from 34000 to about 24000.

We plan to use 17-pair twisted pair cable for routing our signals from the STBs to the chamber backplate. The cable is round-jacketed with a 0.025-in pitch so that the overall cable dimension is smaller than the standard 17-pair cable. This smaller outer diameter cable will only be used from the STBs to the on-chamber "service panels". The standard 17-pair cable will be used from the chamber service panel to the readout electronics racks.

Component	Number
STB boards (6 types)	252 total
HVTB boards (6 types)	252 total
low-voltage cables	252 total
high-voltage cables	252 total
signal cables (17-pair)	1512
total signals	24192

Table 2.10: Electronic channel counts for the readout, high voltage, and low voltage.

Post-Amplifiers, Discriminators, Multiplexers, TDCs

We plan to re-use our post-amplifier and discriminator boards, as well as the associated multiplexing scheme. We also plan to re-use our LeCroy 1877 TDC modules. For details of these systems, refer to our drift chamber technical paper in Ref. [281].

2.8.4 Gas System

We have an extensive gas-handling system that has performed well. We plan to re-use it with only minor modifications of the plumbing. Full details of this system and its design are described in our drift chamber technical paper in Ref. [281].

2.8.5 Drift Chamber Construction

The chambers are being designed with individual holes and holders for each wire, i.e. a "strung" rather than a "wound" chamber. Our inspection and assembly procedures are designed to produce devices with wires placed and known by external survey to an accuracy of 100 μm, in order to achieve our goal of a 250 μm positional accuracy per wire layer. In addition to accuracy, we have chosen materials and designed procedures to insure a quiet and long-lived detector. The construction and winding techniques are based on our already successful CLAS drift chamber design.

Inspection and Cleaning

A visual and tactile inspection will be performed on the endplates and structural frame once we have accepted delivery. If deemed necessary, the surfaces will be sanded using 320-grit paper on a orbital sander to de-burr them in preparation for measurements. The endplates and structural frame will undergo a gross cleaning by soaking in a low residue laboratory degreasing solution with hand scrubbing, followed by a high-pressure water rinse. The parts will then receive their final cleaning using an ultrasonic bath of a laboratory-grade detergent solution. After two hours they will be removed from the bath and rinsed with de-ionized water and then sprayed with methanol to aid drying. Once dry, the parts are heat-sealed in nylon bags with a nitrogen atmosphere to await assembly.

Smaller parts such as feedthroughs and hardware are cleaned using a bench-top ultrasonic cleaner with laboratory detergent, followed by a de-ionized water rinse and a dousing of methanol to facilitate drying. In addition, the injection-molded parts are specified to be free of silicon mold releases.

Box Assembly

The box assemblies for Regions 1 and 3 consist of a structural frame to which the endplates are attached. This is achieved by first welding the frame to a reasonable tolerance then skim-cutting and drilling the endplate-receiving surfaces of the frame in a 5-axis milling machine. The cleaned endplates and cleaned structural frame are then joined using pins to locate them with low out-gassing epoxy (Shell Epon 826 resin/Versamid 140 hardener) on the contact surfaces and bolts to clamp and secure them. When the epoxy has cured, the box assembly is

sent to the measurement lab for fiducialization. Once this is complete, the feedthroughs are inserted and set in place using the same epoxy that was used to bond the endplates to the frame.

Internal Survey

A statistical sampling of the feedthrough hole locations and diameters will be performed on all endplates and structural components upon receipt from the vendor as part of the normal verification procedure. The JLab Survey Group will be using a Faro hard probe configuration on their portable coordinate measuring machine in a temperature-controlled laboratory for these measurements. The goal is to ensure the feedthrough holes are within the 0.200-mm true position tolerance and that the hole diameters are within the specified tolerance range.

Once the box frame and endplates are assembled, and before the feedthroughs are installed, a seven parameter least squares transformation is used to fiducialize the assembly in the measurement laboratory using a Faro laser tracker. This translation will provide a reference from the feedthrough hole locations on the endplates to tooling on the outside of the chamber that can be seen once it is installed in `CLAS12`. The chamber location in the hall will be ascertained also using the Faro laser tracker. The measurement group will then provide a formula that we can use to determine the wire locations in space. We can expect an overall wire location accuracy of approximately 0.2 mm using this system.

Because of the difficulty in producing the metal inserts of the feedthroughs, there is a high incidence of cracks and unwanted ovality in the flared section of the parts. We will be measuring and qualifying each of the metal inserts using magnifiers and run-out jigs before shipping them to the injection molders.

Note: 1) Faro tracker quoted precision, point-to-point = 0.061 mm. Total volumetric precision (25 m cubed) is 0.086 mm.

Note: 2) Error budget for the installed feedthrough points/line:

a. Initial inspection/fiducialization of endplates = 0.086 mm.

b. Secondary fiducialization of assembled box frame fiducials = 0.05 mm.

c. Installation survey standard error = approx. 0.1 mm.

The rms value for each feedthrough hole location in the installation would be approximately 0.14 mm. To define a point on the wire you would need to take the standard error for its two

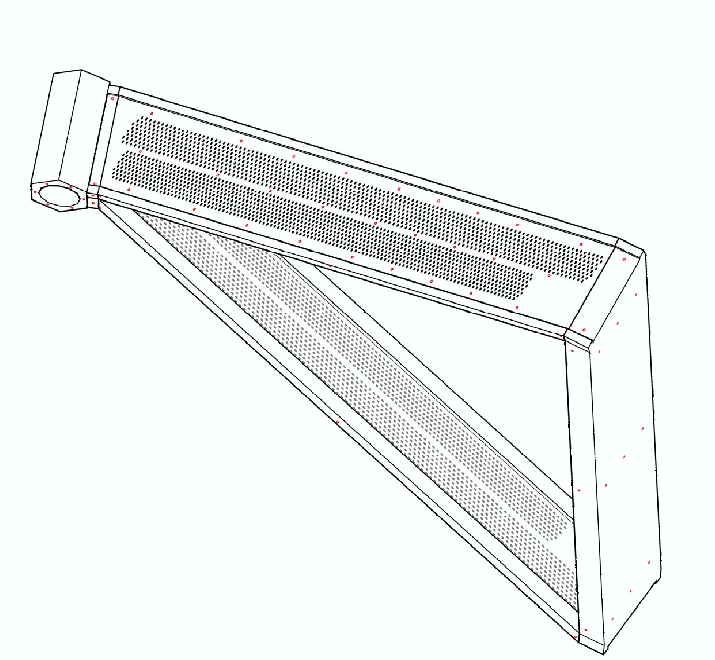

Figure 2.46: Location of the fiducial holes that allow transfer of wire feedthrough locations to the front (upstream) edge of the chamber frame.

feedthrough holes. Therefore, the rms of any calculated point on the wire would be almost exactly 0.2 mm (assuming the wire is straight). This value would then be translated in x and y for each end of the wire to account for the offsets due to the feedthroughs.

Stringing

The detector will be gravity-strung using the same basic methodology used when stringing the current CLAS drift chambers. The detector box assembly will be mounted to a stringing fixture. The frame will connect to the fixture using attachments that place the detector-frame system such that they rotate along the center of mass. This will permit safer and easy rotation of the detector by hand. A gantry crane will be used to lift the detector onto and off the stringing fixture and to raise the small end of the detector to account for the stereo angles.

The stringing fixture is very basic. It is mounted to the floor using concrete anchors. This minimizes floor obstruction as the box must be rotated to the opposite side to string the second set of wires. The box and frame assembly should be far enough away from the uprights such that they do not interfere with stringing activities. There is sufficient adjustment to gravity string the wires. There is a gross adjustment using the gantry crane to lift the telescoping side and pin it on the adjustment collar. The collar has a fine adjustment to allow setting

it at the most favorable stringing angle. The detector box will be rotated 180° to string the second superlayer.

Once the detector is installed onto the fixture, wire feedthrough insulators will be inserted and glued into each hole. Special care must be taken to use only the minimal amount of glue required to provide a solid gas seal and to prevent glue contamination inside the detector. Once one endplate is filled, the assembly will be rotated such that the other side can be done. Once all wire feedthrough inserts are in place, the box will be pre-tensioned.

Mounting Electronics Boards

The signal side of each chamber is tiled with multi-layered printed circuit boards called Signal Translation Boards (STBs). These boards were designed to capacitively decouple high voltage from the signals, and then to route the signals to the single in-line package (SIP) transimpedance preamplifiers mounted on these boards. The amplified differential signals are then sent via 20-m long twisted-pair lines to the main `CLAS12` readout electronics.

The connections between the sense-wire crimp pins and the plated-through holes of the STB boards are made using short conductive-rubber tubes. This material consists of silver-plated and/or nickel-plated glass spheres embedded in a silicon-rubber matrix. These tubes pass through the plated-through hole and over the end of the crimp pins, making the electrical contract between the wire and the circuit board. A small plastic cap inserted into the end of the tube ensures good contact with the circuit board. This approach has the advantages of reducing the space needed for connections, preventing crimp pins from being pulled from the feedthroughs when disconnecting the boards from the wires, and reducing the cost compared to metal connectors. This detail is shown in Fig. 2.47.

Positional Error Budget

In order to achieve a position resolution of 250 μm, the chambers have to be built accurately, positioned precisely, and carefully calibrated. There are three main categories of error: internal geometry, positioning accuracy, and uncertainties in the time-to-distance translation. Table 2.11 lists the main contributors to the error on the internal geometry or position of the wire relative to fiducial marks on the endplates. The quadratic sum of these terms gives 130 μm. Errors in external surveys can be compensated by "straight-track" alignment runs to the level of 60 μm.

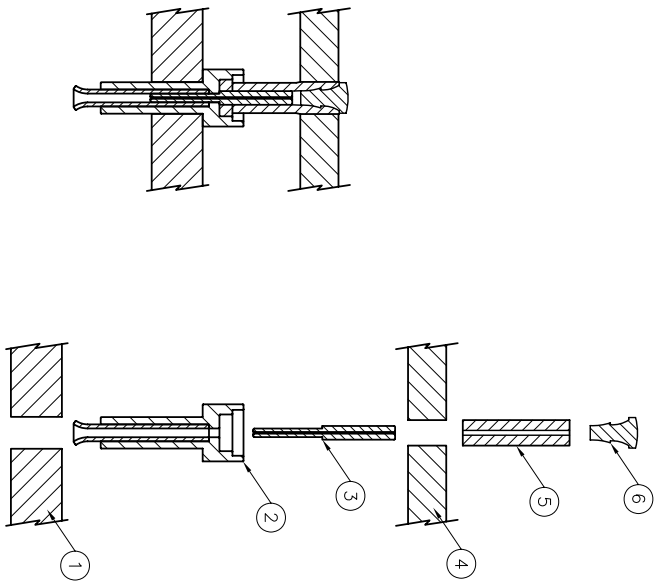

Figure 2.47: An assembly drawing showing how the crimp pin is inserted into the feedthrough and how the conductive elastomer tube fits over the crimp pin and inside the plated-through hole on the printed circuit board to make the electrical connection.

Intrinsic resolutions due to random-walk in the ion drift will be approximately 100 μm times the square root of the drift distance in centimeters; i.e. 90 - 150 μm for Region 1 and Region 3. This term has to be added to a variety of "time-slewing" effects due to amplifier rise-time and discrete location of ions. These time-slewing mechanisms mainly affect the resolution near the wire and near the edge of the drift cell. We see this clearly in our present data. In an approximate sense, this term has a size of about 150 μm. Adding the time-walk and time-slewing terms in quadrature gives us about 200 μm for the drift velocity dependent error. A total quadratic sum of the internal positional error (130 μm), the external positioning error after alignment (60 μm), and the drift velocity dependent error (200 μm), yields our estimate of 250 μm error per layer of measurement.

Quality Assurance

The detector will be strung in a class-10000 clean room to maintain clean wires and detector surfaces. Wire tensions will be monitored daily during the stringing process. All tension test results will be collected and saved in a database. All out of range wires will be replaced on a daily basis. Each step completed during the stringing process will be independently checked at the end or beginning of each shift.

Contribution	Size σ
Endplate hole placement	100 μm
Location in feedthrough	50 μm
Grav. wire sag (uncorrected)	250 μm
Grav. wire sag (corrected)	25 μm
Endplate deflection (uncorrected)	0.8 mm
Endplate deflection (corrected)	40 μm
Transfer of feedthrough locations to tooling balls	50 μm
Quadratic sum	130 μm

Table 2.11: Various contributions to inaccuracies in the internal wire positions.

Once stringing is complete, wires will be checked for shorts and cross-talk prior to installing the HV boards. Wire tensions will be randomly tested and the results will compared to those previously determined. HV testing will be completed prior to installing the signal translator boards.

2.8.6 Drift Chamber Operation

The chambers will operate for many years in a wide variety of experimental conditions. We will draw on the present CLAS infrastructure to supply gas and power (low voltage and high voltage) to the chamber, to monitor these systems, and to provide shift-takers with an online determination of various key tracking parameters: the number of hits per track, the online position resolution, the number of hits per layer and wire, the maximum drift time, and a plot of time differences for nearby wires that show characteristic peaks when coherent noise is present. We will follow procedures similar to those described in our technical article [281] on the CLAS drift chambers. We do not anticipate any changes in the concepts for these operations.

Alignment

During CLAS operation we have had numerous occasions to remove a chamber in order to inspect or fix some problem. After such a repair period, we found it necessary to do a

special "B=0" run in order to line up the removed and replaced chamber with the untouched chambers in the same sector. Our mechanical procedures allowed us to replace the chamber with millimeter accuracy; the alignment procedure fine-tuned our positional knowledge to an accuracy of better than 100 μm.

The CLAS12 chambers have a simpler and smaller geometry (planar chambers in a triangular box) and the positioning fixtures will be located closer together, thus we hope to replace a removed chamber with much better accuracy.

2.9 Expected Tracking System Performance

We have studied rate effects in the central SVT (the BST). A GEANT4 study shows that the primary accidental background impinging on the BST is γ rays, and that the total rate will be about 60 MHz per layer. The vast majority (>90%) of these photons produce only one hit in a particular layer. We have conducted two studies of the effect of background on the BST: in one we studied the effect of uncorrelated background while in the second we used a realistic GEANT4 simulation of the electromagnetic and hadronic background.

The first study considered uncorrelated, evenly-distributed background. Because the number of strips per layer is very large, the main deleterious effect of such a background is to produce 'fake' tracks from these accidental hits. We applied a cut-based track-finding algorithm to a set of events generated from random hits in each layer, augmented with a 10% 'punch-through' probability, that is, for each hit, there was a 10% chance that a strip in the adjacent layer would also be hit. We tuned up the cuts so that true tracks were found with greater than 95% probability. Fig. 2.48 shows the number of reconstructed fake tracks plotted vs. the assumed rate of accidental hits per layer for two cases: one with a 6-layer BST and the other with an 8-layer BST. For each configuration, we see a similar behavior: at low background there are few fake tracks and the number begins to grow exponentially at some background level. Note that these fake tracks can be significantly reduced using other information, e.g. the central TOF counters, but nevertheless, we would like to keep the number of fake tracks as found in the BST alone below some number, for example, five per event. Fig. 2.48 shows that if we wish to stay below five fake tracks per event, an 8-layer BST design will extend the luminosity reach of the detector by about 40% over a 6-layer design. We also note that a 60-MHz accidental background integrated over the 150-ns live-time of the SVT will create

only about 8 accidental hits per plane. At this level of background, we should find essentially no fake tracks and the accidental background will be dominated by real, out-of-time hadrons from other events.

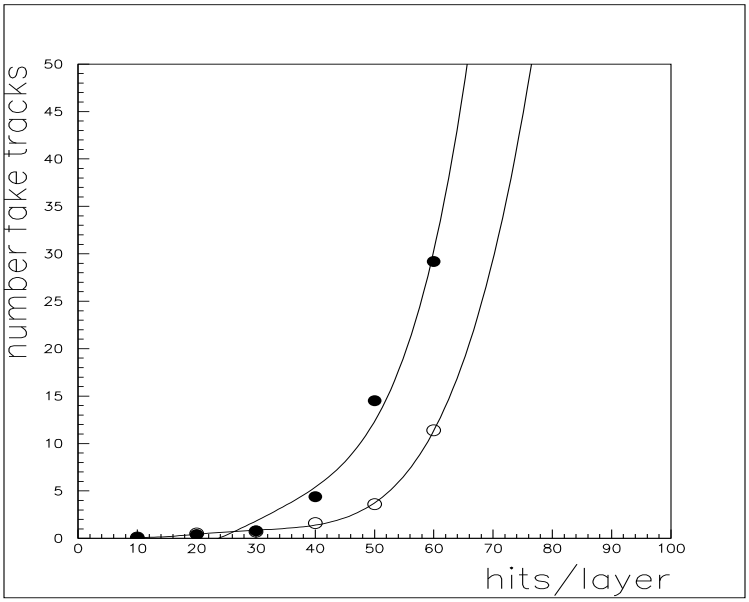

Figure 2.48: A plot of the number of reconstructed fake tracks as a function of the number of accidental hits per layer in the BST for two cases: a 6-layer (filled) and an 8-layer (open circles) version.

The second study was a full GEANT4 simulation followed by realistic event reconstruction in the presence of the background. After optimizing our reconstruction code on clean events, we turned it to the task of finding one (known) track embedded in a sea of background. As expected from the simpler study, we saw very little loss of efficiency in finding the known track, but we did find accidental tracks. The number of these accidental tracks was proportional to the background rate and had a characteristic shape. If there was a real track in the simulated event, then the background consisted of two parts:a number of "sister" tracks with nearly the same momentum as the real track and a smooth background of fake tracks with no connection to the real track. This smooth component peaks at small values of momenta. The "sister" tracks are caused by using most of the hits from the real track along with the wrong choice of hit, when an accidental hit was adjacent or very near a real hit. These combinations would probably be removed during an analysis, but they will worsen the resolution.

Our studies also show that the number of fake tracks is very sensitive to a cut on the energy deposited in a single strip. It seems that we can remove most of the fake track candidates with

a 20 keV cut on the hits from the BST. Note that a minimum ionizing particle is expected to deposit about 140 KeV of energy on traversing one strip.

2.10 Charged Particle Tracking

This section presents the SOCRAT package that has been developed for charged particle reconstruction with the future CLAS12 spectrometer. This spectrometer has been designed to run at luminosities of 10^{35} cm^{-2} s^{-1}, providing an efficient and accurate detection of particles over a wide kinematic range. This has lead to split the spectrometer into two independent parts:

- a central tracker, ensuring the detection of baryons with moderate momentum and polar angles θ between 35° and 125°.
- a forward tracker, covering the region between 5° and 35°.

The requirements in terms of resolutions are summarized in Table 2.12 for these two subsystems.

	Central Tracking	Forward Tracking
σ_p/p	5%	$< 1\%$
σ_θ	< 20 mrad	< 1 mrad
σ_ϕ	5 mrad	< 3 mrad

Table 2.12: Required performances in the central and forward trackers for particles at 1 and 5 GeV, respectively.

This tracking section is organized as follows: Section 2.10.1 is dedicated to details on the event generation. We present in Section 2.10.2 a brief overview of the Kalman Filter algorithm that we use for the final track fitting. The tracking in the central region is described in Section 2.10.3, where we detail our track finding and track fitting methods. The resulting performance of the tracking is then derived and compared with the initial requirements. The effect of the background in terms of fake track reconstruction is also discussed. Finally, we study the effect of various misalignments on the performance, thus deriving constraints on the accuracy of the alignment of the detectors. Section 2.10.4 is dedicated to the forward

tracker, and is basically organized as in Section 2.10.3. In this region, the matching of tracks reconstructed in the DC and in the FST is particularly important, and is discussed in detail.

2.10.1 Event Generation

In order to test the tracking code and evaluate its performance, realistic tracks and events should be generated. For the moment, these events can be simulated in two different ways:

- using a GEANT4 simulation of the `CLAS12` spectrometer. The development of the `gemc` package already allows Socrat to reconstruct tracks from GEANT, using hit information stored in a root tree;
- using a Socrat internal routine.

Ultimately, we want to use only events coming from GEANT, as they are much more realistic. However, because of the number of electrons needed in GEANT to simulate full luminosity (more than 60,000), the event production is very time consuming. The internal routine, on the other hand, is relatively fast (a track with background is generated in about 10 ms in the central tracker, less than 100 ms in the forward), and was made quite realistic by taking into account:

- the multiple scattering;
- the available magnetic field tables (and linear interpolation);
- a full digitization for all detectors (SVT and DC);
- (uncorrelated) background. This is in fact the less realistic point, as the correlation of background hits is neglected.

If both the forward and the central tracking code are tested, the routine generates one track in each region, with the same vertex position.

2.10.2 The Kalman Filter Algorithm

We present here a practical approach to the Kalman Filter, which we used for all our track fitting, both in the central and forward regions; further details can be found in Refs. [285,

286]. This algorithm provides a recursive way to estimate the state of a system evolving in space and time, by using discrete measurements and minimizing the corresponding χ^2. If we assume the system can be described by an n-vector $\vec{x}_k$ at some discrete step k of its evolution, where a *measurement* $\vec{m}_k$ is performed. The m-vector $\vec{m}_k$ is related to $\vec{x}_k$ via some unitary transformation that can be written:

$$\vec{m}_k = \mathbf{H_k} \cdot \vec{x}_k. \tag{2.1}$$

We then define the state of the system, extrapolated to a next step (in practice, to the next measurement), as:

$$\vec{x}_k^{k+1} = \mathbf{F_k} \cdot \vec{x}_k, \tag{2.2}$$

where $\mathbf{F_k}$ is some known propagation operator. At the step $k+1$, the algorithm has to perform an update of the system state, using both an extrapolated vector (i.e. all previous measurements) and the current measurement. Writing $\mathbf{C_k}$ (resp. $\mathbf{M_k}$) the covariance matrix of $\vec{x_k}$ (resp. $\vec{m_k}$), and defining the covariance matrix of the extrapolated state $\vec{x}_k^{k+1}$:

$$\mathbf{C_k^{k+1}} = \mathbf{F_k} \cdot \mathbf{C_k} \cdot \mathbf{F_k}^T + \mathbf{Q_k}, \tag{2.3}$$

with some process noise matrix $\mathbf{Q_k}$, the χ^2 can be written as:

$$\begin{aligned}\chi^2 = &(\vec{x}_{k+1} - \vec{x}_k^{k+1})^T \cdot \left(\mathbf{C_k^{k+1}}\right)^{-1} \cdot (\vec{x}_{k+1} - \vec{x}_k^{k+1}) \\ &+ (\mathbf{H_{k+1}} \cdot \vec{x}_{k+1} - \vec{m}_{k+1})^T \cdot (\mathbf{M_{k+1}})^{-1} \cdot (\mathbf{H_{k+1}} \cdot \vec{x}_{k+1} - \vec{m}_{k+1})\end{aligned} \tag{2.4}$$

The minimization gives:

$$\vec{x}_{k+1} = \mathbf{C_{k+1}} \cdot \left(\left(\mathbf{C_k^{k+1}}\right)^{-1} \cdot \vec{x}_k^{k+1} + \mathbf{H_{k+1}}^T \cdot (\mathbf{M_{k+1}})^{-1} \cdot \mathbf{H_{k+1}} \cdot \mathbf{H_{k+1}}^T \cdot \vec{m}_{k+1} \right), \tag{2.5}$$

with the updated covariance matrix:

$$\mathbf{C_{k+1}} = \left(\left(\mathbf{C_k^{k+1}}\right)^{-1} + \mathbf{H_{k+1}}^T \cdot (\mathbf{M_{k+1}})^{-1} \cdot \mathbf{H_{k+1}} \right)^{-1}. \tag{2.6}$$

Application for Central Tracking: In our case, $\vec{x}$ is a 5-vector and, due to the approximate ϕ symmetry of the BST, we chose the following state vector for the filter:

$$\vec{x} = (z, \phi, p_x, p_y, p_z)^T, \tag{2.7}$$

where z is the coordinate along the beam axis, ϕ is the azimuthal angle (calculated from the origin of the frame), and p_x, p_y, p_z are the momentum components.

It is easy to show that the evolution of this state vector between t and $t + dt$ is:

$$\begin{pmatrix} z \\ \phi \\ p_x \\ p_y \\ p_z \end{pmatrix}_{t+dt} = \begin{pmatrix} 1 & 0 & 0 & 0 & \frac{dt}{m} \\ 0 & 1 & \frac{-ydt}{mr^2} & \frac{xdt}{mr^2} & 0 \\ 0 & 0 & 1 & \frac{qBdt}{m} & 0 \\ 0 & 0 & \frac{-qBdt}{m} & 1 & 0 \\ 0 & 0 & 0 & 0 & 1 \end{pmatrix} \begin{pmatrix} z \\ \phi \\ p_x \\ p_y \\ p_z \end{pmatrix}_t , \tag{2.8}$$

where $r = \sqrt{x^2 + y^2}$. Multiplying all these matrices between two BST double layers directly gives the propagation matrix $\mathbf{F_k}$ introduced above.

As a double layer measures exactly z and ϕ at a given r, the measurement matrix is simply:

$$\mathbf{H_k} = \begin{pmatrix} 1 & 0 & 0 & 0 & 0 \\ 0 & 1 & 0 & 0 & 0 \end{pmatrix} \tag{2.9}$$

Finally, the multiple scattering effect can be correctly taken into account using the process noise matrix $\mathbf{Q_k}$.

2.10.3 Central Tracking

BST Design

Charged particle reconstruction in the central region of `CLAS12` is provided by the Barrel Silicon Tracker (BST) that is located inside a 5-T solenoid. The strip angles of the BST run between 0° and 3° for one layer, and between 0° and -3° for the next one. Because the strips with small angles are longer, the average crossing angle for a superlayer is around 2° (and depends on the polar angle θ).

Track Finding and Track Fitting

Track Finding: The basic idea of the track finding procedure is to find hit candidates in each double layer, and to find combinations that could define a track. Because the strips have a graded angle on a polygonal structure, they are not at a constant radius from the beam line. For this reason, it would be complicated to directly run the fitting procedure using the strip information. So, the finding routine first tries to associate strips from the two layers of a double layer to define a 3-dimensional point. In a first step, this 3-dimensional point is the intersection of the strips, assuming the particle crosses the tile with a 90° angle[1]. Only the strips whose intersection is in the BST acceptance (within a 10-cm margin) are kept and considered as hit candidates.

Once all the hit candidates have been found, the program loops over hits in each double layer, and searches for combinations that are relatively close to a circle. If there are hits on each superlayer that can be associated, the following requirements have to be fulfilled:

- the first two hits should be close in ϕ: $|\phi_2 - \phi_1| < 0.7$ or $> (2\pi$ - 0.7);
- the transverse momentum calculated with the first three hits should be in a reasonable range, $p_T > 0.2$ GeV and < 4 GeV; also the hits should be close in ϕ, $|\phi_3 - \phi_2| < 0.7$ or $> (2\pi$ - 0.7); last but not least, the circle should not be too far from the beam axis ($(x, y) = (0, 0)$): $|R - \sqrt{x_C^2 + y_C^2}| < 8$ mm;
- the last hit (on the 4^{th} double layer) should be close to the previously fitted circle C, $d(P_4, C) < 0.07R + 0.01/R$ (the second term takes into account the multiple scattering), and the angle $\theta_{23,34}$ between the lines (P_2P_3) and (P_3P_4) should be small, $\cos\theta_{23,34} > 0.75$.

If one of the double layers cannot produce a hit satisfying these requirements, the search is not abandoned, as the redundancy allows for finding tracks with only 3 out of 4 double layers, but the criteria and values defined above are slightly modified. These values have been tuned to reach a 99% efficiency of track finding, assuming a perfect acceptance[2].

[1] This is because at this stage, we know nothing about the angle of the track candidate.

[2] Using the internal track generation routine, a perfect acceptance can be easily simulated by putting all the dead zone sizes to zero.

Once a combination of 3 or 4 hits has been found to be a good track candidate, it is possible to quickly obtain a relatively good estimate of the track parameters, assuming the track is a helix. We then use these parameters to derive the incident angle of the track on all the double layers, and recalculate the intersection points of the corresponding strips. As the involved strips do not have the same stereo angle, this recalculation is not straightforward: it is equivalent to find two 3-dimensional points on 2 non-parallel lines, joined by a given unit vector. To make the calculation fast enough, Socrat directly uses the inverted 6×6 system that we solved with Maple. It turned out that, for small momentum particles, this recalculation has a non-negligible effect on the track parameters themselves, so a few iterations are needed in practice.

The total track finding efficiency (including the acceptance) is shown in Fig. 2.49 as a function of some track parameters. One can see some zones of inefficiency that correspond to ϕ values for which at least two edges of the polygons are crossed by the particles. The positions of these zones slightly depends on p_T (directly related to the curvature), especially at small momenta. The resulting inefficiency may be lowered by rotating the double layers separately to decrease the probability of crossing at least 2 dead zones.

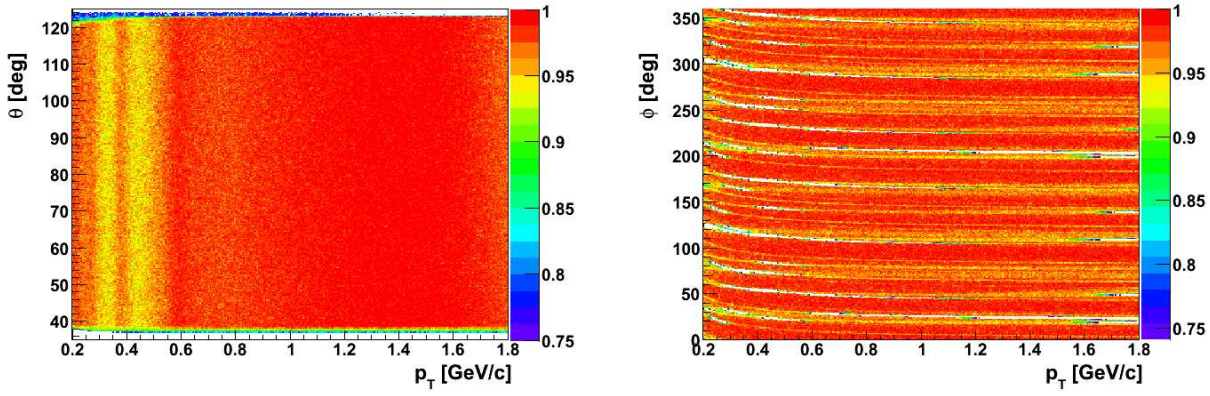

Figure 2.49: Track finding efficiency as a function of the transverse momentum p_T and the polar angle θ (left) or the azimuthal angle ϕ (right).

For a 1-mm long target, the integrated efficiency is:

$$\langle \epsilon \rangle = 94\%. \tag{2.10}$$

For a 10-cm long target, this efficiency is around 90%. If we use only 3 double layers (no

redundancy), the inefficiency reaches around 1/3.

Track Fitting: Once good track candidates have been identified, the corresponding list of hits is sent to the fitter algorithm. This algorithm is based on the Kalman Filter that we described in Section 2.10.2. An important issue is the initialization of the state vector and its corresponding covariance matrix. An analytic estimation of $\vec{x}$ is obtained assuming the track is a helix, the solenoid field being quite homogeneous across the entire BST. The initial covariance matrix we choose is diagonal, with *relatively* large values for the diagonal terms: around 2 mm for the z uncertainty, 1° for ϕ, 40 MeV for p_x and p_y, and 100 MeV for p_z. We also introduced a p_T dependence on these terms to take into account the uncertainty due to the multiple scattering. A further improvement would be to also introduce a θ dependence, as small biases were observed for angles close to 35° and 125°.

Finally, the Kalman Filter is run, starting from the last available measurement, and going backwards. It is stopped when it reaches the distance of closest approach to the beam axis, the corresponding point defining the *vertex* of the current track.

Tracking Performance

The resolutions in p_T, θ, ϕ, and z have been obtained using proton tracks at 90°. Because of the multiple scattering, these resolutions depend on the transverse momentum, and we used the following expressions to fit the different distributions:

$$\sigma_{p_T}/p_T = \sqrt{(\sigma_{1,p} \times p)^2 + \left(\frac{\sigma_{2,p}}{p\beta}\right)^2} \tag{2.11}$$

$$\sigma_\theta = \sqrt{(\sigma_{1,\theta})^2 + \left(\frac{\sigma_{2,\theta}}{p\beta}\right)^2} \tag{2.12}$$

$$\sigma_\phi = \sqrt{(\sigma_{1,\phi} \times p)^2 + \left(\frac{\sigma_{2,\phi}}{p\beta}\right)^2} \tag{2.13}$$

$$\sigma_z = \sqrt{(\sigma_{1,z} \times p)^2 + \left(\frac{\sigma_{2,z}}{p\beta}\right)^2}. \tag{2.14}$$

The 8 $\sigma_{i,X}$ extracted from the fits are summarized in Table 2.13. We see that the original requirements from Table 2.12 are satisfied, even if we are at the upper limit for the θ resolution.

	σ_1	σ_2
p	2.72%	1.06% GeV
θ	21.6 mrad	1.75 mrad GeV
ϕ	4.60 mrad	1.50 mrad GeV
z	2.30 mm	0.13 mm GeV

Table 2.13: Resolutions obtained in the central tracker for protons tracks at 90°.

The performance obtained with the Kalman Filter algorithm were also compared with estimates that can be analytically derived using the MOMRES program [284]. To do this, we used only tracks with hits in all the double layers. Fig. 2.50 shows that very good agreement is found between the two estimates, thus giving us confidence in our tracking code. We can also note that the p_T dependence of the obtained resolutions is very close to the expected ones (used for the fits).

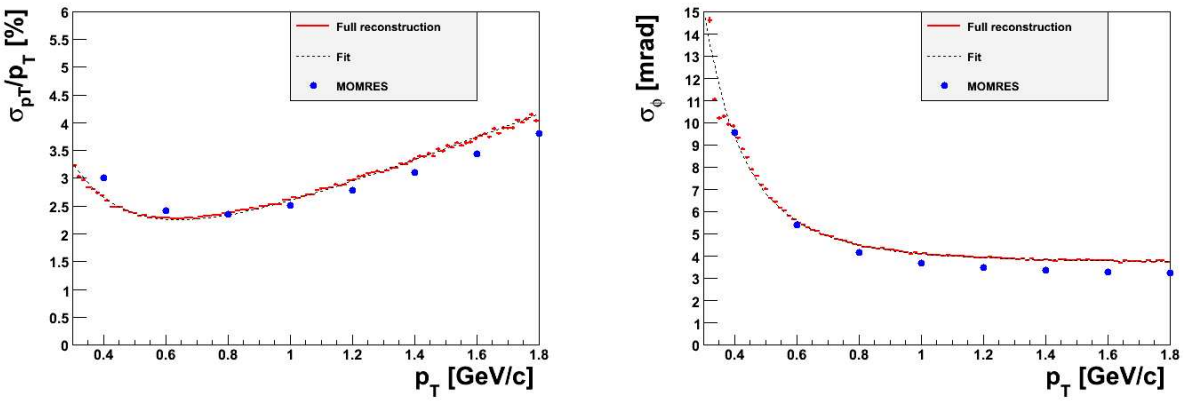

Figure 2.50: Comparison of the resolution in p_T (left) and ϕ (right) obtained with the full reconstruction code and with the MOMRES program (proton tracks at $\theta = 60°$).

Finally, Table 2.14 shows the effect of the maximum strip angle on the resolutions, using the sample of tracks that has been used for the MOMRES comparison. We see that the θ resolution can be improved significantly by using a larger angle, without significantly affecting the p_T and ϕ resolutions. However, a larger crossing angle will increase the reconstruction of fake tracks in the presence of background, which still needs to be quantified.

α_{max} (°)	$\sigma_{1,\theta}$ (mrad)	$\sigma_{1,p}$ (%)	$\sigma_{1,\phi}$ (mrad)	$\sigma_{1,z}$ (mm)
3	18.9	2.69	4.50	2.35
6	12.0	3.04	5.09	1.43
12	9.77	3.26	5.48	1.12
15	8.74	4.05	6.66	0.93

Table 2.14: Evolution of the resolutions with the maximum strip angle α_{max}.

Effect of the Background

Background hits in the BST can degrade the tracking resolution, and produce fake tracks that will complicate the data analysis. The first case happens when a fake hit is accidentally close to a good one, creating a *sister* track that is similar to the original one. But thanks to the good spatial resolution of the BST, only very close sister tracks can pass all the tracking filters (including a final χ^2 cut), so that the effect on the resolution is very limited. The creation of purely fake tracks, on the other hand, can be more problematic, and needs precise simulation on the background rate to be estimated.

The total number of tracks reconstructed in the BST for single particle events with uncorrelated background is presented in Fig. 2.51. We see that below 100 MHz per BST layer, the number of reconstructed tracks is rather limited, but tends to increase more rapidly above 100 MHz. A detailed analysis shows that below this critical rate, additional tracks are mainly sister tracks, whereas they are essentially fakes above, when the density of hits is high enough.

More detailed simulations were done using GEANT3 and GEANT4 they indicated that, with a luminosity of 10^{35} cm^{-2}s^{-1}, the background rates do not exceed 60 MHz in the BST, i.e. well below the critical 100 MHz limit. But they also showed that the background is slightly correlated, so a few fake tracks are indeed seen, as illustrated in Fig. 2.52. However, the Central Time-Of-Flight (CTOF) allows for rejection of some of them (see Fig. 2.52 left), thanks to its very good time resolution. The remaining tracks have almost the same momentum as the original one (*sister* tracks, see Fig. 2.52 right). Using a merging algorithm for these tracks (to be written), the overall reconstructed events will be clean enough for most of the data analyses.

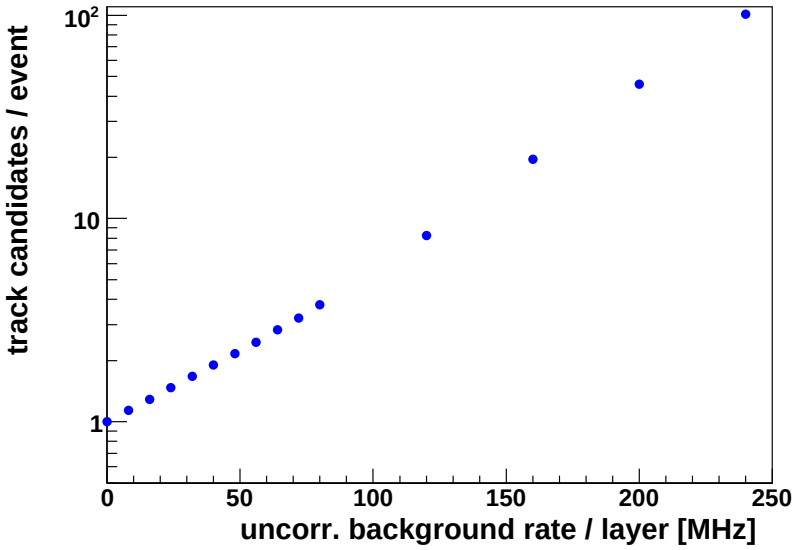

Figure 2.51: Number of reconstructed tracks for single track events as a function of the (uncorrelated) background rate in the BST (see text for details).

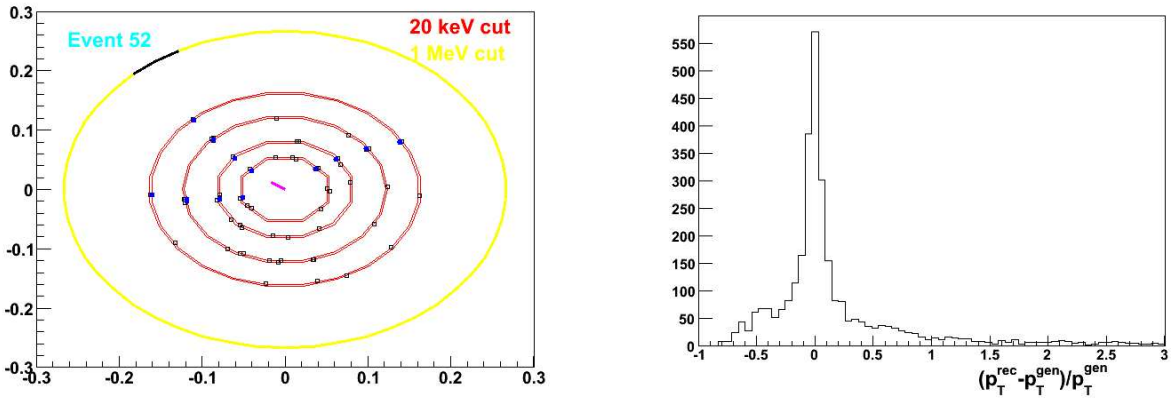

Figure 2.52: (Left): DVCS event generated with GEANT4 at full luminosity. The proton track (indicated by the pink line) has been correctly identified. Two fake tracks are also visible, but can be rejected using the CTOF information. (Right): reconstructed momentum of tracks from DVCS events. On average, three tracks per event are reconstructed, most of them are very close to the original one.

Misalignments

All the resolutions and performances presented up to now assume a perfectly aligned BST. In practice, many reasons – from manufacturing to installation – can introduce misalign-

ments [287], thus degrading the resolution, not to mention introducing systematic shifts in momentum or angles. To study these effects, we studied the use of different geometrical parameters in the track generation and the track reconstruction routines of Socrat. For each BST double layer, the following parameters can be misaligned:

- its radius R (expansion/contraction);
- its global ϕ (rotation around the beam axis);
- its z position (translation along the beam axis).

In practice, one specifies the accuracy of the alignment for all these parameters (the accuracy can be different between two double layers), and the program generates misalignments on Gaussians with the corresponding widths. The average effect on the resolution can then be estimated by running the program many of times to avoid bias from particular configurations. Fig. 2.53 illustrates the effect of misalignment in R. On the left plot, no misalignments are introduced: the resolution found is independent of the sample of events, and no systematic shifts in momentum are observed. On the right plot, one can see that a 200 μm accuracy on R has a limited effect on the momentum resolution, but introduces a shift in momentum of the order of 0.8%.

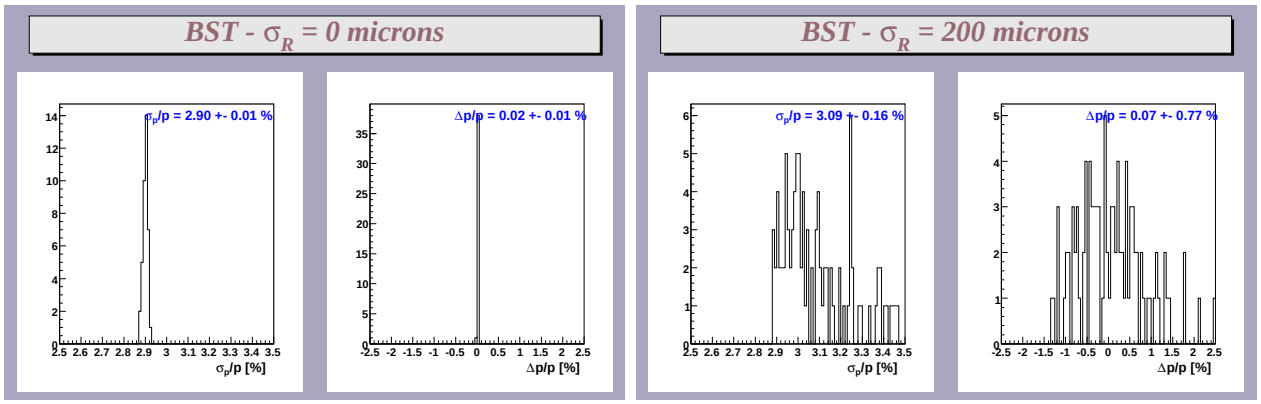

Figure 2.53: Momentum resolution and shift of 0.6 GeV protons at 60° without any misalignment (left) and with R misalignment of 200 μm (right). Each entry of these histograms corresponds to a sample of 50k tracks, and a setup with misalignments randomly generated with a Gaussian of 0 and 200 μm widths, respectively.

As this shift is the largest effect of misalignment, it has been studied as a function of misalignments in R and ϕ (the misalignment in z has almost no effect on momentum resolution,

and limited effect on other track parameters). These studies are summarized in Fig. 2.54. If we want to keep the momentum shift below 0.5%, the plots tell us we need an accuracy:

- better than 100 microns in R;
- better than 0.2 mrad in ϕ.

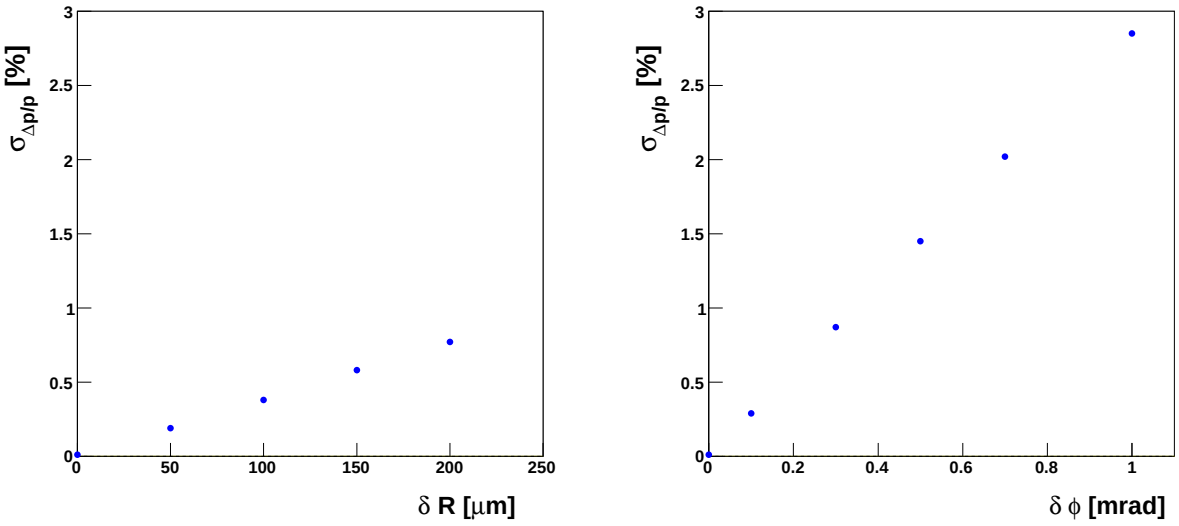

Figure 2.54: Typical size of the momentum shift as a function of misalignments in R (left) and ϕ (right) (0.6 GeV protons at 60°).

These constraints seem to be compatible with what can be reasonably achieved.

Finally, we checked that misalignments in all the variables simultaneously have effects that are compatible with the ones obtained with separate misalignments, as illustrated in Fig. 2.55.

2.10.4 Forward Tracking

DC and FST Design

The FST allows the detection of particles between 5° and 35°. Its major component is a set of 36 planes of Drift Chambers, divided in three regions of two superlayers each, ensuring highly efficient detection with large redundancy. Each region is divided in six sectors of 60°, each of them containing six planes of 112 wires. From studies of the current CLAS DC, the

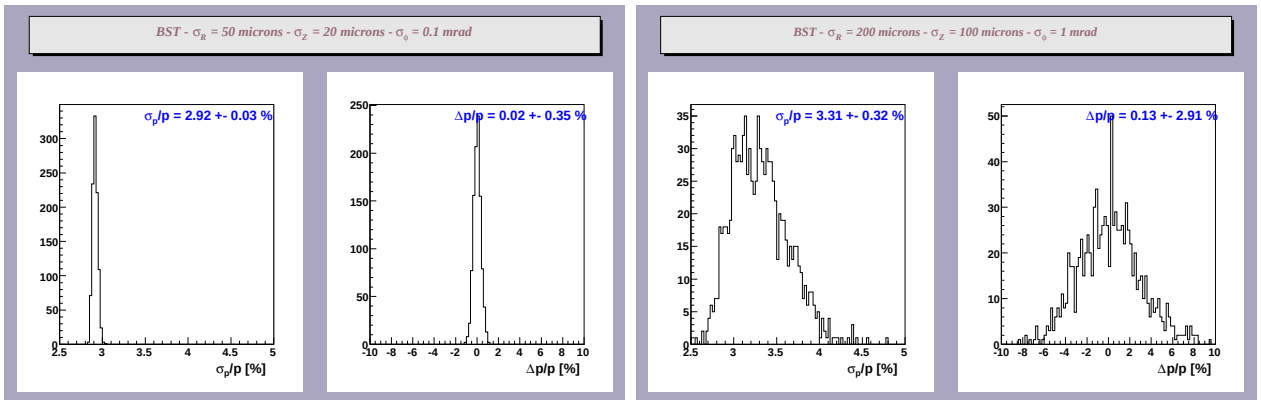

Figure 2.55: Momentum resolution and shift of 0.6 GeV protons at 60° with two different sets of misalignments: $\delta R = 50$ μm; $\delta z = 20$ μm; $\delta\phi = 0.1$ mrad (left); $\delta R = 200$ μm; $\delta z = 100$ μm; $\delta\phi = 1$ mrad (right).

space resolution is expected to be around 250–300 μm. The momentum determination will be provided by the use of a toroidal magnetic field surrounding Region 2.

The other element of this tracker is the FST, which consists of three double layers of silicon strips located between the target and the DC. Each layer is made with 15 trapezoids, with stereo strip angles of $\pm 12°$.

Tracking in the DC

The tracking in the Drift Chambers is performed in three successive steps that will be described below:

- first, we look for combinations of *clusters* that can define a track candidate;
- then we identify a *road* in each of the selected clusters (and solve the left-right ambiguity of the corresponding hits);
- finally we run the Kalman Filter algorithm on the track candidates for which roads were successfully identified.

Cluster and Track Finding: If a particle goes through a DC superlayer, it will leave a collection of hits forming a continuous series of wire numbers (e.g. wire number 37 in first plane, 38 in second, 37 in third, etc.). The very first step of the tracking is therefore to loop over all the hits of an event to find these series (called *clusters*), with hits in all the planes

of the current superlayer. To have overall fast and efficient tracking, the number of found clusters should be limited, so the occupancy in the DC should not exceed a few percent, as illustrated in Fig. 2.56.

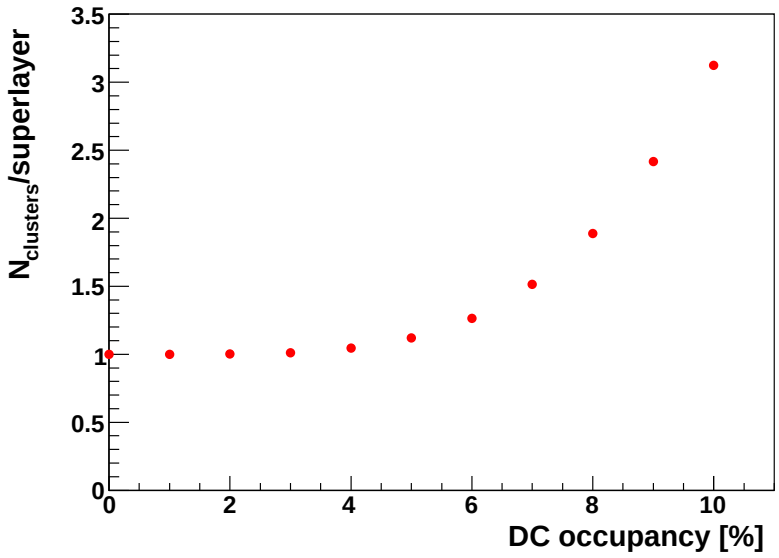

Figure 2.56: Evolution of the number of clusters per DC superlayer for single track events with (uncorrelated) background.

The next step is to form a *track segment* candidate, that is a combination of two close clusters in a given region. for real tracks, the average wire numbers W_1 and W_2 of two consecutive clusters satisfy the inequality $|W_1$ - $W_2| < K \times W_1$, with K around 0.15. In practice, we obtained a cluster matching efficiency close to 100% by using:

$$|W_1 - W_2| < 0.18 \times W_1 + 5. \tag{2.15}$$

Finally, we look for a combination of track segments in all the DC regions that could define a track candidate. As the number of track segments is limited with the expected occupancy, we simply require at this stage that they all are in a single sector. The very few remaining bad candidates will be rejected during the fitting procedure.

The result of the track finding is illustrated in Fig. 2.57, which shows the initial distribution of hits in the DC, and the final remaining candidates.

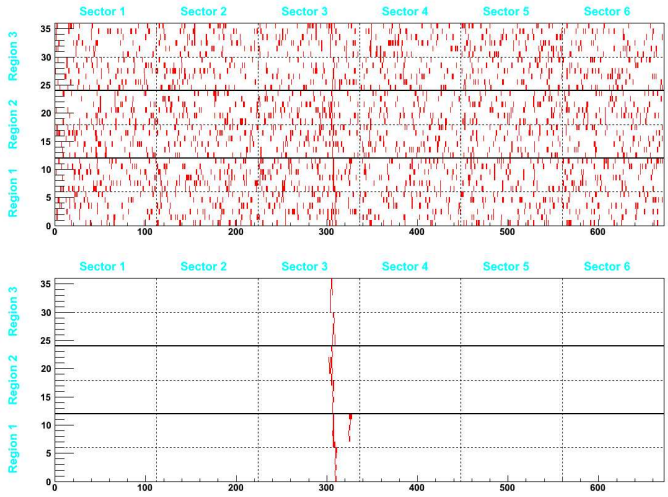

Figure 2.57: (Top): distribution of initial hits in all the DC planes (single track event with 10% uncorrelated occupancy); (bottom): remaining track candidates.

Road Finding: Even without any background, a real cluster cannot be used directly for the fit, as left-right ambiguities should be solved. In the presence of background, a real cluster may also contain fake hits that are accidentally close to the real ones. To solve these two problems, we developed the following iterative procedure:

- we first try to fit each hit combination of a cluster with a straight line, in a plane perpendicular to the wire direction. At this stage, we only use the wire position, with an uncertainty corresponding to the drift distance;
- this preliminary fit allows us to discard some hits (on the edges of the cluster), and to solve, for a particular combination, some left-right ambiguities. The next iteration uses only the remaining hits, with the real hit position if the left-right ambiguity has been solved. The fits are then more and more precise, so that more and more ambiguities are solved;
- after four iterations, all of the remaining ambiguities are solved using the latest fit.

Note that for the moment, the final road cannot contain more than one hit per plane, even if particles with large incidence angle can indeed leave two good hits within a single layer.

If the initial track is relatively close to a wire, it is sometimes not possible to decide whether it was on the left or on the right: in total, our procedure makes the correct decision for 90%

of the hits. In the presence of background, this probability decreases, as a fake hit can "kill" a good one, or be close enough to be identified as good, and then spoil the fit. However, this effect is limited, as shown in Fig. 2.58, proving that our procedure is relatively robust.

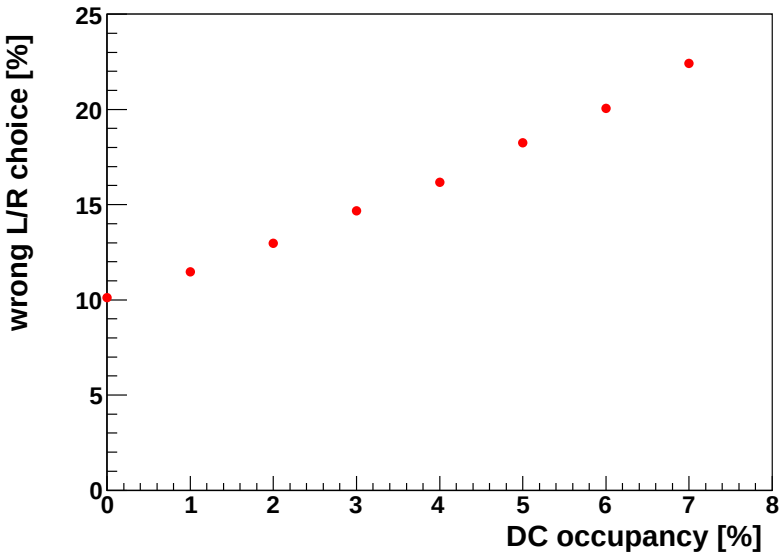

Figure 2.58: Probability to wrongly solve the left-right ambiguity as a function of the DC occupancy.

Track Fitting: The final sets of hits are then sent to the Kalman Filter algorithm, as for the central part. Because of the geometry of the Forward Tracker (measurements at approximately constant z), the state vector chosen is now:

$$\vec{x} = (x, y, u_x, u_y, Q/p)^T, \tag{2.16}$$

where x and y are the coordinates in a plane perpendicular to the beam axis, u_x and u_y are the slopes of the projected track in the xz and yz planes, respectively, and Q/p is the charge divided by the momentum.

The first four components of this state vector are easily initialized at the last plane of Region 3. The last component is estimated using the angles before (using a linear fit in Region 1) and after (using Region 3) the toroidal field, θ_1 and θ_3. We then use the well known formula:

$$Q/p = \frac{\theta_3 - \theta_1}{0.3 \times \int Bdl}, \tag{2.17}$$

with a parameterization of the field integral $\int Bdl$ as a function of the position in Region 1 (this parameterization is different for positively and negatively charged particles).

The initial uncertainties on these components (used in the covariance matrix) were chosen to be 3 cm for the position terms, 80 mrad for the slopes, and 50% for Q/p.

As for the central part, the fit is then stopped at the closest distance to the beam axis. However, for some specific reactions, we may want to determine the vertex position more accurately, and the DC are then used in combination with the FST. The key issue is then the accuracy of the extrapolation of the track parameters between the first DC plane and the last FST layer (located more than 2 m upstream).

Matching with the FST

The track finding procedure in the FST is quite simple, as the double layers are very close to each other, so track candidates are almost straight lines. We therefore select combinations of strips producing three almost aligned points in space, pointing not too far from the beam axis. The corresponding cuts have been optimized to identify at least 99% of the *reconstructable* tracks.

As the FST is always used with the DC, and not as a standalone tracker, we do not need *a priori* to require a hit in each layer. However, all the dead zones are aligned in the current design, so that a particle missing one layer will miss at least another one with a probability of around 99.5%. Besides, requiring only two out of three double layers increases the reconstruction of fake tracks by a large factor. We thus require three out of three double layers to define a track candidate in the FST. The resulting acceptance efficiency is shown in Fig. 2.59 as a function of the polar and azimuthal angles of the particles.

For a 1-mm long target, the integrated efficiency of the FST is:

$$\langle \epsilon \rangle = 92\%. \tag{2.18}$$

The next step is to be able to match track candidates from the FST and from the DC. To do this, we run the Kalman Filter algorithm on DC candidates, extrapolate down to the FST, and look for a *close* FST candidate. The accuracy of this extrapolation should be good enough

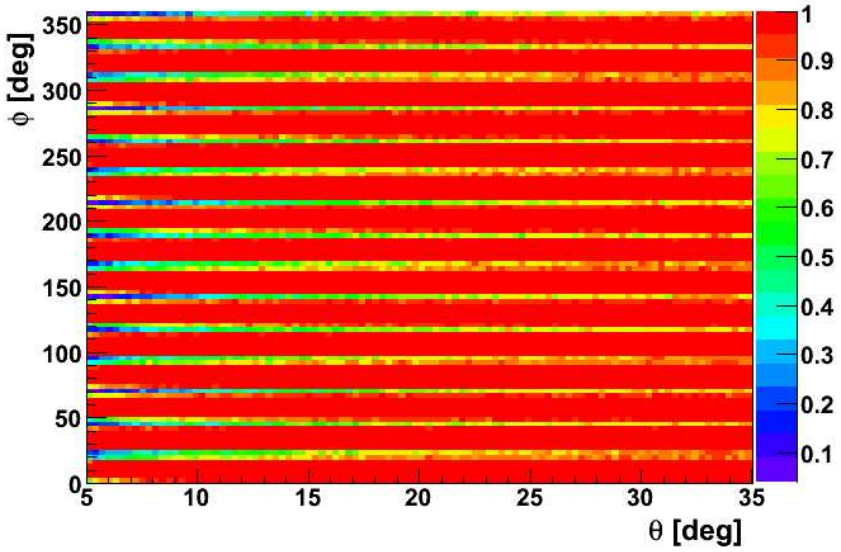

Figure 2.59: Acceptance efficiency of the FST as a function of the polar and azimuthal angles of the tracks, requiring three out of three double layers.

not to match with another track (fake or not). Fig. 2.60 shows that, for a large fraction of tracks, the extrapolated position is within a few mm circle around the original position of the particle. A 1-cm cut is therefore applied on the distance between the extrapolation and the FST track to match the two candidates. This allows a 98% matching efficiency without background; the effect of the DC occupancy (that deteriorates the accuracy of the fit) is shown in Fig. 2.61.

When the matching is successful, it appears that the fit is too unstable to be performed in a single step. We thus introduced some iterations as follows: in a first step, the Kalman Filter fits the track backwards, assuming a larger space resolution for the FST (7 times larger); the track is then extrapolated forwards, and refit using only the DC. The final fit is performed backwards again, using the real resolution for the FST. We are now able to derive the resolutions obtained in the Forward Tracker, and to study the effect of the FST.

Tracking Performance

The resolutions of momentum, polar angle θ, azimuthal angle ϕ, vertex position z, and distance of closest approach to the beam axis b are presented in Fig. 2.62 for proton tracks at 15°, using the DC alone, or in combination with the FST. Fig. 2.63 shows the same resolutions for

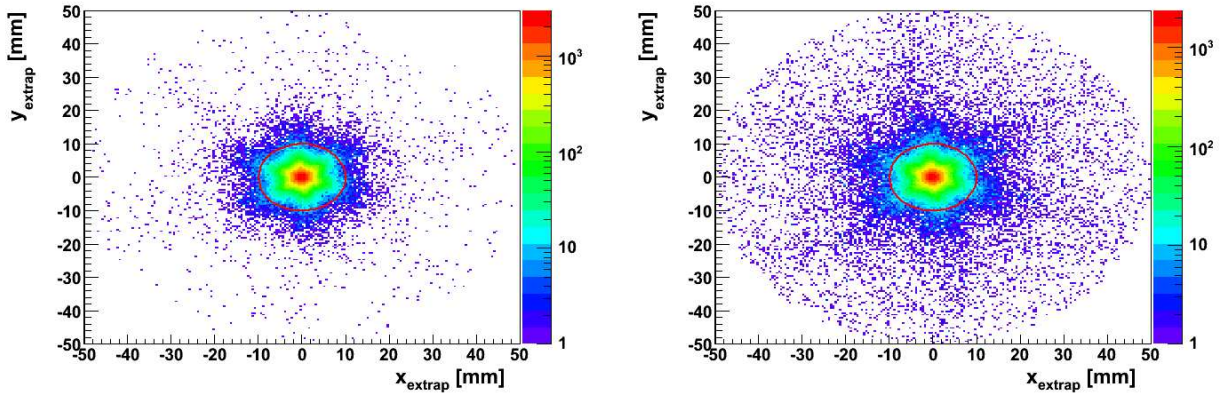

Figure 2.60: xy distribution of the DC track extrapolated down to the last FST layer with respect to the original position of the track. (Left): without any background; (right): with a 4% occupancy in the DC.

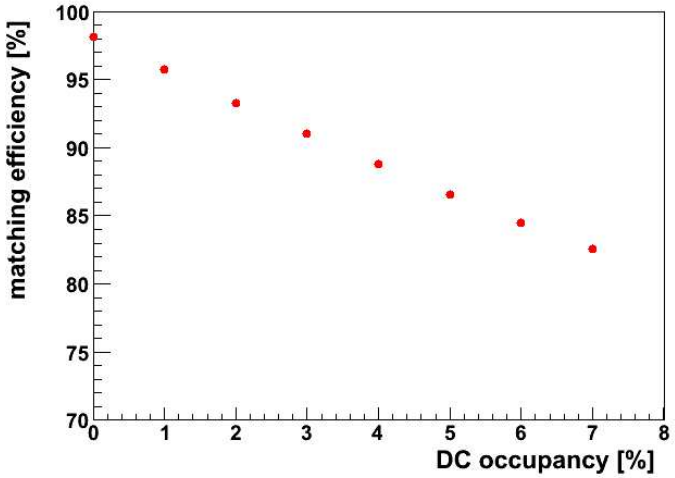

Figure 2.61: FST-DC matching efficiency as a function of the DC occupancy. A 4% occupancy degrades the efficiency by around 10%.

electron tracks. The effect of the DC occupancy on the resolution is very limited, as illustrated in Fig. 2.64 for the ϕ resolution.

If we compare with the original requirements from Table 2.12, we see that the DC design satisfies all of the proposed performances. Concerning the FST, it largely improves the vertex determination (up to a factor 10 on b), and also allows a better determination of p and ϕ at large momenta.

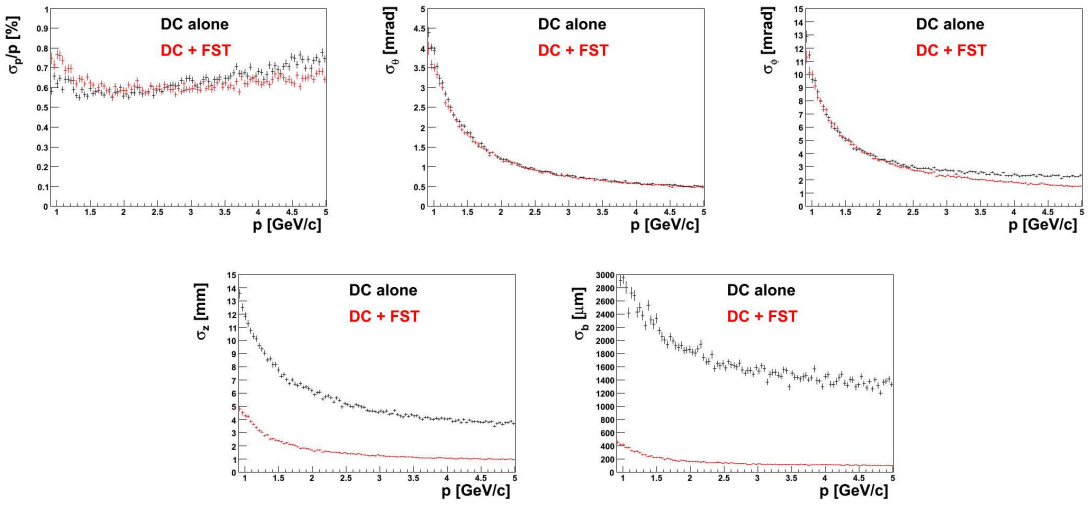

Figure 2.62: Resolutions in p, θ, ϕ, z, and b (distance of closest approach to the beam axis) for 15° protons with and without the FST. A 4% occupancy in the DC and 40 MHz in the FST have been assumed.

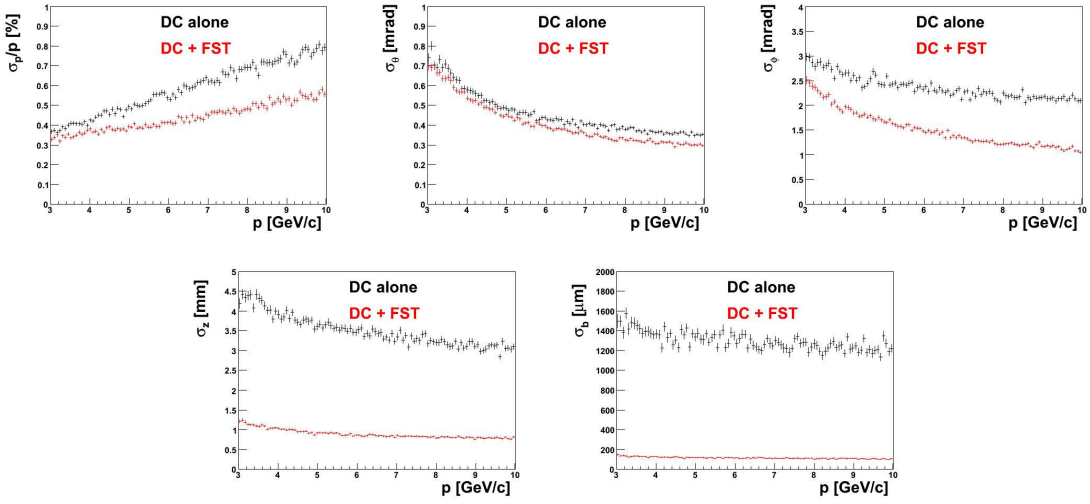

Figure 2.63: Resolutions in p, θ, ϕ, z, and b (distance of closest approach to the beam axis) for 15° electrons with and without the FST. A 4% occupancy in the DC and 40 MHz in the FST have been assumed.

Misalignments

As for the BST, we implemented in Socrat the possibility to misalign the detectors or the magnetic fields. For a given region of the DC, the following parameters can be misaligned:

- the distance R to the target;

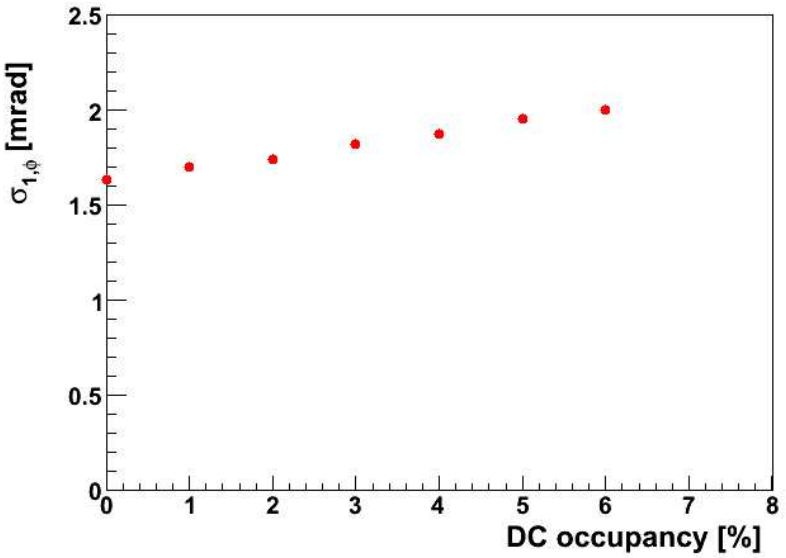

Figure 2.64: Evolution with the DC occupancy of the ϕ resolution (the p independent term) in the forward tracker.

- the tilt around its local x' axis (25° being the nominal value);
- the distance of the first wire to the beam axis.

Two parameters of an FST double layer can also be misaligned. These are:

- its azimuthal position ϕ;
- its position along the beam axis z.

Finally, Socrat can misalign the toroidal field in x, y, and z, with respect to the rest of the spectrometer.

Due to the large number of parameters, we illustrate only the effect of misalignment in R for Region 3 of the DC, and in z for the torus, as shown in Fig. 2.65. We see that both the DC and the torus should be aligned within a fraction of a millimeter. In general, our studies are consistent with the rule saying that a detector needs to be aligned within a fraction of its space resolution for a given parameter: e.g. less than 50 μm for the transverse position of the FST, and a few hundred microns for the longitudinal one (because of the angle of the tracks).

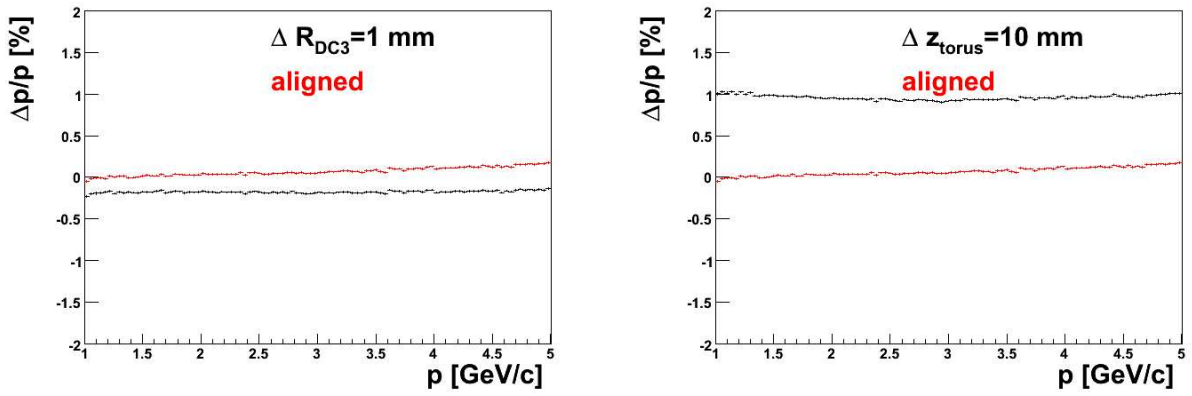

Figure 2.65: Effect of misalignments on the reconstructed momentum as a function of p: (left): R translation of DC Region 3 by 1 mm; (right): z translation of the toroidal field by 10 mm.

2.10.5 Conclusion

We described in this section the program we developed for charged particle reconstruction with the `CLAS12` spectrometer. In the central and forward parts, track finding procedures, as well as a Kalman Filter algorithm, were successfully applied. They provide for efficient reconstruction with resolutions that are in agreement with initial estimations and fulfill the physics requirements. The effect of the background has been quantified, and seems to be limited . Misalignments of all the detectors have also been studied, providing constraints on the position accuracy that will be needed, in particular for the BST. For the Forward Tracker, we showed that a highly efficient matching can be obtained between the FST and DC tracks, and we quantify the large improvement of the FST on the vertex determination.

The global track reconstruction is however not yet finished. More studies will be needed using GEANT4 simulations, particularly to study the effect of the correlated background on the tracking efficiency in the DC. A vertex fit, gathering information from the central and forward regions, has to be developed. Some smaller improvements can also be implemented, for example to take into account double hits from a single track in the DC.

2.11 Expected Physics Performance

We have used a series of programs to calculate the acceptance and reconstructed physics parameters for event types of interest. The program CLASEV [288] served as an event generator

and analysis program. Depending on the value of input flags, it generates certain types of events, that is, it produces a set of 4-momenta for the primary hadrons in the hadronic center-of-mass and allows some of them to decay into the final-state hadrons and transforms their momenta to the lab system. For each final-state track, it calls FASTMC (our fast, parametric Monte Carlo program for CLAS12) to determine if the track falls within a fiducial acceptance window and to determine its final, smeared lab momentum. It then produces selected physics analysis variables (e.g. missing mass) from calculations involving the smeared momenta of the tracks that were accepted. Fig. 2.66 shows the expected missing mass resolution expected for CLAS12 from FASTMC simulation studies based on the current design specifications for a number of different reactions. For all cases studied, the results are quite encouraging in terms of identifying the missing particle cleanly for each reaction. Our GEANT3 results are in accord with the FASTMC results.

We also show some results from our FASTMC simulation of $e\pi^+$ events in which the recoil baryon is detected by missing mass. Fig. 2.67 shows the missing mass spectrum expected when the π^+ is detected in the forward tracker (left) or central tracker (right). We have sufficient resolution to study resonant production and to compare, for example, u-channel, s-channel and t-channel processes.

2.12 Safety and Quality Assurance Issues

2.12.1 Safety

There are safety issues in the construction, installation, and operation phases of the CLAS12 drift chamber and SVT projects that we address in this section. Safety will be addressed from the start as an integral part of all activities and plans. All of our workers will receive appropriate training prior to being permitted to perform any activities on the detectors.

Drift Chamber

Table 2.15 briefly summarizes the issues and the mitigation strategies employed for the drift chamber system.

The only significant safety issues are in the construction, installation, and operation of the chambers. During the construction phase, we receive a number of machined parts from

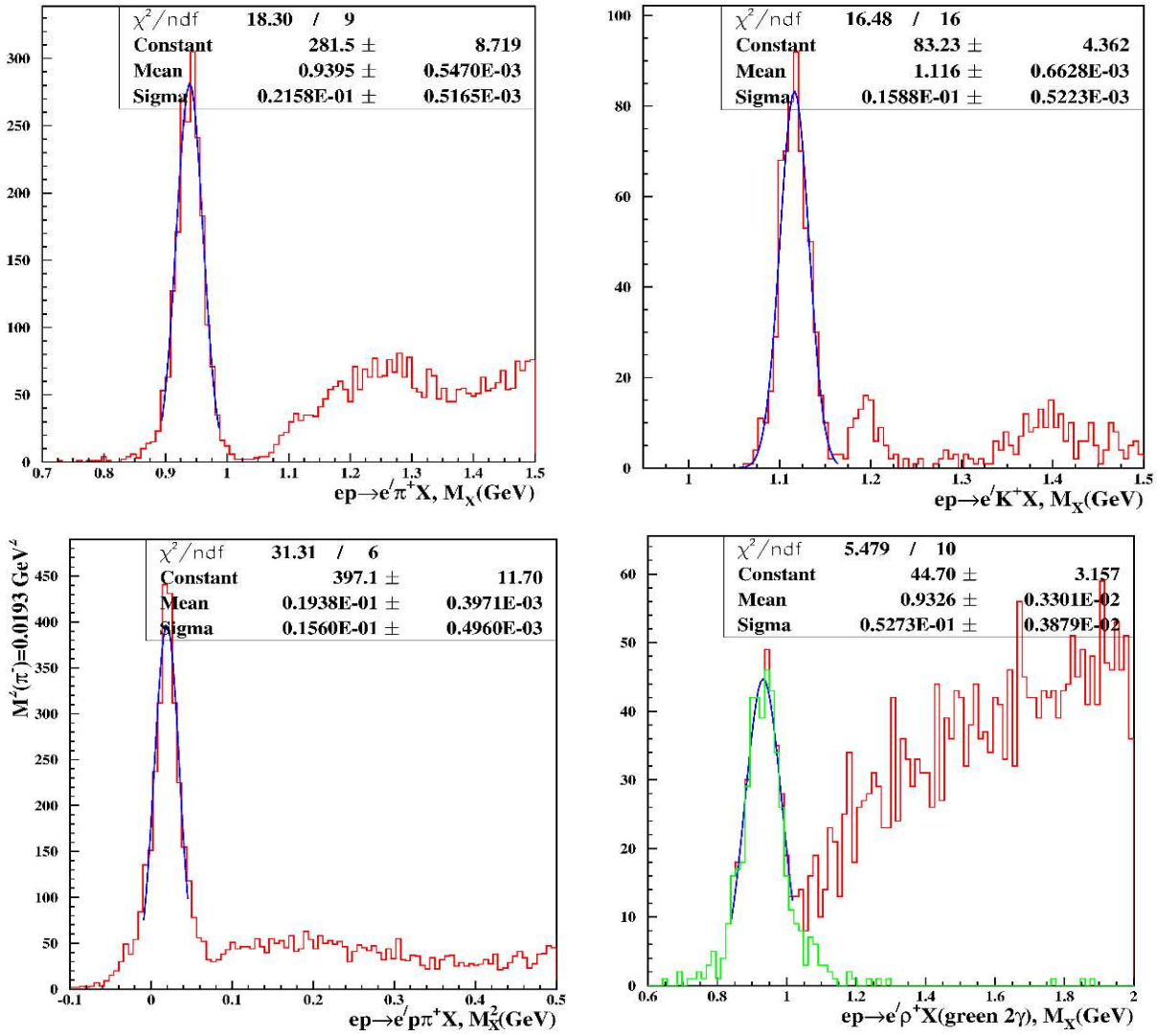

Figure 2.66: Simulation results from FASTMC highlighting the expected missing mass resolution of CLAS12 with the nominal design specifications for the tracking detectors (drift chambers and SVT). Shown are the spectra for the reactions $ep \to e'\pi + X$ (UL), $ep \to e'K^+X$ (UR), $ep \to e'p\pi^+X$ (LL), and $ep \to e\rho^+X$ (LR).

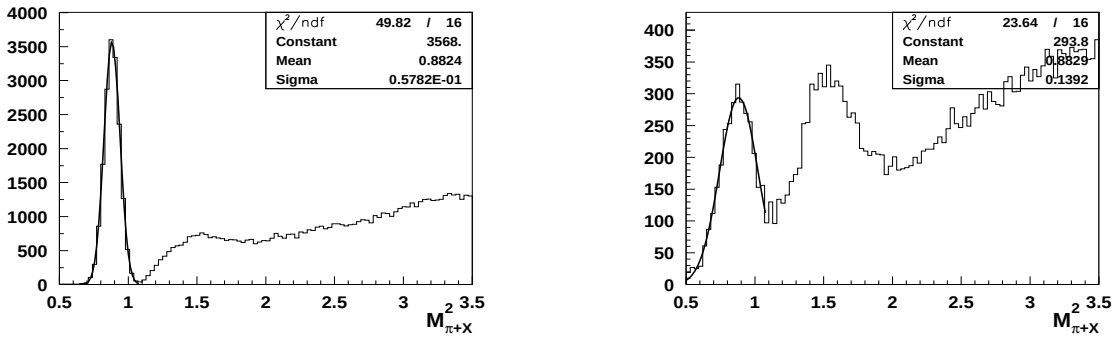

Figure 2.67: Simulation results from FASTMC highlighting the expected missing mass resolution of CLAS12 for events in which we detect only a π^+ and the electron for two cases: on the left when the π^+ is detected in the forward tracker, and on the right when detected in the central tracker.

Operation	Issue	Mitigation
Cleaning parts	Solvents	Use of non-volatiles; masks
Box assembly	Material handling, welding	Standard procedures
Stringing	Material handling	Design overview, reviewed procedures
Installation	Material handling	Design overview, reviewed procedures
Gas delivery	Flammability; ODH	Non-flammable mixture, small lines
Gas delivery	Over/under pressure	Active controls, passive bubblers
LV power	Over-heating	Each line individually fused
HV power	Shock	Current-limited supplies, reviewed procedures
Routine operation	Sparking	Fast-trip supplies
Repair	Material handling	Design overview, reviewed procedures

Table 2.15: Safety issues in the CLAS12 drift chamber project.

industry that must be cleaned thoroughly before assembly into a chamber. Our anticipated cleaning strategy is to use safe, non-volatile cleaning agents that are friendly to the environment and to human health. All of our activities are coordinated by written procedures that are reviewed by our safety staff at the lab.

During construction of the chamber boxes, we handle heavy metallic items and bolt or weld certain items. All of these activities are handled by personnel with adequate safety training, wearing suitable protective gear. The designs of all mechanical assemblies are reviewed by trained mechanical engineers and experienced technicians.

During stringing of the chamber, the technicians and stringers work on elevated platforms. The platform designs are reviewed in a similar fashion to the chamber mechanical designs, and all work is closely supervised by experienced technicians.

Operation of the chambers involves the use of a gas-handling system. We use non-flammable gas mixtures delivered to the chambers at low pressure. There are intermediate storage tanks filled with gas at moderate (a few atmospheres) of pressure. The gas-mixing and delivery system will be the same as the present `CLAS` system with minor modifications, so we will continue to follow our present safety procedures that include some engineering controls in the gas-mixing shed to mitigate possible ODH conditions and extensive active and passive controls to mitigate over- and under-pressure conditions that could harm the drift chambers.

The normal operation also involves delivery of low-voltage power to the on-chamber amplifiers. Although the low voltage (less than 8 V) means that there is no electrocution hazard, there is a potential for over-heating and fire ignition because of the relatively high currents involved. Each supply is capable of supplying up to 50 mA of current. Our mitigation strategy is to not allow more than 3 A of current on any output line, enforced by the placement of individual fuses on every wire that leaves the supply.

The Hall B Drift Chamber Low Voltage (DCLV) supply and distribution system consists of 18 HP 6651A power supplies. Each power supply has a maximum current output of 8 VDC and 50 A of current. The power supplies are connected to the Hall B 120 VAC clean power located in the individual racks of the space frame that are protected by an electrical breaker panel. The supplies have a 10 A current limiting fuse for its own A.C. line protection. The DCLV system supplies DC power to the drift chamber Signal Translator Boards (STBs). The output voltage can be set at the supply, as well as a current limit. In Hall B the current limits are individually set for each region/sector. The power is then supplied to the STBs via

a distribution chassis. Each chassis is safety interlocked and contains 3 bus bars (positive, negative, and earth ground), of which the positive and negative are connected to the individual STBs through current limiting fuses. The individual fuses provide the nominal current draw plus 20% for transient spikes. The distribution system for Region 3 was upgraded in 2003 to provide segmentation of the axial and stereo boards, thus reducing the damage of a permanent short by half. The upgrade consisted of adding new power wires from the distribution to the STBs and adding an additional breakout chassis. The breakout chassis provided individual fuses for each side of the STB in front of the distribution fuse. Each breakout fuse is rated for the nominal current draw of its respective channel on the STB plus 40% for transient spikes. In the event of a short on the chamber there is a written procedure for changing out fuses located in the Hall B counting house and the drift chamber expert manual. Monitoring of the supplies is done using a PC-based LabView program from the Hall B counting house.

Operation also involves the delivery of high-voltage to the drift chamber wires. The operating voltages are between 1000 and 2000 V, depending on the section in question. In all cases, the high voltage supplies are current-limited. No channel can deliver more than 40 μA of current. Administrative procedures are in place to prevent accidental shocks from taking place.

The Hall B Drift Chamber High Voltage (DCHV) system consists of 3 CAEN 527 supplies, with each containing up to 10 A934 (P/N) modules, distribution chassis, and software-based monitoring and control system. Each module has a safety interlock that controls the output of power. The entire system has programmable firmware to set the current limit, voltage, and ramp rate, as well as system monitoring. The crate is connected to the Hall B clean power system and the A.C. input power is fused at the chassis. The modules output high voltage to a distribution system that consists of a summation and distribution chassis for the areas of the drift chamber. The current is limited to 20 μA output from the modules. Monitoring and control is done via the DCHV TCL/TK program.

SVT

The only significant safety issues are in the construction, installation, and operation of the SVT. During the construction phase, we receive a number of machined parts from industry that must be cleaned thoroughly before assembly. Our anticipated cleaning strategy is to use safe, non-volatile cleaning agents that are friendly to the environment and to human health.

All of our activities are coordinated by written procedures that are reviewed by our safety staff at the lab.

The normal operation also involves delivery of low-voltage power to the on-board amplifiers. Although the low voltage (less than 8 V) means that there is no electrocution hazard, there is a potential for over-heating and fire ignition because of the currents involved. The design of the low voltage system will include appropriate current fusing to ensure safety to personnel and to the equipment.

Operation of the SVT also involves the delivery of high-voltage to the detector. The design of the high voltage supplies will include over-current and over-voltage protection. Administrative procedures are in place to prevent accidental shocks from taking place.

2.12.2 Quality Assurance

Quality Assurance (QA) begins before the procurement of components and detector construction and continues beyond detector installation and commissioning. This section details plans for QA for the drift chambers and SVT for `CLAS12`.

Drift Chambers

QA issues include not only the drift chambers themselves, but also the associated high voltage system, low voltage system, gas system, and the actual environment the detector lives in. There will be six identical units of each of three detector regions, for a total of 18 drift chambers. The challenge here will be to tightly control detector fabrication, stringing, instrumentation, and testing, while staying within the project's budget and schedule. The following summary outlines some of the QA procedures that we will be implementing.

The electronics components will be accepted from the vendor by the JLAB Fast Electronics Group (FEG). The FEG will inspect, test, and clean all components in accordance with written procedures that they will develop. All components will be sealed in anti-static bags and stored in a proper environment until needed. Written certifications will be kept for all components.

The detector frame or box will be a mechanical assembly. This assembly will be built on an alignment fixture. Precision positioning pins to locate reference points to the actual wire positions will be one of the features of the fixture. The JLAB survey group will be involved in this process from its inception. Each completed assembly will be surveyed to verify it is

within tolerance. The detector frame or box will then be cleaned before it enters the clean room for final component assembly and stringing.

All of the components will be inspected and cleaned prior to use as it is critical for maximizing detector lifetime. Written procedures will be followed and records will be kept to identify the cleaning and inspection status of all components. Components will be stored in sealed bags in the clean room where feasible.

The CLAS12 drift chambers will be strung in a clean room environment. Technicians will wear clean room coats, gloves, shoe covers, and hair nets. Only clean gloves and clean tools will come into contact with the detector and its components. All technicians who work in the clean room will be trained in proper clean room practices. Written cleaning procedures and schedules will be developed to insure proper clean room maintenance. Supervisors will frequently inspect all areas to verify proper practices are followed.

Written procedures will be developed from the prototype experience for all detector assembly and stringing steps. Fabricators and stringers will be trained by experienced persons in all required steps and procedures. They will be closely supervised to ensure compliance with written procedures and to prevent any deviation from accepted practice.

At the end of each stringing shift, the wires will be tested for proper tension using a magnetic field and variable frequency oscillator. The frequency measured at the wires first fundamental for that length wire will be used to determine the wires tension. Wires with out of specification tension will be removed and new wires will be strung in their place. This test also verifies proper continuity of the wire from pin to pin. It will also identify crossed or twisted wires because those will show a decrease in signal amplitude.

The next tests are a redundant check for shorted or twisted wires missed during visual inspection and tension testing. Prior to signal and high voltage board installation, the field and guard wire layers are wire wrapped. Once the high voltage side is wrapped, a multimeter will be used to determine if there are any shorts between layers or between and sense wires and the wire wrapped layers. A multimeter will also be used to determine shorts and twisted wires in the same layer by measuring the resistance of each wire between the wire-wrap side and the pin on the opposite side. Since wire lengths are all known, the resistance of each wire is also known. Twisted wires will have much lower resistance than would be expected from that wire length. The high voltage boards are installed and connections are made. A multimeter is then used to measure the resistance between sense layers. There should be

infinite resistance between layers, and any other result indicates a short or twisted pair. The multimeter is then used to measure the resistance from the signal side of the wire to the high voltage bus. This should read $\approx$1 MΩ, which is the value of the current-limiting resistor in the circuit. A reading of 0.5 MΩ indicates a shorted or twisted pair.

Final testing includes high voltage tests and cosmic ray tests before and then after the final cabling and patch panel installation. The detector will then be stored in a temperature and humidity controlled area until installation.

SVT

QA planning for the SVT system includes the following areas:

- Bench testing of each of the individual components of the SVT hardware prior to module assembly. This includes the silicon sensors, readout chips, circuit boards, wire bonds, and cabling;
- Testing of complete stave assemblies and modules prior to assembling the detector as a unit;
- Encapsulation of the wire bonds to prevent breakage or stress;
- Including fiducial marks on all custom silicon components for alignment;
- All assembly will be done in a clean room following established clean room conventions;
- Use of custom fixtures to prevent damage during shipment of components;
- Use of alignment markers on the support structure for detector installation.

The quality assurance planning is being done in conjunction with a value engineering (VE) approach for the design. It is expected that the VE for the SVT will improve the QA rating for the design. The steps that are being taken include:

- Use of one silicon sensor design for the barrel SVT and one design for the forward SVT for a total of only two total different sensors in the system. This allows for a lower number of spares to be purchased and also allows for the possibility that sensor blocks can be interchanged between regions;

- The SVT design employs previously design readout chips. The design of these chips has therefore been extensively studied and detailed performance evaluations have been completed;
- Common circuit boards and electronic components will used for the barrel and forward SVT. These boards will follow industry and JLab standards for design;
- Whenever possible, the SVT design makes use of "off-the-shelf" components to improve reliability.

2.12.3 Conformance with JLab ES&H Manual

All activities will be analyzed in accordance with the JLAB ES&H Manual to identify any and all hazards associated with the work and any and all safety requirements mandated. All persons involved and all persons in the vicinity will be briefed on all potential hazards involved in all activities. However, all activities are considered low risk, common, and routine in nature and are all fully covered by the ES&H Manual.

Many operations will be performed around and in the vicinity of equipment and other activities. Procedures to identify and mitigate risks due to trip and fall hazards will be developed. Similar procedures will be developed for work involving the use ladders, work platforms, and scaffolds. Standard safety procedures will be followed for all work involving the use of cranes and hoists. Instrumenting, testing, and troubleshooting the detectors may require Class 1 Mode 1 and Class 1 Mode 2 limited testing and diagnostics and will be performed according to EH&S requirements.

Chapter 3

High Threshold Čerenkov Detector

3.1 Introduction

The High Threshold Čerenkov Counter (HTCC) is one of the major components of the CLAS12 spectrometer. It will be used for electron identification in all experiments with electron beams. In combination with the Low Threshold Čerenkov Counter (LTCC), it will make possible the identification of charged π-mesons over the entire momentum range up to a maximum of 5 GeV. An overall view of the CLAS12 spectrometer is given in Fig. 3.1. Part of the infrastructure in the Hall B experimental area and other equipment are shown as well.

The HTCC is located between the central and forward detectors of CLAS12, and is mounted on a separate cart that can be moved along the beam direction. The radiating gas for the HTCC is CO_2 at room temperature and pressure. The threshold for the detection of charged π-mesons is 4.9 GeV. In the entire momentum range below threshold in which the detection efficiency for electrons is 99.99%, the pion rejection factor is greater than 300. For 2.0 GeV pions, it is greater than 750. The optical configuration in the HTCC is chosen to be similar to the LTCC currently used in CLAS. However, since the detector is positioned upstream of the drift chambers and therefore has to be "thin", it was decided to use one reflection from a single mirror in a given module, as opposed to two for the LTCC. The current design comprises 48 light reflection and collection modules. The main working parameters of the HTCC are given in Table 3.1. The overall performance requirements and the scope of the primary problems that need to be solved are shown in Table 3.2.

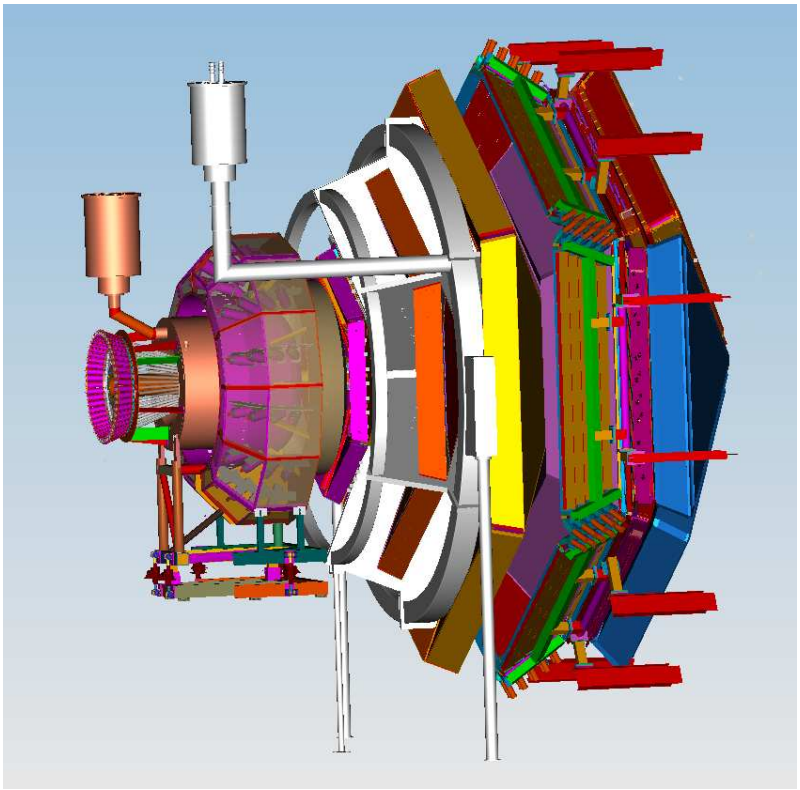

Figure 3.1: CLAS12 spectrometer in experimental Hall B. The HTCC is shown mounted on the extension of Level-1 of the space frame just downstream and outside of the solenoid.

Channels	48 (6 sectors of (2×4) channels each)
Working Gas	CO_2 at 1 atm and room temperature
Mirror Type	Ellipsoidal, 48 segments
Photomultipliers	XP4508 (5 in, quartz face-plate)
Pion Threshold	4.9 GeV
Electron Threshold	15 MeV (electrons)
Rejection Factor	>300 at $p < 4.9$ GeV

Table 3.1: The main working parameters for the design of the HTCC.

Performance Requirement	R&D tasks to be addressed
High electron detection efficiency	Development of technology of ellipsoidal mirror construction. One reflection of Čerenkov photons in most events.
Run at luminosity $\geq 10^{35}/\mathrm{cm}^2\mathrm{s}$	48 channels. Flexibility in assigning certain angular acceptance to a particular channel.
Acceptance $\Delta\phi = 2\pi$ in angular range $5^\circ \leq \theta \leq 35^\circ$	Designing mirrors with no support/alignment parts within the acceptance. No dead zones between mirror segments.
Total thickness ≤ 200 mg/cm^2	Developing technology of mirror construction using components of low density and no residual stress.
Reliability	Safe maintenance and operation of the detector. PMTs and other components can be reached and replaced if necessary in-situ.

Table 3.2: The overall performance requirements of the HTCC and the scope of the primary problems that need to be solved.

3.1.1 Optical Requirements

The upgraded CLAS12 spectrometer incorporates several major components inherited from CLAS, such as the Forward Time-of-Flight Counters, the Low Threshold Čerenkov Counters, and the Forward Electromagnetic Calorimeters. CLAS12 will be built in the same experimental area. This places constraints on the overall CLAS12 design, and consequently, on all detector components, while requiring the most efficient acceptance coverage.

The HTCC occupies very limited space downstream of the central detector and is mounted between the Silicon Vertex Tracker and the Region 1 drift chambers. Fig. 3.2 illustrates the basic optics of the detector, and Fig. 3.3 shows a 3-dimensional view of the mirror and PMTs for one sector. The design is such that the photons are reflected only once by one of the ellipsoidal mirrors and then directly impinge on the photocathode of a photomultiplier tube. However, since the optical design must be forgiving in the sense that the light collection efficiency must be relatively insensitive to the target length and position, the 5-inch PMTs are equipped with *Winston* light collection cones to account for the smearing of the photon distributions due to the influence of the magnetic field of the central solenoid on the particle trajectories,

The optical properties of the mirrors, Winston cones, and PMTs are optimized for maximum reflection and detection of the Čerenkov light. Since much of the Čerenkov light is in the ultraviolet (UV), the working surfaces of the mirrors and cones will consist of evaporated coatings of aluminum, which has a high reflectivity from the near UV through the visible wavelength regions. An evaporated magnesium fluoride (MgF_2) protective coating will be provided to prevent oxidation of the aluminum, while transmitting light through the required wavelength range. The photomultiplier tubes will be Photonis XP4508 units with a quartz face plate, again, to maximize efficiency in the UV range.

3.1.2 Physical Environment

The HTCC is a single module detector covering all six sectors for scattering angles in the range $\theta = 5^\circ$ to 35° in the entire $\Delta\phi = 2\pi$ range. Since the detector is a single unit, it can be moved along the beam direction or removed from the beam if necessary. It is located in the strong magnetic field of the superconducting solenoid of the central detector. The light collection geometry of the HTCC is such that all 48 PMTs are located in the fringe field domain at radial

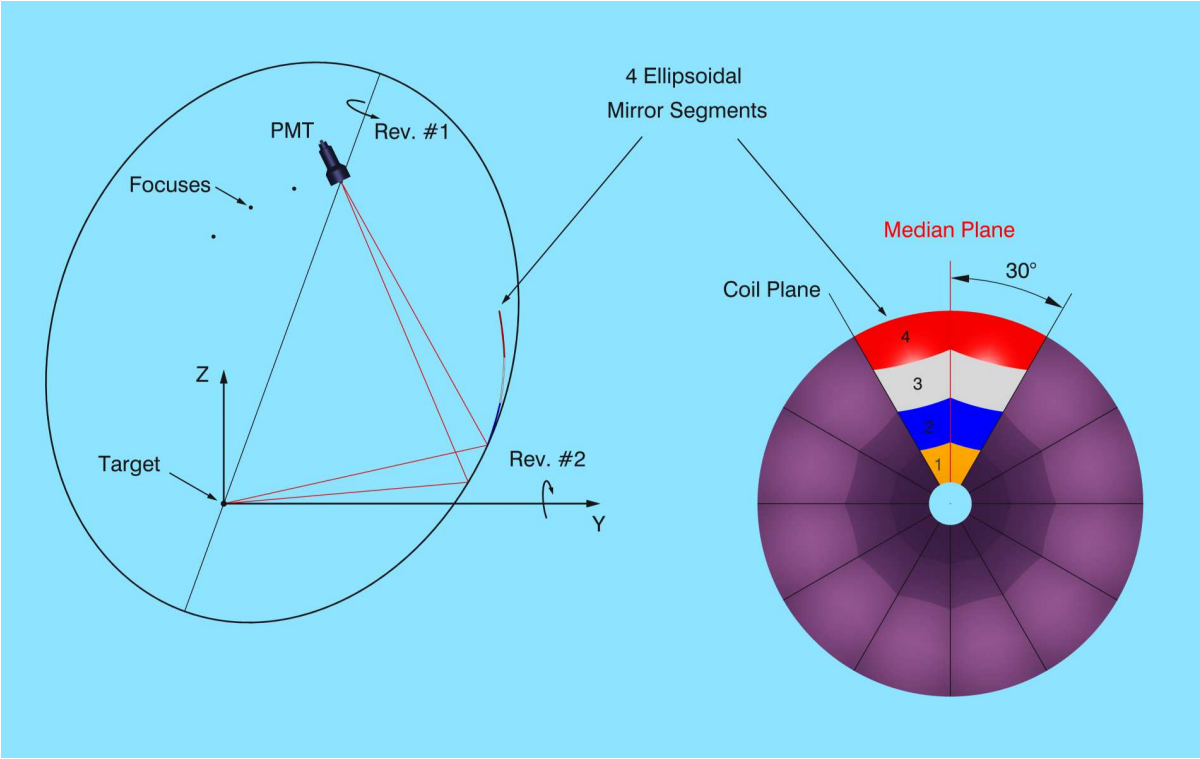

Figure 3.2: Geometry of the HTCC: an ellipsoidal mirror segment is obtained by revolving a corresponding ellipse about its major axis. Adjacent segments intersect along planes. The resulting 4 ellipsoidal segments are revolved about the y-axis (the beam direction) through $\pm 15°$. The two highlighted mirror portions are cut to accept polar angles from 5° to 35°, and by the median and coil planes for one sector, as shown in the right figure.

distances from 161.3 cm to 194.7 cm from the electron beam. These distances are chosen to be maximal, while still small enough to fit in the Hall B tunnel and space frame infrastructure, while allowing movement of the detector upstream for CLAS12 alignment and maintenance purposes.

The space occupied by the HTCC along the beam direction defines the intensity of the Čerenkov photons expected at a given pressure of the working gas. The design of CLAS12 specifies that the entrance window of the Čerenkov counter is located ~0.5 in downstream of the SVT of the central detector, and the exit window is 10 cm upstream of the Region 1 drift chambers. That leaves the distance that the scattered electrons travel in the CO_2 radiator of ~131 cm at $\theta = 5°$ and ~181 cm at $\theta = 35°$. The geometry of the HTCC is optimized to keep the differences in path lengths minimal. The distribution of magnetic fringe fields was taken into consideration in locating the PMTs. The optics and estimated signal strength are

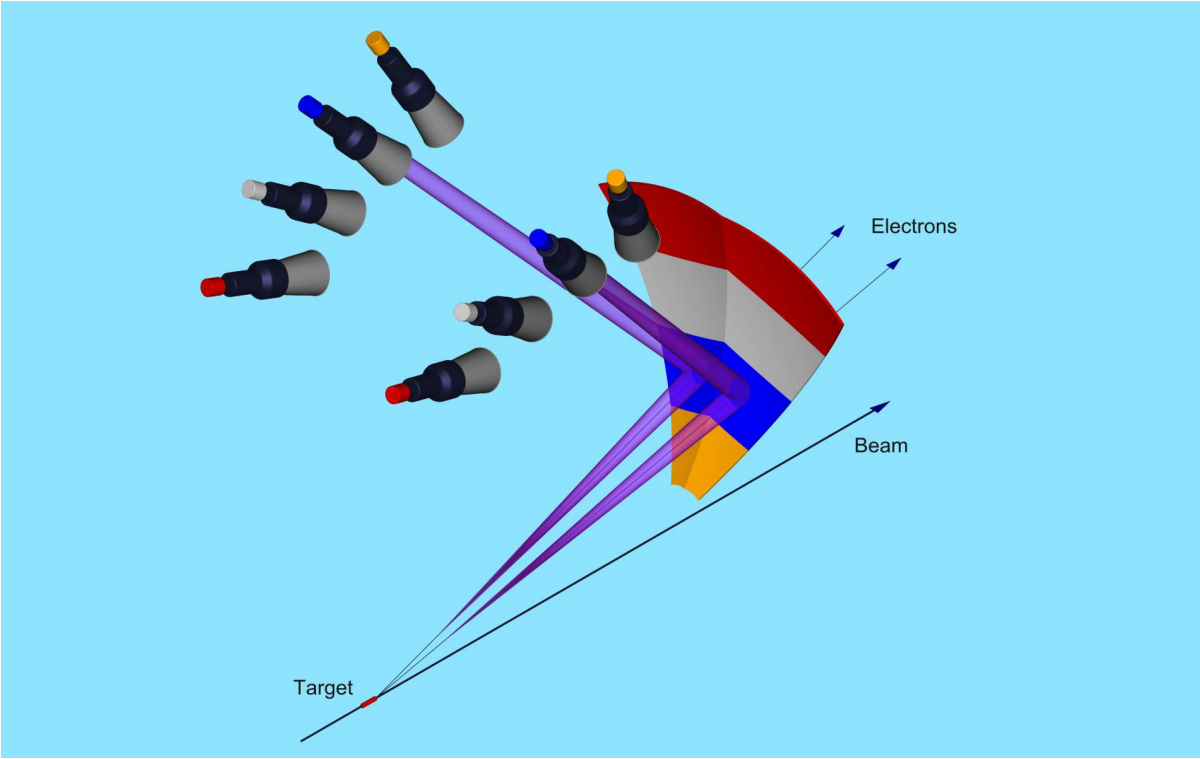

Figure 3.3: 3D-view of the mirror and the PMTs for one HTCC sector.

discussed below.

The intrinsic angular and momentum resolutions of CLAS12, along with its capability of running at high luminosities, puts serious constraints on both the thicknesses and materials that can be used in the HTCC mirror construction. These limitations on materials and estimates of required and achievable mirror thicknesses are given in Section 3.2.1.

Another constraint comes from the acceptance specifications for the Region 1, 2, and 3 (R1, R2, and R3, respectively) drift chambers, which are located downstream of the HTCC. The polar angle acceptance for the drift chambers, $\theta = 5^\circ$ to 40°, is greater than for the HTCC. The support structure for the elliptical mirrors has to be located in the relatively narrow *shadow* region of the coil planes of the CLAS12 torus magnet, and the mirror substrate support built of as light materials as possible.

3.1.3 Overall Design

The overall approach to working out the HTCC design is a two-fold task, first to outline the general demands on the HTCC performance and then to define the ranges for critical

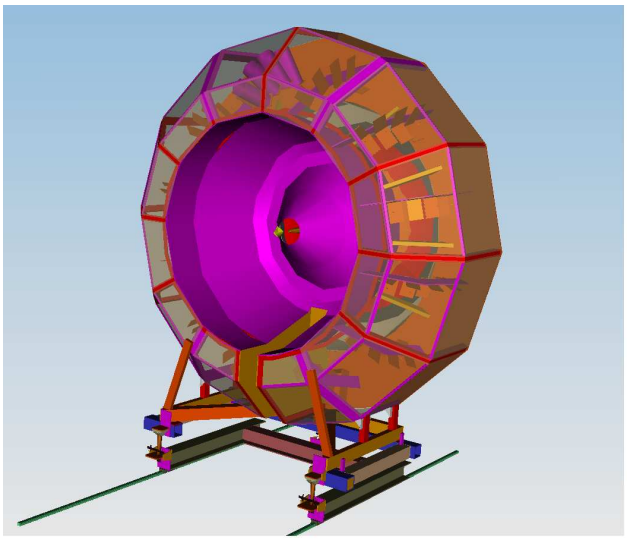

Figure 3.4: A view of the front face of the HTCC showing the entrance window in red.

parameters of the major components such as the ellipsoidal mirrors.

The main requirements are:

- High electron detection efficiency, low background;
- Capability of running at a luminosity of 1×10^{35} cm^{-2}s^{-1};
- Angular acceptance $5^\circ \leq \theta \leq 35^\circ$ and $\Delta\phi \approx 2\pi$;
- Lightweight – as little material as possible within the acceptance to meet the expected angular and momentum resolutions of CLAS12 ($\delta\theta \leq 1.5$ mrad, $\delta\phi \leq 5$ mrad, and $\Delta p/p \leq 1\%$).

A front view of the HTCC is shown in Fig. 3.4. Some specific features of the HTCC design include:

- Thin entry and exit windows of black Kapton or Tedlar film (~3.5 mg/cm^2 and ~11 mg/cm^2, respectively);
- Ultra-thin, self-supporting mirror structure;
- Capability of working with different types of Tungsten Møller shields.

The total radiation length of the detector is ∼1.7%, including contributions of the CO_2 radiator gas (∼0.9%), and of the mirror (< 0.8%). Since the number of photons per event is proportional to the total radiation length of the radiator, the only way to decrease the thickness of the detector without compromising its performance is to use thinner mirror backing. Figs. 3.5a, b, and c illustrate the changes in the CLAS12 resolution for different mirror thicknesses: standard (∼200 mg/cm^2) and reduced to ∼100 mg/cm^2. The results show relatively small improvements in momentum, angular, and spatial resolutions for thinner mirrors, indicating that the influence of the mirror thickness is small or comparable with contributions of other CLAS12 detector components.

3.2 Optical Design and Construction

The most challenging aspect of the HTCC is the construction of the elliptical mirrors. In addition to being very lightweight and self-supporting, there must not be shadowing among adjacent mirrors or gaps between them. This problem has been worked out as follows: each mirror surface is an ellipsoid of rotation, so the line of intersection of adjacent mirror surfaces is curved. Two coplanar ellipses, each revolved about its major axis, give two ellipsoids of rotation, (1) and (2), represented by the following equations:

$$\begin{aligned} \frac{x^2+(y-y_1)^2}{a_1^2} &+ \frac{(z-z_1)^2}{b_1^2} = 1 \\ \frac{x^2+(y\cdot\cos\theta - z\cdot\sin\theta)^2}{a_2^2} &+ \frac{(y\cdot\sin\theta - z\cdot\cos\theta)^2}{b_2^2} = 1. \end{aligned} \tag{3.1}$$

In the above, $(0, y_1, z_1)$ are the coordinates of the center of the ellipse (1), a_1, a_2, and b_1, b_2, respectively, are the minor and major radii of the ellipses, and θ is the angle between the major axis b_2 and the z-axis in the $y-z$-plane. Considering the system in the $x = c < a_1$ plane, we get (assuming $a_1 < a_2$):

$$\begin{aligned} \frac{(y-y_1)^2}{a_1^2} &+ \frac{(z-z_1)^2}{b_1^2} = c_1^2 \\ \frac{(y\cdot\cos\theta - z\cdot\sin\theta)^2}{a_2^2} &+ \frac{(y\cdot\sin\theta - z\cdot\cos\theta)^2}{b_2^2} = c_2^2. \end{aligned} \tag{3.2}$$

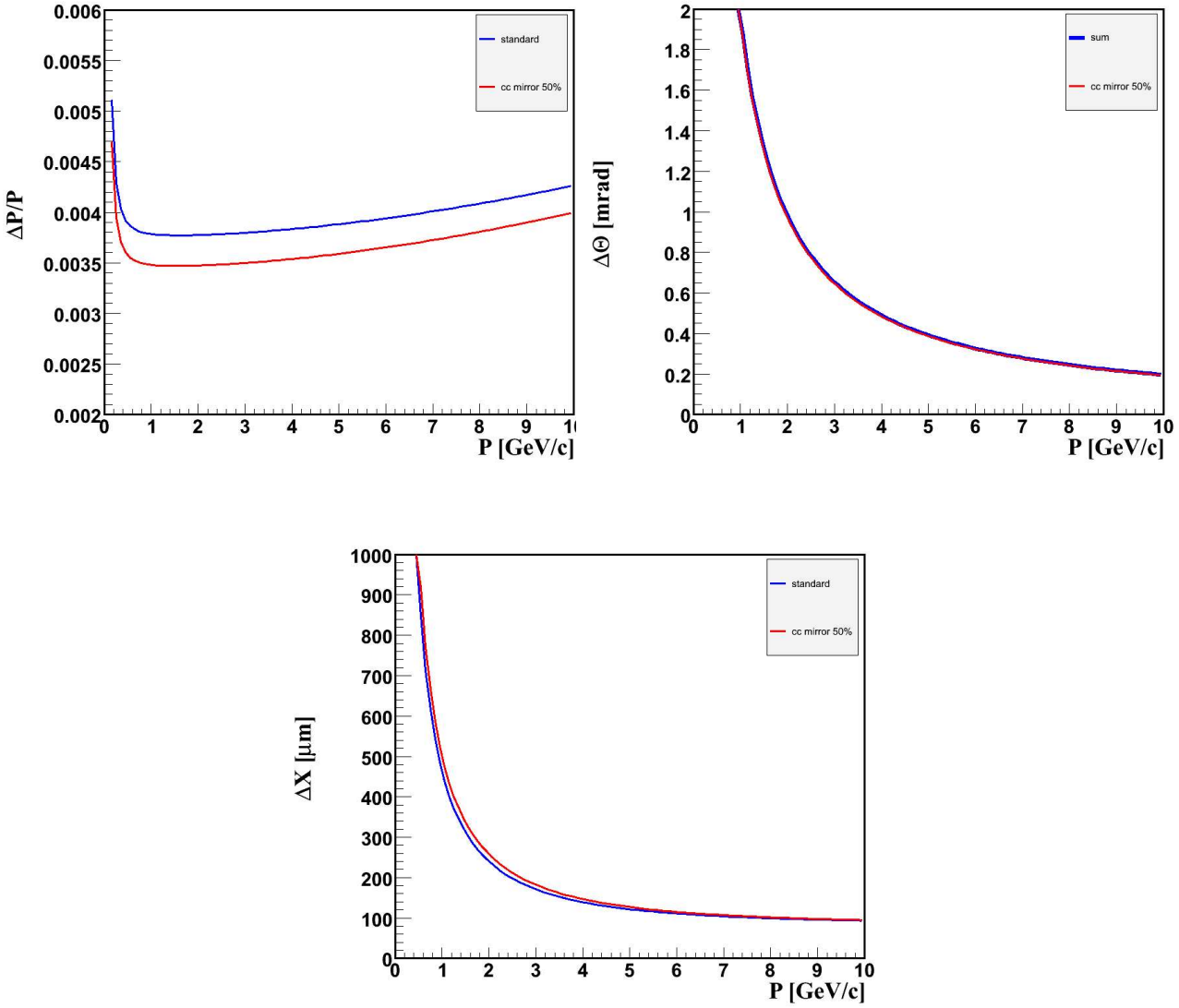

Figure 3.5: Momentum, angular, and spatial resolution of CLAS12 for pions.

By excluding one variable from eq.(3.2), we arrive at a general quartic equation:

$$p_0 z^4 + p_1 z^3 + p_2 z^2 + p_1 z + p_4 = 0,$$

which always can be solved, and in the case of the HTCC geometry, has two roots (see Fig. 3.6). So, from eq.(3.2), we obtain two roots $P_1^{(c)}(y_1, z_1)$ and $P_2^{(c)}(y_2, z_2)$ in the plane $x = c$; they also satisfy eq.(3.1) at $x = c$: $P_1^{(c)}(c, y_1, z_1)$ and $P_2^{(c)}(c, y_2, z_2)$ are the roots of eq.(3.1). Two other roots of eq.(3.1) can be found at $x = 0$ (the $y - z$-plane): $P_3(0, y_1, z_1)$ and $P_4(0, y_2, z_2)$. Three out of any four roots define a plane. It can be shown that the remaining root belongs to the same plane as well. Since we arbitrarily used $x = c$, all points of intersection (intersection curve) of the two ellipsoids belong to the same plane. This allows us to build mutually self-supporting ellipsoidal mirrors in which there are no gaps or shadowing of one mirror by the next. As a result, the cutting of the segments along the perimeter and the final assembly become relatively simple. Moreover, there will be no shadowing of one mirror by another, and no "dead" zones for any electrons from the target within the acceptance. This also eliminates the need of having a support structure for any single mirror segment, and consequently makes it possible to construct the most efficient and lightweight mirror.

Fig. 3.7 shows four intersecting mirrors forming half of the mirror array for one sector. The coordinates of the points defining the planes of intersection between segments were used in the corresponding Monte Carlo simulations. Fig. 3.8 illustrates the concept of the compound elliptical mirror assembly. The approximate dimensions of segment #4 are given in inches.

The tolerances for construction are critical for HTCC performance. The typical tolerances for cutting the substrates are of order 0.001 in and have been achieved in prototyping. So, the expected average deviation from the nominal geometry would be mostly due to the accuracy that can be achieved at the assembly stage. It is anticipated to keep the assembly tolerance within ± 0.010 in for one mirror segment. Parallel shifts will not affect the light collection because of the large overall acceptance, whereas unwanted rotation of a segment during assembly might require some adjustment of the PMT positions, which would be unacceptable. At the given average half width of the segments, $\sim$5 in (see Fig. 3.8), the angular equivalent of ± 0.01 in is $\sim$2 mrad or less. This is the worst possible case since all segments except #1 are of length greater than 5.60 in. The average distance between the mirrors and the corresponding PMTs is $\sim$80.5 in. Therefore, the shift of the image in the focal plane of the PMTs is less then 0.15 in ($\sim$3.8 mm). This estimate will be examined in R&D.

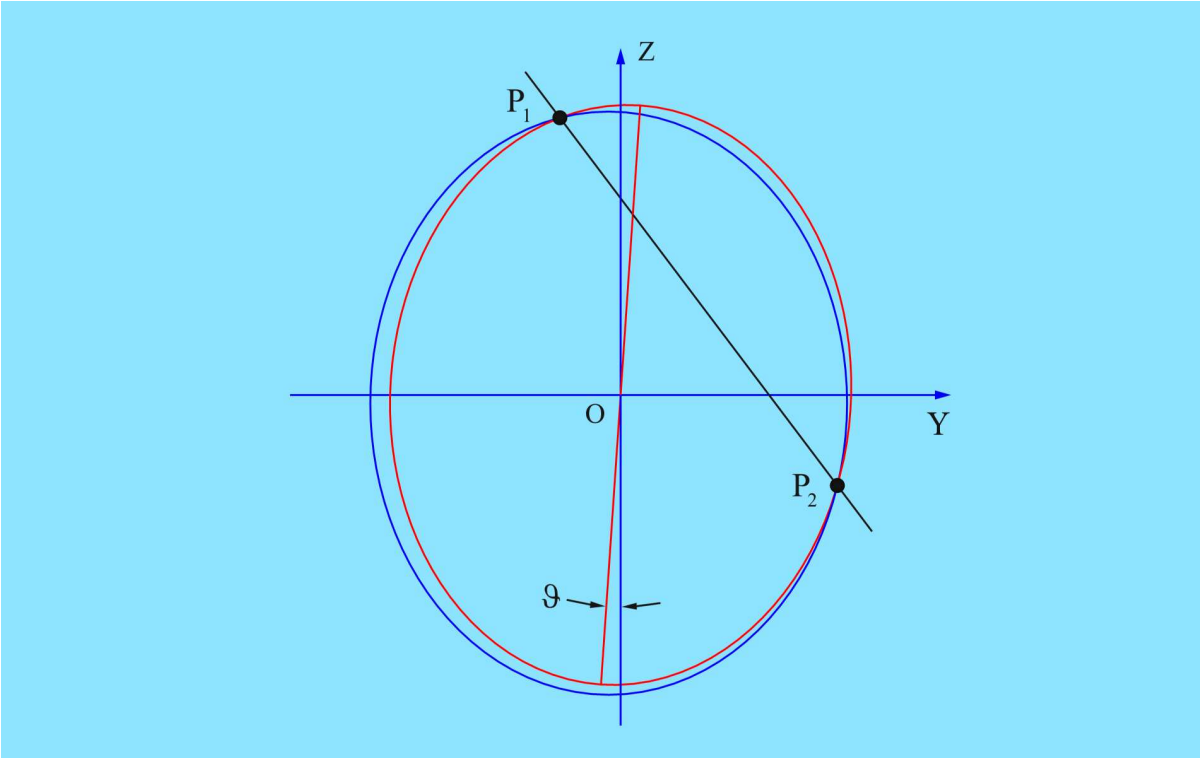

Figure 3.6: Ellipses of adjacent mirrors intersecting in two points.

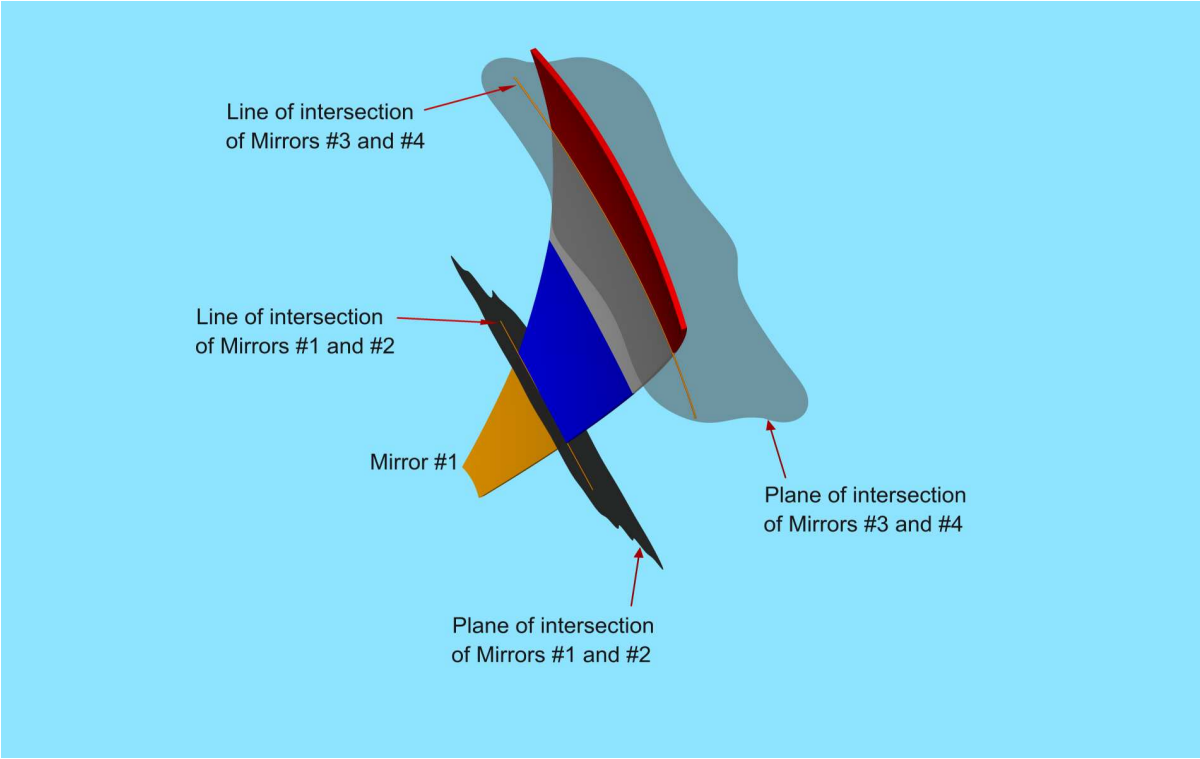

Figure 3.7: Planes of intersection of adjacent mirror segments.

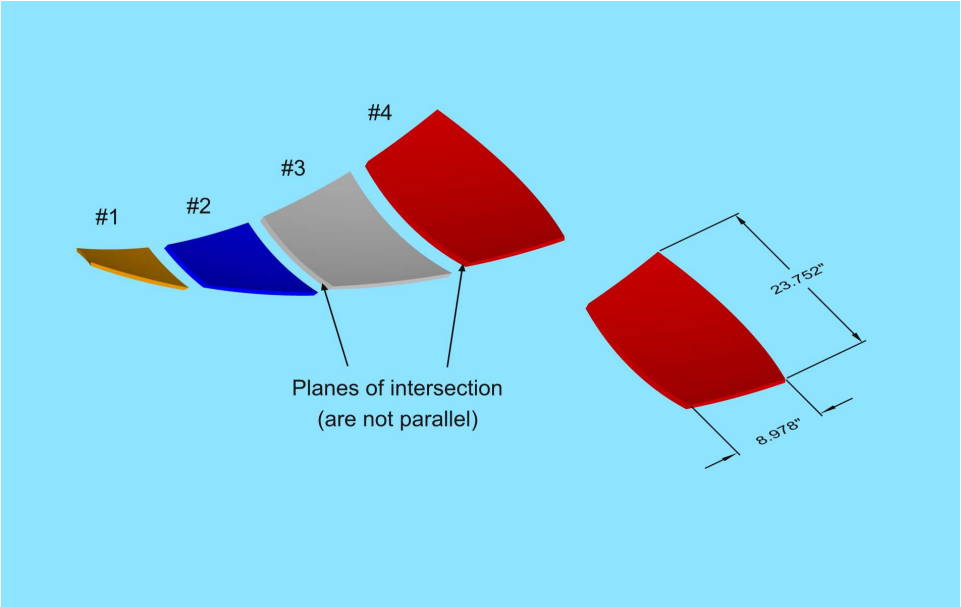

Figure 3.8: Elliptical mirror segments cut along the planes of intersection. A set of four segments cover half of the acceptance of one sector. An identical set covers the other half of the acceptance.

3.2.1 Mirror Prototyping

All of the main features of the HTCC and the properties of its components will be examined and checked by prototyping and testing of the key elements. In this section we present results on the prototyping of one mirror segment obtained in FY06, and describe current R&D efforts on building a mirror consisting of 3 mirror segments. The main R&D goal is to find ways of building an elliptical mirror of:

- 200 mg/cm^2 total thickness;
- minimal residual stress (no adjustment in-situ);
- highest possible specular reflectivity of working surface;
- reasonable cost.

A mirror substrate consists of a thermally shaped plain Mylar film of thickness 0.005 in, laminated to an ellipsoidal substrate made of rigid Polymethacrylimide polymer foam Rohacell HF31 ($\rho \approx 31$ mg/cm^3). In the entire construction procedure, the working surface of the Mylar film stays untouched. The aluminum reflector and optical coating of magnesium fluoride

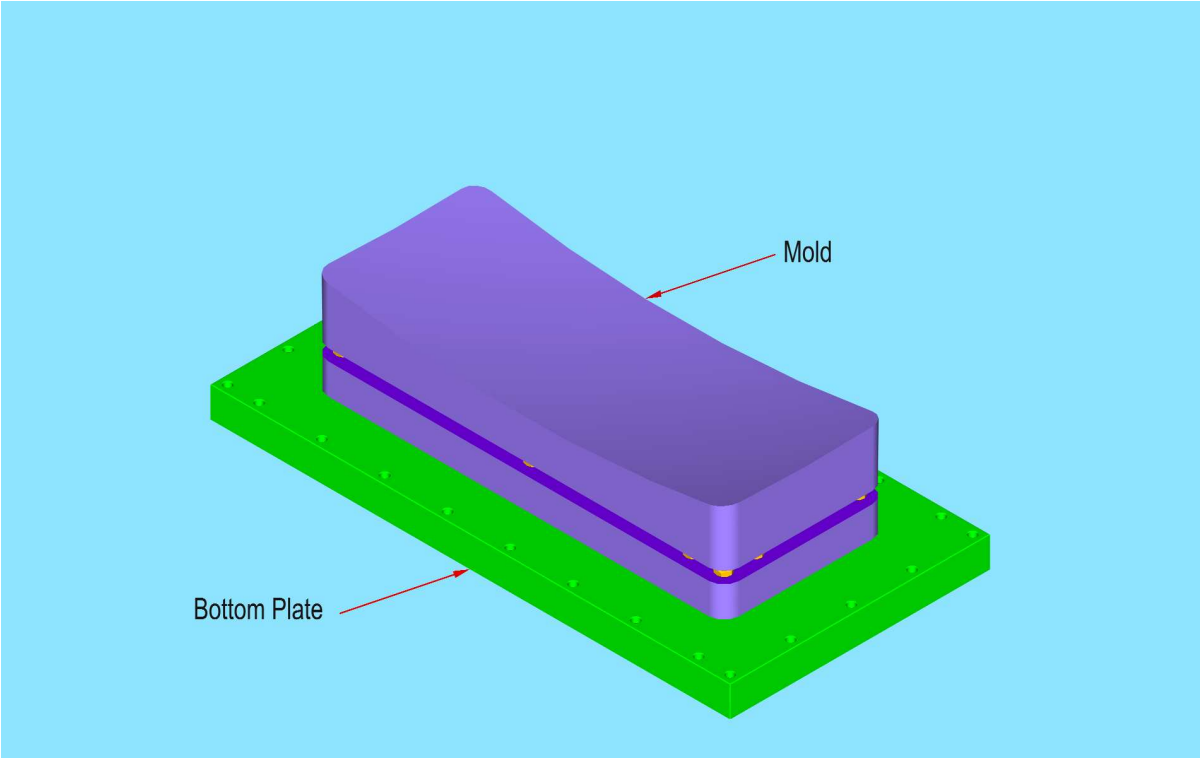

Figure 3.9: The mold installed on the bottom-plate.

(MgF_2) will be vacuum deposited onto the mylar surface after the substrate and mylar are joined as a completed unit. A set of molding tools is used for the shaping of the Mylar film into the ellipsoidal shape that mates precisely with the Rohacell substrate to avoid residual stresses. One of the mold fixtures attached to the bottom-plate of the vacuum chamber is shown in Fig. 3.9. The top surface of the mold is cut to the precise shape of the specified ellipsoid of rotation by computer-controlled milling using a ball-end mill. The thickness of the film is taken into account. The top of the mold is then polished to remove scalloping left after milling. The Mylar film is shaped by this surface, so the finish has to be smooth enough to avoid a *" telegraph wire"* effect, although the surface does not have to be of mirror quality.

For better control of the Mylar film edges and to minimize effects of thermal contraction, a thin aluminum support guard is installed surrounding the mold, as shown in Fig. 3.10. There is a small gap of 1/8-in width left between the support and mold. The support has a profile (shown in red) parallel to the edge of the ellipsoidal surface of the mold. The gap is so small that the edge of the shaped Mylar film is defined not by the mold, but by the support. This results in a better alignment of the film with the foam substrate while gluing.

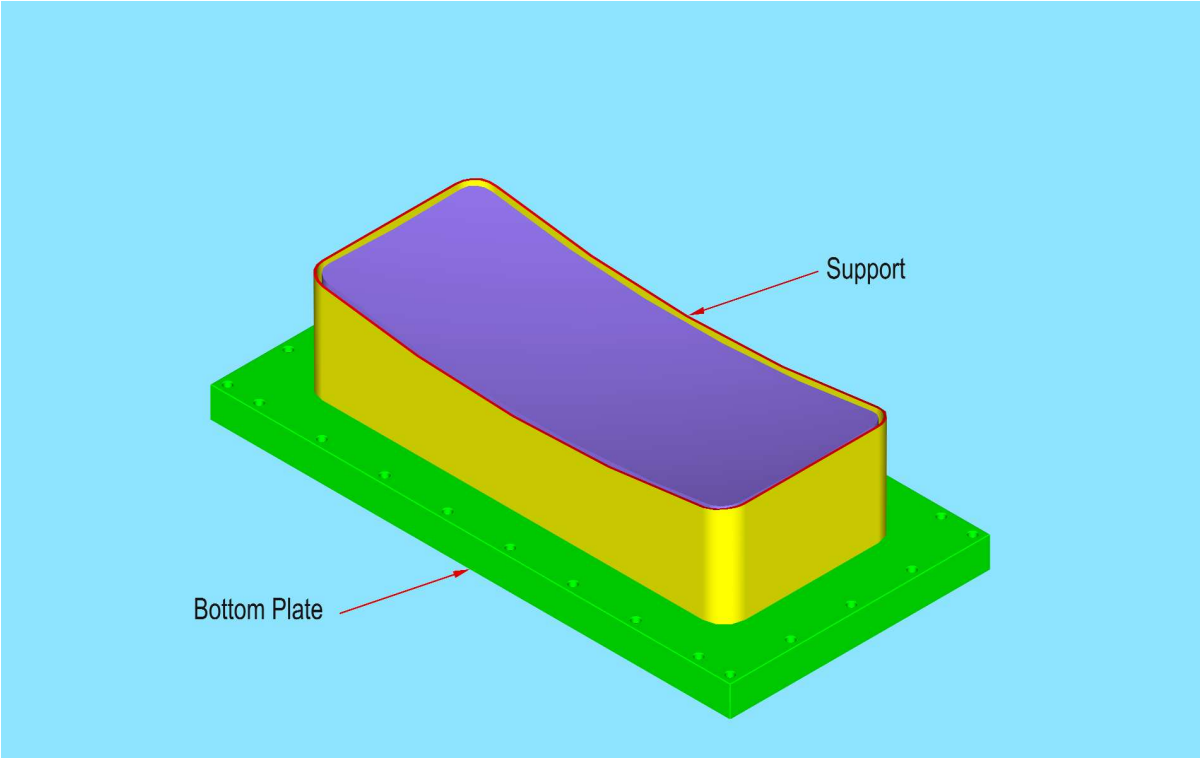

Figure 3.10: The support installed around the mold.

In Fig. 3.11 the wall of the vacuum chamber (molding box) attached to the bottom plate is shown. There are high-temperature-rated vacuum o-rings installed both on the top and bottom of the wall.

The profile of the top of the wall is cylindrical, such that there is an approximately constant clearance of $\sim 1/4$ in between this surface and the ellipsoidal surface of the mold. The inside gap between the wall and support is quite wide. It has to be wide enough for the Mylar film to form concave channels under applied pressure. These channels are formed all the way around the support and are necessary for tension relief when the chamber is being cooled down and then depressurized.

A portion of Mylar film is placed on top of the vacuum chamber, as shown (in transparent yellow) in Fig. 3.12. The top surface of the Mylar remains untouched during cutting and installation of the film. A flange is placed on the top of the Mylar and tightened down to the wall. Then the air in the chamber is pumped out so that the Mylar is deflected under atmospheric pressure, as in Fig. 3.13.

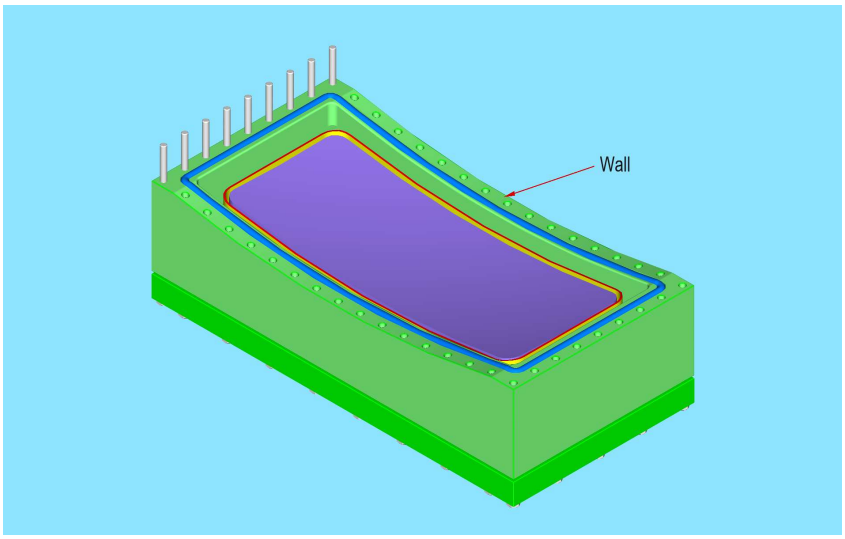

Figure 3.11: The vacuum chamber with the mold.

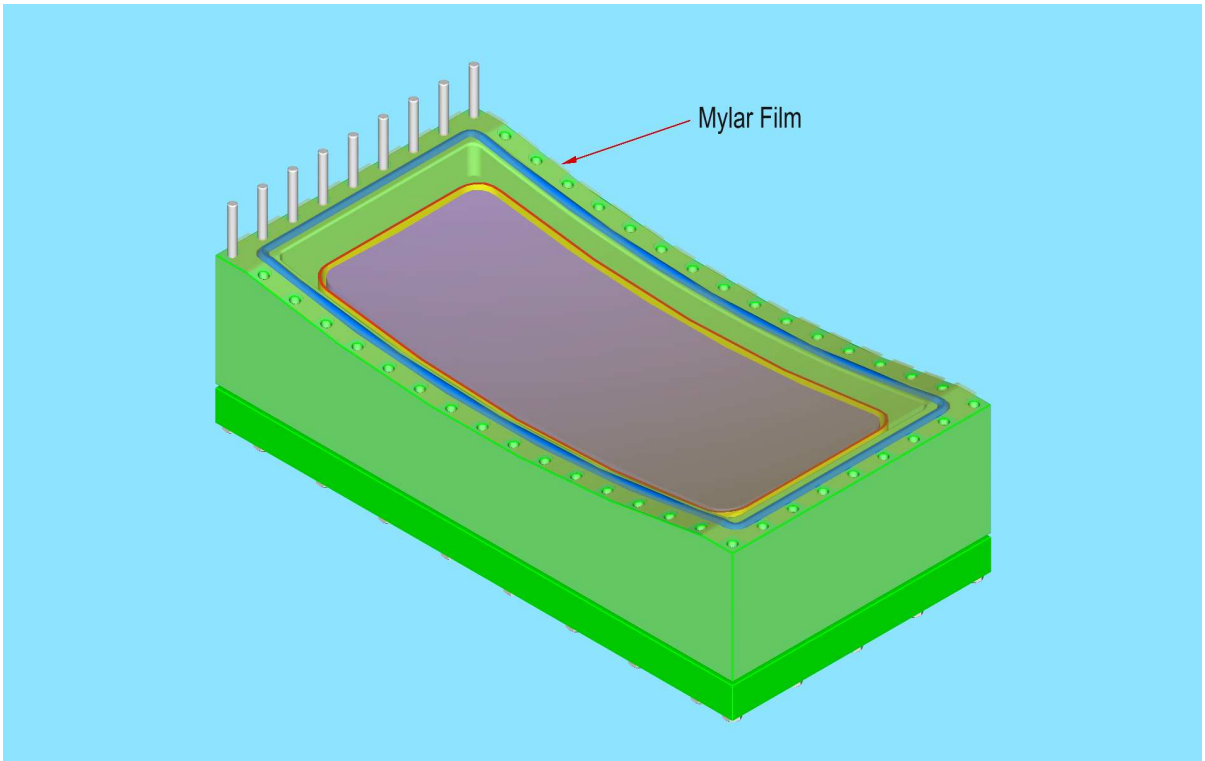

Figure 3.12: The vacuum chamber with the mold and the pre-cut Mylar film.

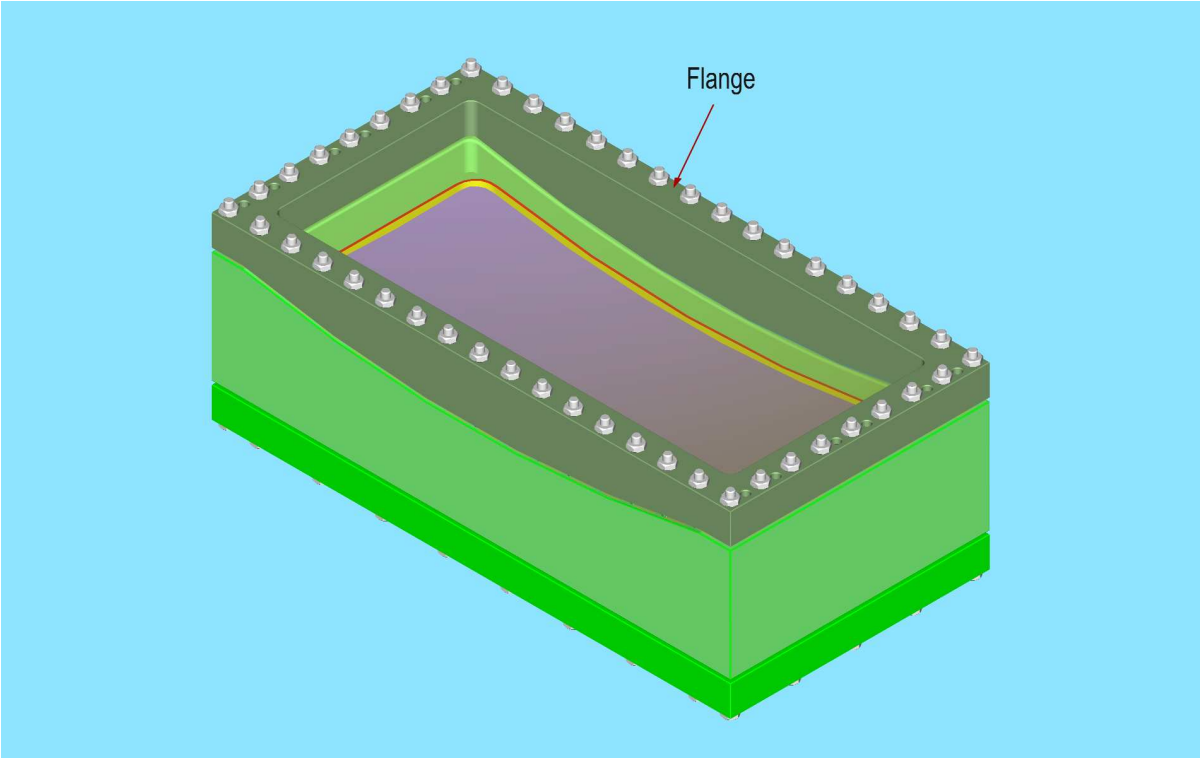

Figure 3.13: The vacuum chamber with the mold and the Mylar film.

At this point, while still at room temperature, the Mylar is touching the mold, and the area of contact between them is about 60-70% of maximum. To provide a 100% contact, the vacuum chamber is heated in an oven to a temperature of 170°C. During the heating process, which takes about 4 hours, the chamber remains connected to a vacuum pump located outside the oven. To increase the deflection of the unsupported portion of Mylar film (along the wall), additional pressure is applied to the film. This is done by covering the vacuum chamber with a lid installed on the top of the flange, as shown in Fig. 3.14. The volume under the lid is then pressurized with dry nitrogen.

The maximal differential pressure applied to the Mylar can be as high as 3 kg/cm^2. Tested stable results were obtained at differential pressures in the range from 2.0 to 2.55 kg/cm^2, depending on the temperature. The cooling of the chamber back to room temperature is the last step in the thermal shaping. The working differential pressure, once reached, is monitored and kept constant during the entire cooling cycle. After completion, the differential pressure is brought back to atmosphere and the lid is removed. A frame, shown in Fig. 3.15, is glued onto the already shaped Mylar film. The bottom surface of the frame has the required ellipsoidal

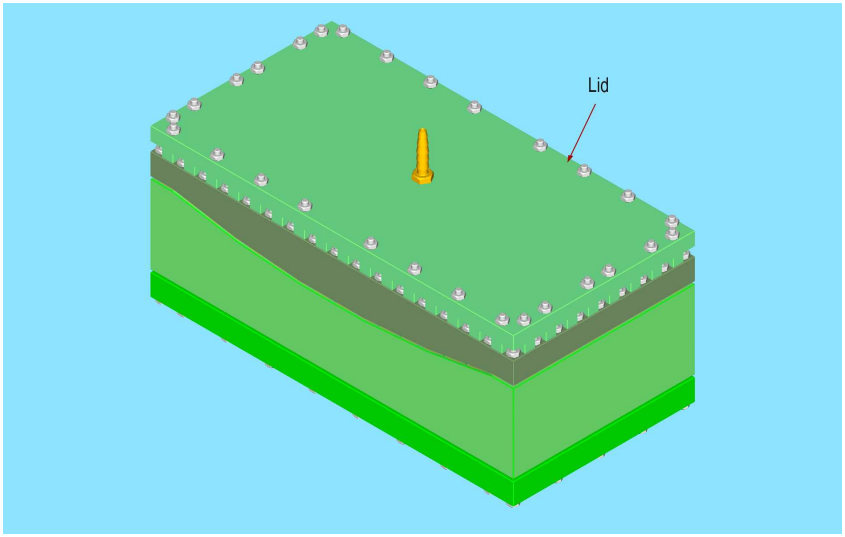

Figure 3.14: Vacuum chamber equipped with lid allowing molding of Mylar film at higher pressures.

shape. On the top there is a groove cut for a vacuum o-ring. In the figure, several installed studs are shown in red. Fig. 3.17 illustrates the gluing of the frame onto the pressurized thermally shaped Mylar. The largest portion of the Mylar, even while pressurized, is stress free. That portion of the surface that is in full contact with the mold, is leaning on it, and therefore no stresses are involved here. Only the unsupported deflected portion of Mylar that is out of the gluing frame is under stress. After the glue is polymerized, a flat Plexiglas lid is attached to the frame, and the vacuum chamber is released. The deflected portion of Mylar provides stress relief. The Mylar film, shaped at no residual stress, together with the frame and lid, is cut out as a single unit for future use.

The other important component of the mirror is the mechanical support substrate, which is made of rigid foam. A sheet of polymer foam is sanded down, under its own weight, until it provides a flat base. The top of the flat sheet is cut by CNC milling to the concave ellipsoidal shape, which mates to the back surface of the Mylar mirror substrate, as seen in Fig. 3.18. The length and width are appropriate for gluing the frame and mold.

In order to process the front (working) surface, the substrate is mounted on an auxiliary table and glued to it along the edges at several locations, as shown in Fig. 3.19. The top of the table and back of the substrate have precisely the same ellipsoidal shape, thus providing the required rigidity for further processing.

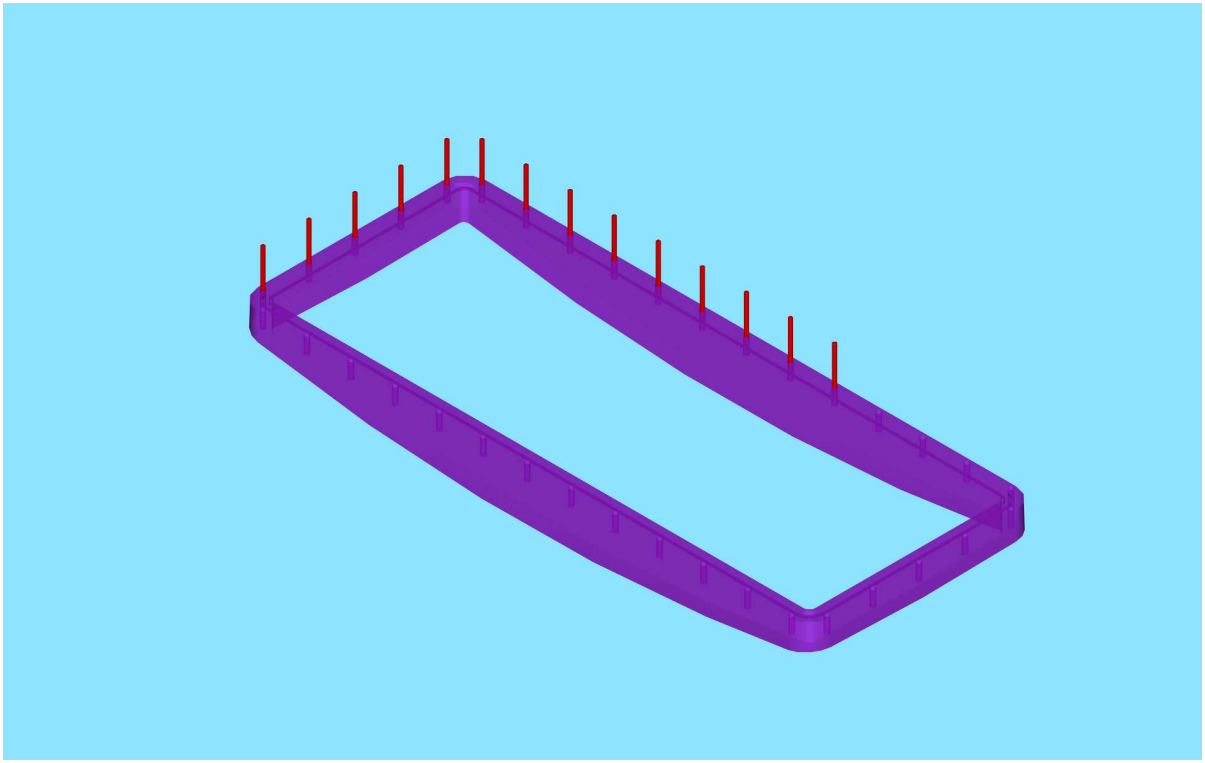

Figure 3.15: The HTCC gluing frame.

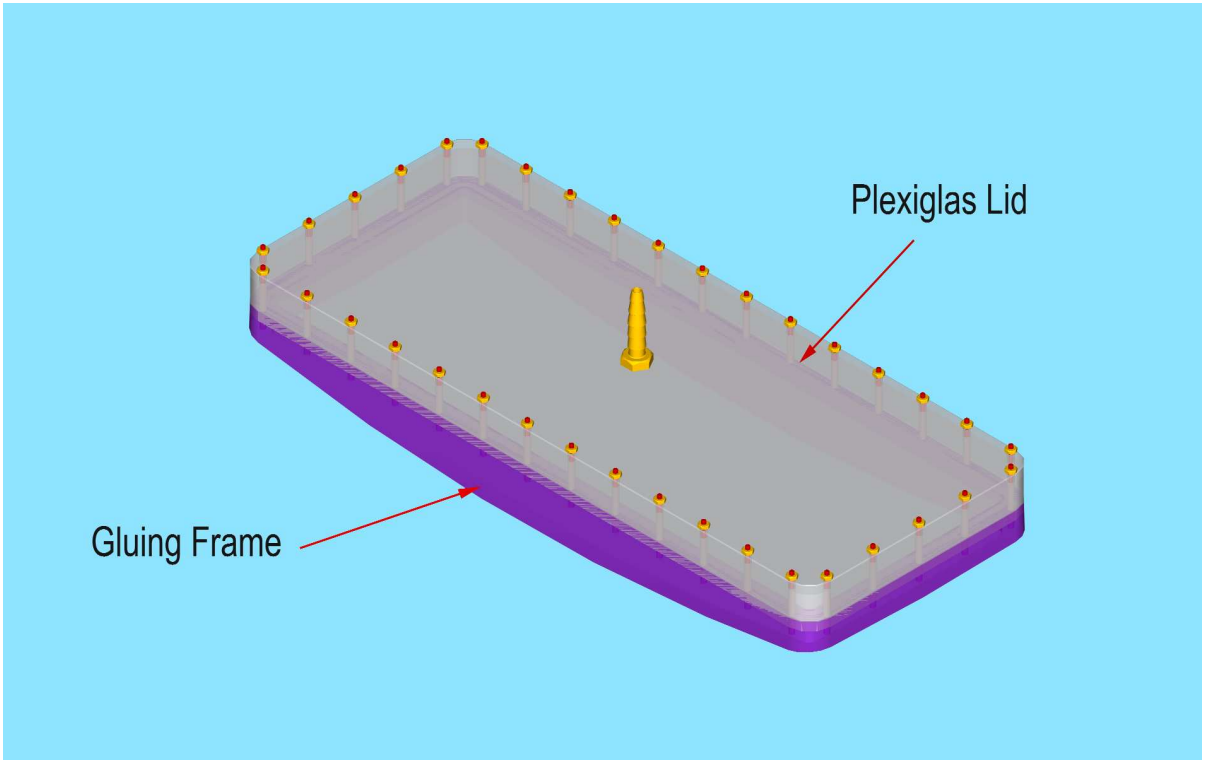

Figure 3.16: Gluing frame with Plexiglas lid on the top and Mylar attached to the bottom.

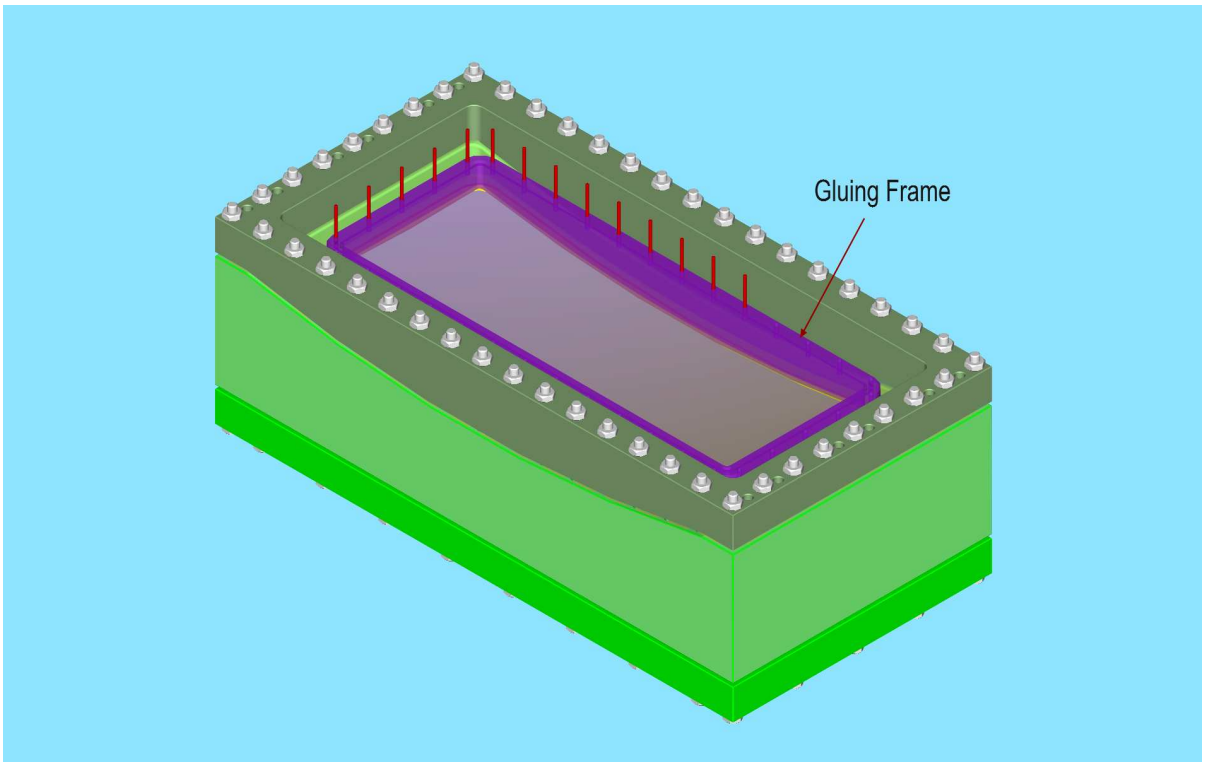

Figure 3.17: The frame glued onto the thermally shaped Mylar film leaves the film stress free after the chamber is depressurized.

Figure 3.18: The substrate: flat face down, cylindrical top.

Figure 3.19: The substrate mounted on the auxiliary table.

Figure 3.20: Computer-controlled cutting of the ellipsoidal surface of the foam substrate.

Fig. 3.20 shows the cutting of the working surface to the shape of an ellipsoid. The ellipsoid parameters were defined by taking into account the thickness of the anticipated glue joint and of the thermally shaped Mylar film. The process was optimized to achieve a surface finish on the foam smooth enough so that no polishing would be necessary. Due to the properties of foam structure, there were no scallops observed after milling. In Fig. 3.21 sample pieces of the thermally shaped Mylar films are shown, along with the mold used in shaping them, and the completely processed foam substrate mounted on the auxiliary table.

The final step in mirror construction is the gluing of the shaped Mylar onto the ellipsoidal substrate. The gluing frame, with transparent Plexiglas lid on the top and the Mylar film attached to the bottom (see Fig. 3.16), is pressurized at a differential pressure up to $\sim 2\times10^{-2}$ Torr, so that the film bulges out beyond its normal convexity. Low viscosity degassed epoxy with extended polymerization time is uniformly applied to the ellipsoidal surface of the substrate that remains attached to the auxiliary table. Then the pressurized frame with bulged Mylar is placed on top of the substrate slowly enough to let trapped air bubbles escape. A transparent lid allows visual control of the quality of the joint. The Mylar is fully

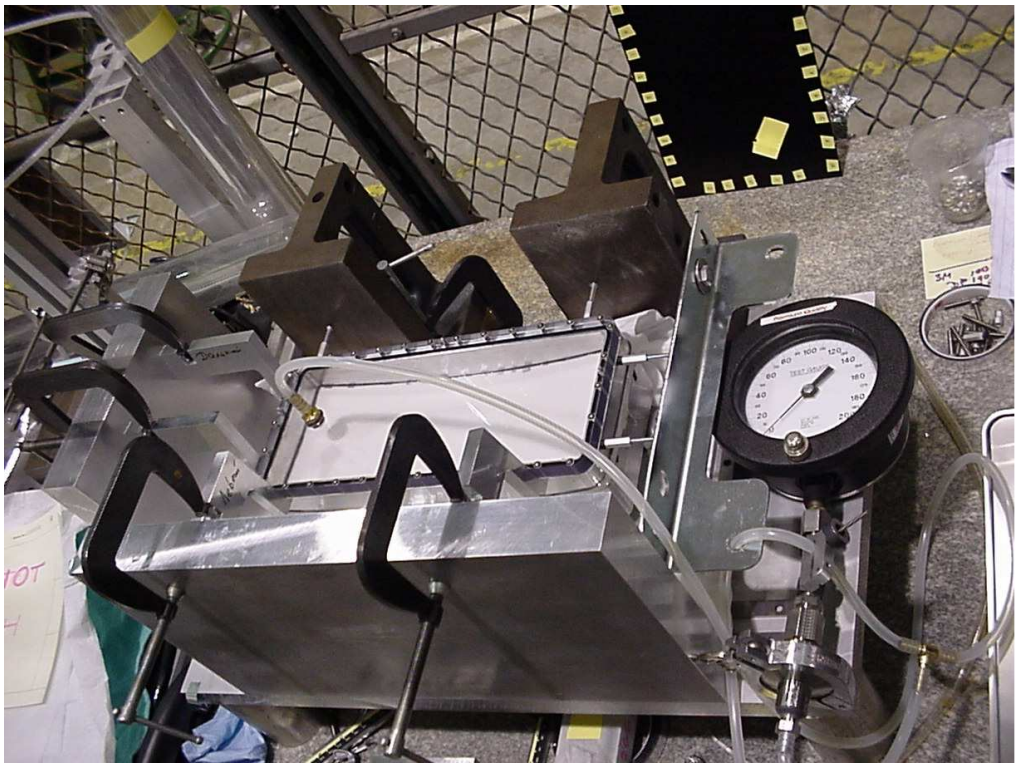

Figure 3.21: Precision assembly of the mirror substrate.

pressed against the substrate, and stays under uniformly distributed pressure until the epoxy is cured. The position of the frame relative to the table is controlled by using special tooling for precision assembly of the mirrors. After curing, the frame is depressurized, the lid removed, and the auxiliary table with its components is placed back on the CNC milling machine. The inner portion of the composite substrate is directly cut out through an opening on the frame. Measurements have shown that the total thickness of the composite substrate was 73-74 mg/cm^2. There is a potential of further decreasing a mirror's thickness without altering the technology described in this section. It would leave some contingency in varying the mirror thickness within a factor of $\sim$2, while optimizing the overall rigidity.

In 2007-2008 R&D is planned to check the last step of construction of the mirror consisting of three different ellipsoidal segments. A critical issue to be addressed is whether the estimated tolerances of assembly can be achieved.

Each of the three mirror segments, once built according to already established technology, is put on the modified auxiliary table with special trim grooves for compound-angle cuts. Then all four sides (one at a time) are cut on a 5-axis milling machine at appropriate angles

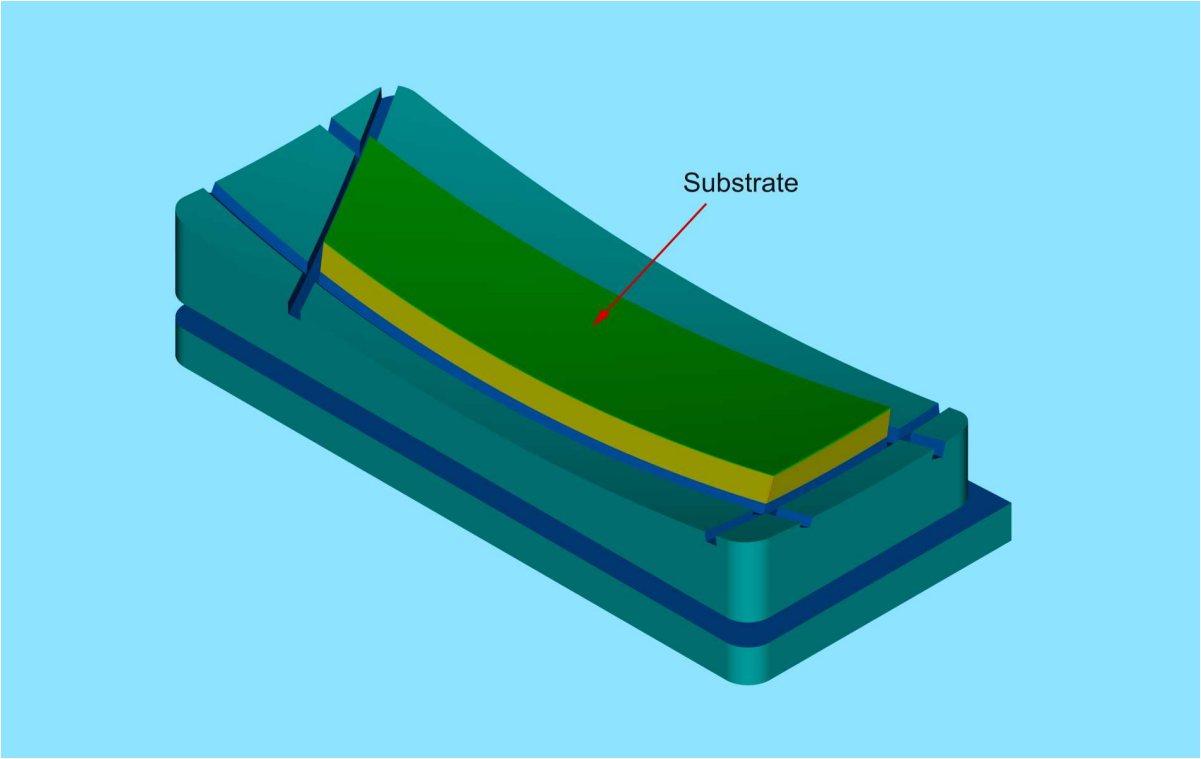

Figure 3.22: Completely cut substrate mounted on the modified auxiliary table.

(all different), defining the orientation of the planes along which the ellipsoids intersect. The accuracy of cutting (including positioning) is typically ± 0.001 in or better. Fig. 3.22 shows a substrate that has been processed along all sides (in yellow) mounted on the modified auxiliary table.

The sides of all segments are trimmed using their own tables since the angles and dimensions are different for each. But, the back surfaces of all three segments, and the top of the corresponding tables, are cylindrical with the same parameters. So, the segments can be mounted next to each other on a larger table with the top surface of the same cylindrical shape. This is illustrated in Fig. 3.23. After alignment checks of the substrates, they will be glued together along the planes of intersection.

3.2.2 Light Collection Cones

GEANT simulations of the HTCC optics and performance show that for a point-like target with no magnetic field, almost all Čerenkov photons from each segment are focused on its corresponding PMT photocathode of diameter 110 mm. This is minimal for the Photonis 5-in

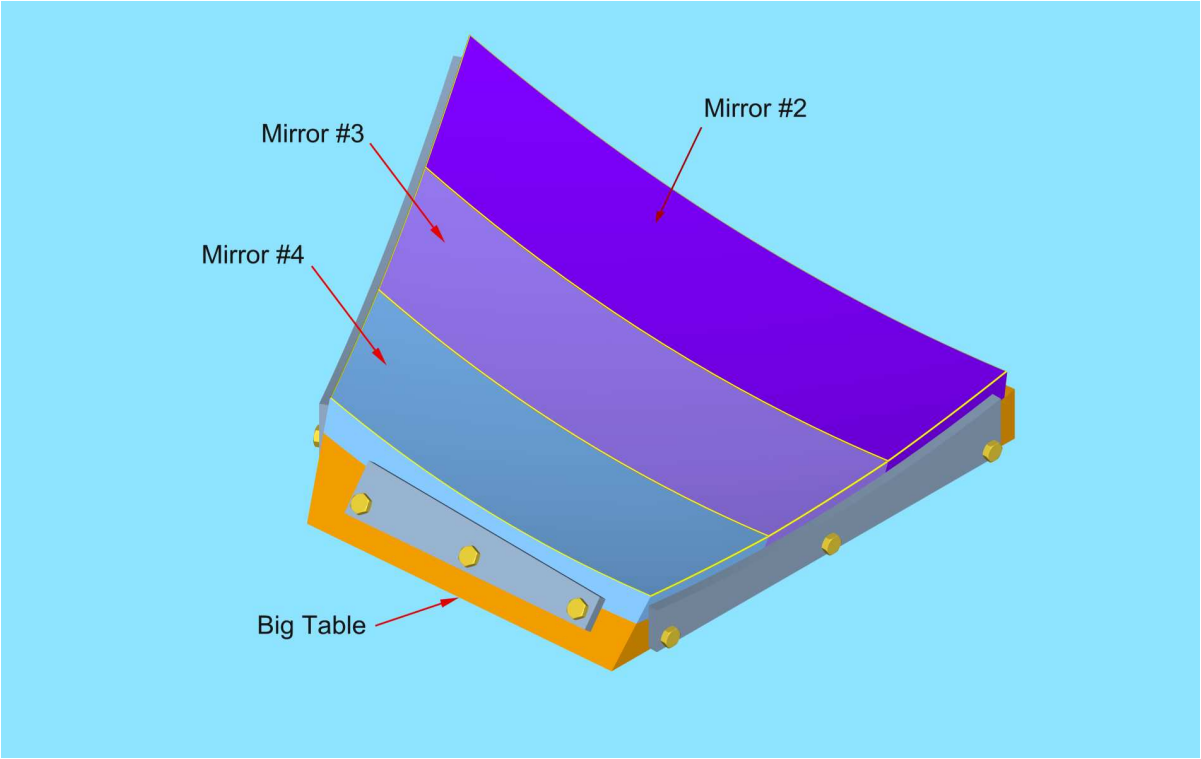

Figure 3.23: Mirror segments mounted on the Big Table. The left and right sides of the mirrors are planes along which will be glued adjacent combined mirrors.

PMTs. In experiments with CLAS12, standard cryogenic targets are 50-mm long, and in some experiments, targets as long as 100 mm can be used. For all experiments with electron beams, the superconducting solenoid and the Čerenkov counters will be used. As was mentioned in Section 3.1.1, to have efficient Čerenkov light collection for extended targets in magnetic fields, light collection (Winston) cones are necessary. To define the main parameters for the Winston Cones, we required an opening diameter of 7.5 in and a distance from the PMT photocathode to be equal to 8 in, allowing magnetic shields to be extended far enough beyond the photocathode. Direct comparison of the angular acceptance of the Winston Cones with results from Monte Carlo simulations, showed that the Winston Cone's acceptance is much wider, and the opening diameter is big enough to collect at least 95% of the Čerenkov light in experiments with both polarities of the CLAS12 torus magnet without any adjustments of the PMT locations or orientations.

There are well established and experimentally checked technologies for constructing Winston Cones. Such light concentrators were built for the existing Low Threshold Čerenkov Counter (LTCC) of CLAS by electro-forming technology and have shown sustained undiminished performance for more than a decade. The technical specifications and requirements of the proposed Winston cone for the HTCC, similar to those used in CLAS, are given in Table 3.3. The corresponding parameters are given in Fig. 3.24.

3.3 DAQ for HTCC

Signals from the Čerenkov counter will be used in generation of the CLAS12 event trigger and for timing purposes. The PMTs will supply an anode signal over a coaxial cable to a passive splitter installed on the forward carriage. One of the output signals from the splitter will go to a flash ADC (see Fig. 3.25) and the other one to will go to a timing discriminator connected to a pipeline TDC.

The flash ADC will have 12-bit resolution and a 250 MHz clock. The pipeline TDCs will provide 85 ps time resolution. The timing discriminators will have built-in scalers for each channel. The sums from the flash ADCs will be delivered to the trigger processing boards and will be used to generate the Level-1 trigger, along with the other fast detectors of CLAS12. The mirror segmentation in polar angle will allow use of the HTCC for selecting angle ranges at Level 1.

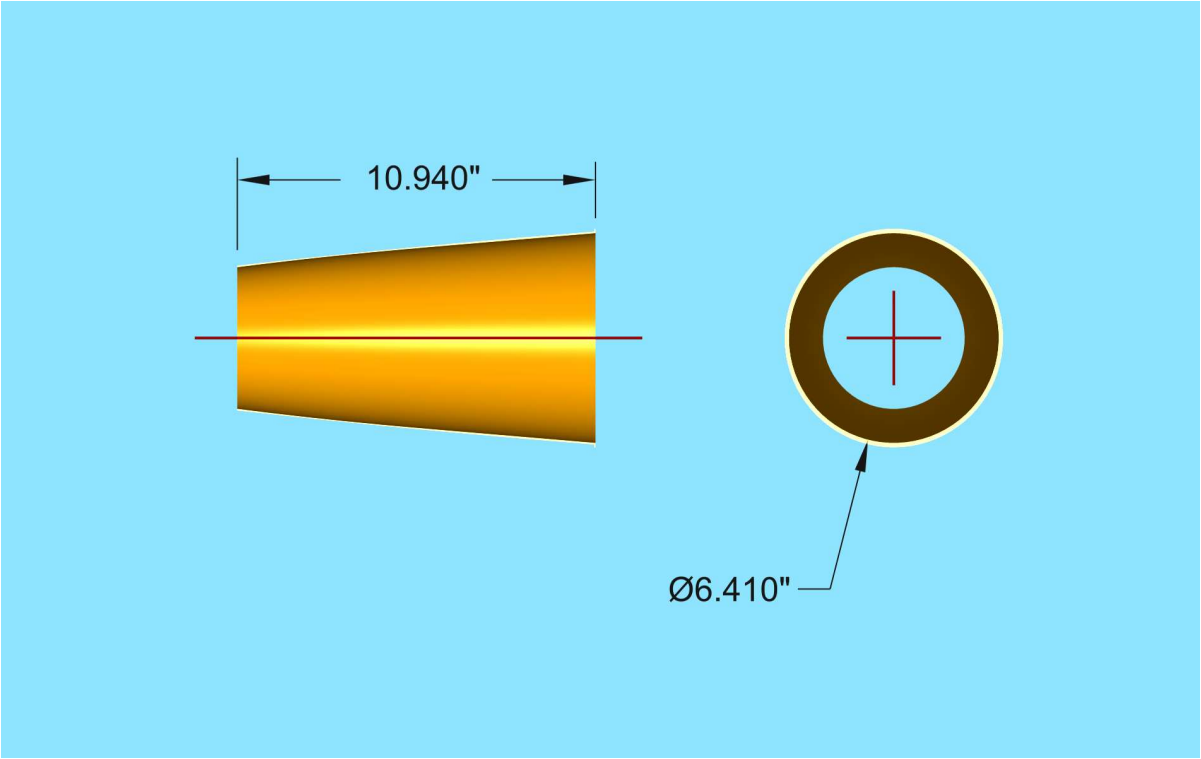

Figure 3.24: Winston cones for the HTCC.

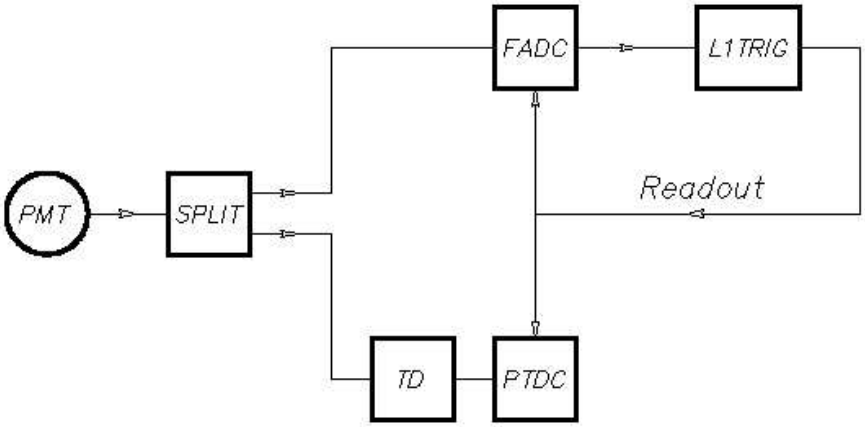

Figure 3.25: Single channel scheme of readout for the HTCC.

Specification	Date	Source
Winston Cone Definition		
A Winston Cone is a non-imaging light collector designed to collect light from a range of incident angles on a given circular area and to collect that light onto a smaller area. The Winston Cone is not a focusing device, but it is highly efficient in collecting light. In general, the shape is that of a parabola that revolves about the axis of symmetry of the parabola.		
Basics		
Material = nickel alloy outer surface with inner coatings of aluminum and magnesium fluoride (see below)	12/2006	P. Stoler
Weight = $\sim$4 lbs	12/2006	Y. Sharabian
Life time = 30 years with no optical degradation	12/2006	P. Stoler
Dimensions = 7.5 in $\times$ 8.0 in long	12/2006	Y. Sharabian
Optical and structural properties tolerant to a high radiation dose of 20 Mrad/20 years	09/1991	C. Zorn
Most radiation consists of x-rays with some relativistic particles	05/1992	C. Zorn
Manufacturing = electroforming		
Slope errors $< 1^\circ$	12/2006	D. Kashy
Surface finish of Root Mean Square = 0.5 μm	12/2006	Y. Sharabian
Scratches occurring in forming operation, etc. need not be removed provided in the final product there are less than 4/cone and 1) they are less than 2.54 cm in length 2) they are less than 0.15 μm deep Open ends flat within 0.03 in	12/2006	Y. Sharabian
Optics	12/2006	Y. Sharabian
Acceptance angle for incident light = 28.3° Reflectivity >88% between 220 nm and 600 nm for all glancing angles $<30^\circ$		

Table 3.3: Specifications for the HTCC Winston cones for CLAS12.

MATERIAL	12/2006	P. Stoler
Nickel Alloy: Thickness = 0.040-in nominal Application method = electro-formed Aluminum: Thickness $\approx$ 0.04 μm Application method = vacuum (vapor) deposition Non-magnetic Magnesium fluoride (protective coating) Thickness = as required to meet reflectivity specifications Application method = vacuum (vapor) deposition Non-magnetic		
ENVIRONMENTAL	12/2006	Y. Sharabian
Operating in CO_2 at 1.001 atm, temperature = 22°C; Stored in plastic bag w/ambient air to avoid dust contamination; DO NOT contact reflective surface with anything; Wash reflective surface w/only optical liquid.		

Table 3.4: Specifications for the HTCC Winston cones for `CLAS12`.

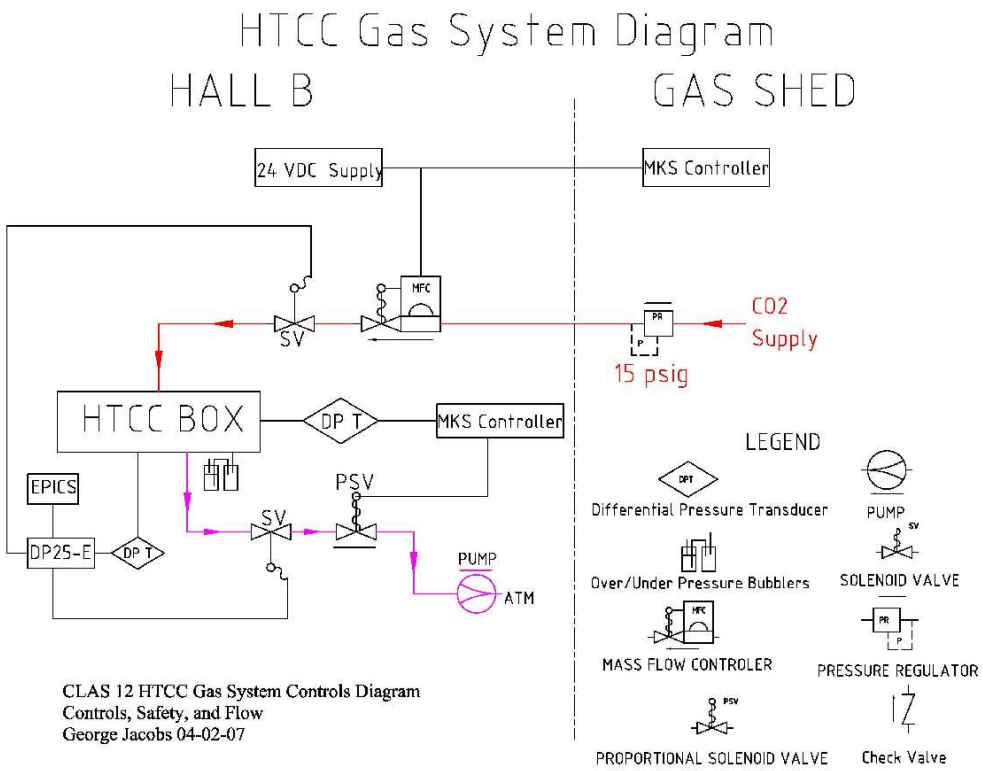

Figure 3.26: A diagram of the HTCC gas system.

3.4 HTCC Gas System Overview

The CLAS gas supply system for the existing LTCC counter will be used for the HTCC, with minor upgrades of two reserved lines. Gas will be supplied via CO_2 dewar boil off of Coleman-grade gas, 99.98% minimum purity. The pressure is reduced in three stages. The dewar output will be set to 175 psig, the house line regulator will be set to 35 psig, and the hall supply to 15 psig. A continuous flow of gas, CO_2, will be supplied to the detector via an MKS Mass Flow Controller (see Fig. 3.26).

The pressure in the detector is controlled by pumping gas out of the detector via a pump and an MKS proportional control valve. An MKS pressure controller adjusts the valve position to maintain 0.05-in water equivalent pressure in the detector. Both the supply and exhaust systems will fail safe on loss of power and will require a manual restart when power is restored.

Both active and passive over-pressure and under-pressure protections for the detectors will be used. Active protection will use an Omega process controller to operate the solenoid isolation valves. One valve isolates the detector from the gas supply to prevent an over-pressure

condition. The other solenoid isolates the detector from the exhaust manifold to prevent an under-pressure condition. These solenoid valves also isolate the detectors in case of power failure. The active level automatically provides action to mitigate the pressure problem. Passive protection uses oil-filled bubblers that will be installed on the detector itself. If the differential pressure inside the detector exceeds 0.125-in water equivalent, gas will either vent to atmosphere or be sucked into the detector to prevent damage. The bubblers will be sized such that they can vent the full gas system supply or exhaust flow in case both the pressure control system and active safety systems fail.

3.5 Simulations of Detector Performance

Extensive Monte Carlo simulations were carried out as part of the detector design procedures. This section describes some of the features of the expected detector performance based on the current design.

3.5.1 Optical Properties of Physical Components

The criterion for the choice of physical components is to maximize the production and detection of electron Čerenkov light with the maximum threshold energy for pion Čerenkov radiation. Fig. 3.27 is a composite showing the properties of the various materials that play important roles in the Čerenkov performance.

Radiator Gas

The choice of radiator gas is CO_2, which has excellent optical transparency for wavelengths as low as 200 nm (see Fig. 3.27). This is an important feature since the spectrum of Čerenkov light is approximately $dn/d\lambda \propto 1/\lambda^2$. The low index of refraction, $n \sim 1.00041$, corresponds to a pion threshold energy of 4.7 GeV. The trade-off is that fewer photons are produced at such low values of n. However, as will be seen, the number of collected photons is high enough to ensure a high detection efficiency.

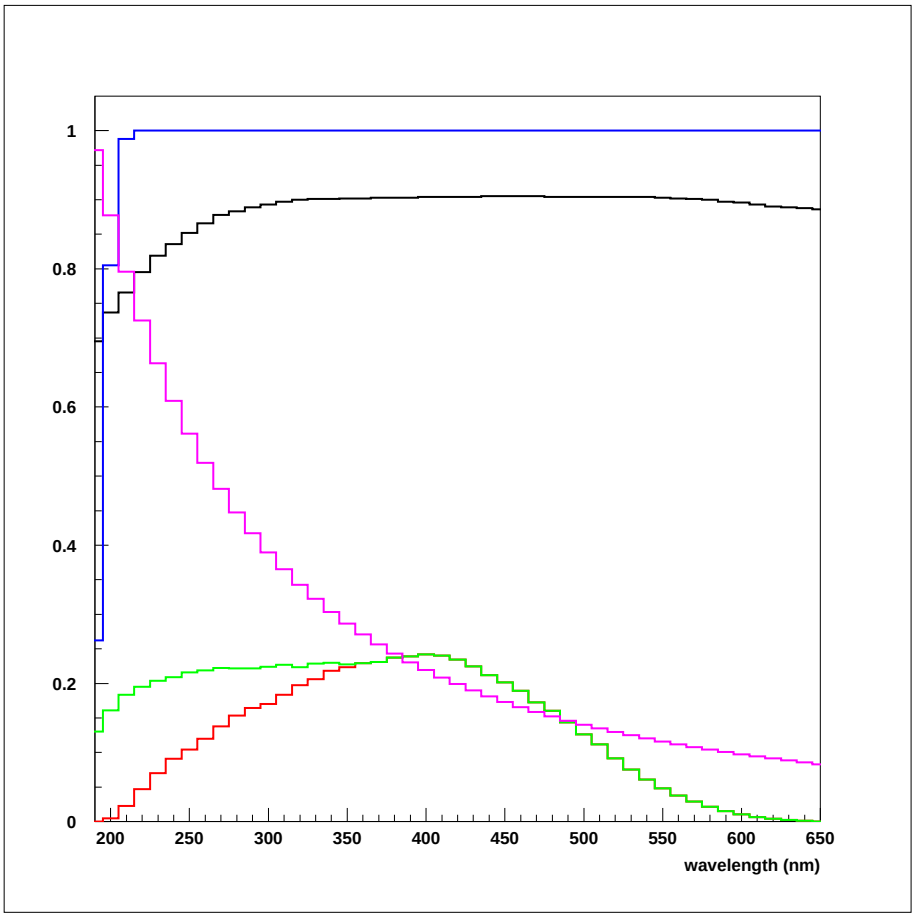

Figure 3.27: The optical properties of components of the HTCC relative to maximizing the number of detected photoelectrons as a function of photon wavelength. The transparency of CO_2 is shown in blue, the reflectivity of aluminum in black, the photo-efficiency of a PMT with a UV glass window in red, and a quartz window in green. The magenta line represents the Čerenkov spectrum (in arbitrary units).

Photomultiplier Tubes

The use of 5-in photomultiplier tubes was chosen as the best match for the optical properties of the HTCC. This will be clear in the section on the photon spacial distributions at the face of the PMTs. After consideration of PMTs from several manufacturers [1], the Photonis XP4508 was chosen to have the best overall characteristics for our requirements. The window material is an important consideration. Fig. 3.27 compares the quantum efficiency of the Photonis XP4508 with UV glass and quartz windows. Clearly, the quartz window is superior in the low wavelength regime in which there are a large number of photons, and it matches the transparency range of the CO_2, as well as the reflectivity of the Al-MgF_2 mirror surfaces, which are also shown in Fig. 3.27.

The intensity and spectrum of Čerenkov photons is given by the Frank-Tamm relation:

$$\frac{dN_\gamma}{dE} = \left(\frac{\alpha}{\hbar c}\right) Z^2 L \left[1 - (\frac{1}{n(E)\beta})^2\right], \tag{3.3}$$

where Z is the particle charge, $n(E)$ is the index of refraction, L is particle trajectory length, and $(\frac{\alpha}{\hbar c}) = 370\ \mathrm{eV}^{-1}\mathrm{cm}^{-1}$. The expected number of obtained photoelectrons is then:

$$N_{ph.e.} = \int \frac{dN_\gamma}{dE}\varepsilon(E)dE, \tag{3.4}$$

where $\varepsilon(E)$ is the detection efficiency of photons with energy E. $\varepsilon(E)$ depends on the Čerenkov gas transparency, reflection losses, quantum sensitivity of the PMT, and the probability of missing the PMT because of geometry factors.

The calculated mean number of photoelectrons per 1 cm of the trajectory is 0.1477 for a UV glass PMT window and 0.2086 for a quartz PMT window. The difference is essentially because of the fact that the Čerenkov photon spectrum has an enhancement at low wavelengths – see Fig. 3.27. For our Monte Carlo simulations we assume quartz PMT windows. The number of obtained photoelectrons was corrected for mirror imperfections and possible misalignments. The correction coefficient, derived from the ratio of the Monte Carlo simulations and the experimental number of photoelectrons for the CLAS LTCC, was equal to 2/3.

The shape of the PMT surface has also been considered, since the reflectivity of the PMT window, and thus the quantum efficiency, depends on the distribution of the angles of the photons relative to the PMT surface. Fig. 3.28 shows the simulated distribution of photon

[1] ElectronTubes, Burle, Hamamatsu, Photonis

angles relative to the normal to the PMT surface for convex and flat windows, respectively. It is seen that the distribution for the flat surface is closer to the surface normal than for the convex surface, and thus the flat surface quartz window was chosen as most appropriate for our purposes.

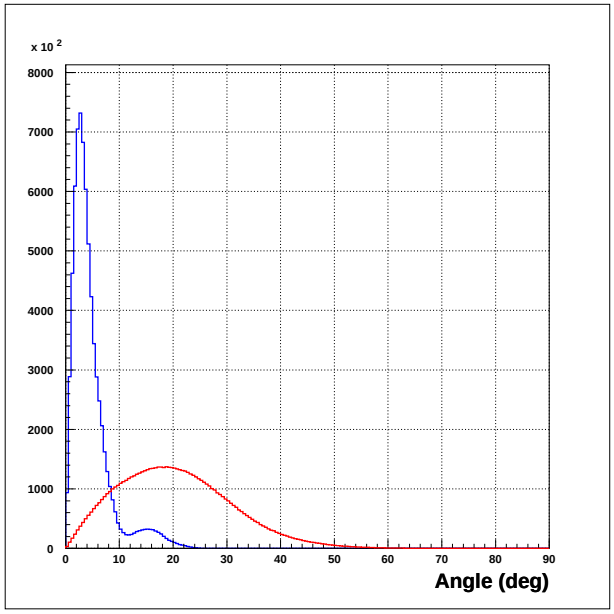

Figure 3.28: The simulated distribution of photon angles relative to the normal to the PMT surface for convex (red) and flat (blue) windows, respectively. The enhancement near the 15° (blue curve) is due to the photons, reflected off the Winston cone.

3.5.2 Distributions of Photons Incident on the PMT Faces

Simulations were carried out to assess the HTCC response to scattered electrons as a function of scattering angle in both θ and ϕ. The results discussed in this section are for electrons of energy 2 GeV uniformly distributed in $d\Omega = \cos\theta d\theta d\phi$. Each mirror is designed to direct the Čerenkov light that impinges upon it onto the face of a specific PMT. Fig. 3.29 shows the distribution of photons reaching PMTs in the PMT surface plane.

The electrons originate from a target of length 10 cm, which is centered at the nominal central target position, with the full magnetic field configuration. It is observed that the photons are constrained to circles of diameter approximately 16 cm, which is somewhat larger than the 11 cm PMT active diameters. Thus, light collection cones (Winston Cones) have been designed to redirect the photons that arrive outside of the photosensitive areas of the

PMTs into the photosensitive areas. All calculations were made for a Winston Cone window diameter of 7.5 in.

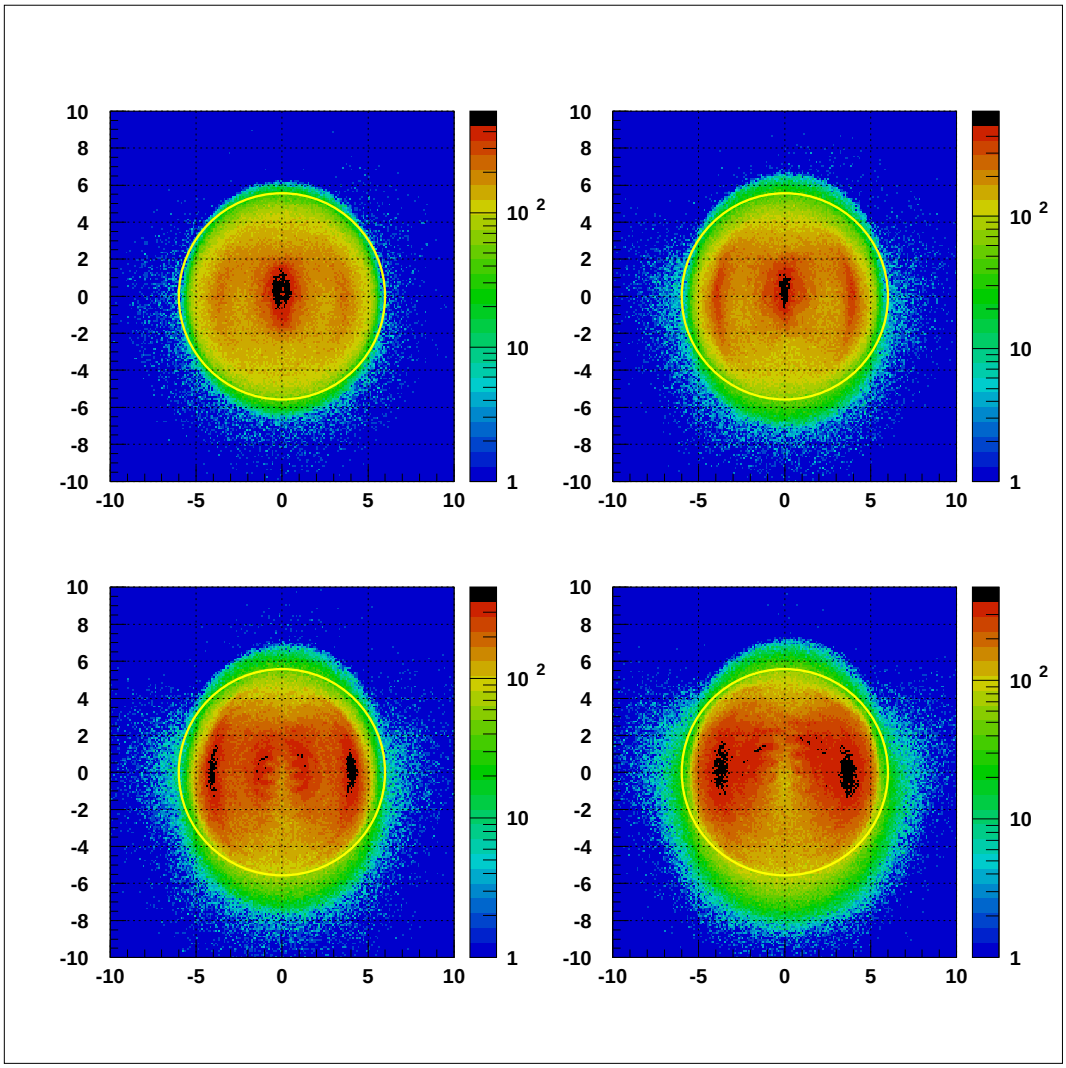

Figure 3.29: The distribution of photons reaching the PMTs in the PMT surface plane. Circles show the PMT size.

Fig. 3.30 shows the overall acceptance in the number of photoelectrons as a function of θ and ϕ for one half of a sector, corresponding to the *standard* conditions described above. The results are the same for the 12 symmetrically placed half sectors corresponding to full $\Delta\phi = 2\pi$. Fig. 3.31 shows the projections of Fig. 3.30 vs. θ and ϕ, respectively. One observes that the mean number of photoelectrons is greater than 10 for scattered electrons in the angular range from about 5° to 36°. The θ dependence of the photoelectron number reflects the trajectory length dependence.

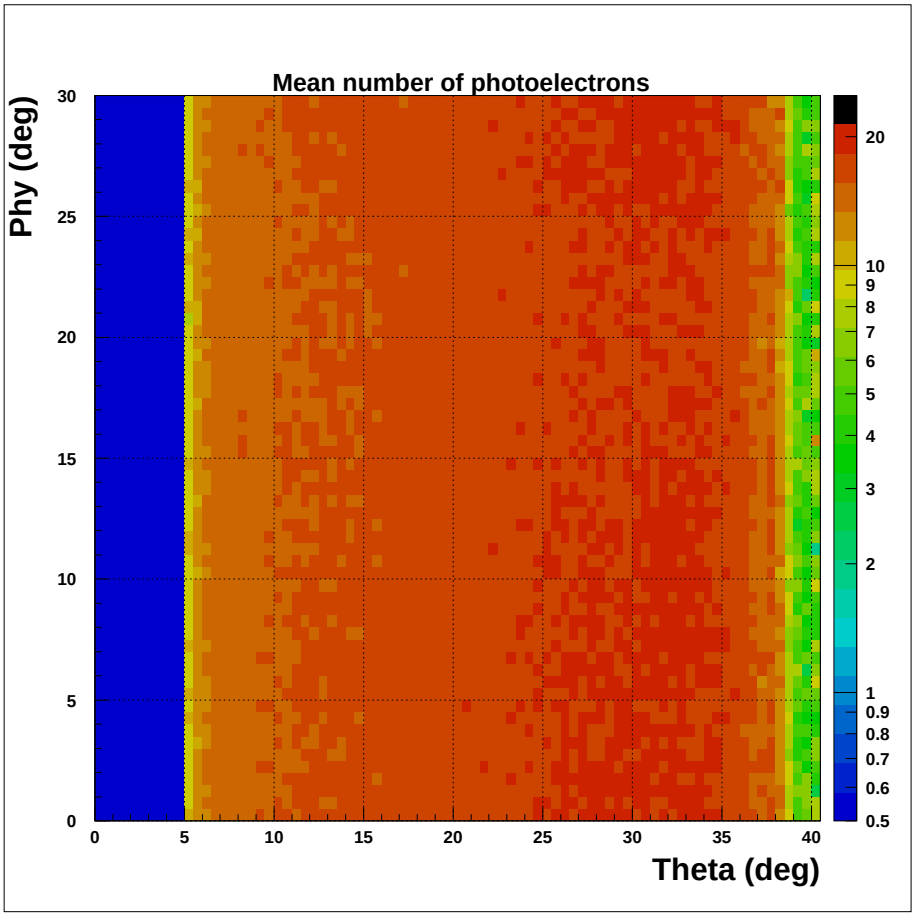

Figure 3.30: The overall acceptance in the number of photoelectrons as a function of θ and ϕ for one half of a sector.

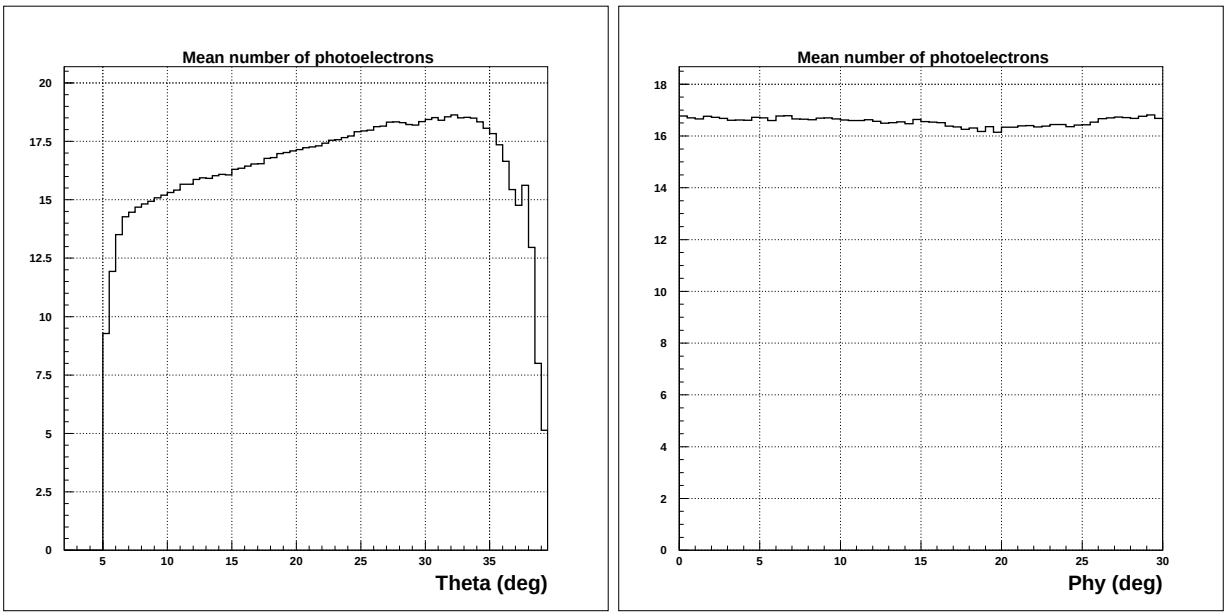

Figure 3.31: The projections of Fig. 3.30 vs. θ and ϕ, respectively.

The effect of the fields and target length on the performance of the detector are illustrated in Fig. 3.32a, b, c, and d, which show the distribution of photons on one PMT, number 2. Case a) is a point-like target without magnetic field and case b) is a 10-cm target without magnetic field. Cases c) and d) are the point-like target and 10-cm target, respectively, in the 5-T solenoid magnetic field. Fig. 3.32 shows that the distortions due to the target length and magnetic field are not very large, and the 7.5-inch diameter Winston Cone is an adequate choice to collect all Čerenkov light.

3.5.3 Background Rates

GEANT was used to estimate the background rate due to scattered electrons, and electrons and positrons from secondary interactions with the detector materials. Initial electrons with energy 11 GeV interact with the 5-cm liquid-hydrogen target in the 5-T solenoid magnetic field. The beam pipe shielding starts from about 40 cm from the target. The beam pipe shielding is between 2° and 4°. The PMT rates were reduced to the standard luminosity at 11 GeV, 10^{35} cm^{-2}s^{-1}. The beam pipe shielding material was tungsten.

Fig. 3.33 illustrates the beam pipe shielding setup and background PMT rates. The highest rate is for the PMT at the lowest polar angle.

For possible using the Inner Calorimeter for DVCS studies the other shielding was designed.

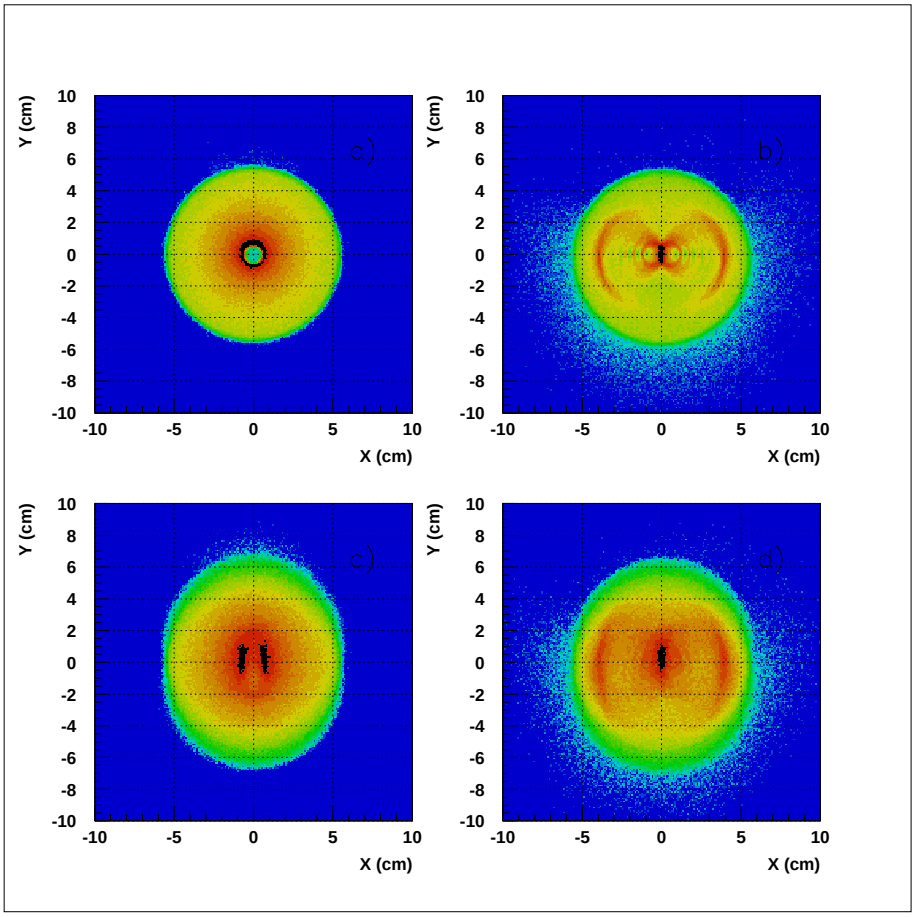

Figure 3.32: The effect of the magnetic field and target length on the performance of the detector. (a) is a point-like target, no magnetic field; (b) 10-cm target, no magnetic field; (c) and (d) are for a point-like target and a 10-cm target, respectively, in the 5 T solenoid magnetic field.

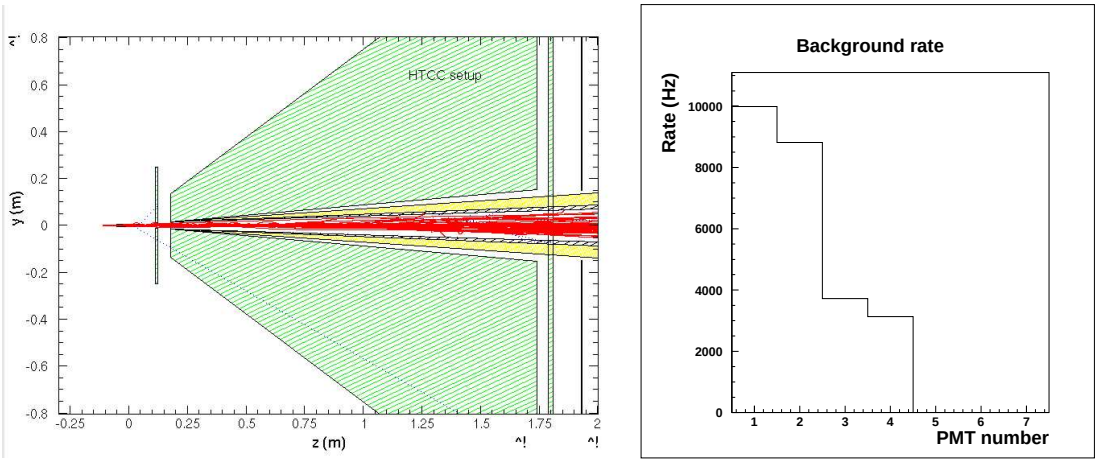

Figure 3.33: The experimental setup and background rates estimate.

It covers the open angle from 1° to 1.5°, and also the angle from 5° to 5.5° . The setup and the estimated background rate in this case is shown in Fig. 3.34. The background rate is a bit higher in this case, but it can be easily handled by the data acquisition system.

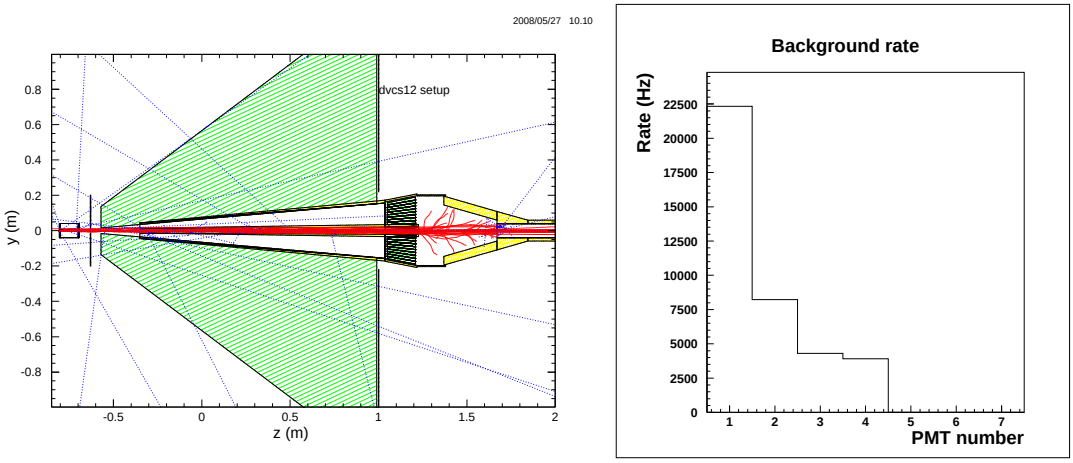

Figure 3.34: DVCS12 setup and background rates estimate.

The π/e rejection factor is very important for the Čerenkov detector. Pions can produce δ-electrons, which can be detected in the HTCC. However, the amplitude distribution of such events is low. Fig. 3.35 shows the amplitude distribution of detected pions (in photoelectrons) for 2 GeV (blue curve) and 4 GeV pions (red curve).

Fig. 3.36 shows the π/e rejection factor, calculated as the ratio of electron to pion detection efficiency, for 2 GeV and 4 GeV pions. The red line shows the π/e rejection factor with a threshold of one photoelectron, green - two photoelectrons, and blue - three photoelectrons. The π/e rejection factor can be as high as 500 even for high momentum pions. It must be noted that the electron detection efficiency is still very high at thresholds up to three photoelectrons: 99.99% for two photoelectrons and 99.90% for three photoelectrons.

3.5.4 Timing Parameters

GEANT can be used to estimate the trajectory length and the ray-tracing length difference for Čerenkov photons for different PMTs. The detection time difference is shown in Fig. 3.37. It is evident that HTCC signals can be used for good time-of flight measurements, because even at larger θ angles, the timing is within ± 0.2 ns.

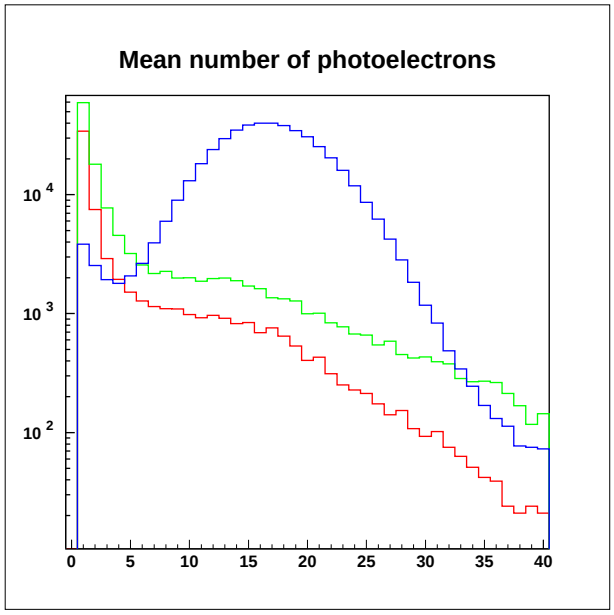

Figure 3.35: The amplitude distribution of detected pions (in photoelectrons) for 2 GeV (red curve) and 4 GeV pions (green curve). The blue curve shows the amplitude distribution for the detected electrons.

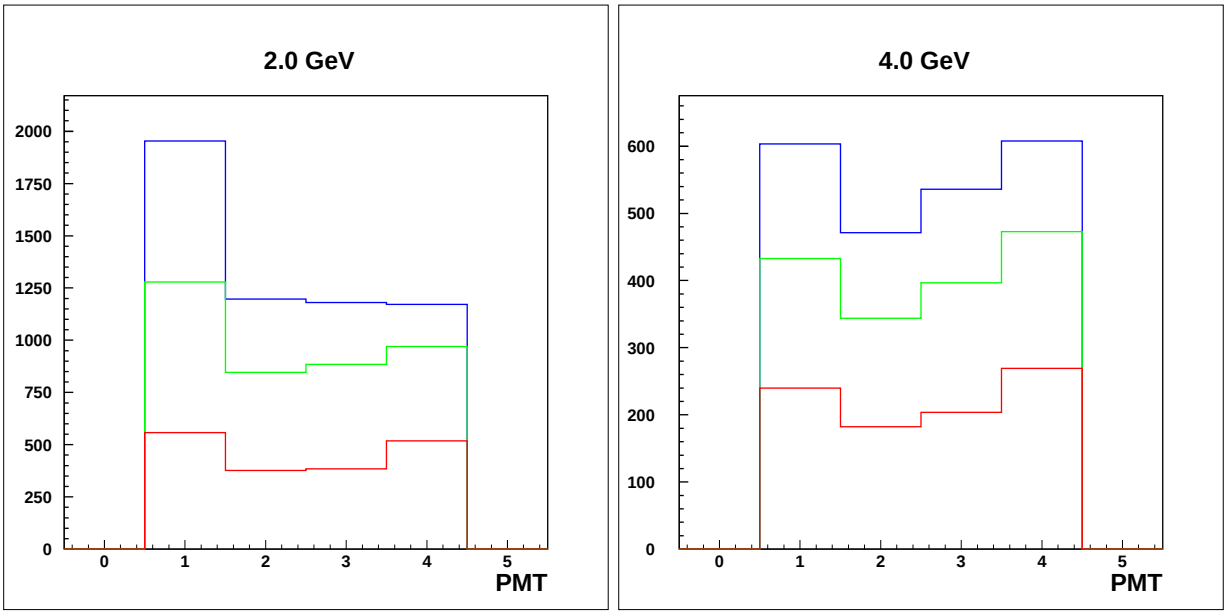

Figure 3.36: The simulated pion rejection factor of pions to electron identification for initial 2 GeV and 4 GeV pions. The different curves represent different amplitude thresholds: red is for one photoelectron, green for two photoelectrons, and blue for three photoelectrons.

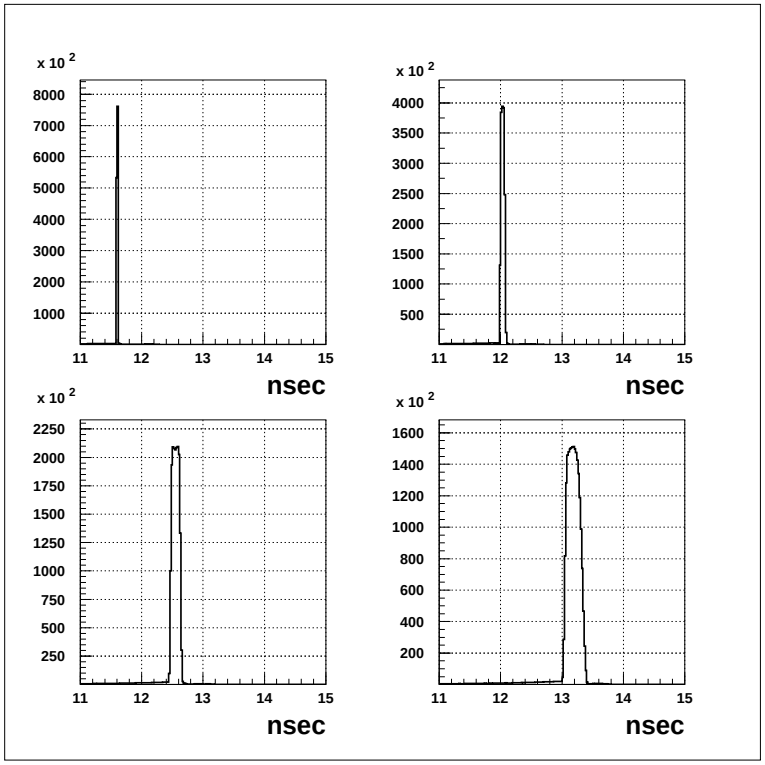

Figure 3.37: The detection time difference for different HTCC PMTs.

3.6 PMT Studies

3.6.1 PMT Magnetic Shielding Studies

The PMTs of the HTCC will be located in a region in which there will be a significant magnetic field, primarily from the solenoid magnet that surrounds the target and central detector system. The field varies considerably with distance from the solenoid, with a maximum value of as much as 50 G in the region of the PMTs closest to the solenoid. To give an idea of the magnitude of the problem, we note that for tests we have carried out, the PMT gain is reduced by a factor of two for a magnetic field of 0.4 G perpendicular to the PMT axis and 1.3 G parallel to the PMT axis. The standard PMT magnetic shield that can be obtained from the PMT manufacturer is totally inadequate to reduce the ambient field to even these levels, so that it is necessary to custom design a magnetic shielding system appropriate for the CLAS12 HTCC configuration. The design is being carried out with the aid of the TOSCA magnetic field program.

Figs. 3.38, 3.39, 3.40, and 3.41 present the residual magnetic field at the PMT axis for a

standard single-layer PMT magnetic shield for three values of the field: 50 G, 40 G, and 30 G, with the direction of the magnetic field perpendicular and parallel to the PMT axis (linear and logarithmic y-scales are shown). In the first case, the residual magnetic field inside the PMT volume is around 8 G, 2 G, and 1 G for a magnetic field of 50 G, 40 G, and 30 G, respectively. For the second case (the field is along the PMT axis), the field residual is significantly higher. The residual magnetic field inside the PMT volume is around 30 G, 10 G, and 1-2 G for magnetic fields of 50 G, 40 G, and 30 G, respectively. We may conclude from this calculation that:

- We need additional magnetic shielding to suppress the residual magnetic field to the level of 0.5 G;
- The residual field is significantly (several times) higher when the magnetic field is directed along the PMT axis;
- The shielding needs to extend beyond the PMT window for at least one PMT diameter.

We modeled three-layer magnetic shielding configurations using the TOSCA program. Fig. 3.42 shows the residual field for 3 different configurations with cylindrical PMT magnetic shielding with the magnetic field directed along the PMT axis. The magnetic shielding has 1-mm thickness for every layer. For these studies, the following conditions apply:

- Single layer tube made of co-netic μ-metal (shown in black),
- Two layers made of netic and co-netic μ-metals (shown in red),
- Three layers made of netic, co-netic, and co-netic μ-metals (shown in blue).

The residual magnetic field with the three-layer shielding is below 1 G in the region ± 5 cm, which is inside the specifications for the magnetic field parallel to the PMT axis. The perpendicular field will be several times lower, based on our calculations with the standard PMT magnetic shielding.

3.6.2 Magnetic Shielding Test Stand

A test stand (Fig. 3.43) was used to study the magnetic shielding properties. The magnetic shielding was placed inside a black box that is located between two circular magnetic coils that

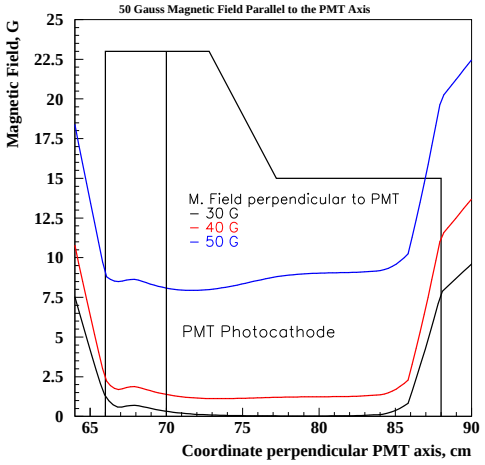

Figure 3.38: Standard single-layer PMT magnetic shielding (shown in black). The magnetic field is perpendicular to the PMT axis. The result with applied external fields of 50 G is shown in blue, 40 G in red, and 30 G in black. The PMT photocathode position is shown by the black vertical line.

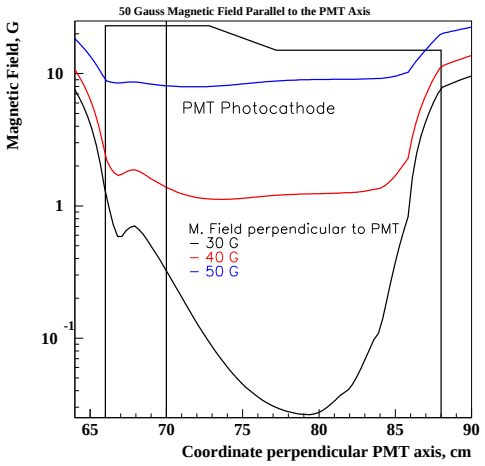

Figure 3.39: Same as in Fig. 3.38 but with a logarithmic y-axis. The PMT photocathode position is shown by the black vertical line.

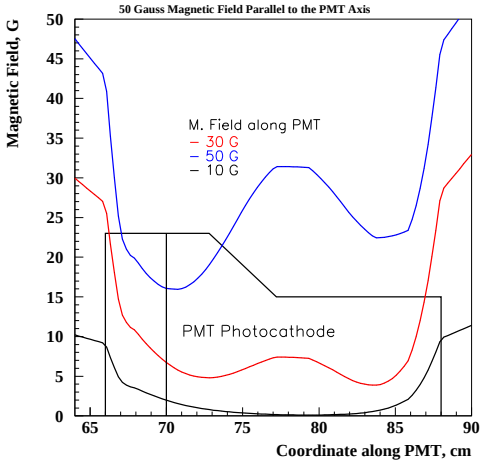

Figure 3.40: Standard single-layer PMT magnetic shielding (shown in black). The applied magnetic field is along the PMT axis: 50 G is shown in blue, 40 G in red, and 30 G in black. The PMT photocathode position is shown by the black the vertical line.

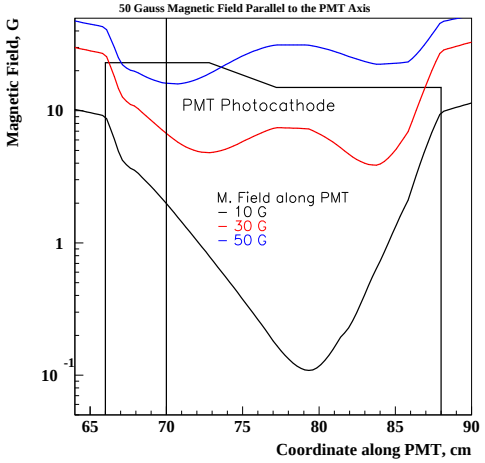

Figure 3.41: Same as Fig. 3.40 but with a logarithmic y-axis.

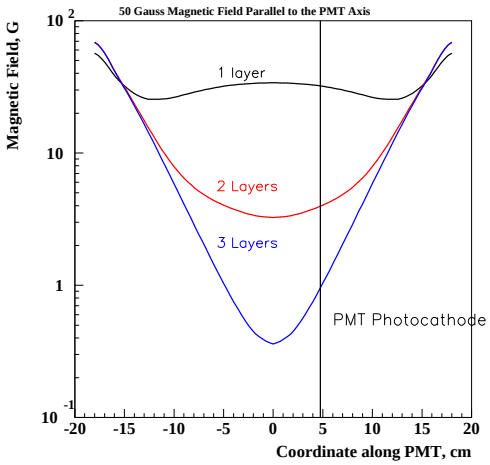

Figure 3.42: The effect of cylindrical PMT magnetic shielding, in which the applied magnetic field is 20 G along the PMT axis. Single-layer shielding is shown in black, two-layer shielding is shown in red, and three-layer shielding is shown in blue. The PMT photocathode position is shown by the black vertical line.

produce an external magnetic field. A high-current power supply allows us to vary the current up to 107 A, which corresponds to a magnetic field value of 68 G. The calibration line showing the relation between current and the magnetic field is shown in Fig. 3.44. We have measured the magnetic field along the PMT axis inside the shielding by using the Gauss/Teslameter (Model 5070) measuring device. The results of the measurements for the single shielding layers are shown in Fig. 3.45. Note that the first shielding layer is a prototype shield that was ordered for testing from the manufacturer. It is a cylindrical magnetic shield, 50% alloy of NiFe with a 6.19-in outer diameter, 6.06-in inner diameter, and 18.7-in long. The second shield layer is a standard PMT magnetic shield. Fig. 3.46 shows a drawing of the PMT and Winston Cone inserted inside the prototype shield. Results of the measurements for the double-layer shielding are shown in Fig. 3.47. According to Fig. 3.47, we expect a 0.3 G magnetic field on the PMTs with the two-layer shield in a nominal 30 G external magnetic field. Studies of the PMT performance affected by different magnetic field conditions are underway.

Figure 3.43: Photograph of the magnetic shielding test stand. The black box that contains the test shielding is located between the magnetic coils.

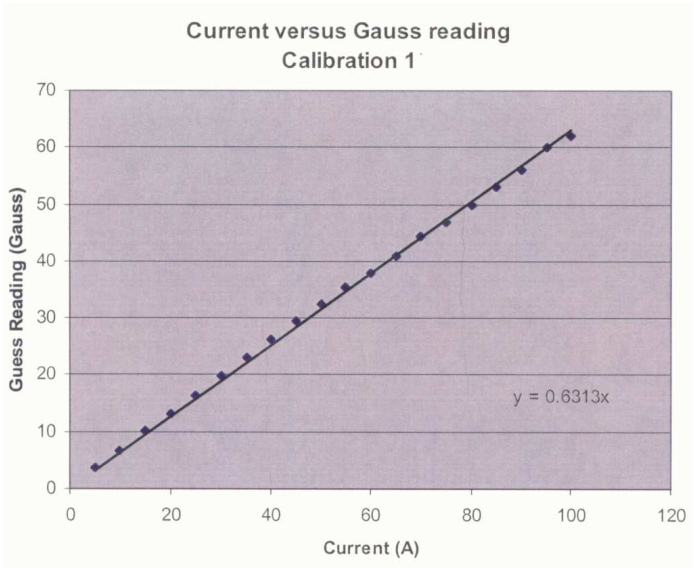

Figure 3.44: The current to magnetic field value calibration curve.

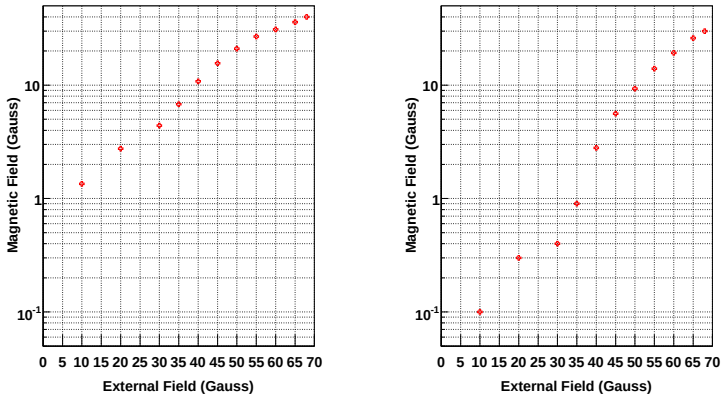

Figure 3.45: Results of the measurements of the magnetic field along the PMT axis inside the single-layer shield. Left panel: The cylindrical shielding. Right panel: The conventional PMT shielding.

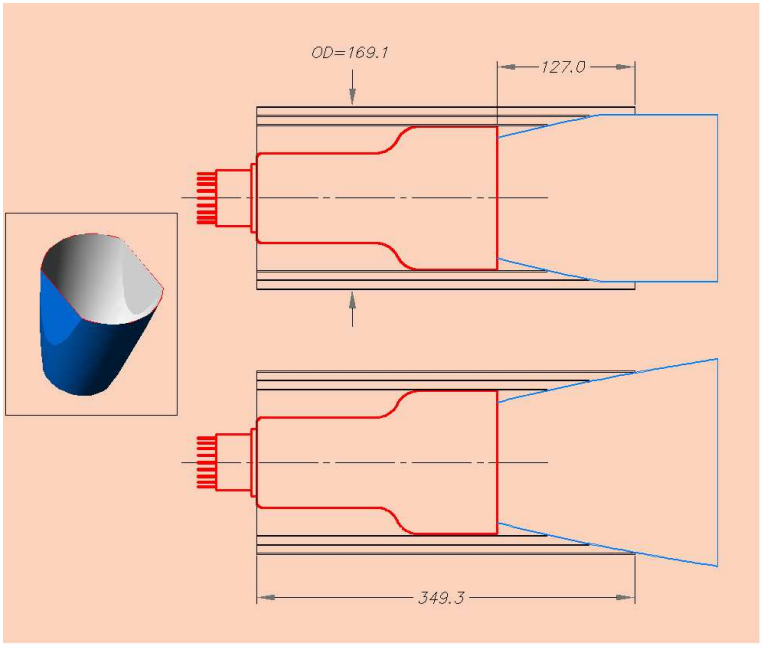

Figure 3.46: Assembly of a photomultiplier tube with a Winston Cone magnetic shield.

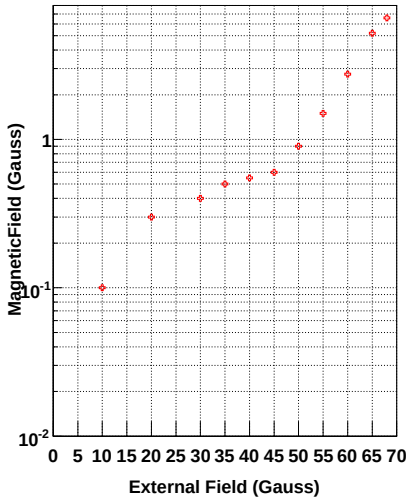

Figure 3.47: Results of the measurements of the magnetic field along the PMT axis inside the double-layer shield combined from the two single layers shown in Fig. 3.45.

3.6.3 PMT Laboratory Studies

Introduction

Particles that pass through a medium with a higher velocity than the phase velocity of light in that medium electromagnetically radiate photons. This is called Čerenkov radiation. The Čerenkov photons are produced at an angle relative to the particle direction given by:

$$\cos\theta = \frac{1}{n\beta}, \tag{3.5}$$

where n is the index of refraction and $\beta = v/c$ is the particle velocity.

Čerenkov detectors are usually used for particle identification. Threshold Čerenkov detectors make a yes/no decision based on whether the particle is above or below the threshold velocity $\beta_t = 1/n$. The more powerful use of Čerenkov radiation comes from measuring the ring-correlated angles of emission of the Čerenkov photons in a Ring Imaging Čerenkov Counter (RICH).

The High Threshold Čerenkov Counter for `CLAS12` contains three main elements:

- a radiator through which the charged particle passes;
- a mirror;
- a photodetector.

As Čerenkov radiation is a weak source of photons, light collection and photodetector efficiency must be as high as possible.

The number of photoelectrons ($N_{p.e.}$) per unit path length of a particle with charge ze is:

$$\frac{dN_{p.e.}}{dx} = 2\pi\alpha z^2 \int \frac{\epsilon(\lambda)}{\lambda^2}\left(1 - \frac{1}{\beta^2 n^2(\lambda)}\right) d\lambda, \tag{3.6}$$

where x is the path length, $\epsilon(\lambda)$ is the efficiency for collecting the Čerenkov light and transducing it into photoelectrons, and $n(\lambda)$ is the index of refraction of the radiator, which is a function of photon energy or photon wavelength λ. The typical energy-dependent variation of the index of refraction is modest, so we can write

$$\frac{dN_{p.e.}}{dx} = 2\pi\alpha z^2 \left(1 - \frac{1}{\beta^2 n^2}\right) \int \frac{\epsilon(\lambda)}{\lambda^2} d\lambda. \tag{3.7}$$

The Čerenkov detector quality factor (figure of merit) N_0 is defined as:

$$N_0 = 2\pi\alpha z^2 \int \frac{\epsilon(\lambda)}{\lambda^2} d\lambda, \tag{3.8}$$

So that

$$N_{p.e.} \approx L N_0 < sin^2\theta >, \tag{3.9}$$

where L is the radiator length.

Careful designs of the Čerenkov counter give values of N_0 for a PMT detection system working in the visible and near UV, that collect most of the Čerenkov light of about 100 cm^{-1}.

The overall efficiency and rejection factors of the Čerenkov counters are controlled by Poisson fluctuations, which can be especially critical for the separation of species where one particle type is dominant. The effective number of photoelectrons is often less than the average number calculated above due to additional noise from the photodetector. So, it is extremely important to design the detector with as high an average number of photoelectrons as possible.

The number of detected photoelectrons ($N_{p.e.}$), which is directly connected with the efficiency for collecting the Čerenkov light and transducing it in photoelectrons $\epsilon(\lambda)$, contains several components:

$$\epsilon(\lambda) = \epsilon_{gas}(\lambda) \times \epsilon_{mirror}(\lambda) \times \epsilon_{PMT}(\lambda), \tag{3.10}$$

where $\epsilon_{gas}(\lambda)$ is the gas transparecy, $\epsilon_{mirror}(\lambda)$ is the mirror reflectivity, and $\epsilon_{PMT}(\lambda)$ is the PMT quantum efficiency.

One of the ways to increase the figure of merit N_0 is to use a PMT with a quartz input window. The intensity of the photons produced in Čerenkov radiation varies as $dN/d\lambda \sim 1/\lambda^2$. Therefore, it is critical to use PMTs that are efficient at low wavelengths where most of the light is produced. The wavelength cutoff for a quartz PMT is in the region from 160–180 nm, in comparison with the 220–240 nm range for the UV glass PMT. However, the quartz PMTs are more expensive.

Čerenkov Light Detection

The High Threshold Čerenkov Counter (HTCC) for `CLAS12` will contain a total of 48 mirrors and 48 PMTs. The shape of the mirrors and distribution of the PMTs for one sector of

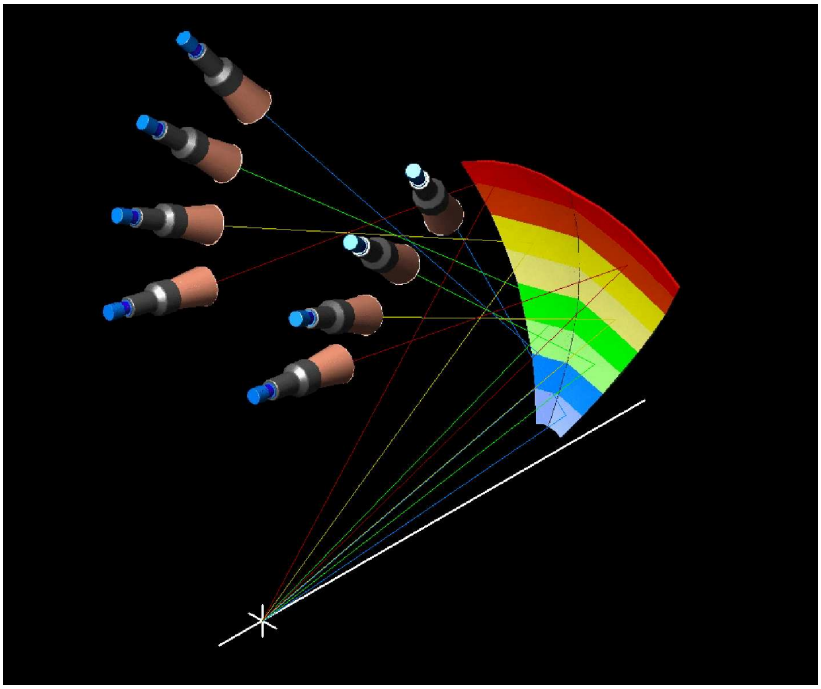

Figure 3.48: The current optical design for one sector of the HTCC. Eight PMTs will collect the Čerenkov light reflected off of four mirrors.

the detector is illustrated in Fig. 3.48. Two different types of PMTs were considered for the Čerenkov Counters: the Photonis XP4508 quartz-faced PMT and the XP4500 UV glass-faced PMT. Both models have uniform electron collection over their bialkali photocathodes and measure 5 in in diameter. However, as seen in Fig. 3.49, the quartz PMTs are expected to have better quantum efficiency at low wavelengths than the UV glass PMTs. With increased efficiency, the quartz PMT should be able to detect more photons at higher energies than standard UV glass PMTs.

To study the performance of PMTs, a cosmic ray stand was used, which is described in Section 3.6.3. In addition to studies of light collection by two different PMT types, we also measured the impact on light collection from different gas environments. We used air and nitrogen. Note that the HTCC will use CO_2 gas, but we will neglect the difference between CO_2 and nitrogen gas in our tests. Nitrogen gas absorbs less light than air at low wavelengths. The absorption factor of a gas, detailed in Fig. 3.49, is the fraction of light that the gas will allow to pass through it. PMTs in a nitrogen gas environment should be able to detect more Čerenkov light than those in air due to this improved transparency at low wavelengths.

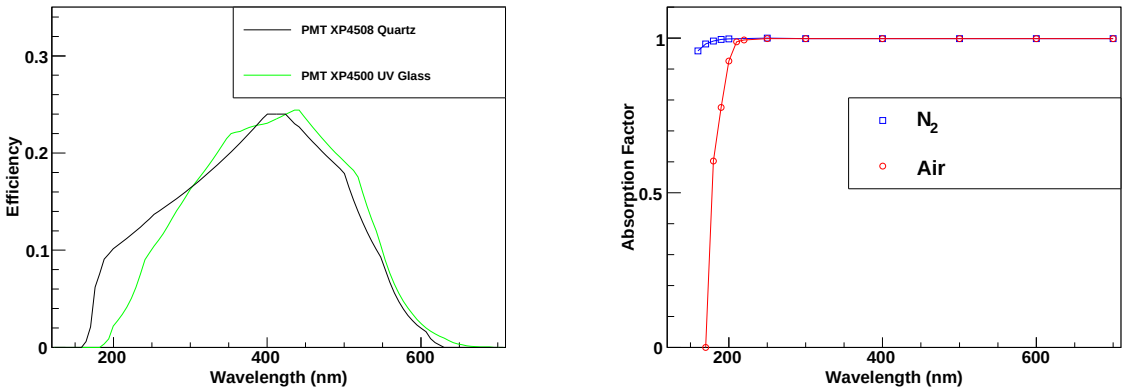

Figure 3.49: Left: The quantum efficiency as a function of wavelength of the two Photonis PMT models being tested. Right: The absorption factors of nitrogen gas and air as a function of wavelength.

Multiplying the gas absorption factor by the PMT quantum efficiency and the $1/\lambda^2$ Čerenkov light production dependence gives, to a constant factor, the amount of Čerenkov light collected as a function of wavelength. The predicted amounts of light collected for different gas and PMT-face configurations are plotted in Fig. 3.50. Taking the ratio of their integrals for quartz and UV-glass in air gives:

$$\frac{\text{Light}_{Quartz,\ Air}}{\text{Light}_{UV-Glass,\ Air}} = \frac{\int_0^\infty QE_{Quartz}(\lambda) * AF_{Air}(\lambda)/\lambda^2 d\lambda}{\int_0^\infty QE_{UV-Glass}(\lambda) * AF_{Air}(\lambda)/\lambda^2 \lambda} = 1.2, \tag{3.11}$$

yielding a predicted 20% improvement in light collection. Similarly, in a nitrogen gas environment, this improvement increases to 25%. However, comparing the air and nitrogen gas environments for the quartz-faced PMTs only results in a 4.5% predicted increase in light collection. The UV glass-faced PMT is predicted to achieve no appreciable improvement in light collection in a nitrogen gas. This is because the quantum efficiency of the XP4500 rapidly approaches zero for light with $\lambda < 200$ nm, the region where nitrogen gas has the most improvement over air. These predictions are only preliminary, rough estimates as the quantum efficiency measurements of the PMTs supplied by the manufacturer are only characteristic approximations.

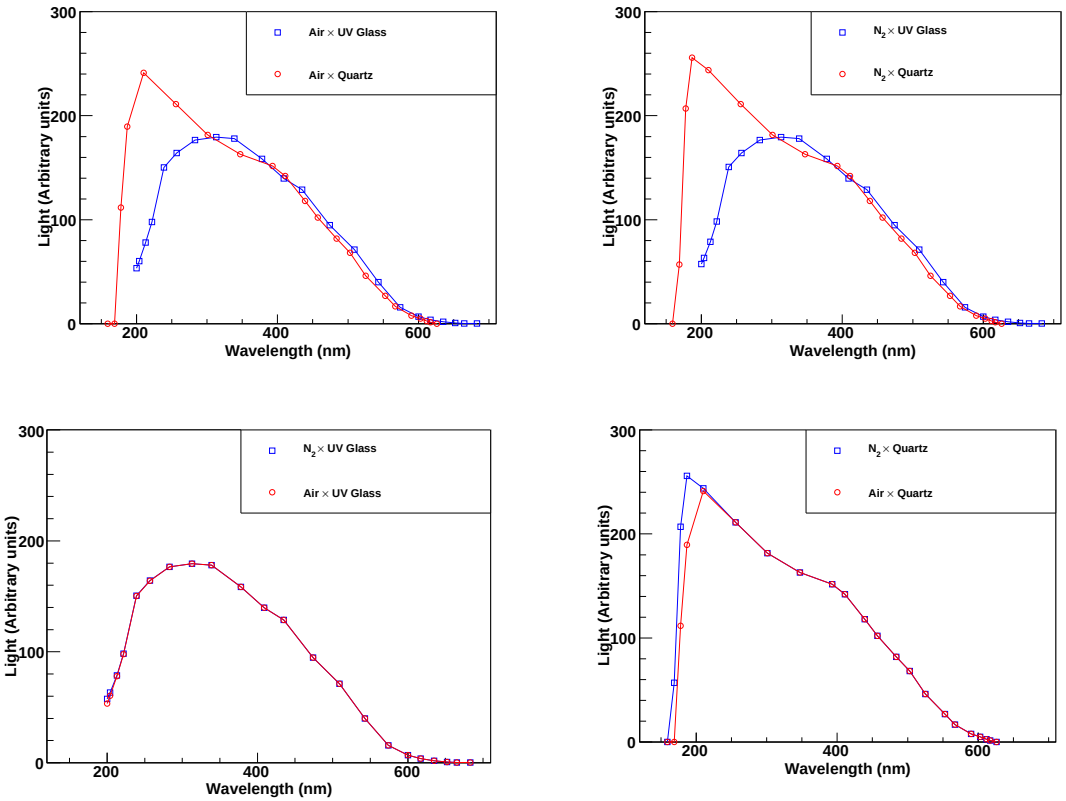

Figure 3.50: To a constant factor, the predicted amount of light collected as a function of wavelength for different PMT face and gas configurations, plotted against each other for comparison.

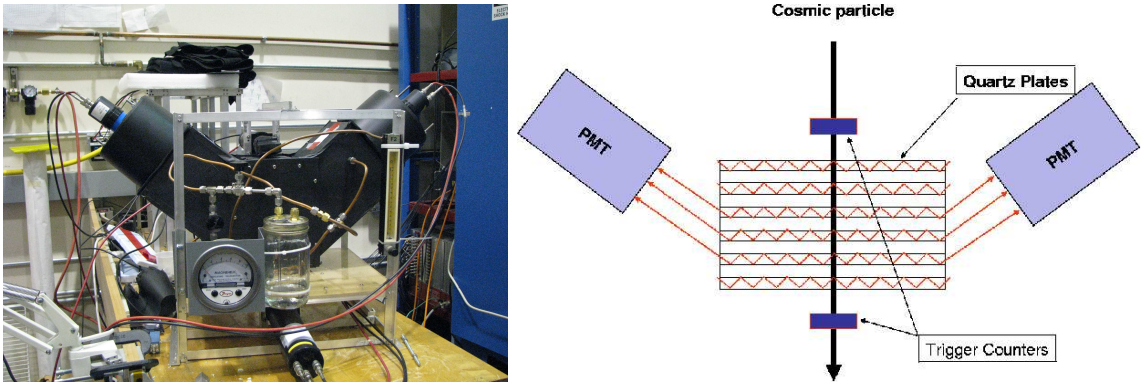

Figure 3.51: A photograph (left) and schematic (right) of the cosmic ray stand used for testing the Čerenkov light collection of different PMTs. Trigger counters above and below the chamber detect a signal when a cosmic ray has passed through the quartz plates, and the two PMTs collect the resulting Čerenkov radiation. A flow meter and pressure gauge are used to supply and regulate nitrogen gas to the chamber.

Cosmic Ray Stand

The predicted increase of detected photoelectrons in quartz-faced PMTs is significant, so a test stand (see Fig. 3.51) was constructed to determine whether this performance increase is reproducible. A stack of 32 quartz plates was used as a medium for Čerenkov light generation as cosmic muons passed through them. As diagrammed in Fig. 3.51, the Čerenkov light was produced at a 46.7° angle from the incoming cosmic rays and was internally reflected until passing out of the end of the quartz plate. In a light-tight and air-tight box, the Čerenkov radiation emitted by these cosmic rays was collected by two PMTs located an average of 11 cm away from the quartz plates. While one of the PMTs was being tested, a second PMT was used as a reference to confirm the consistency of the experiment from test to test. Three Photonis XP4508 quartz-faced PMTs and three Photonis XP4500 UV glass-faced PMTs were tested in air, and one of each type in nitrogen gas, which is close in optical properties to CO_2, which will be used in the HTCC. A flow meter and pressure gauge were used to regulate the supply of nitrogen gas to the chamber during the final tests.

To collect data, small scintillators attached to PMTs above and below the test chamber were used to trigger event recording. A coincidence between both PMTs indicated that a cosmic ray had passed through the quartz plates, producing Čerenkov light. The trigger and

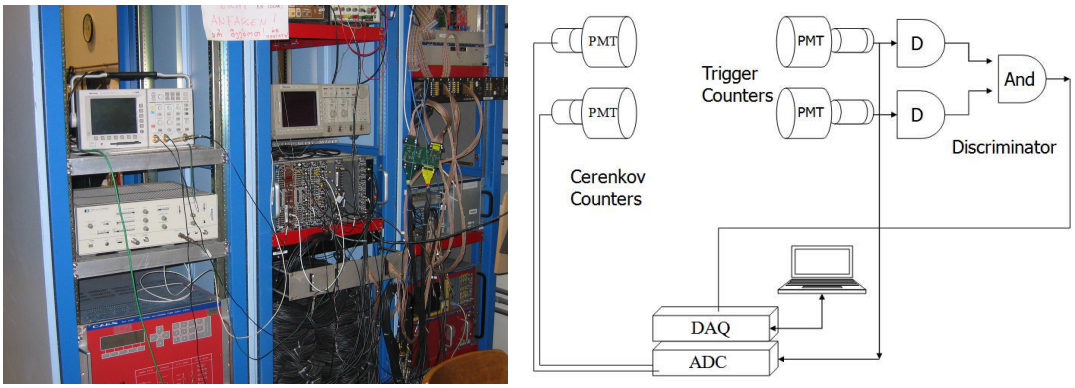

Figure 3.52: Left: Data acquisition hardware. Right: Diagram of the triggering and DAQ process.

data acquisition systems are pictured and diagrammed in Fig. 3.52. The pulse height of the electrical signals from the PMT dynodes were converted to digital ADCs for analysis. The ADC spectra of the two trigger counters and the two Čerenkov counters for one test run are shown in Fig. 3.53. Cuts were placed around the peaks of the ADC spectra of the trigger PMTs to remove background events. Also, the high voltage supplied to the PMTs was fixed throughout the experiment to make sure that the response of each of the PMTs was consistent.

Calibration of the ADC Scale

The ADC spectra of the test PMTs must be converted into units of collected number of photoelectrons ($N_{p.e.}$) to judge PMT performance. This conversion is linear because the multi-stage signal amplification process of the PMTs is independent of the number of photons detected. The ADC conversion factor for each PMT was found by using an LED to fix the source intensity. The LED and test PMTs were placed in a light-tight box for testing. Multiple tests were performed for each PMT, each with a different intensity of LED source photons.

The energy response of a PMT to a fixed intensity source of photons is described by a Poisson-like distribution,

$$N(ADC) = \frac{N_0 \mu^{\frac{ADC}{\mu_1}} e^{-\mu}}{\mu_1 \Gamma(\frac{ADC}{\mu_1} + 1)}, \ \Gamma(x) = \int_0^\infty t^{x-1} e^{-t} dt, \tag{3.12}$$

where μ is the average number of photoelectrons, μ_1 is the ADC to $N_{p.e.}$ conversion factor, and N_0 is the scaling factor. The Poisson distribution fits to the ADC spectra of different light

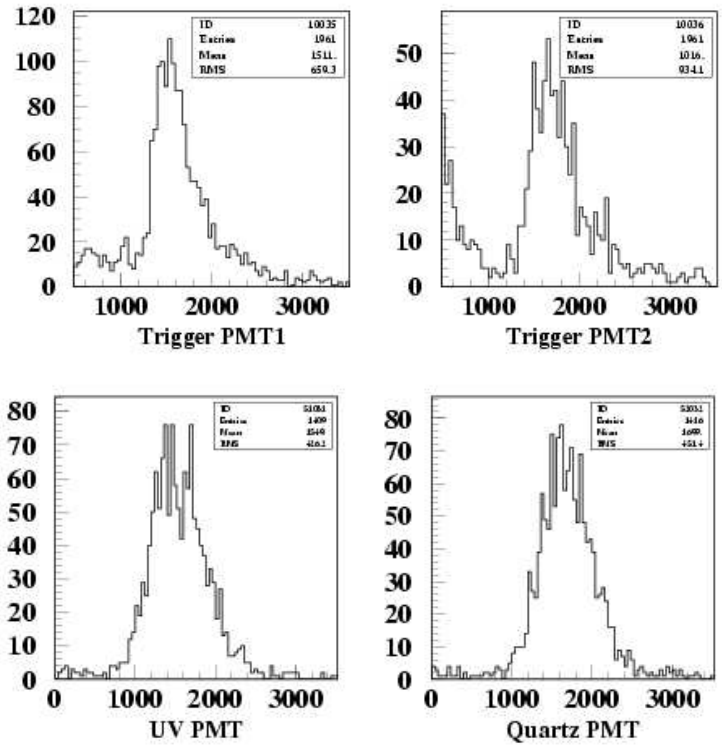

Figure 3.53: ADC spectra of the two trigger counters (top) and two Čerenkov counters (bottom) for one test run.

intensities for the three UV-glass-faced PMTs and the three quartz-faced PMTs are shown in Figs. 3.54 and 3.55, respectively. To find the average conversion factor, the average ADC vs. the average $N_{p.e.}$ were plotted in Figs. 3.56 and 3.57 and fit to a linear function. The slope of these fits gives the ADC to $N_{p.e.}$ conversion factor for each test PMT.

To check that these conversion factors were correct, each PMT was tested with the LED emitting only a single photon. As seen in Fig. 3.58, the conversion factors were applied to the ADC spectra and the mean number of photoelectrons for each distribution was approximately one, indicating that the conversion factors are correct.

Čerenkov Light Test Results

Using the ADC to $N_{p.e.}$ conversion factors, the three Photonis XP4508 quartz- and three Photonis XP4500 UV glass-faced PMTs were tested with the cosmic ray stand filled with air. The results of the tests, with each measured for about a week, are shown in Fig. 3.59, which highlights the $N_{p.e.}$ spectra from collecting the Čerenkov radiation. Fig. 3.60 illustrates the average $N_{p.e.}$ for each PMT-face type, yielding an increase of $45 \pm 4\%$ in the number of detected Čerenkov photoelectrons in quartz-faced PMTs over UV glass-faced PMTs. This result is larger than the predicted increase of 20% found in eq.(3.11). This difference is most likely due to an error in the rough quantum efficiency estimate that the manufacturer supplied. Fig. 3.61 shows a fit to the average number of photoelectrons collected by the quartz reference PMT throughout the two months of testing. In five tests, the maximum deviation from the average of 58 photoelectrons was 4.1%, which may be considered as an estimate of the systematic uncertainty of the experiment.

One quartz- and one UV glass-faced PMT were tested in the cosmic ray stand with the chamber filled with nitrogen gas. Fig. 3.62 illustrates the $N_{p.e.}$ spectra for these tests, yielding an average photoelectron detection increase of 82%. This is much larger than the predicted increase of 25% from Section 3.6.3. As mentioned previously, the rough quantum efficiency distributions supplied by Photonis are likely incorrect. Additionally, only one PMT of each type was tested; thus this difference may be inflated by the inconsistent response between PMTs of the same model. So, this estimate based on a single measurement is very crude. The amount of light collected by the quartz-faced PMT in a nitrogen gas environment was 7% more than in air, similar to the predicted increase of 4.5% from Section 3.6.3. The amount of light collected by the UV glass-faced PMT actually decreased by 2% in nitrogen gas, as

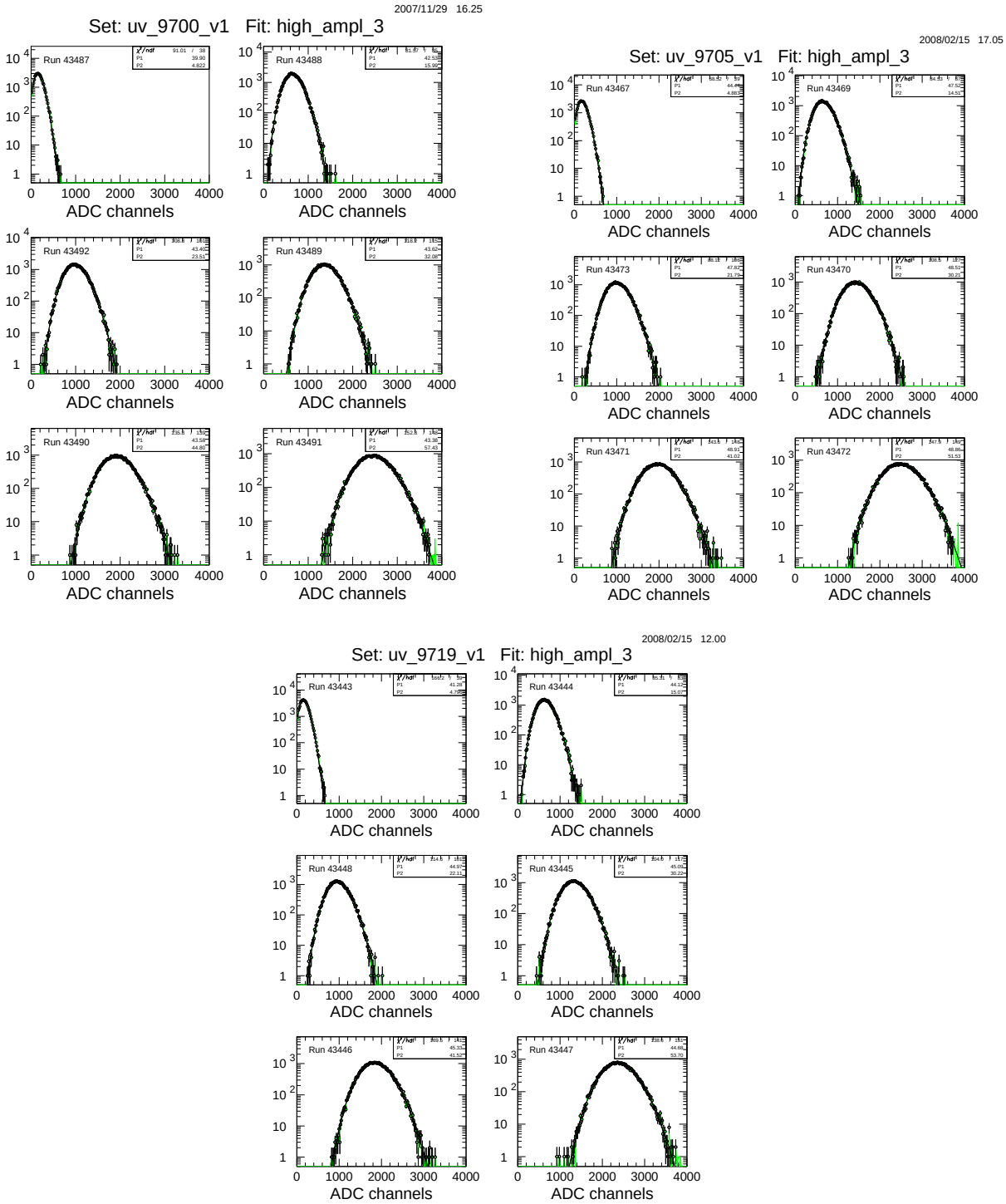

Figure 3.54: Poisson fits to ADC spectra of the three UV glass-faced PMTs. Here, $P1$ is the ADC to $N_{p.e.}$ conversion factor μ_1, and $P2$ is the average number of photoelectrons, μ.

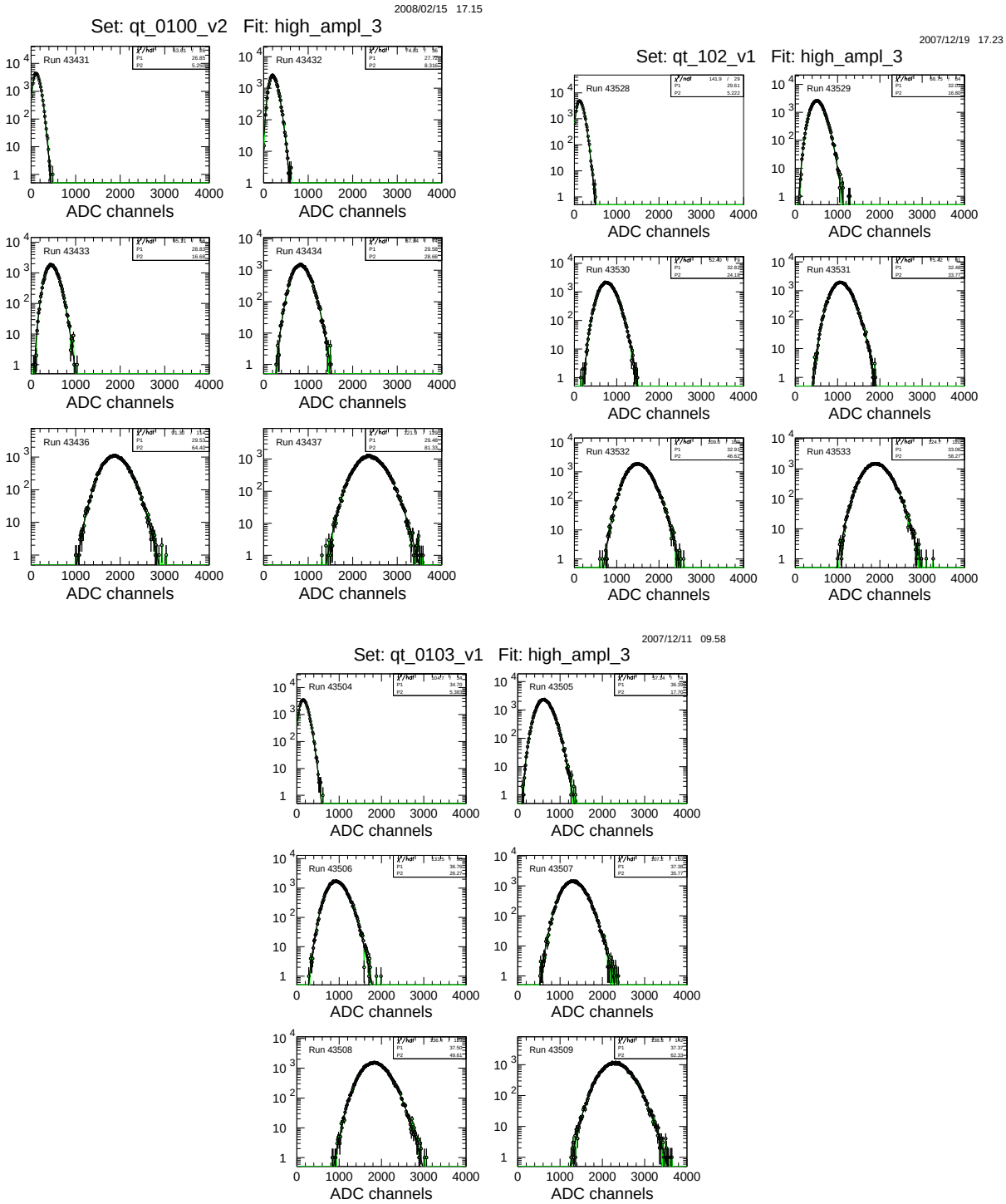

Figure 3.55: Poisson fits to ADC spectra of the three quartz-faced PMTs. Here, $P1$ is the ADC to $N_{p.e.}$ conversion factor μ_1, and $P2$ is the average number of photoelectrons, μ.

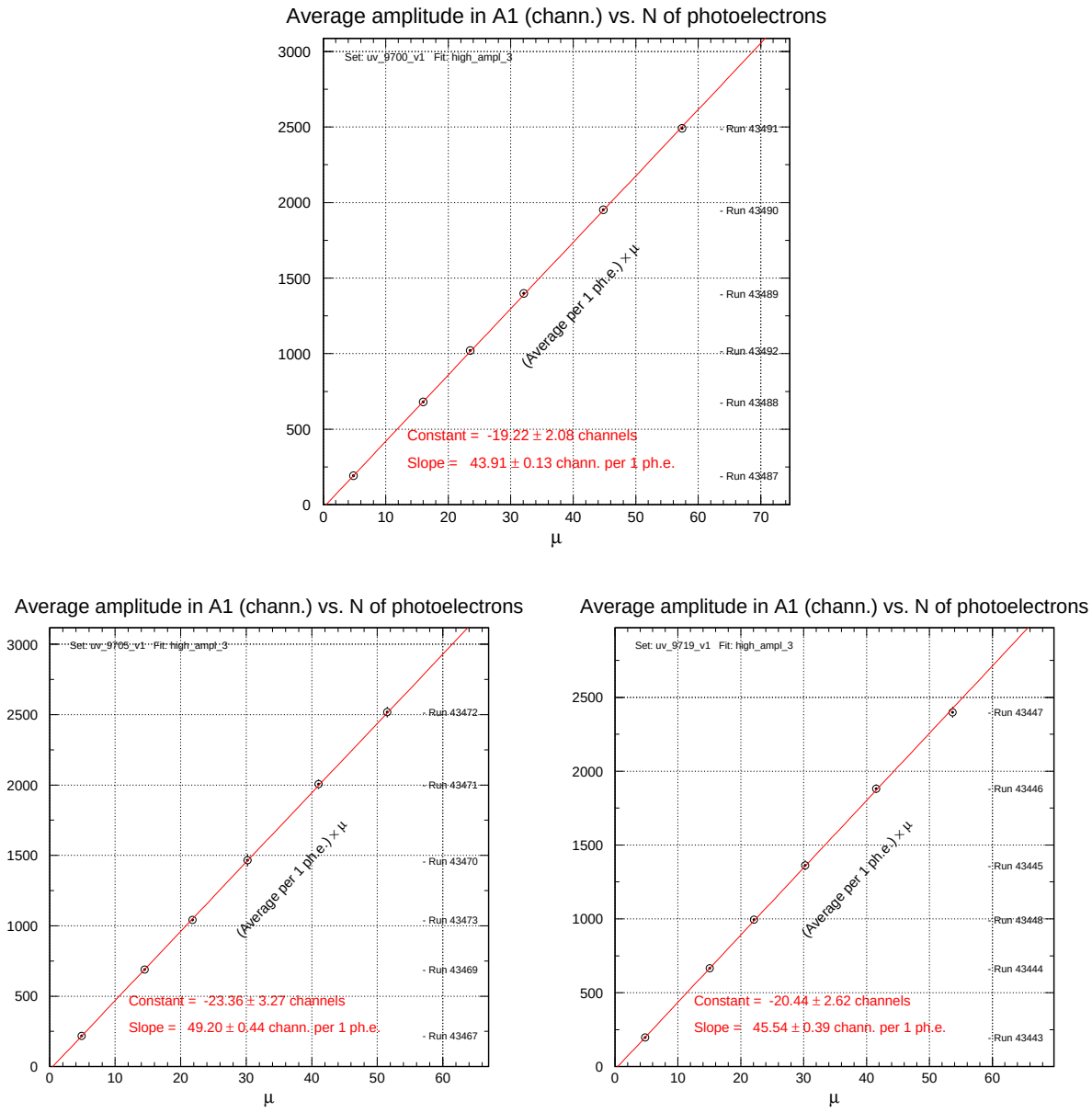

Figure 3.56: Linear fits to the average ADC value vs. the average $N_{p.e.}$ of the Poisson distributions of the three UV glass-faced PMTs. The slopes are the ADC to $N_{p.e.}$ conversion factors.

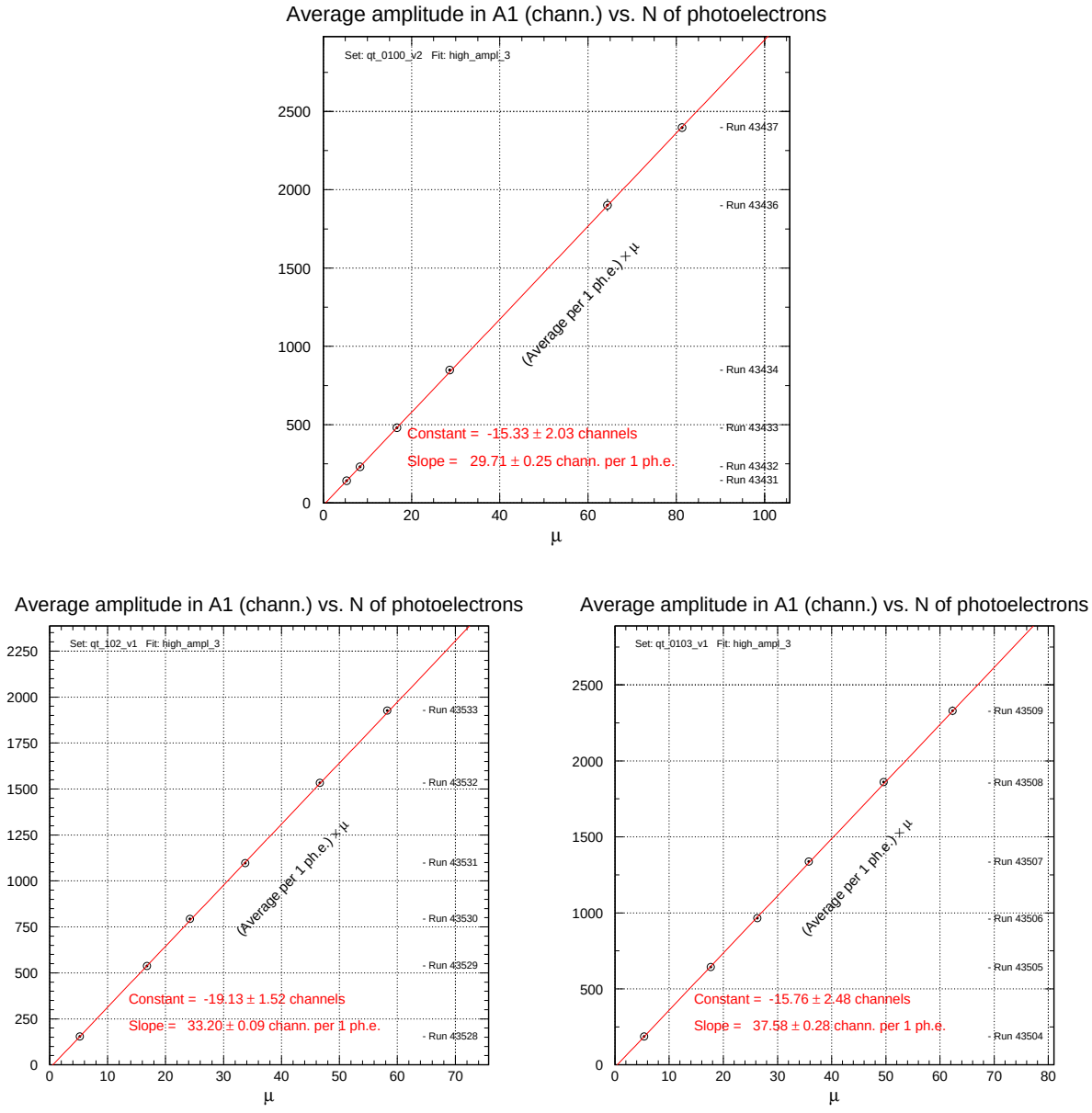

Figure 3.57: Linear fits to the average ADC value vs. the average $N_{p.e.}$ of the Poisson distributions of the three quartz-faced PMTs. The slopes are the ADC to $N_{p.e.}$ conversion factors.

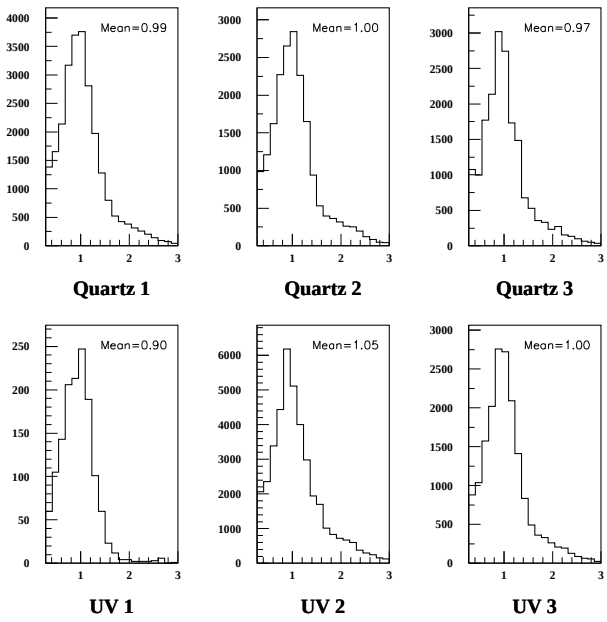

Figure 3.58: $N_{p.e.}$ spectra for a single-photon LED source for the six test PMTs. The means of each distribution are all near one, indicating that the ADC to $N_{p.e.}$ conversion factors are correct.

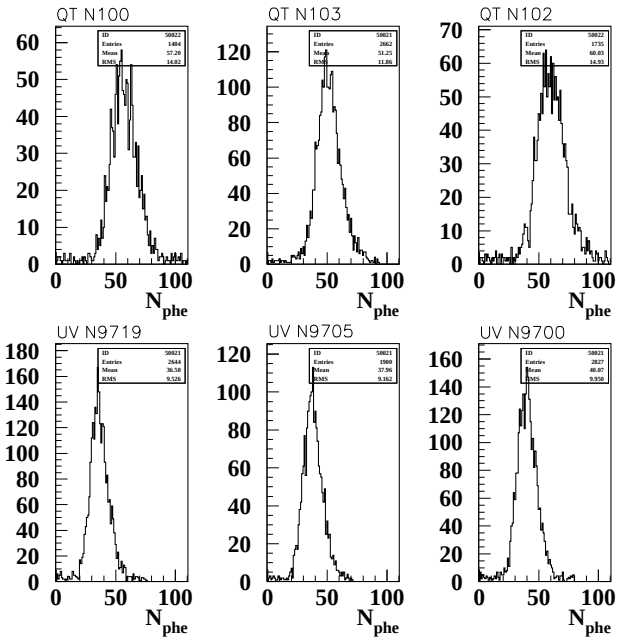

Figure 3.59: $N_{p.e.}$ spectra from collecting Čerenkov light in the cosmic ray stand for the three UV glass- and three quartz-faced PMTs.

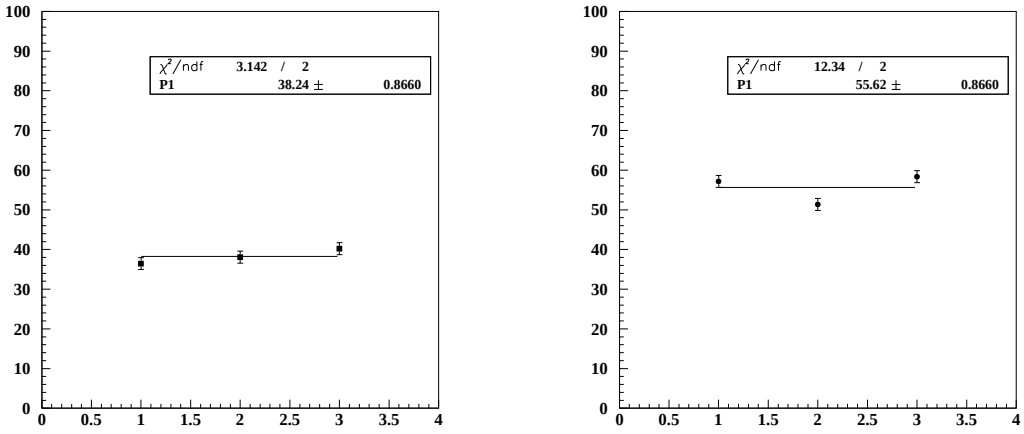

Figure 3.60: Fits to find the average $N_{p.e.}$ for UV glass- and quartz-faced PMTs.

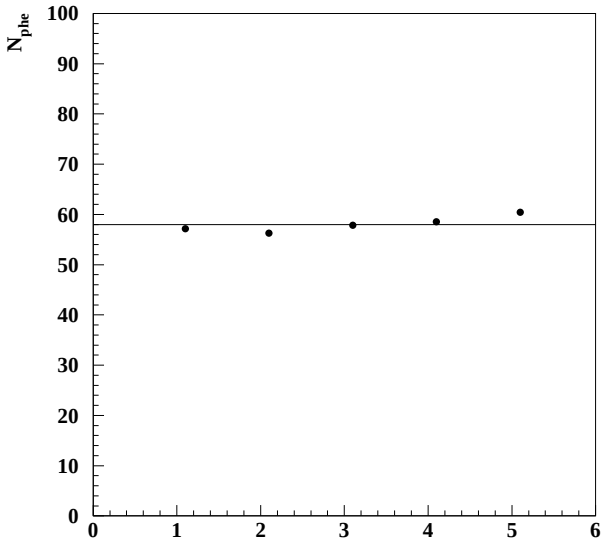

Figure 3.61: The number of photoelectrons collected by the reference PMT during testing. The maximum deviation of 4.1% is a reflection of the systematic uncertainty of the experiment.

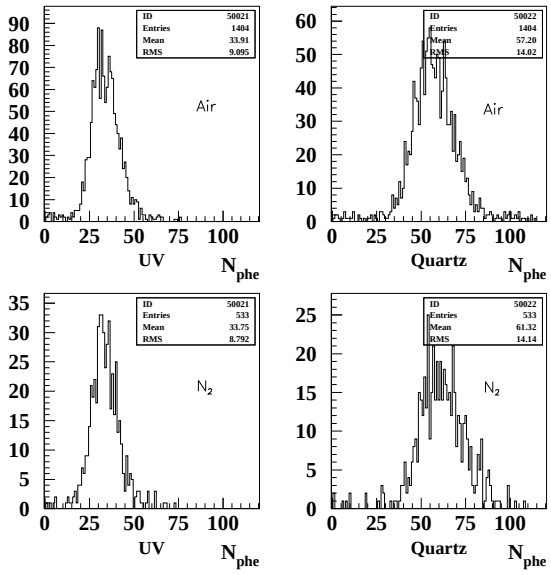

Figure 3.62: $N_{p.e.}$ spectra for UV-glass and quartz-faced PMTs in a nitrogen gas environment.

opposed to the negligible difference that was predicted (see Fig. 3.63).

In summary, using a cosmic ray test stand, the Photonis XP4508 quartz-faced PMTs were found to collect 45% more Čerenkov radiated photoelectrons in air than the Photonis XP4500 UV glass-faced PMTs. In a nitrogen gas environment, the Čerenkov light collection of the quartz-faced PMTs improved by an additional 7%, so the total gain is estimated to be 55% (1.45×1.07=1.55).

3.7 Mechanical Design

The basic shape of the HTCC is naturally generated by a combination of the dimensions and positions of the surrounding equipment, certain required acceptance angles, and the planned focal points of the mirror within. The body will serve primarily as a gas volume container, and should have as little material as possible within to obstruct either the Čerenkov light, or particles to other detectors. An overall view of the appearance of the HTCC is shown in Fig. 3.64.

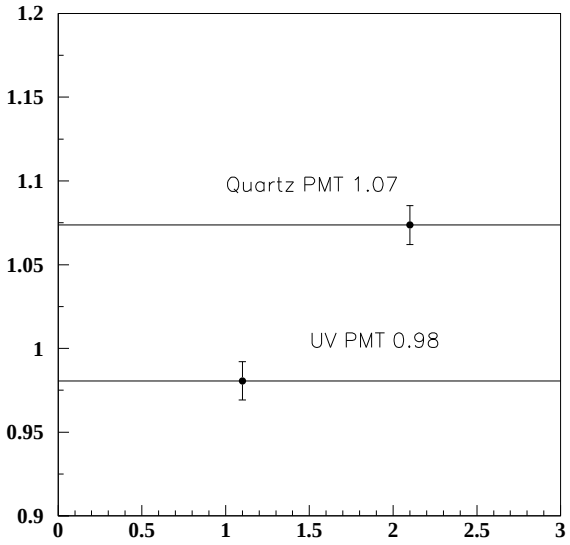

Figure 3.63: Ratio of light collection in nitrogen gas to the air environment for UV-glass and quartz'faced PMTs.

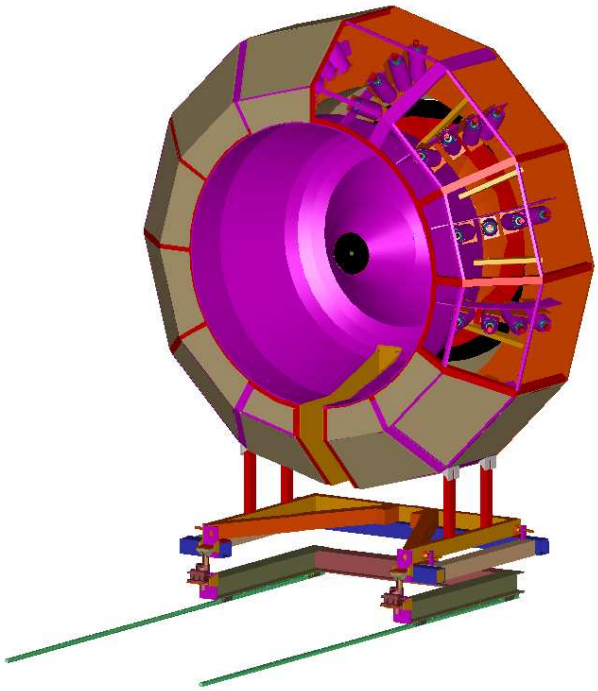

Figure 3.64: Overall appearance of the HTCC viewed from upstream side.

3.7.1 Main Structure

The geometry of the detector strongly dictates the shape of the HTCC's main structure. The mirror design is a twelve segment combined mirror, and the light is focused to twelve banks of 4 photomultiplier tubes per bank. For this mirror, a twelve-sided shell centered around the beamline was designed, with space on each segment to mount one row of four PMTs. The shell was designed to completely enclose all of the PMTs, mounting hardware, shielding, etc.. The strength of the structure comes from the entry cone, the downstream mirror housing, and the connecting ribs of rectangular tubing. The outer web of aluminum angles and tees will add to the strength of the unit, but is primarily to serve as a frame for panels used to seal the gas volume. The structure is still simple, and can be constructed of flat and rolled, machined and welded plates, tees, and/or angles of Aluminum (see Fig. 3.65).

3.7.2 PMT Mount

Our original goal was to have the PMTs mounted to the outer surface of the HTCC to make maintenance easier, but finding an effective way to seal the gas volume, while maintaining

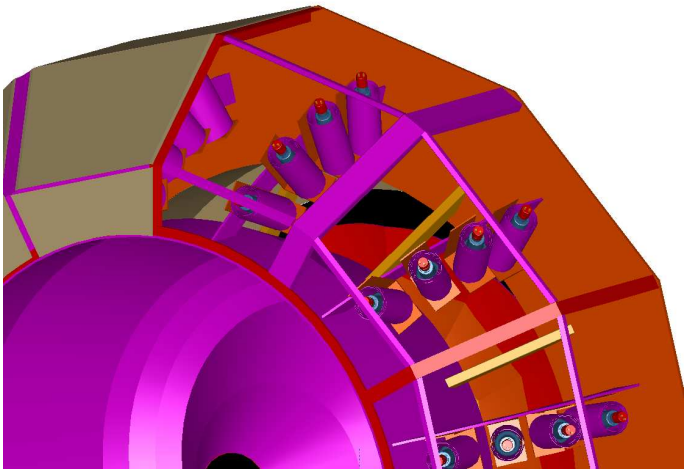

Figure 3.65: Mechanical housing of the HTCC.

some degree of adjustability at each PMT within the space available proved to be challenging. Instead, each PMT, Light Concentrator, and any shielding is mounted to one bracket, as shown in Fig. 3.66. The brackets are mounted to a plate (eight each) as shown in Fig. 3.67, and the gas volume of the HTCC is sealed via access panels located radially beyond the PMTs as shown in Fig. 3.68. This system is relatively easier and less expensive to manufacture, easy to assemble, and each PMT is independently adjustable.

3.7.3 Mirror Positioning and Alignment

Using six dual ball-socket adjustment linkages that contact the mirror in three places, the mirror can be securely supported and adjusted in all directions without inducing any torsional stress upon the mirror. With this system (see Fig. 3.69), the mirror would also be protected from possible stresses that the main shell may sustain, whether via temperature changes, transport, maintenance, or other unforeseen events.

3.7.4 Upstream and Entry

The upstream end of the HTCC must wrap closely around the CTOF and solenoid magnet, to both avoid interfering with the light paths, and to allow for the greatest possible acceptance angle from the target. This results in a cup shape that reaches from the outside of the solenoid magnet, around the downstream CTOF light guides, with a cone in the center that follows the light guides back in toward the center of the solenoid, stopping just before the SVT. This entry

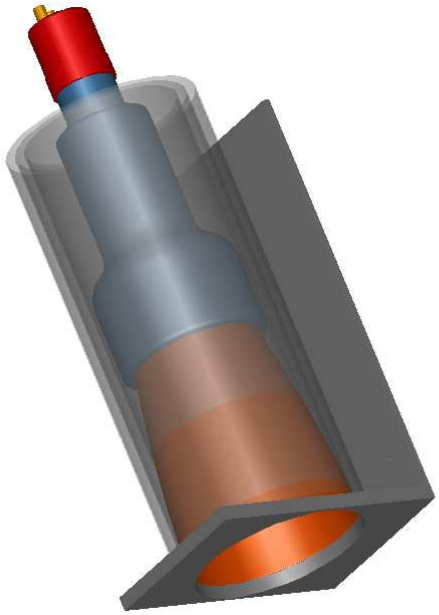

Figure 3.66: Photomultiplier tube with Winston Light Concentrator, magnetic shield layers, and mounting block.

cone must be as thin as possible to retain every available degree of entry angle. Currently, the optimized entry acceptance angle of 36° is limited by the solenoid shape and the position of the CTOF light guides. This angle is only achievable using equipment clearances as low as 0.20 in, and an entry cone thickness of 0.040 in. At this thickness, the cone could be made of aluminum or a carbon composite; it is not a structural member, and only needs to be strong enough to support itself and the entry window. A view of the entry structure is shown in Fig. 3.70.

3.7.5 Exit Scheme

From the portion of the shell where the photomultiplier tubes are mounted, a cylindrical tube reaches downstream to house and support the mirror and adjustment fixtures, and finally interfaces with the exit window. The exit window of the HTCC is located approximately 0.5 in past the mirror of the HTCC. It must allow up to 41° particles to pass through the gas volume unobstructed. Because of the shape of the next detector in the beamline (Region 1 drift chamber), the outer edge of the HTCC exit window must be beveled to avoid interference with Region 1, see Fig. 3.71.

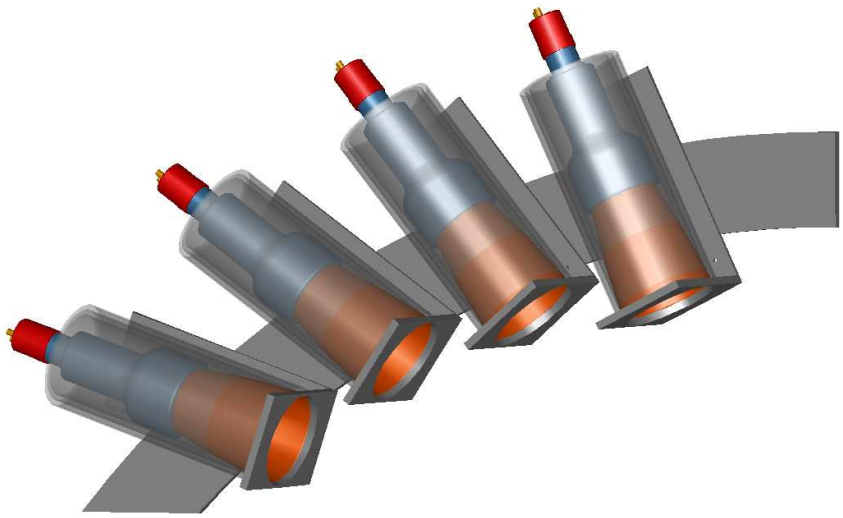

Figure 3.67: Four photomultiplier tubes with Winston Light Concentrators and magnetic shield layers mounted to a plate.

3.8 HTCC System Quality Assurance Procedures

This section provides a list of quality assurance (QA) steps for the construction of the HTCC counter for CLAS12. The information given here is based on experience from construction of the Čerenkov counter for the existing CLAS detector and on the HTCC R&D results.

3.8.1 QA Procedures for the Combined Mirror Construction

Quality assurance procedures for the HTCC combined mirror construction include several items:

- *Mirror Substrates*: All constructed mirror substrates (96 segments) will be checked to ensure all dimensions and tolerances meet the design requirements. The substrates will then be sent to the vendor for the reflector and protection coating deposition;
- *Reflectivity*: All coated mirror segments will be tested in several randomly chosen points to provide input control to ensure the reflectivity is as specified in the design requirements;
- *Assembly*: The assembly of the sections of the mirror sector will be done separately using positioning tables and a class-2 laser for orientation checks;

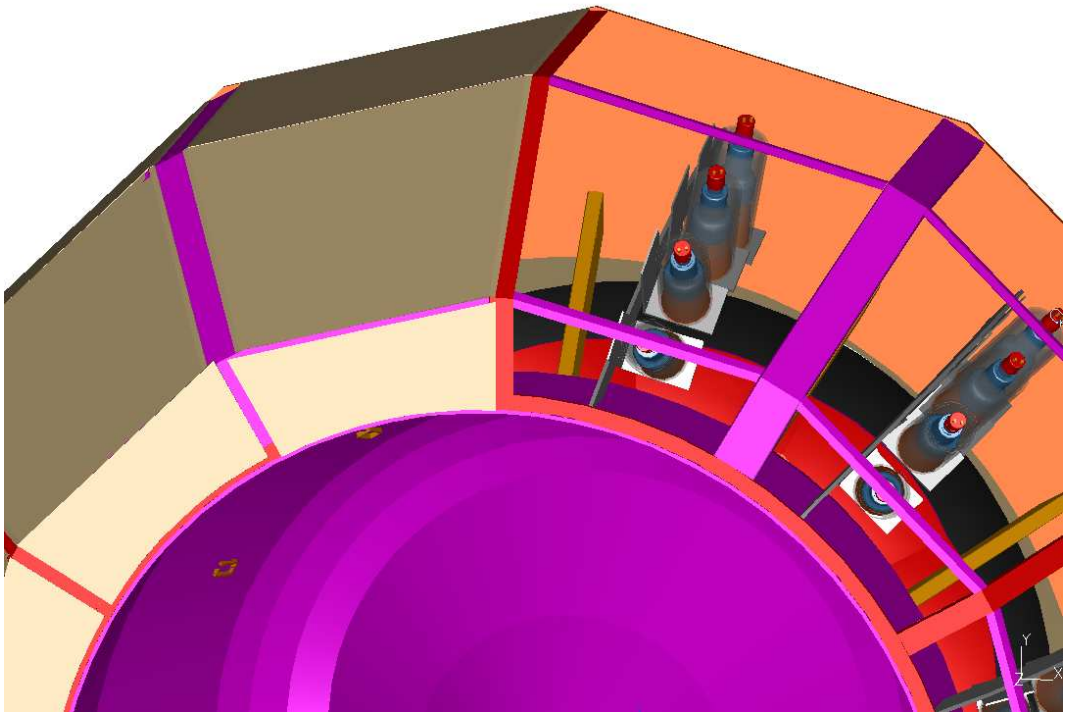

Figure 3.68: Access panels covering identical banks of 4 PMTs.

- *Preparation for Assembly*: The overall dimensions of the portions will be checked one more time before final assembly;

- *Final Assembly*: Assembly will be performed using a foam assembly table that will consist of 12 separate identical portions of smaller size, aligned and attached to the flat metal base plate. A metal ring with inner diameter equal to the outer diameter of the combined mirror will be used as a part of the final assembled product. The alignment (position and orientation) for each of the left and right mirror portions will be controlled with a laser.

3.8.2 PMT Quality Control

- *PMT Handling*: The PMTs are susceptible to damage from shock, and care must be taken when handling them both before and after they are mounted. In addition, care must be taken to avoid any scratches on the PMT face during handling and installation;

- *PMT HV Testing*: HV checks of the detectors will be performed and the dark current will be measured for each PMT. Any measured dark current more than 100 nA is an

Figure 3.69: HTCC mirror supported in three places using adjustment linkages.

indication of a bad PMT;

- *PMT Testing*: The PMT output signals will be checked using light emitting diodes (LEDs). During these measurements, the HV will be adjusted to make sure that the one-photoelectron signals have the same pulse height. The output signal will be checked by studying the ADC spectrum. All ADC spectra will be written to a database for future reference.

3.8.3 QA for Magnetic Shielding

The PMT magnetic shielding consists of several layers of magnetic material. It is very important to check that the magnetic properties of the PMT shielding correspond to specifications. The assembled magnetic shielding should be tested at the magnetic test stand. The PMT signal from an LED should be within specifications at a magnetic field of 50 G.

3.9 HTCC System Safety Issues

There is potential shock hazard if the high voltage is contacted or if grounding fails. The safety concerns include:

- Grounding scheme - necessary to prevent electrical shock;

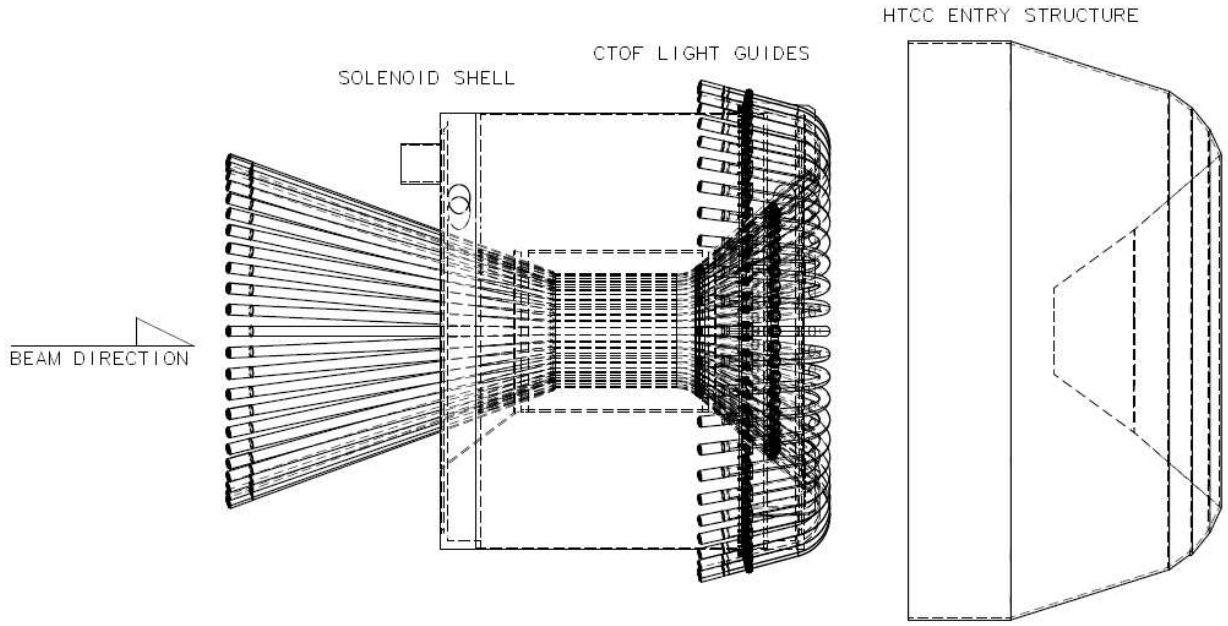

Figure 3.70: HTCC mechanical entry structure.

- Every PMT should have a cover that electrically protects the PMT from the support structure;
- The HV to the phototubes should be turned off if maintenance of the tubes or based required;
- An interlock on the HV should be implemented to protect personnel and equipment;
- Access to the test area and dark box should be key protected;
- Eyes should be protected when handling PMTs;
- Under normal operation the HV should be controlled by a slow-controls system. The control should indicate an *off for maintenance* option;
- The HV power supply should have low current trip limits on each PMT line, thus sustained currents are not possible;
- Only HV-rated connectors and coaxial cables should be used;
- Elevated work areas - access to the HTCC system for installation and repairs will be via man-lifts. Operators will employ appropriate harnessing and fall protection;

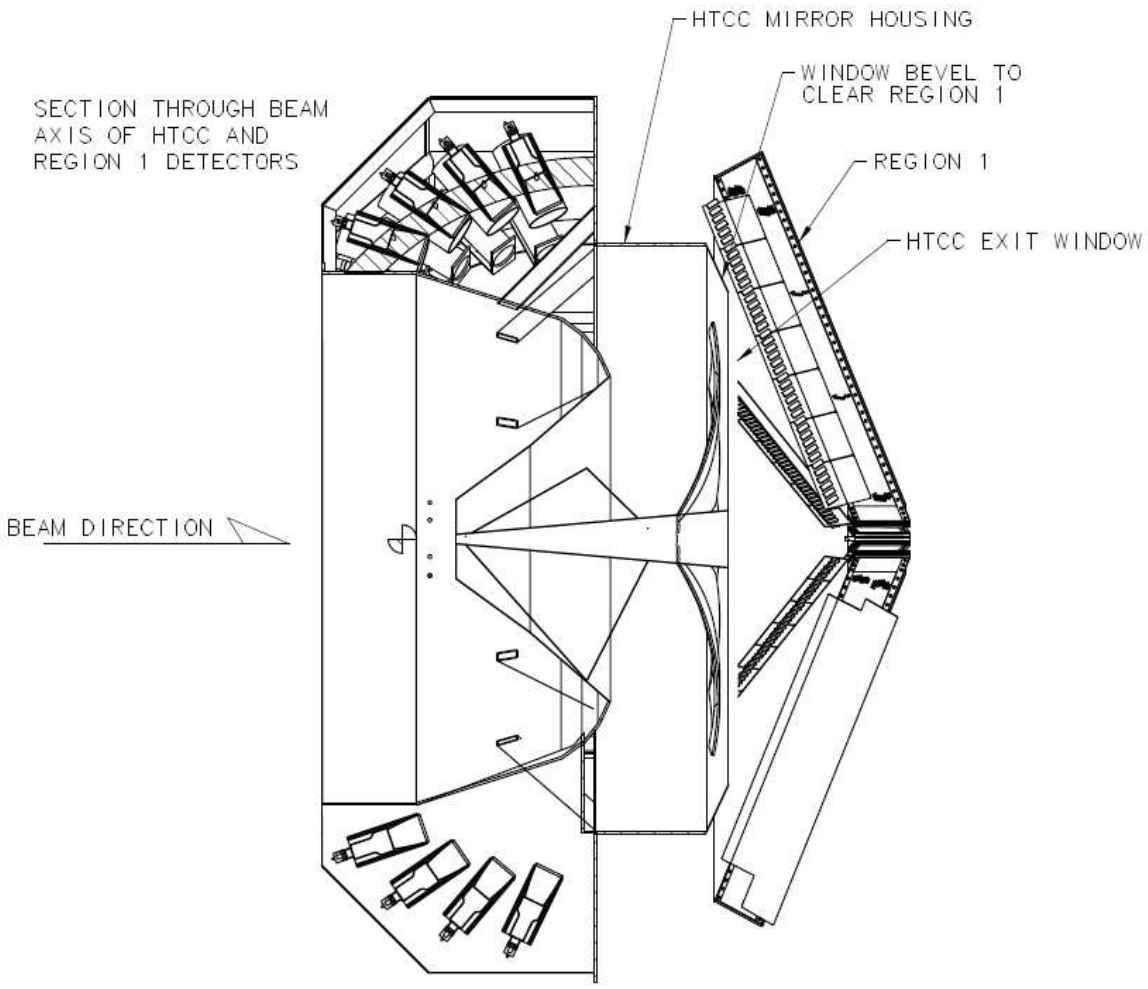

Figure 3.71: View of the mechanical components of the outer shell.

- Staging and installation - special procedures will have to be detailed for the installation of the mirrors and PMTs.

It is expected that the safety issues involved with this work involve low risk for personnel injury or equipment damage, especially with the use of appropriately planned and supervised work activities.

Chapter 4

Central TOF Detector

4.1 Introduction

The new time-of-flight system for CLAS12 will have a refurbished forward-angle detector and a barrel scintillation detector for triggering and time-of-flight measurements in the central region – the central time-of-flight (CTOF) detector. The design of the CTOF barrel includes 50 counters as shown in Figs. 4.1 and 4.2. Each CTOF counter is 66-cm long and $\approx$3.5$\times$3 cm^2 in cross section. These counters will be placed inside the superconducting solenoid (nominal field 5 T) at a radius from the beam axis of $\approx$25 cm. Our goal in the CLAS12 upgrade program is to achieve a timing resolution, $\sigma_{TOF} \approx 50$ ps, which will allow ≥ 200 ps separation [1] of pions from kaons up to 0.64 GeV and pions from protons up to 1.25 GeV. Fig. 4.3 shows the flight time for charged particles incident upon the CTOF counters as a function of momentum.

The timing information in CLAS12 [289] will be referenced to a stable radio-frequency signal from the accelerator. Therefore, the time-of-flight resolution is determined as $\sigma_{TOF} = 0.5\sigma_{PMT}$. Thus we aim to develop a CTOF counter with an effective resolution of a single photomultiplier, with $\sigma_{PMT} \leq 72$ ps. We refer to σ_{PMT} as an "effective resolution" since it is determined by the scintillator rise time (≤ 1 ns), light collection efficiency, discrimination, and the experimental environment, as well as by the excellent intrinsic timing characteristics of modern photomultipliers tubes (PMTs).

In our R&D program we are following a conservative strategy, i.e. we are aiming for the

[1] This value corresponds to $4\sigma_{TOF}$ separation at the given momenta in the transverse direction. A resolution change to $\sigma_{TOF} \approx 60$ ps translates to a $3.3\sigma_{TOF}$ separation between the different hadron species at the same momenta.

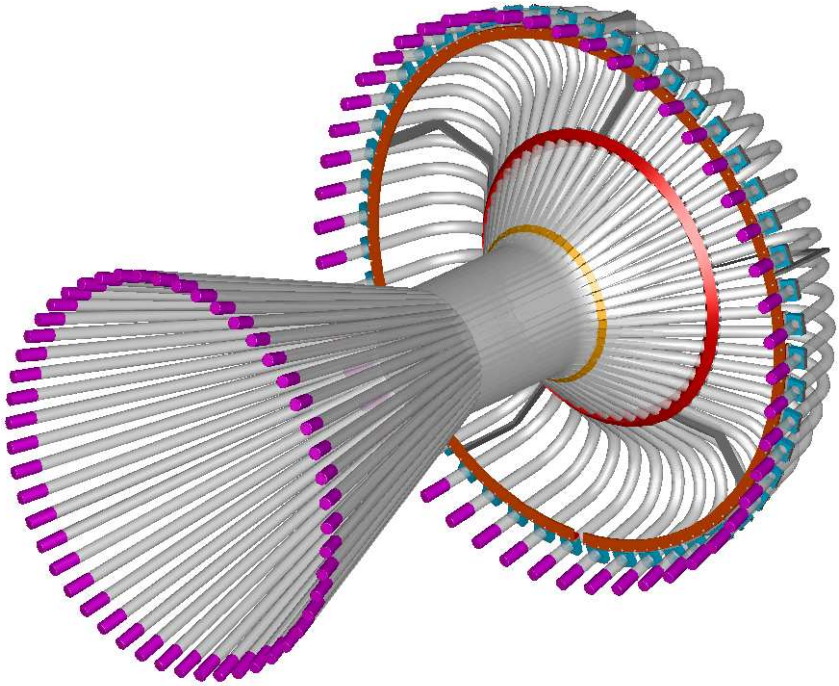

Figure 4.1: The design of the CLAS12 central TOF detector.

best possible resolution using double-sided readout with conventional PMTs and very long light guides ($\leq$ 1.5 m), delivering light to an area outside of the central solenoid where the associated magnetic fields are low (see Fig. 4.4).

We have proven both experimentally and with calculations that long light guides should have an increasing cross section moving from the scintillator to the PMT. This feature allows delivery of about twice as much light compared to a light guide of a constant cross section. Therefore it is preferable to use PMTs with large photocathodes. The actual length and configuration of the light guides will be defined by the maximum magnetic field that can be tolerated by a conventional PMT. Bent light guides, shown on the downstream side of Fig. 4.2, will be used with ordinary PMTs, which have to be protected against magnetic fields $\leq$ 1000 G. On the upstream side magnetic fields are below 500 G.

In parallel, we are pursuing other possible solutions based on modern PMTs that are capable of operating in high magnetic fields, such as micro-channel plate, fine-mesh, and metal-channel PMTs. The review of possible candidates is given in Section 4.3. At the current time, all of the aforementioned PMTs are being considered as options for the CTOF system.

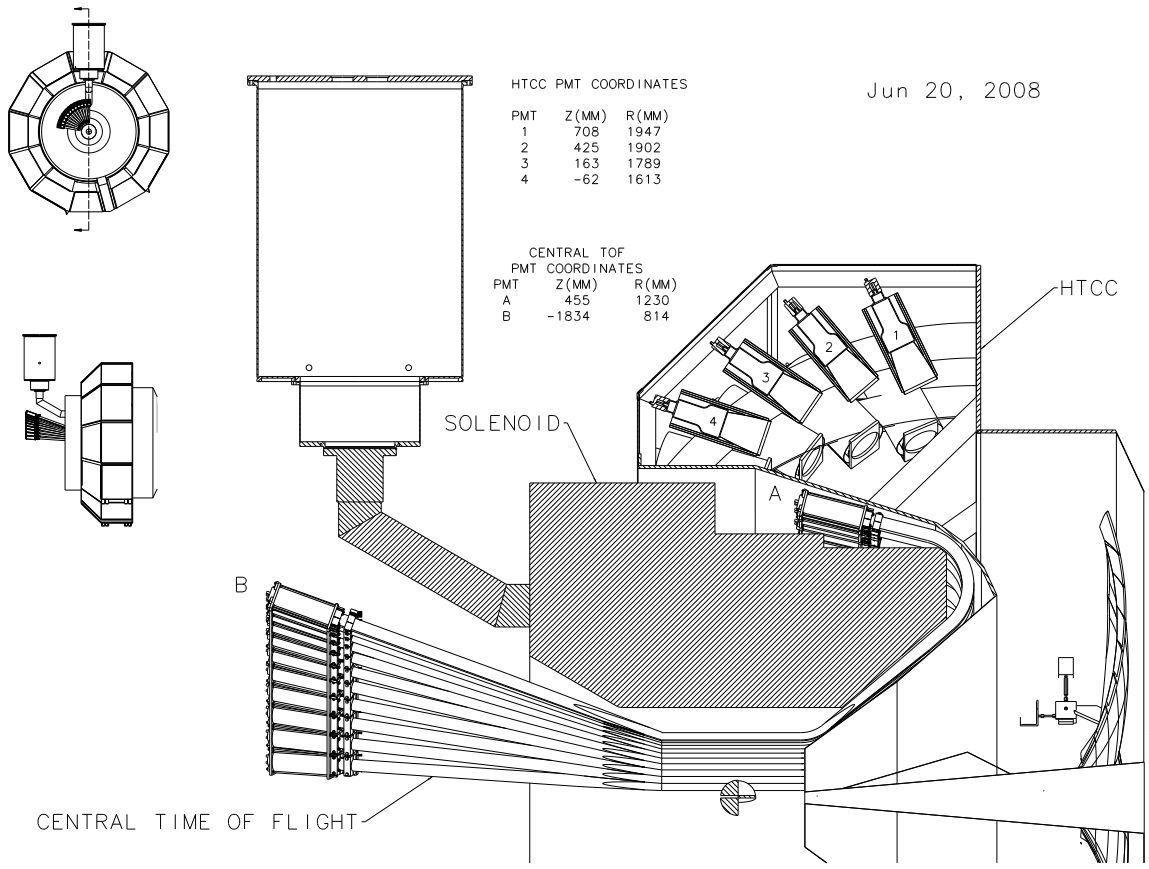

Figure 4.2: The layout of the CLAS12 central TOF detector. The solenoid is shown by the hatched area. The scintillators form a barrel, 66-cm long with an inner radius 24.945 cm. At the upstream and downstream ends, 50-mm diameter light guides are included that have a pitch of 20° and 41°, respectively. The 1.4 – 1.6-m long light guides for conventional PMTs may be replaced with ≤1-m long light guides to accommodate magnetic-field-immune photo-detectors.

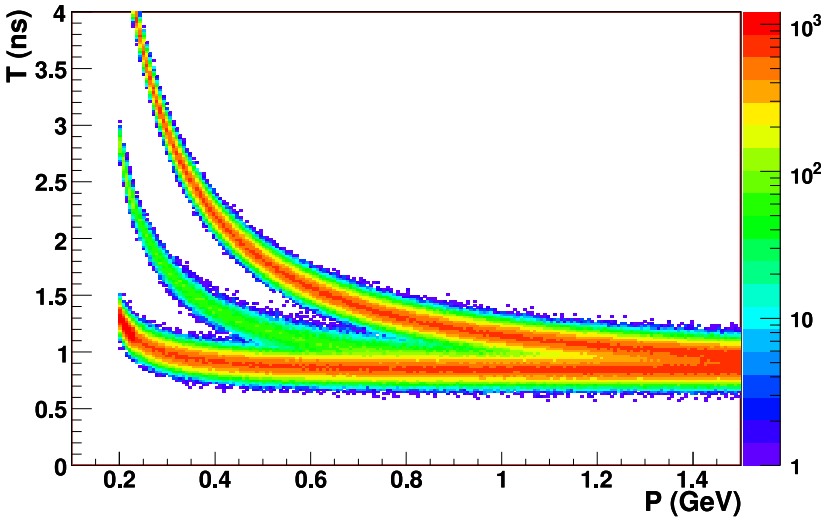

Figure 4.3: Time of flight in the transverse direction vs. particle momentum for protons (top), kaons (middle), and pions (bottom).

At the 5 T nominal solenoid field, long light guides of complex shape are unavoidable elements of the CTOF counter instrumented with both ordinary and/or fine-mesh PMTs. In order to investigate the design and technology for bent light guides (see Section 4.4), we consider a realistic pilot design for the CTOF barrel with light guides shaped as a narrow pyramid. In Section 4.7 we focus on the design of long light guides and optimization of the light guides via Monte Carlo calculations. Prototyping and reference measurements of σ_{PMT} with ordinary and magnetic field insensitive photo-detectors are described in Section 4.2. From our R&D program, coupled with the results of detailed Monte Carlo calculations, we estimate σ_{PMT} for different possible CTOF designs (see Section 4.8).

Within the program of employing magnetic-field-immune PMTs, we have measured the timing resolution of counters instrumented with micro-channel plate (MCP) PMTs with an on-board preamplifier. We describe details of our measurements in Section 4.2.2. Such PMTs are supposed to be attached directly to the scintillators. The corresponding pilot design is given in Section 4.10. However, the performance of MCP PMTs with on-board amplifiers is the subject of future tests in magnetic fields up to 4.5 T.

Another magnetic-field-immune ($\leq$ 1 T) photo-detector is the fine-mesh (FM) PMT. We also plan to test more precise metal-channel (MC) PMTs for their performance in magnetic

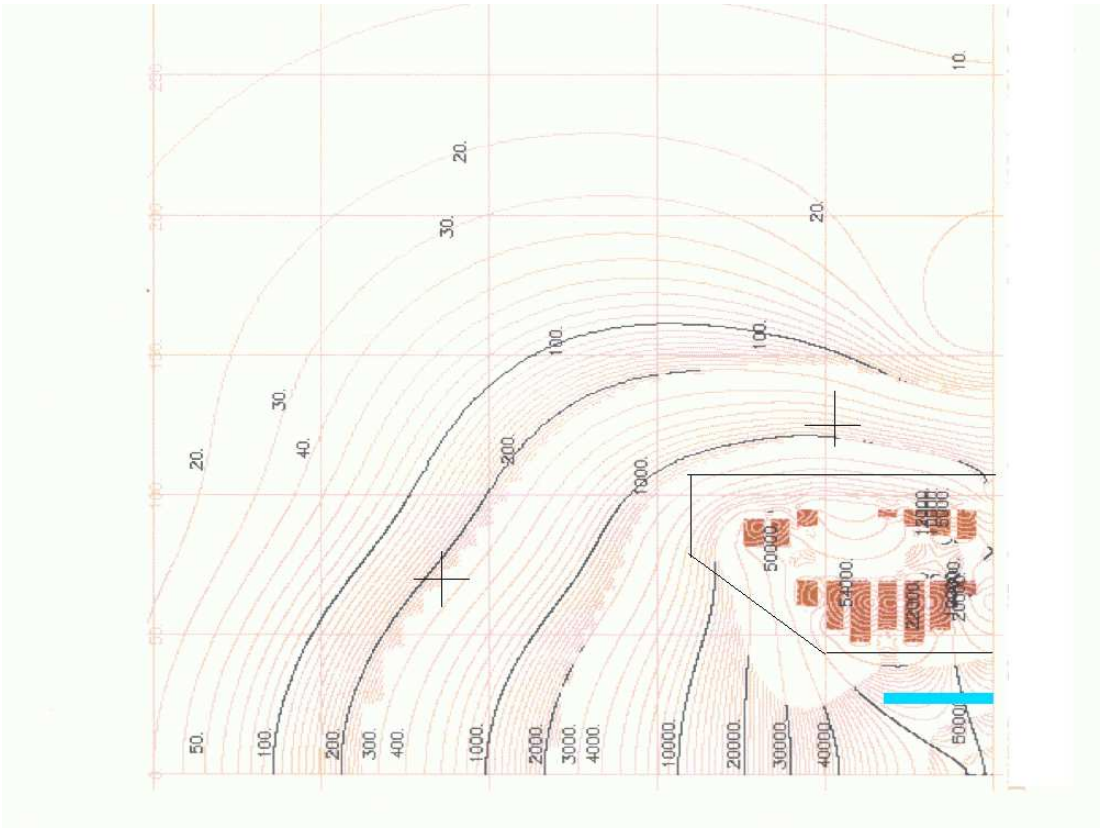

Figure 4.4: Location of R2083 PMTs (cross-hairs) in relation to the magnetic field map for the central `CLAS12` solenoid.

fields up to ≤ 0.2 T with magnetic shielding. Both types require significantly shorter ($\leq$1 m) light guides to deliver light to the locations with a low enough field.

We emphasize that our conservative design with ordinary PMTs may accommodate new photo-detectors, provided the space reserved for the long light guides can be used to house the new PMTs.

4.2 Counter Prototyping and Reference Measurements

Several prototype scintillation counters were manufactured at Kyungpook National University (KNU) in 2004-2007. In cooperation with the Detector Group at JLab, two reference counters were made with double-sided readout via MCP PMTs. In all of our prototypes, we have used Bicron-408 scintillators $2 \times 3 \times 50$ cm^3 in size. Each prototype counter was instrumented with test PMTs on both ends for a double-sided readout. The detailed description of the prototypes, test measurements, analysis methods, and results are published in several `CLAS` notes and NIM papers [290, 291, 292, 293].

We have used two basic configurations for measuring the effective PMT time resolution. Our main setup for express measurements consists of only one counter. In order to measure the effective resolution of the PMTs, we placed a radioactive source on the surface of the scintillator. Using the double-sided readout of the signal time and amplitude, we determined the location of the source via the difference between the arrival times of the two signals. The standard deviation of the determined source location is proportional to the product of σ_{PMT} and the known effective speed of light in the scintillator.

For reference we use a triplet of identical counters exposed to cosmic rays. The reference triplet consists of three identical scintillator bars with double-sided readout. The spacing between the middle and top counters and the middle and bottom counters was matched. To determine the effective resolution of the PMTs we use the method of cosmic ray tracking. The track coordinates are determined in each of the three counters via time difference measurements in each counter. For each counter we also determine the time of a light flash in the scintillator as the mean value of the arrival times at both ends. Thus we exclude coordinate-dependent delays caused by light propagation from the hit point to the PMTs. For the straight tracks with constant velocity, the hit time of the middle counter equates to the mean value of the top and bottom hits. This fact results from the simple geometry of the setup. Therefore,

the difference in timing between the top and middle and the bottom and middle counters should be zero, while the distribution of the residual values is determined by fluctuations in the PMT timing. In order to determine the effective σ_{PMT}, we study the distribution of the residuals. The standard deviation of residuals is proportional to σ_{PMT}.

In our studies we have shown with different measurement methods [290, 291, 293] that the effective time resolution of a Hamamatsu R2083 PMT attached directly to our test scintillators may be as good as ≈52 ps. This value relates to a minimum ionizing particle energy deposition of ≈6.6 MeV in 3 cm of plastic. However, if the 1-m long light guides, shaped as a cut pyramid, mediate the light signal, then the resolution drops to ≈78 ps.

The effective resolution of the Burle 85011 multi-anode (64 anodes) micro-channel plate PMT of ≈75 ps was measured using a single counter setup with the radioactive source method. Amplification of the PMT signal via an on-board amplifier, which was designed at JLab for this purpose, was required for these measurements. The amplification allows the MCP to operate at a reduced gain, thus its counting rate capability is higher [290].

Recently at Kyungpook National University [294] we studied a setup with six Hamamatsu R7761 fine-mesh PMTs attached directly to our reference scintillators. With this setup we have determined the effective σ_{R7761} to be ≈60 ps in the central region of the triplet. The method of time resolution measuring with the radioactive source was also used with a narrow 45-MeV proton beam incident on the center of our reference counter with double-sided readout. The effective σ_{R7761} was determined to be ≈34 ps. The full range of 45 MeV protons in plastic scintillator is 25 mm, therefore the protons stop completely in the scintillator. However, due to the Birk effect, the energy deposition of 45-MeV protons is only ≈35 MeV. We plan further studies with this setup to address the coordinate and angular dependence of the effective resolution.

Below we describe in more detail the studies with the setup of three counters instrumented with six 1-m long light guides [292] and single counters instrumented with Burle 85011 micro-channel plate PMTs and Hamamatsu R7761-70 fine-mesh PMTs.

Comparing the various tests, we conclude that the effective time resolution of the PMTs in our prototypes is mostly dictated by the statistical fluctuations in the number of primary photoelectrons. Therefore, we conclude that further progress in improving the effective time resolution may be provided with better light guide design and optical properties, better coupling of the PMTs to the light guides, and improved scintillator output in the corresponding

wavelength area.

4.2.1 Time Resolution Measurements with R2083 PMT Triplets

Six light guides with our pyramid shape were manufactured at KNU. The light transportation efficiency (LTE) of these light guides was found to be $LTE = 0.44 \pm 0.04$ via Monte-Carlo calculations [295] and various measurements [292]. In order to increase the produced light, the orientation of the scintillators was changed to 3 cm along the cosmic particle track. The obtained values of the effective σ_{PMT} are listed in Table 4.1 in comparison to other measurements at different conditions.

The best σ_{PMT}=52 ps=σ_{NLG} was obtained with our no light guide (NLG) setup (see Fig. 4.5), while with the 1-m long pyramid-shaped light guides (LLG), we have measured $\sigma_{PMT} = 77.9$ ps $= \sigma_{LLG}$ (see Fig. 4.6). One can see from these two figures that x-dependent systematics in the residuals are significant only in the case of direct contact to the scintillators, while in the measurements performed with light guides, these effects are negligible.

This systematic effect reflects a combination of at least two phenomena. The first one is the coordinate dependence of the effective speed of light in the scintillator bar. The reason is that the closer the hit is to the PMT, the more d irect light with higher longitudinal speed participates in the PMT signal developing at the threshold level. The second effect is the well known time walk effects associated with the discriminators.

However, if long light guides are implemented, then the direct light does not share in the signal build-up and the signal size becomes significantly longer due to the larger light path variations. As one can see from Figs. 4.5 and 4.6, both effects are much less pronounced in the measurements with the long light guides.

To estimate the effective σ_{PMT} in different counter designs (i.e. with different dimensions of the light guides, etc.) we use the above declared values and the empirical relations deduced from Monte Carlo simulations [295] for "extrapolation" of the measured σ_{PMT} to the different designs.

We emphasize that the resolution with 1-m long light guides, σ_{LLG}, is worse due to the absorption of $\approx$56% of the light in the light guides. The amount of light at the photocathodes is proportional to the light transmission efficiency (LTE) of the light guides and, assuming the statistical nature of the resolution, we can estimate σ_{LLG} as:

	Setup & Method	Year	lg(N)	ΔE (MeV)	σ_{PMT}(ps)	Status
1	2×R2083,2cm,2×LG(1 m) coordinate meth.;^{90}Sr	2004	6 *vs* x	$T_\beta < 2.28$ $\rightarrow$ 4.4	89.1±4.0	Publ.
2	2×Burle 8501-501,NoLGs coordinate meth.;^{90}Sr	2004	6 *vs* x	$T_\beta < 2.28$ $\rightarrow$ 4.4	≈80, 125±4	Publ.
3	6×R2083,2 cm,No LGs cosmic ray tracking	2004	6 *vs* x, θ	cosmic ≈4.4	59.1±0.7	Publ.
4	Same as #3	2005	5 *vs* x, θ	≈4.4	62.3±0.4	Publ.
5	6×R2083, 3 cm, NoLGs cosmic ray tracking	2005	5 *vs* x, θ	≈6.6	52.0±0.6	Publ.
6	Same as #5 **reference with no LG**	2006	5 *vs* x, θ	≈6.6	**52.2±0.4**	Publ.
7	6×R2083, 2 cm, 2×LG (1 m), cosmic ray tracking	2005	5 *vs* x, θ	≈4.4	92.3±0.5	Publ.
8	6× R2083, 3 cm, 2×LG (1 m)	2005	5 *vs* x, θ	≈6.6	83.6±0.6	Publ.
9	Same as #8 **reference with LGs**	2006	5 *vs* x, θ	≈6.6	**77.9±0.6**	Publ.
10	2×Burle 85011, NoLGs coordinate method; ^{90}Sr	2006	6 *vs* x	$T_\beta < 2.28$ $\rightarrow$6.6	86.6±1; 10^6 s^{-1} 71.4±1; 10^5 s^{-1}	Publ.
11	2×FM R7761-70, NoLGs cosmic ray tracking	2007	3 $x \approx 0$	cosmic ≈6.6	$60 - 66$	Discon-tinued
12	2×FM R7761-70, NoLGs cosmic ray tracking	2008	3 $x \approx 0$	protons ≈45	≈ 34	In Progr.

Table 4.1: Reference measurements of the effective time resolution (standard deviation) of different PMTs. The values of σ_{PMT} in rows 1–10 of this table are averaged over -25 cm< x <25 cm and -45° < θ <45°. The uncertainties shown in this table are derived from the fitting procedures. The possible systematic uncertainty is 6% on the given values.

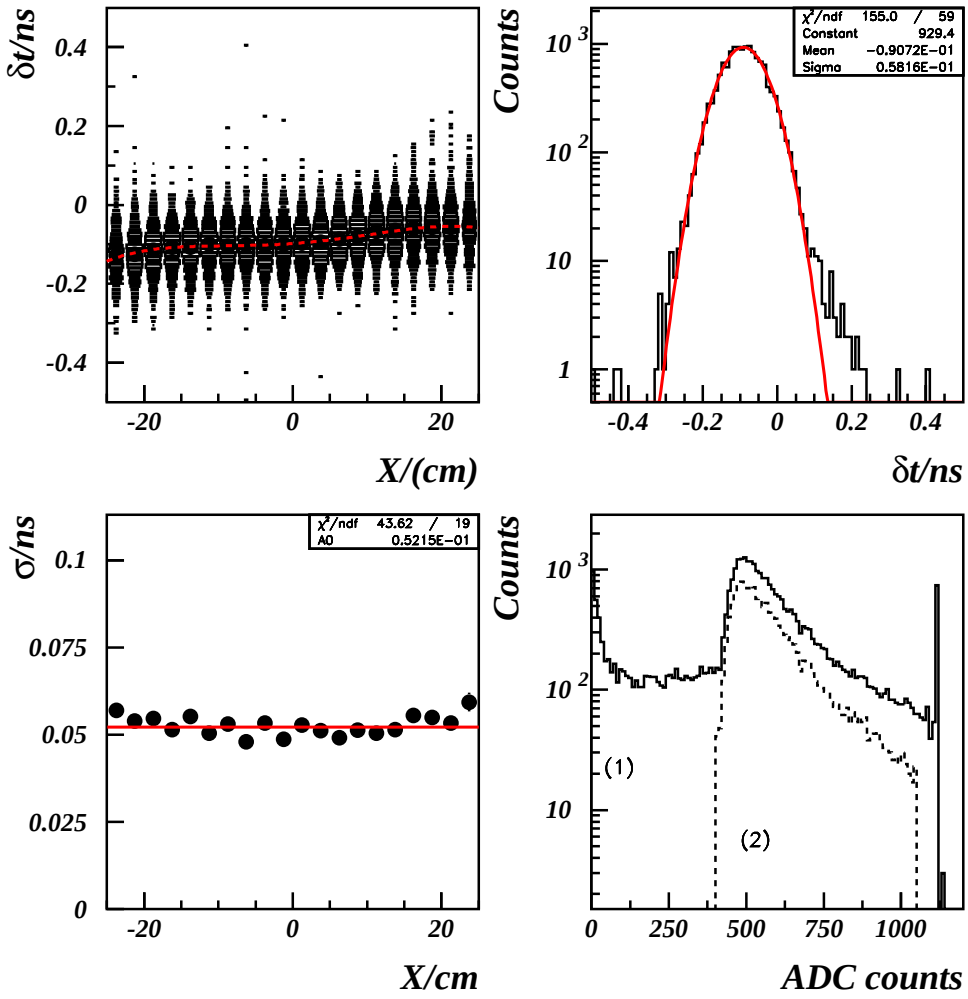

Figure 4.5: Effective time resolution of a PMT (σ) in the triplet without light guides. (UL) scatter-plot of residuals vs. longitudinal coordinate x; the dashed line shows mean values, (UR) overall distribution of residuals, (LL) local σ vs. x with mean value $\sigma = 52.2 \pm 0.4$ ps, (LR) ADC values.

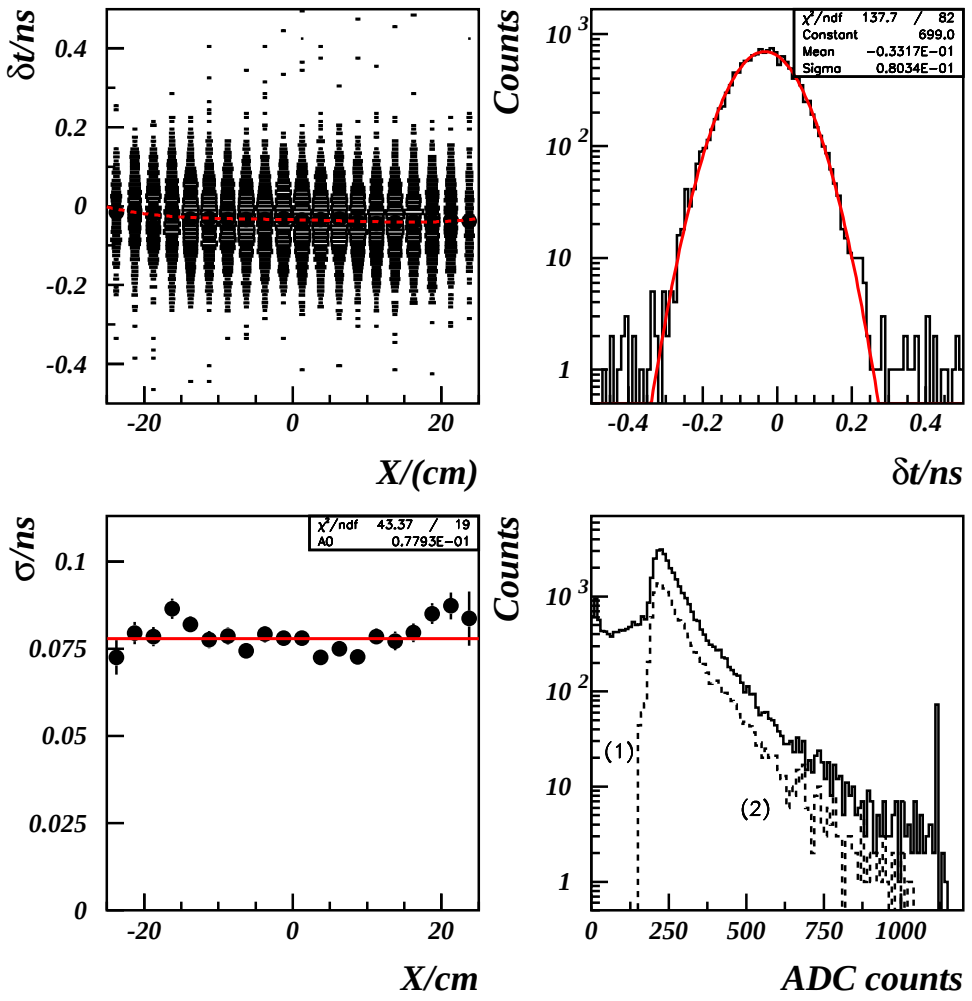

Figure 4.6: Effective time resolution of a PMT (σ) in the triplet with 1-m long straight light guides. (UL) scatter-plot of residuals vs. longitudinal coordinate x ;the dashed line shows mean values, (UR) overall distribution of residuals, (LL) local σ vs. x with mean value $\sigma = 77.9 \pm 0.6$ ps, (LR) ADC values.

$$\frac{1}{\sqrt{LTE}}\sigma_{NLG} = \frac{1}{\sqrt{0.44}} \times 52.2 \text{ ps} = 78.7 \text{ ps}, \quad (4.1)$$

where σ_{NLG} is the measured resolution. The resulting value matches to the reference from row–9 of Table 4.1 within a 1% accuracy. Therefore, we conclude that in our test setup the effective σ_{PMT} is determined mostly by the statistics of the primary photoelectrons, i.e. by the amount of light at the photocathodes. We use this experimental fact as the main rule in our further estimations of σ_{PMT} in various environments.

4.2.2 Time Resolution Measurements with a Burle 85011 PMT

For these measurements the new assembly of a Burle 85011 PMT with an "on-board" preamplifier (with a gain value of $\times 50$) and a high voltage divider that was designed at JLab was employed. The design of the circuit board is described in Ref. [296]. This design follows the requirement implied by the final goal of $\sigma_{PMT} \leq 72$ ps in time resolution.

The Burle 85011 photocathode is formed by 64 pads 0.6×0.6 cm^2 in size. We took into account the fact that the MCP PMT resolution may be limited by the signal propagation time through the pad, which is spread between 0 at the point of the pad-wire contact and l_{max}/c for the most remote point, at the distance l_{max}.

We used the central 6×6 pads as a single photocathode. In order to avoid additional jitter due to propagation from the individual pads, the central 36 pads were grouped into three amplification channels via isochronous transmitting lines. The resulting three signals are summed up, also isochronously, at the last stage of amplification. Thus we guarantee that the jitter caused by signal propagation is defined by the size of a single pad, which amounts to only 10 ps (i.e. negligible).

The test counter with our "standard " scintillator was assembled at KNU and resolution measurements with a radioactive source were recently performed. We present the results below.

Effective Time Resolution at the Ultimate Gain: A sample plot given by the coordinate method with extrapolation to the energy loss in a 3-cm thick scintillator is shown in Fig. 4.7. The extrapolated time resolution σ_{PMT}=71.4 ps was obtained at the ultimate MCP gain of 0.89×10^6. This resolution is very close to our goal. Unfortunately the counting rate at such a high gain is limited to $10^5 s^{-1}$ [290]. Therefore, we have measured the resolution at

lower gains and present below the measured dependence upon the MCP gain. Prior to determining the gain, one has to measure the number of primary photoelectrons (N_{ppe}) emitted from the photocathodes.

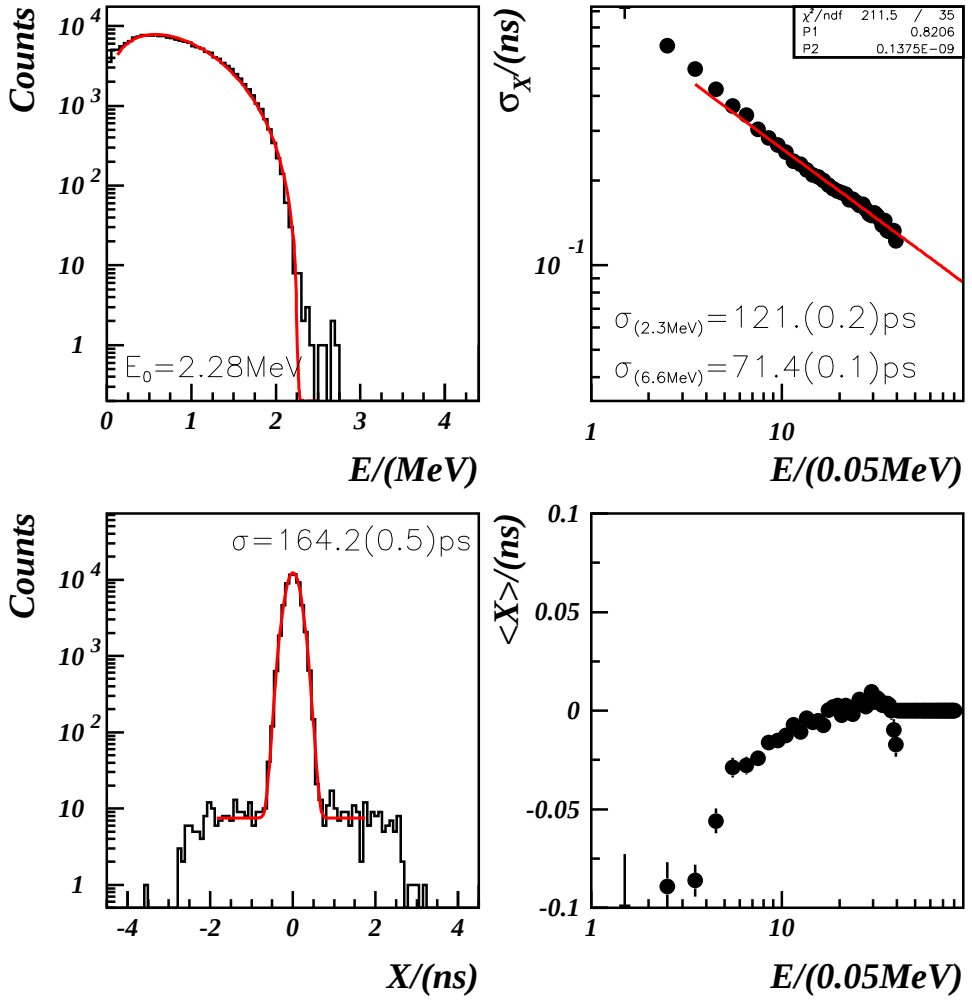

Figure 4.7: Effective time resolution of a Burle 85011 MCP PMT obtained with the location method of the ^{90}Sr source placed in the center of the counter. (UL) energy (E) spectrum of β-particles, (LL) coordinate distribution (x) of β-particles with $E > 1$ MeV, (UR) σ_x of the peak vs E, (LR) $< x >$ vs E.

Number of Primary Photoelectrons in the MCP: We have measured the number of primary photoelectrons produced by MIPs using the technique developed within the coordinate method [290]. The PMT output signals were split in order that a fraction f=0.16 of the initial current fed the ADC inputs, while the rest triggered the corresponding discriminators.

The ADC spectrum of β-particles was then used to determine the number of primary photoelectrons and their dependence upon β-particle energy. The corresponding graphs are shown in Fig. 4.8. These results were extrapolated to determine the expected number of primary photoelectrons in a 2-cm thick scintillator, which was found to be $N_{ppe} = 370 \pm 8$ (note that this value relates to both photocathodes). This result is in good agreement with expectations using the quantum efficiency (QE) specified in the Burle 85011 data sheet.

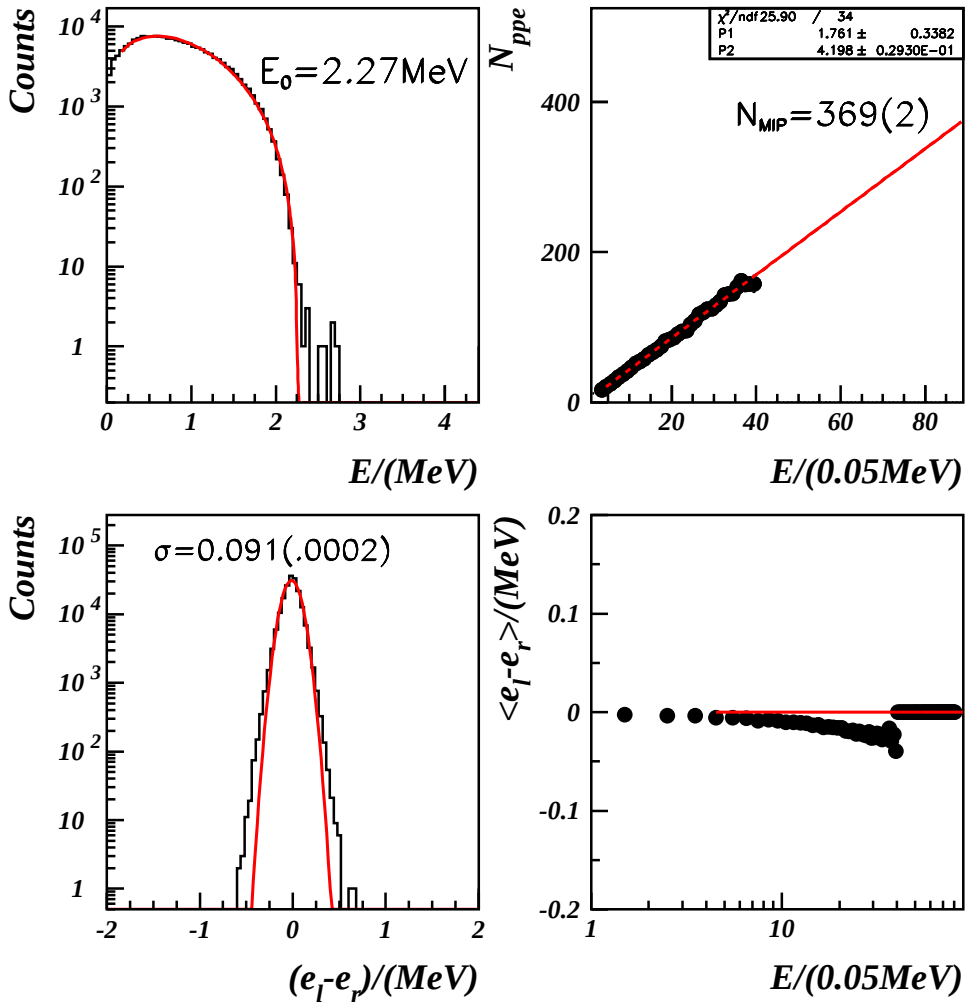

Figure 4.8: Determination of the number of primary photoelectrons. (UL) Energy (E) spectrum of β-particles, (UR) N_{ppe} vs E. We expect the number of primary photoelectrons to be 369 ± 2 for a MIP energy of $\approx$4.4 MeV, (LL) spectrum of $(e_l - e_r)$, where $e_{l,r}$ are the energies measured from the two sides of the counter, (LR) mean value of $(e_l - e_r)$ vs. β-particle energy.

Measurements of the MCP Gain: The MCP gain (G) was determined using the measured N_{ppe} and the β-particle spectra measured with the ADCs as:

$$G = \frac{2 \times \alpha \times A_0}{f \times e \times N_{ppe} \times G_a}, \tag{4.2}$$

where A_0 is the pedestal-subtracted ADC value corresponding to the upper edge of the β-spectrum, E_0=2.28 MeV, α is the ADC channel width (0.25 pC), G_a is the amplification factor of the preamplifier (50), f is the aforementioned spitting factor, and e is the charge of the electron. The factor of 2 in the numerator is from the number of photocathodes. A plot of the determined gain as a function of the MCP voltage is shown in Fig. 4.9.

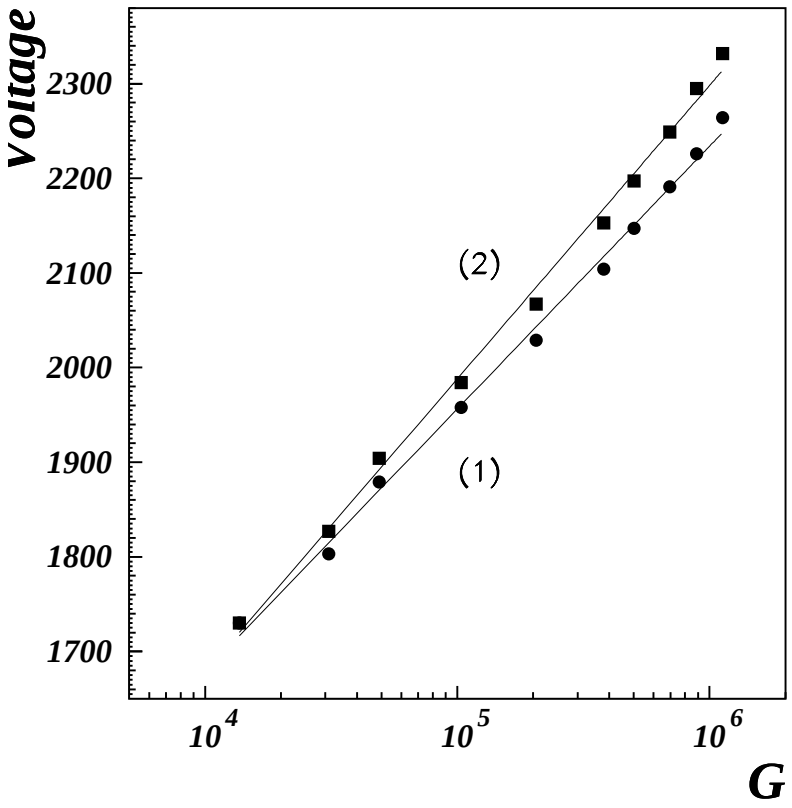

Figure 4.9: High voltage vs. MCP gain. Curves (1) and (2) are fits to a power law form. (1)-left PMT, (2)-right PMT.

Time Resolution vs. MCP Gain: We have measured the effective time resolution of a Burle 85011 PMT at different high voltage settings. The resolution yielded by the coordinate method is shown in Fig. 4.10 as a function of the MCP gain. One can see that at a gain

of 0.5×10^5, where the MCP can operate at a 1 MHz counting rate [290], the effective time resolution with a 3-cm thick scintillator is only 86.6 ± 1 ps. With this value we are 20% away from our goal of 72 ps. Thus a further significant improvement of N_{ppe} is required.

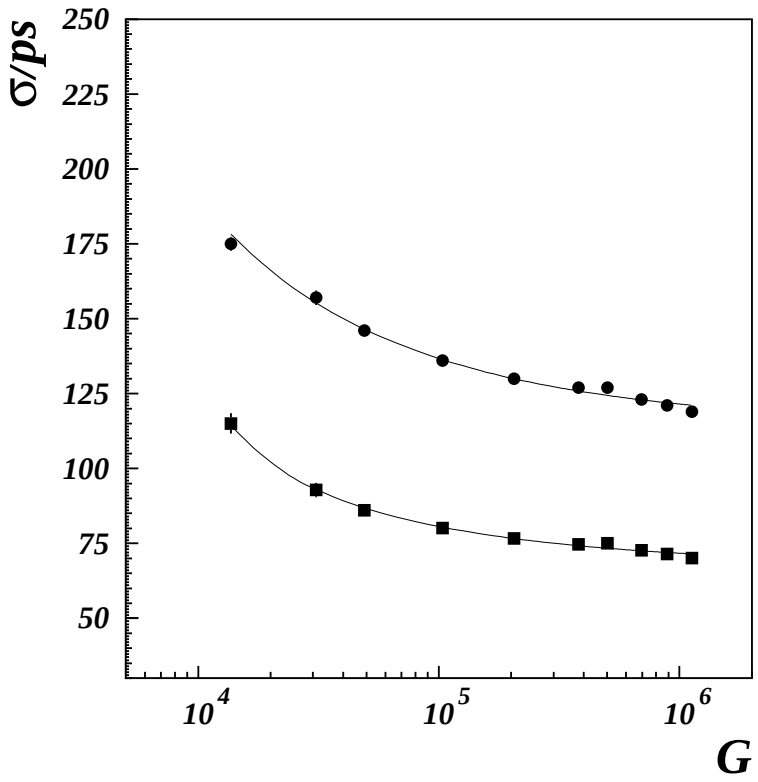

Figure 4.10: Resolution of the Burle 85011 PMT vs. the MCP gain (G). The circles are for σ at ΔE=2.28 MeV. The squares are for ΔE=6.6 MeV (which corresponds to MIPs in a 3-cm thick scintillator). The curves are fits to the G^{-2} dependence. The amplification factor of the PMT signals is 50.

4.2.3 Measurements with Fine-Mesh Photomultipliers

Using the same triplet technique as for the R2083 PMTs, we have measured σ_{PMT} of the fine-mesh PMTs. In our standard counter triplet [290, 292] the ordinary PMTs in the middle counter were replaced with 27-mm Hamamatsu R7761 fine-mesh PMTs. All PMTs were in direct contact with the scintillators. The corresponding σ_{R7761}=64 ps is shown in Fig. 4.11 in comparison to the Hamamatsu R2083 PMTs. It was further improved to ≈60 ps with cuts in the central region of the triplet instrumented with R7761 PMTs and identical discriminators [294].

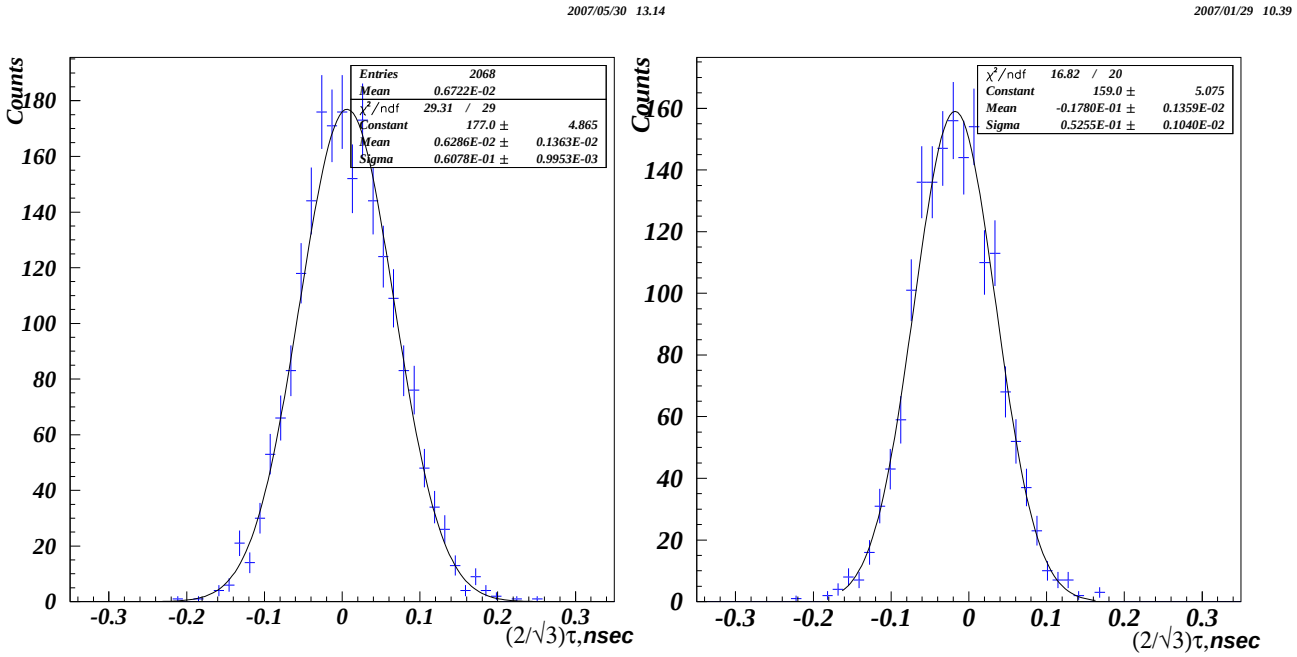

Figure 4.11: Spectra of the 6 PMT time residuals scaled by $2/\sqrt{3}$. Left panel: distribution with two R7761-70 PMTs and four R2083 PMTs (right). Right panel: distribution obtained with six R2083 PMTs. The actual effective σ_{R7761}=64 ps is derived from the RMS width of the left panel. The reference $\sigma_{R2083} = 52 \pm 1$ ps from the right panel coincides with the previously reported value from Table 4.1.

The time residual spectrum at the center of the reference counter instrumented with two R7761-70 PMTs is shown in Fig. 4.12. It was obtained with the 45-MeV proton beam at an $\approx 10^5 s^{-1}$ counting rate [2]. Protons completely stop in the bulk of the scintillator, therefore the deposited energy is ≈10 times higher than the reference MIP energy deposition. The standard deviation σ=24 ps of this distribution translates into $\sigma_{R7761} \approx 34$ ps for a single PMT. In order to compare this result to our reference from Table 4.1 (line 5), this value has to be scaled to the reference energy by a factor of $\sqrt{(45 \text{ MeV}/6.6 \text{ MeV})}$. The additional factor of $\sqrt{0.77}$[3] accounts for the reduced light output of 45-MeV protons compared to the electrons of same energy (Birk's effect). Since PMTs were attached directly to the scintillator, the effective PMT area was reduced by a factor of ≈0.8. All of this results in the following preliminary resolution of:

$$\sigma_{R7761} \approx 34 \text{ ps} \times \sqrt{\frac{45}{6.6} \times 0.77 \times 0.8} = 70 \text{ ps}. \quad (4.3)$$

[2] For details see KNU presentation http://www.jlab.org/~baturin/KNUpresentation0208.pdf.
[3] This number was obtained from the manufacturer's specifications.

However, the uncertainty on this value has to be determined experimentally. This result was obtained in direct contact to the scintillator and the proton beam hit the center of the counter, where the left and right signals are almost identical. Therefore, effects related to the signal shapes cancel out.

In this test, one PMT signal was used as a TDC "start", while another provided the TDC "stop". Therefore, all events were concentrated within a few TDC channels. In this situation, the differential nonlinearity of the TDC, which may be as high as 15%, directly affects the measured time resolution.

Therefore, further studies of differential nonlinearity effects, as well as of coordinate and angular dependence with realistic light guides, are required in order to establish the ultimate effective time resolution of the fine-mesh PMTs.

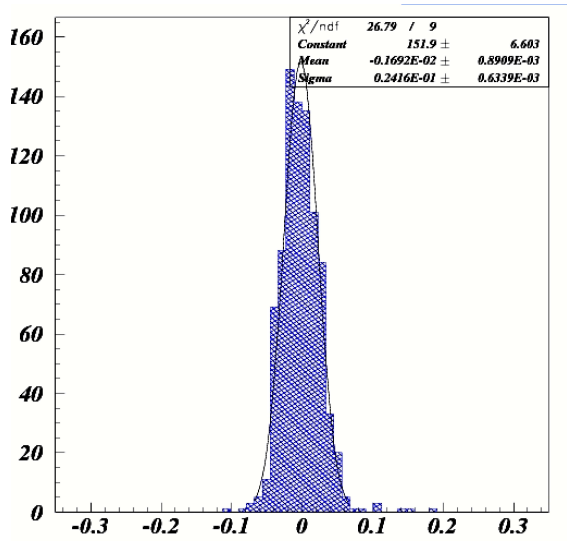

Figure 4.12: The time residual spectrum at the center of the reference counter obtained with R7761 fine mesh PMTs with a 45-MeV proton beam. The standard deviation is 24.2 ± 0.6 ps.

4.3 Review of Modern Photo-Detectors

Different possible approaches to the design of the CLAS12 CTOF counter are considered below in relation to the advantages and disadvantages of different photo-detectors.

4.3.1 Ordinary Dynode PMTs

Following our conservative strategy, we will maintain our effort to achieve the desired timing resolution with ordinary Hamamatsu R2083 PMTs. The gain and timing characteristics of R2083 PMTs are very good for this purpose (see Table 4.2). However, for ordinary PMTs there is no other option than to be placed outside of the region of high magnetic field. Therefore, $\approx$1.5-m long light guides are required to deliver the light to an area with $B \leq 30$ mT. Shorter light guides will require a heavy magnetic shield composed of 3 concentric cylinders. In addition, according to the preliminary design shown in Fig. 4.2, the light guides on the downstream side will have to be bent by 139°. This reduces the net light at the PMT, the ultimate limit of which is dictated by the desired time resolution. Therefore significant progress is required in the light guide design and manufacturing technique.

4.3.2 Micro-Channel Plate Photomultipliers

An alternative solution with micro-channel plate (MCP) PMTs is very attractive for the following reason. Due to the immunity of MCPs to magnetic fields, proven up to ≤ 2 T[297], micro-channel plate PMTs could be attached directly to the scintillators. Therefore, the mechanical design of the barrel may be significantly simpler. The intrinsic timing properties of MCP PMTs are perfect. The properties of one such photomultiplier (Burle 85011) are shown in Table 4.2.

The single photon timing resolution (see Fig. 4.13) remains below σ_{TTS}=35 ps up to $\approx$2 T and perhaps higher fields. The gain (see Fig. 4.14) also does not degrade in such high magnetic fields [297].

Unfortunately, the quantum efficiency of MCP PMTs is about one-half that of ordinary PMTs, which has a direct adverse effect on the TOF resolution. However, very good resolution of a MCP photo-detector was already shown in Fig. 4.13. In addition, it was shown [298] recently that the effective σ_{PMT} of a Burle 85011 may be as good as 70 ps in a magnetic field up to 1.5 T. In our aforementioned measurements, we have achieved a resolution of $\approx$75 ps, which is almost sufficient for our goals.

Hence, the two approaches look almost equivalent with respect to the timing resolution. The advantage of a R2083 PMT with its higher quantum efficiency is compensated by the loss of about half of the light in the light guides. Almost nothing can be done with the quantum

PMT Model Characteristics	R2083 Dynode	H8500 MC	R6504 FM	R5924 –	R7761 –	85011 MCP
Photocathode sizes, mm	d=46	49 × 49	d=51	d=39	d=27	49 × 49
Anode configuration	1	8 × 8	1	–	–	8 × 8
Area ratio PMT/SC (9.6 cm^2)	1.77	2.19	2.14	1.24	0.6	2.19
Wavelength max. response, nm	420±80	–	–	–	–	400±80
-//- at 10% of max. QE, nm	300 – 650	–	–	–	–	–
Window thickness, mm	1	1.5	1	–	–	2
Number of stages	8 dyn.	12dyn.	19 fm	–	–	2MCP
Photocathode material	Bi-alk.	–	–	–	–	–
Photocathode radius, mm	55	flat	–	–	–	–
Sensitivity@420nm, μA/lm	80	55	70	–	–	55
Sensitivity in blue, μA/lm	10	8	9	–	–	8
Quantum efficiency@420mn	.22	0.2	0.22	0.22	0.22	0.12
Anode rise time, ns	0.7	0.8	2.7	2.5	2.3	0.3
Transit time (t_T), ns	16	6	11	9.5	7.5	4
t_T spread (FWHM), ps	370	400	470	440	350	80
Gain×10^{-6}	2.5	1	10	–	–	0.5
Dark current, nA	100	32	50	50	30	1

Table 4.2: Technical data of the R2083 PMT from Hamamatsu in comparison with other candidates.

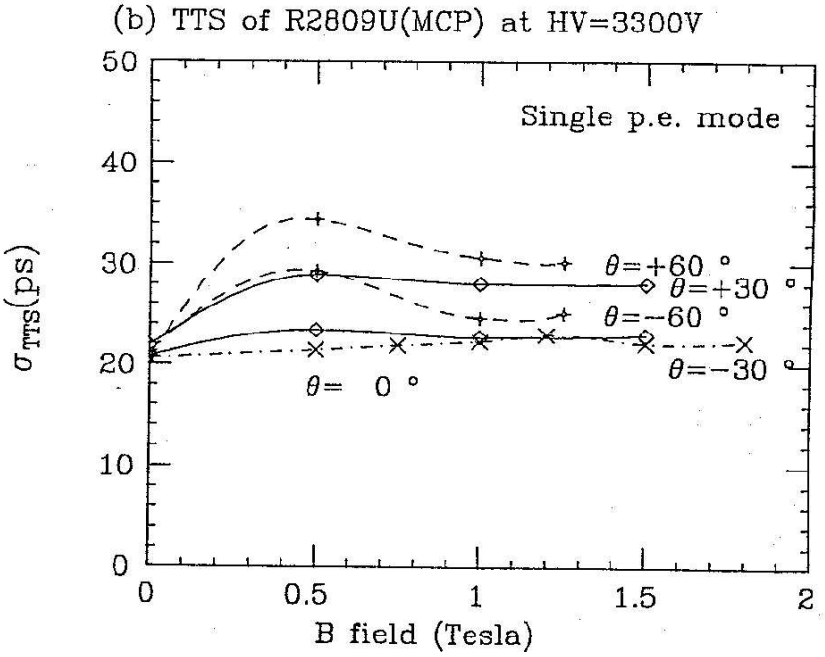

Figure 4.13: Transition time spread of the MCP PMT vs. magnetic field.

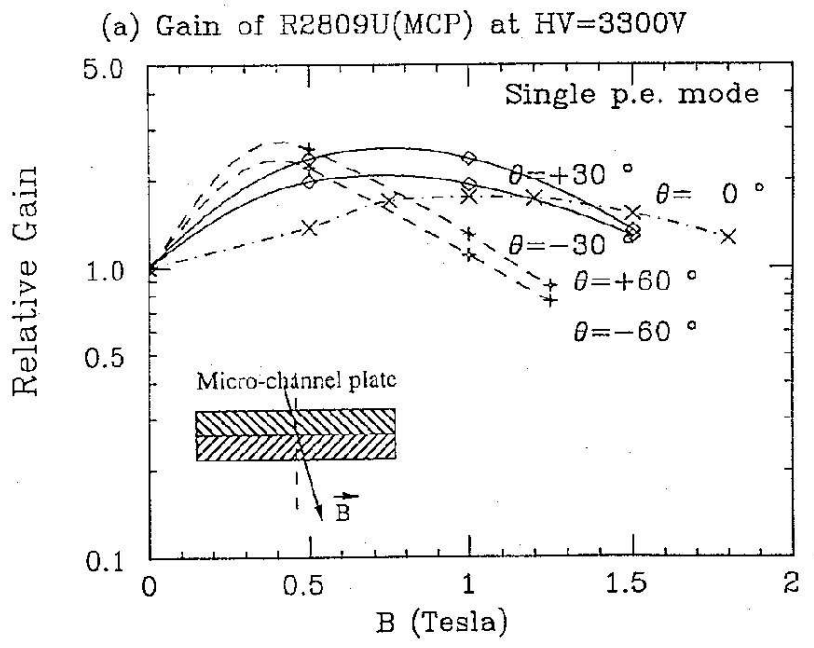

Figure 4.14: Gain of the MCP PMT vs. magnetic field at different orientations.

efficiency of MCP PMTs unless the PMT design is completely changed.

In the design with long light guides, we can try to optimize the light guides via Monte Carlo simulations for a maximum possible LTE, including the solution with PMTs capable of operating in moderate magnetic fields of ≈0.5 T. In addition, we can use more refractive materials, such as Lexan. It has a refractive index equal to that of the scintillators. However, its attenuation length is higher. Thus the gain in resolution may be achieved with relatively short light guides (0.5 m – 1 m).

4.3.3 Fine-Mesh and Metal-Channel Photomultipliers

The light deficiency problem may be solved with fine-mesh (FM) PMTs, which have been shown to operate at $\leq$ 1 T or metal-channel (MC) PMTs, provided they can be shown to operate well in fields up to 0.2 T with a proper shield. The light guides can be about a factor of two shorter and we can use all of the experience that we have obtained with the design implementing the long light guides (see Section 4.4).

Fine-Mesh PMTs: In fine-mesh PMTs, the conventional dynode system is replaced with a ladder of fine-grade metal mesh at a certain potential. The gain and resolution [297] of a fine-mesh PMT vs. magnetic field are shown in Figs. 4.15 and 4.16, respectively.

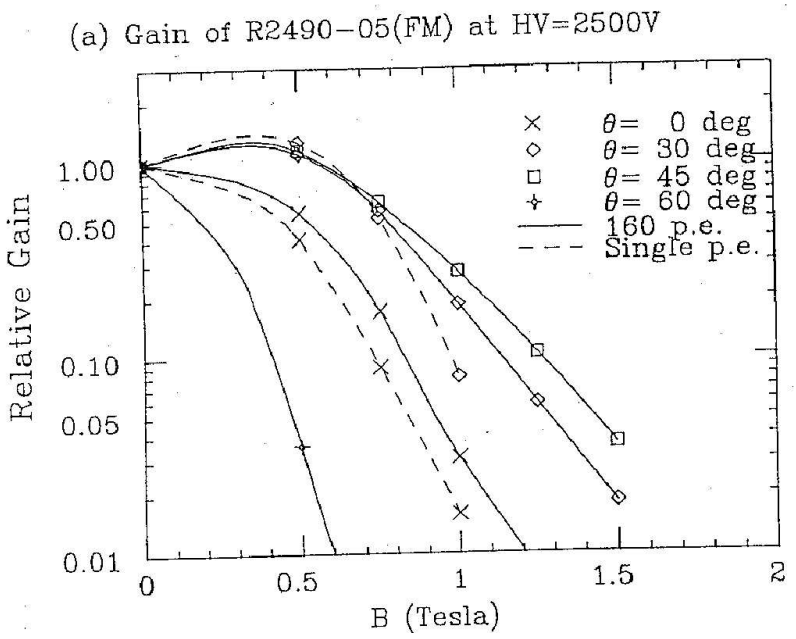

Figure 4.15: Gain of the R2490-05 fine-mesh PMT vs. magnetic field at different orientations.

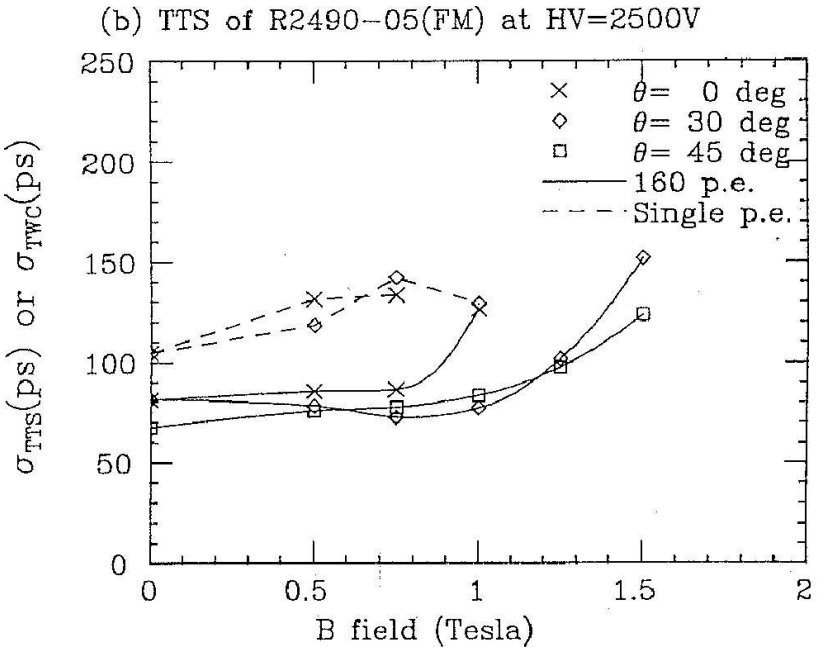

Figure 4.16: Transition time spread of the R2490-05 fine-mesh PMT vs. magnetic field.

The behavior of modern FM PMTs R5505, R7761, and R5924 from Hamamatsu has been recently studied in magnetic fields up to 1.2 T [299]. The generic time resolution of the 2-in R5924 PMT (≈60 ps) was found unchanged up to a field of ≈0.8 T. This characteristic was measured with light pulses equivalent to ≈300 photoelectrons. In our recent measurements, in which Hamamatsu R7761 FM PMTs were in direct contact with the scintillator, we also have achieved a similar time resolution [294].

The counter instrumented with two fine-mesh PMTs attached to a 1-m long scintillator was tested in Ref. [300]. This counter may be considered as a rough approximation a single element of the CTOF system. For this setup with a 6-cm thick Bicron-408 scintillator, we estimated $\sigma_{TOF} \approx 70$ ps. The effective timing resolution of fine-mesh PMTs of $\sigma_{FM} \approx 63$ ps may be extracted from the data obtained [301] with $50 \times 2 \times 5$ cm^3 Bicron-408 and ≈50-cm long light guides.

The closest in size to the R2083 PMT is the R6504 fine-mesh PMT (see Table 4.2) from Hamamatsu with a QE ≈ 20% at 420 nm. We emphasize that with expanding light guides (toward the PMTs), we gain about a factor of two in light collected at the PMT [292]. Therefore, PMTs with wide enough photocathodes are required to accommodate this design. Unfortunately, this PMT is already discontinued. The timing characteristics of the R5924 PMT are almost the same, but it has a two times smaller sensitive area. However, it is still

larger than the scintillator cross section, therefore we plan to test it. The R7761 PMT has almost a twice smaller sensitive area (5.6 cm^2) compared to the size of the scintillator cross-section (9.6 cm^2). Therefore, it is unlikely to collect enough light with realistically long light guides of 0.7–0.8 m length. The reason is that even without attenuation, the transmittance of a light guide cannot exceed 0.58.[4]

Unfortunately, the rise time of the R6504/R5924 PMT signal is ≈4 times longer than that of the R2083 PMT. In addition, the transition time spread is 100 ps higher than the 370 ps for the R2083. We plan to measure the resolution of the R5924 PMT in addition to smaller FM tubes, metal-channel PMTs, the R2083 PMT, and MCP PMTs, using the same test setup and methods.

Metal-Channel Photomultipliers: Another interesting photo-detector worthwhile to investigate as a component of the CTOF counter is the metal-channel PMT, such as the H8500 or R7400 PMTs from Hamamatsu. The H8500 is a 64-channel PMT with a square photocathode. The dynode system is formed by channels in precisely machined metal sheets. Such PMTs have excellent timing characteristics, which are very close to that of the R2083 PMT, i.e. σ_{TTS} ≈400 ps, QE≈ 20%, and they have a high gain (see Table 4.2).

In our future tests we are going to verify whether such PMTs can operate at fields of ≤0.2 T with appropriate shielding. This photo-detector may be a good candidate for further consideration in combination with light guides of moderate length.

4.3.4 Silicon Photomultipliers

In recent years a variety of semiconductor devices (see Table 4.3) have been developed for light detection. Their advantage of operating in high magnetic fields and with a small size detecting element is very attractive for designers of TOF systems. A matrix of such detectors, with arbitrary dimensions, could be attached directly to the scintillators inside the magnetic field.

A silicon photomultiplier [302] is a 3 × 3 mm^2 matrix of 5625 pixel photodiodes (30 × 30 μm^2) with a common output. The photodiodes operate in the Geiger regime of bulk carrier amplification. Therefore, an almost immediate (no drift required) signal from a single

[4] This is the ratio of the PMT area to the input area, which limits the acceptance due to phase space conservation.

APD name	Size mm	Drift dist. μm	FWHM ps	σ_t ps	Rate s^{-1}	QE 420 nm
5343	d=1	10	82	35	10^7	1-5%
5344 LC	d=3	20	160	68		1-5%
SPL 2625	d=3	120	1300	550	10^7	1-5%
Beveled Edge						1-5%
LAAPD	d=16	40	400	115		1-5%
30719	5×5	10	170	72		1-5%
C 30626	5×5	100	800	340	10^7	1-5%
C 30703	10×10	180	1600	680		1-5%
SiPM	3×3	0	155	66	10^7	14-20%
MPPC S10362-33-10C	3×3	0	200	85	10^7	70%

Table 4.3: Semiconductor device characteristics.

photon may be seen with a standard shape and amplitude (≈2.5 mV). The time resolution of a SiPM may be as high as 66 ps [302] with 3-mm thick BC-418 scintillator. It is very important that the output may be triggered by the first arriving "direct" photons. However, the noise at the nominal operating voltage is as high as $10^5 - 10^6$.

The QE is a product of the pixel packing efficiency (≈0.5) and the Geiger mode efficiency (≈0.6). At 420 nm, the quantum efficiency is ≈14%, and it is likely that this may be improved to reach the QE of ordinary photo-detectors. In addition, the signal has a tail ≈5 μs long. Thus the recovery time may be as high as 5 μs. However, due to the large number of pixels, the SiPM count rate capability of light flashes with ≈500 photons, for example, is limited by a rate of ≈ 10^7 s^{-1}, which is typical for conventional PMTs. Nevertheless the optical cross-talk may significantly reduce its count rate capability. For use in CLAS12, the SiPMs would have to reside in a high radiation environment. Therefore, their radiation hardness has to be addressed. Due to all of the above reasons, SiPMs may be considered as a candidate for future studies and an upgrade possibility for the CLAS12 CTOF system.

4.3.5 Avalanche PhotoDiodes

In the avalanche photodiode [303], the carriers are drifting with a velocity of 0.1 μm/ps toward the narrow region in which the avalanche develops. In such a device, the single photon time resolution is determined by the drift distance x, thus, roughly, $\sigma_{APD} \propto x$. In addition, the dependence on the sizes is quite significant. For example, the x=10-μm thick device 5343, roughly 1 mm in diameter, manifested a time resolution $\sigma \approx 35$ ps, while the 5×5 mm^2 30719 x=10-μm thick device shows $\sigma \approx$72 ps. The thicker the device the higher is its QE, but the worse its time resolution. The related parameters of available APDs are listed in Table 4.3. The quantum efficiency of such a photo-detector is roughly 2% – 5% in the region of BC-408 emittance, while for longer wavelengths, it may be as high as 70%. In addition, their gain is quite low ($\approx 10^4$) and amplification is required. The behavior in a high radiation environment is not determined yet. Therefore, at the present time, such photo-detectors may be considered as unlikely candidates for use in the CLAS12 CTOF system.

4.4 Pilot Design with Conventional R2083 PMTs

This design is based on a traditional and well-established approach of using ordinary photomultipliers coupled to scintillators via long light guides. Hamamatsu R2083 PMTs have excellent timing characteristics. In order to approach our goal for the effective σ_{R2083}=72 ps, we have been developing long (1 m) light guides of non-trivial shape with significantly improved light transmission efficiency (≈44%). Also we are thinking about implementing a better light guide manufacturing approach using cast Acrylic, which is a widespread technology for commercial applications. The advantage of cast Acrylic is that the product has a near-perfect surface. Thus, time-consuming polishing is not required. In addition, we will keep an eye on the progress in organic materials with a refractive index close to that of scintillators, such as commercially available Lexan.

4.4.1 Detector Specification and Design Criteria

The nominal CTOF design, which starts with ordinary R2083 phototubes, may accommodate other types of photo-detectors, such as magnetic-field-immune micro-channel, fine-mesh, or more sensitive metal-channel phototubes of similar sizes. The only thing that would have to

be done in the design is to change the lengths (cross section) of the corresponding light guide at the PMT side. However, the space reserved for the light guides in the design has to be wide enough to accommodate these PMTs. The independent parameters that determine the design of a single CTOF counter, including its light guides, are listed in Table 4.4.

Diameter of PMT in μ-metal case	60 mm
Diameter of the PMT photocathode	46 mm
Number of scintillators	50
Thickness of scintillator along r-axis	31.5 mm
Inner radius of the barrel	25.0 cm
Lengths of the scintillator barrel	66 cm
Length of Upstream light guides	130–140 cm
Length of Downstream light guides	150–160 cm
The downstream opening angle	$\pm 36^\circ$

Table 4.4: Basic values determining the CTOF counter design.

The CTOF barrel has to be as hermetic as possible. Therefore, due to the cylindrical symmetry of the setup, all elements of a single counter, including the scintillator, both downstream and upstream light guides, and PMTs, all have to fit into a ϕ range of 7.2° in the (r, ϕ)-plane. A schematic view of such a counter is shown in Figs. 4.17 and 4.18.

Scintillator Dimensions

The length of the scintillators is predefined to be 50 cm. Other dimensions of the scintillator are determined by the total number of counters (predefined as 50) and the inner radius of the scintillating barrel (predefined as 25 cm). The scintillator cannot be a rectangular bar due to the cylindrical geometry of the setup. The cross section of the scintillator is shown in Fig. 4.19. Since a single counter has to fit into a sector $2\gamma = 7.2^\circ$, the cross section of the scintillator has to be a symmetric trapezoid with the sizes 31.46 mm and 35.4 mm for the bottom and top sides, respectively, and 31.5 mm high. In this figure the trapezoid is inscribed into the cross section of the photocathode of the R2083 PMT.

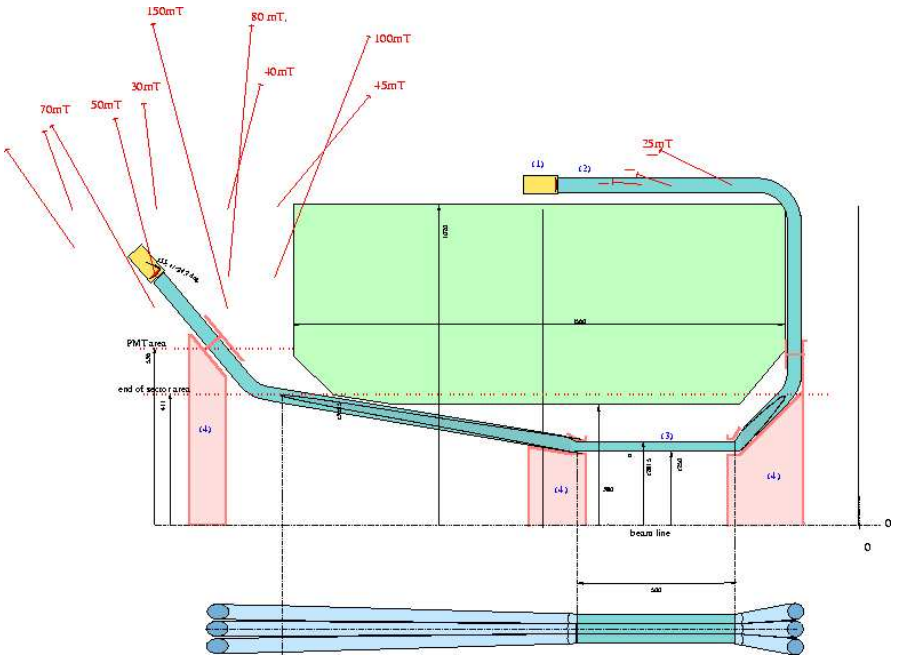

Figure 4.17: The pilot design of the CLAS12 CTOF counter. (1) R2083 PMT from Hamamatsu, (2) Acrylic light guides, (3) scintillators, and (4) supporting cones and rings. The magnetic field is shown by the vectors.

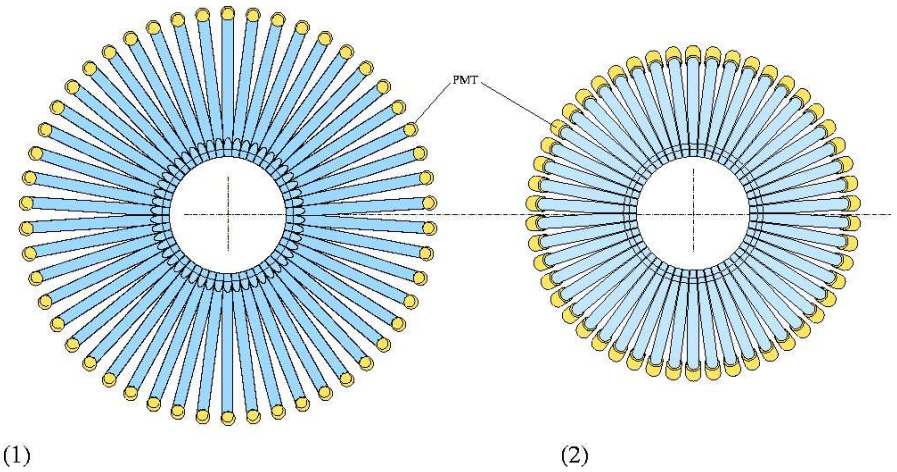

Figure 4.18: Upstream (1) and downstream (2) view of the CTOF detector.

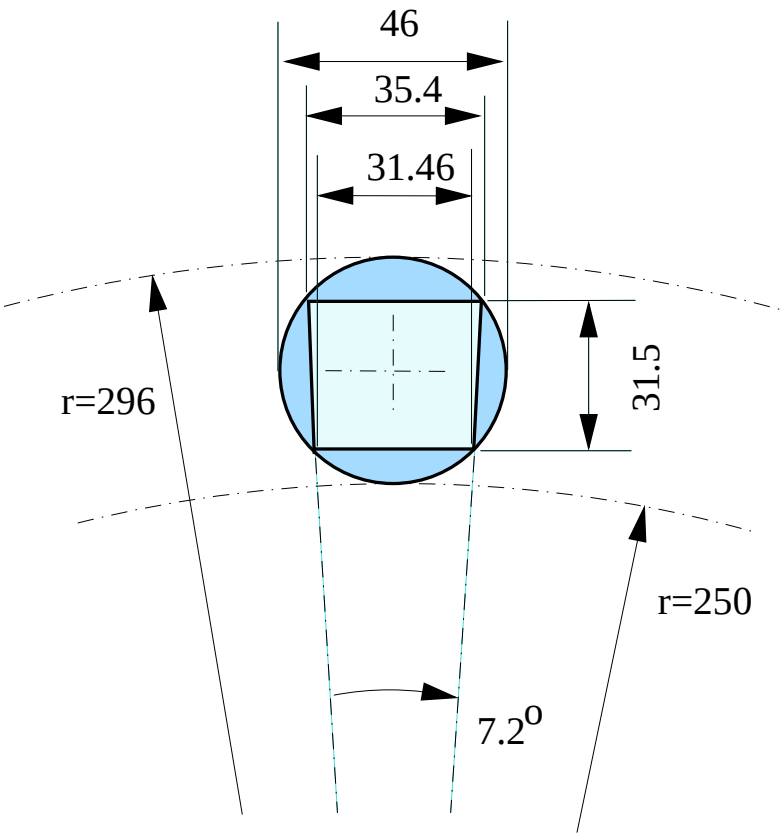

Figure 4.19: The cross section of the scintillator inscribed into the photocathode of the R2083 PMT from Hamamatsu. Light guides will join the PMTs via the cylindrical side of the same diameter as the R2083 photocathode, i.e. 46 mm.

Dimensions of the PMT Housing

In this design we assume that R2083 PMTs from Hamamatsu will be used, and that they will be housed in a metal case 60 mm in diameter. This determines the divergence of the upstream light guides. It is clear that 50 adjacent PMTs with the specified diameter will form a ring of $\approx 50 \times (60 + 10)$ mm$/\pi = 111.4$ cm in diameter (we add 10 mm to the diameter of the PMT case as tolerance). With this number we set the radius of the "PMT area" R_{PMT}=55 cm. Note, that it is not possible to place 50 adjacent PMTs, mounted on the ends of 1-m long light guides, at an r-coordinate below R_{PMT}.

Dimensions of the PMT Photocathode

In the hermetic configuration, the expanding light guide has to match the cross section of the scintillator from one side. At the PMT end, it has to match the photocathode of the PMT. Therefore, it is natural to manufacture the "pyramid" light guides from Acrylic cylinders with a diameter of 46 mm, corresponding to the diameter of the R2083 PMT photocathode.

4.4.2 Light Guides

From the PMT-end, the 1-m long light guide has to match the circular photocathode of the PMT. Therefore, light guides will be manufactured from Acrylic cylinders $\geq$ 46 mm in diameter, which is the specified diameter of the R2083 PMT photocathode. From the opposite side, it has to match the trapezoidal cross section of the scintillator.

It was shown via Monte Carlo calculations [295] that the light transportation efficiency depends significantly on the length of the cylindrical part of the light guide. The corresponding dependence upon the length of the non-cylinder part of a 1-m long light guide is shown in Fig. 4.20.

The design of the upstream light guide is shown in Fig. 4.21. The sides of the cylinder will be milled to form a wedge up to a radius of 36.55 cm in the (r, ϕ)-plane in order to fit into the $\Delta\phi = 7.2^\circ$ sector. The straight cylindrical parts will be longer in order to deliver light to the area of $B < 30$ mT. Therefore at the nominal field B=5 T, the total length of the light guide will be $\approx$1.5 m.

The scintillator ends of the light guides will be further machined in order to form focusing mirrors on the inner and outer surfaces, respectively. Such machining is also necessary to form

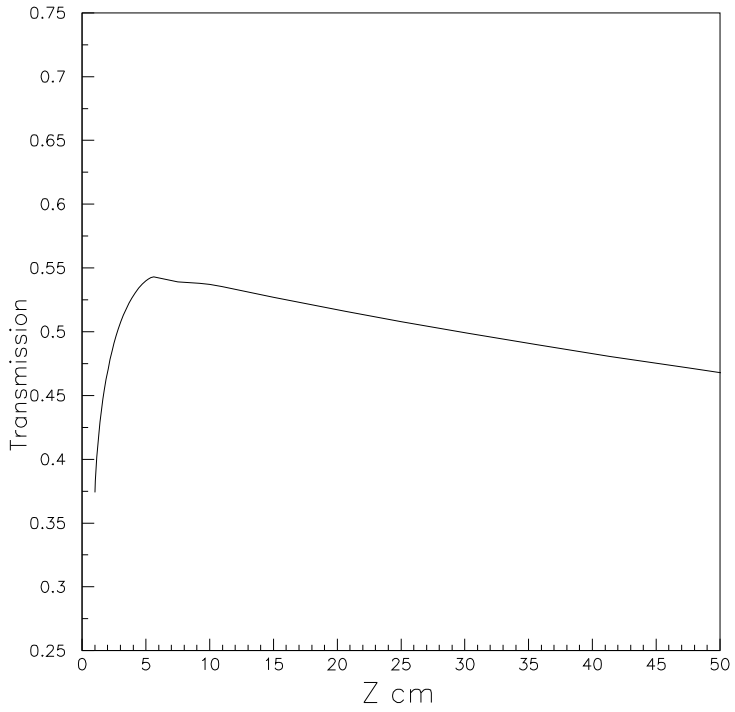

Figure 4.20: The light transportation efficiency (vertical scale) of the "pyramid" light guide vs. the length (horizontal scale) of the milled surface.

a trapezoid at this end for coupling to the scintillator.

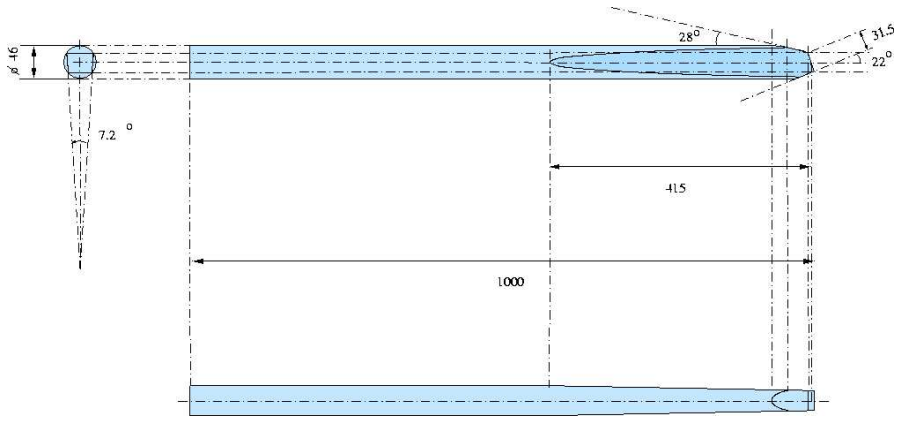

Figure 4.21: The design of the upstream light guide.

4.4.3 Downstream Light Guides

From the PMT-end, the light guide will match the circular photocathode of the PMT. Therefore, the light guides will be manufactured from bent Acrylic rods of corresponding diameter. From the opposite side, it has to match the trapezoidal cross section of the scintillator. In addition, these light guides have a pitch of 45° relative to the scintillator to provide an immediate opening for forward-going particles. Another complication is that these light guides have to be bent twice by 45° and 90°, respectively.

The pilot design of the downstream light guide is shown in Fig. 4.22. The mirrors at the scintillator end will be milled similarly to the upstream light guide. The minimum length of this light guide will be ≈1.6 m, provided the magnetic field at the PMT end will be ≤50 mT at a nominal field B=5 T.

4.5 PMT Magnetic Shields

The main CTOF design is based on using ordinary PMTs coupled to the scintillators via ≈1.5-m-long light guides of a complex design[5]. Our reference PMT is the 51-mm R2083 PMT from Hamamatsu. It has a spherical photocathode in order to equalize the travel distances of

[5]We anticipate that at the final design stage, regular PMTs may be replaced with fine-mesh PMTs with two times shorter light guides. These PMTs are insensitive to fields up to 5000 G.

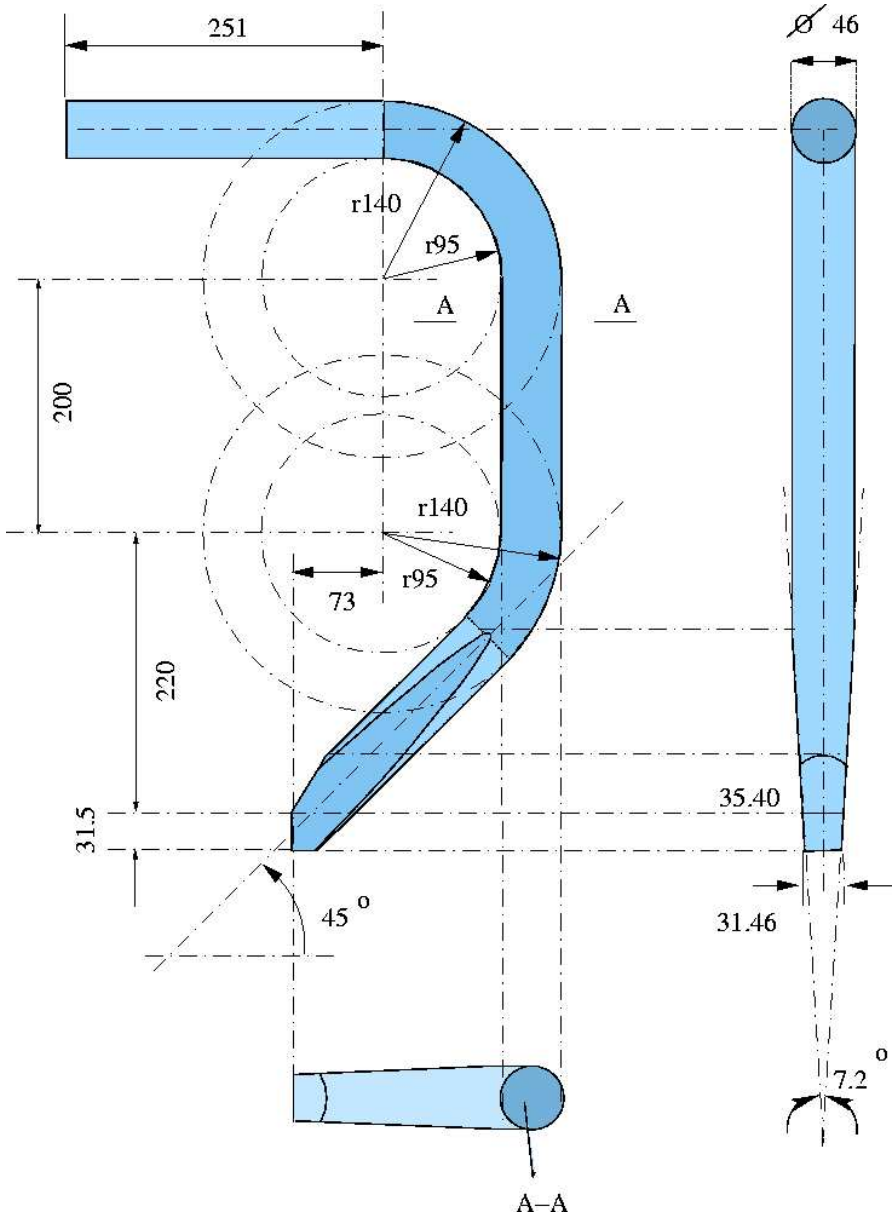

Figure 4.22: The design of the downstream 1-m long light guide.

the primary photoelectrons and is quite similar to the Phillips XP4312 PMT, which is 76 mm in diameter, hence it is less sensitive to magnetic fields. The XP4312 PMT was thoroughly studied in 1993 by J. Flint and E. Smith as a candidate for the CLAS TOF detectors [6]. It manifests an additional time smearing of $\sigma \approx 30$ ps at fields of 0.25–0.4 G at the photocathode, which corresponds to an external field of 30 G, reduced by the 1-mm thick μ-metal shield that is 80 mm in diameter[7]. Since our PMT is similar in design, we can estimate that the maximum field at the photocathode would be 0.2–0.4 G.

Two kinds of PMT shielding are possible in principle: passive and active shielding. Active shielding means using a solenoid around the PMT to cancel the internal field. We do not plan on using active shielding because, firstly, in our case, the fringe fields are not solenoidal, and secondly, such shields would be more complex and more costly, and thirdly, it may be a source of additional electronic noise.

With passive shielding, a diamagnetic superconducting cylinder could be used to block the magnetic field inside the cylinder. Such shielding would be very complex and expensive, as well as requiring cryogenics for cooling.

Therefore, we plan to study a traditional approach based on the properties of ferromagnetic cylinders. In such shielding, the magnetic field lines are concentrated in the bulk of a ferromagnet, reducing the fringe fields inside the cylinder. However, the efficiency of such shielding at high fields is limited by the effect of saturation.

We plan to achieve field reduction to the 0.25-G level with a shield composed of three concentric ferromagnetic cylinders. The important parameter in the CTOF design, is the external diameter D_s of the magnetic shield. This parameter is determined by the radial coordinate r_{50} of the 50 adjacent shields:

$$D_s = 2\frac{r_{50}}{\sin(3.6^\circ)} = 134.277 \times r_{50}. \tag{4.4}$$

The characteristics of the PMTs relevant to the design of the magnetic shields are given in Table 4.5.
Here,

- D_{pm} - nominal diameter of the PMT;

[6] J. Flint and E. Smith, "Tests of Phillips XP4312/D1 PMTs in a Magnetic Field", CLAS-Note-94-008.
[7] See the corresponding field map in Fig. 13 of CLAS-Note-94-008.

PMT	D_{pm} mm	S_a mm^2	L_m mm	B_t G	M kg	r_{50} mm	D_{sm}	L_{LG} mm	B_o G
R2083-u	54	1662	120	0.25	$\approx$5	826	88.	1400	≤ 500
R2083-d	–	–	–	–	$\approx$10	1090	146.4	1600	≤ 1000
H8500-u	72	2400	15	≤ 500	$\approx$10	596	80.1	945	2000
H8500-d	–	–	–	–	$\approx$10	890	119.5	945	3000

Table 4.5: Characteristics of the PMTs relevant to the CTOF magnetic shield design.

- S_a - PMT sensitive area;
- L_m - maximum length to protect against the magnetic field;
- B_t - maximum tolerated field by the "naked" PMT;
- M - expected shield mass;
- r_{50} - radial coordinate according to the current design;
- D_{sm} - maximum possible diameter of the PMT shield via Eq.(4.4);
- L_{LG} - shortest possible light guide length in current design;
- B_o - magnetic field at the PMT location at the specified light guide length.

According to this table, the upstream R2083 PMTs have to withstand against a field $\leq$ 500 G, provided the light guide length is 1400 mm. In this case, the diameter of the magnetic shield has to be below 88 mm. The downstream R2083 PMT meets a significantly higher non-uniform magnetic field. Provided the downstream light guide length is 1600 mm, the maximum field would be $\leq$ 1000 G, while the magnetic shield diameter may be as high as 146 mm.

The metal-channel H8500 PMT may operate at 200 G without magnetic shielding. However, with a powerful enough shield, both kinds of PMTs could operate at higher fields. In such a situation, shorter light guides could be used, which would lead to an improved resolution.

R2083 PMTs will be used in the assembly H2431, enclosed into the 200-mm long, 0.8-mm thick μ-metal of 60 mm external diameter. However, we plan to change the H2431 design in

order to arrange a overhang of 50–60 mm from the photocathode side. This is required for a more efficient shielding design [8].

4.5.1 Ferromagnetic Shielding

In ferromagnetic shields, the field lines are concentrated in the bulk of the ferromagnetic, thus reducing the fringe fields inside the protecting area. The problem with infinite hollow ferromagnetic cylinders in uniform transverse magnetic fields may be solved analytically[9], as well as the problem of ellipsoids in axial fields. Therefore, the following practical formulas are recommended by the Magnetic Shield Corporation for rough estimates of magnetic shield parameters:

$$S = \frac{B_o}{B_{in}} \approx \mu(B_m)\frac{t}{D_+} \quad ; \quad B_m \approx B_o\frac{D_+}{0.8t} \quad ; \quad t \approx B_o\frac{D_+}{0.8B_m}, \tag{4.5}$$

where S is the shielding factor of a cylinder, $\mu(B_m)$ is the permeability as a function of the field B_m in the shielding material, B_o is the external field, B_{in} is the field inside the ferromagnet, t is the thickness of the shielding material, and D_+ is the external diameter of the cylinder. For a set of separated coaxial cylinders, the shielding factor may be estimated as the product of the individual factors.

Finite Element Analysis

Two external layers are the most important element for shield performance. Therefore, we have analyzed a double-layer magnetic shield against 3000 G. The parameters of such a pilot shield are listed in Table 4.6.

[8] The internal field drops significantly at a depth of one radius of the shield.
[9] See E. Smith, GlueX-doc-843.

Cyl n	B_o G	D_+ mm	D_- mm	t mm	B_m G	$\approx \mu$	S	B_{in} G	Fm
1	3000	136	86	25	20000	600	40	80	Netic
2	80	84	80.8	1.6	5300	150000	2850	0.03	Hiperm-49

Table 4.6: Two-layer shield design parameters. n - layer number starting from the external layer, B_o - external field, D_+ - external diameter, t - ferromagnetic thickness from Eq.(4.5), B_m - field in the ferromagnetic from Eq.(4.5), μ - permeability from the magnetization curve, S - shielding factor, B_{in} - field inside the shielding or the external field for a next layer, and Fm - ferromagnetic material.

The result of the finite element analysis (FEA) calculations[10] in a perpendicular field is shown in Fig. 4.23. According to this plot, the minimum field inside the shield is 0.23 G, which is 15 times higher than the naive estimate from Table 4.6. This means that the interaction between layers is important and has to be analyzed via more advanced FEA calculations.

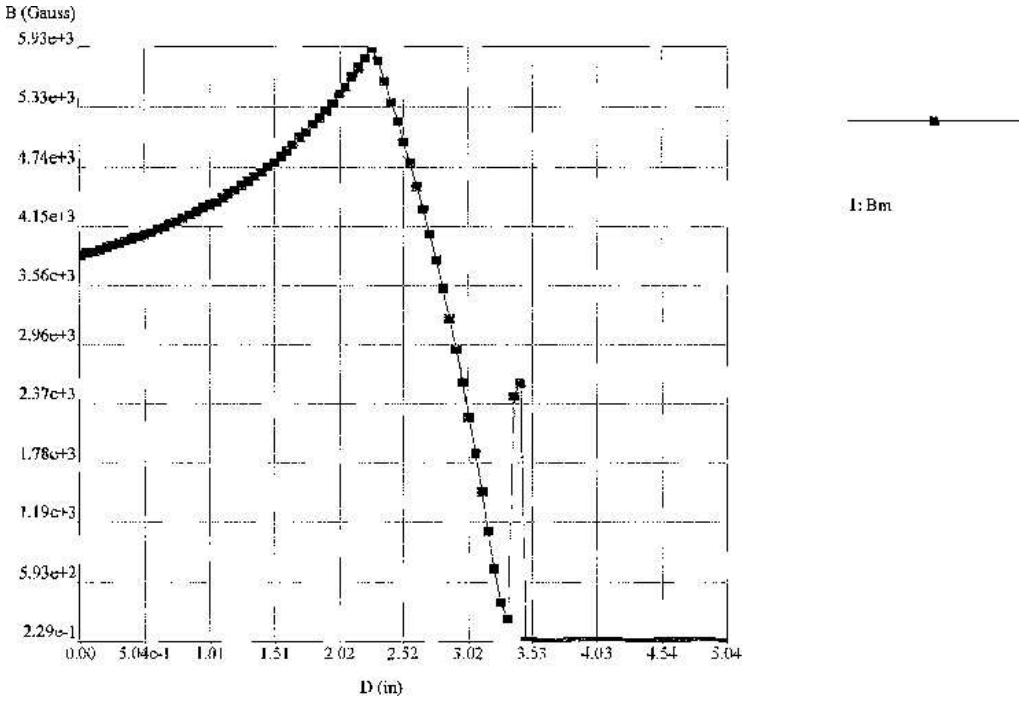

Figure 4.23: Sample of a field map for the 2-layer PMT shield in the 3000 G external field. The field in the center is 0.23 G.

In Fig. 4.24, the pilot design of a 3-layer shield is shown. A very high permeability Netic will be used for the external layer. For the middle layer, Hiperm-49 may be used, since it has higher permeability at lower fields. For the inner shielding, a very soft Co-Netic may be considered. The dimensions will be further optimized via FEA calculations.

In Fig. 4.25 we show a sample of the shield performance in a 1000 G axial field. This field map was obtained with the POISSON-Superfish program, which performs two-dimensional net calculations in limited space. The boundary conditions applied enforced that the field lines be parallel to the axis at the borders. An axial uniform field inside the area has been created with a current running over a thin cylinder. The resulting field in the center is determined to be 0.5 G. Further optimization is required in order to achieve 0.25 G in the region of the PMT dynodes.

[10] Calculations were performed by the Mu-shield Company (D. Grilli).

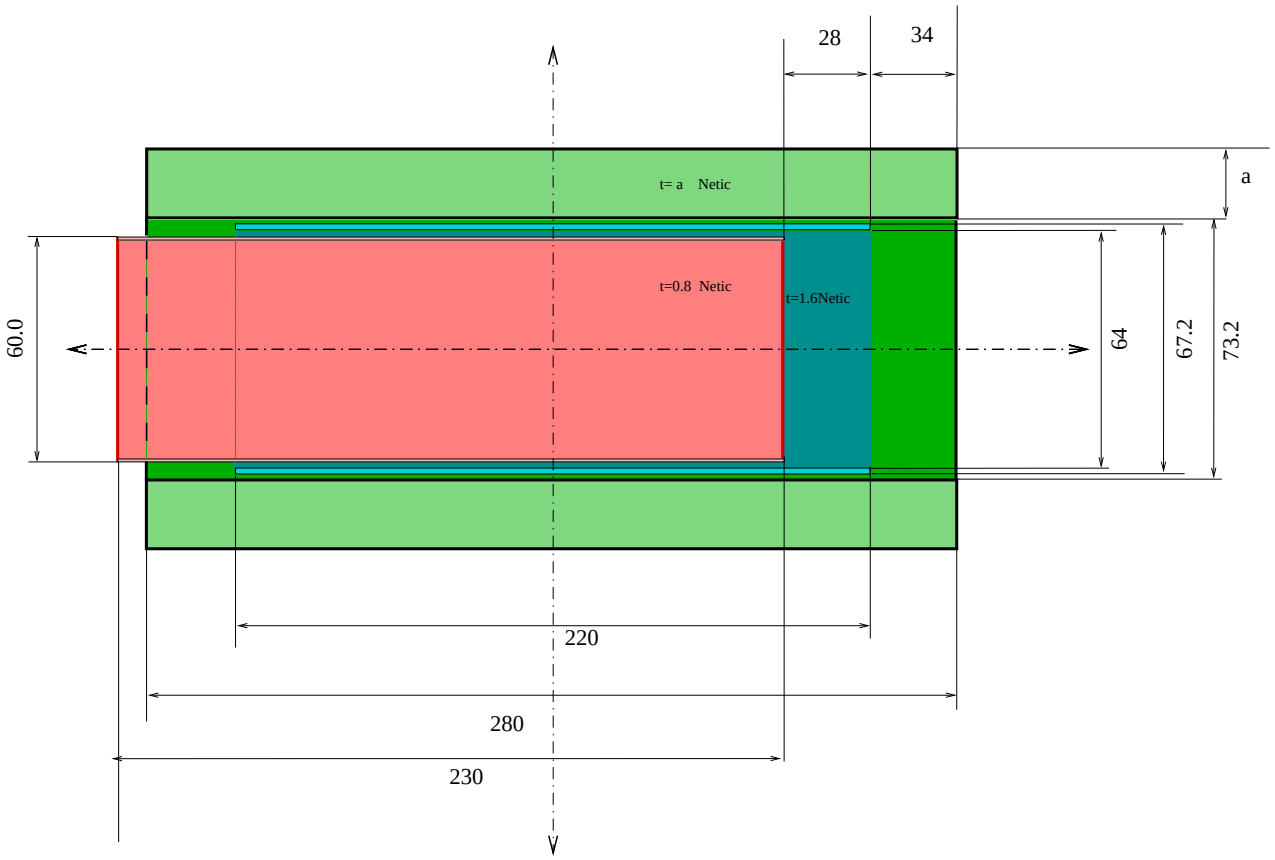

Figure 4.24: Pilot design of the PMT magnetic shield.

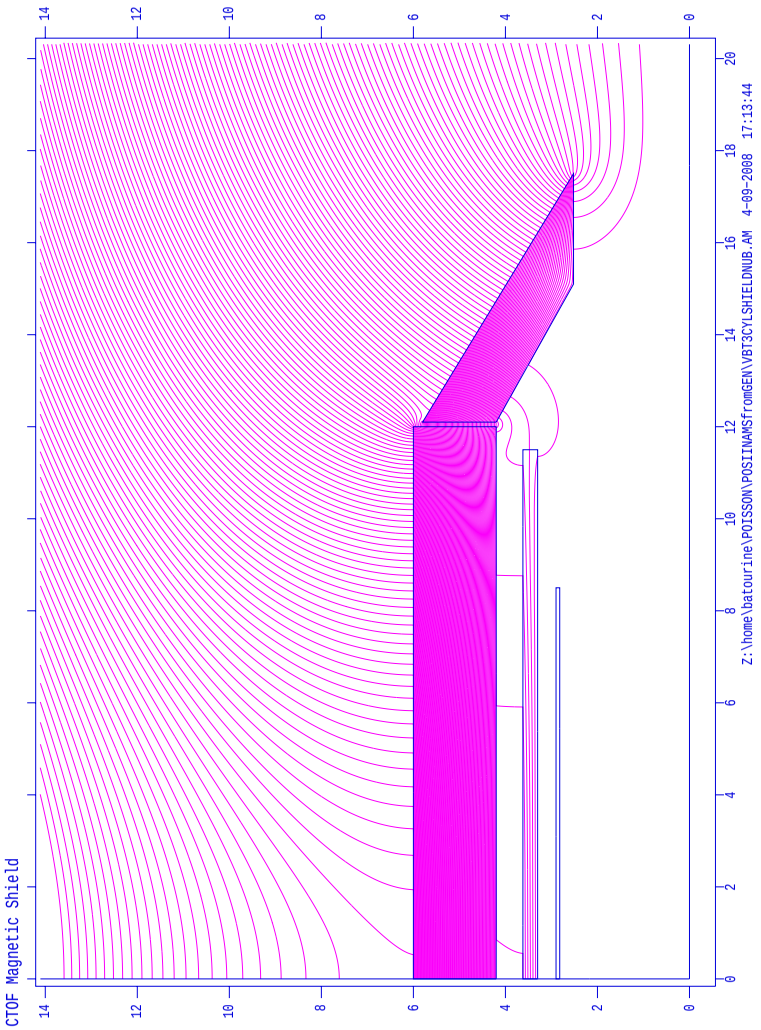

Figure 4.25: Sample of a field map for the 3-layer PMT shield in the 1000 G external field. The field in the center is 0.5 G.

Hybrid Magnetic Shield with Compensating Coil

The inner magnetic field strongly depends on the ferromagnetic properties, which are very sensitive to the fabrication technology. Therefore, we are looking for more robust protection of the PMTs. For this purpose, we can consider use of a combination of passive and active elements of shielding. In Fig. 4.26 we present the novel design of a magnetic shield with a compensating coil inside the shield assembly. A small current on the order of 0.1 A running through a 1-mm thick wire, is enough to reduce the inner PMT field to the desired values below 0.1 G. The detailed magnetic field map inside the PMT is shown in Fig. 4.27. As seen from this figure, the internal field is below 0.1 G, while the external field is 400 G.

The total current running through the compensating coil is ≈50 A, while the coil is ≈200-mm long. Thus it may contain 200 turns of 1-mm thick wire with a current of only 0.25 A. Certainly, higher fields may be exterminated with a higher currents in the compensation coil. Thus, hybrid magnetic shields are very promising. We plan further developments and prototyping of this type of shielding.

4.6 Optical Tests of Acrylic

In our studies of Acrylic light guides [291, 292], we have almost doubled the transmittance of our 1-m-long Acrylic light guides, fashioning it as a pyramid at the scintillator side and as a cylinder at the PMT end. In order to achieve the desired $\sigma_{TOF} \approx 50$ ps, a further ≈50% improvement of the light guide transmittance is necessary. Since the light guide geometry is almost optimized, a sensible gain may be achieved via modest improvement of several factors, e.g. we need shorter and more transparent Acrylic with better surface properties, more reflective wrapping, and better coupling to the PMTs.

First we concentrated on the optical properties of commercial cast Acrylic rods, which are of special interest for use as our light guides. Our primary motivation was a confusion with manufacturer's specifications for the Acrylic transparency. In their reference measurements, the transparency (92%–94%) has been determined as a percentage of the radiance passed through a ≈3-mm thick Acrylic film. Thus surface reflections are included into the specified numbers, which appears to be almost irrelevant to the bulk attenuation. Otherwise, the attenuation length would be unrealistically low. Moreover, a better reflection from surfaces is an advantage for light guiding. Hence, using the manufacturer's specifications, one may even

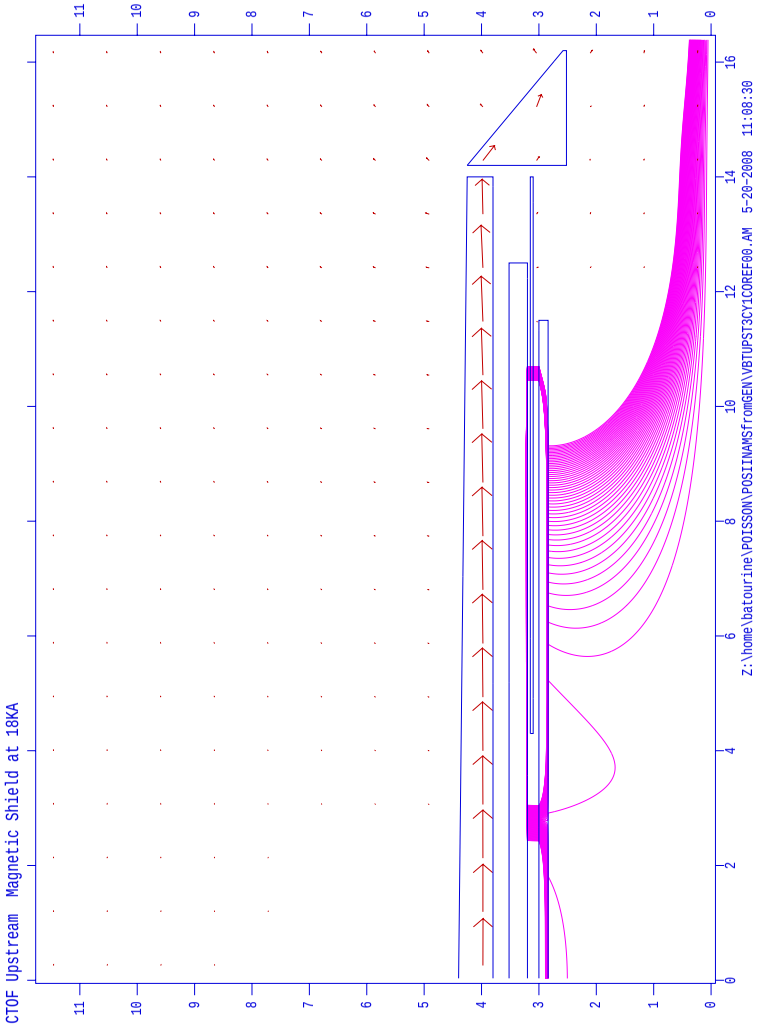

Figure 4.26: Hybrid magnetic shield for the R2083 PMT with the compensating coil wound around the H2431 assembly. At in the 400 G external field, the inner PMT field is below 0.1 G.

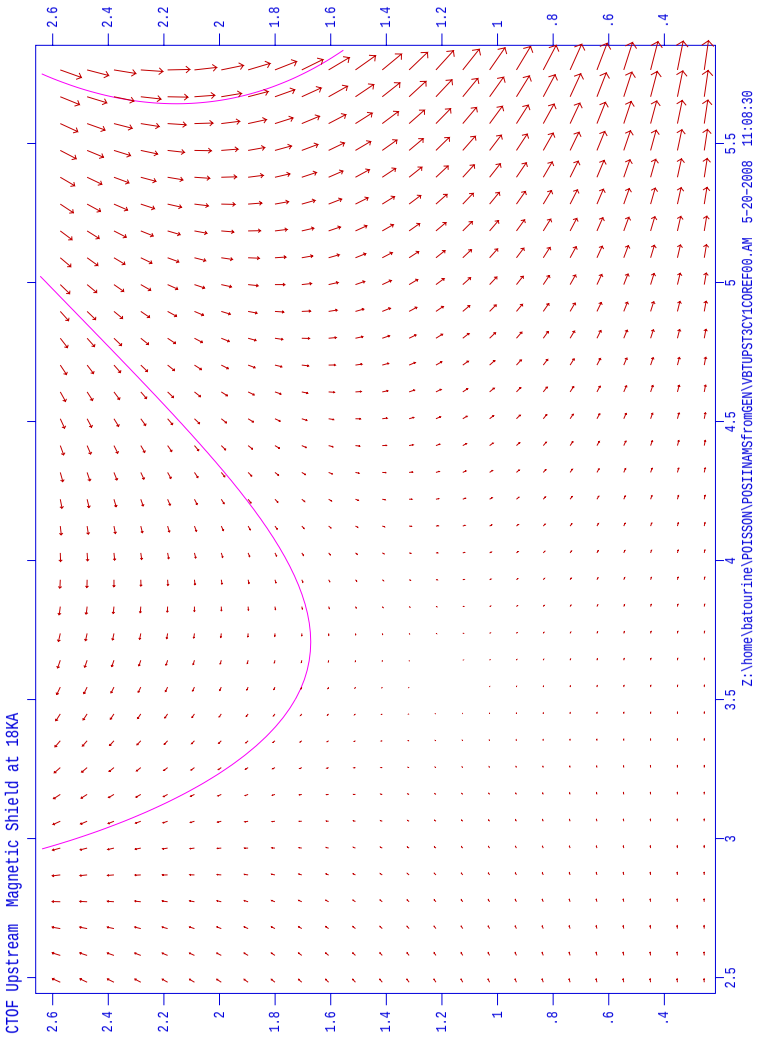

Figure 4.27: Hybrid magnetic shield for the R2083 PMT with the compensating solenoid around the H2431 assembly in a 400 G external field. "Zoomed in" field map inside the PMT. The length of arrows indicate the magnetic field. The maximum field, corresponding to the longest arrow, is 1 G. As seen from this figure, in the region of the PMT photocathode at an axial coordinate of ≈4 cm, the field is 0.1 G.

neglect what could be a good guiding material.

With this purpose, we have developed simple hand-held tools and methods for the express evaluation of Acrylic optical properties. Such methods are very desirable for the detector quality assurance during development and construction. We briefly describe these methods in the following sections.

4.6.1 Practical Transmittance Measurements

We define the practical transmittance of Acrylic light guides as the ratio of the light guide output radiation to the input radiation. These values are the main subject of our efforts, and therefore, we need to measure it quickly and precisely, with an accuracy of ≈1%. This allows us to monitor all steps of development and fabrication.

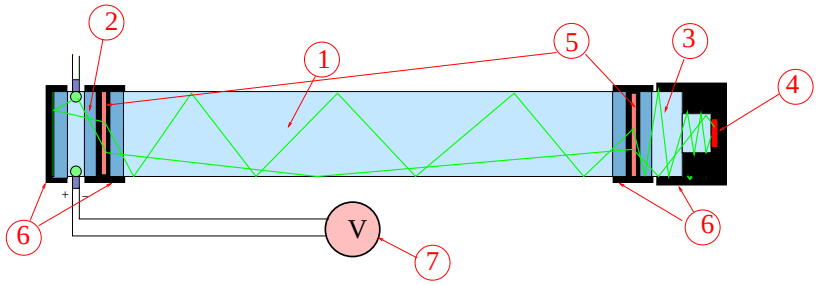

Figure 4.28: Transmittance measurements. (1) Acrylic rod, (2) light source, (3) Acrylic piece, (4) silicon photodetector, (5) Teflon film as a diffuser, (6) mount units, and (7) digital voltmeter.

We measure the practical transmittance in the following way (see Fig. 4.28). Diffuse light is injected into the Acrylic rod (light guide) along its axis from one side. At the opposite end we mount a IL1400 radiometer, which functions as a photodetector. In order to determine the transmittance T we compare two measurements of the transmitted radiation R. The

first value has been measured with a very short reference rod and the second value has been measured with a long Acrylic rod. The difference between the two measurements is due to the transmittance of the Acrylic light guide. This has been estimated as:

$$T = \frac{R(l_x)}{R(l_s)}, \tag{4.6}$$

where l_x is the length of the long rod under test (141.5 cm), l_s is the length of the short rod (2.52 cm), and $R(l)$ is the radiation measured with a sample of length l. We also determine a more "practical" attenuation length λ_p using:

$$\lambda_p = \frac{(l_s - l_x)}{ln(T)}, \tag{4.7}$$

assuming an exponential attenuation along the light guide.

For monitoring the luminosity we have developed a method based on precise measurements of the consuming power. For this purpose we record the voltage and current of the light source power supply. We observe a strong correlation between the precise voltage and the radiometer's readout. This correlation has been used to bring it to the same voltage, thus to the same radiation power.

In our first tests, the surface of the Acrylic rod remained as it was processed at the factory. We then had it polished and remeasured the transmittance. A sample of the measured radiance vs. voltage is shown in Fig. 4.29.

From this figure we conclude that the practical transmittance of this Acrylic rod is 55.6%. In order to test the reproducibility, we repeated measurements a second time and measured 58.8%. After changing to a stabilized power supply for the lamp, we measured 58.9%. Thus, we have approached the desired ≈1% level of accuracy in the transmittance measurement. Note that re-polishing the Acrylic rod at the JLab mechanical shop resulted in slightly reduced transmittance of 54.4%.

4.6.2 Bulk Attenuation Length and Surface Quality

We assume that attenuation of light in the bulk Acylic rod is proportional to the inhomogeneity and foreign inclusions. That is the reason for a luminous line in the bulk Acylic irradiated with a strong laser beam (≈1 W). Therefore, we assume that one can estimate the light attenuation length via precise measurement of the luminosity of this line.

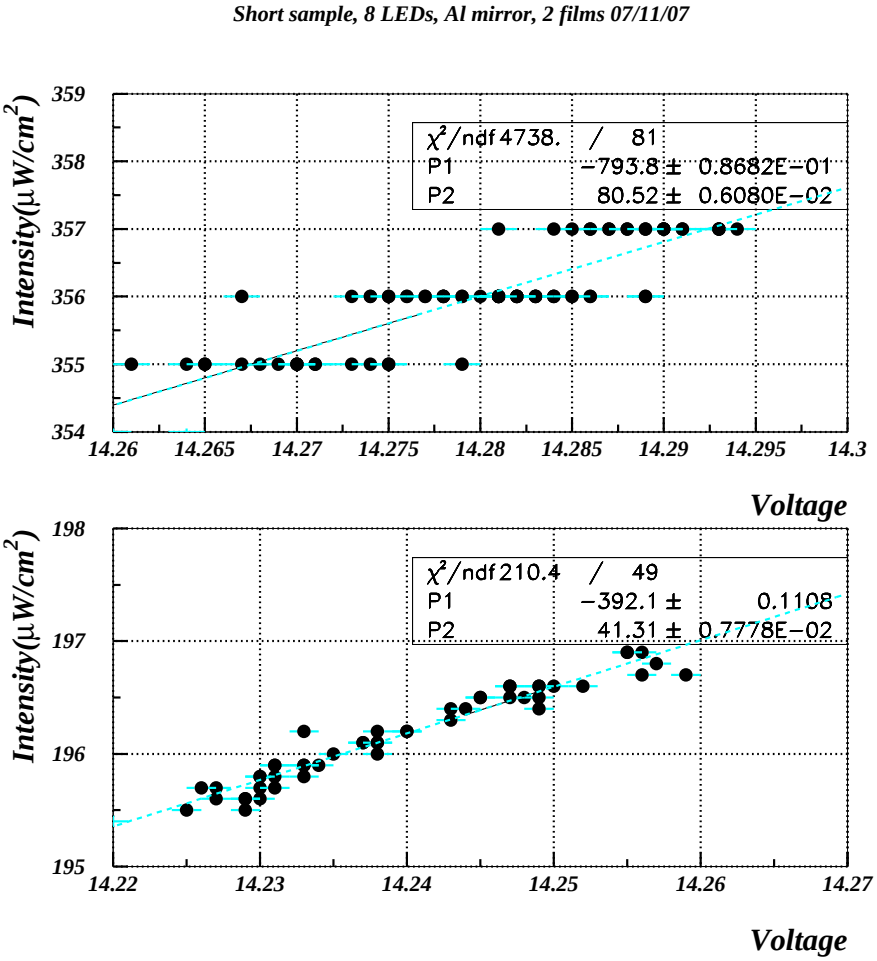

Figure 4.29: Practical transmittance measurements. Top panel: radiance of short reference sample. Bottom panel: radiance of the Acrylic rod under test. Vertical axis: radiometer readout. Horizontal axis: power supply voltage (V).

Absolute Measurements

With a narrow laser beam one can determine the absolute value of the bulk attenuation length. The setup and method is similar to that shown in Fig. 4.28. As in the former method, we compare two successive measurements performed with short and long samples, respectively. The only difference is that the laser beam is now axial. However, the sensitive area of the IL1400 photodetector (1×1 cm^2) is wide enough to cover the transmitted beam, which is just slightly wider than the original beam at the same distance. The bulk attenuation length was then determined using Eq.(4.7). The obtained values for various setups and monitoring methods are listed in Table 4.7.

Light (nm)	Power Supply	Monitor	λ (m)
Laser 475	$\approx$3 V	light	5.4 ± 0.7
Laser 532	$\approx$3 V	light	5.5 ± 0.7
Laser 532	3.0 V	current	6.7 ± 0.2
Laser 532	3.0 V	current	6.6 ± 0.2

Table 4.7: Bulk attenuation length (λ) of the reference Acrylic rod.

We have convinced ourselves that the measurements with a monitored voltage (current) of the power supply are more reliable than monitoring of the laser luminosity. Therefore, we determine the bulk attenuation length of the Acylic rods from our manufacturer as $\approx 6.65 \pm 0.5$ m, from the last two lines of Table 4.7.

4.6.3 Relative Measurements

We have developed a simple express method for relative measurements of attenuation in Acylic rods. For this purpose we detect the light scattered at large angles from the area exposed to the laser beam. A special hand-held tool provides a certain acceptance for the radiometer. The laser beam creates a luminous line across the rod. The radiometer reads the light scattered in transverse directions; the surface is excluded from the acceptance. We have checked 2-in rods from several distributors. The results are listed in Table 4.8.

The dispersal of the radiometer readout is significant. These values are calibrated in units of attenuation length, as was described in the previous section. The samples vary in

Purchased from	Technology	Comment, status	Radiance (nW/cm^2)	$\lambda(m)$
Prof. Plastic-0	cast,1.41 m	reference	17.7	6.65 ± 0.2
Plast. Craft-1	cast,148 mm	pol. butt-ends	16.1	7.31 ± 0.3
Plast. Craft-2	cast,153 mm	unpol.butt-ends	21.6	5.44 ± 0.3
Plast. Craft-3	cast,200 mm	unpol.butt-ends	32.1	3.66 ± 0.2
KNU sample	cast,205 mm	pol. butt-ends	≥ 18.2	≤ 6.1
McMaster-Carr Supp.Cmp.	extr.,400 mm	unpol. butt-ends	48.7	2.42 ± 0.2

Table 4.8: Bulk attenuation length (λ (532 nm)) of 2-in Acrylic rods from different manufacturers.

attenuation length[11] by almost a factor of three. The 2-in Acylic rods from Professional Plastic Inc. gives $\approx$18 nW/cm^2 in our hand-held tool. This value will be our future reference. The best readout (over the length) for the Acylic sample from South Korea is about the same. However, this sample has numerous local inclusions separated by a few mm. These inclusions manifest themselves as a reduced practical transmittance (λ_p $\approx$1.5-2 m) of the sample. In addition, due to the fact that this rod was machined (with a lathe) from a flat piece of Acylic, its surface was damaged, perhaps to the depth of a few microns, which resulted in a hazy view from the end of the rod.

We have selected Professional Plastic Inc. as our provider of Acylic for the CTOF project. However, we plan further casting for better Acylic samples.

4.6.4 Surface Quality Measurements

We have developed an express method for estimating the quality of a polished surface. This method is based on measuring the scattered light from the light guide surface illuminated with a laser beam. A special hand-held tool provides a certain surface impact angle and acceptance for the IL1400 radiometer. Note that in this case some part of the bulk scattered light is also accepted by the radiometer. However, it may be subtracted from the readout. The method has been calibrated with the reference Acrylic rod. The typical reference readout of the IL1400 with this rod was 20 nW/cm^2.

[11] The readout values are calibrated in units of attenuation length as described in Section 4.6.2.

Practical Transmittance After Polishing: Unfortunately, after we had the JLab mechanical shop polish our Acrylic samples, the surface readout increased by 50%. The scratches on the polished surface indicate that this problem was caused by the environment in the shop.

Practical Transmittance After Painting with Lacquer: The technique of vapor polishing is very close to painting. Therefore, we have checked the effect of painting on the practical transmittance of a previously buffed 20-cm long Acylic rod. The result is quite confusing. The surface readout dropped almost by a factor of two after painting with Acylic lacquer. The surface looks quite smooth. However, the practical transmittance of a 205-mm long sample dropped by $\approx$10%. The possible reasons for this unexpected effect are firstly, the higher refractive index, secondly, surface cracks due to aggressive solvents, and thirdly, worse transmission spectrum of the laser. All of this has to be carefully investigated in future.

4.6.5 Future Applications

We have developed express hand-held methods for measuring both the bulk and the surface attenuation of light guides. Our basic assumption on the proportionality of the attenuation to the scattering has to be verified. The developed methods allow us the following:

- to assure a proper attenuation length of Acylic in the light guides;
- to monitor the surface quality of light guides;
- to perform R&D for better light guide transmittance.

The immediate practical results of these methods include:

- we have selected the manufacturer of Acylic rods with the lowest attenuation;
- customer buffing does not necessarily improve the surface quality; other methods should be used;
- manufacturer's specifications should be interpreted with care.

We plan to use these methods for comparison of Acylic surfaces after ordinary buffing, flame polishing, and, perhaps, vapor polishing.

4.7 Studies with Monte Carlo Calculations

We have calculated the transport efficiency of the light guides using the code BARTIM described in the Appendix of Ref. [295]. In this Monte Carlo program, a photon is either totally internally reflected or reflected or refracted according to the Fresnel equations. Imperfections on the surface are modeled by reducing the total internal reflection co-efficient, IR, below 100%. The light that escapes the scintillator (or light guide) is specularly reflected with the appropriate reflection co-efficient R. The calculations were performed for the light guide configuration shown in Fig. 4.17. The dimensions given in Figs. 4.21 and 4.22 for the upstream and downstream light guides, respectively, were used. The beam was taken to be incident normally at the center of the scintillator. The transmission and loss of light at various positions are tabulated in Table 4.9.

Percentage lost at a given position	Upstream	Downstream
Scintillator - light guide interface	5.9	16.9
Absorption (all sections)	20.7	16.8
Lost in straight sections	25.0	17.6
Lost in bends	–	10.2
Lost at PMT	3.8	2.9
Transmitted	44.6	35.5

Table 4.9: Calculated values of the light guide transmission efficiency and losses for the two sides.

The parameters used in this calculation were R=0.9, IR=0.99, and a bulk attenuation length of 4 m in the Acrylic. It was assumed that the wrapping was a radiant mirror film VM-2000 from 3M as described and measured in Ref. [295].

4.7.1 Effect of Trapezoidal Shape of Scintillator on Light Propagation

The effect of the scintillator's trapezoidal cross section was investigated. It was found that only about 7.2% of the light generated in the center of the scintillator was lost, compared with a rectangular scintillator bar. The sloped sides of the light guide, that allowed the 46-mm cylinder to mesh with the smaller scintillator, may actually improve the light transport

efficiency. It directs the light upward, which is needed to match the direction of the light guide.

4.7.2 Effect of Coupling Angles Between Light Guides and Scintillators

The effect of changing the pitch angle of the upstream light guide from 18° to 30° was investigated. The transmission varied by less than 1%. Varying the downstream angle is more difficult as it would impinge on the forward acceptance. Therefore we did not investigate this.

4.7.3 Effect of Bending

The effect of varying the bend radius of the upstream light guide was examined. The radius was varied from 10.0, 11.75, 13.3 to 14.3 cm. Surprisingly, the results were insensitive to the radius of the bend. The smaller the radius, the smaller the losses in the bend, but this was compensated for by increased losses in the straight sections, which were now longer. This seems counterintuitive, but the bend radius appears to be sufficiently large that the losses are dominated by the length of a given section.

4.7.4 Effect of Up and Down Mirrors of Light Guides

The effect of the angle and the quality of the polish, IR value, are shown in the top and bottom panels of Fig. 4.30. There is a weak dependence on the lower angle, with a broad maximum at about 9°. This angle was used in the calculations shown in Table 4.9. The dependence on the upper angle is even weaker. We took it to be 9° also, but any angle between 7° and 15° is acceptable.

4.7.5 Light Guide Transmission Efficiency vs. Refractive Index

We compared the light guide transmission efficiency for two materials – Acrylic (n=1.49) and Lexan (n=1.58) – to estimate the benefit of using a more optically dense material for the light guides. If we assume equal attenuation lengths, Lexan transmits 10% more light, primarily by eliminating the losses at the scintillator – light guide interface. Unfortunately the transparency of Lexan is about half that of Acrylic. Taking this into account, the Lexan

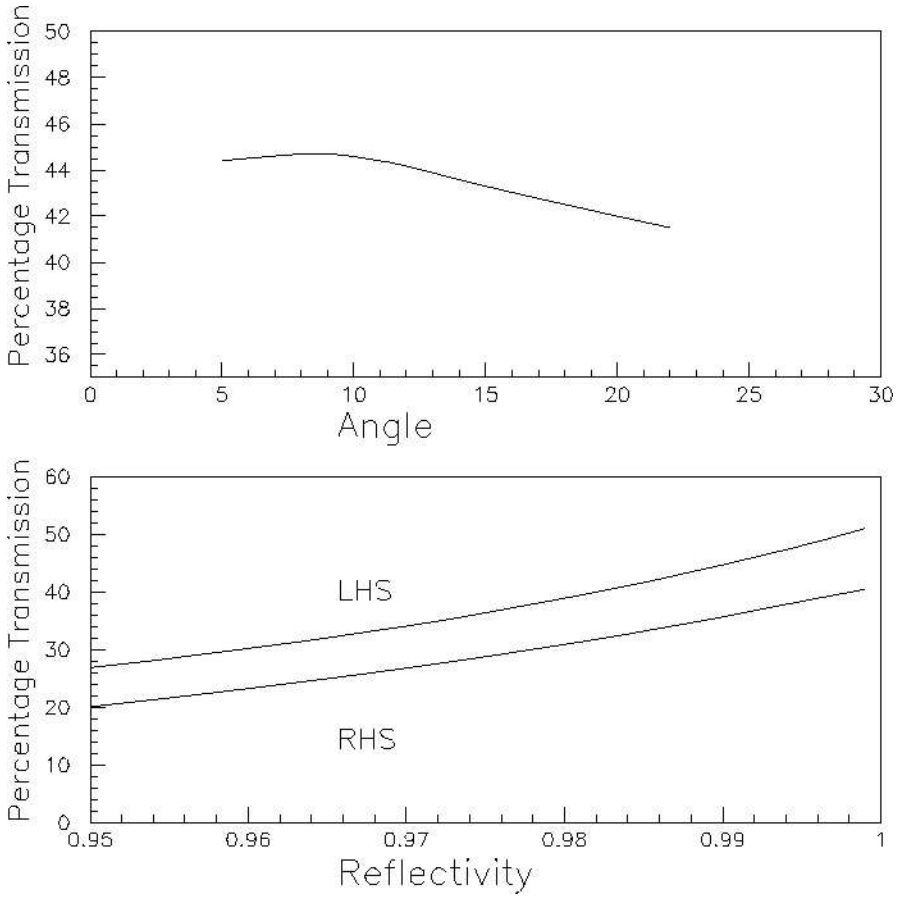

Figure 4.30: Light transmission vs. 1). the "down mirror" orientation angle (left panel) and 2). the reflectivity of the light guide surface (right panel).

transmits only 93% of the light. However, we have to consider this option, keeping in mind possible progress in the plastic industry.

4.7.6 Matching of the Light Guide to the PMT Entrance Window

The photocathode of the R2083 PMT is ≈1-mm thick in the center. According to the information obtained from the Hamamatsu experts, the shape of the photocathode is a sphere of 55 mm in radius with ≈ ±25° polar opening. On the other hand, the entrance window is flat. Therefore, the distance between the flat end of the light guide and the photocathode ranges from 1 mm in the center to 6 mm at the edge of the photocathode. That may cause significant loss of light through the edges of the PMT entrance window. If the scintillator is directly coupled to the PMT, 32% of the light output is lost. However after the light has been transported through the light guide, the phase space has been restricted to mostly forward angles. In this case the loss is only 8-9%.

4.7.7 Effect of the Photocathode Diameter

The number of reflections drops if the light guide has a larger diameter in its cylindrical part. The downstream light guide was modeled with a 52.0-mm diameter light guide. This transported about 6% more light to the PMT, but it was then lost. A larger diameter tube could collect most of this light, giving a net gain in the signal.

Another possibility that we have investigated is the use of a reducing cone at the end coupled to the PMT. The length of the cone was varied, keeping the overall length of the cone plus the last straight section constant at 250 mm. In accordance with Fig. 4.20, the optimum length of the cone was found to be about 50 mm. However this did not improve the light guide transmission. Once again the extra light was lost at the PMT. (Note, the effect of the curvature of the photocathode was taken into account in these calculations).

4.7.8 Effect of Light Guide Length

We investigated the effect of decreasing the light guide length by about 250 mm. This yields a transport efficiency of 48.8% for the upstream light guide and 37.8% for the downstream light guide. This is an ≈10% and 6% improvement over the numbers quoted in Table 4.9 for

1-m long light guides, respectively. This result may be used for further estimations of longer light guides.

4.7.9 Light Guides to Metal-Channel Photomultipliers

Finally, we investigated the possibility of using rectangular Hamamatsu metal-channel tubes with shorter light guides. If a tandem of such PMTs and on-board preamplifiers can tolerate magnetic fields up to ≈0.3 T, then it may be placed closer to the scintillator.

A tube that might be suitable is the Hamamatsu H8500 that has a photocathode 49 × 49 mm^2. The minimum light guide length is constrained by the requirement that the tubes (52 × 52 mm^2 external size) are at a radius sufficient to provide clearance between the tubes. This would be about 70 cm for the upstream light guide and 50 cm for the downstream one.

For preliminary estimations the light guides were taken to be straight guides 40-mm wide by 47.5-mm thick. The transmission and loss of light at various positions are tabulated in Table 4.10. The loss at the PMT was not estimated since the light guide is smaller than the photocathode and the photocathode is flat.

Percentage lost at a given position	Upstream	Downstream
Scintillator - light guide interface	5.9	16.9
Absorption	15.9	10.4
Lost from sides	19.9	16.0
Lost at PMT	N/A	N/A
Transmitted	58.3	56.7

Table 4.10: Calculated values of the light guide transmission efficiency and losses for rectangular light guides. The upstream side guide is 70-cm long angled at 22° and the downstream guide is 50-cm long angled at 45°. There are no other bends in the light guides. The light guides are coupled to rectangular Hamamatsu H8500 tubes 49 × 49 mm^2. The light guides are 40-mm wide and 47.5-mm thick.

This is a 30% and 58% increase in the light transmission efficiency, respectively, over the results in Table 4.9. However these gains will be offset by the reduced photocathode efficiency of a metal-channel tube, which is typically 20–22% vs. the 26–28% of regular tubes. However,

there will be a net gain on the downstream side and the pulse height on the two ends will be approximately equal.

4.8 Estimations of σ_{TOF} for Different CTOF Designs

According to Table 4.9, the light transport efficiency of an optimized straight light guide is LTE=44.6%. This value is in agreement with the previous experimentally determined value $44.2 \pm 4\%$. The LTE of the bent light guide is lower, 35.5% (see Table 4.9).

Using the previously measured σ_{PMT}=77.9 ps (see Table 4.1), obtained with a symmetric counter and 1-m long straight "pyramid" light guides, we can estimate the time-of-flight resolution of optimized asymmetric counters in the following way. As was shown in Ref. [304] for asymmetric light collection, the best timing is achieved by using a weighted average of the two PMTs with σ_A and σ_B respectively:

$$\sigma_{TOF} = \sqrt{\frac{(A\sigma_A)^2 + (B\sigma_B)^2}{(A+B)^2}}, \tag{4.8}$$

where A and B are proportional to the pulse heights (amount of light) of the two tubes, attached to straight (A) and bent (B) light guides, respectively. Note that $A \propto LTE_A$, as well as $B \propto LTE_B$. If we define $f = A/B$ and $\sigma_{PMT} = \sigma_A = \frac{1}{\sqrt{f}}\sigma_B$, then

$$\sigma_{TOF} = \sigma_{PMT}\sqrt{\frac{f}{1+f}}. \tag{4.9}$$

Resolution with 1-m Long Light Guides: Using data from Table 4.9 we find:

$$f = \frac{A}{B} = \frac{LTE_A}{LTE_B} = 44.6/35.5 = 1.256. \tag{4.10}$$

Thus for an asymmetric counter with 1-m long light guides we estimate:

$$\sigma_{TOF} = 0.746 \times \sigma_{PMT} = 0.746 \times 77.9 \text{ ps} = 58.1 \text{ ps}, \tag{4.11}$$

which is only 16% worse of the desired value 50 ps. However, that means that the amount of light would have to be increased by a factor of 1.16^2=1.346.

Resolution with 1.5-m Long Light Guides: If the total length of the light guides is 1.5 m, the amount of light will drop by ≈22% (see Ref. 4.7.8), thus the resolution will be ≈64 ps, which is 28% worse than the desired value. In this regard, we hope that improving the surface quality up to IR-0.995 using cast Acylic for the light guides and wrapping them with VM2000, may gain us a factor of ≈1.2 in the number of photons at the PMT window. Thus we may gain a total factor of $\approx 1.1^{-1}$ in the resolution, i.e. σ_{TOF} ≈58 ps. In a pessimistic scenario we may simply increase the thickness of the scintillator to 4 cm to get an additional factor of $\approx 1.15^{-1}$.

Resolution with Metal-Channel PMTs H8500 and Light Guides: Below we consider a counter with two H8500 MC PMTs viewing the scintillator via light guides $700 \times 40 \times 47$ mm^3 and $500 \times 40 \times 47$ mm^3 in size. In this estimation we assumed that in direct contact to the scintillator the resolution of the H8500 is the same as for the R2083. This is a reasonable assumption since the timing characteristics of these PMTs are almost identical. The estimate was done in the same way as above for the R2083 PMT, using the calculated parameters of the light guides given in Table 4.10. The resulting estimate for σ_{TOF} ≈49 ps is listed in Table 4.11, row 5. Of course, we plan to measure the resolution of the H8500 PMT in the environment of a high magnetic field.

4.9 Pilot Design with FM/MC Photomultipliers

In parallel we will develop the design with PMTs capable of operating in high magnetic fields. In addition to measurements with fine-mesh PMTs, we plan to measure the time resolution with metal-channel PMTs. Unlike fine-mesh PMTs, such photo-detectors are sensitive to magnetic fields. However, the signal rise time of metal-channel PMTs is significantly shorter compared to fine-mesh PMTs (0.8 ns vs. 2.7 ns). We plan to test H8500 PMTs, with a magnetic shield, up to fields of 0.2 T, most probably with amplification to the PMT signals, as was done in our studies with MCP PMTs.

In the low-field area of ≤0.3 T, fine-mesh/metal-channel PMTs may be used with light guides ≤0.8-m long. In addition, their sensitive surface is wider (49×49 mm^2), therefore an expanding light guide may deliver more light to the photocathodes.

The pilot design, utilizing advantages of fine-mesh/metal-channel PMTs, is shown in

Counter design LG $\leftrightarrow$ LG	f	LTE_l/LTE_r	$\sqrt{\frac{f}{1+f}}$	RF reference σ_{TOF}/ps	Light deficiency factor
Pyr. $\leftrightarrow$ Pyr. 1 m, 2$\times$ R2083	1.00	.44/.44	0.71	**55** ref. measur.	1.21
Pyr. $\leftrightarrow\supset$ Pyr. 1 m, 2$\times$ R2083	1.25	.446/.355	0.75	58 *estimate*	1.35
Pyr. $\leftrightarrow\supset$ Pyr. 1.5 m, 2$\times$ R2083	1.19	.372/.313	0.737	63 *estimate*	1.58
Bar $\leftrightarrow$ Bar 0.7 m, 2$\times$ H8500	1.03	.583/.567	0.712	49 *estimate*	0.94
MCP PMT$\leftrightarrow$MCP PMT 2$\times$ Burle 85011	1.	1./1.	0.71	61 at 1.0 MHz 50 at 0.1 MHz	1.5
CTOF counter (1.4m & 1.6m)	1.33	.4/.3	0.76	60 *estimate*	1.4

Table 4.11: TOF resolution for different CTOF counter designs. The measured reference values from lines 6, 9, and 10 of Table 4.1 were used to evaluate σ_{TOF}.

Fig. 4.31. The scintillators are of the same shape as in the design with conventional R2083 PMTs. The upstream and downstream light guides, delivering light to the area of tolerable magnetic fields are 86-cm and 50-cm long, respectively, with corresponding pitch angles of 21° and 45°. These parameters provide room for the 50 adjacent H8500 PMTs at $r \approx 55$ cm.

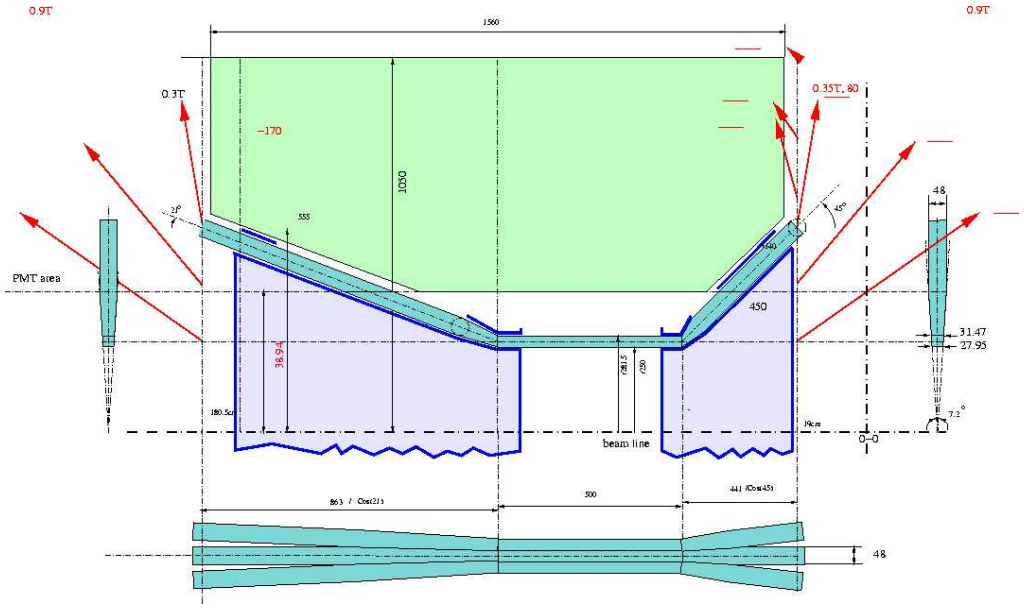

Figure 4.31: The design of the CLAS12 CTOF counter with H8500 PMTs from Hamamatsu. Acrylic light guides may be rectangular in cross section at the photocathode (49×49 mm^2). The length of the upstream/downstream light guides is 863/441 mm, respectively. At the scintillator end, the light guides and the Bicron-408 are trapezoids in cross section. Magnetic fields are shown with vectors.

The light guides will be rectangular in cross section at the PMT side for the metal-channel H8500 PMTs. At the scintillator side, they will have a trapezoidal cross section of variable size, which couples to the cross section of the scintillator at the corresponding end. Up to a certain radius of ≈39 cm, the light guides are in close contact to each other, thus forming a body enclosed between two cones. Above this radius the light guides form a "fan". Similar to the light guides for the R2083 PMT design, they have "focusing mirrors" at the scintillator side. These relatively short straight scintillators may be easily machined or casted. The expected resolution (≈49 ps) of counters with metal-channel PMTs is listed in Table 4.11.

In the design with fine-mesh PMTs, the light guides may be even shorter. We plan future resolution tests with fine-mesh PMTs of large sensitive area, such as the R5924, instrumented with realistic light guides.

4.10 Pilot Design with Micro-Channel Plate PMTs

A general view of the pilot CLAS12 CTOF counter with 85011 MCP PMTs from Burle is shown in Fig. 4.32. A detailed view is shown in Fig. 4.33. One multi-anode PMT is supposed to convert the light from two scintillators, left and right.

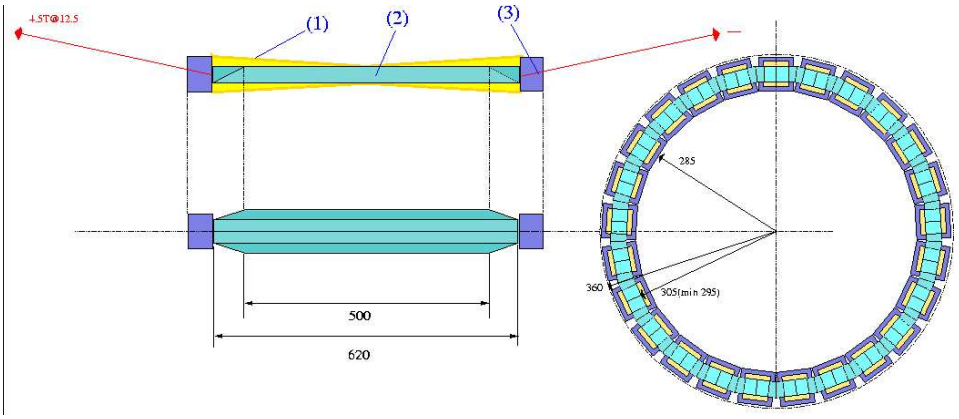

Figure 4.32: General view of the CLAS12 CTOF counter with Burle 85011 MCP PMTs. (1) Mirror film, (2) two adjacent scintillators, and (3) Burle 85011 multi-anode assembly.

The outputs of the corresponding anodes will be assembled to produce a common signal for each scintillator. The scintillators, Bicron-408, are machined with a trapezoidal cross section. We note that the inner radius can be reduced in two different ways, provided that the sizes of the PMT housings remain the same (72×72 mm^2). The first way is via implementing staggered counters, as shown in Fig. 4.34. In this case r_{min}=206 mm, but the length of scintillators has to be increased by 52 mm (the thickness of the 85011 PMT assembly). The second option is to reduce the number of counters from 50 with r_{min}=275 mm to 44 with r_{min}=250.4 mm.

4.11 Outlook

We have experimentally verified that the resolution of our test installation is mostly dictated by the statistics of the primary photons. We have measured a reference resolution for the setup of three counters with long light guides. With this reference value we have estimated the time-of-flight resolution (relative to the RF signal of the accelerator) for different counter designs. Estimations were done using Eq.(4.8) and Eq.(4.9). The resulting values are listed in Table 4.11 together with the deficiency factors in the amount of light.

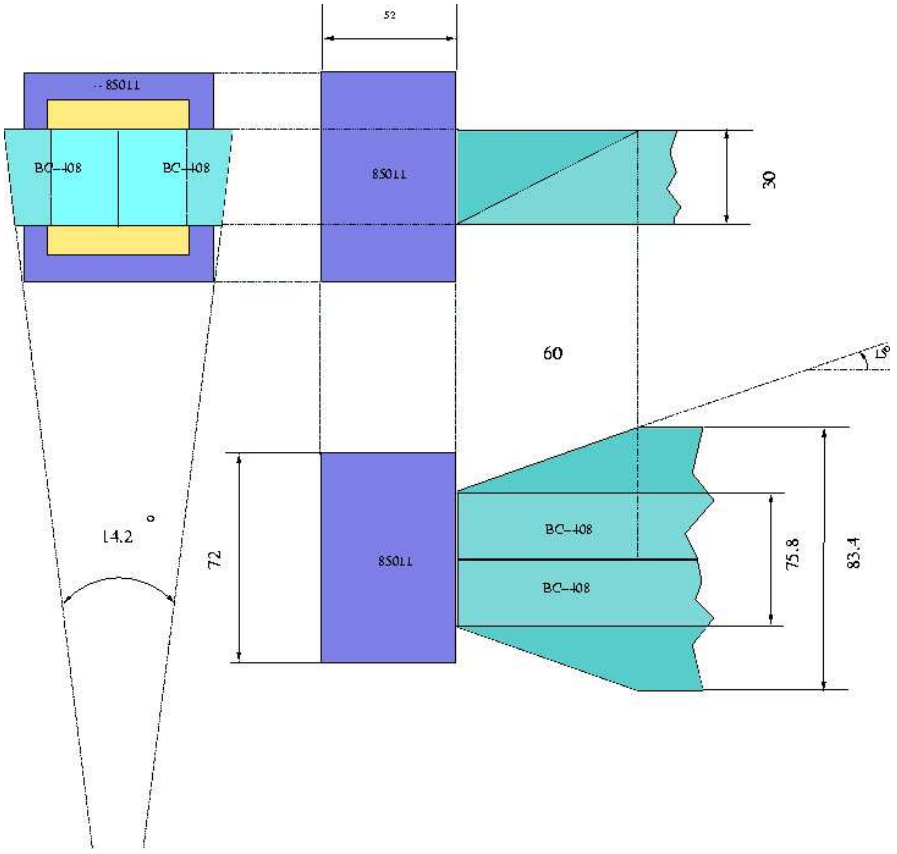

Figure 4.33: A closer view of the CLAS12 CTOF counter with Burle 85011 MCP PMTs.

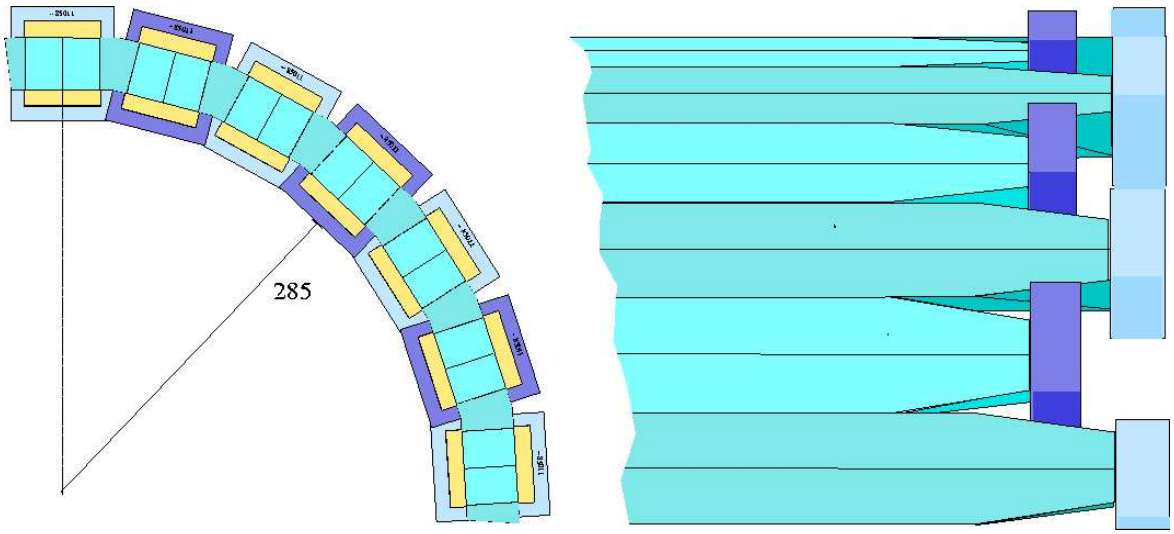

Figure 4.34: Staggering the CTOF counters with Burle 85011 MCP PMTs.

CTOF Counter with Conventional R2083 PMTs: For the current design with 1.3–1.5m long light guides (row-7) the resolution is likely to be improved to the desired value with better technology for the light guide production and further optimization of the design, including bent and thicker scintillators (≈4 cm). The desired increase of total transmittance is about 40%, i.e. the transmittance has to be 50% and 60% for the downstream and upstream light guides, respectively.

CTOF Counter with MCP PMTs: Recently we found a way to form a dense barrel with MCP PMTs from Burle, or similar PMTs from Hamamatsu. The design with MCPs looks promising. According to our recent measurements with Burle 85011 PMTs, the timing resolution may be as good as 61 ps (see Table 4.11, row-6) at a 1 MHz rate. It may even be as good as 50 ps at a 0.1 MHz rate. Thus this approach may be an alternative to the counters with 1.5-m long light guides at fields below 1.5 T. In order to operate at higher fields, short light guides (≈50 cm) have to be implemented, but in combination with the reduced QE, this will have a significant adverse effect on the resolution.

The main disadvantage of MCP PMTs is that their counting rate capability is significantly lower compared to ordinary PMTs. This is an effect of a positive charge, created by the avalanche on the inner surface of the micro-channels, which leaks out slowly through the resistive material of the micro-channel plate. This effect has been reduced with a combination of a MCP PMT operating at low high voltage and a preamplifier [290]. We hope that progress on the design with MCP PMTs may be achieved via further development of the on-board preamplifier. In addition, a new MCP PMT from Burle with 10 and 5 /*mu*m may be available in the future. With their smaller capillaries, they may withstand higher magnetic fields and higher counting rates.

CTOF Counter with Fine-Mesh/Metal-Channel PMTs: As seen from Table 4.11, the design with the H8500 PMT (row-5) looks promising. We hope that the actual light transmission efficiency will be better for light guides shaped as "pyramids" with focusing mirrors. However, a strong magnetic shield is required in order to use 1-m long light guides. We plan a further study of light guides with Monte Carlo simulations and Finite Element Analysis of multi-layer magnetic shields.

The advantages of metal-channel PMTs are as follows: 3.5 times lower signal rise time

compared to fine-mesh PMTs and higher counting rate capability compared to micro-channel plate PMTs. We plan to make a CTOF counter prototype with magnetic field shielding and perform resolution tests in magnetic fields $\leq$0.2 T.

Fine-mesh PMTs have an advantage of experimentally confirmed immunity of their time resolution to magnetic fields up to 0.6 T [299]. However, due to $\approx$3.5 times longer signal rise time, their resolution has to be worse. In the near future we plan to perform resolution tests of fine-mesh R5924 PMTs as a component of a realistic CTOF counter with 0.8-m long light guides.

4.12 Construction

The steps involved in the construction of the CTOF scintillators are listed below along with general quality assurance guidelines.

1. **Wrapping the light guides with reflecting & opaque materials:** The reflecting material will be procured in sheets of size $14'' \times 18' \times 65\mu$m. The sheets must be precisely assembled to avoid gaps that could introduce light leaks. Sheets of Enhanced Specular Reflector (ESR) from 3M-Vikuity will be glued to the inner surface of the opaque plastic (Tedlar from DuPont). Therefore, the opaque plastic will be shipped with adhesive on one side.

   The thickness of the reflecting wrapping (65 μm) of the scintillators and light guides has to be uniformly equal, otherwise the radius of the scintillating barrel becomes larger. No double layers are allowed.

   All wrapping materials must be handled with gloves to avoid deposits. A clean work area should prevent dust and debris from adhering to the surfaces, especially to the adhesive side of the opaque plastic. All wrapping steps must ensure that no wrinkles or air pockets are introduced.

   The bent part of the long light guides cannot be wrapped with the ESR sheets. Instead, a narrow customer-made tape of ESR may be used for the helix-like wrapping. All seams have to be at the outer surface of the cones formed by the light guides. The wrapping has to stop at $\approx$1 mm from the ends.

2. **Scintillators:** The scintillators will be procured by EJ Technologies with diamond cut surfaces according to our specifications. During the wrapping process care must be taken that all seams are at the outer surface of the barrel, i.e. at the wide side of the scintillator. All wrapping has to stop ≈1 mm away from the ends.

3. **Scintillating barrel mounting:** Careful visual inspection of the rubber foam tape that is being employed to protect the scintillators from direct contact to the metallic backing structure. Also procedures must be carefully followed to be sure that any tape employed has good adhesion to all contact surfaces. Sufficient measurements must be made when positioning the scintillators on the support structure to ensure that all alignment tolerances are met.

4. **Boot attachment:** Light tight boots must be attached prior to mounting the light guides. The light tight boots must be individually inspected for holes, seams, and proper joining. Any boots with noticeable defects should be discarded.

5. **Mounting light guides to the supporting cones:** Care must be taken to avoid any damage to the light guides. The light guides will be spring-loaded along their axis in order to provide good optical contact to the scintillators. This load has to be carefully adjusted for each light guide after final assembly of the CTOF. Careful visual inspection must be made of the rubber foam tape that is being employed to protect the light guides from direct contact to the backing structures. Also procedures must be carefully followed to be sure that any tape employed has good adhesion to all contact surfaces.

6. **Optical contact:** Procedures to eliminate air bubbles in the optical grease between the scintillators and light guides must be followed.

7. **Joining the barrel to the light guide cones:** Care should be taken to ensure proper orientation of the three parts in radius, azimuth, and the z direction. The stagger structure of the scintillators and light guides must ensure precise compliance between the scintillators and light guides. The final alignment will be guaranteed by conic flanges. Prior to doing this, all optical contacts must be inspected.

8. **PMT mounting:** The PMT and magnetic shield will be first assembled together to form a single unit. The PMT inside will be spring-loaded in the axial direction for good

and gentle mechanical/optical contact to the light guide. These 100 units have to be mounted on two supporting rings at the upstream and downstream ends of the CTOF. Care must be taken to provide good optical contact with the light guides and to ensure proper orientation along the axial axis. The units must be secured from any possible future displacements under magnetic forces from the solenoid.

9. **Workmanship:** Accuracy in workmanship is very important as mishandling and poor construction procedures can reduce the detector resolution noticeably. All measurements have to be precise and all construction procedures and tolerances have to be rigidly followed.

4.13 CTOF System Quality Assurance Procedures

This section provides a list of quality assurance (QA) steps prior to the construction of the CTOF system.

Scintillators, light guides, and reflecting materials: Upon arrival of the scintillator material and light guides from the manufacturer, all pieces should be visually inspected with UV light for scratches, marks, and defects. All pieces should be measured for tolerances. The light transmission efficiency of each light guide must be measured with a radiometer and compared to the reference samples. Any product outside of acceptable size, light transmission, or condition should be shipped back to the manufacturer. The all-plastic pieces have to be packed properly for storage until the assembly period.

In all steps of handling the scintillators and light guides, white gloves and lab coats should be worn. Wrapping with reflective films has to be performed in the clean room. Any naked plastic should be covered if it needs to be left exposed for any period of time. The scintillator material is very susceptible to damage from scratches, heat, cold, shock, and alcohol. Care must be taken at each step of the construction process to monitor the environmental conditions.

Magnetic shields and light guide handling: The PMTs and magnetic shielding are susceptible to damage from shock, and care must be taken to handle them with care both before and after they are mounted. Care must be taken to avoid any damage on the light

guides and PMTs during handling and installation. The magnetic shielding has to be reliably secured in order to avoid even small displacements due to magnetic forces induced by the solenoid. The magnetic forces may be very strong and the forces applied to the magnetic materials have to be estimated and taken into account.

Detector testing: HV checks of the detectors should be performed and the dark current should be measured for each PMT. Any measured dark current more than 100 nA is an indication of a possible light leak. Attempts to find light leaks should continue to ensure that the measured currents are the same in the testing area with the lights on and off. Light guide transmission measurements should be performed on all light guides to ensure that they are within specifications.

Installation: Quality assurance during installation must involve procedures for proper and safe handling of the detector structures to be sure that they are not subject to any shocks or stresses, as well as to ensure that support frames and lifting structures do not put any stresses on the light guides, scintillators, or PMTS. Care must be taken so that the installation procedure does not affect the integrity of the surface wrapping. Finally, procedures must be followed regarding voltage and signal connections to the detectors to be sure that all cables are labeled and sufficient strain-relief or slack is allowed so that no stresses are put on the detectors or readout electronics.

4.14 Personnel Safety Issues

There are several important areas of personnel safety concern:

1. **Chemical injury:** The construction procedure involves the use of glues and epoxies that can cause irritation if they come in contact with skin or eyes. Safety precautions dictate the requirements to use gloves when mixing or handling glues, epoxies, or paints, as well as appropriate eye protection.

2. **Cutting tool injury:** A sizeable number of construction tasks involve the use of scissors and Exacto blades. Extreme care must be taken when undertaking activities using these instruments to avoid personal injury and cuts.

3. **Fall protection:** During construction the light guide and scintillator assemblies will have to be handled and manipulated. Personnel protecting shoes and helmets must be used when lifting or supporting loads. Operators will employ appropriate harnessing and fall protection. Signage and personnel barriers will be installed to prevent trip and fall hazards.

4. **Magnetic fields:** High magnetic field environments require that only non-magnetic tools and hardware should be used for assembly in order to avoid potential damage to the detector components or injuries to personnel.

4.15 CTOF System Safety Issues

The main areas of the detector safety concern are the following:

1. Grounding scheme - necessary to prevent electrical shock.

2. Elevated work areas - access to the CTOF system for installation and repairs will be via man-lifts and crane lifts.

3. Staging and installation - special procedures will have to be detailed for the installation of light guides and PMTs, as well as of the upstream and downstream assemblies.

4. Cable installation - floor grating will be removed and care should be taken to prevent personnel injury and damage to unprotected cables.

5. Magnetic shielding - in addition to gravity, the force induced by a very high magnetic field has to be taken into account in the design of the detector supports.

It is expected that the safety issues involved with this work involve low risk for personnel injury or equipment damage, especially with the use of appropriately planned and supervised work activities.

4.16 Conclusions

The development of the prototype detector is attributed to the Nuclear Physics Group of Kyungpook National University. Two experienced researchers and four students are engaged in

this R&D work. KNU provides infrastructure for this project: there are mechanical, computer, and administrative services. Generous private workshops situated around the University are available as well.

The R&D is done in connection with the Hall B staff physicists at JLab. The significant support of the JLab Detector Group made it possible to perform resolution measurements with a novel micro-channel plate PMT. Monte-Carlo simulations were performed at Bonner Nuclear Laboratory at Rice University. A NIM paper and 5 CLAS-Notes describing the R&D results have been completed.

The Korean Advanced Institute of Science and Technology will provide expertise and assistance in testing the prototype counters in a magnetic-field environment. Test measurements will be carried out at the 50-MeV proton beam of the M-50 cyclotron of Seoul University. The approval for such measurements and the appropriate funding have been obtained. The test measurements of the timing resolution in the magnetic field are scheduled to begin in the second half of 2007. The results of these measurements will be the basis for the construction of the first real counter, which will take place in the fall of 2008. However, prior to launching this program, measurements with long light guides will be performed.

Chapter 5

FTOF System

5.1 FTOF System Overview

The Forward Time-of-Flight System (FTOF) will be a major component of the CLAS12 forward detector used to measure the time-of-flight of charged particles emerging from the target. The average path length from the target to the FTOF counters will be roughly 650 cm. The requirements for the FTOF system include excellent timing resolution for particle identification and good segmentation for flexible triggering and prescaling options. The design parameters were chosen to allow for separation of pions and kaons up to roughly 3 GeV. The most energetic particles are produced at small angles. The system specifications call for a time resolution of σ_{TOF}=80 ps at the more forward angles of CLAS12 and 150 ps at angles larger than 36°. The system must also be capable of operating in a high-rate environment. The maximum counting rate occurs in the forward direction where, at an operating luminosity of 1×10^{35} cm^{-2}s^{-1}, the average rate per scintillator is approximately 250 kHz.

The discriminated scintillator signals will be used in certain situations in the CLAS12 Level-1 trigger. Therefore, the system must provide signals representing a uniform response with adequate granularity to select particles reaching the detectors. The timing in the trigger hardware will be limited by the flight time variations between fast particles (e.g. electrons) and slow particles (e.g. protons), which can be as large as 50 ns. Therefore, precise timing information will only be achieved in off-line software analysis using the momentum and position measured with the drift chamber system.

The FTOF system will also be used for energy-loss measurements in specific instances.

Pulse height information, being directly proportional to energy deposited, provides an independent means for the identification of slow particles. In this regard, the flight time can provide for a more accurate measurement of particle energy than magnetic analysis for slow particles, where the effects of multiple scattering are the largest.

In order to meet the requirements for the tight timing resolution, the major considerations in the design of the FTOF system are:

- *Scintillator Size:* The overall size of the system will demand careful consideration of light collection in order to optimize the time resolution of the system. Also, the width of each scintillator determines the granularity of the scattering angle definition in the trigger.

- *Geometry:* The projected space behind the coils of the main CLAS12 torus is inactive and therefore useful for locating the light guides, photomultiplier tubes (PMTs), voltage dividers, and cables. The remaining area in the forward direction is the fiducial region of the detector and must be covered with scintillator counters.

- *Magnetic Field:* The PMTs will have to be properly shielded from the stray magnetic fields of the CLAS12 torus.

- *Crossing Tracks:* Particle trajectories from the target can intersect adjacent TOF counters. Therefore light from both counters will have to be summed to optimize particle identification in the data analysis.

Each component of the design must satisfy these design constraints and be optimized against cost considerations.

In each sector of CLAS12, the FTOF system will be comprised of three sets of TOF counters, referred to as panels (called panel-1a, 1b, and 2), in each sector. Each panel consists of an array of rectangular scintillators with a PMT on each end. Panel-1 refers to the sets of counters located at forward angles (roughly 5° to 36°) (where the two panels are necessary to meet the 80 ps resolution requirements) and panel-2 refers to the sets of counters located at larger angles (roughly 36° to 45°). The positioning and attachment of the FTOF system panels to the forward carriage of CLAS12 are shown in Fig. 5.1.

The panel-1 counters will consist of the current CLAS panel-1 TOF counters (called panel-1a) and a new set of panel-1 counters (called panel-1b). The existing panel-1a counters

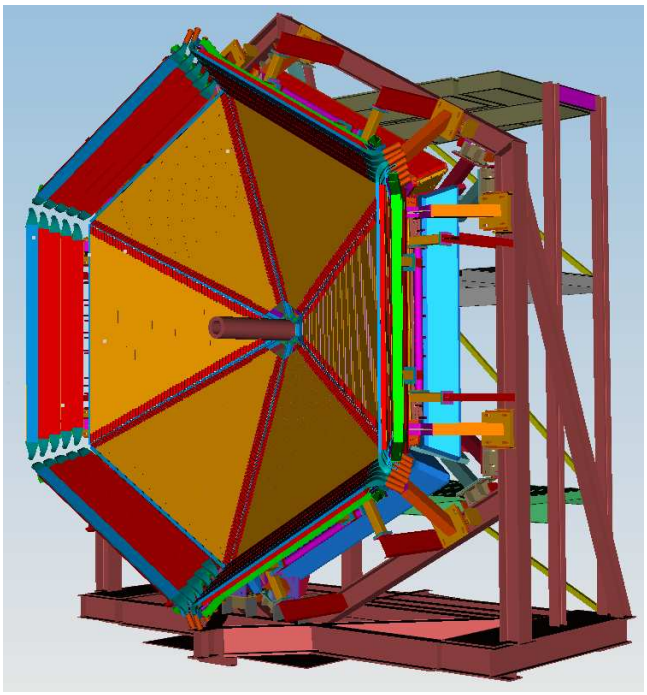

Figure 5.1: View of the FTOF counters for CLAS12 highlighting the location of the panel-1 and panel-2 counters. This figure was generated from our 3–D CAD model.

consist of 23 scintillators, each measuring 5.08-cm thick and 15-cm wide. The lengths of these counters range from roughly 32 cm at the smallest scattering angles to roughly 375 cm at the largest scattering angles. The scintillators are constructed from Bicron BC-408 and are read out through short acrylic light guides to 2-in Thorn EMI-9954A PMTs. The new panel-1b counters will consist of an array of 58 scintillators constructed from Bicron BC-404 scintillator for the shorter counters and BC-408 for the longer counters, each 6-cm wide and 6-cm thick with a range of lengths to match the panel-1a counters. This new panel will be mounted off of the forward carriage in front of the existing panel-1a counters. One sector of the FTOF system highlighting the panel-1 counters is shown in Fig. 5.2. Note that the existing panel-1a arrays extend down to only 8° in the CLAS geometry. As the positioning of the forward carriage in CLAS12 becomes finalized, we will then decide on the number, lengths, and widths of additional scintillator bars to add at the small-angle apex of the panel-1a arrays to ensure acceptance down to 5°.

The panel-2 counters will consist of the current CLAS panel-2 TOF counters, which include 11 22-cm wide, 5.08-cm thick scintillators in each sector. The length of these counters ranges from roughly 370 cm to 430 cm. The scintillators are constructed from Bicron BC-408 and are

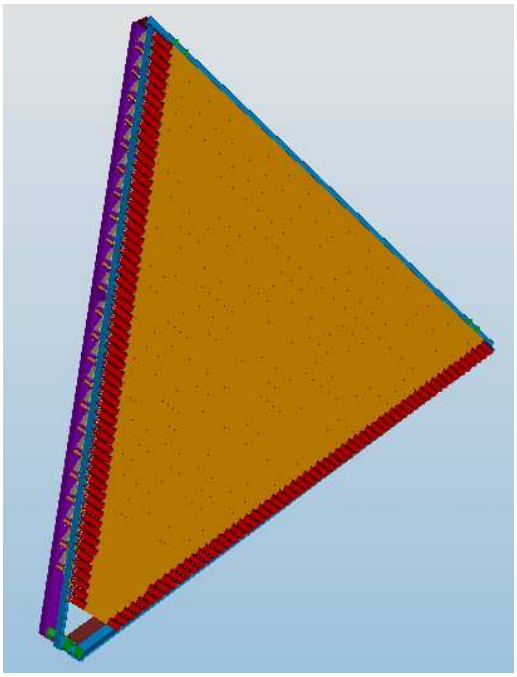

Figure 5.2: View of the FTOF panel-1 counters for CLAS12 for one sector from the 3-D CAD model of the detector.

read out through curved acrylic light guides to 3-in Philips XP4312B PMTs. These scintillators are included to give complete acceptance for outbending charged particles incident upon the CLAS12 drift chambers. Monte Carlo simulations are currently underway to determine how many of the panel-2 counters will need to be included in CLAS12 to match the acceptance of the drift chamber system. Note that the exact number of the panel-2 counters that is required depends directly on the final size of the Region 3 chambers (which is still being optimized). Given the present design of the outermost CLAS12 drift chambers, it appears that no more than 5 to 6 of the existing panel-2 counters will be required in each sector.

In the current CLAS detector, the panel-2 counters are mounted to the side carriages (called the north and south clam shells). However, in the CLAS12 design these panels will be mounted on the existing forward carriage. Work is presently underway to engineer and design the supports and attachment scheme. A schematic representation of the layout of panel-1 and panel-2 for a single sector of the existing CLAS TOF system is shown in Fig. 5.3.

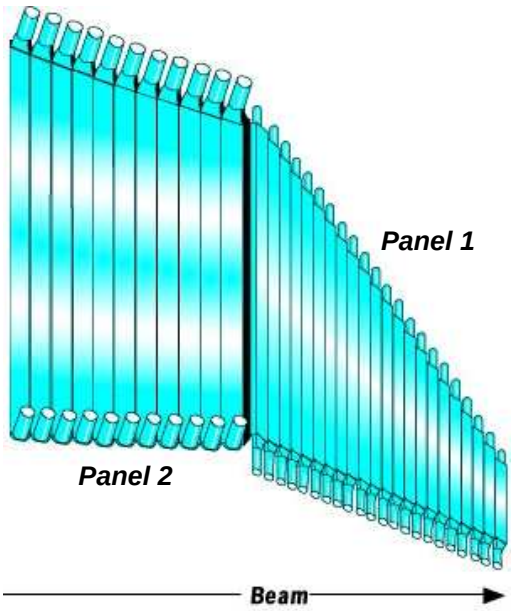

Figure 5.3: View of the forward TOF panel-1 and panel-2 scintillators for a single sector for the existing CLAS TOF system.

5.2 Design Requirements

In CLAS12, operated with a maximum beam energy of roughly 11 GeV, forward-going charged hadrons will have momenta up to roughly 5 - 6 GeV. Mounted in front of the FTOF system will be the existing CLAS low threshold Čerenkov system. The planned radiator gas for this system will be C_4F_{10} (perfluorobutane), as in the current detector system. This gas has an index of refraction of n=1.00153, and thus a threshold for pion detection of roughly 2.6 GeV. This threshold sets the momentum range where the FTOF system must be able to separate kaons from pions. To separate pions from kaons up to 2.6 GeV and pions and kaons from protons up to 5.6 GeV, a timing resolution of σ_{TOF} ≈80 ps has to be achieved for the panel-1 counters (see Fig. 5.4). This assumes a 4σ difference in flight-time between the two particles over a 650-cm path length and allows identification of a hadron species in the presence of other hadrons with up to ten times higher rates.

The requirement of 80 ps for the FTOF timing resolution is expected to be achievable for the panel-1 system with the planned design. The TOF counters from the existing CLAS detector have a timing resolution of about 150 ps [305]. The new FTOF system is expected to have an improved timing resolution relative to the existing TOF panel (panel-1a) by a factor of $\sqrt{15/6}$, or the square root of the ratio of the scintillator widths. Thus, due to the improved light collection efficiency, the new TOF panel-1b should provide a timing resolution

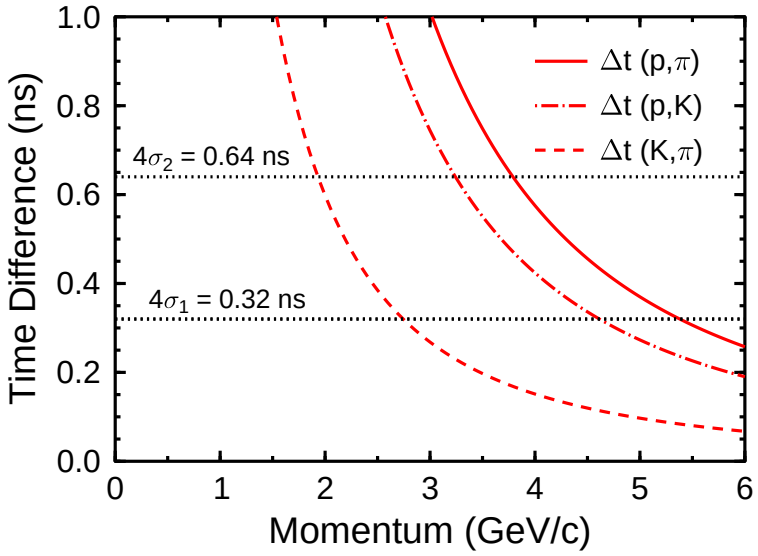

Figure 5.4: Time differences, Δt, between protons and pions, between protons and kaons, and between kaons and pions (as indicated) over the 650-cm path length from the target to the FTOF system. The horizontal lines indicate the 4σ separation time differences for the panel-1b and panel-1a counters.

of about 95 ps or less. The resolution expected from the two timing measurements in panel-1 is then expected to be $\sigma_{TOF} = ((1/150 \text{ ps})^2 + (1/95 \text{ ps})^2)^{-1/2} = 80$ ps. Timing resolutions of 60 ps have been achieved with small scintillator counters [306]. For counters 200 cm in length, prototypes have achieved a resolution of about 70 ps [307].

As with the design of the current CLAS TOF counters, the inactive components of the detector for the FTOF system must be designed to fit fully within the projected space (the shadow) behind the superconducting coils of the main torus. Therefore all light guides, PMTs, voltage dividers, and cables have tight constraints on how much space they can take up. Fig. 5.5 shows the shadow created by the main torus cryostats and drift chambers as projected on the face of the FTOF system. This picture comes from our CAD model of the CLAS12 system for one particular design assumption for the drift chamber endplate design. The limits of the shadow region are actually defined at the current time by the Region 2 drift chamber system. While the Region 1 and Region 3 chambers have their endplates, on-board electronics, and readout cables located in the shadow of the torus cryostats, the Region 2 chambers are located fully between the cryostats. Thus the Region 2 endplates define the ultimate shadow for the definition of the FTOF panel-1 inactive region. Fig. 5.6 shows the ϕ angle coverage for each counter of the FTOF system.

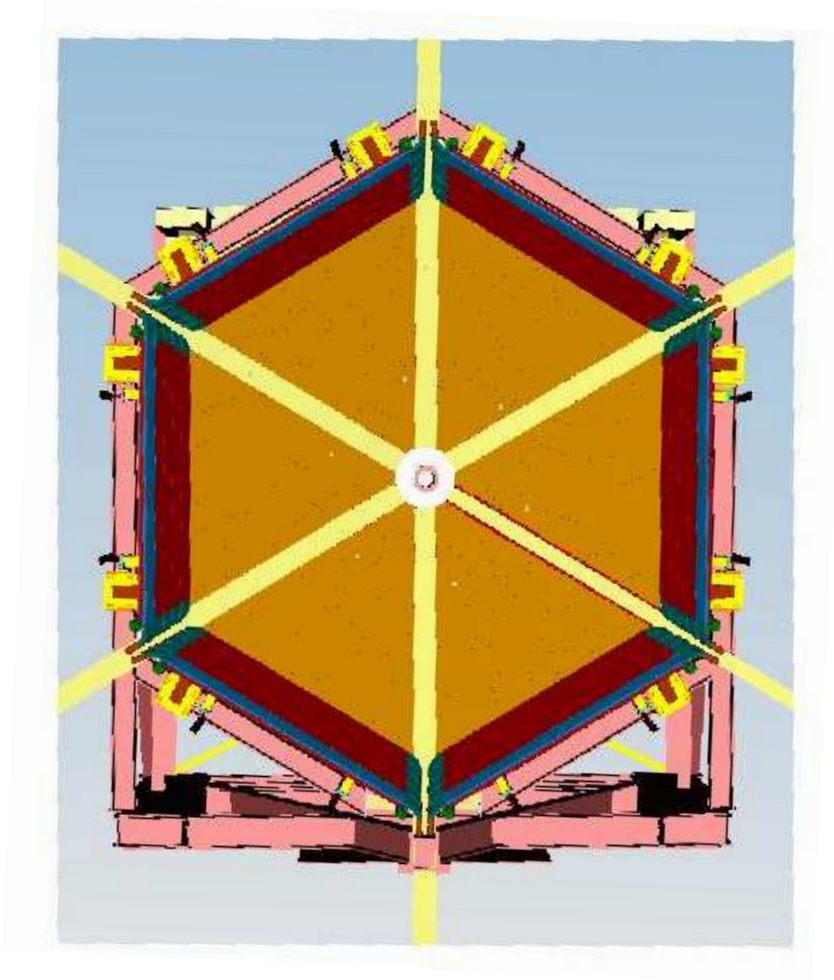

Figure 5.5: View of the projected shadow (in light yellow) created by the main torus cryostats and drift chambers as projected on the face of the FTOF system (shown in orange and dark red).

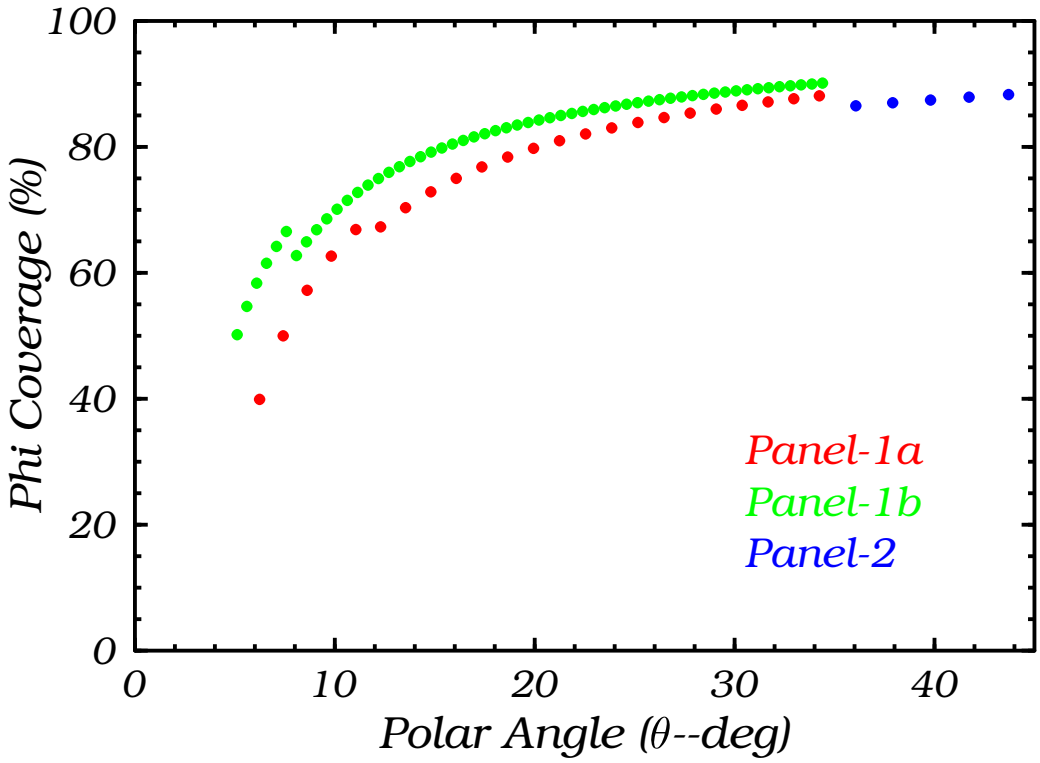

Figure 5.6: Calculation of the ϕ angle coverage of each counter in the FTOF system using the nominal design for the FTOF system. The discontinuity in the ϕ coverage for panel-1b is due to the use of shorter PMTs for the first six counters (97-mm long Hamamatsu R9779 PMTs), whereas the larger angle counters employ slightly longer PMTs (131-mm long Photonis XP20D0B PMTs).

5.3 FTOF System Description

The time-of-flight detectors provide an electronic signal for the data acquisition system, which reflects the time a particle passes through the scintillator. Passing through the scintillator, the particle ionizes the material and subsequently generates scintillation light; these photons travel on various paths inside of the scintillator and the light guide, may get absorbed, reflected (internally or on outer coatings), and ultimately impinge on the photocathode of the photomultiplier tube (PMT), producing a current of photoelectrons. In several stages this current gets amplified within the PMT and is then available as an electronic output pulse. The pulse finally passes through various components of the electronics system, including a discriminator and a time-to-digital converter (TDC) for computer readout. These various processes influence and determine the total time resolution σ_{TOF}. It is convenient to parameterize σ_{TOF} with the following formula:

$$\sigma_{TOF} = \sqrt{\sigma_0^2 + \frac{\sigma_1^2 + (\sigma_P L/2)^2}{N_{pe}\exp(-L/2\lambda)}}. \tag{5.1}$$

The parameters in this formula quantify the characteristics of the detector geometry and components (i.e. scintillator, PMTs, and electronics). In particular, λ is the attenuation length of the scintillator and L its length; σ_0 represents the intrinsic resolution of the electronics and other processes that are independent of the light intensity, σ_1 models the jitter in the combined single-photoelectron response of the scintillator and PMT, and σ_P accounts for path length variations in the light collection. Path length variations in the scintillator scale with the distance from the source to the PMT, which we take to be half the length of the counter ($L/2$), since the scintillators are read out at either side. The statistical behavior of the last two terms is indicated by scaling the single-photoelectron responses by $\sqrt{N_{pe}}$, where N_{pe} is the average number of photoelectrons seen by the PMT of a counter with an infinitely long attenuation length. For scintillators that are several meters long, the dominant contribution comes from transit time variations of photon paths in the scintillator. Parameters for the present `CLAS` TOF system are given in Ref. [308].

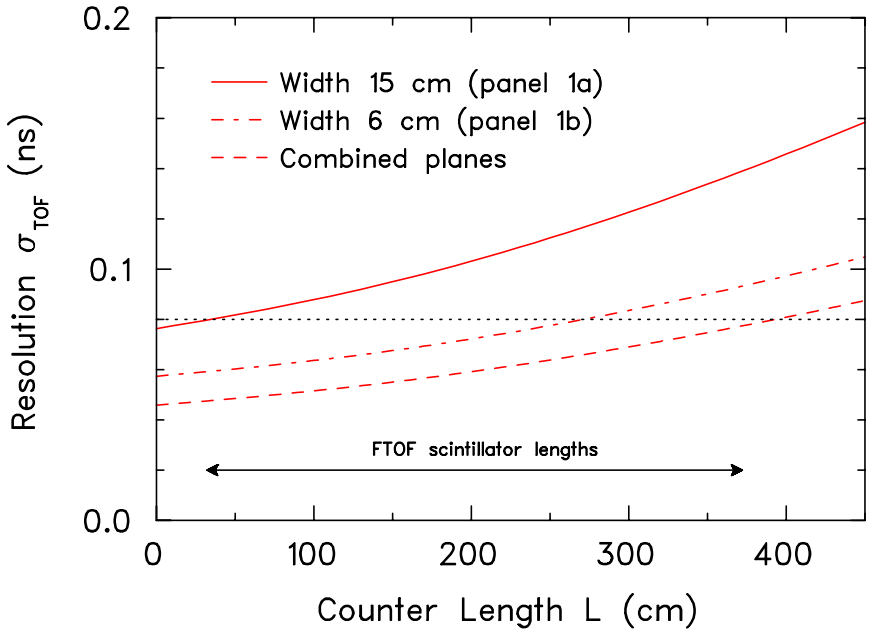

Figure 5.7: Expected time resolution for the existing panel-1a counters (15-cm wide) with an assumed intrinsic electronic resolution of 40 ps. Also shown are predictions for the new panel-1b counters (6-cm wide) and for the combined panel-1a and panel-1b counters. The arrow along the bottom of the plot shows the range of scintillator lengths in the FTOF panel-1 counters.

5.3.1 Geometry

Fig. 5.7 illustrates how the detector size (width and length) affects the timing resolution. As a guide to necessary improvements in the time resolution of the system, we scale the parameterization of the CLAS system from the present 15-cm wide counters down to 6 cm in width. An important consideration is a good match of the detector cross section to the size of the PMT entrance window. How exactly the connection is optimized (e.g. with or without a light guide), needs to be studied with Monte Carlo simulations and detector prototypes, which are being built at the University of South Carolina. Preliminary results indicate that the best time resolutions are obtained without light guides. Fig. 5.7 also shows how, by means of a combined measurement from the two detector planes, one can improve on the time resolution.

5.3.2 Scintillation Material

The parameterization of σ_{TOF} is used to study the possible improvements in resolution based on a trade-off between the decay time of the scintillator (σ_1) and the number of photoelectrons (N_{pe}) arriving at the PMT, which depends on the attenuation length λ. The bulk attenuation

length and the scintillator decay times for three typical scintillators are listed in Table 5.1. The actual value for the attenuation length in a given setup may differ and will be measured on prototype detectors. In Fig. 5.8 the expected resolution is plotted as a function of counter length for the three scintillators listed in Table 5.1. For the figure we have used bulk attenuation lengths for BC-404 and BC-418, while we have used the measured values for BC-408, which is used in the current CLAS TOF system. The plot illustrates that the overall performance of short counters, less than 200 cm in length, is improved by the use of fast scintillators with small decay times τ, whereas for long counters, the existing material BC-408 with its larger attenuation length is the better choice. The final choice for the short FTOF counters is an open question and will be explored experimentally.

The new scintillation counters, which are formed in a casting process against glass surfaces, will be milled using a diamond-edge fly cutting technique on two sides of the counters and the ends. This process has been shown to leave the surface typically flatter and smoother than hand-polished surfaces. Costs associated with diamond-tooled finishes on all four sides of the scintillator bar are significantly more than on two sides only. The technical representatives at Saint-Gobain Crystals have indicated that scintillation bars with only two sides diamond-tool finished and two casted against glass, perform better than bars with all four sides machined. We will perform bench tests to verify these claims before making a final decision.

The geometry and materials for the interface between the scintillator and PMT, and the wrapping material for the scintillator to provide for light-tightness and improved light collection are important design parameters and will be studied on prototypes to provide for a maximum of photoelectrons.

Scintillator	Bulk (λ) (cm)	τ (ns)
BC-408	380	2.1
BC-404	160	1.8
BC-418	100	1.4

PMT (2″)	Rise Time (ns)
XP20D0B	2.5
XP2020	1.5
XP2020/UR	1.4
R9779	1.8

Table 5.1: Attenuation lengths λ and decay times τ for various scintillators (left) and rise times (right) for various photomultiplier tubes. The present CLAS TOF system utilizes BC-408 scintillator coupled to 2-in Thorn EMI9954A PMTs (panel-1a) and 3-in Philips XP4312B PMTs (panel-2).

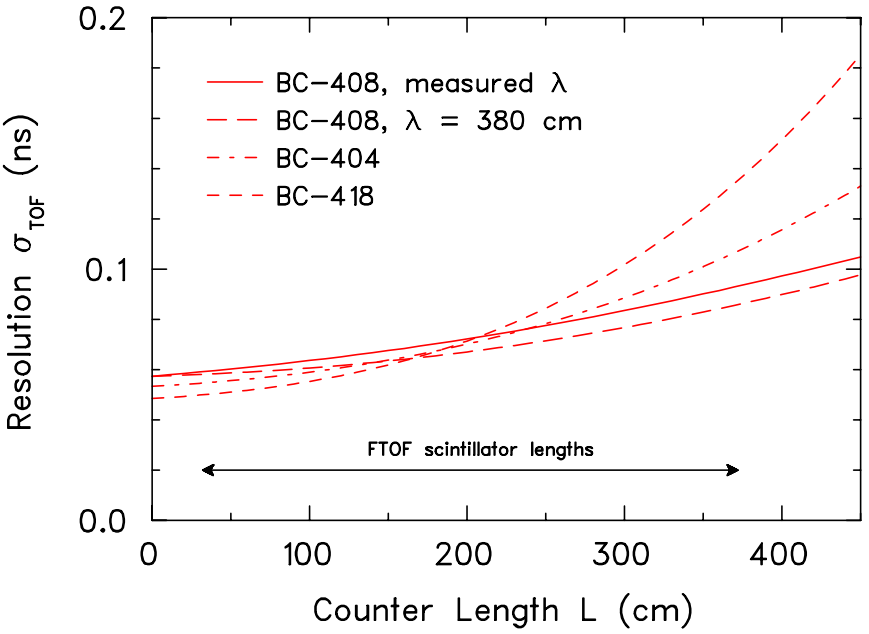

Figure 5.8: Resolution for various scintillation materials showing the trade-off between attenuation length and decay time. Estimates assume 6-cm wide scintillators and an intrinsic resolution of the electronics of 40 ps. The arrow along the bottom of the plot shows the range of scintillator lengths in the FTOF panel-1 counters.

5.3.3 Light Guides

Preliminary simulation studies indicate that the best time resolutions for the panel-1b counters will be obtained without light guides since the number of photons entering the PMT window is higher by a factor of two than with the best optimized light guide of non-zero length. Eliminating the light guides altogether allows for long enough scintillators to cover the full fiducial region given the constraints of the PMT, voltage divider, and cable sizes.

5.3.4 Photomultiplier Tubes

Prototypes have realized a timing resolution of 70 ps for 200-cm long detectors using Philips XP2020/UR PMTs, which have 25% faster rise times than the more standard Philips XP2262 PMTs. This is achieved with an improved transit-time spread across the photocathode. PMTs contribute to a large fraction of the total hardware costs for the FTOF system. Careful prototyping of the detectors is therefore especially important for the selection of a specific tube and voltage divider network, as, e.g., the XP2020/UR is about twice as expensive as the XP2262. While we plan to perform detailed prototyping efforts to optimize the choice of

components, we expect that a faster PMT will be required. In Table 5.1 we give the rise times for various common tubes. Faster PMTs are available, but in practice should be matched to the rise times of the combined scintillator-light guide system.

PMT performance must be carefully weighed against the tube geometry. An important criterion for the new panel-1b counters is that they cover the same ϕ range as the drift chambers. In other words, all of the inactive system elements must reside within the projected shadow of the torus coils/drift chambers. Thus it is imperative to select a PMT model that meets this requirement. The choice of the PMTs for the panel-1b counter readout will employ two different PMTs. For the first six counters, we will employ Hamamatsu R9779 PMTs (97-mm long). For the remaining counters we will employ Photonis XP20D0B PMTs (131-mm long). The design requirement to match the acceptances of the FTOF system to the drift chambers is an important consideration. The coverage specification for the drift chambers is to provide 50% ϕ coverage at θ=5°. This specification is only met for the FTOF system when using the shorter PMTs. This ϕ coverage of the panel-1b counters with this design choice is highlighted in Fig. 5.6. The final number of counters readout with the Hamamatsu PMTs still needs to be finalized. The issue will be a compromise between the physics requirements for large ϕ coverage at small polar angles and the increased costs of the Hamamatsu PMTs compared to the Photonis PMTs. Also the timing specifications for the Hamamatsu PMTs are slightly worse than for the Photonis PMTs. However, this is offset by the improved light collection for the shorter counters.

5.3.5 Voltage Dividers

A schematic diagram of the high-voltage divider currently used for the CLAS TOF panel-1a and panel-2 readout is shown in Fig. 5.9 [305]. For the panel-1b counters we are presently planning on using the Photonis Imaging Systems VD127K/T transistorized hybrid voltage divider as shown in Fig. 5.9. Each of these active dividers use high-voltage transistors to fix the PMT gain by stabilizing the voltage and to protect the PMT against high light levels by shutting down the circuit in an over-current situation.

The tube-base assembly for the current CLAS panel-1a counters is shown in Fig. 5.10. In order to allow the scintillator to span the maximum area of the detector, the PMT and voltage divider are required to fit in the shadow of the main torus magnet. The same constraint will be imposed on the tube-base assemblies for CLAS12. A design of this sort meets our requirements

of an extremely compact design.

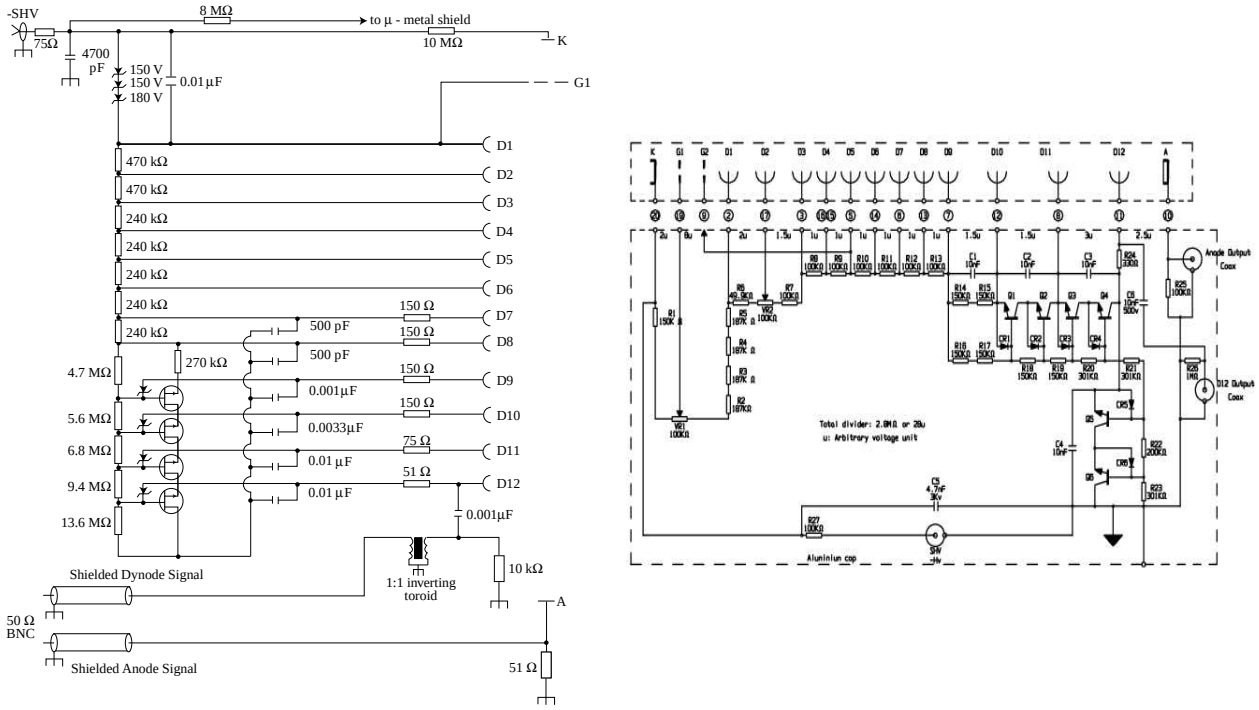

Figure 5.9: (Left) Schematic diagram of the high-voltage divider for the EMI-9954A PMT used for the current CLAS panel-1 readout. The last four stages of the divider are stabilized by high-voltage FETs. (Right) Schematic diagram of the active Photonis VD127K/T dividers planned for the panel-1b counters.

5.3.6 Assembly

Each scintillation counter will be individually wrapped, and assembled with two photomultiplier tubes, one at each end. The layers are shown in Fig. 5.11 for the existing panel-1a and panel-2 counters. The outer coverings of the scintillator consist of two layers of aluminum foil, one strip of 5-mil lead foil on the side facing the target, and finally, one layer of black Kapton. The lead foil was included to shield the scintillators from background x-rays produced in the target. This is the only extra material facing the target.

For the new panel-1b counters, studies are underway to decide on the final wrapping materials, especially with regard to adding a thin lead sheet for x-ray absorption on the side facing the target. Currently we plan on wrapping the counters in a single layer of metalized mylar film and then a double layer of Tedlar PVF film for light tightness. Presently we are

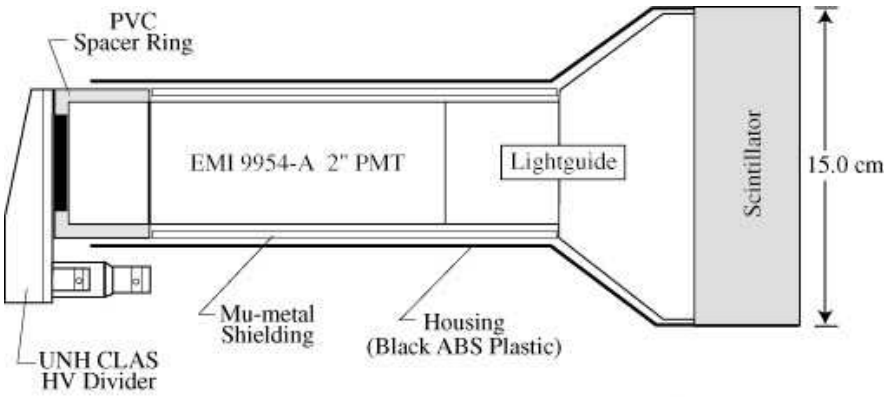

Figure 5.10: Side view of the PMT-base assembly mounted on the CLAS panel-1a TOF scintillators. The compact design is required by space limitations in the detector for the 2-in PMT.

not planning to change the wrapping of the existing panel-1a and panel-2 counters as a cost reduction measure.

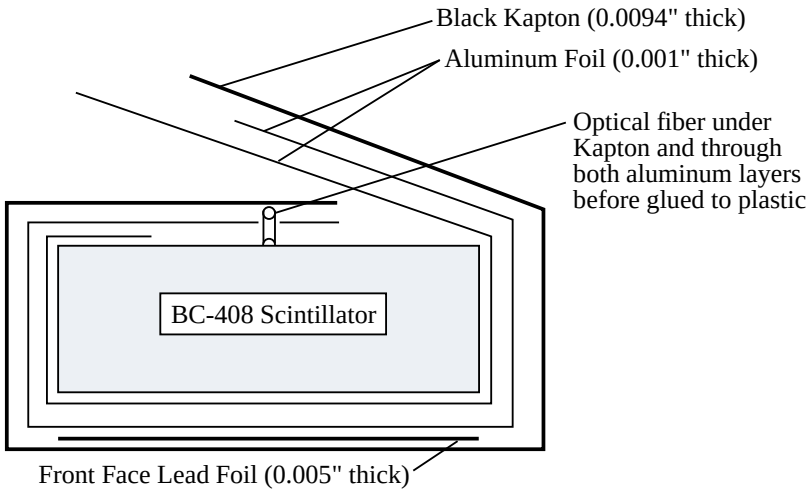

Figure 5.11: Cross section of counter wrapping for the existing CLAS panel-1a and panel-2 counters. The UV-transmitting fiber is used for the laser calibration system. The lead foil is to absorb low-energy background x-rays from the target.

After wrapping, each panel-1a and panel-2 scintillator was attached to a support structure, light guides and photomultiplier tubes were glued in place, and an optical fiber installed for the laser calibration system. Dymax 3-20262 UV-curing optical cement was used as a bond for the light guide/scintillator interface, as well as the PMT/light guide interface. This approach is also planned for the panel-1b counters.

The panel-1a and panel-2 counters are each supported individually by a composite sandwich structure of stainless steel skins on structural foam that is attached to the detector frame

only at the two ends. The composite structure, which mounts on the scintillator side facing away from the target, provides uniform material thickness to the scattered particles. The support was undersized so the counters could be placed as close together as allowed by the wrapping material. The assembly with support is shown in Fig. 5.12.

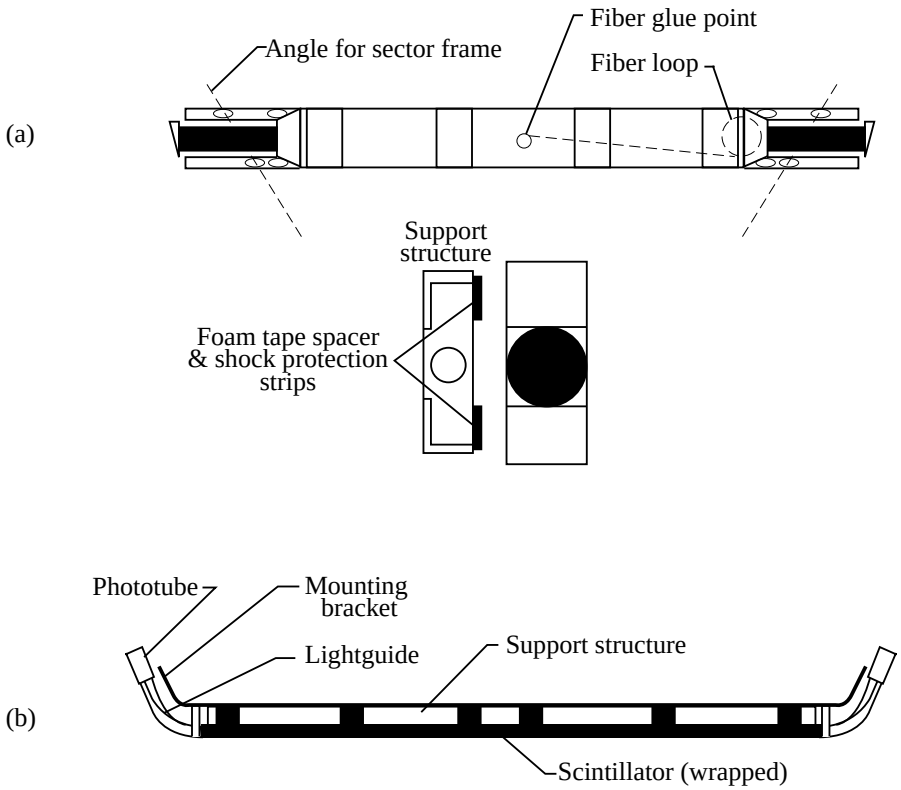

Figure 5.12: Counter and support assembly. a) Top view and enlarged end view of the panel-1a and panel-2 assemblies. b) Side view of the panel-2 mounting assembly.

The panel-1a counters were mounted on 1-in-thick supports to minimize the thickness of the package from the standpoint of Coulomb multiple scattering and energy loss considerations. The maximum deflection for the installed scintillators is 4.4 mm, as estimated from deflection tests and the compound angle of each detector, which relieves the overall support requirements. The space for the panel-2 counters allowed for 3-in-thick sandwich supports, which were mechanically much stiffer and resulted in no appreciable deflection.

The mounting of the panel-1b counters in front of the existing panel-1a counters is being designed to allow for minimal additional material in the active area of the detectors. Fig. 5.13 shows the current mounting plan for the panel-1 counters. Here the panel-1b counters will be mounted on a triangular support frame very similar in design to that employed for the

existing panel-1a counters. Side views of the panel-1 counters showing the individual support frames is shown in Fig. 5.14. The support frames for the two panels in each sector will be mounted to the forward carriage using legs that project through the gaps between the PCAL and EC detectors.

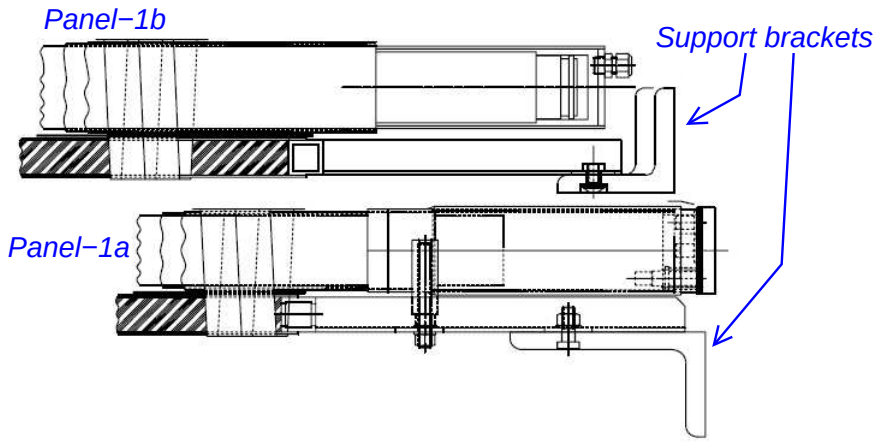

Figure 5.13: Panel-1 counter support structure diagram showing the angle brackets used to attach the counters in the different panels to their associated support frames.

5.3.7 Magnetic Shielding

The FTOF PMTs will be located roughly 650 cm from the target in a local magnetic field that should be less than 24 G (maximum that occurs in the axial direction with respect to the PMT), given the field map for the current design of the CLAS12 torus. A magnetic shield for the PMTs must be included to reduce both the axial and transverse components of the field, especially near the photocathode. These conditions are similar to those of the PMTs in the current CLAS TOF system. In the existing panel-1a and panel-2 counters, the magnetic shield consists of a cylinder made from 0.020-in thick μ-metal, with the shield extending 2-in beyond the front face of the PMT. For the panel-1b counters, we are planning on a design that consists of a cylinder made from 1 to 2-mm thick μ-metal, with the shield ending at the front face of the PMT. The outside face of the cylinder will have a μ-metal endcap to improve the shielding against the axial field and the cable connections to the voltage divider (anode, dynode, and high voltage) will be made through the shield. Detailed studies of these PMTs will be carried out in various magnetic fields to optimize the final design of the magnetic

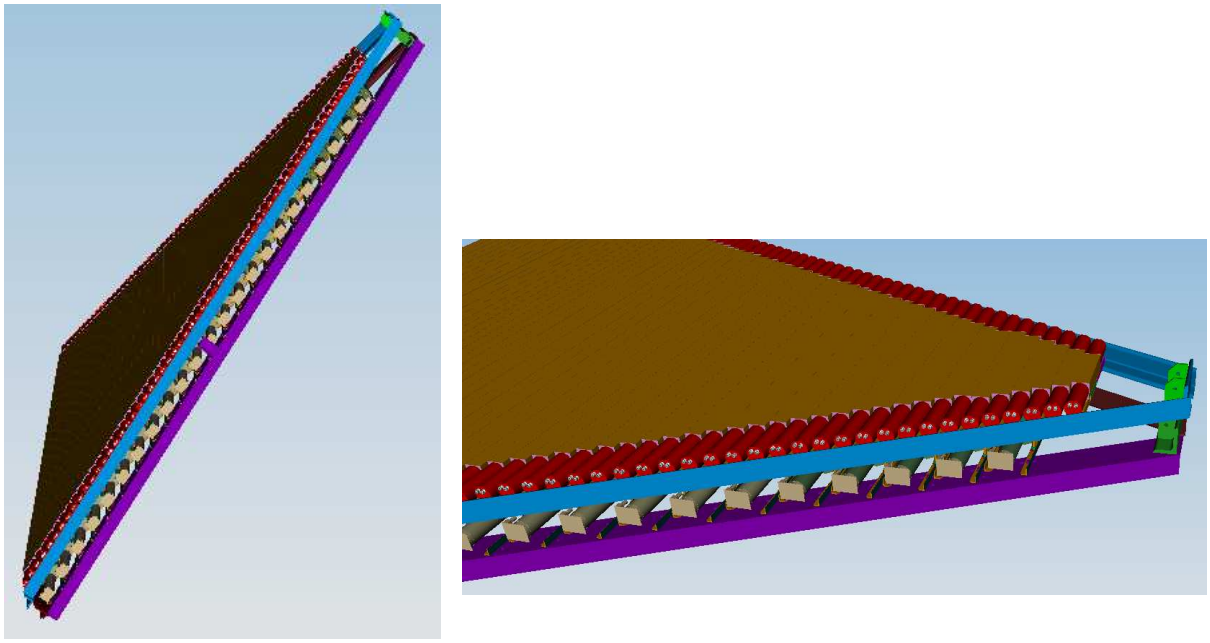

Figure 5.14: Side views of the panel-1 counters in a single sector showing the panel-1a and panel-1b counters mounted on their associated support frames. These figures were generated from our 3–D CAD model.

shielding.

5.3.8 Laser Calibration System

A system of ultraviolet (UV) lasers is used to test and calibrate the existing CLAS TOF counters. This system will continue to be employed and will be updated to include connections to the new panel-1b counters. The UV light is delivered to the center of each scintillator via a silica optical fiber. The fiber core diameter is 200 μm with a 240-μm cladding. The TDC and ADC information from the laser pulses is then used to calibrate the overall timing and pulse-height time-walk.

The calibration system consists of optical tables located near the counters. Each optical table contains a Laser Photonics LN203C nitrogen laser operating at 337 nm enclosed in an aluminum box for RF shielding and personnel safety. The laser beam is directed through an opening in the aluminum enclosure to a series of optical and mechanical elements. The laser beam first encounters a flat quartz plate that reflects a small fraction ($\approx$ 4%) of the light

back to a fast photodiode circuit that is used as a reference to time the laser to the TOF scintillators. Most of the laser light passes through a variable neutral-density filter with a dynamic range of 1:40. This filter can be used to attenuate the light over a range of values suitable for measuring the time-walk correction of the scintillators. The filter is adjusted by a remotely controlled stepping motor. Downstream of the filter, the beam is expanded by a CTR 5×3 diffuser. The diffused beam incident on the fibers is uniform to within 30%. The beam can then be partially intercepted by a "mask" controlled by a stepping motor. Several different hole patterns along the "mask" can be positioned to illuminate various combinations of fiber bundles. Each bundle consists of seven all-silica 100-μm-diameter fibers (numerical aperture is 0.22) that are 13-m long and distributed to the various scintillators. For the panel-1a counters, there are 24 bundle ends that are arranged in a four-by-six rectangular array behind the "mask" within an area of 3.0 cm^2.

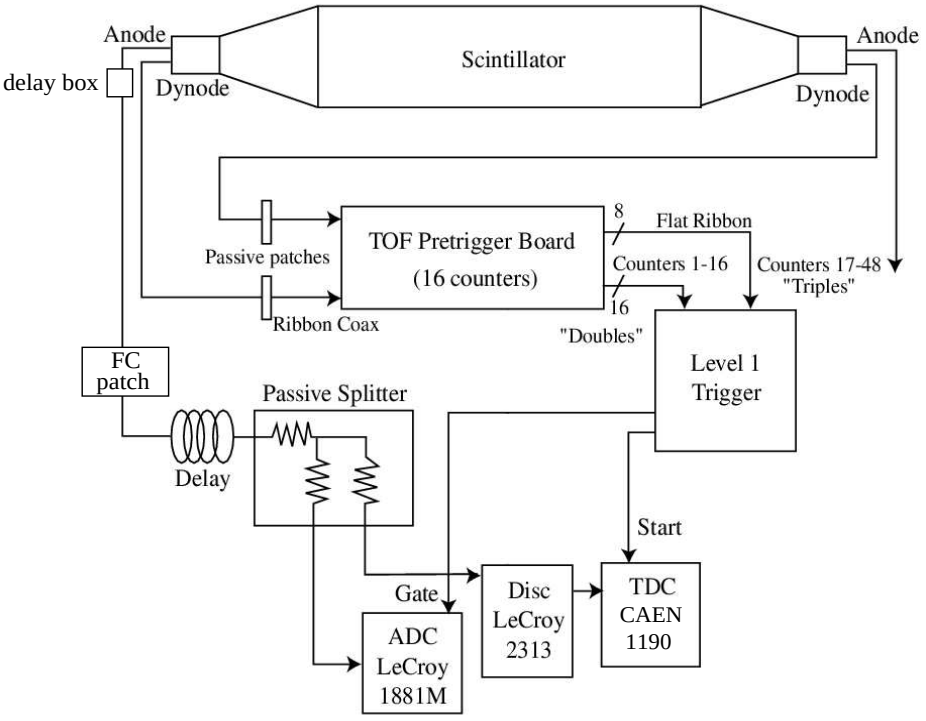

Figure 5.15: Overall schematic of the electronics used in the current CLAS TOF system.

5.3.9 Electronics

The FTOF counters will generate prompt signals for the CLAS12 Level-1 trigger electronics, as well as signals for pulse-height and timing analysis. The overall layout of the TOF electronics

currently used in CLAS is shown in Fig. 5.15. In this design the PMT dynode pulses go to a pretrigger circuit to generate the Level-1 trigger. Each PMT anode pulses go to a LeCroy 1881M FASTBUS ADC and a CAEN VME 1190 pipeline TDC (100 ps LSB) for readout. A simplified design using pipeline TDCs, flash ADCs (or pipeline ADCs), and improved electronics for forming the trigger signals is planned for CLAS12 (see Fig. 5.16). With the incorporation of the new ADCs, the miles of delay cables employed in the current TOF system can be eliminated.

The intrinsic resolution of the electronics system (σ_0) must be reduced and it has been measured to be as small as 14 ps in various setups [309]. There are many contributions to this term, and each electronic component will be chosen to insure that it meets our specifications. In order to achieve the rate capability at a luminosity of 1×10^{35} cm^{-2}s^{-1}, a high-resolution pipeline TDC will be used for the new panel-1b counters. These modules may be the commercially available modules used for the readout of the existing CLAS TOF counters, or may be electronics developed at JLab. For instance, the JLab Fast Electronics group is developing such a TDC based on the COMPASS F1 chip. Presently, we assume $\sigma_0 = 40$ ps in our estimates in Figs. 5.7 and 5.8, limited by the resolution of the COMPASS F1 TDC chip.

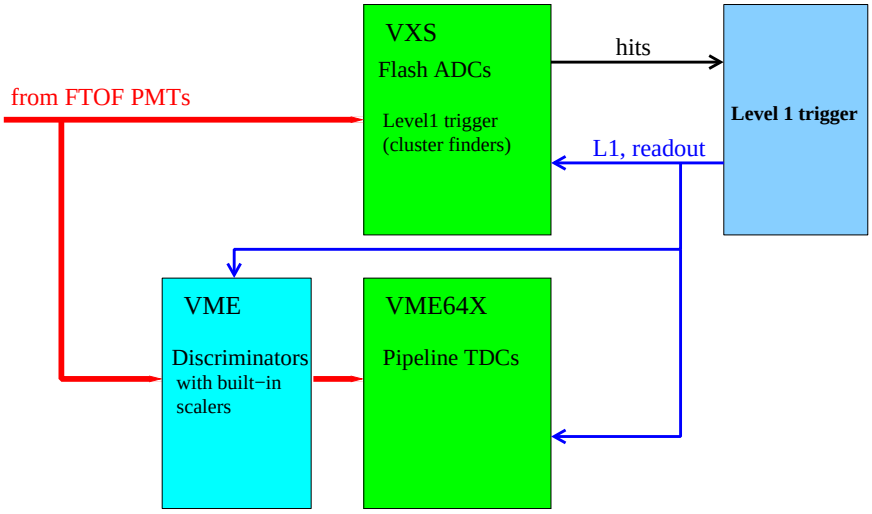

Figure 5.16: Overall schematic of the electronics planned for the new CLAS12 FTOF system.

Cables

Fast timing of signals from the FTOF system requires cables with low signal distortion. Measurements were made of the response of several types of coaxial cable for the existing CLAS

TOF system, including RG-58, the usual cable for fast NIM electronics, RG-213, and Belden 9913, a low-loss semi-solid polyethylene cable. The lengths of the cables (∼400 ns) were chosen to match the time required to form a first-level trigger for CLAS. The response of the cables to a NIM logic signal, -0.75 V and 10 ns duration, was measured, and the transmission of pulses through the cable was simulated. Note that the cable dispersion in high quality Belden 9913 is approximately equal to the dispersion in standard RG-213 cable for the same delay because the slower velocity in RG-213 ($\beta = 0.66$) compared to Belden 9913 ($\beta = 0.84$) compensates for the larger attenuation. We plan to keep the Belden 9913 cable from the PMT dynode to the trigger electronics and RG-213 from the anode to the ADC and discriminator for panels-1a and 2. The faster trigger cables reduce the need for additional signal delay. Since the panel-1b counters will typically not be in the trigger for CLAS12 electron runs, the preferred choice of readout cable for the new panel-1b counters is to use short standard RG-58 cables to feed into a nearby pipeline TDC and ADC readout system.

High-Voltage Supplies

The photomultipliers for the FTOF counters will operate at about 2000 V with negative polarity. The maximum dark current drawn by the PMTs for the existing panel-1a counters is about 20 nA and is about 30 nA for the panel-2 PMTs. The current CLAS TOF system is powered by five LeCroy 1458 mainframes that can contain up to sixteen cards, each supplying 12 independent channels for a maximum of 192 channels per mainframe. This system will be reused for the FTOF system, however due to the number of HV channels in the panel-1b system, additional HV channels will have to be added to the system.

5.4 Simulations and Reconstruction

The FTOF system is being modeled within our GEANT4 Monte Carlo framework. Fig. 5.17 shows a representation of the counters in this model, including panel-1a, panel-1b, and panel-2 in each sector of CLAS12. The output of the Monte Carlo are the ADC and TDC values associated with the two ends of each counter where there is a hit, modeled with the appropriate resolution expected for these detectors. At the current time, the coding for the full FTOF reconstruction is being implemented in the Monte Carlo. Studies of the angular coverage of the counters, particle identification vs. momentum, reconstruction for tracks that cross

multiple counters, and the impacts of the panel support frames will be carried out in the near future. However, even with the low-level ADC and TDC information currently available, we can already gain some insight into the expected coverage and response of this system.

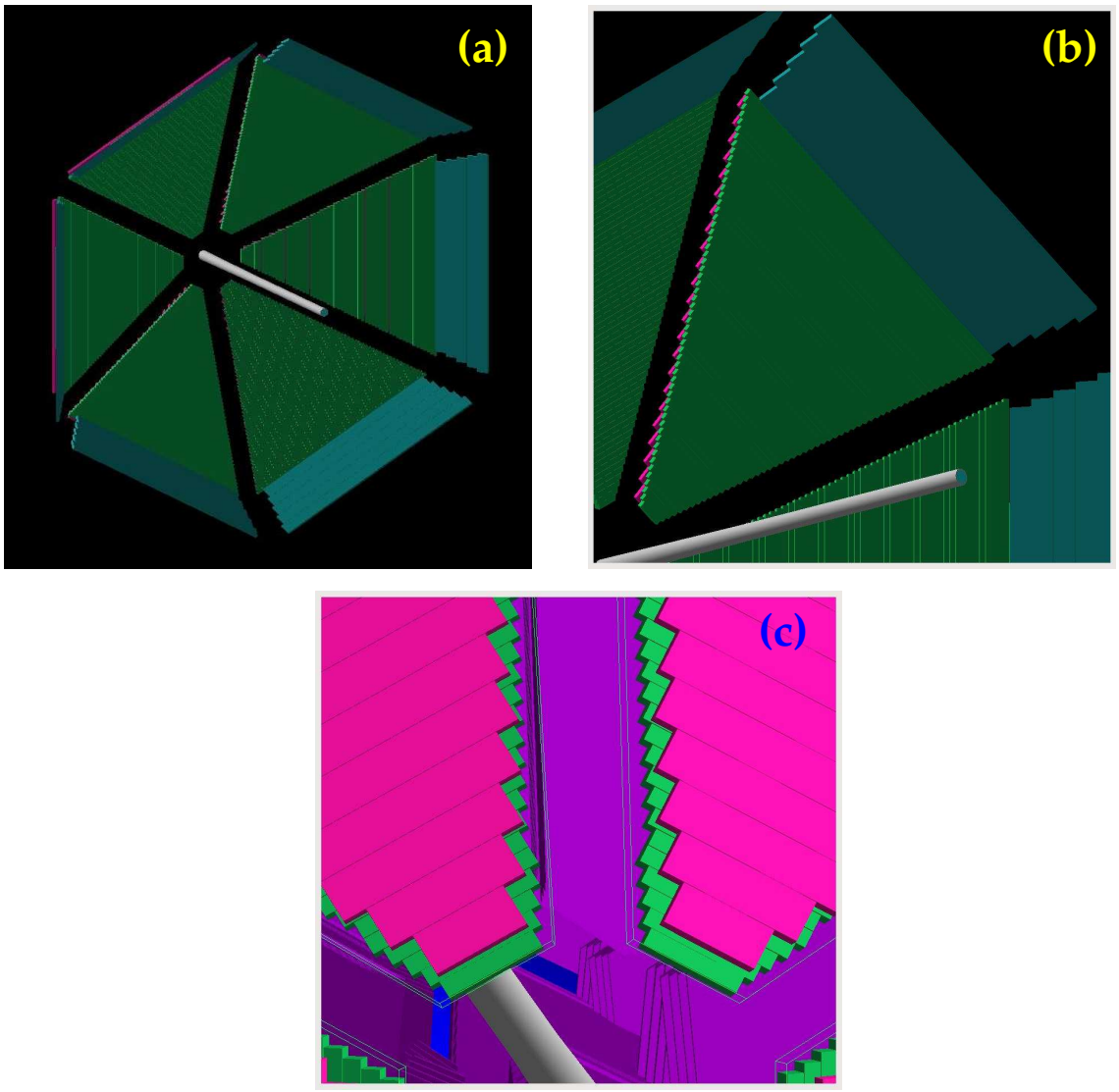

Figure 5.17: Model of the FTOF system included in our GEANT3 Monte Carlo. (a). Perspective view looking downstream of the six FTOF sectors divided into panel-1a, 1b, and 2. (b) Close-up view of (a) focussing in on a single sector. (c). View of the back of panel-1a (looking upstream) showing details of the definitions of panel-1a (pink) and panel-1b (green).

Fig. 5.18 shows the acceptance of the CLAS12 FTOF system in terms of ϕ and θ. Plots of this sort serve to define the shadow region in terms of ϕ vs. θ defined by the main torus cryostat and the drift chamber system. In this shadow, all of the inactive components of the detectors

must reside, including light guides, PMTs, voltage dividers, magnetic shielding, support frames and structures, and cables. Fig. 5.18 shows the thrown particles in the simulation and the particles reconstructed by the FTOF system. The final definition of the shadow region serves to define the lengths of the new panel-1b counters as a function of polar angle, as well as the number of required panel-2 counters.

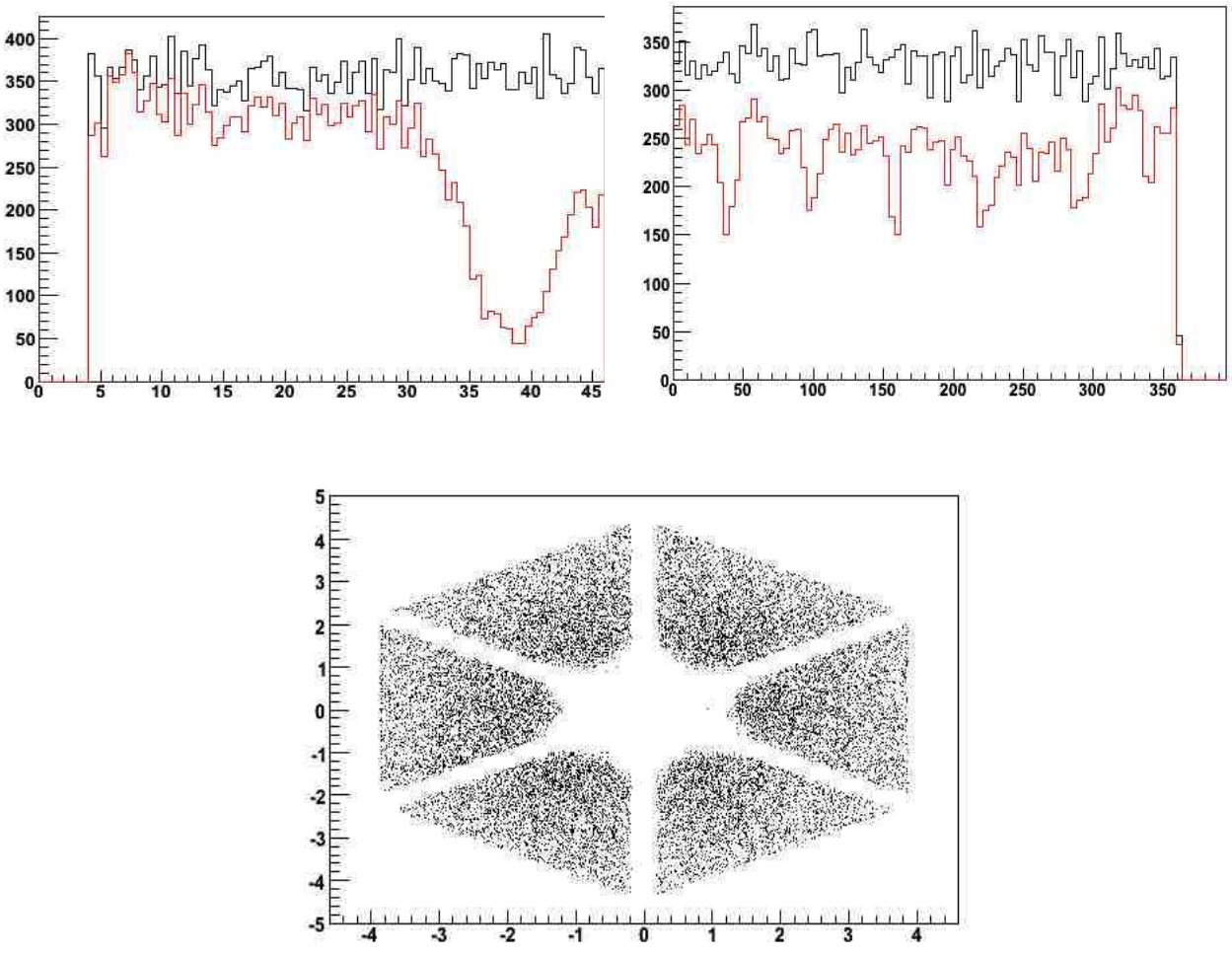

Figure 5.18: Preliminary GEANT4 Monte Carlo output showing the geometric coverage of the panel-1b FTOF system in terms of θ (deg) (UL) and ϕ (UR) (deg). Here the black curves are the thrown events and the red curves are the reconstructed events. Also shown for panel-1b is the reconstructed y-coordinate vs. x coordinate (m) (bottom) for the full FTOF system.

5.5 FTOF System Quality Assurance Procedures

This section provides a list of quality assurance (QA) steps for the construction of the FTOF system for CLAS12. The information given here is based on experience from construction of the TOF system for the current CLAS detector system.

Scintillator Material: Upon arrival of the scintillator material from the manufacturer, all scintillator should be unwrapped and inspected with UV light for scratches, marks, and defects. All pieces should be measured for tolerances. Any plastic outside of acceptable size, clarity, or condition should be shipped back to the manufacturer.

Scintillator Handling: In all steps of handling the scintillator material, white gloves and lab coats should be worn. Whenever possible, observe clean room-like procedures. Naked plastic should be covered if it needs to be left exposed for any period of time. The scintillator material is very susceptible to damage from scratches, heat, cold, and shock. Care must be taken at each step of the construction process to monitor the environmental conditions and to be sure that the detectors and materials are handled with care.

Workmanship: Accuracy in workmanship is very important as mishandling and poor construction procedures can reduce the detector resolution noticeably. All measurements have to be precise and all construction procedures and tolerances have to be rigidly followed.

Construction Steps: The steps involved in the construction of the FTOF scintillators are listed below along with general QA guidelines.

- Preparation of wrapping layers: The dimensions of the wrapping materials must be precise to avoid any gaps that could cause local efficiency problems or introduce light leaks. Proper cutting implements must be employed with sharp blades always in use. All wrapping materials must be handled using gloves to avoid surface deposits. A clean work area is required to avoid any debris adhering to the surface. Finally all wrapping steps must ensure smooth material finishes to ensure optimal resolution.

- Fiber preparation and gluing: Fibers must be cut so that the ends are perfectly flat. Any ridges in these fibers will give rise to a surface for reflections that could impact the calibrations. Also the cut ends must be properly polished and cleaned. Care must be

taken when gluing the fibers into position to ensure that no glue gets on the ends of the fibers. Care in handling and routing of the fibers is required to ensure that they are not bent in such a manner that they could crack or break.

- Wrapping: Strict procedures must be followed when wrapping the aluminum and Tedlar about the scintillator material. The wrapping materials and the tape employed tend to curl or wrinkle when under stress. When smoothing the materials during the wrapping process care must be taken not to rip the materials or introduce scratches in the material layers or the scintillator itself.

- Support structure preparation and mounting: Careful visual inspection must be employed of any tape that is being employed to attach the counters to the backing structure to be sure it is free from defects. Also procedures must be followed carefully to be sure that any tape employed has good adhesion to all contact surfaces. Sufficient measurements must be made when positioning the scintillators on the support structure to ensure that all alignment tolerances are met.

- Mounting the PMTs: Care must be taken to ensure that instructions for mixing epoxy used to attach the PMTs are precisely followed. Procedures to eliminate or reduce air bubbles in the epoxy must also be followed.

PMT Handling: The PMTs are susceptible to damage from shock and care must be taken to handle them with care both before and after they are mounted. In addition, care must be taken to avoid any scratches on the PMT face during handling and installation.

Detector Testing: HV checks of the detectors should be performed and the dark current should be measured for each PMT. Any measured dark current more than 100 nA is an indication of a possible light leak or bad PMT. Attempts to find light leaks should continue to ensure that the measured currents are the same in the testing area with lights on and lights off. Attenuation length measurements should be performed on selected detectors to ensure that they are within the manufacturers stated specifications.

Installation: Quality assurance during installation must involve procedures for proper and safe handling of the detector structures to be sure that they are not subject to any shocks or

stresses, as well as to ensure that support frames and lifting structures do not put any stresses on the detector, the light guides, or the PMTs. Care must be taken that the installation procedure does not affect the integrity of the surface wrapping. Finally, procedures must be followed regarding voltage and signal connections to the detectors to be sure that all cables are labeled and sufficient strain-relief or slack is allowed for so no stresses are put on the detectors or readout electronics.

5.6 FTOF System Safety Issues

During construction there are three important areas of safety concern. These include:

- The construction procedure involves the use of glue, epoxy, and paints that can cause irritation if they come in contact with skin or eyes. Safety precautions dictate the requirements to use gloves when mixing or handling glues, epoxies, or paints, as well as appropriate eye protection.
- A sizeable number of construction tasks involve use of scissors and Exacto blades. Extreme care must be taken when undertaking activities using these instruments to avoid personal injury and cuts.
- During construction the scintillator bars and scintillator assemblies will have to be handled and manipulated. Care must be taken when lifting or supporting loads to avoid personal injury.

There are four main areas of safety concern for installation and operation of the FTOF system. These include:

- Grounding scheme - necessary to prevent electrical shock.
- Elevated work areas - access to the FTOF system for installation and repairs will be via man-lifts. Operators will employ appropriate harnessing and fall protection.
- Staging and installation - special procedures will have to be detailed for the installation of these large and heavy detector panels.
- Cable installation - floor grating will be removed and signage and personnel barriers will be installed to prevent trip and fall hazards.

It is expected that the safety issues involved with this work involve low risk for personnel injury or equipment damage, especially with the use of appropriately planned and supervised work activities.

5.7 Collaboration

The design, prototyping, and construction of the FTOF system is the primary responsibility of the University of South Carolina and Jefferson Laboratory. USC is currently in the stage of R&D to optimize the design of the panel-1b counters and to demonstrate that the combined panel-1a/panel-1b system will meet the design specification of 80 ps timing resolution.

Chapter 6

Pre-Shower Calorimeter

6.1 Overview and Physics Requirements

The primary goal of experiments using the CLAS12 detector at energies up to 11 GeV is the study of internal nucleon dynamics by accessing the nucleon's generalized parton distributions (GPDs). This is accomplished through the measurement of deeply virtual Compton scattering (DVCS), deeply virtual meson production (DVMP), and single spin asymmetries (SSA). Towards this end, the detector has been tuned for studies of exclusive and semi-inclusive reactions in a wide kinematic range.

The CLAS12 program of experiments goes further than just GPDs and includes experiments such as the space-time characteristics of hadronization. Detection of π^0s and K^0s is important to complement the measurements of nuclear attenuation seen for charged pions and kaons. These experiments depend on the ability to detect neutral and charged pions at high momentum.

Copious amounts of high-energy particles, both charged and neutral, will be produced at experiments to be done at CLAS12. Electromagnetic calorimeters for the CLAS12 detector should have sufficient radiation length to absorb the full energy of the electromagnetic showers produced by high-energy electrons and photons. High-energy neutral pions present a challenge as well, as they decay immediately into two photons with an opening angle that decreases as the π^0 momentum increases. Unless there is sufficient position resolution in the electromagnetic calorimeter of the CLAS12 detector, the two photons from π^0 decay could be seen as a single high-energy photon.

The separation of single high-energy photons from the photons of π^0 decay is very important to the deeply virtual Compton scattering (DVCS) experiments that represents a major physics program planned for CLAS12. A single high-energy photon is produced in the reaction $ep \rightarrow ep\gamma$ and the largest background to this process is from single π^0 production, $ep \rightarrow ep\pi^0$. Clearly, good π^0 detection is crucial to separate these two processes. In addition, direct π^0 production complements the DVCS measurements by accessing GPDs at low and high momentum transfer $|t|$.

Simulations have shown that the existing electromagnetic calorimeter (EC) of CLAS [310] will not be able to absorb the full energy of the electromagnetic showers produced by electrons and photons with momenta above 5 GeV. The leakage from the back of the calorimeter will diminish the energy resolution, see Fig. 6.1a. For the simple kinematics of π^0 decay, above a momentum of 5.5 GeV the opening angle of the decay photons becomes too small to be resolved with the existing EC system, which is at a distance of about 6 m from the target. The readout segmentation of the EC is only ∼10 cm. Simulations with the GEANT software for the CLAS12 geometry show that these pions would be seen as a single cluster (i.e., one photon) by the event reconstruction software, see Fig. 6.1b.

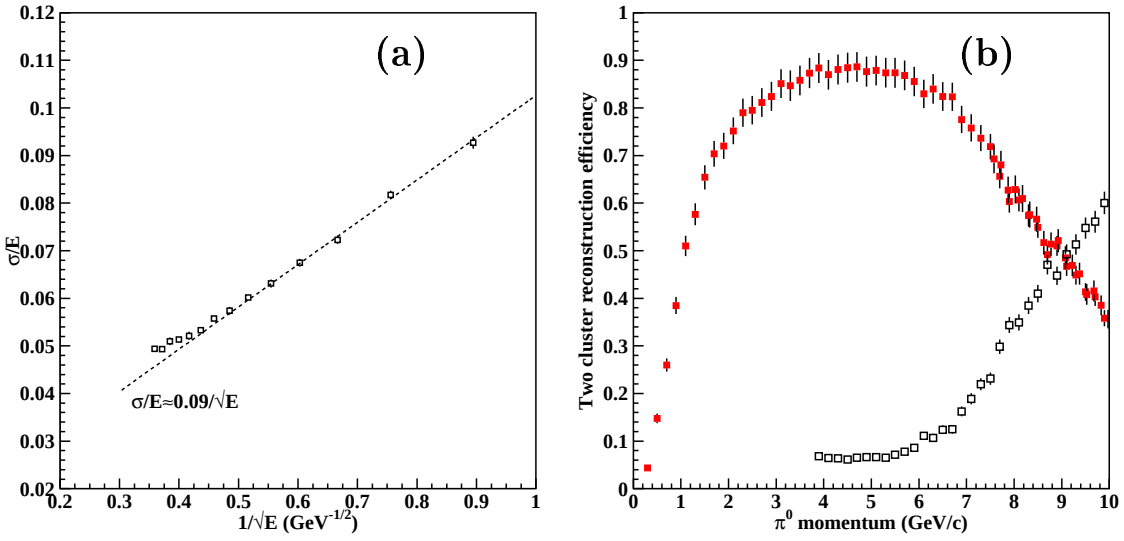

Figure 6.1: Performance of the EC at high energies. a) The energy resolution of the EC as a function of the inverse square root of energy. b) The efficiency of reconstruction of two clusters from π^0 decay photons as a function of pion momentum, filled red squares. The open symbols correspond to the probability that a single cluster is reconstructed with the same energy as the simulated pion.

To reconstruct the energy of high-energy showering particles and to separate high-energy

π^0s and photons, a pre-shower detector (PCAL), with finer granularity, will be built and installed in front of the current EC. The PCAL will have a similar geometry as the current EC. It will consist of a lead-scintillator sandwich with three stereo readout planes. Initial simulations have shown [311, 312] that 15 layers of 1-cm thick scintillator layers, segmented into 4.5-cm wide strips, sandwiched between lead sheets of 2.2-mm thickness, corresponds to about 5.5 radiation lengths, and will be sufficient to address issues arising at high energies.

In summary, accurate reconstruction of high-energy electromagnetic showers and detection of π^0s, and in particular the ability to distinguish single high-energy photons from the two-photon clusters from π^0 decay, is essential to the experimental program using the CLAS12 detector at high energies that will be part of the GPD program. Efficient detection of high-momentum π^0s is also needed for a variety of other CLAS12 proposals. The physics dictates the need for a pre-shower calorimeter to be placed in front of the existing EC. Simulations show that good π^0 identification can be obtained with full coverage of the EC front surface. In addition to the improved performance in the reconstruction of electromagnetic showers, the increase of the overall scintillator thickness in the CLAS12 forward electromagnetic calorimeters will increase the detection efficiency for neutrons.

6.2 Conceptual Design

The design parameters of the PCAL were established using the full GEANT simulations of the PCAL-EC system. As a tool, a modified GEANT simulation computer program for the CLAS detector was used. The PCAL was positioned in front of the current EC as shown in Fig. 6.2. These studies are described in detail in Refs. [311, 312] and are summarized below. The mechanical design depends on the number of scintillator-lead layers, on the angular coverage of the PCAL, and on the size of the readout segmentation. These parameters were determined by the physics requirements for the detection and identification of high-energy electrons, photons, and π^0s via 2γ decay.

Initial simulations were carried out with 15 layers of lead and scintillator (similar to the inner part of the EC), using 35-mm wide segmentation for the scintillator layers, corresponding to about 108 readout channels in each stereo view. Events were generated in a uniform distribution of π^0 and photon events at the target with momenta up to 12 GeV. Reconstruction of clusters was done using the standard cluster reconstruction algorithm of the EC, but applied

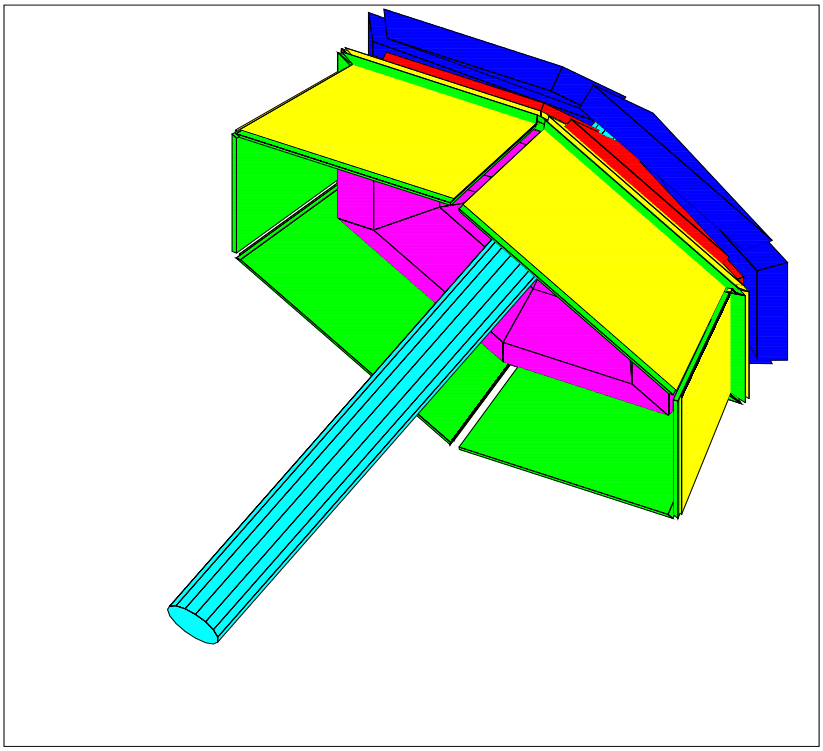

Figure 6.2: Particle ID detector package of the CLAS12 forward region. The low threshold Čerenkov counter is shown in magenta, two layers of FTOF counters are shown in green and yellow, the PCAL is shown in red, and the EC in blue.

to both the PCAL and EC. As shown in Fig. 6.3, the combined PCAL and EC system retains good energy resolution, $\sigma_E \sim 0.1\sqrt{E}$, and a constant efficiency for two-cluster reconstruction up to the highest momenta.

Keeping the number of layers at 15, the width of the readout segments (strips) was varied from 35 mm (108 channels) up to 60 mm (65 channels). In Fig. 6.4a, the two-cluster reconstruction efficiency is presented for different strip widths. The magenta points correspond to a 60-mm strip width, the blue points are for 50-mm segmentation, the green points for 43-mm strip width, and the red points are for 35-mm width. The efficiency decreases with energy for wider strips, but remains reasonably high if the strip size is kept at less than 50 mm.

Other simulations were performed using 9 or 12 layers in the PCAL design, clearly showing a loss of two-cluster reconstruction efficiency. In Fig. 6.4b, the two-cluster reconstruction efficiency is shown as a function of π^0 momentum for 9 (red), 12 (green), and 15 (blue) layers. Clearly, the 15 layer configuration has the highest efficiency. The reduced efficiency in the other cases is mainly due to insufficient radiation thickness for high-energy photons to convert

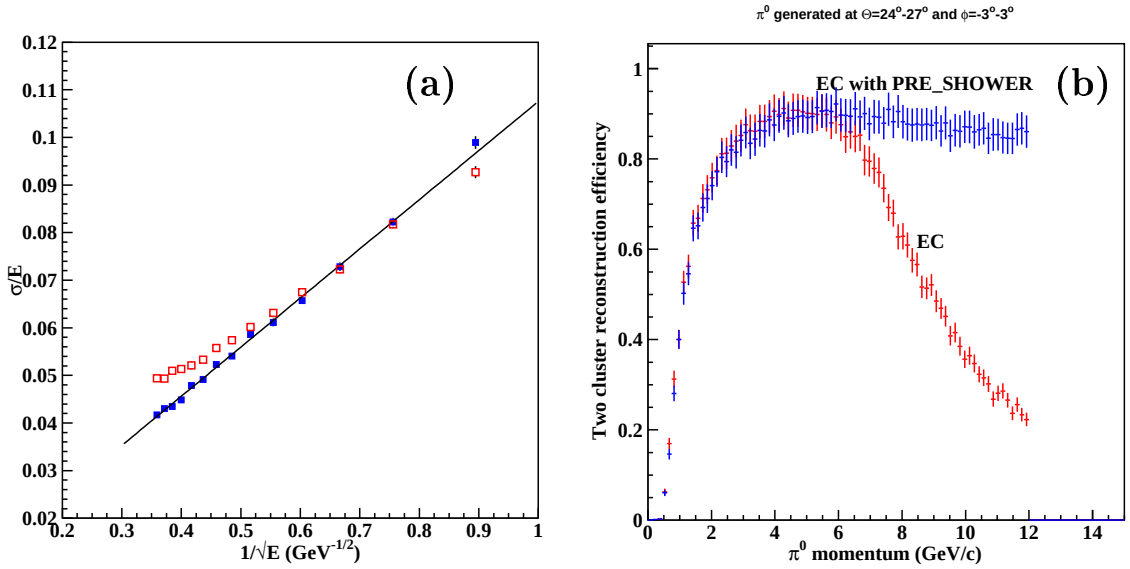

Figure 6.3: Performance of the combined PCAL-EC detector at high energies, shown with blue points. a) The energy resolution of the CLAS12 electromagnetic calorimetry system as a function of the inverse square root of energy. b) The efficiency of reconstruction of two clusters from π^0 decay photons as a function of pion momentum. Red symbols correspond to the EC performance presented in Fig. 6.1.

and deposit sufficient energy for the shower to be detected. Simulations were repeated for the 12-layer case, by doubling the thickness of the first 3 layers of lead. This configuration had a comparable two-cluster reconstruction efficiency as the original 15-layer design, but poorer energy resolution.

Additional simulations were performed using variable segmentation of the scintillator layers. Keeping constant the total number of readout channels per sector, it was found that the maximum efficiency can be obtained if half of each stereo layer is equipped with 45-mm wide strips and half with 90-mm wide strips (double-strip readout). The triangular stereo layers overlap such that there is always a region with 45-mm wide strips in one of the stereo layers, as shown in Fig. 6.5. There is only a small loss of two-cluster efficiency at the highest momenta for this geometry compared with 45-mm wide strips in all stereo layers, see Fig. 6.6. It should be noted that at forward angles (short U-strips), where most of the high-energy π^0s are produced, all three stereo readout views have small readout segmentation.

The proposed design of the PCAL covers the full angular range of the EC. The PCAL has 15 scintillator and 14 lead layers, confined between two endplates. A variable width of the readout segmentation will be used to minimize the number of readout channels, while

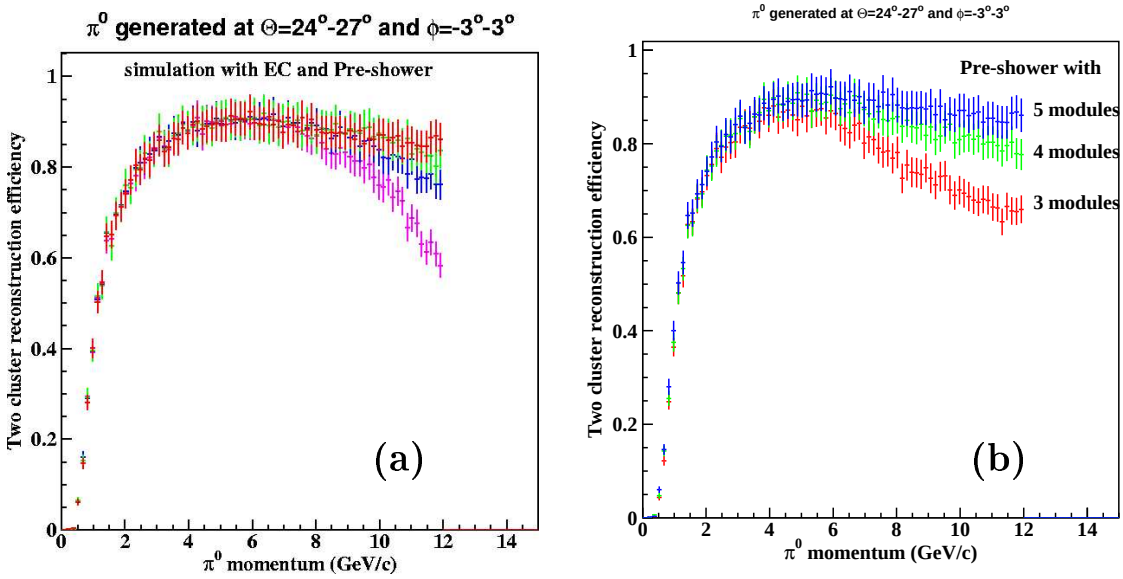

Figure 6.4: Performance of different configurations of the PCAL. a) The reconstruction efficiency for two clusters from π^0 decay photons as a function of pion momentum for different readout segmentation. The magenta points correspond to 60-mm strip width, the blue points are for 50-mm segmentation, the green points for 43-mm strip width, and the red points are for 35-mm width. b) The reconstruction efficiency for two clusters for different numbers of scintillator-lead layers. The red points correspond to a 9-layer configuration, the green points are for 12 layers, and the blue points are for 15 layers.

retaining sufficient resolution for the separation of close clusters. It is proposed to use 45-mm segmentation for the short strips in U, and for the long strips in the V and W stereo readout planes, at least half of the height of the layer. For the remaining part, 90-mm wide segmentation can be used (two strips). The total number of readout channels will be limited to 192 per sector.

6.3 Mechanical Design

Experience gained in the design and construction of the CLAS electromagnetic calorimeters, followed by 10 years of successful operation of these detectors, forms the basis of the PCAL design. A calorimeter of sampling structure with lead as the radiator and scintillator as the active medium is an economical way of covering a large detection area. The triangular shape of the EC with sides of order of 4.5 m in length, matches well the forward-angle acceptance of CLAS12. In the EC, three stereo readout planes were used, segmented into 36 transverse

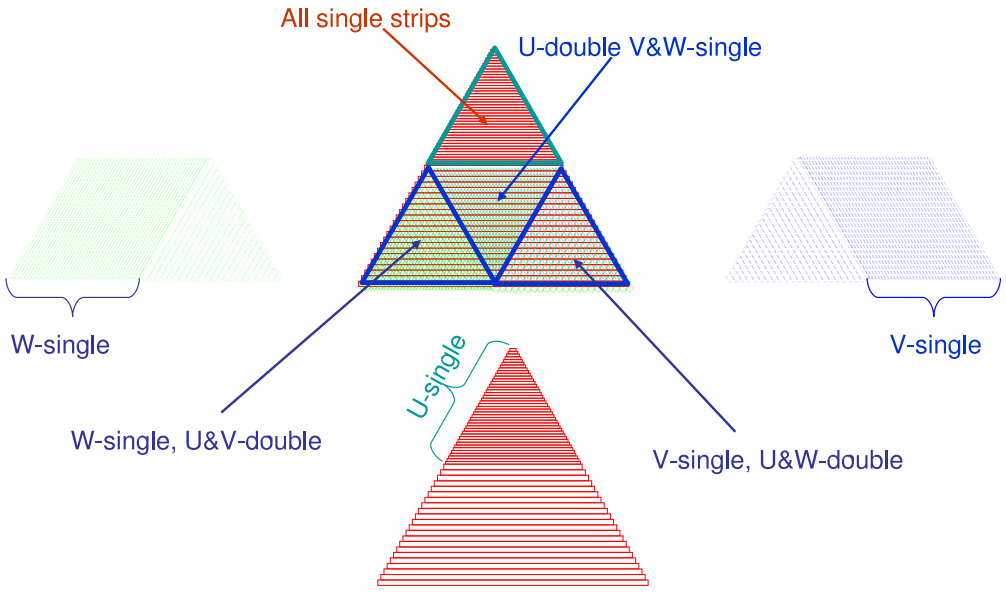

Figure 6.5: Variable segmentation for different stereo readout planes (U, V, and W). There is always a region with single strip (45-mm segmentation) readout in one of the stereo layers.

stacks and into two longitudinal parts. The calorimeter showed good performance in terms of energy and position reconstruction of showering particles. The proposed geometry of the PCAL is similar to the geometry of the existing EC, however the mechanical design will have a few essential differences.

The 15 layers of the PCAL will have all the same size, i.e. no pointing geometry as in the EC. This will simplify the design of the container, including the individual elements inside, and the assembly process. The triangular boxes will contain scintillators, lead, and support elements, and will have 1.5-in thick aluminum side walls and two composite endplates. The endplates will be constructed from 2-in thick composite foam, sandwiched between 2-mm thick stainless steel sheets connected with aluminum bars. Initial FEA calculations showed that the deflection of the plates is less than 1.5 mm in the center in the installed position [313], see Fig. 6.7.

Light from the scintillator strips will be transported to a photo-detector via wavelength-shifting fibers embedded in grooves on the surface of the scintillator strips. There will be no need for optical connections inside the box. This will allow for use of simple bars to secure the scintillator and lead layers in place inside the box, see Fig. 6.8. Spacers will be used to

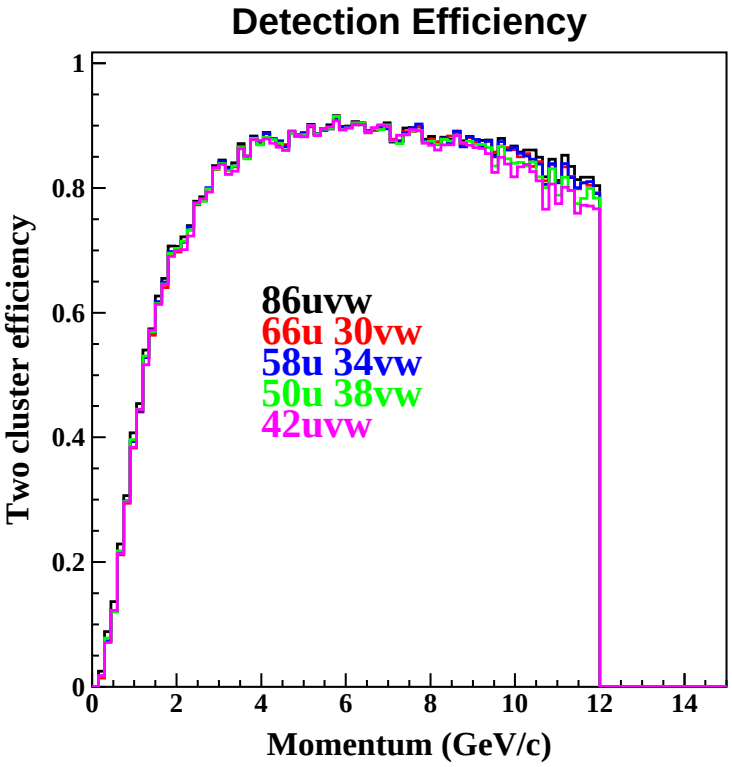

Figure 6.6: Various combinations of 45-mm and 90-mm readout segmentation. For the black histogram only 45-mm readout is used, amounting to a total of 258 channels per sector. The other histograms correspond to cases when part of the layer was read out in 90-mm segments, keeping the total number of channels to 192 per sector.

position the scintillators and lead sheets inside the box within 1-2 mm tolerances.

The fibers will be brought to the outside via feedthroughs in the side walls. There will be only a few feedthroughs, spaced along each side of the triangle. Fibers from several scintillator strips will be routed to a single feedthrough inside the box and will be spread out to the PMT adapters on the outside. There will be shelves mounted along the side walls at the level of the backplate that will hold adapters for the fiber-PMT connections. The shelves for the two sides will be located in the space between neighboring sectors to allow access to PMTs from the forward carriage (from behind the EC), see Fig. 6.9. For the side perpendicular to the beam direction, the location and the length of the shelves will be defined by the space free from the mounting arms of the low threshold Čerenkov counter. There will be thin aluminum covers along the shelves to make the PCAL container light tight.

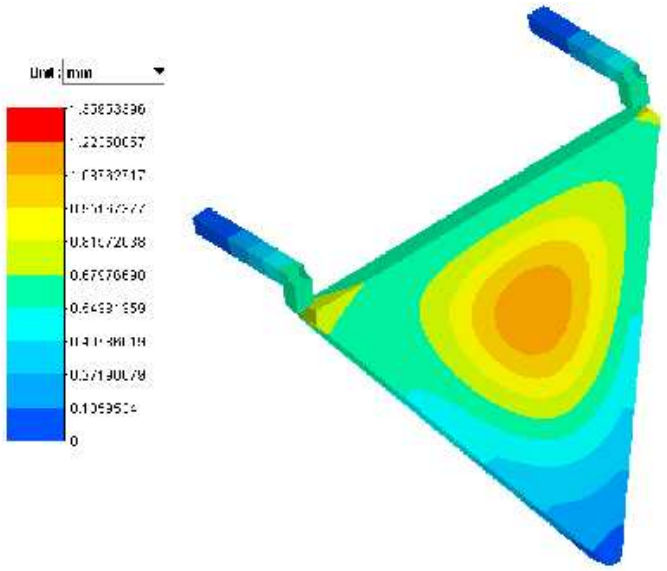

Figure 6.7: FEA simulation of the endplate deflection in the position of the PCAL in CLAS12 Sector 2. The maximum deflection with 2-in thick Rohacell foam sandwiched between 2-mm thick stainless steel sheets is less than 1.5 mm.

6.4 Signal Readout and Triggering

The electrical connections of the PCAL PMTs will be as follows: the voltage dividers for the PCAL PMTs will have high voltage (HV) as input and the anode signal as an output. Each PMT will be furnished with a separately regulated HV power source. The charge and the time of the anode signals for each PMT will be measured using a flash ADC (FADC) and a multi-hit TDC (MTDC), respectively. The PMT anode signal will be sent to a splitter through about 15 m of RG-58 cable, with approximately a 1 : 3 split. The larger portion of the split, ∼75%, will be sent to a discriminator input. Outputs from the discriminator will feed the MTDC and a scaler. The second output of the splitter, ∼25% of the signal, will go to the FADC. The PCAL will be included in the trigger system of CLAS12. The trigger signals from the PCAL modules will be formed using the fast readout of the FADCs and the FPGA programming of the mainframe controller. This type of trigger organization will allow for more sophisticated and robust trigger configurations compared to the total energy sum trigger configuration that is available in the current CLAS detector.

The energy uniformity of the calorimeter response is one of the important aspects in the configuration of the trigger system. The response of the PCAL to electromagnetic energy

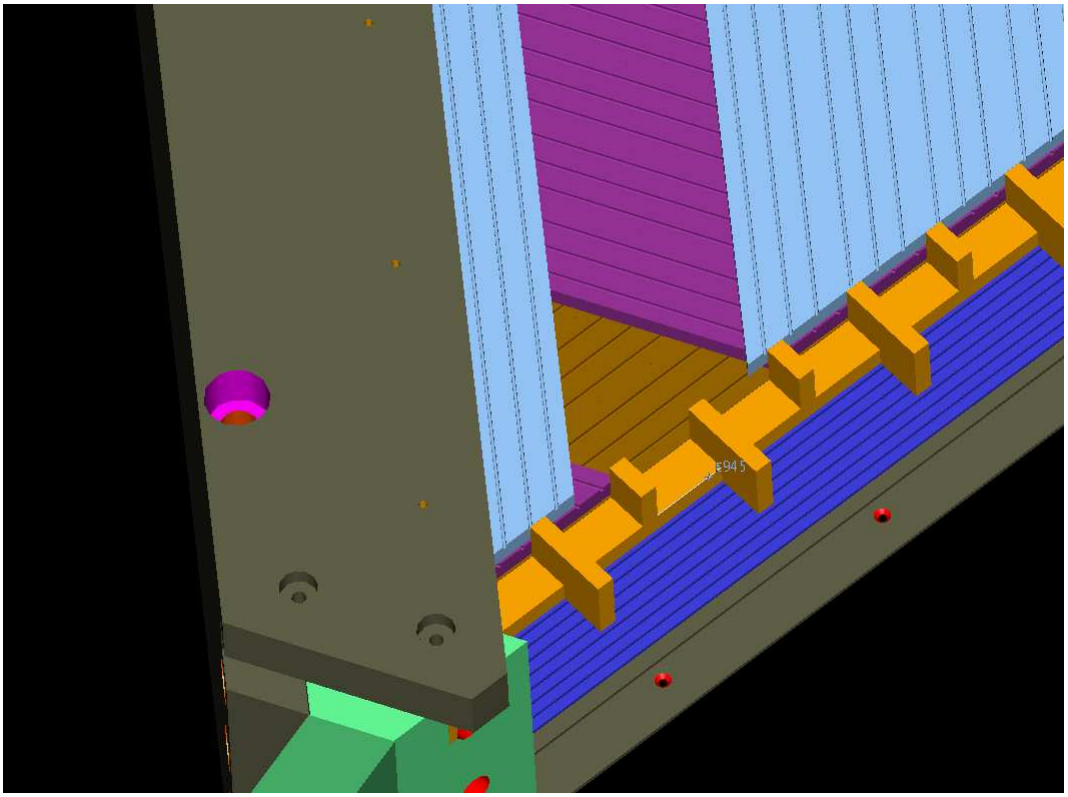

Figure 6.8: View of the opening of one PCAL sector. Three subsequent scintillator layers have strips oriented parallel to one of the sides of the triangle.

deposited in the scintillator material across the calorimeter front face depends upon several factors. Assuming that the same amount of energy deposited in the scintillator generates the same amount of light in the scintillating fibers independent of the position across the calorimeter, the light attenuation along in the fiber remains the major factor that determines the PMT response for a given scintillator stack in the U, V, and W views. A typical light attenuation length for green fibers is $L_0 = 300$ - 400 cm. Depending upon the $X-Y$ position at the calorimeter face, the light may travel up to nearly 500 cm before it reaches the photomultiplier. Therefore, the signal may be attenuated by a factor of $\sim$4 when reaching the PMT photo-cathode. Therefore the response of the individual U, V, or W stacks can vary by large factors, making the response highly non-uniform. However, the triangular structure of the PCAL with nearly equal side lengths, and with the scintillators oriented approximately 120° relative to each other, reduces this non-uniformity drastically when the signals from all strips are added together. In fact, in the case of linear attenuation, the sum of the signals from the U, V, and W strips is independent of the $X-Y$ position at the calorimeter face.

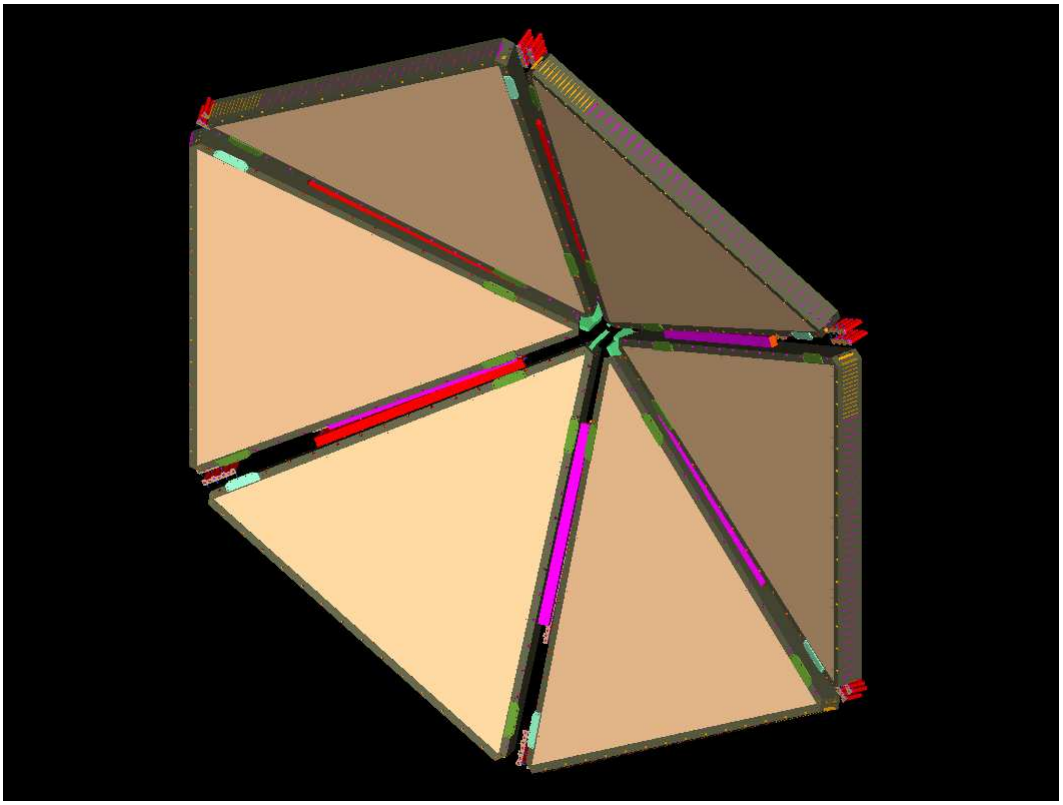

Figure 6.9: Six sector view of the PCAL. The PMTs are shown in red and magenta. The PMTs for two sides are aligned along the openings between the sectors. On the third side, the side perpendicular to the beam direction, the PMTs will occupy the space along the side where no fixtures for mounting other detectors exist.

However, in a more realistic case, the signal drops like an exponential function of the distance, i.e. $I(L) = I_0 \times \exp(-L/L_0)$, where L is the distance along the fiber from where the signal was generated. Adding all signals up will generate significantly higher sums ($\sim$40%) at the edges and corners of the calorimeter than in the center. While this effect can be corrected in the offline analysis, it could, however, significantly bias the calorimeter response towards lower energy deposition near the edges when used in a total energy trigger. To avoid this non-uniformity, the PCAL response can be made more uniform by giving lower weight factors to the shorter strips than to the longer strips in the trigger logic using the FADCs and the FPGA programming. The non-uniformity can be reduced to a few percent across the entire PCAL face.

6.5 Prototyping and Component Testing

The design goals for the PCAL detailed in the previous sections are based on the proposed geometry for CLAS12, the combined performance of the PCAL, the existing EC for CLAS12, and experience gained from the construction followed by 10 years of successful operation of the EC [310]. In addition, several factors have established the preliminary design. These principle considerations include:

- Comparable geometric coverage for the PCAL with respect to the EC;
- Good resolution/calorimetry coverage for up to 10 GeV photons and electrons;
- Improved particle identification ability to enhance final state reconstruction at higher energies;
- Information on the longitudinal shower development for e/π discrimination;
- Fast calorimeter response for use in the Level-1 trigger;
- Sufficient position information to resolve $\pi^0 \rightarrow \gamma\gamma$;
- Compatibility with the present EC and other CLAS components;
- Mechanical stability;
- Mechanical support viability;
- Constructibility (reasonable facilities, manpower and resources to assemble the detectors);
- Reasonable options for testing components in order to establish PCAL operational parameters.

In the construction of the existing EC system, the components were carefully characterized (e.g. scintillator attenuation, light transmission, photo-electron efficiencies). Calibration procedures were developed and continue to be improved to update the relevant properties (e.g. PMT gains and pedestal). This information has been used to construct algorithms for extracting particle identification, particle position, and particle energy [314]. An EC electronic sum is available as part of the current trigger options for CLAS and has proven to be

essential for limiting the amount of recorded data, while identifying useful final states. The calorimeter has operated reliably, providing critical information on reaction final states, with sound performance in terms of maintenance and stability. The mechanical structures for the calorimeter movement and support work well. Thus part of the PCAL design has been based on the existing EC.

To match the above goals, a lead-scintillator sampling calorimeter with a wavelength shifting fiber readout was chosen. Scintillator light readout systems with embedded fibers are well known. This technique was used, for example, in the MINOS FAR detector [315], and many other "tile" calorimeters.

The main design features of the PCAL are:

- Triangular shape with sides of order 4.0 m in length;
- Sampling structure with Pb as the radiator and scintillator as the active medium;
  - Lead 2.2 mm (available sheets) [simulation verifies this choice of sheet depth];
  - Scintillator strips:
    * Scintillator 10-mm longitudinal depth;
    * Strip width will be important in determining position resolution;
    * Simulation suggests that 4.5-cm width is adequate to reach required position resolution;
    * U, V, and W readout;
- Light readout needs to reach several photo-electrons/MeV of deposited energy;
- Components need to be combined to reduce the required number of PMTs;
- Wavelength-shifting fibers are the chosen method for light collection.

Component testing was primarily focused on finding the components that did not compromise the design goals, while minimizing costs. Tests were conducted to find the optimal:

- Wavelength-shifting fibers;
- Photomultiplier tubes;

- Number of fibers per strip;
- Grooved scintillators;
- Glue that binds fibers and scintillators and improves optical properties.

Tests were also designed to characterize combinations of components in terms of the number photo-electrons/MeV and to verify the expected attenuation lengths for the scintillator and the fiber.

For these test measurements, several different types of scintillator, wavelength-shifting fibers (WLS - single and multi-clad), and PMTs were studied, see Table 6.1. Extruded scintillators from Fermilab (FNAL) and Kharkov, as well as commercial scintillators from Eljen were compared on the basis of light yield and cost. The FNAL and Kharkov strips are grooved during the extrusion by the die [316, 317], whereas the grooves for the Eljen scintillators were machined by the manufacturer. The grooves provide insets for the WLS fibers. The fibers are held in place by either a UV-cured glue or an epoxy. Light absorption by the fiber is influenced by the optical properties of the glue. Preliminary results indicate that an optical epoxy is adequate, both in terms of bonding and light transmission. The more expensive UV-cured optical glues were used during these tests. The FNAL and Kharkov scintillator strips were coated with a reflective material (1-mm titanium dioxide, excluding the inside surface of grooves) to improve light collection. Tests on the Eljen scintillator were done with and without an additional aluminized-mylar surface. The Hamamatsu R1450-13 and R6095 PMTs were tested because of their high quantum efficiency at 500 nm. R1450-13 and R6095 PMTs were chosen with QE $>$ 18 and $>$16% at 500 nm and studied as possible options. Light yield measurements were done with Kuraray 1.5-mm and 2-mm diameter Y11 fibers to determine the dependence of the light yield on the fiber diameter. Finally, a sufficient sample of scintillator-WLSF-PMT combinations was studied to determine the optimal combination.

6.5.1 Setup

Measurements were performed in the semi-clean room in the EEL building at JLab using a 4-m long dark box (see Fig. 6.10). The box was instrumented with a moving cart. In Fig. 6.11, a schematic view of the setup is shown. Scintillator strips with fibers were secured inside the box. The trigger PMT was attached directly to the end of the scintillator strip through

PMT	Type	Photo-cathode	# of stages
Hamamatsu	R7899EG	25 mm	10
	R1450-13	19 mm	10
	R6095	28 mm	11
ElectronTubes	9124B	30 mm	11
Photonis	XP1912	19 mm	10
	XP2802	19 mm	10
WLS fibers	Type	Diameter	Cladding
Kuraray	Y11	2 mm	Single
	Y11	1.5 mm	Single
	Y11	1 mm	Single
	Y11	1 mm	Multi
Bicron	BC-91A	1 mm	Single
	BC-92	1 mm	Single
Scintillators	Type	Cross section	# of grooves
Eljen Tech.	EJ-204	3×1 cm^2	4
	EJ-204	3×1 cm^2	No grooves
FNAL	MINOS	4×1 cm^2	1
Amcrys-Plast, Kharkov		2.6×1 cm^2	2
		2.6×1 cm^2	3

Table 6.1: Pre-shower calorimeter readout components used in the test.

an acrylic light guide. For the scintillator-light guide and the light guide-PMT connections, Bicron BC-630 optical grease was used.

WLS fibers were glued inside the scintillator grooves using Dymax UV-curable optical glue OP-52. The fibers were extended about 40 cm from the end of the scintillator in order to connect to the photo-cathode of a test PMT. The test PMT was installed inside a plastic housing, a tube with μ-metal shielding inside. The housing tube had two end-caps, one with connectors for the HV and signal cables, and the another with an adapter for the fiber connection [318]. To secure the fiber on the photo-cathode of the test PMT, several plastic

Figure 6.10: Picture of the dark box. The moveable cart is mounted on rails.

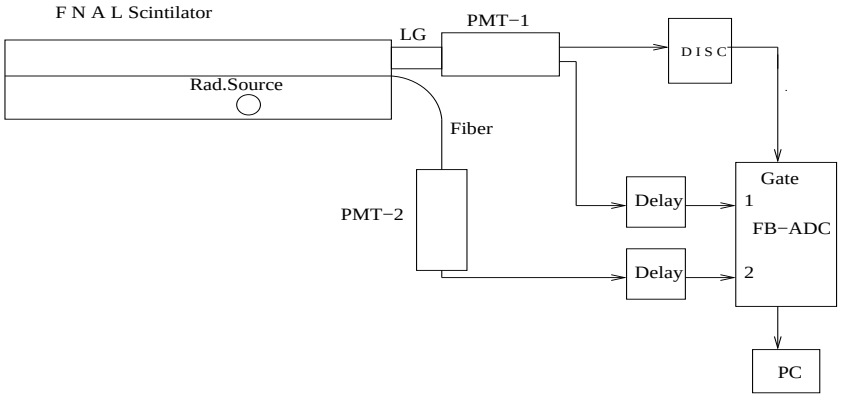

Figure 6.11: Schematic view of the setup for the light yield measurements.

adapters were built with thin metallic tubes as inserts. The inner diameter of the tubes was chosen to have a tight fit for the fibers. The tubes were aligned along the axis of the PMT and guided the fibers in the direction perpendicular to the photo-cathode. Bicron BC-630 optical grease was used between the fiber and the photo-cathode for good optical contact.

The readout electronics of the system consisted of a LeCroy 1881M ADC and a Philips 704 discriminator. As a gate for the ADC, the discriminated pulse from the trigger PMT was

used. Signals of the test and the trigger PMTs were delayed and connected to the ADC inputs, see Fig. 6.11. The ADC information was read out using the standard CLAS data acquisition (DAQ) software.

6.5.2 Determination of the Number of Photo-electrons

For the analysis of the photo-electron statistics, the method developed in Ref. [319] was used. Each ADC spectrum was fit with a sum of a Poisson distribution, $P_i(N_{pe})$, convoluted with a Gaussian function, $C_i(n_{ch})$. Poisson distributions describe the photo-electron distribution, while the Gaussians are used to describe the PMT response. The predicted ADC spectrum for a given average number of photo-electrons will be:

$$A = c \cdot \sum_i P_i(N_{pe}) \times C_i(n_{ch}) \quad (6.1)$$

$$P_i(N_{pe}) = \frac{N_{pe}^i \cdot e^{-N_{pe}}}{i!} \quad (6.2)$$

$$C_i(n_{ch}) = \frac{1}{\sigma_1 \cdot \sqrt{i}} \cdot \exp\left(-(\frac{n_{ch} - (a_1 + (i-1) \cdot a_0)}{\sigma_1 \cdot \sqrt{2i}})^2\right). \quad (6.3)$$

In eq.(6.1), the summation goes over the possible number of photo-electrons in the spectrum, i. The coefficient c is for the overall normalization and N_{pe} is the average number of photo-electrons. In eq.(6.3), n_{ch} is the pedestal-subtracted ADC channel number. The parameters a_1 and σ_1 are the position and the standard deviation of the single photo-electron peak in units of ADC channel. a_0 is the distance between two adjacent photo-electron peaks in units of ADC channel (not necessarily equal to a_1). The fit parameters were c, N_{pe}, and a_0.

The parameters a_1 and σ_1 were defined from fits to a single photo-electron distribution for each of the test PMTs. Two examples of single photo-electron peaks are shown in Fig. 6.12. The left plot shows the response of the Photonis XP2802 PMT as the light intensity is lowered. The right graph shows a single photo-electron peak for the Hamamatsu R6095 PMT.

6.5.3 Determination of the Absolute Light Yield

Since the measurements were carried out with a β-source, the amount of energy deposited for a given event will vary significantly. Most of the measurements were done with a ^{90}Sr source that provided a 2.3-MeV β based on the decay $^{90}\mathrm{Sr} \rightarrow 0.546\ \mathrm{MeV}\beta^- + ^{90}\mathrm{Y} \rightarrow 2.28\ \mathrm{MeV}\beta^-$.

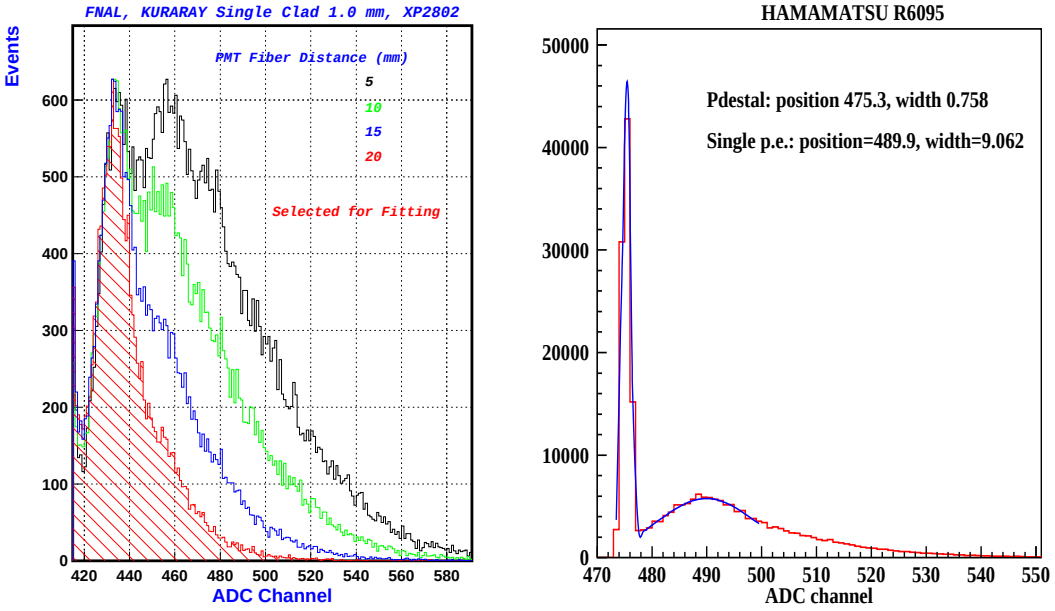

Figure 6.12: (Left) ADC distribution of the XP2802 PMT corresponding to a few and single photo-electrons. (Right) Fit to the single photo-electron distribution of the Hamamatsu R6095 PMT. The fit was done using the sum of two Gaussians, one for the ADC pedestal and a second one for the single photo-electron distribution.

The measured responses will, however, depend on the part of the β spectrum that was selected by the trigger PMT. A typical spectrum is shown in Fig. 6.13. To reduce the systematics due to variations in the trigger conditions and to estimate the deposited energy, events from the endpoint of the β spectrum ($\sim$2 MeV) were used in the comparisons. The endpoint was identified by increasing the trigger threshold until the average N_{pe} remained constant. In Fig. 6.14, fits to the ADC distributions of the Hamamatsu R7899EG and R6095 PMTs for different trigger settings (ADC channel 550 to 600) are presented. The dependence of N_{pe} on the trigger PMT ADC channel is shown in Fig. 6.15. As one would expect, the number of photo-electrons increases with increasing trigger ADC channel and flattens out at the end. The number of photo-electrons at the endpoint was taken as the light yield corresponding to a $\sim$2 MeV energy deposition.

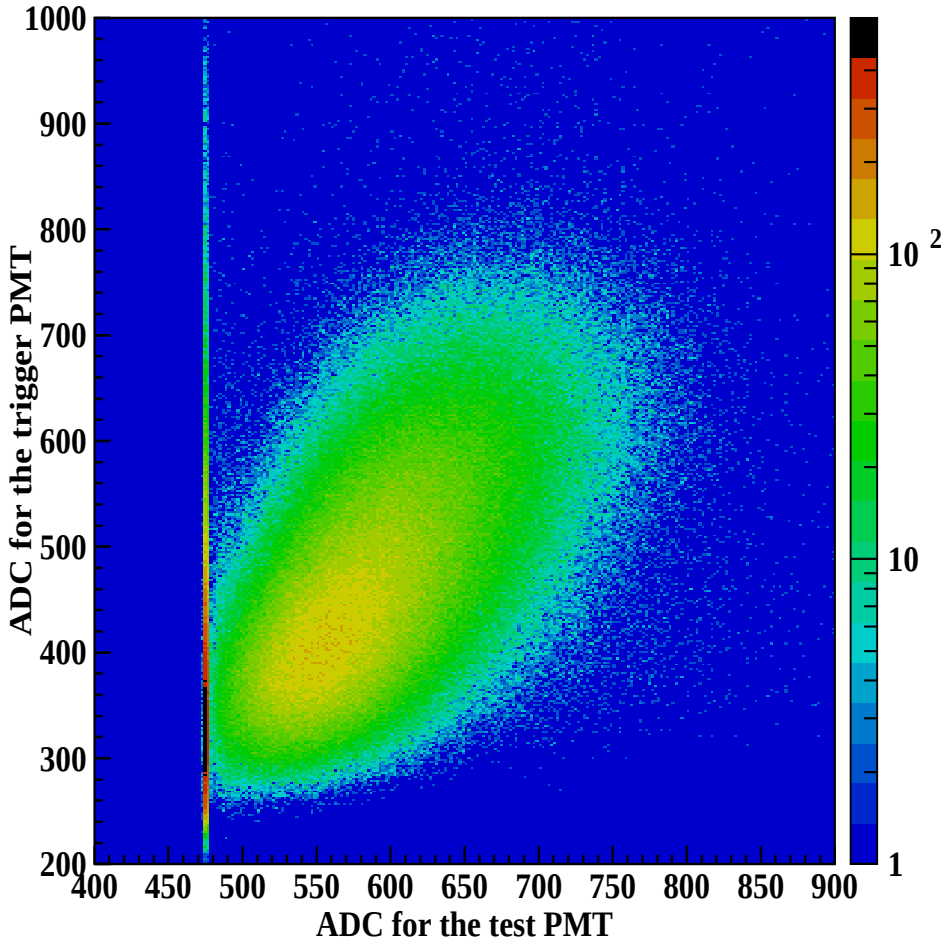

Figure 6.13: ADC spectra of the trigger and test PMTs. The test PMT ADC distributions for different slices of the trigger PMT ADC were fitted to get the photo-electron statistics.

6.5.4 Light Yield with Single-Fiber Readout

Studies of the PMT response were performed with the same FNAL scintillator and the single-clad 1-mm diameter Y11 WLS fiber (WLSF). Sample results are shown in Fig. 6.16. The response was extrapolated to the endpoint energy by increasing the trigger thresholds. All of the fits show the expected flattening at the end of the spectrum. The tabulated yields (see Table 6.2) are based on the endpoint extrapolation to ∼2 MeV energy deposition.

The Hamamatsu R7899EG (green extended photo-cathode) PMT has the highest light yield, followed by the Hamamatsu R6095 PMT with ∼26% fewer photo-electrons. The other PMTs, the PHOTONIS XP2902, the ElectronTubes 9124B, and the Hamamatsu R1450, did not perform as well.

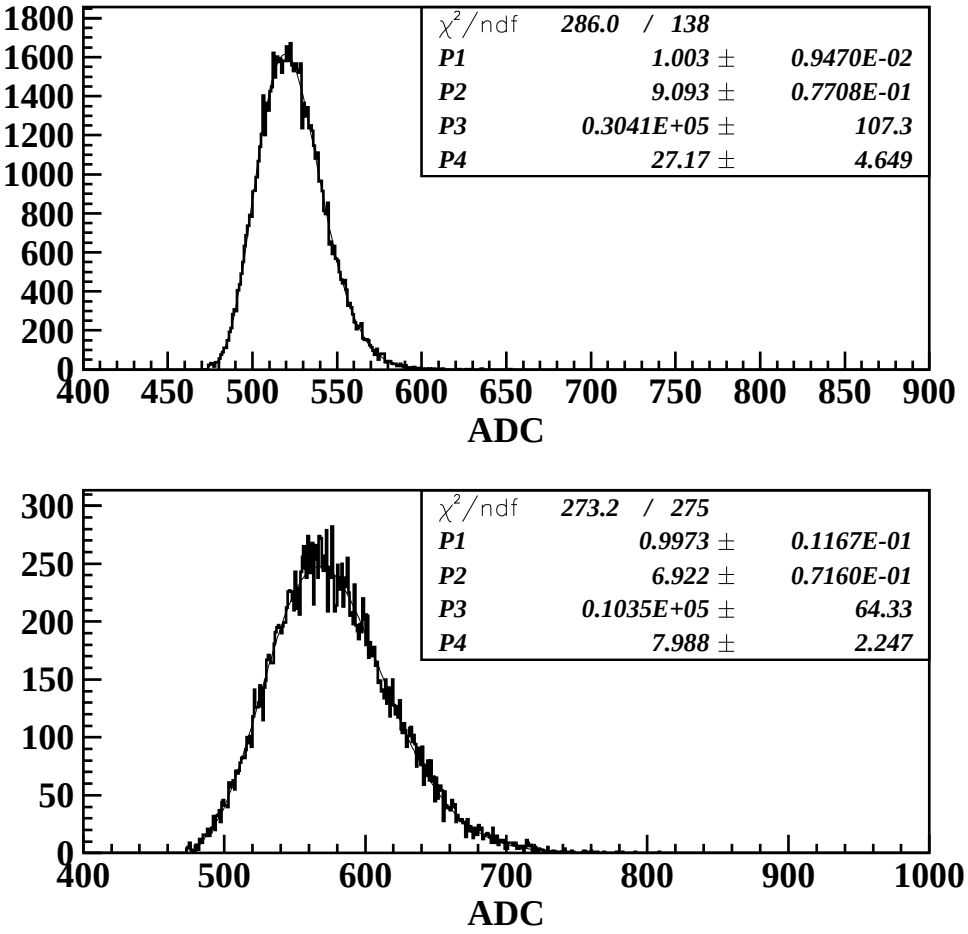

Figure 6.14: Fit to the ADC spectra of the Hamamatsu R7899EG and R6095 PMTs with eq.(6.2). The spectra correspond to the trigger PMT ADC channels 550 to 600.

PMT	R7899EG	R6095	XP2802	R1450	9124B
N_{pe}	10.3	7.6	7.3	6.5	4.7
$\sigma_{N_{pe}}$	0.53	0.57	0.39	0.17	0.14
χ^2	1.7	0.92	1.16	1.23	0.7

Table 6.2: The number of photo-electrons for different PMTs corresponding to a 2 MeV energy deposition in the FNAL extruded scintillator with one groove. Readout employed a 1-mm diameter, single-clad Y11 WLS fiber.

Comparison of the scintillators was done using an R6095 PMT. All of the strips had a 1-mm, single-clad Y11 fiber glued in the groove on the surface of the strip. The EJ204 scintillator did not have a reflective coating, therefore two measurements with and without

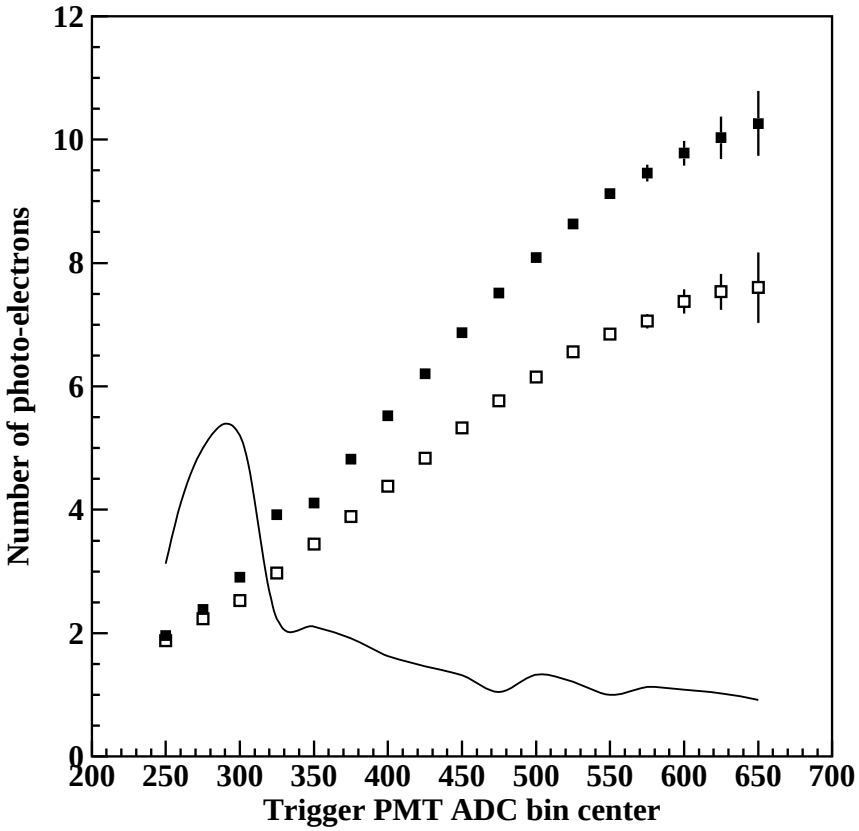

Figure 6.15: Dependence of N_{pe} on the trigger PMT ADC channel. The closed squares are N_{pe} for the R7899EG PMT and the open squares are for the R6095 PMT. The solid line curve is the χ^2 distribution for the fit to the spectra of the R7899EG PMT.

wrapping were done. The results are tabulated in Table 6.3 and are shown in Fig. 6.17. The FNAL extruded scintillator showed the highest light yield.

	FNAL	Eljen	Eljen wrapped	Kharkov
N_{pe}	7.6	2.5	5.7	6.8
$\sigma_{N_{pe}}$	0.57	0.55	0.33	0.23
χ^2	0.92	1.08	1.1	1.02

Table 6.3: The number of photo-electrons for 2 MeV of energy deposition in different scintillator strips. Readout was with 1-mm, single-clad Y11 WLS fibers and an R6095 PMT.

The candidate WLS fibers were studied. Different fiber types and fiber diameters were

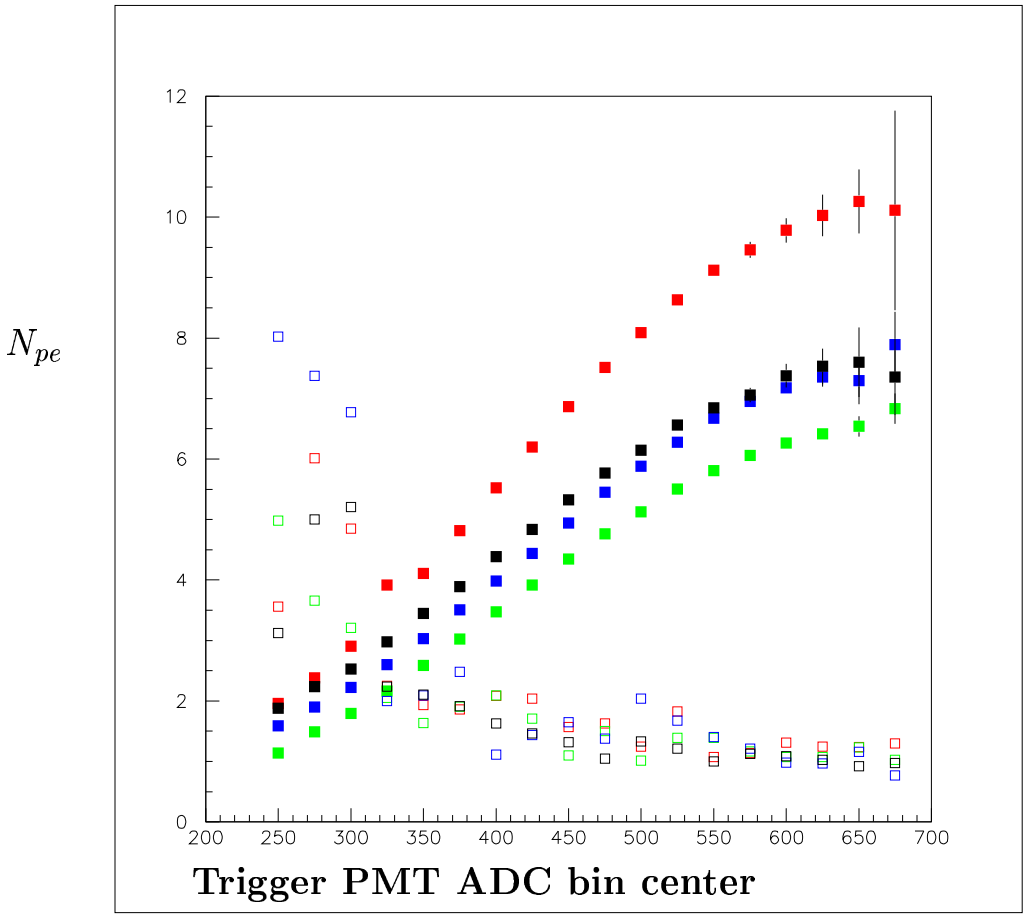

Figure 6.16: Dependence of N_{pe} on the trigger PMT ADC channel. The closed squares are N_{pe} for R7899EG (red), R6095 (black), XP2802 (blue), and R1450 (green) PMTs. The open squares are the χ^2 distributions for the fits (in the same color coding).

glued into the FNAL scintillator strip and the photo-electron statistics were measured with the Hamamatsu R7899EG PMT. The relative light yield for different fibers is presented in Fig. 6.18. The light yield for the Bicron G92 fiber is not presented because it was too low (not a surprise since G92 is designed to have a fast response time and has a small attenuation length).

The number of photo-electrons was observed to increase with the diameter of the fiber. A 1.5-mm fiber has ~25% more light than a 1-mm diameter fiber, and a 2-mm fiber has ~40% more light. The light yield is also higher for multi-clad fibers compared to single-clad by about 20%. Bicron G91A 1-mm diameter, single-clad fiber has about 10% less light yield

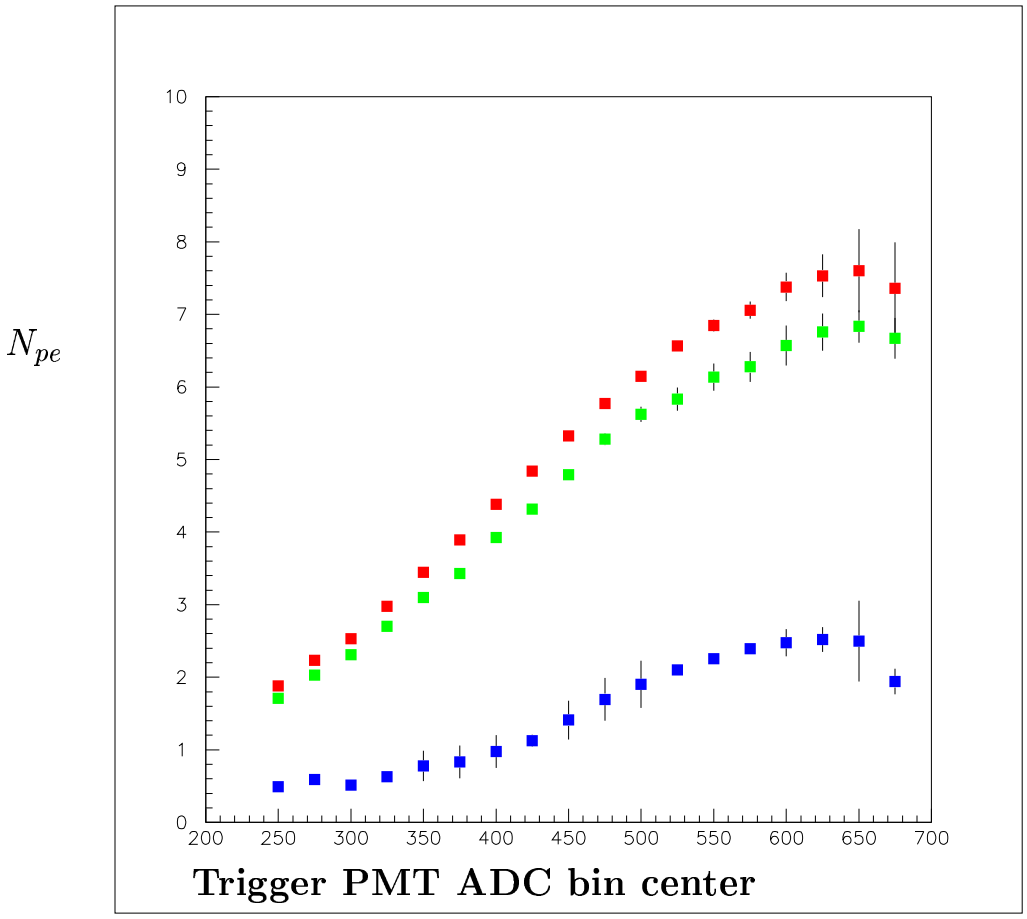

Figure 6.17: Dependence of N_{pe} on the trigger PMT ADC channel. The closed squares are N_{pe} for the FNAL extruded scintillator strip (red), Kharkov extruded scintillator strip (green), and the Eljen diamond-cut strip (blue). Note that the FNAL and Kharkov scintillator strips have a reflective coating, while the Eljen scintillator was wrapped only in aluminized mylar.

than Kuraray 1.0-mm, single-clad Y11 fiber.

6.5.5 More Measurements

Additional measurements have been performed to check the systematics of the results. The same scintillator-WLSF-PMT combinations were measured at several settings. Results from different measurements were consistent to within a few percent. One of the major sources of uncertainty is the determination of the single photo-electron peak position and the Gaussian width for a given PMT. Therefore, measurements for one PMT but several different voltages were performed. In Fig. 6.19, the dependence in the measured number of photo-electrons vs.

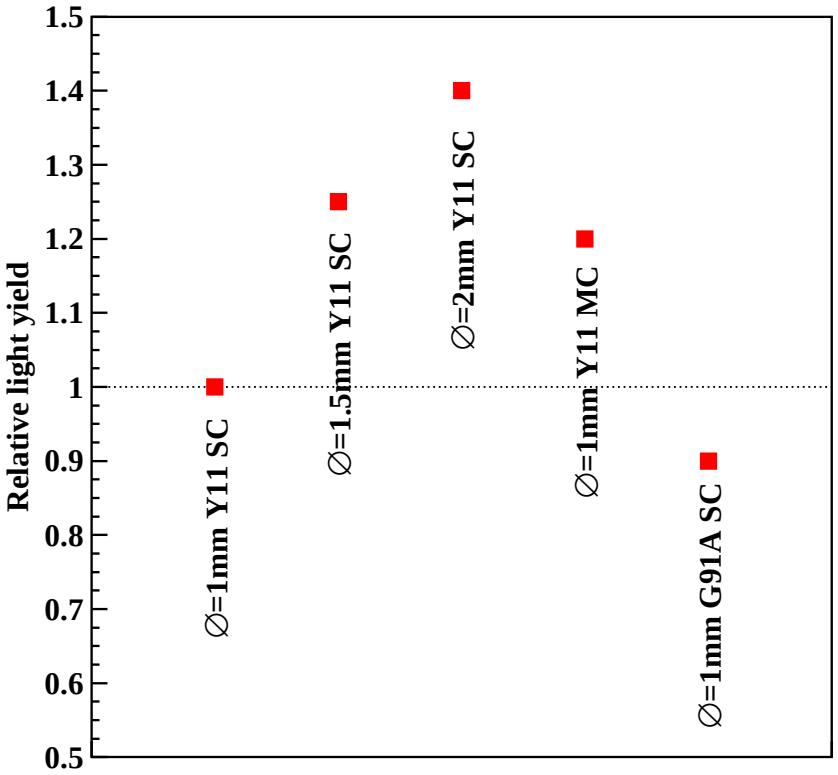

Figure 6.18: Light yield for different WLS fiber readout relative to 1-mm diameter, single-clad Y11 fiber. In all cases, the fibers were glued to the FNAL extruded fiber and the Hamamatsu R7899 PMT was used for the readout.

the trigger PMT response for different HV settings is shown. The maximum difference in the estimated number of photo-electrons for the extrapolated end point is <10%.

Measurements were made with cosmic ray muons in order to verify the above results. The light yield for the R6095 PMT with FNAL scintillator and 1-mm diameter single-clad Y11 fibers was determined. As a gate for the ADC, the coincidence of the trigger PMT and the scintillator counter positioned above the scintillator strip was used. The counter had 1-cm thick, 1.5×4 cm^2 scintillator. A fit to the test PMT spectrum, selected with a cut on the trigger PMT ADC in the range of MIP energy deposition, yielded ∼9 photo-electrons. There is a difference of ∼20% compared to the number of photo-electrons obtained with the ^{90}Sr source (∼2 MeV energy deposition). This difference can be explained by the fact that in the cosmic setup, the average path of particles is >1 cm. Also the energy loss in the 1-mm titanium dioxide coating would lower the β energy deposited, but it would not influence the cosmic ray muon energy deposition. More precise measurements of the absolute photo-electron yield will

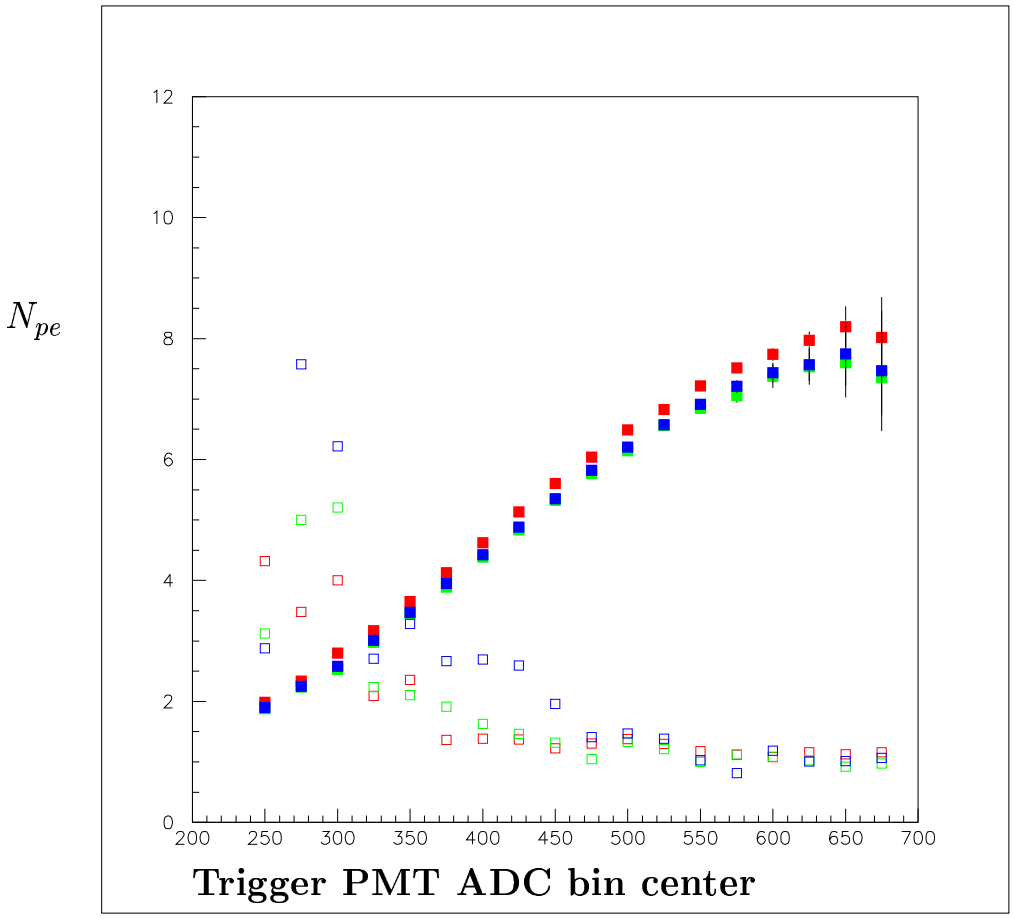

Figure 6.19: Light yield for the Hamamatsu R6095 PMT operated at different HV settings. The blue squares correspond to 800 V, the red squares are at 850 V, and the green squares are at 900 V. The open squares correspond to the χ^2 distributions of the fits.

be done with a box prototype (see below).

6.5.6 Multiple Fiber Readout

In the final design of the PCAL, each scintillator strip will be read out with three WLS green fibers embedded in the grooves on the surface of the scintillator strip. To estimate the expected light yield for the three fiber readout, the Amcrys-Plast, Kharkov extruded scintillator strips with three grooves were used with Kuraray 1-mm diameter, single-clad Y11 fibers. In Fig. 6.20, the light yield dependences on the trigger PMT ADC bin center are shown for one, two, and three fiber readout. The source (^{90}Sr) position was unchanged during these measurements. As one can see, the number of photo-electrons is proportional to the number of fibers. In the

figure the open squares represent the χ^2 distribution for the fit to the two fiber readout case.

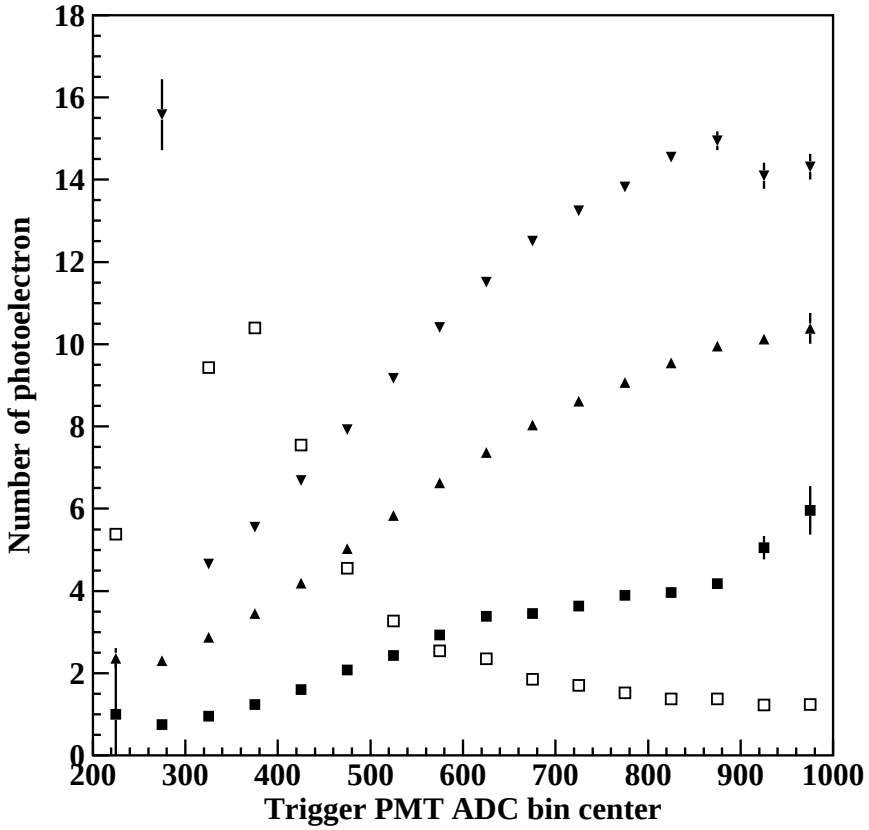

Figure 6.20: Dependence of N_{pe} on the trigger PMT ADC channel for one (closed squares), two (closed upward triangles), and three (closed downward triangles) WLS fiber readout from the Kharkov scintillator strip with three grooves on the surface. The source was ^{90}Sr and the readout PMT was the R6095. The open squares represent the χ^2 distributions for the fit to the two fiber readout case.

The source position dependence was studied using three fiber readout. The source was moved on the surface of the strip from one side to the other, and the measurements of the light yield were performed at four points. The results are shown in Fig. 6.21. No dependence on the position of the source is observed. However, it should be noted that the multi-fiber readout and the position dependence should be checked with the final strip geometry since the Kharkov scintillators are only 2.63-cm wide, while for the pre-shower, 4.5-cm wide scintillators will be used.

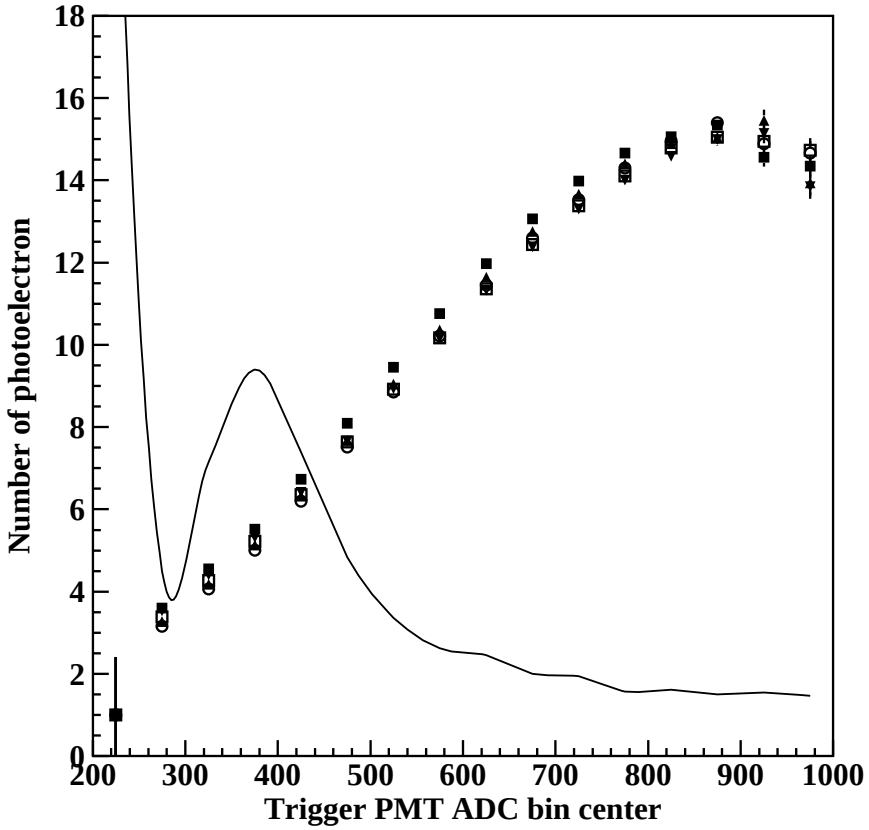

Figure 6.21: Dependence of N_{pe} on the trigger PMT ADC channel for the three fiber readout of the Kharkov three-groove scintillator strip. Different color symbols correspond to different position of the ^{90}Sr source. For light readout, the R6095 PMT was used.

6.5.7 Summary of the Test Measurements

The light yield for several different types of scintillator strips, WLS green fibers, and PMTs was measured. The purpose of these measurements was to select the best combination of the scintillator-WLSF-PMT based on the performance and price. Systematic uncertainties of the relative light yield measurements of different combinations of scintillator-WLSF-PMT were <10%. For the absolute light yield, the estimated systematic uncertainty was ∼20%.

The best results were obtained with the FNAL extruded scintillator, Kuraray Y11 fibers, and the Hamamatsu R7899EG PMT. The Hamamatsu R6095 PMT, selected with QE >16% at 500 nm, showed only ∼25% less light yield, while in price it is about 33% times less expensive. Multi-clad fiber readout showed ∼20% more light than single-clad fiber readout, but it is about 35% more expensive.

Based on the measurement results and the available price estimates, the choice for the

pre-shower will be: the FNAL extruded scintillator, Kuraray 1-mm diameter, single-clad Y11 fiber, and the Hamamatsu R6095 PMT, selected with QE >16% at 500 nm. It should be noted that by the performance and price, extruded scintillators from Amcrys-Plast, Kharkov (Ukraine), Bicron G91A wavelength-shifting fibers, and the Hamamatsu R1450 PMT, selected to have >18% quantum efficiency at 500 nm, were not too far from the best choice set and generally meet the requirements for the pre-shower.

Component	Optimal Choice
WLS Fiber	Kuraray 1-mm diameter, single clad WLS fiber (Y11)
PMT	Hamamatsu R6095 PMT, selected with QE >16% at 500 nm
Scintillator	FNAL extruded scintillator

Table 6.4: Final choice for the pre-shower calorimeter components.

6.5.8 Prototype of the PCAL Module

A small-size prototype has been designed and constructed from existing materials. The cross section of the prototype has a rectangular shape and is on the order of 30 cm. The prototype contains 15 layers of scintillator and 14 layers of lead. Top and side views of this prototype are shown in Fig. 6.22. The scintillator layers were read out on three sides ($X1$, Y, $X2$), so as to mimic the final (UVW) readout planned for the PCAL. In each view there were five readout strips channels. The scintillator and lead layers were stacked using horizontal supports to secure them inside the box. There were openings made in these supports and on the side walls to allow the WLS fibers to come out of the box. To connect to the PMTs, the fibers were glued inside holders located on shelfs that were attached along the side plates, outside of the box. The ends of the fibers were polished and the PMTs were attached to the fibers using an optical gel. Only $X1$ and Y views were furnished with Hamamatsu R6095 PMTs. On $X2$, 5 different PMTs were used. The full five module longitudinal depth in each view of the prototype will allow accurate characterization of the shower and a fairly complete determination of the combined response of the components in terms of energy and timing. The prototype will be placed in the Hall B beam for direct studies with electrons.

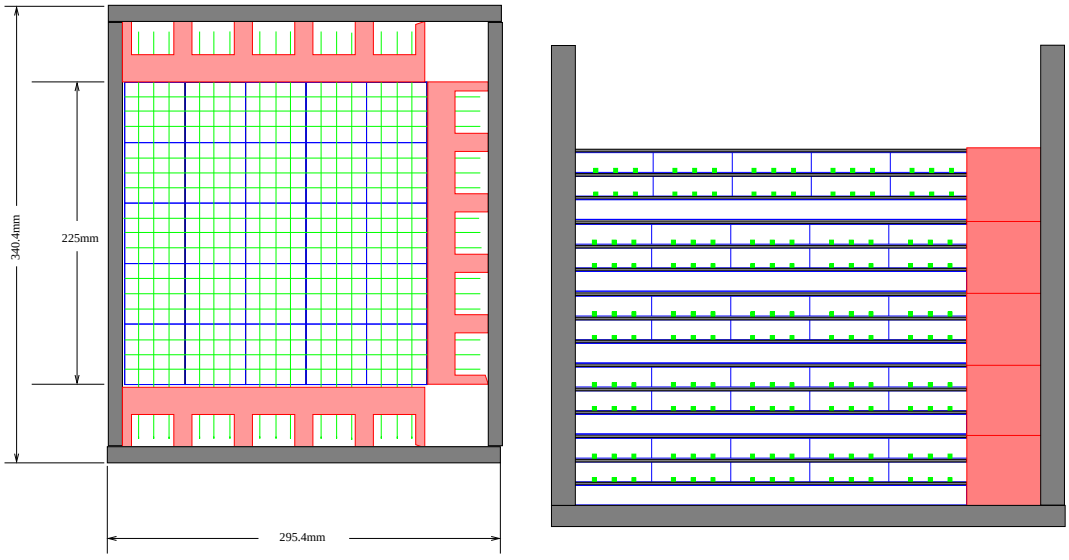

Figure 6.22: Two views of the box prototype currently under construction. The full 5 module longitudinal depth will allow study of the behavior of shower development and actual sampling features using cosmic rays or possibly from in-beam tests.

The first measurements with the prototype were performed using cosmic ray muons. In Fig. 6.23, a schematic of the test setup is shown. As a trigger, a coincidence of a scintillator counter, located on top of the prototype, with an OR of one of the prototype layers was used. The signals from each PMT were split into two parts with a ratio of 2 : 1. The larger part was sent to the discriminator and then to the trigger logic and TDCs. The smaller part was delayed and sent to the ADC inputs.

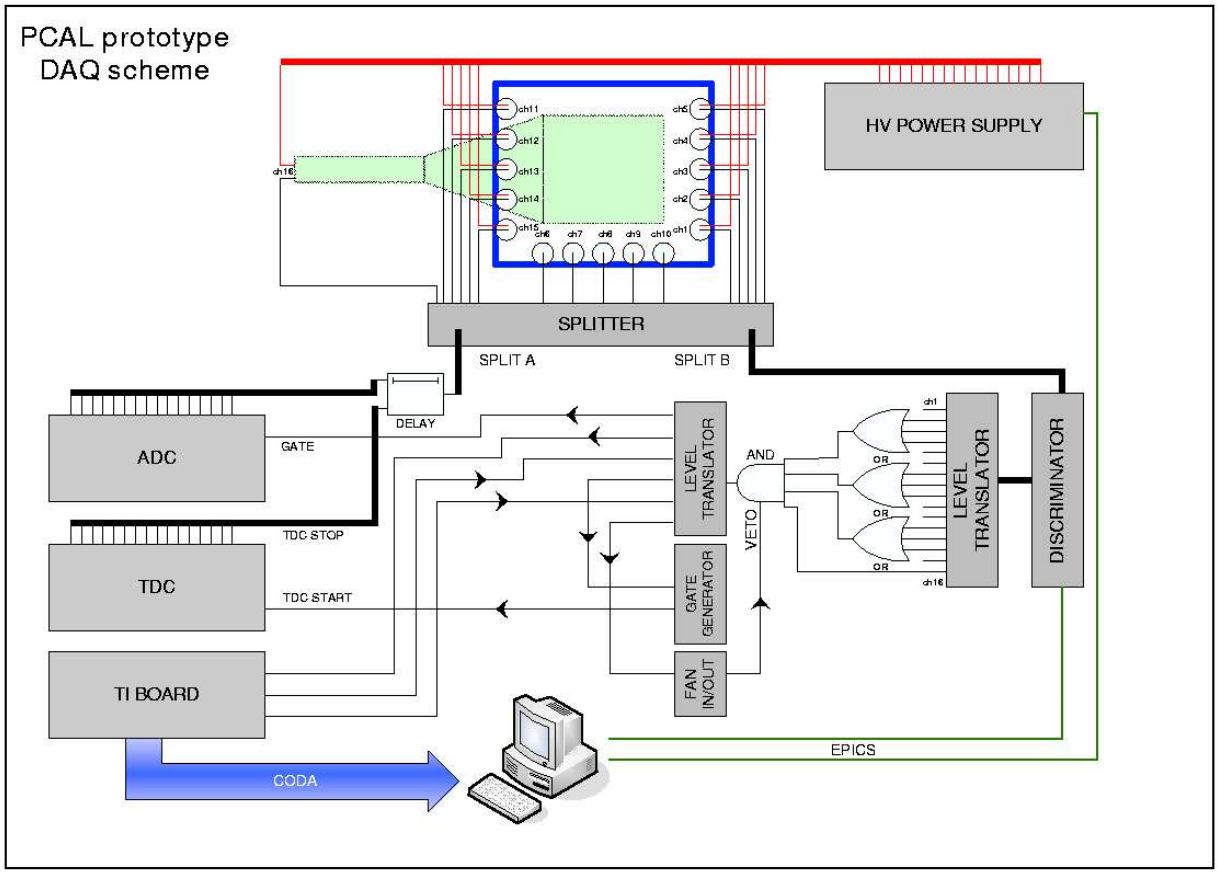

Figure 6.23: Schematic layout of the cosmic test setup of the PCAL prototype.

The main purpose of the cosmic test was to determine the average number of photo-electrons per MeV of energy deposition, and to compare this with the single strip measurements presented above. In Fig. 6.24, ADC spectra of all five PMTs on the $X1$ view are shown. In these distributions, events when only a single PMT is fired in all three views are selected. This selection ensures an MIP crossing through the system. The ADC distributions in the figure correspond to the MIP energy distribution and have a characteristic Landau shape.

Fits were performed using two Gaussian functions and the peak position of the Gaussian with the narrower width was taken as the point of 2 MeV energy deposition in a single scintillator strip. The corresponding distribution of the Y view is shown in Fig. 6.25.

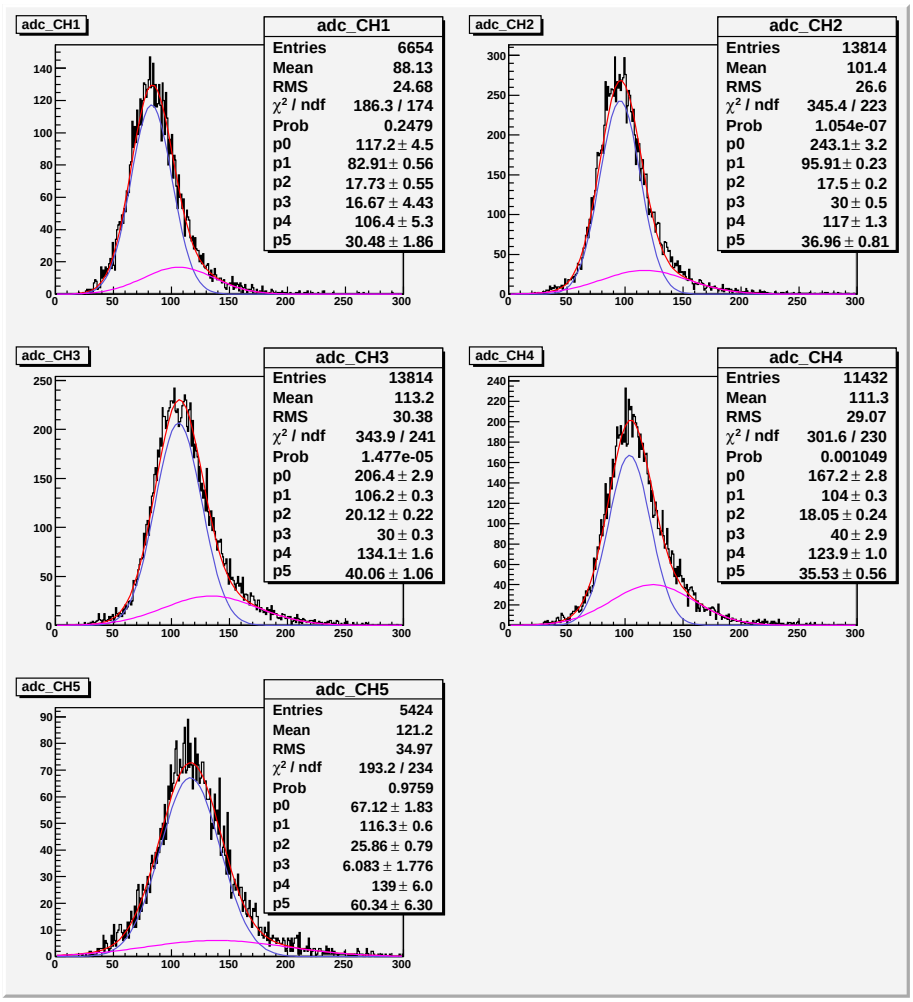

Figure 6.24: ADC spectra of the $X1$ view PMTs corresponding to the MIP energy deposition.

To determine the photo-electron statistics, for each PMT position, the single photo-electron peak at a given voltage was measured using a setup with a trigger PMT and a LED. For accurate determination of the single photo-electron peak position, the gain vs. voltage for each PMT was measured in the single photo-electron regime and in the regime when a large amount of light was directed to the photo-cathode. Corrections to the light emission stability of the LED were applied using the trigger PMT pulse. In Table 6.5 the obtained photo-electron statistics for all 10 R6095 PMTs are presented. The average number of photo-electrons

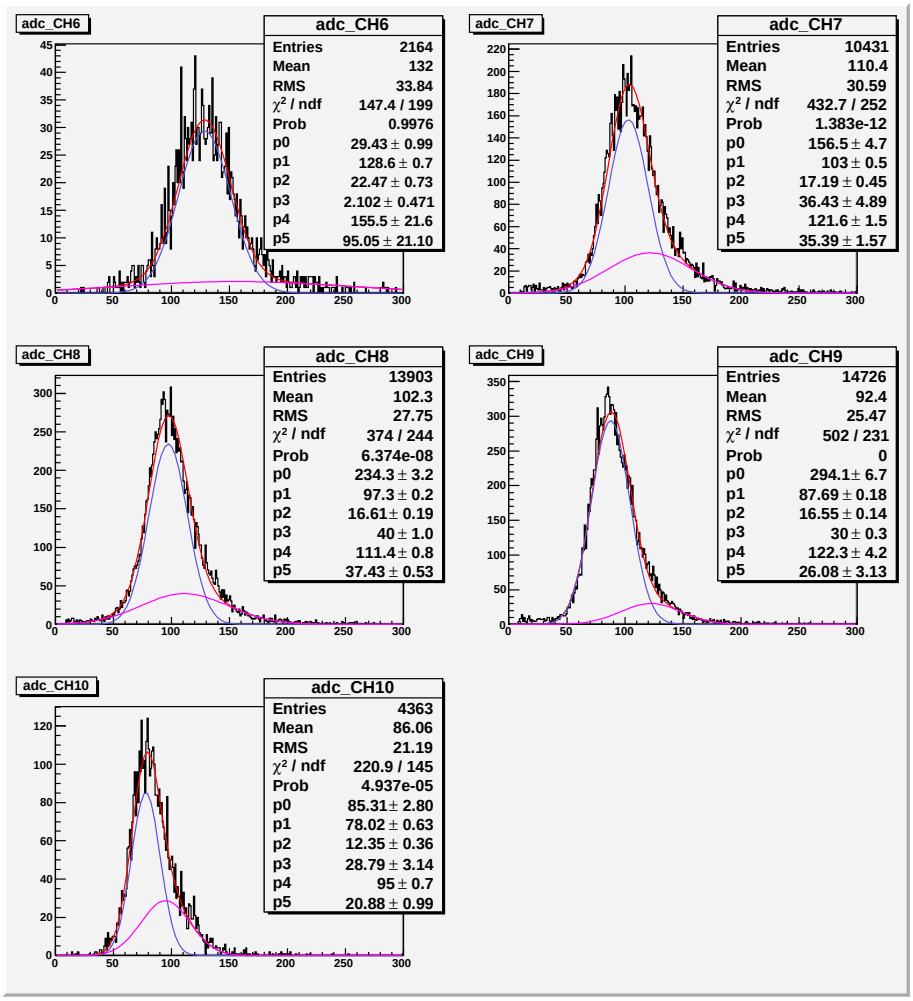

Figure 6.25: ADC spectra of the Y view PMTs corresponding to the MIP energy deposition.

obtained is in good agreement with the expected number of photo-electrons from previous test measurements with single strips.

Channel	# of fibers	PMT HV (V)	ADC peak for MIP (1/3)	ADC peak for s.p.e.	# of p.e. for 1 MeV
X1-1	15	786	82.9 ± 0.5	3.3	7.5
X1-2	15	791	95.4 ± 0.2	2.9	9.7
X1-3	15	841	105.5 ± 0.3	4.3	7.2
X1-4	15	825	$104. \pm 0.3$	3.8	8.1
X1-5	14	855	116.3 ± 0.6	5.1	6.7
Y-1	15	865	128.3 ± 0.7	3.4	11.3
Y-2	14	822	102.9 ± 0.5	3.7	8.1
Y-3	15	818	96.4 ± 0.3	2.2	12.8
Y-4	15	762	87.4 ± 0.2	2.9	8.8
Y-5	15	733	78 ± 0.6	1.9	11.9

Table 6.5: Results of cosmic test measurements for the $X1$ and Y PMT views. The ADC value for the MIP energy deposition corresponds to 1/3 of the PMT signal after the splitter.

6.6 Construction

Construction of the PCAL consists of several quasi-independent processes. Each process requires independent manpower and work space. Most of these processes require a clean environment. The handling of many items, such as scintillator strips, fibers, μ-metal shields, lead, PMTs, etc., requires the use of gloves. Below are the steps/processes involved and the resources needed in the construction of the PCAL.

1. Preparation of scintillator strips with WLS fibers requires a semi-clean area with a 4.5-m long table and open shelves for about 3000 m of scintillator strips. A table should be instrumented with fixtures for gluing. This process requires tools for measuring dimensions and tools for cutting and gluing the optical fibers. Preparation of the scintillator-fiber assembly will be done for one sector at a time. The work will include:

   - visual inspection of the scintillator strips;
   - cut the strips to the correct length and measure dimensions;
   - cut and inspect the fibers;
   - glue the fibers into the grooves;
   - inspect the gluing quality.

2. Assembly and tests of the PMTs and dividers requires a room with a dark box and storage shelves. The process requires tools for mechanical assembly, an oscilloscope, a HV system for the PMTs, cables, electronics, and a DAQ system. Work will include:

   - assembly of dividers to the end-caps of the PMT housing;
   - assembly of the PMT housing, cleaning the plastic tubes and end-caps, and installation of the μ-metal shield;
   - full assembly of the PMT, divider, and housing system;
   - measurement of the relative sensitivity to green light (500 nm) and the gain of each PMT using a photo-diode, and compare with specifications.

3. Stacking of the scintillator and lead layers requires a semi-clean room 8×8 m^2 in area. The room should have access to an overhead crane or other lifting device to move the

lead sheets. The process will require wide paper or Teflon sheets to place between the lead and scintillator layers. The stacking will be done one sector at a time. The work will include:

- cleaning and assembly of the backplate and the side walls of the box;
- stacking scintillator and lead layers;
- after scintillator layer is in place, add fixtures and shims to secure the position of the scintillator layer from all sides; cover the layer with paper or Teflon sheets and add the lead sheet;
- after all layers are stacked, put enough paper or Teflon sheets on top of the last layer to have a tight, uniform compression of the scintillator-lead layers between the two endplates;
- put on the front-plate and bolt it to the side walls;
- inspect that all fibers are in place and that there are no broken fibers;
- move the PCAL module where a high-load crane is available and rotate it to have the front-plate down;
- move the module to the area where the PMTs will be assembled.

The plate that holds the weight of the PCAL should have a strong-back support to prevent bowing. There should be at least two strong-backs, one for stacking and a second for the PMT assembly.

4. Mounting of fiber-adapters and PMTs requires a semi-clean room of 6×6 m^2 area, with gluing fixtures, polishing instruments, black masking tape, tools for mechanical assembly, an oscilloscope, a HV power supply, and HV and signal cables. The work will include:

   - mount shelves and fiber-PMT adapters;
   - position fibers inside the adapters according to the readout channel distribution and glue them into place;
   - cut and polish the ends of the fibers;
   - clean shelves and adapters;

- mount aluminum sheet covers;
- mount PMTs;
- check for light leaks; if there are light leaks use black masking tape to cover;
- move the PCAL module to the test area.

5. Test of the PCAL module with cosmic particles requires a room of about 6×6 m^2 area, that is air conditioned, and includes cables and electronics for one module and a working DAQ system. The work will include cabling, checking each channel, data taking, and analysis.

6.7 PCAL Quality Assurance

In each process of the PCAL construction, appropriate steps will be taken to ensure the quality of the final product. Quality controls will include – accuracy of mechanical assembly of the box, quality of scintillator strips, quality of fiber gluing, and checks of the PMTs and dividers. Quality assurance of the mechanical assembly will include verification of the dimensions of the parts, and the assembly will be checked to be within the specified tolerances. During the assembly, after installation of each layer, mechanical dimensions will be measured to ensure correctness of the assembly procedure. As for quality checks for the gluing process and for the scintillators and fibers, we will follow practices used during the assembly of the existing `CLAS` calorimeters. The scintillator strips will undergo visual and dimensional checks. The glued fibers will be checked using a UV light to identify any cracks on the cladding or bad gluing. The frequency of these checks will be defined after we have more experience with the scintillators and fibers, and the gluing process is determined. Each PMT will be tested to verify the required QE for green light and the required gain. After a module is assembled, the light yield and time response of each channel will be tested using cosmic particles.

6.8 PCAL Safety Issues

There are no major hazards in use of materials, high-power electrical supplies, mechanical tools, or radioactive materials. Construction of the PCAL includes work with lead sheets, adhesives, HV power supplies for the PMTs, and some heavy lifting. In current operation of

the CLAS detector, work with lead, heavy lifting, and work with adhesives are done routinely. These types of work practices are covered by the JLab EH&S manual and routine monitoring practices.

Lead work will be handled by personnel who have "Lead Worker Training" (SAF 136). Lead work practice includes use of appropriate PPEs, wet washing the lead or using HEPA vacuums to clean oxides from the surfaces, appropriate cleansing of personnel in contact with the lead, appropriate TOSPs or OSPs and task hazard analysis, and using HEPA vacuums to clean the work areas after lead handling.

Adhesives will be used to glue the fibers. Gluing will be done in a clean, well-ventilated room. All personnel working on the gluing process will be trained in the use of adhesives. Different types of adhesives are routinely used in Hall B operation, and all technical staff and users are familiar with the associated hazards and follow the JLab ES&H manual with regards to chemical hygiene and respiratory protection. Material Safety Data Sheets (MSDS) for all chemicals in use will be available, and every worker will be familiarized with the hazards in the MSDS.

Moving the PCAL modules will be done by qualified personnel using appropriate lifting and moving tools and procedures. One of the requirements for the work area is access to an overhead crane for this purpose.

6.9 Collaboration

Several institutions are involved in the design, prototyping, and construction of the PCAL. The main contributions by these institutions will be in the manpower needed for the pre-design simulations, as well as for the design, testing, and prototyping. In the construction stage, individual institutions can take over separate tasks or participate in different activities. The main groups are:

- Yerevan Physics Institute (YerPhI) – will provide scientists experienced in the detector design, construction, and simulation, as well as students to help during the assembly and testing of the PCAL modules. It is expected also that some parts needed for the prototyping and construction can be made at YerPhI facilities (e.g. adapters for the fiber-PMT connection). The YerPhI collaboration already has made significant contributions in the simulations, design, and prototyping of the PCAL.

- James Madison University (JMU) – will provide scientists and students to participate in the design, prototyping, and construction of the PCAL. The JMU group already has made significant contributions to the testing of the PCAL components.
- Institut de Physique Nucleaire d'Orsay (INP) – will provide engineers to participate in the design of the PCAL. The INP group has already made significant contributions to the design of the PCAL.
- Ohio University (OU) – will provide scientists and students to participate in the design, prototyping, and construction of the PCAL. The OU group has already made contributions to the design of the PCAL components.
- Norfolk State University (NSU) – will provide scientists and students to participate in the prototyping and construction of the PCAL.
- Jefferson Lab (JLAB) – will manage the project, and will lead the design, prototyping, and construction of the PCAL. JLab will provide infrastructure for the project, work space for different activities, and engineering and technical help.

Chapter 7

Beamline Elements

7.1 Longitudinally Polarized Solid Target

7.1.1 Physics Requirements

The proposed experimental program requires use of a polarized solid state target. The target will be polarized via the method of Dynamic Nuclear Polarization (DNP), which is a well established technique that has been used extensively in nuclear and particle physics experiments, including the ones performed in Hall B. Dynamically polarized target systems consist of a hydrogenated (polarized protons) or deuterated (polarized neutrons) compound containing paramagnetic centers, such as unpaired electrons, placed in a high magnetic field and cooled to low temperatures, with a B/T ratio of the order of 5 T/K. In these conditions, the free electron spins can approach polarization of 100%. The high polarization of unpaired electrons is then transferred dynamically to the nucleons by irradiating the target material at a frequency near that of the electron spin resonance. This technique typically achieves a proton polarization of 80-90% and a deuteron polarization of 30-40%. The nucleons in the target will be polarized either parallel or anti-parallel to the electron beam direction. The main systems required to realize DNP are a superconducting magnet to provide a strong (5 T) field, a ^{4}He evaporation refrigerator to maintain the target material at $\sim$1 K, a target insert that will house the target material and some additional instrumentation, a microwave system to transfer the polarization to the nucleon spins, and a Nuclear Magnetic Resonance (NMR) system to determine the state of the polarization.

7.1.2 Polarized Target Design

Polarizing Magnet and the Cryostat

In CLAS12 the polarizing magnetic field will be provided by the superconducting solenoid of the central detector. The target will be placed in the center of a warm solenoid bore with the center of the target approximately 2 m away from the upstream entrance of the magnet. A diagram for such a setup is shown in Fig. 7.1.

The solenoid magnet is in the design stage, and not all parameters are well known at the moment. Some additional correction coils might be necessary to improve the field uniformity around the target cell. The DNP method requires that the target material is placed in a magnetic field of uniformity $\Delta B/ < 10^{-4}$. The current magnet design provides for such a region of field uniformity in a cylinder of 30 mm in diameter and 100 mm in length. Some properties of the magnet are listed in Table 7.1.

Type	Superconducting solenoid
Aperture	0.78 m warm bore
Central field	2.5-5 T
Dimensions	1.10 m OD x 0.78 m ID x 1.800 m long
Region of $\Delta B/B < 10^{-4}$	cylinder: 10 cm long, 3 cm OD

Table 7.1: Solenoid magnet properties.

The target cryostat will house the evaporation refrigerator, the target insert, and some instrumentation necessary for the microwave and NMR operations. The cryostat needs to be designed to allow its operation in a warm bore magnetic field. The 'target ladder' used in previous experiments is not compatible with this geometry. The cryostat will contain a single cell filled with a polarizable target material. It would also be possible to place a carbon target upstream or downstream of the polarized target cell. A conceptual design of the target cryostat is shown in Fig. 7.2. The main component of the cryostat is a ^{4}He evaporation refrigerator. The refrigerator is inserted horizontally through a pumping tube between the pumps and the evaporation chamber. One important difference between this design and the previously used polarized target in Hall B is that the refrigerator will reside along the beam line, so that the amount of material in the way of the beam needs to be minimized.

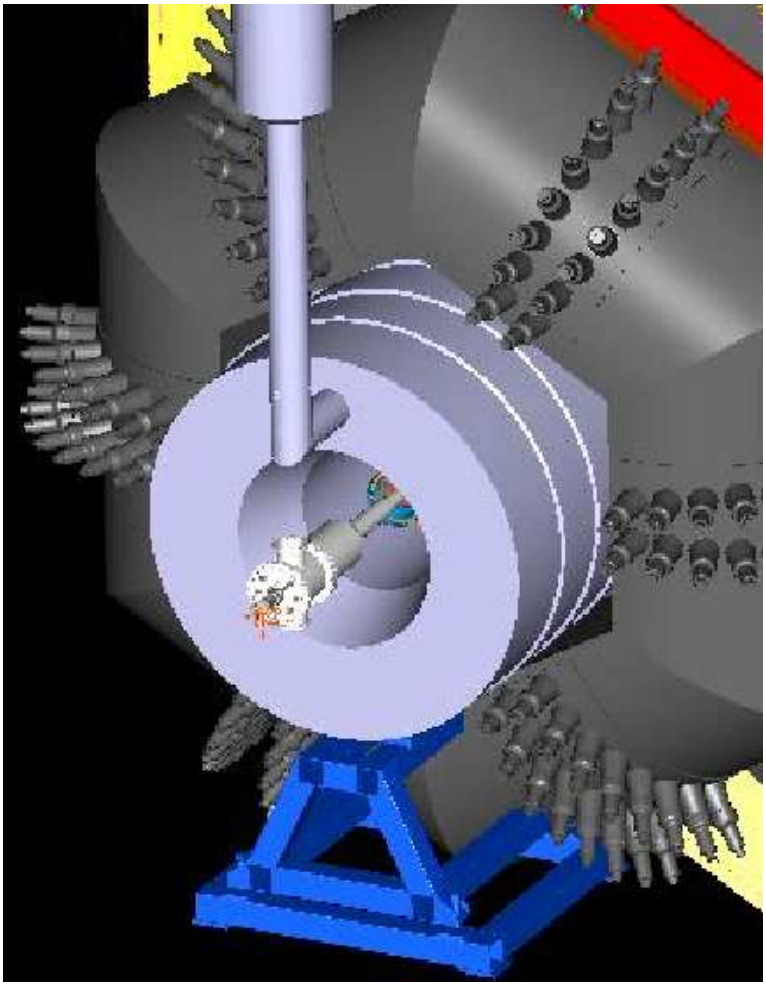

Figure 7.1: A schematic drawing of the polarized target cryostat inside of the solenoid magnet.

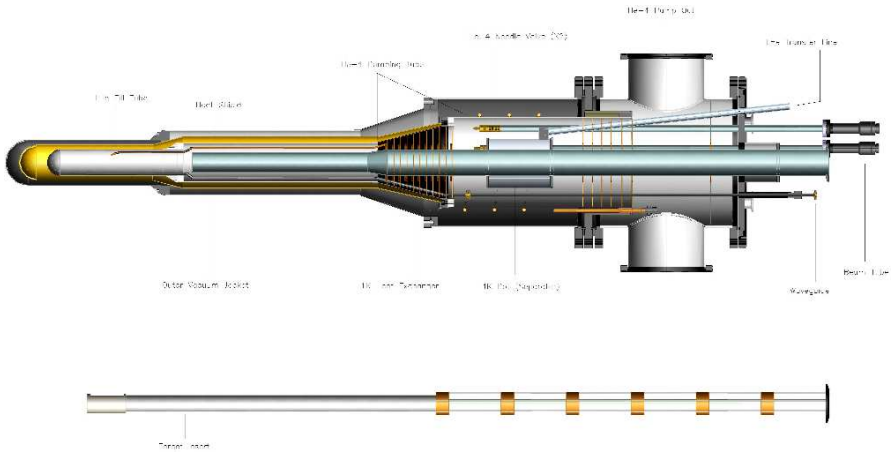

Figure 7.2: A schematic drawing of the polarized solid target cryostat and target insert for CLAS12.

The evaporation chamber will be situated in the bore of the magnet. The silicon vertex tracker (SVT) will also be installed in the magnet bore, surrounding the target, and imposing constraints on the chamber dimensions. The constraining radius of the SVT is 40.25 mm in the current design, which is NOT compatible with the current target design, in which the minimum outer diameter of the target cryostat is 10 cm. This volume of the cryostat will contain the outer vacuum space, heat shield, and the evaporation chamber. Diagrams of the cryostat section surrounded by the SVT planes are shown in Fig. 7.3. To make this picture possible, the cryostat diameter had to be shrunk to 7.6 cm.

Name	Material	Dimensions
Outer Vacuum Jacket	Al	0.5 mm
Heat Shield	Al	0.5 mm
Cup Wall	Kel-F	0.5 mm
Cup/Cell Windows	Al	0.025 mm
Cell	Kel-F/torlon	0.3 mm

Table 7.2: New cryostat and insert design parameters.

Target Insert, Cells, μ-waves, and NMR

The target material will be placed in the cell inside of a cup, with both containers made of hydrogen-free plastic. The cup will be attached to a thin aluminum structure that can

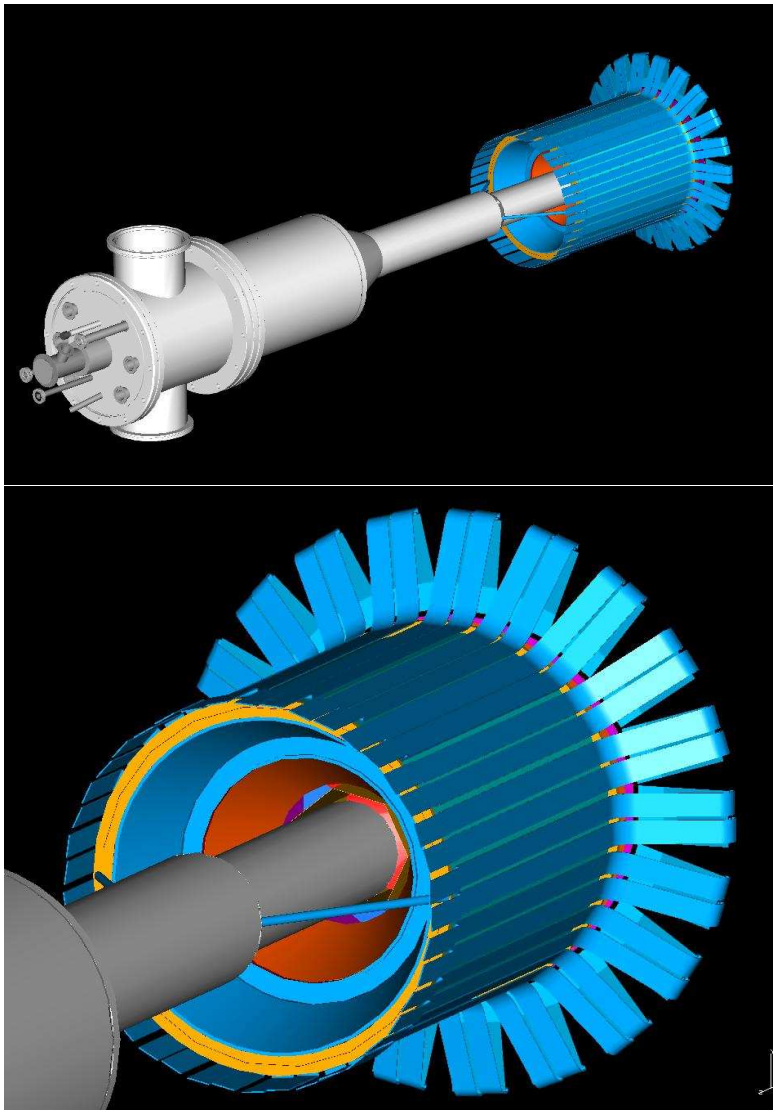

Figure 7.3: Diagrams of the target cryostat surrounded by the SVT planes.

be inserted through the beam tube. The schematic of the insert is shown on the bottom of Fig. 7.2. The dimensions of the target cell are determined by the size of the region of field uniformity, and geometric constraints of the cryostat. The cup will have an opening on the top for the LHe fill, while the cell will have small holes so that the target material will be sitting in a bath of LHe, while also being showered by LHe coming from the run valve. The flow of LHe in the cryostat will be maintained by a series of pumps located outside of the cryostat. The entrance and exit windows of the target cell and cup could be made out of thin aluminum or Kapton foils. The microwave radiation needed to polarize the target will be guided through a designated waveguide inserted through the upstream entrance window of the cryostat. The guide will have a slit directly underneath the target cup, providing continuous microwave radiation directed at the target cell. With this arrangement, the target cup will act as a resonating cavity.

Ammonia and deuterated ammonia will be used as target material with the electron beam and `CLAS12`. (We will also investigate the possibility of using ^{6}LiH(D) as a target material). Ammonia will be frozen and broken up into small beads (to optimize the cooling surface) that fill the target cup. Some parameters of frozen ammonia are listed in Table 7.3. These targets offer high polarization, good resistance to radiation damage, and a relatively high ratio of polarizable nucleons per total number of nucleons. With the goal luminosity, L, of 1×10^{35} cm^{-2}s^{-1} and the tentative target dimensions of 3.0 cm in diameter and 3.3 cm in length, we can estimate the rate of charge accumulation, J. We estimate the packing factor to be $f_{eff} \sim 0.6$.

$$
\begin{aligned}
J &= f_{\rm eff} \times l \times \rho \times N_A \times N_{nucl} \times (1 \text{ mole}/17 \text{ g}) \times L \qquad (7.1)\\
J &= 0.6 \times 3.3 \times 0.91 \times (1 \text{ mole}/17 \text{ g}) \times 6.02 \times 10^{23} \times 17 \times 10^{35}\\
J &= 9.22 \times 10^{10} e^-/\text{s}\\
I &= J \times 1.60 \times 10^{-19} \text{ C}/e^- = 14.7 \times 10^{-9} \text{ A}.
\end{aligned}
$$

Compared to the existing target (4 nA current, 1-cm long), this represents an increase by a factor of $\sim$12.

The target polarization will be monitored during the run via the NMR system in the field of the solenoid magnet. The calibration of the proton NMR can be done by measurements of polarization in thermal equilibrium, taken with the polarizing magnet. In cases when the

Chemical Structure	$NH_3(ND_3)$
Target Diameter	3 cm
Target Length	3.3 cm
Density	0.917(1.056) g/cm^3
Dilution Factor	$\approx$ 0.15(0.22)
Packing Factor	$\approx$ 0.6

Table 7.3: Some parameters of the ammonia targets.

deuteron signal is too small for the thermal equilibrium measurement, the polarization can be monitored through the ratio of the two peaks of the NMR signal (R-ratio method). The target cell size in the current design is relatively large, which will allow for placement of the coils inside of the cell, resulting in a measurable thermal equilibrium signal, so the polarization of deuterium will be monitored by the area and ratio methods.

Heat Load and Pumping Requirements

Assuming the energy loss of 2 MeV/g/cm^2, the heat load due to the beam will be:

$$J \times (2 \times 10^6 \text{ eV/g/cm}^2) \times \rho \times f_{\text{eff}} \times l \times (1.602 \times 10^{-19} \text{ J/eV}) = 0.053 \text{ W}. \qquad (7.2)$$

The heat load due to the microwaves is more difficult to estimate. Systems with movable target ladders, such as the existing Hall B polarized target and the UVa-SLAC target, use horns to direct microwaves toward the target. In these systems the target is not located inside a microwave cavity and the microwave power delivered to the target region is typically 0.5 W to 1 W. In systems with a single, fixed target, it is possible to locate the target inside a multi-mode cavity with highly conductive walls. The Yale-SLAC polarized target operated with 0.5 W of microwave power even though the volume of target material was relatively large (25 cm^3). A value of 0.5 W of microwave power should be a relatively safe assumption for this target. The total heat load is expected to be 0.55 W.

The heat of evaporation of ^{4}He at 1 K is approximately 80 J/mole. To provide 0.55 W, a flow rate of 0.0069 moles/s will be required. At 1.0 K the vapor pressure of ^{4}He is 0.160 mb. The displacement of the pumping system will be:

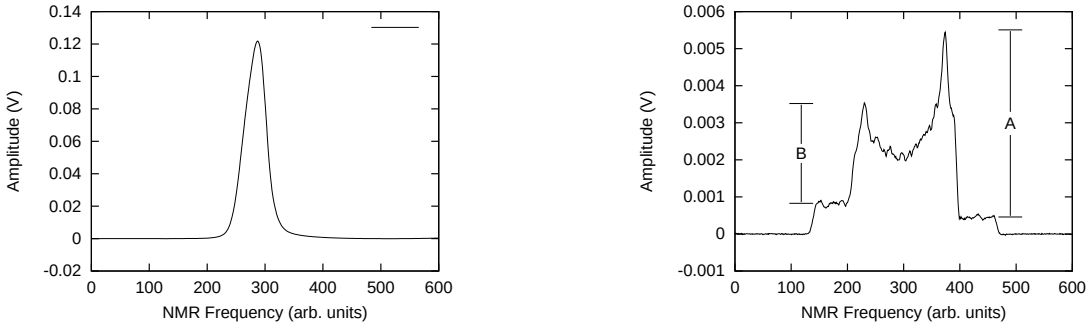

Figure 7.4: NMR signals for polarized NH_3(left) and ND_3(right).

$$.0069 \text{ mole/s} \times (22.4 \text{ l/mole}) \times (1 \text{ b}/0.160 \times 10^{-3} \text{ b}) = 966 \text{ l/s} = 3480 \text{ m}^3/\text{hr}. \quad (7.3)$$

The measured pumping speed for the existing Hall B polarized target pump set is 3300 m^3/hr. A larger pumping system will be required. It is desirable to use hermetically sealed pumps in order to avoid contamination of helium gas that is returned to the liquefier. A system based on the WKP6000 AM series (Pfeiffer) would be suitable.

7.1.3 Expected Performance

With the magnetic field of 5 T and temperature of ∼1 K, we expect to obtain polarization values of 80-90% (30-40%) for the ammonia (deuterated ammonia) targets. Target polarization will be monitored using the NMR system. The target cell size in the current design is relatively large, which will allow for placement of the NMR coils inside of the cell resulting in a measurable thermal equilibrium signal. The polarization of deuterium will be monitored by the area and ratio methods. Typical NMR signals for the proton and deuterium targets are shown in Fig. 7.4. The signals are obtained from the small target cells with NMR coils wrapped on the outside, and represent the minimum expected quality.

Ammonia can accumulate a charge of $\sim 10^{15}$ electrons/cm^2 before showing signs of deterioration. Accumulated radiation damage can be mostly restored through the annealing process, in which the target material is heated to temperatures of 80-90 K for short periods of time. At a flux of 9.22×10^{10} electrons/s (14.7 nA), a 3-cm diameter target would accumulate a dose of $\sim5\times10^{15}$ e^-/cm^2 in 4 days (106 hours). If ammonia is used as the target material then frequent target anneals and target changes should be anticipated. Experience with the

existing Hall B polarized target has demonstrated that withdrawing the target to a heated region, rather that attempting to heat the 1 K section of the cryostat, is an effective method of annealing the target. A load lock for the target insert could be useful both for frequent target anneals and changes. It may also be desirable to increase the diameter in order to extend target lifetime. A history of target polarization as a function of accumulated charge and anneal cycles is shown in Figs. 7.5 and 7.6.

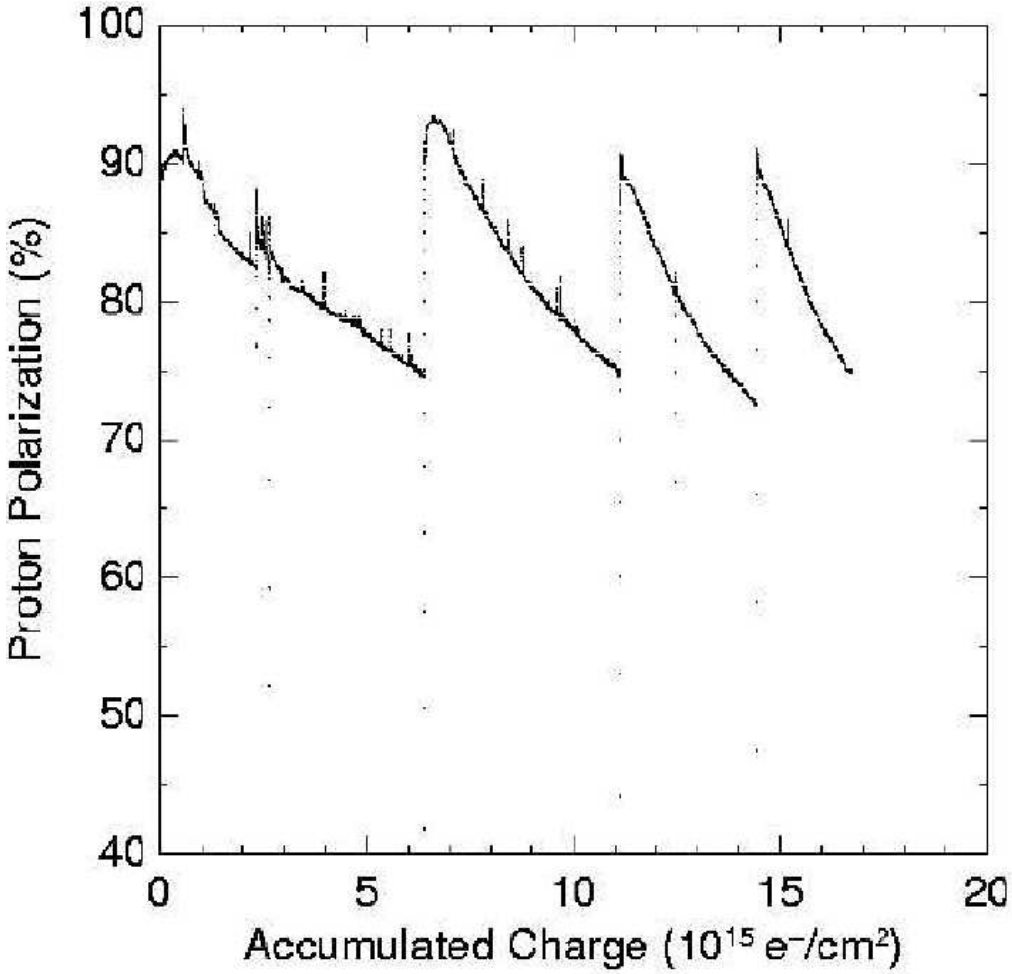

Figure 7.5: $^{15}NH_3$ polarization as a function of time.

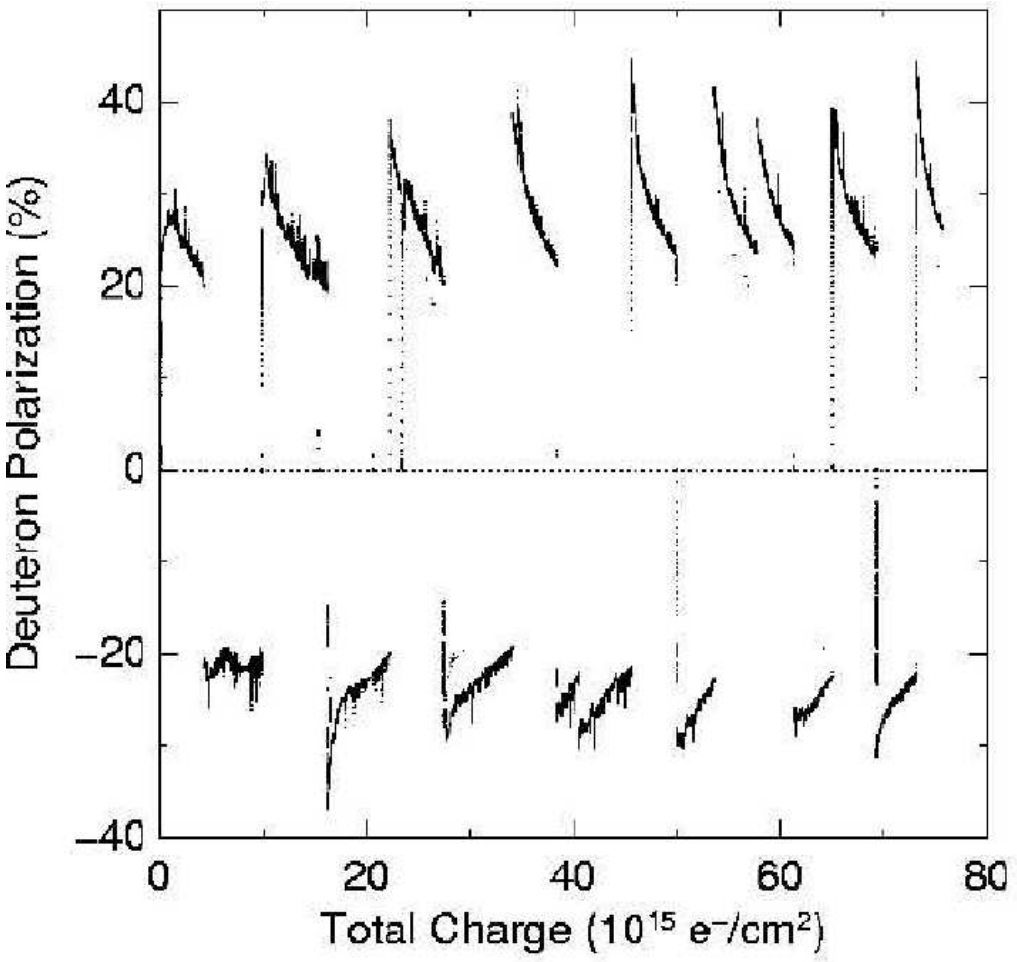

Figure 7.6: $^{15}ND_3$ polarization as a function of time.

7.2 Møller Polarimeter

7.2.1 Physics Requirements and Polarimeter Design

Several experiments in the proposed experimental program require the use of polarized electron beams. The design of the polarimeter for the upgrade is similar to the present polarimeter and will provide a similar uncertainty in the polarization measurement: $\Delta P_B/P_B \approx 2.5\%$.

The polarimeter is based upon elastic electron-electron scattering. The electrons are detected in coincidence at center-of-mass scattering angles near 90° where the analyzing power of the reaction, and therefore the beam asymmetry, is a maximum. For a beam of polarization P_B^z and a target of polarization P_T^z, the measured beam-helicity asymmetry is given by:

$$A = \frac{N_+ - N_-}{N_+ + N_-} = \bar{A}_{zz} P_B^z P_T^z, \tag{7.4}$$

where N_+ (N_-) is the number of counts with positive (negative) beam helicity and $\bar{A}_{zz}$ is the average analyzing power for the beam and target polarized along the beam direction. By detecting both of the scattered electrons over a small range of scattering angles, the reaction kinematics are fixed. Thus, this method has the advantage, as compared to single-arm Møller polarimetry, of producing a clean data set without having to do energy-dependent background subtractions. In the present CLAS Møller polarimeter, accidental rates are typically less than 5% of the real rate for normal operating conditions. Furthermore, the accidental rate is measured and included in the corrections.

The general layout of the present Hall B polarimeter is shown in Fig. 7.7. It is located in the beamline immediately upstream of the tagger. The system consists of a target chamber, two quadrupole magnets, and two detectors in the horizontal plane on either side of the beamline. The target is a permendur foil that is magnetized with a small Helmholtz-coil system. The two quadrupoles separate the scattered electrons from the unscattered beam. The two detectors are lead/scintillating fiber composites. The magnets are powered by a power supply providing currents up to 2676 A but is capable of providing 4800 A.

The major components of the polarimeter – target, magnets, detectors, and power supply – will be reused for 11 GeV operation, however, the relative positioning of these elements will need to be modified and the water-cooling system will need to be upgraded. At a beam energy of 11 GeV, the scattered electrons are not sufficiently deflected by the magnetic field to reach the detectors in the present configuration. Our simulations indicate that running the

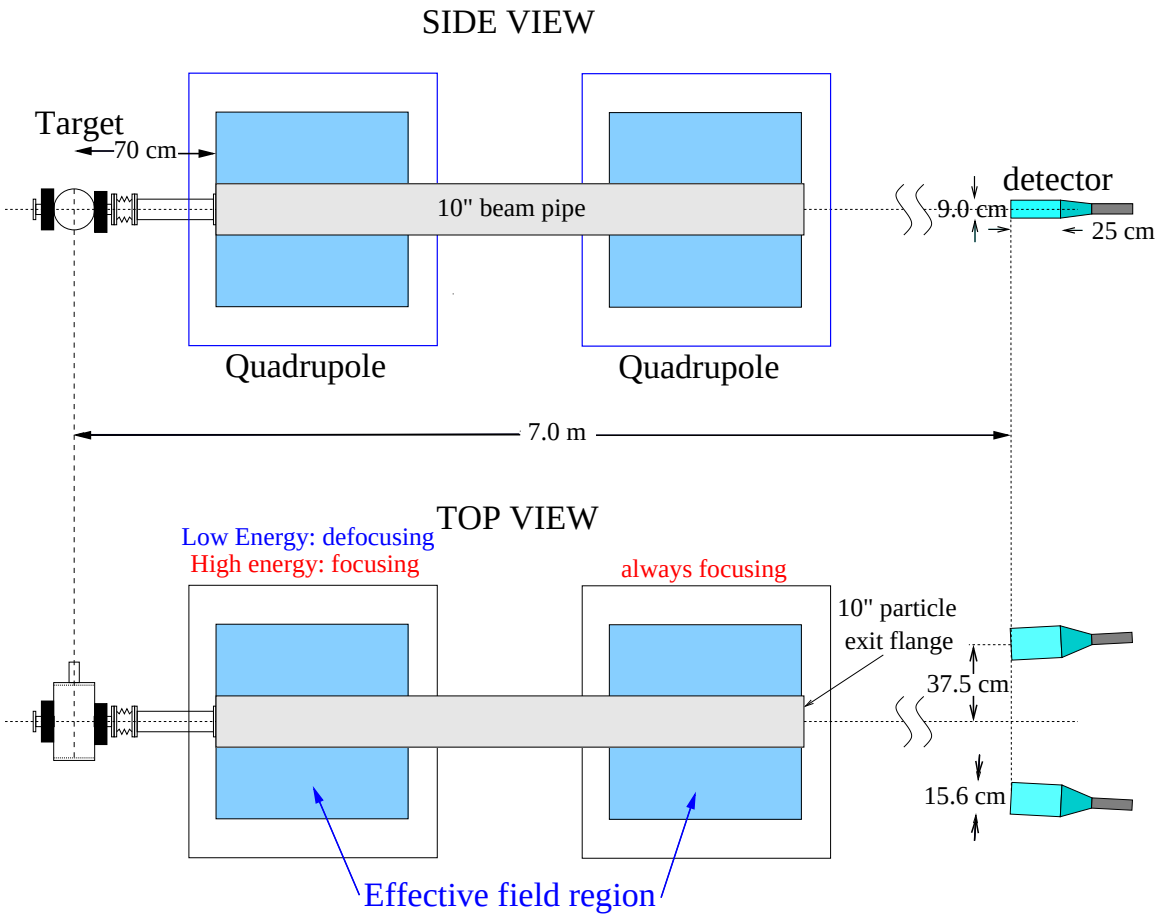

Figure 7.7: Layout of the Hall B Møller polarimeter.

power supply at the maximum current of 4800 A, improves the situation. At this current, the present cooling system cannot handle the heat load, thus the need for an upgraded cooling system.

In addition, while the deflection angle of the scatted electrons increases with the larger magnet currents, it is still not sufficient for the electrons to be detected in the present configuration. Simulations indicate that this can be remedied by a combination of increasing the flight path from the downstream quadrupole to the detectors, moving the detectors closer to the beamline, and increasing the separation between the quadrupoles. This will likely require moving both quadrupoles as well as the target. More simulations are necessary to determine the geometrical configuration required for optimal operation. We are thus planning for all three changes.

The changes to the geometrical configuration of the present polarimeter will require several changes to the beamline and auxillary hardware. This includes new beam pipes, bellows,

anchors, cables, and beam exit windows.

At 11 GeV a larger center-of-mass scattering-angle range will be detected with the present detector system. This reduces the effective analyzing power of the polarimeter and thus increases measurement times required to achieve the desired statistical precision. Therefore, it will be necessary to increase the segmentation of the detectors to restrict and/or identify electrons in the desired angle range. This can be done placing a smaller scintillator in front of each of the existing detectors. These detectors would be half as wide and the same height as the present detectors: 8 cm wide by 9 cm high. This is preferable to simply reducing the size of the present detectors, since the full present width is required if polarization measurements are ever needed for beam energies in the range of 5-8 GeV.

Finally, the existing polarimeter target system can be reused in its present configuration. However, since has been in use now since 1998, it would be prudent to remeasure the target polarization, and if necessary, replace the target material. Replacement target material is in our possession as well as the equipment to do the measurements.

7.2.2 Collaboration and Responsibilities

Florida International University is actively involved in this project. The FIU nuclear physics group (5 faculty, 1 post doc, and 8 graduate students) is currently supported by a DOE grant. The group's contribution to CLAS12 will be the design of the polarimeter, construction of additional detectors, and refurbishment of the target. Design of the final polarimeter configuration will require further simulations to optimize performance.

7.3 Other Beamline Devices

The other beamline devices concerned by the upgrade are:

- Raster. The raster is used to evenly spread the heat load of the beam on the surface of the target. It consists of two pairs of kicking magnets for vertical and horizontal rastering. The water-cooled magnet coils can be used to raster an 11-GeV beam. The present power supplies are not powerful enough to provide a suitable magnetic field, but they will be upgraded for the CLAS 6 GeV DVCS experiment. The new power supplies

will be powerful enough for a 11 GeV beam. Consequently, no upgrade will be necessary for the raster.

- Faraday Cup. The Faraday cup (FCup) is the device presently used for monitoring of the absolute beam current in Hall B. The higher luminosity and beam energy will make standard operations of the FCup impossible. However, the FCup can be used at low luminosity for calibration of other devices measuring beam current. The beam stopper will then be inserted at high luminosity and the current will be provided by nanoAmps BPMs (see next item). Consequently, no hardware or software upgrade is necessary for the Faraday cup.

- Beam Position Monitors (BPMs). The BPMs measure both the position and the current of the electron beam. The BPM can work with an 11-GeV beam as they are. They are currently read out by the slow controls system. However, upgrading the data acquisition to 60 Hz is necessary in order to monitor the beam current and beam charge asymmetry at a large enough speed in the absence of Faraday cup monitoring. This necessitate a fast intensity 60 Hz signal. The lock-in amplifiers will have to be reconfigured. It is necessary to provide VtoA for the 6 channels (phase/amp) per nA and scalers for the 18 channels, as well as writing the corresponding software.

Chapter 8

Additional Equipment Required for Physics Program

8.1 Transversely Polarized Target

Measurements of the transverse target single spin asymmetry (SSA) for different final state particles in semi-inclusive and exclusive hard processes, including photon deeply virtual Compton scattering (DVCS), and pseudoscalar and vector meson production in a wide range of different kinematic variables are a critical part of the CLAS12 physics program. Our preliminary studies show that it is technically possible to run a polarized target with CLAS12. Two main options for a transversely polarized target are currently under consideration:

- Standard transverse target with 4.2 T field;
- HD target.

8.1.1 Standard Transversely Polarized Target

For CLAS12 operation with the standard transversely polarized target, the solenoid magnet and central detector will be removed and replaced by a stand-alone polarized target, similar to the existing polarized target used in electron scattering experiments. As the magnetic field orientation is transverse to the beam direction, the electron beam will be deflected vertically. This will be compensated for by installing a magnetic chicane system upstream of the target so that the beam after the target is again in the horizontal plane. Special care is needed

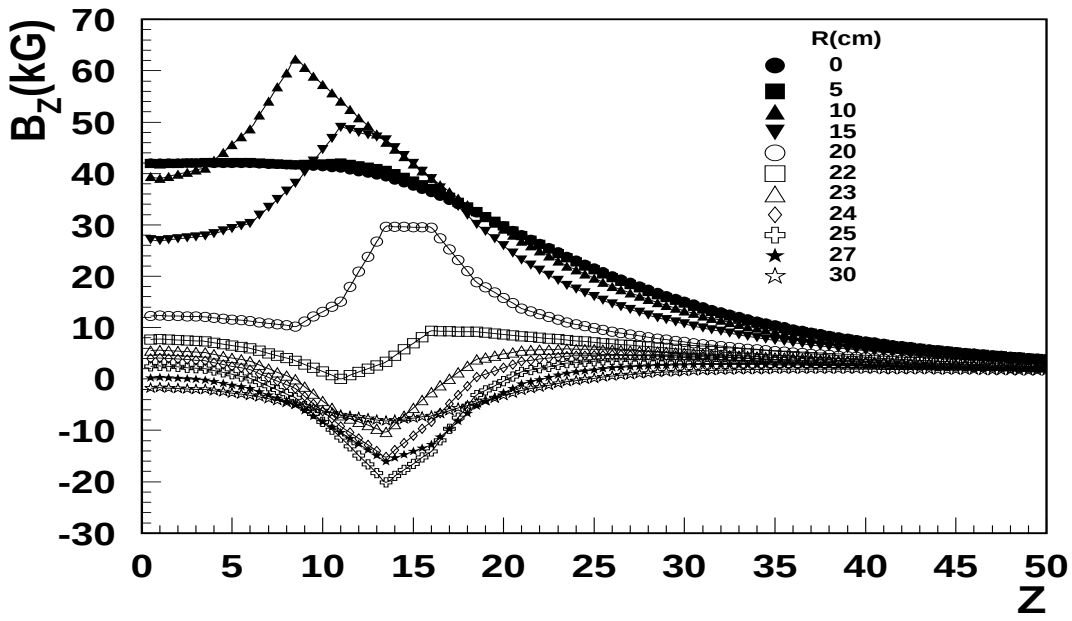

Figure 8.1: Transverse target magnetic field distribution in terms of B_z (kG) vs. z-coordinate (cm) for different radial distances.

for shielding of the electromagnetic background, especially Møller electrons. Note that the chicane system is necessary for transverse target operation, and has to be robust enough to allow the beam to go through the center of the target and restored afterwards to go into the beam dump.

The basis for the design of a transversely polarized target is the 5 T magnet, which has been used very successfully in SLAC and JLab, along with a 1 K ^{4}He evaporation refrigerator. The 5 T magnet was optimized for scattering with longitudinal polarization, but allowed a reasonable aperture for scattering with a transverse field. This mode was used at both SLAC and JLab. A similar magnet was built and operated successfully with `CLAS` in Hall B; modifications to the design were mandated by the magnet having to be supported inside `CLAS`, and it could not be configured to operate with a magnetic field transverse to the electron beam. Both magnets were designed and built by Oxford Instruments, and through a cooperative effort with JLab and the University of Virginia, Oxford Instruments produced an optimized design for a high-field transverse magnet to be used in `CLAS` for the 6-GeV program. However, the target concept is such that it can be operated with `CLAS12` as well.

The target will have a warm bore for the target cryostat that also allows detection of slow protons in specially designed magnetic field insensitive detectors located around the target

cryostat. The target field map is shown in Fig. 8.1. The magnet specifications are listed in Table 8.1.

Central Field	4.2 T at 4.2 K
Homogeneity	1 part in 10^4 over a 15 mm DSV (diameter spherical vol.) 3 parts in 10^4 over a 25 mm DSV
Cold vertical access (for target access)	100 mm (helium temperature)
Bore access	$\pm 35^\circ$ onto a 25-mm diameter sphere. Removable room temperature re-entrant cones on axis to within 12 cm of central field position.
Split access	Vertical: $\pm 35^\circ$ onto 25-mm diameter sphere. Horizontal: $\pm 22.5^\circ$ onto a point.

Table 8.1: Listing of polarized target magnet parameters.

The refrigerator is vertical and will be very similar to that used in the UVA/SLAC/JLab system with the target samples easily inserted and removed. The target can operate in a beam of up to 100 nA, but it will be much less in `CLAS12`. Initial ammonia polarizations give $\pm 95\%$ for protons and 38% to 48% for deuterons. The target is polarized continuously by applying microwaves, and the most important process affecting the polarization value is radiation damage. However, this can be repaired by warming the ammonia to about 100 K for up to an hour, after which the polarization returns to its starting value or, in the case of deuterons, actually improves. This process can be repeated many times before the target material must be changed. Fig. 8.2 shows the kinematic coverage of `CLAS` and `CLAS12` with the transversely polarized target.

8.1.2 Transversely Polarized HD Frozen-Spin Target

The magnetic holding fields accompanying transversely polarized targets can deflect an electron beam and create challenging background conditions. A magnetic chicane can be installed upstream of the target and arranged in such a way that the target's magnetic field bends the electron beam back on axis. However, bremsstrahlung created in the target material will be peaked along the direction of the incoming electrons, which will then be at several degrees to

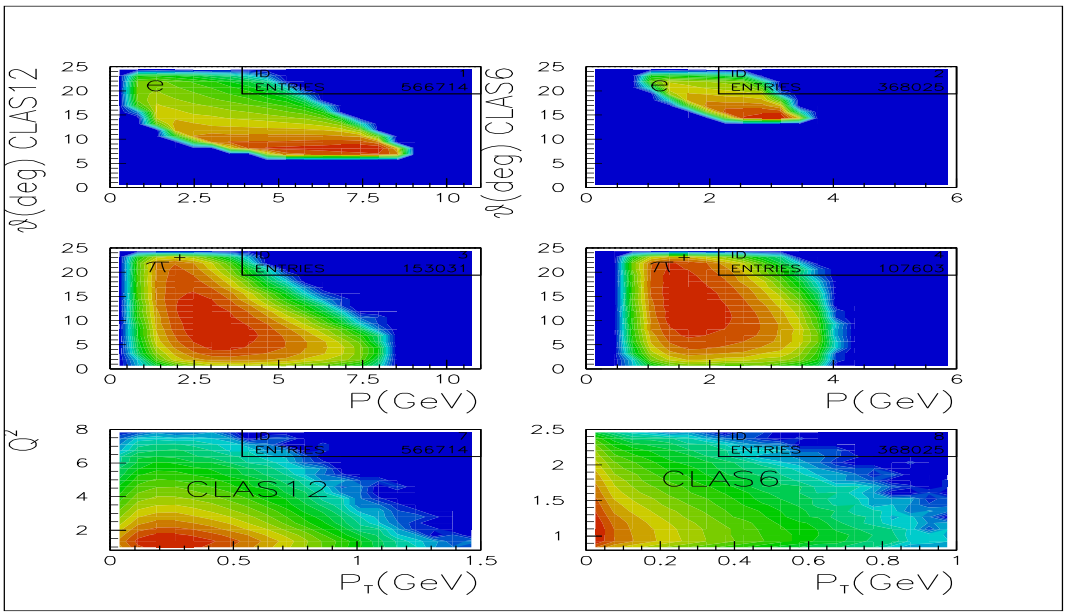

Figure 8.2: Kinematic coverage with the transversely polarized target (electron angles below 22.5°). The plots on the left show (top to bottom) θ_e vs. p_e, θ_π vs. p_π, and Q^2 vs. p_t for CLAS12. The plots on the right are the same but for CLAS at 6 GeV.

the detector axis. Generally, one can arrange to have either the electron beam or the target bremsstrahlung centered at 0°, but not both. A transversely polarized target in a frozen-spin state that requires only small holding fields would greatly mitigate such background problems. Problems associated with beam deflection are virtually eliminated by the small holding fields, and this potentially allows the target to be located in the center of the detector, thus dramatically increasing the acceptance. In addition, the target has almost no dilution. The only unpolarizable nucleons are associated with the target cell and these can be sampled and subtracted in conventionally empty-cell measurements. At the same time, the low Z of the target material results in a long radiation length and comparatively few bremsstrahlung photons.

The HDice target developed at LEGS in Brookhaven and now migrating from BNL to JLab, has been used successfully in photon beam experiments. The factors affecting the target polarization are complex and intertwined; a direct test of the performance of polarized HD with electrons is essential. This will be carried out during the course of the E06-101 run with CLAS.

At BNL, HD target polarizations of 60% H and 35% D have been achieved in photon experiments with spin-relaxation times in excess of a year, and polarizations are expected

to be higher with the smaller diameter cells that will be used at JLab. The deuterium polarization is particularly stable; spin-relaxation times of 2 months have been measured with only a 0.01 T holding field at 0.2 K. The projected D decay time for a 0.04 T saddle coil, 0.12 m in length ($\int B \times dL = 0.005$ T-m), is $\sim$7 months. Comparable H relaxation times require higher fields, but should be possible with $\int B \times dL = 0.050$ T-m, which is still about 30 times less than a dynamically polarized ammonia target. The beam heating expected from 5 nA of 10 GeV electrons traversing a 2-cm HD target is $\sim$5 mW (as calculated with GEANT). This is about the cooling power of the existing BNL In-Beam-Cryostat (IBC) at 0.5 K, and will be significantly increased in the CLAS-IBC now under design for E06-101. Beam heating is considerably less in HD, as compared to butanol, due to the lower Z of the target material and, unlike butanol, HD relaxation times are not such strong functions of temperature, so long life-times are achievable up to about 0.7 K.

Free radicals generated by electron bremsstrahlung will have randomly oriented polarizations. While their absolute number is small, they can generate polarization sinks within the target if the spin-diffusion time is short. This time constant has been indirectly measured at BNL by using RF waves to punch a local polarization hole within a highly polarized target. The rate at which this hole heals after the RF power is lowered reflects the in-diffusion of spin from other regions of the target. At 2 K, this measured spin-diffusion is $\sim$1 day for H, but unmeasurably long for D (greater than a year). Whether or not the H performance improves at lower temperatures is a matter for further study, but the extremely slow spin-diffusion for D already suggests that frozen-spin HD could maintain its deuterium polarization during electron experiments. Frozen-spin HDice may provide an attractive alternative for electron experiments with at least transversely polarized deuterons in CLAS12.

8.2 The BoNuS Radial Time Projection Chamber

The BoNuS experiment needed to detect very low-momentum recoil protons at backward scattering angles used as a tag on quasi-free electron-neutron scattering from a deuterium target. For that experiment, a radial time projection chamber (RTPC), surrounding an integrated thin-walled target gas cell, was built. This detector is going to be used for the conditionally approved experiment PR12-06-113, using the upgraded 11 GeV electron beam and CLAS12, and can be used for other experiments with other target gases as well.

The RTPC will be placed inside the central detector solenoid magnet, which will provide the analyzing magnetic field for the momentum determination via the track curvature of scattered charged particles.

The 283-mm long, thin-walled Kapton target tube can contain up to 7 atm of target gas, like deuterium, and is surrounded by the radial time projection chamber. The sensitive drift region of the 200-mm long RTPC is an annulus with an inner radius of 30 mm and an outer radius of 60 mm. Materials between the target gas cell and the sensitive detector volume are minimized to prevent energy loss of the scattered particles and to minimize the interaction of background particles. These background particles are mostly Møller electrons forced into helical trajectories along the beam axis.

The amplification of the drifting electrons is achieved by three layers of gas electron multiplier (GEM) foils at radii of 60, 63, and 66 mm. This is surrounded by a cylindrical readout surface at a radius of 69 mm.

The resulting detector consists of two similar half-cylinder units that are mated together on either side of the central beam axis. Axial mechanical structures fit within a $\pm 16^{\circ}$ wedge along the top and bottom of the assembly, as shown in Fig. 8.3. All of the structural components are light-weight and self-supporting. These parts nest together to form the final detector module.

Gas electron multipliers are 50-μm thick polyimide foils coated on both sides with a 5 μm copper layer, and punctured with 70 μm holes. The distance between these holes is about 140 μm. By applying a voltage in the range of 200 V to 300 V across the two copper layers, a very high electric field is formed inside the holes. Electrons drifting towards the GEM foil produce an avalanche of secondary electrons when captured and accelerated through the holes. The gain in each GEM is of the order of 100. The electrons drift to the next GEM foil, and after passing through three GEM foils, the resulting electron pulse is detected on the readout plane. The three GEM support frames were dimensioned such that identical GEM foils of an active area of 200 mm $\times$ 170 mm could be used throughout. The voltage was chosen such that the RTPC was insensitive to minimum ionizing particles, such as electrons and most pions, but had an excellent detection efficiency for highly ionizing recoil protons.

The outermost cylindrical layer of the detector is the readout board made out of a flexible polyimide substrate. It carries gold-plated conductive pads on the inner surface with a pattern of 4.45 mm $\times$ 5 mm, as shown in Fig. 8.4. The pads are connected by closed vias to the outer surface on which groups of 16 pads are traced to a common connector, carrying 16-channel

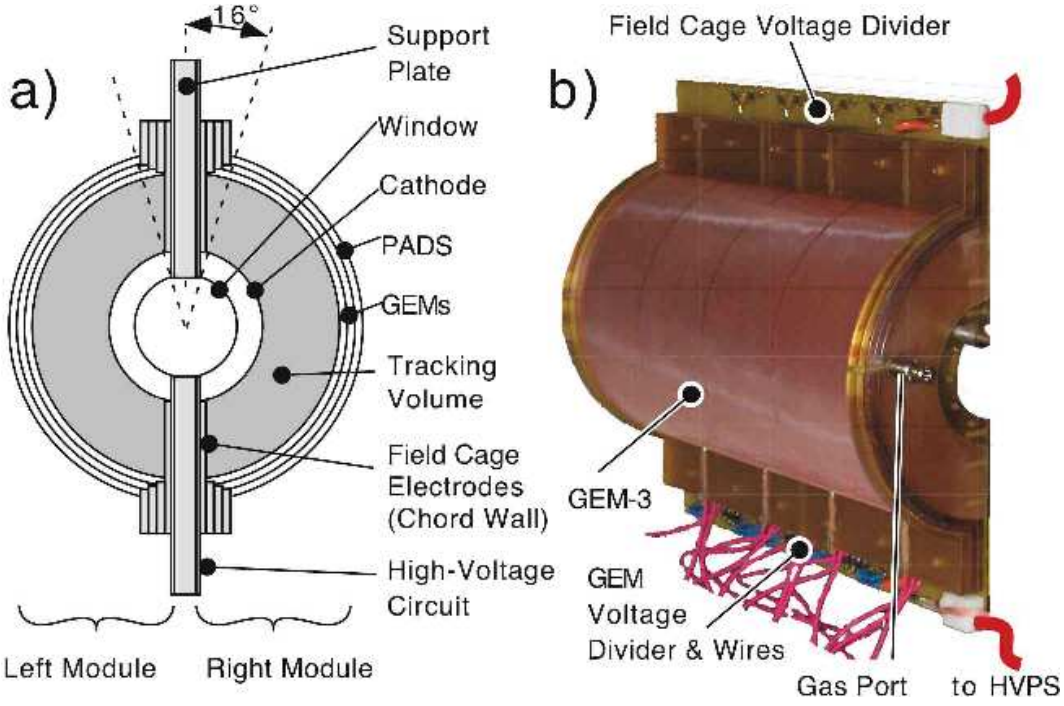

Figure 8.3: Schematic diagram and photograph of the BONUS RTPC. a) Cross-section view through the center of the detector. b) Photograph of the left module with the readout pad board removed.

preamplifier cards.

The signals are inverted on these cards and transmitted via 6-m long cables to a low-impedance receiver circuit, feeding the positive signals into the readout electronics developed at CERN for the TPC of the ALICE experiment, under construction at the Large Hadron Collider for heavy-ion collisions. Each readout card provides 128 channels of pre-amplification, digitization via a 10-bit ADC, signal correction circuits, and a pipeline buffer for eight events. Each event contains the signals of all pads integrated over a selectable time interval in the range of 100 ns for a period of up to 100 intervals, in this case 10 μs. Of the 100 intervals, up to 15 can be before the arrival of the trigger from `CLAS`.

Signals below preset thresholds, taking dynamically calculated and preset pedestals into account, are suppressed in the data stream to decrease the data volume, for an increase of the event rate. Thirteen readout cards are needed to read out one half-cylinder of the detector. They are grouped into one crate, controlled by one readout control card (RCU). Two crates are needed to read out the whole RTPC. Each RCU is connected at present via USB 2.0 to a VME based Motorola crate controller, forming the standard readout unit in the `CLAS` data acquisition system.

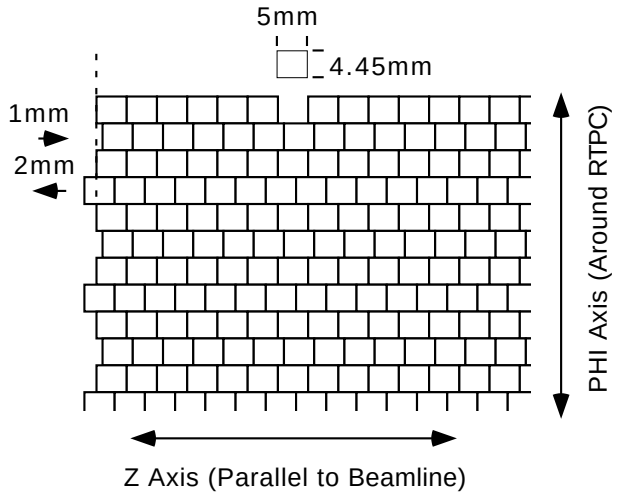

Figure 8.4: Pad geometry in the production RTPC. There are 40 rows and 40 columns of pads. Pad rows (along the cylindrical axis) are offset from one another to improve the track resolution.

8.3 Ring Imaging Čerenkov for CLAS12

The particle identification system (PID) of the CLAS12 forward detector is based on the information from the Forward Time-of-Flight counters (FTOF), the Low Threshold Čerenkov Counters (LTCC), the High Threshold Čerenkov Counters (HTCC), the Pre-shower Calorimeters (PCAL), and the Electromagnetic Calorimeters (EC). The combination of the LTCC, HTCC, and EC counters will allow a good separation between electrons and pions for momenta up to 5 GeV. The performance of the CLAS12 PID system for charged hadrons is summarized in Fig. 8.5. Green indicates good PID and yellow shows where there are limitations of the system and how far it can be pushed. The case of the separation between pions and kaons for momenta between 2.6 and 5 GeV is a good example. By combining the information from the FTOF and LTCC, one can get some kind of separation between kaons and pions, although not very satisfactory. Red indicates the absolute limitation of CLAS12 PID in the high momentum range above 5 GeV.

Good PID is a crucial element in the success of any experimental program as important and as diverse and as rich in physics as the one planned for CLAS12. Good kaon identification over the entire momentum range is very important for the polarized and unpolarized semi-inclusive deep inelastic measurements, such as the contribution of the strange sea to the nucleon spin and the transversity measurements for kaons. The study of hadronization will also benefit tremendously from very good PID.

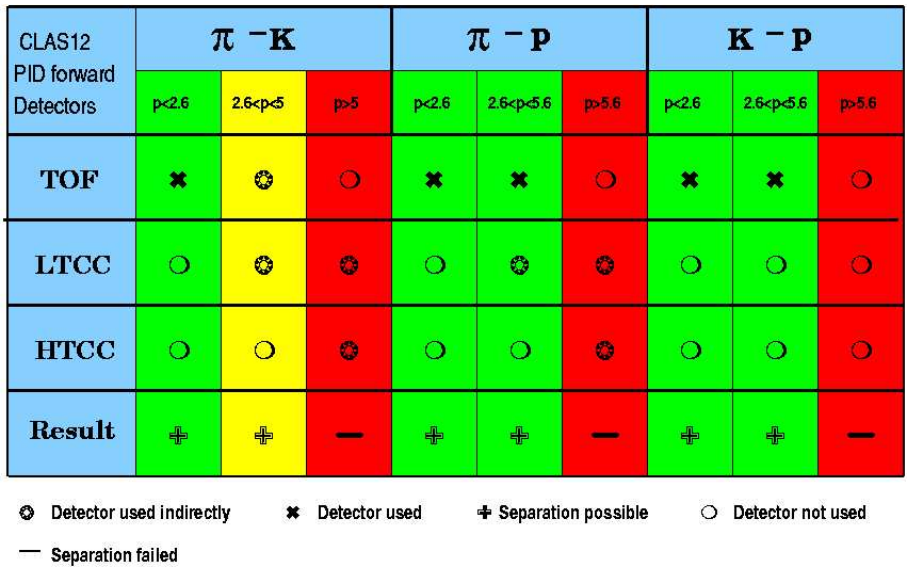

Figure 8.5: Summary of the performance of the CLAS12 PID system for charged hadrons.

	Aerogel	C_4F_{10}
n	1.0304	1.00137
Pions	0.6 GeV	2.7 GeV
Kaons	2.0 GeV	9.4 GeV
Protons	3.8 GeV	17.9 GeV

Table 8.2: Čerenkov light thresholds for pions, kaons, and protons for the aerogel and C_4F_{10} gas radiators.

To improve the CLAS12 PID system from good to excellent, one needs to build a ring imaging Čerenkov (RICH) detector. Due to space limitations, the only place where this detector would fit is the LTCC location. One can think of exchanging one or more sectors of LTCC by a RICH detector. The design of the RICH detector [324] of HERMES experiment would be a good choice for CLAS12. It is a dual radiator RICH detector that uses a clear aerogel in combination with a heavy gas, C_4F_{10}. It can provide a clean separation of pions, kaons, and protons in the desired momentum region. The Čerenkov angles produced by the combination of the aerogel and the C_4F_{10} gas for pions, kaons, and protons are plotted in Fig. 8.6. The corresponding threshold momenta are listed in Table 8.2.

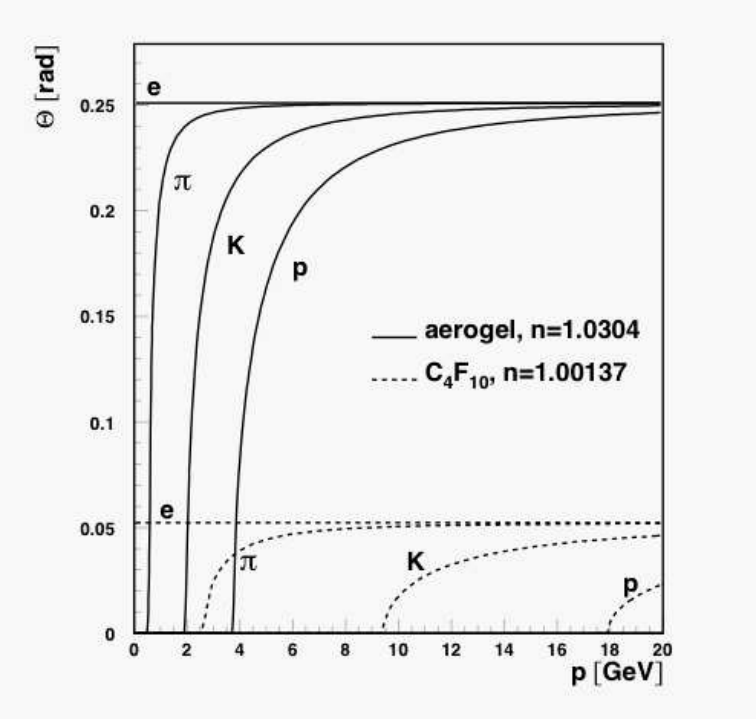

Figure 8.6: The Čerenkov angle vs. hadron momentum for the aerogel and the C_4F_{10} gas radiators.

8.4 Central Electromagnetic Calorimeter

8.4.1 Overview

The central electromagnetic calorimeter is an essential part of the CLAS12 central detector. It covers detection angles in the polar range from $40^\circ \leq \theta \leq 135^\circ$, and in almost the entire azimuthal range. It is designed for the reconstruction of π^0 and η mesons by their neutral decays, therefore, for the detection of multi-γ events. The design parameters are defined to meet an operational luminosity of $L \sim 10^{35}$ cm^{-2}s^{-1}. The following sections describe the technical requirements, the detailed design concept, and the estimates for the calorimeter performance.

8.4.2 Requirements

The compact structure of the entire central detector, which is mounted inside a superconducting solenoid with a strong magnetic field, determines the basic parameters of the calorimeter. The available radial space for the calorimeter material inside the magnet is limited to ~ 10 cm. The calorimeter must provide adequate energy and spatial resolutions to cleanly identify π^0 and η events. The typical energies of decay photons, produced at large angles ($> 40^\circ$) and at

Total Radiation Lengths	10 - 12
Radial Space (radial thickness)	$\sim$ 10 cm
Energy Resolution	$\approx 6\%/\sqrt{E}$
Angular Resolution, $\delta\theta = \delta\phi$	$\sim 1^\circ$
Timing Resolution, δt	few ns
Energy Threshold, E_γ^{min}	$\leq$ 50 MeV

Table 8.3: Central electromagnetic calorimeter design parameters.

beam energies of 12 GeV, are up to $E_\gamma \sim 1$ GeV. Reasonable energy resolution with these size restrictions can only be achieved if very dense materials are used, and at the same time, the sampling ratio and homogeneity of the calorimeter are reasonably high. The π^0 and η mass resolutions are functions of the energy and angular resolutions.

In order to provide sufficient mass resolution, i.e. $\delta m \sim 1/3(m/2)$, for π^0 and η mesons, it is necessary to have energy resolutions of about $\sigma/E_\gamma \leq 6\%$ at $E_\gamma \sim 1$ GeV and angular resolutions of $\delta\theta \sim 0.8^\circ - 1.4^\circ$. The angular resolution depends on the number of channels used to measure ϕ and θ. Taking into account that transverse shower dimensions are expected to be of $\sim$20 mm ($\sim$80% containment), the lower limit of the angular resolution is estimated to be $\delta\theta \sim 1^\circ$. To detect π^0s of the lowest energy, the calorimeter must provide an energy threshold of about $\sim$50 MeV. To prevent major shower energy leakages for photons at angles close to $\theta = 90^\circ$ (worst case), the calorimeter should be $\sim$10 - 11 radiation lengths deep at E_γ = 1 GeV. Table 8.3 shows the main design parameters of the Central Calorimeter.

Scintillating Fiber/Tungsten Powder Calorimeter Design

The overall view and basic dimensions of the cylindrical central calorimeter mounted inside the solenoid magnet are shown in Fig. 8.7. Dense tungsten metal powder is used as the absorber. Thin plastic scintillating fibers run in the direction parallel to the beam and are read out from the upstream end as shown in Fig. 8.8. The fibers are grouped into groups of equal size. Each group of fibers, which cover an azimuthal angle range $\Delta\phi \approx \pm 0.6^\circ$, go to a single photo-multiplier tube that provides energy, ϕ, and timing information. In the radial direction, there are one or two layers of fibers (see Fig. 8.9) that all bend at the same radius with both ends running out of the sensitive volume as shown in Fig. 8.10. This circular layer of

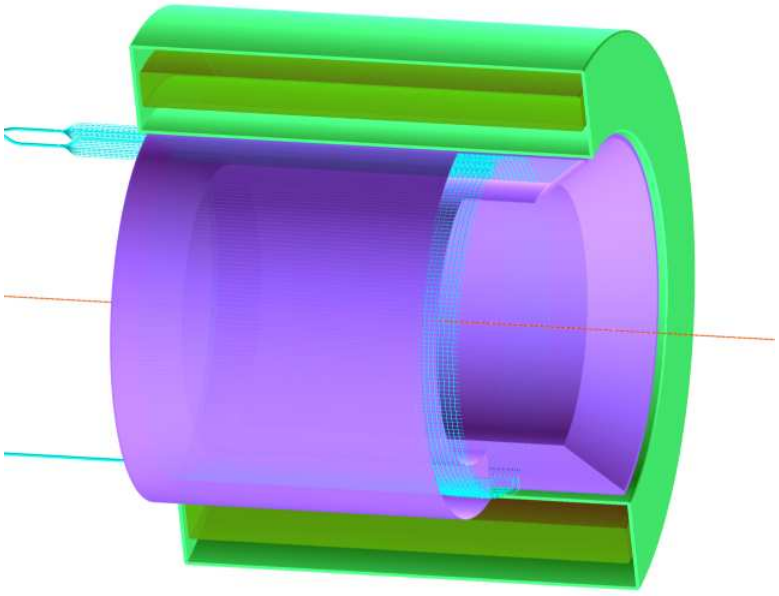

Figure 8.7: A perspective view of the central electromagnetic calorimeter inside the solenoid magnet.

grouped fibers provides independent measurements of the polar angle θ of the shower. To have resolutions of $\delta\theta \approx 1^\circ$, there will be a total of about 50 channels per polar angle measurement. To allow all the fibers to run through the main volume (see Fig. 8.10), there is a narrow gap not wider than 5 mm along the beam direction for readout purposes. This gap produces only a small reduction in the angular acceptance of the calorimeter (about 1-2%).

The implementation for this topology of the calorimeter with two sets of scintillating fibers embedded within essentially the same sensitive volume, is only possible because of the powder technology – the volume is filled by loose metal powder. Since the so-called "green density" of the tungsten powder to be used as absorber is of about 12 ± 0.2 g/cm^3, the entire structure becomes very efficient, especially in providing high sampling ratios with fibers as thin as 0.5 - 0.75 mm (or even smaller diameters), with no air gaps between the fibers and absorber. This particular feature allows matching two requirements, having sufficient energy resolution and small overall dimensions at the same time.

Expected Performance

To estimate the calorimeter response, one can use parameterizations based on simulations and previous calorimeter data. We have used parameterizations during the initial design phase for a fast estimation of the basic dimensions and characteristics of the calorimeter. The containment of the shower is parameterized using [325]:

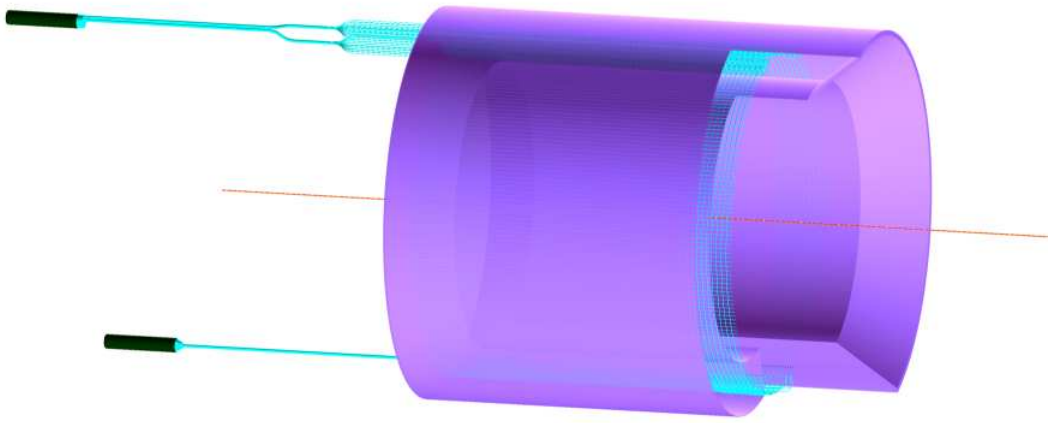

Figure 8.8: Central calorimeter. The tungsten powder volume and some of the axial readout fibers are shown at the left. Some of the radial fibers are indicated on the right side. The radial fibers are brought to the readout end through a slot at the bottom of the calorimeter.

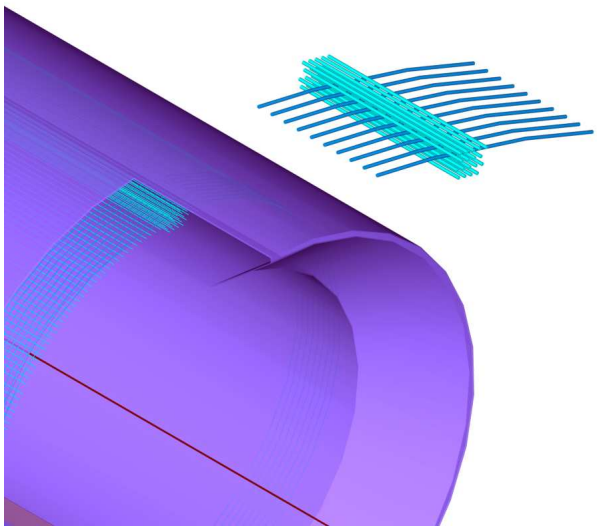

Figure 8.9: Central Calorimeter. The radial fibers are interleaved with the axial fibers. They provide shower position information along the beam direction. Since they are not used for the energy measurement, only a few layers are needed to provide the position information.

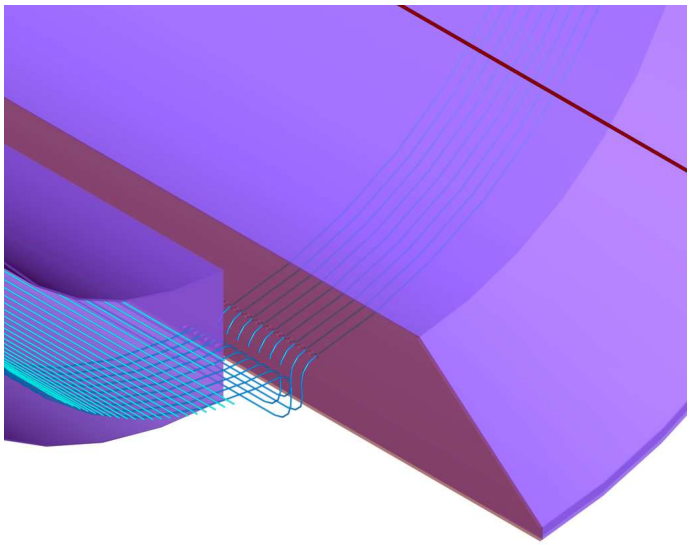

Figure 8.10: Central Calorimeter: radial fibers read out (detail) in the slot at the bottom of the calorimeter.

$$L(98\%) = 2.5 * [\log(\frac{E}{\epsilon}) + 1.2] \times X_o \text{ (cm)}. \tag{8.1}$$

Here, L gives the length in centimeters that contains about 98% of the energy of the shower. E is the energy of the incoming photon, ϵ the critical energy of the material, and X_o is the radiation length of the mix in centimeters. The material in the calorimeter is a mix of tungsten powder and scintillating plastic (Polystyrene) fibers. The radiation length for the mix (X_o) that contains a fraction y of scintillating plastic per volume and a fraction $(1-y)$ of tungsten powder absorber, is obtained using:

$$\frac{1}{X_o} = \frac{y}{X_{Sci}} + \frac{(1-y)}{X_{Powder}}. \tag{8.2}$$

For the powder with a fraction x of the pure tungsten, the total thickness in radiation lengths is given by $X_{Powder} = X_{PureTungsten}/x$. The critical energy of the mix is obtained using:

$$\epsilon = y\epsilon_{Sci} + (1-y)\epsilon_{Powder}. \tag{8.3}$$

The results are shown in Fig. 8.11. The values of L are plotted versus the fraction of scintillating plastic by volume for three values of the powder density: x=0.62 (loose powder),

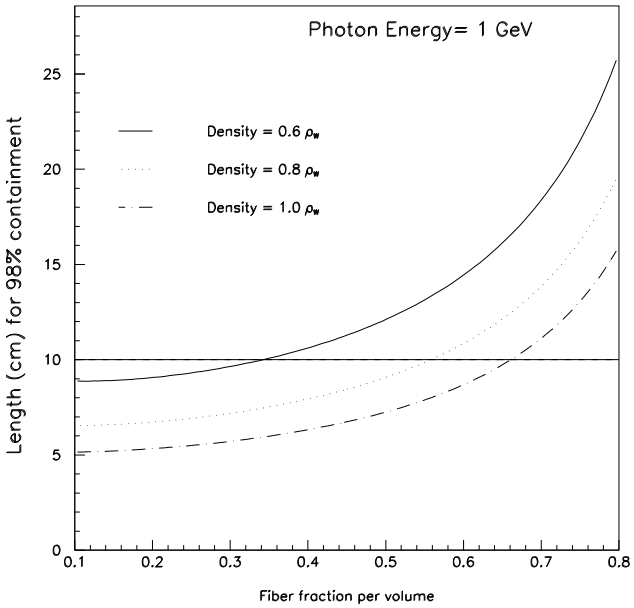

Figure 8.11: Containment vs. fraction of plastic for the central calorimeter.

x=0.8 (cold pressed density), and x=1.0 (pure tungsten). One can see that if the radial thickness of the calorimeter, using loose powder at x=0.62, is limited by ∼10 cm, then the fraction of scintillating plastic should not exceed ∼35% per volume.

The other important figure-of-merit is provided by the sampling errors in the energy measurements. For a given material (x=0.62), these sampling errors are a function of the fraction of scintillating plastic in the calorimeter y (sampling fraction) and the diameter of the fibers ϕ (sampling frequency). The corresponding parameterization for the sampling errors is given by [326]:

$$\frac{\sigma}{E}_{sampling} = 0.02\sqrt{\frac{\phi(mm)}{f_{sampl}}}, \tag{8.4}$$

where f_{sampl} is the sampling ratio for minimum ionizing particles, and is calculated using:

$$f_{sampl} = \frac{1}{1 + \frac{(1-y)}{y} x \frac{dE_W}{dE_{Sci}}}. \tag{8.5}$$

Here, dE_W and dE_{Sci} are the energy depositions by minimum ionizing particles in 1 cm of tungsten (22.1 MeV/cm) and polystyrene (2.0 MeV/cm), respectively.

Fig. 8.12 shows the sampling errors versus the fraction of scintillating plastic by volume

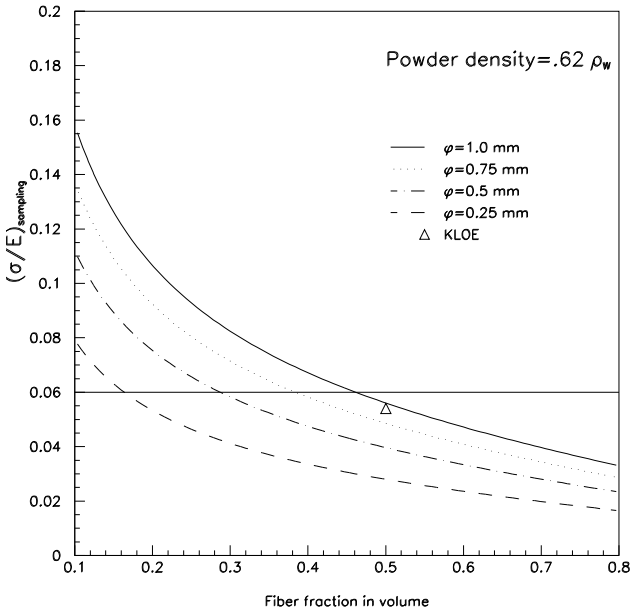

Figure 8.12: Sampling errors vs. fraction of plastic for the central calorimeter.

for four different fiber diameters (0.25, 0.5, 0.75, and 1 mm), at a powder density of x=0.62. One can see that for an absorber density of 11.8 g/cm^3 (x=0.62), a tungsten powder based sampling calorimeter built with fibers of 0.5 mm in diameter and with a fraction of scintillating fibers of ∼35% per volume can reach energy resolutions better than ∼6% at 1 GeV energies. This resolution is similar to that obtained by the KLOE [327] and JETSET [328] calorimeters using a larger number of scintillating fibers. In Fig. 8.12, the value of σ/E obtained by the KLOE collaboration [327] with a sampling calorimeter of 23 cm radial thickness built at y=0.5 using lead absorbers and 1 mm polystyrene fibers is also shown.

Prototyping and Simulations

The proposed sampling calorimeter is to be build using a new calorimetry construction technology. There are open questions that need to be answered, although some initial tests already have been successfully carried out.

- An important test will be to establish the more efficient assembly procedure when fibers having different directions and shapes are installed in the same volume.
- We need to explore the limits on sampling frequencies available with this technique, especially with fibers of small diameters. Small fibers (∼0.25 mm) cannot be used with

other techniques (grooving), unless one allows lots of air gaps or glue. Also the technical limits for sampling ratios with tungsten powder radiator have to be found. First tests have shown that designs are possible with a sampling ratio ∼17% and 340 polystyrene fibers of 0.5 mm in diameter using loose tungsten powder. A density of not less than 11.8 g/cm^3 can be achieved. Further tests are in progress.

- The main features of the calorimeter with a given realistic geometry need detailed simulation (i.e, using GEANT). This simulation will define the expected energy and angular resolutions to be compared with experimental test values that can be used in planning of physics experiments.

- A prototype consisting of 12 channels is currently being designed and built to examine all basic properties of the calorimeter. The final goal is to test the calorimeter in a photon or electron beam in the very near future. This first full prototype will have ∼10 cm of thickness (∼11 radiation lengths) with a fraction of plastic of 35% by volume using polystyrene fibers of 0.75 mm in diameter.

Chapter 9

Data Acquisition and Trigger

9.1 Overview and Requirements

9.1.1 Requirements

The following parameters are required for the CLAS12 Data Acquisition (DAQ) System: at least 10 kHz event rate, at least 100 MB/s data rate at the Event Recorder level, and not more than a 15% dead time under the above listed conditions.

9.1.2 Current DAQ System Analysis

Currently the CLAS DAQ system runs at an 8-10 kHz event rate and a 25-35 MB/s data rate at a dead time of not more than 15%. Since it will be partially re-used in CLAS12, we will discuss its main features and limitations, along with improvements necessary to achieve the CLAS12 requirements.

Front-End Electronics: ADCs

The currently used FASTBUS 1881M ADCs set a limit for the entire DAQ system: 12 μs conversion time projected into 12% dead time at 10 kHz event rate. It can be improved by switching to the low-resolution mode of these units, which sets a 9 μs conversion time. In this case the event rate limit can be pushed up to about 15 kHz. This means that from a performance point of view, the 1881M ADCs can be re-used, however, the number of FASTBUS ADCs must be doubled to equip all new detectors, and delay cables and pretrigger

discriminators must be purchased as well.

We have decided to replace all existing ADCs and equip all new detectors with Flash ADC boards. That decision provides higher performance for the traditional DAQ system and free-running DAQ compatibility for future upgrades. Flash ADC boards with on-board processing units will be used as the first stage of the Level-1 trigger, so no pretrigger discriminators are required (as in the current CLAS DAQ system. The delay cables will be eliminated as well.

It should be mentioned that removing the 1881Ms will increase the Level-1 trigger decision time from hundreds of nanoseconds to at least 3 μs, making it more powerful. In addition, Flash ADCs can deliver more detailed information to the trigger logic than the pretrigger discriminators.

Front-End Electronics: TDCs and Discriminators

All fast detectors in CLAS are already equipped with new pipeline TDC boards, both low (85 ps) and high (35 ps) resolution, and they will be re-used in CLAS12. All new detectors will be equipped with the same types of boards. We are planning to purchase new VME-based JLAB-made discriminators to equip all channels, eliminating the existing CAMAC-based LeCroy discriminators.

Front-End Electronics: TDCs and ADBs in Drift Chambers

The drift chamber readout is equipped with FASTBUS 1877 TDCs, and according to our plan, they will be re-used in CLAS12. All FASTBUS crates needed to accommodate those TDCs were recently equipped with new remotely controllable power supplies and fan units, which will extend their lifetime. The LeCroy 1877 TDC board has the following basic parameters: 500 ns resolution, 20 ns double-pulse resolution, up to 32 μs full scale, 1 to 512 μs fast clear window with 250 ns fast clear settling time, conversion time 750 ns + 50 ns/hit (1.6 μs minimum). The conversion time and readout speed of the 1877s will not limit the DAQ performance until about 15 kHz, however, we may see aging effects and the necessity to increase the event rate beyond 15 kHz in the future. In that case, all FASTBUS 1877 TDC boards can be replaced with pipeline TDCs. Replacement will not require any additional changes in other subsystems such as the trigger electronics.

The Amplifier-Discriminator board (ADB) electronics will be partially re-used, but new ADB crate backplanes, multiplexer (MUX) boards, and trigger boards (segment finders) will

be designed. The number of ADB crates will be decreased from 30 to 18, leaving a significant number of spare power supplies and fan units.

Trigger System

The current CLAS Level-1/Level-2 trigger system will be completely replaced with a new Level-1/Level-2 system capable of a few microseconds decision time. The new trigger system will include segment and track finding capabilities in the drift chambers, cluster finding in the calorimeters, and matching capabilities between different detectors. In addition, a Level-3 trigger will be running between the Event Builder and the Event Recorder for additional event rate reduction and/or data filtering. Level-3 will perform full event reconstruction, including hit-based tracking and time-based tracking, if required. The trigger system, in general, will be flexible to accommodate different running conditions, with the main goal to search for events with electrons.

Online Monitoring

Four practically independent monitoring systems are currently used in CLAS: Nagios-based computer and network monitoring, SmartSocket-based DAQ and Online monitoring, EPICS-based slow controls monitoring, and data monitoring. In addition, a few smaller hardware-specific systems are used. The data monitoring system includes visualization only, with almost no alarm capabilities.

CLAS12 will have one integrated monitoring system, with a standard low-level interface compatible with the CLAS12 equipment. It will also be compatible with the accelerator control and monitoring system on some level. It will have not only monitoring, but also control capabilities. The implementation of such a system is under discussion and concept development will take at least one more year. However, with our experience in developing and maintaining such systems, we are not expecting any problems in developing the new integrated system.

Online Calibration

The online calibration system must provide prompt information for the trigger system and online monitoring, and will be used for preliminary offline data processing. Such a system does not exist in CLAS and will be implemented in CLAS12.

9.1.3 'Free-Running' vs. Traditional DAQ Systems

Since we will employ some old FASTBUS boards in the readout, the new DAQ system cannot be run in 'free-running' mode, however, all new components will be compatible with the 'free-running' concept. This means that the CLAS12 DAQ system will become 'free-running' after all FASTBUS boards are replaced in the future.

9.1.4 SVT Readout

The Silicon Vertex Tracker (SVT) is not a part of the CLAS12 trigger system. The SVT readout is not included in the CLAS12 DAQ section, and is described in detail in the SVT section of this document (see Section 2.5.4. However, it should be mentioned that the current SVT readout design sets a limit for the Level-1 trigger decision time at 3 μs, which may effect its ability to make the desired decisions. Two solutions in the SVT readout are considered to avoid that problem: new readout chips and a 16 μs Level-2 FIFO buffer. More details can be found in the SVT section.

9.2 Hardware Design

9.2.1 Overview

The generic scheme for the CLAS12 DAQ system hardware is shown in Fig. 9.1. This system will be described in detail in the following sections.

9.2.2 Front-End for Fast Detectors

CLAS12 will have two calorimeters, two time-of-flight systems, and two Čerenkov counters with more than 3700 total PMT channels. Every PMT will be connected to a Flash ADC and to a TDC through a discriminator (see Figs. 9.2 and 9.3). Splitter panels will be used to deliver signals to both the ADC and TDC subsystems. Four VME64X and nineteen VXS crates will be used to accommodate the 56 TDC and 244 ADC boards. Sixteen VME crates will contain the 262 discriminator boards.

The 16-channel JLab-made discriminators have a controllable threshold and output signal width. They have built-in scalers, and every VME crate with discriminators will have a readout

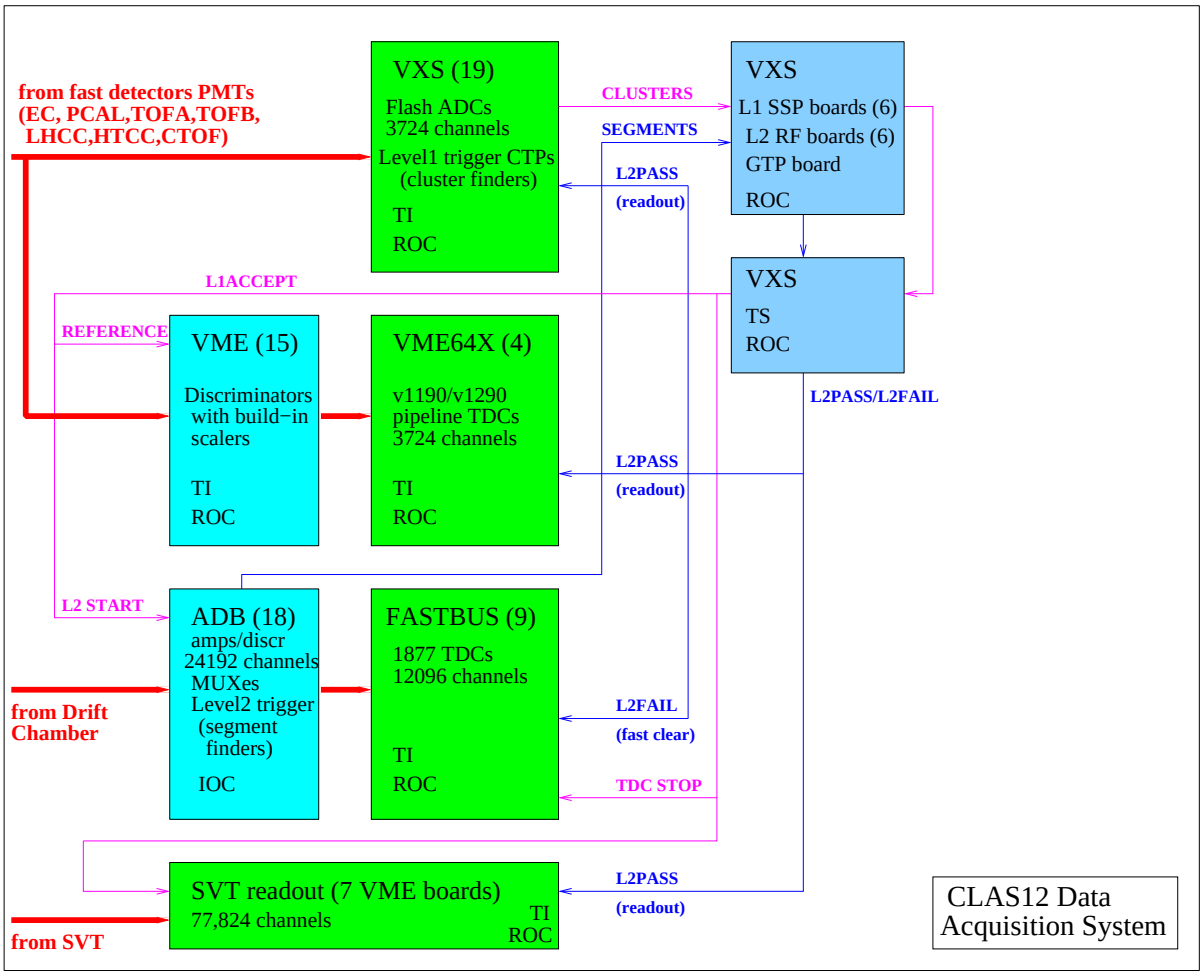

Figure 9.1: Generic scheme for the CLAS12 DAQ system hardware.

controller (ROC), so those scalers can be read out. The discriminators were successfully used in the CLAS tagger system. A new revision of the discriminators for CLAS12 will have a test input for calibration purposes and a channel mask. This is currently under development.

In CLAS12, 128-channel 85 ps resolution and 32-channel 35 ps resolution pipeline TDCs will be used. The first channel of every board will be connected to a reference signal through a discriminator to provide a timing reference. The CLAS system has been using these TDC boards for several years. A recent firmware version for those TDCs has reached 160 MB/s readout speed due to advanced 2eSST data transfer protocols.

The 16-channel JLab-made Flash ADCs are still under development and were not available for testing in CLAS at the time of writing of this document. However, based on our tests with commercially available Flash ADC boards (Struck SIS3320, see Refs. [320, 321]), CLAS12 can be equipped with 12-bit 200 MHz boards. We are expecting that the JLab FADCs will satisfy

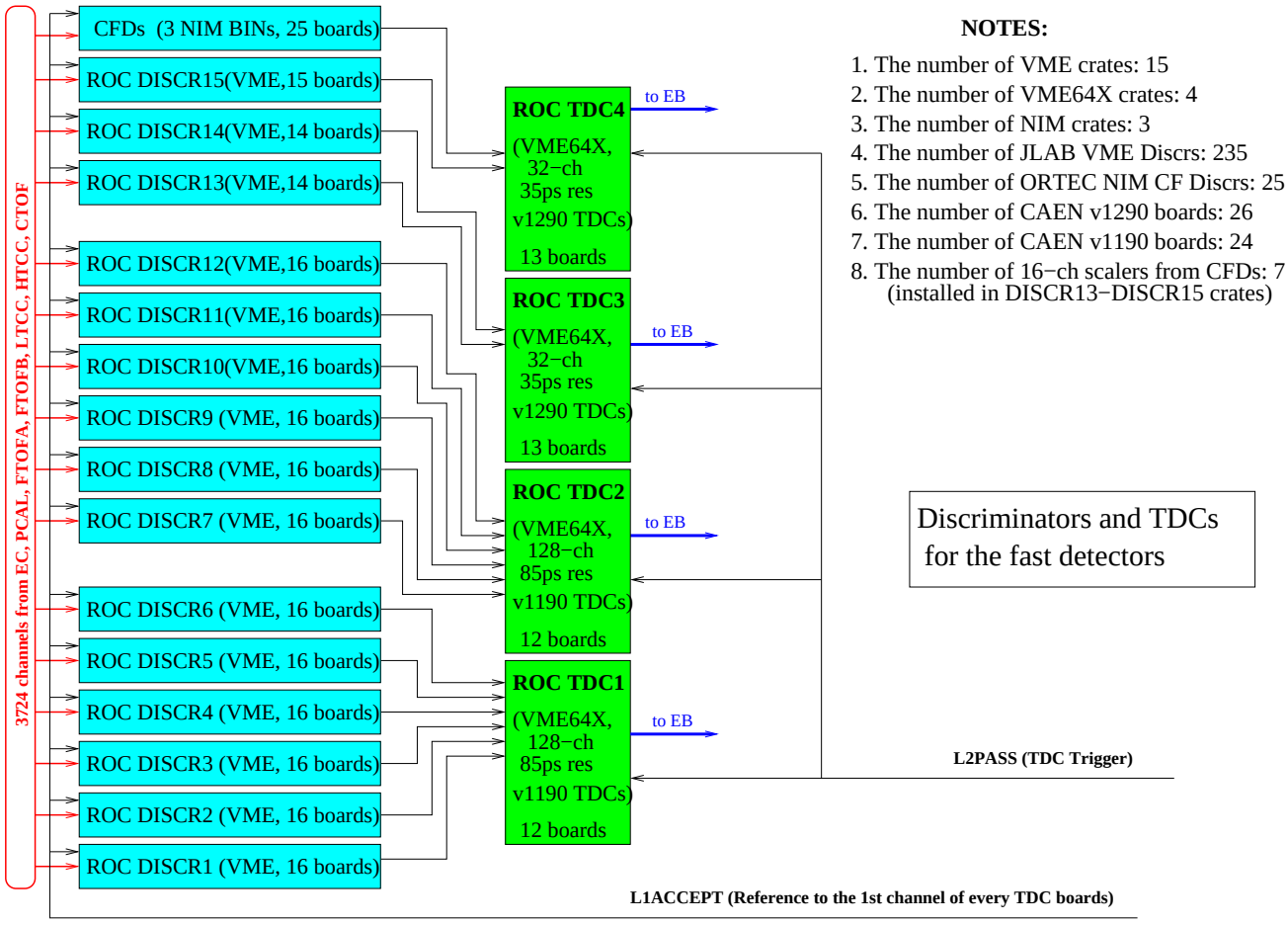

Figure 9.2: Planned scheme for the TDC readout in CLAS12.

those requirements.

The FADCs are a significant part of the trigger system and will send prompt information to the Cluster Finder board installed in the same crate. The cluster information will include energy for every channel above threshold. A threshold will be applied to the energy sum of several consecutive hits. Information will be sent to the Cluster Finder over the backplane serial bus every 16 ns. The Cluster Finder board is described in Section 9.2.4, along with the energy summing algorithm.

9.2.3 Front-End for the Drift Chambers

The existing CLAS preamplifier hybrid boards will be re-used for sense wire signal amplification. The existing MUX boards will be redesigned and the ADB crates will be equipped with new

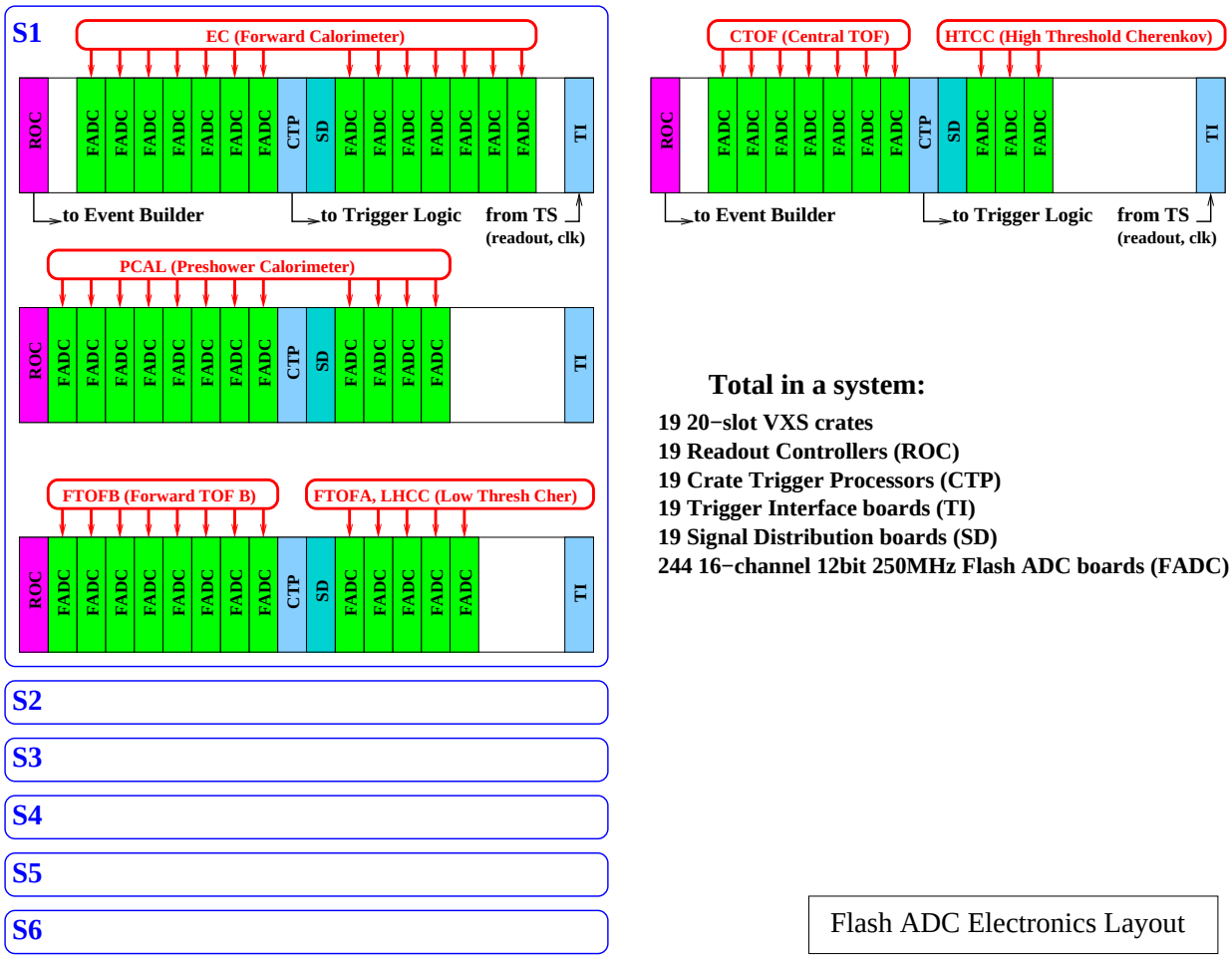

Figure 9.3: Planned scheme for the ADC readout in CLAS12.

backplanes. The ADB crates will be reused, probably with new power supplies installed. Fig. 9.4 shows the new ADB electronics layout that is planned. One ADB crate will have 14 96-input preamplifier boards serving a complete drift chamber region, with 7 boards per superlayer (112×6 wires = 96×7 channels). The new MUX boards will send data to the new Segment Finder using a 96-wire bus and ECL outputs to the TDCs after a 2-to-1 multiplexing. The ADB crate backplane has two 96-line buses, one per superlayer, ending in the middle of crate, where the two-unit-wide Segment Finder is installed. Communication between the various components is described in Section 9.2.4.

18 ADB crates will be connected to 9 FASTBUS crates containing 14 LeCroy 1877 TDC boards each. The FASTBUS crates will be upgraded with new Wiener power supplies that include remote control. In the future, the FASTBUS electronics can be replaced by 6 VME64X crates containing 16 v1190 CAEN TDC boards each (see Fig. 9.5).

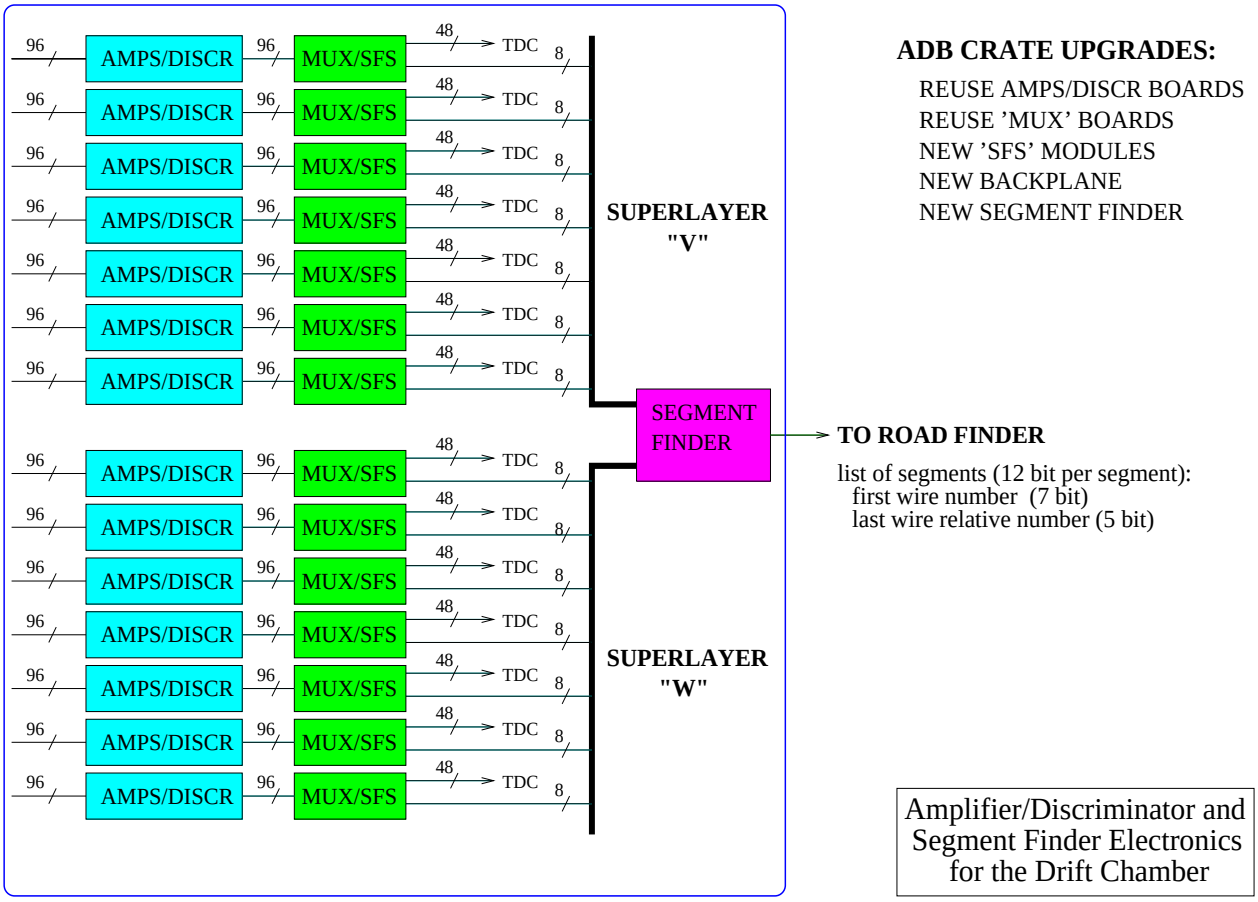

Figure 9.4: Planned layout of an ADB crate for CLAS12.

In addition to aging problems, the FASTBUS TDCs may set another limitation for the CLAS12 DAQ system. Currently they are programmed to accept up to 4 hits during a 2 μs interval, which corresponds to the maximum drift time in the Region 3 CLAS drift chamber. The CLAS12 drift chambers will have similar drift times, so the TDC window will be set to similar values as with the current CLAS configuration. Unfortunately, with the FASTBUS 1877 TDCs, we can only program the window size against a common stop signal. This signal is derived from the Level-1 trigger signal, and can be delayed a few microseconds to the TDC inputs. In that situation, we have to open the TDC window by a few more microseconds, which may lead to more background hits. In that case, we may need to allow 8 or 16 hits per channel to make sure that we are not losing useful hits. That may increase the TDC conversion time (which is hit-dependent) and the data rate from the FASTBUS crates, which would lead to a decrease in the overall DAQ performance. Our backup VME-based solution will be activated if the FASTBUS electronics will not be usable for any reason.

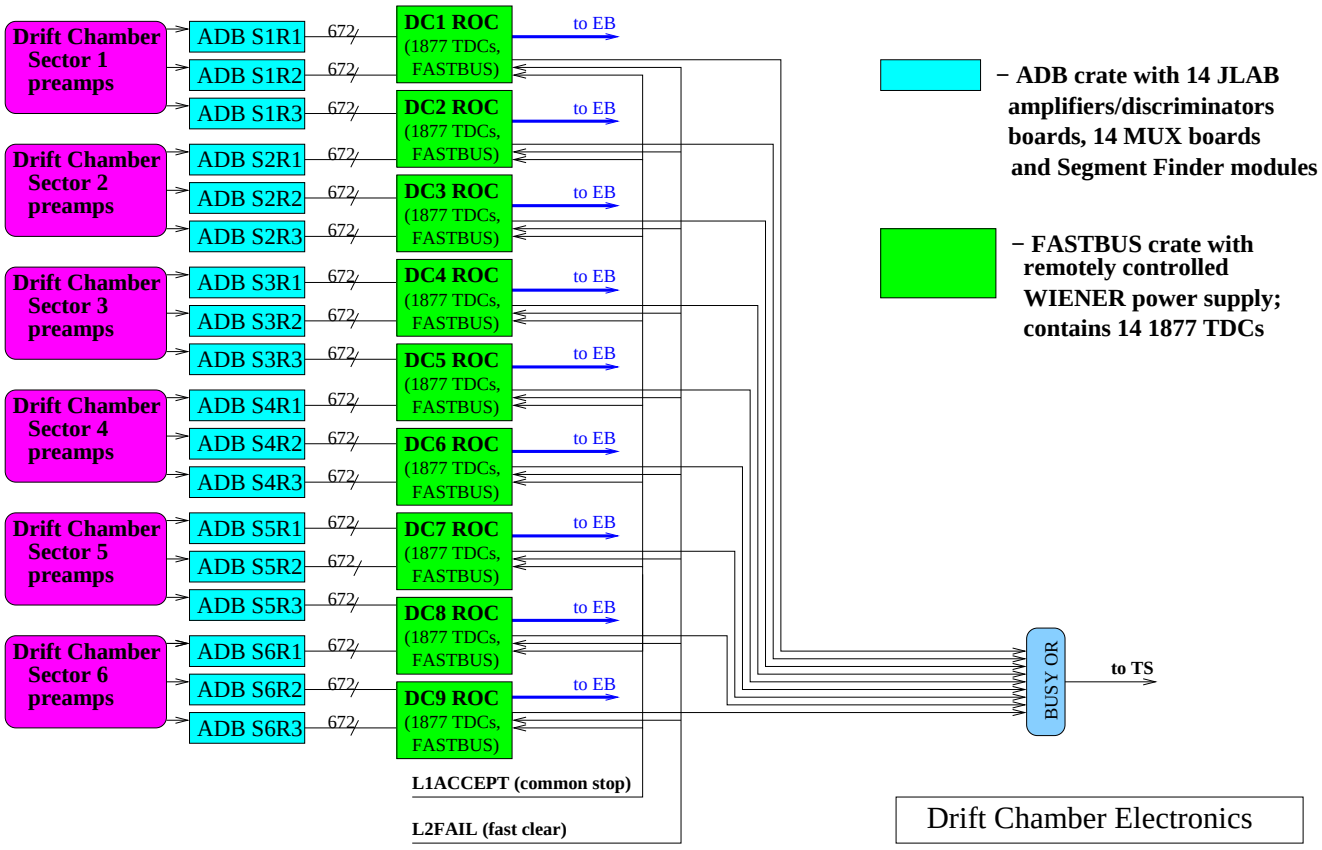

Figure 9.5: Schematic layout of the planned readout configuration for the CLAS12 drift chambers.

9.2.4 CLAS12 Trigger

CLAS12 will have a three-level trigger system. The Level-3 trigger is a software-based component and will be discussed in Section 9.3. The following sections contain a detailed description of the hardware-based Level-1 and Level-2 trigger components.

Trigger Efficiency Study

As a first step in the CLAS12 trigger system design, we studied the efficiency of the current CLAS trigger system. In particular, we studied its efficiency for electrons, which is important for most of the physics program. Detailed results can be found in Ref. [322]. We found that by increasing the Čerenkov counter pretrigger discriminator threshold up to 2 photoelectrons, we can make the electron trigger much more selective. However, CLAS has never run with

that threshold because of the possibility of losing electrons with low energy deposition in the Čerenkov counter. CLAS12 will have two Čerenkov counters, so even with a lower threshold, it is expected that electron selection will be improved. We also found that many non-electron events can be rejected by doing pattern recognition in the drift chambers and matching tracks with the fast detectors. The new CLAS12 trigger system was designed to be flexible enough to exercise different approaches, depending on the particular run requirements.

Trigger System Timing and Layout

The maximum trigger decision time is currently set to 3 μs for Level-1 and 4 μs for Level-2. The first number is defined by the SVT readout chip, and the sum of both times must be less then 8 μs, which is defined by the FADC units. Our preliminary FPGA algorithm development shows that 3 μs for Level-1 may not be enough, for example, to complete the cluster finding in the calorimeters using energy corrections. Those time constraints can be mitigated by using newer SVT readout chips and bigger FPGAs in the FADC boards.

It is important to make sure that logically completed parts of the detector will not be wired to the several FPGAs inside the Cluster Finder boards, which will make cluster reconstruction much more difficult. The current Cluster Finder board design contains two FPGAs, which collect information from 8 FADC modules each. That layout will satisfy all possible Level-1 algorithms.

Level-1 Trigger

The Level-1 trigger system is based on fast detectors equipped with Flash ADCs. The first stage components of the trigger hardware are incorporated into the Data Acquisition elements (VXS crates), while the final decision is made in a specialized trigger crate containing Level-1 Subsystem Processors. The same crate also contains Level-2 Road Finders and Level-1/Level-2 matching logic incorporated into the Global Trigger Processor, as well as Trigger Supervisor boards as shown in Fig. 9.6. The system is driven by a 16 ns global clock with an internal FPGA 4 ns clock.

The VXS crates shown in Fig. 9.3 contain two trigger system components: processing units on the FADC boards (Fig. 9.7) and Cluster Finder (CF) boards that collect data from the Flash ADCs over fast serial lines. The CF boards search for clusters in the electromagnetic calorimeters and other detectors, and send the results to the following stage of the trigger

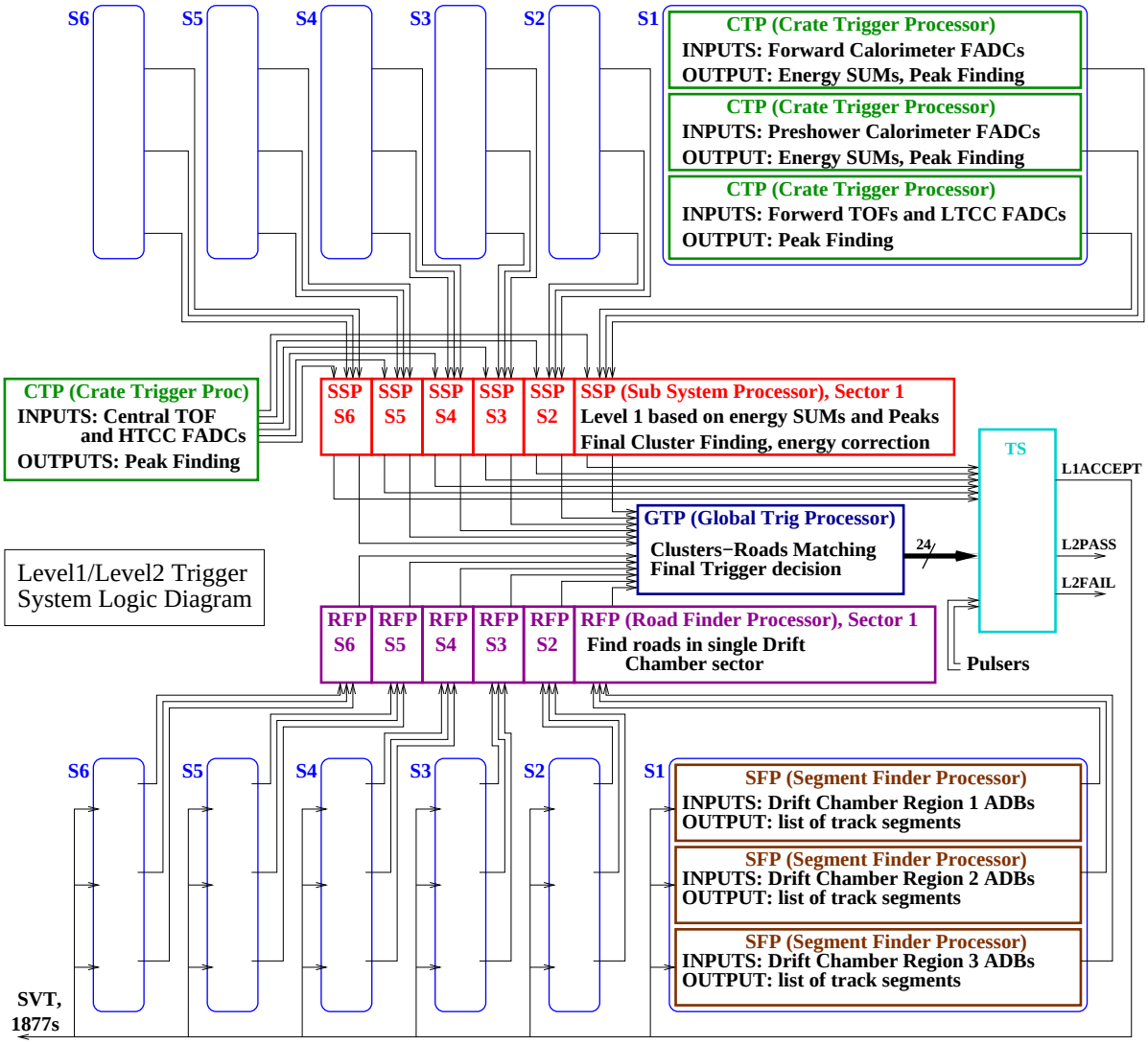

Figure 9.6: Trigger system logic diagram for CLAS12.

system (see Fig. 9.8). A signal processing algorithm running in the FADC board processing unit is shown in Fig. 9.9.

Level-2 Trigger

The ADB crates shown in Fig. 9.4 contain the Segment Finder (SF) boards that collect data from the set of drift chamber MUX boards corresponding to an entire drift chamber region. The SF boards search for track segments and send them onto the following stage. The MUXs send data with a 15 ns strobe, so in a 105 ns interval, all data from both superlayers is injected into a programmable delay (see Fig. 9.10). The Level-1-driven switch and latch units

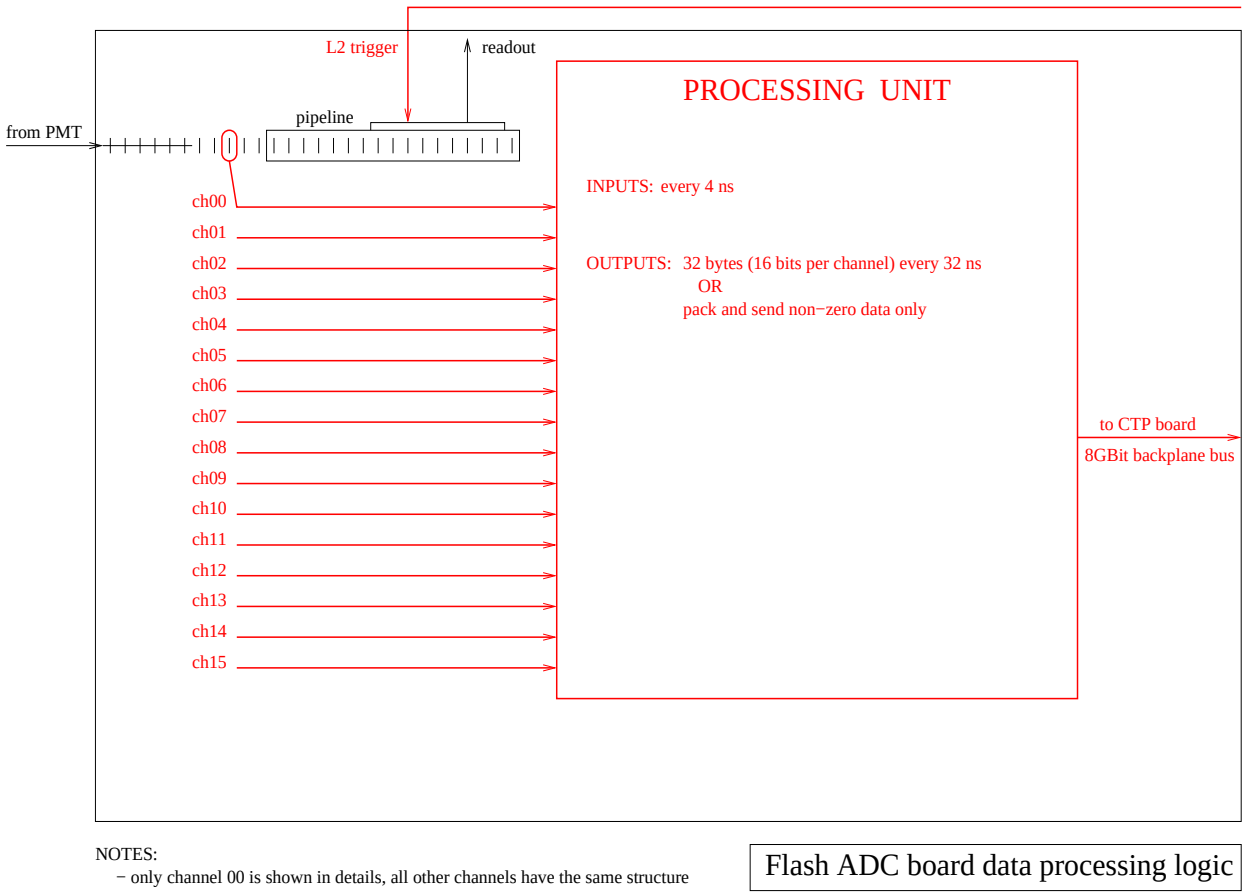

Figure 9.7: Processing unit on the FADC board.

accumulates the drift chamber hits during a 2 μs interval and passes the result to the Segment Finder board for processing.

The Segment Finder searches for segments in both superlayers simultaneously, then performs a region-based segment search, and finally builds a list of region-based segments. The system works as a pipeline and sends sets of segments to the Level-2 Road Finders. Every segment occupies 24 bits: 7 bits for wire numbers in U and 5 bits for the U-V difference for the first and last wires in the region-based segment.

Six Level-2 Road Finder boards are installed in the trigger crate along with six Level-1 Subsystem Processor boards, a Global Trigger Processor (GTP) board, and a Trigger Supervisor (TS) board. The system collects all information from the fast detectors and drift chambers, along with the information from the central detectors. It performs drift chamber-based track finding and matches the tracks with clusters from the fast detectors. The Global Trigger Processor collects the data from the Level-1 Subsystem Processors and Level-2 Road

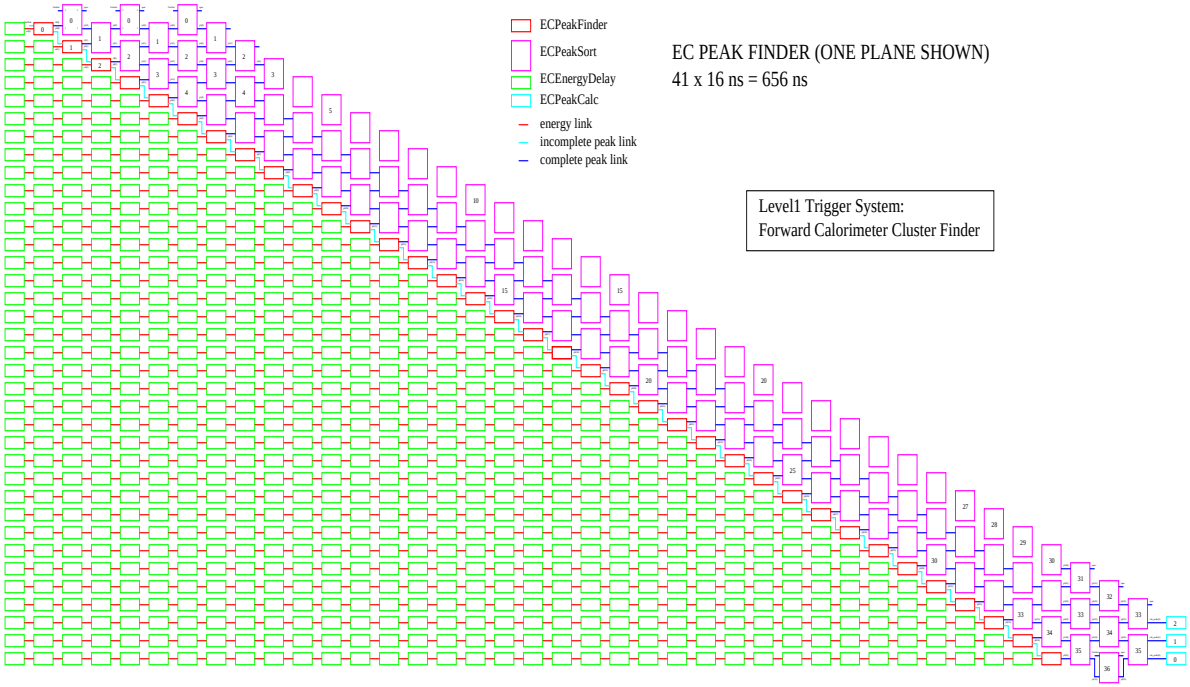

Figure 9.8: Cluster Finding diagram on the Cluster Finder board.

Finders and produces the Level-2 trigger signals (see Fig. 9.6).

The Trigger Supervisor generates the Level-1/Level-2 pass/fail and other signals, and controls the entire DAQ system readout through the Trigger Interface units. The Trigger Interface (TI) units installed in every crate participate in the readout process.

Level-1/Level-2 Timing Diagram

The generic scheme for the Level-1/Level-2 trigger timing is shown in Fig. 9.10. The entire trigger system can be considered as a three-stage process.

The first stage is the Level-1 sector-based trigger, which includes the FADC on-board processing (T1), data transfer over the VXS backplane serial bus (T2), cluster finding (T3), data transfer to the trigger crate (T4), sector-based Level-1 decision (T5), and data transfer to the following trigger stages. During that period of time (T1+T2+T3+T4+T5+T6+T7), the drift chamber signals are delayed by a programmable delay on the MUX boards in the ADB crates. The T3 and T5 time intervals can be different for different run periods, so the programmable delay must be reprogrammed accordingly.

The second stage starts when the Level-1 signal arrives at the ADB crate, initiating the

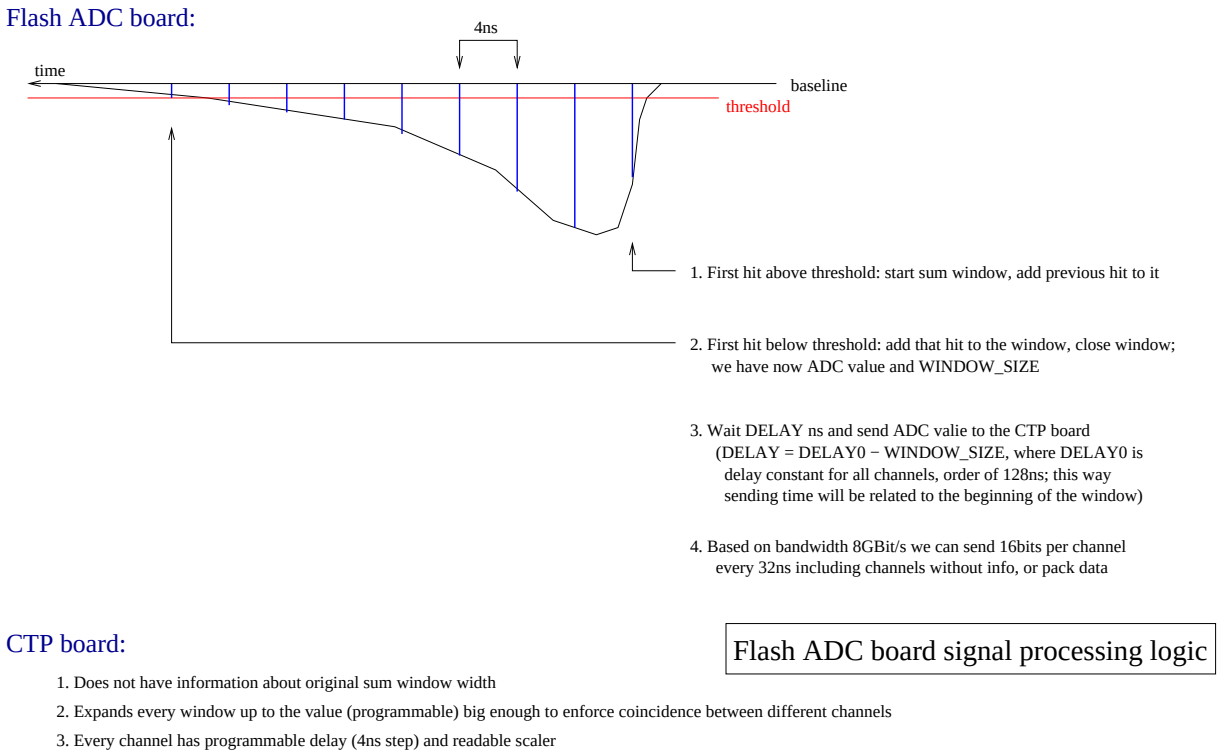

Figure 9.9: Signal processing algorithm on the FADC board.

drift chamber hit-latching process (T8). The typical T8 timing is about 2 μs and is defined by the maximum drift time. Three latch units will be used for every channel, so up to three Level-1 triggers can be processed in parallel. If a fourth Level-1 signal arrives while the first one is still latching, the whole trigger system will be stopped, however, such events will be extremely rare based on the expected trigger rate. After the latching process is finished, the latched hits will be transferred to the Segment Finder (T9), processed there (T10), and the list of segments will be transferred to the Level-2 Road Finders (T11) installed in the trigger crate, and processed there (T12). During that period of time (T8+T9+T10+T11+T12), the Level-1 information (clusters from the Level-1 Subsystem Processors) will be delayed by another programmable delay.

Stage three is the final Level1/Level2 trigger processing stage in the Global Trigger Processor (T13+T14) and Trigger Supervisor (T15). The total trigger decision time must be less than 7 μs to satisfy the Flash ADC range.

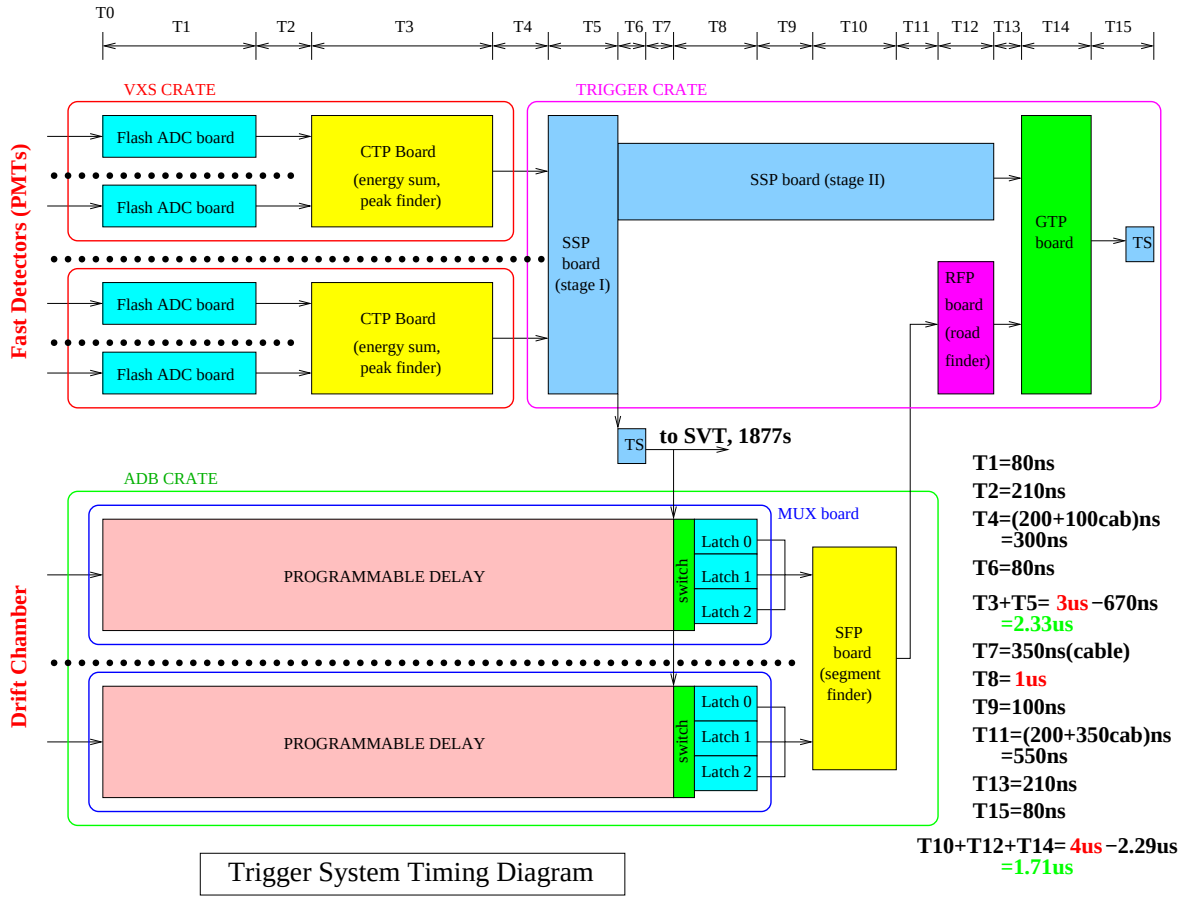

Figure 9.10: Level-1 and Level-2 trigger timing diagram.

9.2.5 Readout Controllers

Readout Controllers (ROCs) are installed in every FASTBUS, VME, VME64X, and VXS crate. The ROCs collect data from the front-end boards, process it, and send it to the Event Builder over the network. Currently we employ mvme6100 controllers with a prpmc880 or pmc280 co-processor module. That configuration is fast enough to meet the CLAS12 requirements and more co-processor modules can be installed if necessary. By the time of CLAS12 startup, a new generation of ROCs (including multi-processor and multi-core units) will be available.

9.2.6 Computing and Network

A Foundry 1500 switch is currently used as the backbone of the DAQ system, and a similar switch will be used for CLAS12. The Event Builder, Event Recorder, and other critical DAQ

components for CLAS are running on 4-CPU Opteron-based servers, and that configuration is sufficient for CLAS12 as well. ROCs are linked to the 1500 Foundry switch through smaller switches with up to four GBit uplinks (see Fig. 9.11). The CLAS data storage system (RAID5) is sufficient for up to a 150 MB/sec data rate.

All available equipment is good enough to satisfy the CLAS12 requirements, but most likely we will upgrade most of the components because of aging and maintenance considerations. The performance of the link to the JLab Computer Center tape storage must be increased up to at least 200 MB/s.

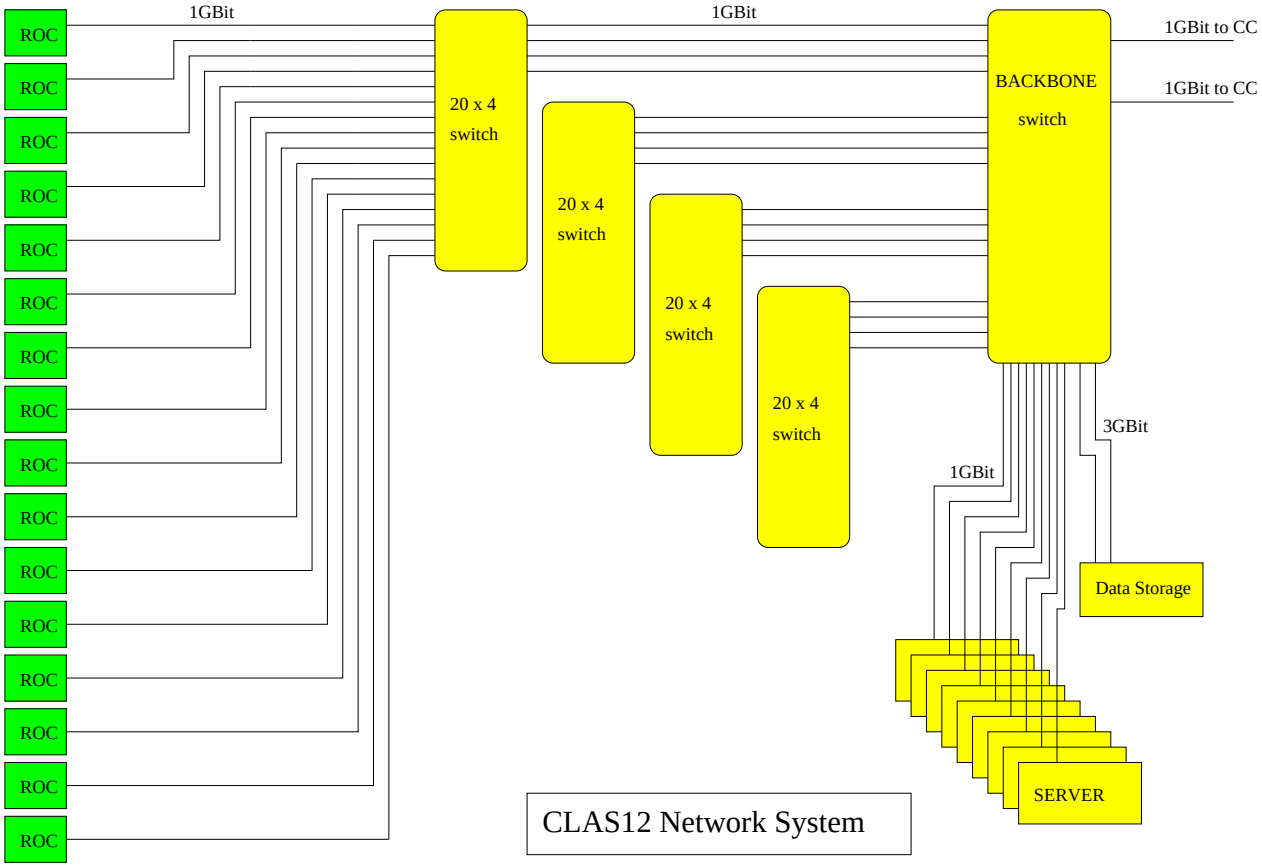

Figure 9.11: Planned scheme for CLAS12 networking.

9.3 Software

9.3.1 CODA Data Acquisition System

CLAS12 will use the CODA data acquisition software [323], similar to what we are using in

CLAS. The CLAS version of CODA was modified in recent years to improve performance and reliability, and those changes will be incorporated into the future version of CODA, along with appropriate redesign and cleanup. The most important changes were 'parallel' front-end readout, multi-processor ROC support, and a multi-threaded Event Builder. As a result, CLAS is running at an 8-10 kHz event rate, which is close to the CLAS12 requirements. We are expecting to get new software from the CODA group by the time of CLAS12 startup. Until then, we will use the current CLAS version of CODA for detector commissioning and test runs.

Recent upgrades have eliminated most of bottlenecks from the DAQ software, but there are still places where improvements can be made. One of them is multi-event readout and corresponding data coping inside the ROC memory. That modification will improve DAQ performance significantly for the free-running DAQ mode, but it will not have a big impact while CLAS12 is using FASTBUS 1877 TDCs. Those TDCs have 6 event buffers and need to be readout on an event-by-event basis to avoid back-logs. When the FASTBUS electronics are replaced, we plan on utilizing multi-event readout.

9.3.2 CLAS12-Specific Components Running as CODA Extensions

Several CODA extensions were developed for the CLAS detector, and some of them will be re-used in CLAS12. The CODA fragment format was expanded by adding an additional data bank header; this way several data banks with different formats could be created and processed by the same ROC. This feature may be implemented into the new CODA version, or we can continue to use it as it is implemented now.

The currently used BOS data format will be obsolete, and the CODA data format will be used instead for all output data files, but data will be organized based on the detectors, not on the readout hardware layout. Again, it can be done by expanding the CODA format or by CLAS12-specific extensions.

The data translation procedure running in the ROCs will be re-used, with possible data format modifications. Two advantages of this method should be mentioned: the data volume reduction (especially in the drift chambers) and the ability to access data using the 'offline' format on the very first stage of the data acquisition process. Also the ROC-level histogram package played a critical role in the DAQ performance analysis, and it will be reused after adjustment to the new data format. The DAQ performance profiler will be reused, although it may be part of the new CODA version as well.

The Event Transfer (ET) system in CLAS was extended by adding a new package to handle multi-threaded attachments to a single ET station, with special care taken for preserving the event order. This method was successfully used by the Event Builder, Level-3, and the fast online reconstruction software running on an 8-CPU Sparc Server, and will be reused in some form in CLAS12.

9.3.3 Level-3 Trigger

A multi-threaded Level-3 (software) trigger was implemented in CLAS, but was used in tagging-mode only. We will redesign that component for CLAS12, implementing full reconstruction up to at least the hit-based tracking level. A single multi-core machine is used right now to run the Level-3 trigger, and a computer farm solution can be used for CLAS12 if needed.

9.3.4 Online Monitoring

Online Monitoring will be addressed in CLAS12 as a part of the Experiment Control System (ECS) concept. This approach was used in previous years by other collaborations. We will use their experience to design the CLAS12 ECS.

ECS will collect all information coming from various CLAS12 components into one processing center, which will perform analysis and report problems with maximum possible precision. To make the whole system work successfully, all information from the low-level components will be reported in standard form, EPICS-channel access format is currently being considered. Special care will be taken to avoid false alarms.

The generic scheme for the CLAS12 Experiment Control System is shown in Fig. 9.12. Low-level hardware and data quality control components will communicate with top-level state machines using EPICS channel access and/or similar protocol. The data acquisition components will have a DAQ-specific communication system. Most state machines will be detector-specific, with one central component supervising the entire CLAS12 setup. A set of logic diagrams will be developed to handle different situations during CLAS12 experiments, such as production data taking, calibration runs, test runs, troubleshooting, recovery, etc. These diagrams will be processed by the state machines.

The Experiment Control System for CLAS12 is currently under development. We are looking into several frameworks that can be used to build the CLAS12 ECS, such as CERN

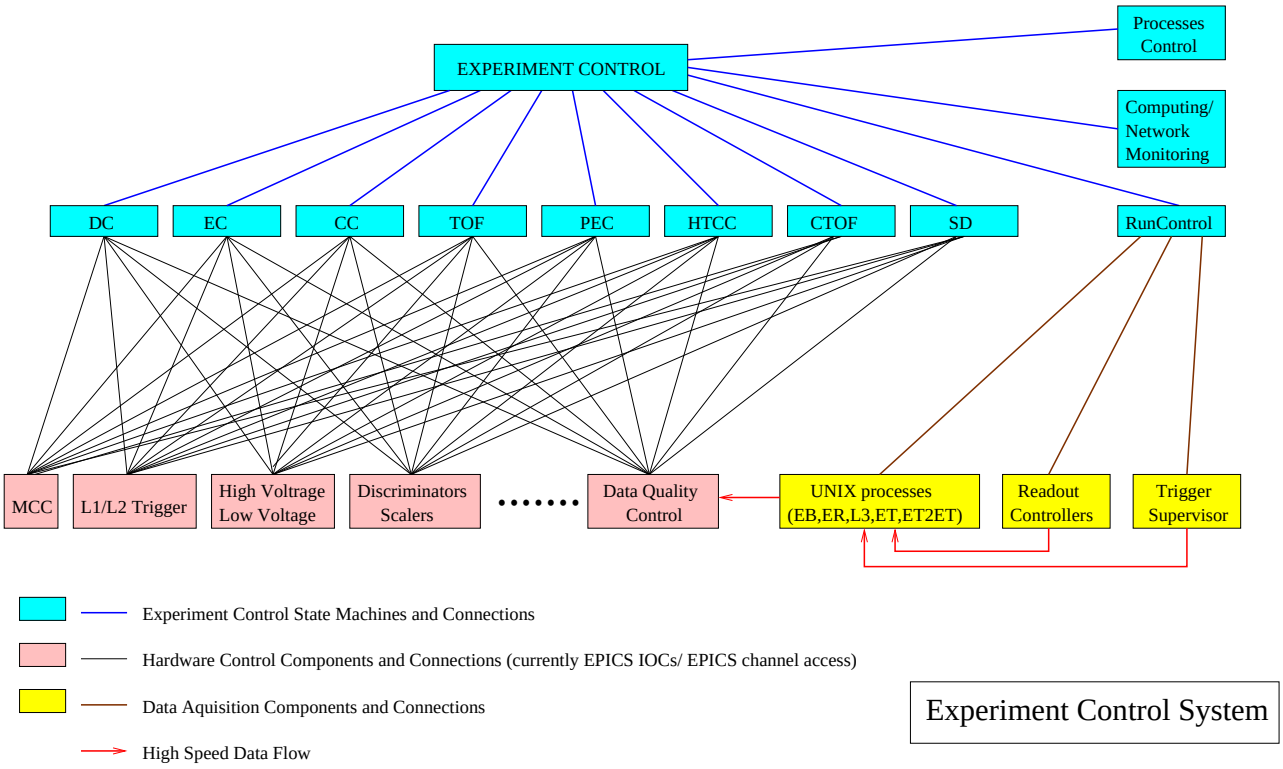

Figure 9.12: Generic scheme of the CLAS12 Experiment Control System.

PVSS (used by all major CERN experiments), AFECS (under development at JLab), and others.

It may take a while to complete the design because of the dependency on the accelerator's control system, which we have to be compatible with on some level. Several approaches are being considering by other JLab groups, and we are planning to participate in joint efforts to obtain the system most suitable for CLAS12.

9.3.5 Online Calibration

The main goal of the online calibration system is to deliver the calibration parameters for the trigger components. Normally, special runs will be taken and analyzed online before production data taking starts. Those runs will be processed and analyzed by software included into the Level-3 trigger component running in tagging mode.

9.4 Conclusion

Since the current CLAS DAQ system already has a performance close to that needed for CLAS12, we are confident that the CLAS12 goals will be achieved with available solutions. All new components designed by the JLab CODA group and the JLab Fast Electronics Group for Hall D will be utilized in CLAS12, since the CLAS12 requirements have already been taken into account.

Chapter 10

Infrastructure

10.1 Overview

The CLAS12 detector will be located in experimental Hall B. It will replace the CLAS detector and re-use many systems, including magnets, beam line components, cryogenic targets, support structures, and some particle detectors. The planned CLAS12 detector is shown in Fig.10.1.

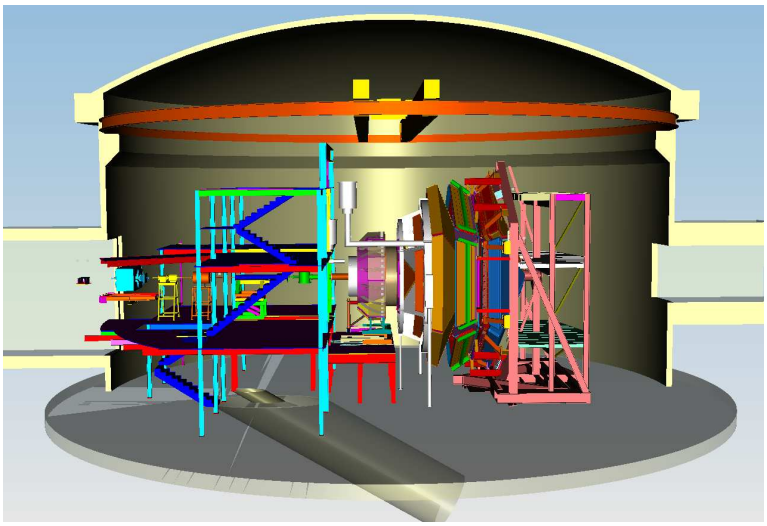

Figure 10.1: Model of the CLAS12 detector in Hall B.

Two of the major structures in Hall B will be retained. The first is the "Space Frame", the structure on the left side of Fig. 10.1, and the second is the Forward Carriage shown on the right side of the figure. The Space Frame is a fixed-deck structure, while the Forward

Carriage, which is movable, is a large structure that supports detectors, cables, and instrumentation racks, and weighs approximately 300 tons. Some modifications will be required for each structure. Major utilities and their distribution systems including electrical power, HVAC, cooling water, and cryogenics that currently service CLAS, will be re-used for CLAS12. Shown in Fig. 10.1 is the 20 ton polar crane. This crane has enough capacity to install all of the new components for CLAS12. Not shown for simplicity are all of the magnet power supplies, electronics racks for detector signal processing and device controls, cable trays, and the handrails on the decks.

10.2 Permanent Platforms

There are four large frame structures in Hall B. Two of which will be re-used for CLAS12. The largest structure is fixed in position to the Hall and called the Space Frame. The other structure we will re-use is the Forward Carriage. It is not fixed in location and must be moved downstream to allow detector installation and maintenance.

10.2.1 Space Frame

The largest structure in Hall B is the Space Frame shown in Fig. 10.2. The Space Frame has three levels, with the electron beam passing between Levels 1 and 2. Level 1 has a set of rails that allow beam line components to be located at various z locations along the beam.

Some modifications to the Space Frame are anticipated, which include:

- removal of the downstream structure and the top beam;
- a deck structure (called Sub-level 1) will be added to support the HTCC and solenoid (see Fig. 10.3);
- Level 2 will have the deck cut out above the beam line to allow the solenoid magnet to move upstream;
- a small raised platform may be required to access the cryogenic distribution can.

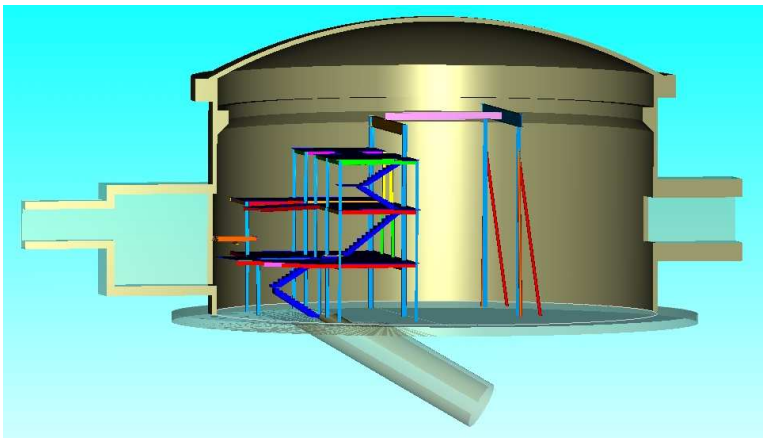

Figure 10.2: View of Hall B without any of the detector elements or the Forward Carriage to highlight the layout of the Space Frame. This figure shows the existing configuration existing in Hall B.

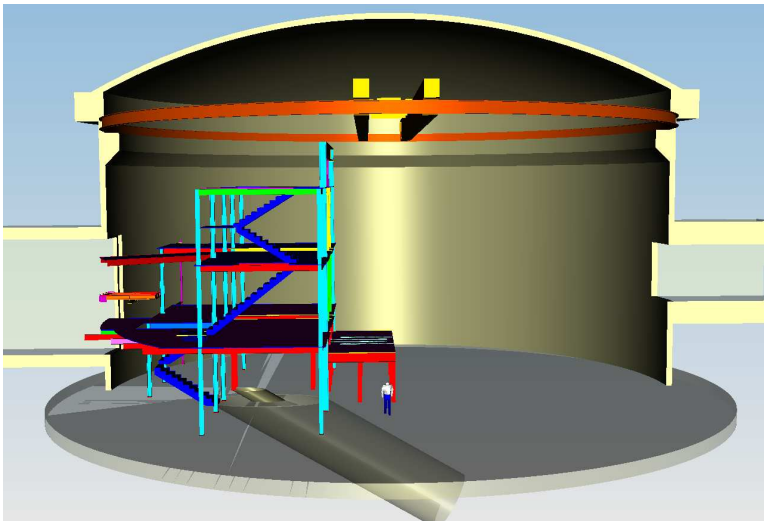

Figure 10.3: View of the Space Frame as modified for CLAS12 showing the addition of the Sub-level 1 deck for the HTCC and solenoid. Also shown is the cut-out for the solenoid on Level 2.

10.2.2 Forward Carriage

The Forward Carriage currently supports 200,000 lbs of calorimeters, 10,000 lbs of TOF, 15,000 lbs of LTCC, and roughly 15,000 lbs of delay cables and electronics (see Fig. 10.4). The carriage was weighed using hydraulic jacks and the total was approximately 600,000 lbs. The CLAS12 upgrade will include adding the following to the Forward Carriage:

- six pre-shower calorimeter modules (PCAL) weighing 70,000 lbs;
- a second layer of forward time-of-flights (FTOF) panels weighing 12,000 lbs;
- a set of large-angle time-of-flight panels (panel 2) weighing 6,000 lbs.

These additional loads may require strengthening of this carriage. A finite element analysis of the carriage is being performed. The results will be analyzed to determine what work will be required.

10.3 Tooling for Detector Installation and Maintenance

Tooling for detector installation and maintenance was a major challenge for the CLAS detector and will be again for CLAS12. The addition of several new detectors and the increased thickness of the drift chambers will impose new constraints on accessing each of the detectors. The fact that all of the forward detectors are planer could make some of the installation tooling simpler. All tooling will be designed to facilitate safe installation and maintenance. Tooling that will carry loads will be tested to 125% of the rated load. Equipment installation will be guided by principles from the EHS&Q manual (Section 6000) and appropriate subsections. Hazard analysis will follow the guidelines in Section 3210 of the EHS&Q manual. In most cases, specific procedures will be developed and followed to assure worker and detector safety. These procedures will be "living" documents and updated as new ideas are developed and processes tested that reduce the likelihood of equipment damage, reduce the possibility of personnel injury, or reduce the time required to carry out the work without sacrificing safety.

10.3.1 The HTCC Lifting Fixture

The HTCC will be lifted to the beam line using the Hall B polar crane. The design of the detector will allow a single lift point with minimal distance to the crane hook. The total

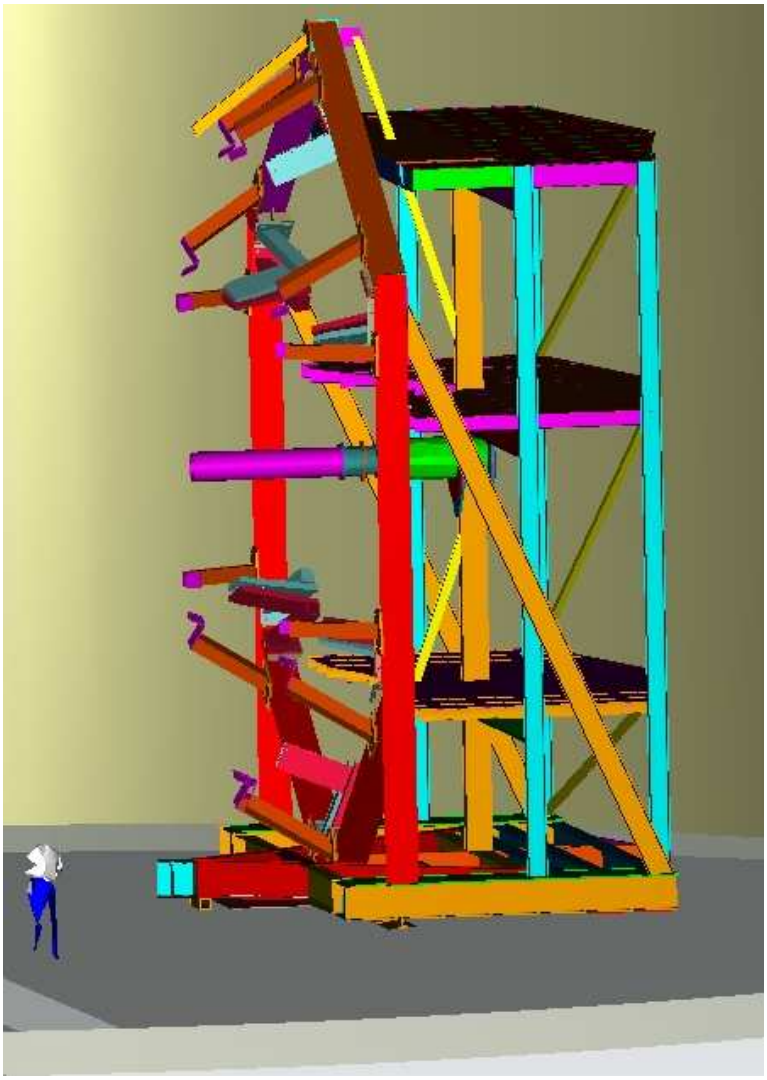

Figure 10.4: Forward Carriage in Hall B with all detectors removed.

weight of the HTCC will be around 5000 lbs.

10.3.2 Drift Chamber Tooling

Drift chamber installation will require very specialized tooling. These chambers are being designed to allow sectors to be installed and removed individually. Due to the delicate nature of drift chambers, the handling and mounting systems must incorporate features that allow accurate placement that impose only known loads. The installation tooling must control the position carefully at all times. The current design uses tooling that is similar in concept to the designs used in CLAS for the LTCC (see Fig. 10.6). The principle is that the detectors arrive in Hall B on a truck or low-boy trailer. A strong-back with a cantilever arm and weight box will allow the individual drift chambers to be positioned near their final positions, where they will be attached to their final attachment linkages. The strong-back is detached from the chamber and pulled back using the crane. Final chamber positioning is done using some fine tuning adjustment screws that are attached to the torus cryostat.

10.3.3 Forward Time-of-Flight

The FTOF system will have three panels mounted in each of the six sectors of CLAS. Panels-1a and 1b will be mounted in front of the PCAL and EC detectors, and panel-2 will be mounted off the side of the forward carriage. Each TOF panel weighs about 2000 lbs. The strong-back shown in Fig. 10.5 was used for CLAS and will be re-used for panel-1a mounting, and with modifications, for panel-1b mounting. The panel-2 counters will be installed using the crane.

10.3.4 Low Threshold Čerenkov Counter

The LTCC will be modified slightly for CLAS12. The modifications include changing the optics and changing the side walls to make the detector upstream window flat. Fig. 10.6 shows the lifting fixture that currently exists for the LTCC, which may need modification because of reduced space in CLAS12.

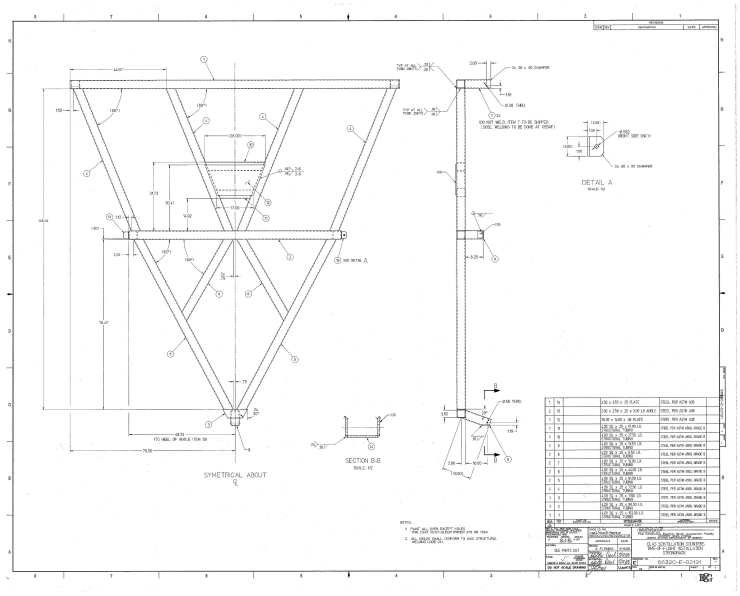

Figure 10.5: Engineering drawing of the FTOF strong-back assembly.

Figure 10.6: Photograph of the LTCC lifting fixture as attached to an existing LTCC sector in CLAS.

10.3.5 Pre-Shower Calorimeter

The PCAL will be installed with tooling similar to the original EC tooling. It may even be possible to re-use the original tooling shown in Fig. 10.7 that was used for the CLAS EC installation.

Figure 10.7: Photograph of the EC tooling used to lift and install the CLAS EC sectors.

10.3.6 Solenoid

The solenoid will be delivered to Hall B as a complete unit inside its cryostat. The Hall B crane will be used to lift the magnet to a cart that is waiting on Sub-Level 1 of the Space

Frame. A lifting bracket will be designed to match the magnet will be bolted to the magnet and used to allow a single point lift. If the solenoid final weight is greater than 20 tons, a backup plan using a mobile 100 ton crane has been put in place (see Fig. 10.8).

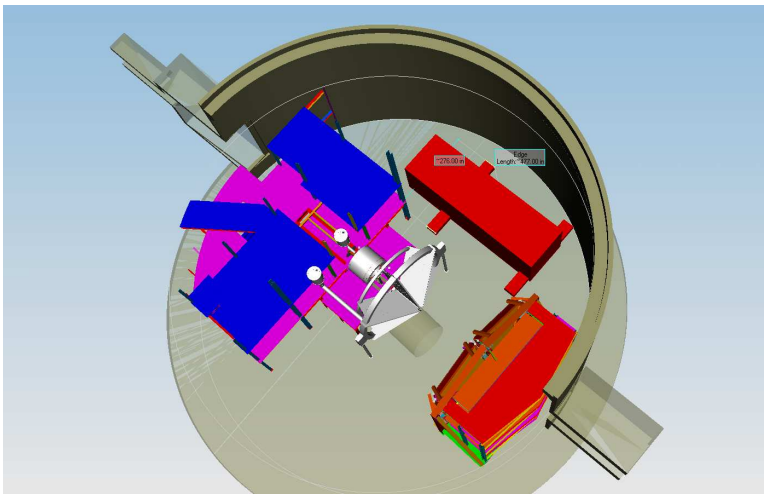

Figure 10.8: Overhead view of Hall B showing the CLAS12 configuration and the positioning of a mobile crane for installation of the solenoid. This plan will be used only if the final weight of the solenoid is more than 20 tons.

10.3.7 SVT

The SVT system is an interesting case. It is so light that no cranes will be necessary to carry the load, but it is very fragile. The current plan is to mount the SVT on an extension tube that is supported from the solenoid. The support fixture is also used for aligning the detector. The SVT is installed into the solenoid using the CLAS insertion cart. Before installation, the SVT will be pre-aligned on the beam line.

10.4 Permanent Support Devices

10.4.1 Torus Support

The torus will be mounted on a support stand that sits on the floor of Hall B. The magnet will be supported from three legs. The support system will be tied to Sub-level 1 of the Space Frame to increase the stability of the system.

10.4.2 Drift Chambers

The three regions of drift chambers will be attached to the torus. This is done to allow accurate, reliable, and repeatable positioning with respect to the magnetic field that is used for bending the charged particles. A six link system (shown in Fig. 10.9) has been prototyped for this attachment system. The prototype has been shown to have a reproducibility of 25 μm for chamber positioning. The system has also been designed to allow for easy access to the individual chambers to facilitate repairs.

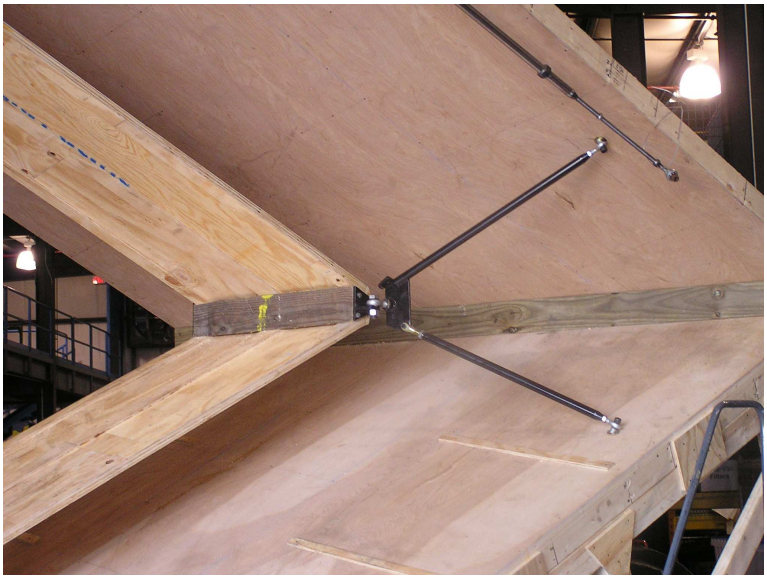

Figure 10.9: Photograph of the link system installed in the Region 2 drift chamber plywood prototype. The link systems for all 18 CLAS12 drift chambers will be of a similar design.

10.4.3 PCAL

The pre-shower calorimeter will be supported from three points. The nose will have a docking ring similar to the drift chambers. The back two corners will have arms that reach from the Forward Carriage upstream, and attach to each sector. These arms will have slots that allow for some misalignment of the brackets that must be welded to the Forward Carriage.

10.4.4 Panel-2 FTOF

FTOF panel-2 will be attached to the Forward Carriage on the outer hex ring. These panels will be hinged to allow them to be folded back such that they are clear of the other detectors.

A jack screw position arm will allow them to be moved in and out. It may be possible to re-use the jack screws from the CLAS panel-4 TOFs.

10.4.5 LTCC Arms

The LTCC supports will be changed. The current support arms slide between the LTCC boxes. There are several good reasons to modify this support system. This system has very little clearance and sometimes the installation or removal process results in making small leaks in the detector. The space that the original arms take is very valuable and is needed for the PCAL phototube assemblies. The current system requires that the LTCC come in parallel to the beam direction. A different support system is being designed to allow the sectors to come in from other angles and this reduces the space required for installation. The nominal design for the new support system includes attachments at the nose and outer corners of each LTCC box.

10.4.6 CTOF Supports

The central TOF will be supported from the solenoid cryostat. Detailed engineering and design work on this support is presently underway.

10.5 Carts

10.5.1 Central Detector Cart

The central detector includes the solenoid, central time-of-flight system, and the silicon vertex tracker. It may in the future also include a central calorimeter. These systems combine to a significant load for this cart. The estimated total weight is 40,000 lbs. The cart must be designed to allow for alignment of the solenoid to the beam axis. The current design of the central detector cart is shown in Fig. 10.10.

10.5.2 HTCC Beam Line Cart

The HTCC weight is approximately 5000 lbs. It will be supported from rails on the deck described in Section 10.2.1. It will have an alignment cart (see Fig. 10.11) that allows positioning

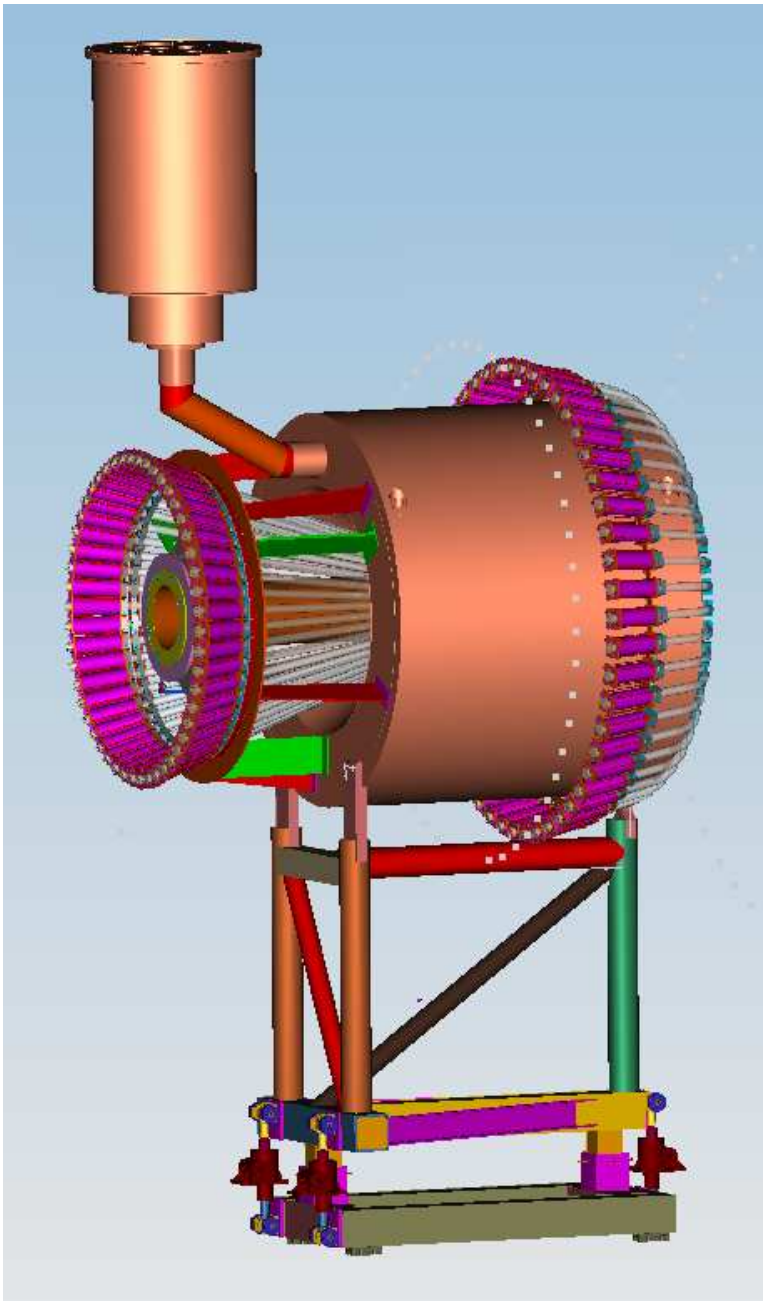

Figure 10.10: CLAS12 central detector cart.

of the detector to better than 0.5 mm.

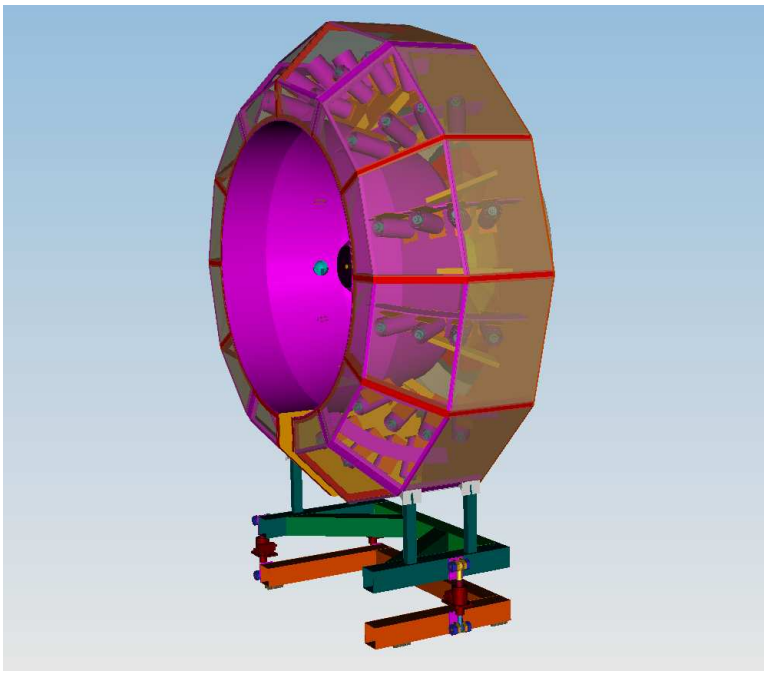

Figure 10.11: CLAS12 HTCC on its installation cart.

10.5.3 Polarized Target Cart

The polarized target will have a cart similar to the Frost target that was designed and built for CLAS. Fig. 10.12 shows a schematic diagram showing the polarized target assembly on its installation cart.

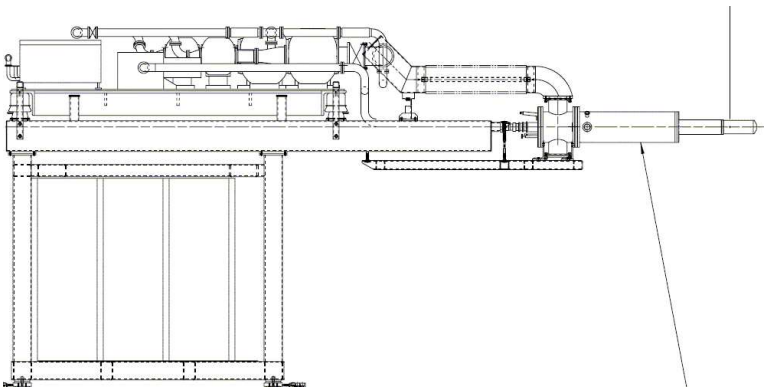

Figure 10.12: Schematic of the polarized target assembly on its installation cart.

10.6 Utilities

10.6.1 Cryogenic Distribution Can and U-tubes

The cryogenic distribution can will be installed in the same location as the CLAS torus service module. The supply transfer line will need no modifications. The new can will have 3 sets of 4 K bayonets, 1 set of 15 K bayonets, and 3 sets of liquid-nitrogen bayonets. Fig. 10.13 shows the planned cryogenic cooling distribution schematic.

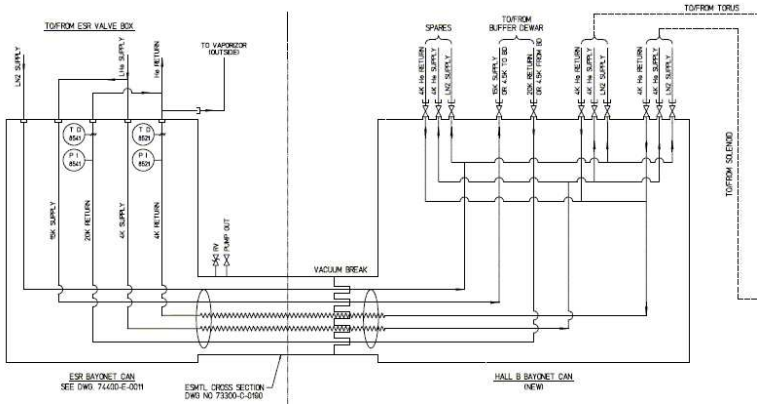

Figure 10.13: Cryogenic cooling distribution schematic.

10.6.2 HVAC Cooling Power

Hall B uses a chilled-water cooling system for meeting the HVAC load requirements. The present system has four compressors, and during normal operations, the load varies such that only 2 or 3 are needed. The upgraded CLAS12 will have more electronics.

10.6.3 LCW

No change in the system will be necessary to accommodate the Hall B loads. Some minor plumbing will be necessary to connect the new magnet power supplies.

10.6.4 Electrical Service

No capacity increase in the electrical service that exists for CLAS will be required for CLAS12. Only minor circuit installation and relocation is currently expected.

10.6.5 SVT and IC Cooling

The SVT and IC detectors will each have a small chiller system installed to remove heat from the electronics.

10.6.6 Cable Trays

Significant cable tray work will be necessary for CLAS12. Most of this will be the cables for the three regions of drift chambers.

10.7 Survey

JLab has a survey and alignment group that provides services lab-wide. Their tooling includes two Faro Laser Tracking Tools, models SI and X. These are used for alignment and to make *as found* measurements of systems throughout JLab. All detectors and beam line devices are fiducialized prior to being installed into the accelerator or one of the Halls. Depending on the design of the alignment system, large detectors can be aligned to accuracies better than 200 μm and knowledge of the location can be ascertained to 50 μm when necessary. Each detector will have tooling ball mounts that are used to facilitate both the fiducialization and alignment. Support connections will be designed to allow precise alignment for detectors where this type of alignment is critical, e.g. the drift chambers and targets. For other detectors such as the LTCC, FTOF, and PCAL, where alignment is not critical, much less precise systems will be used.

10.8 Safety

All persons that will work on CLAS12 detectors on site will receive job specific training. ISM (integrated safety management) principles will be used. Resources from the EHS&Q division will be brought to bear to help developing any new procedures that are not documented in the EHS&Q manual. Specific fabrication and installation procedures will be developed for each detector system by the lead engineers and physicists. All lifting devices will be load tested prior to use and specific lift plans will be developed. The determination of what lifts will be done by who will be done by a rigger with Master Rigger Qualification.

Chapter 11

Offline Software

11.1 Introduction

The goal of the offline software is to provide tools to the collaboration that allow design, simulation, and data analysis to proceed in an efficient, repeatable, and understandable way. The process should be set up to minimize errors and to allow cross-checks of results. As much as possible, software-engineering related details should be hidden from collaborators, allowing them to concentrate on the physical processes and experimental effects they are studying. If the process is efficient in terms of time invested by the experimenter, it will likely be efficient in terms of resource use (CPU, storage, network) as well. Also, when the time invested is minimized, it allows the process to be repeated with variations in assumptions or parameters. These repeated investigations result in more robust scientific results.

Our hope is that by encouraging communication of ideas with multiple discussion formats (meetings with remote access, email lists, websites, wikis), we can make most major design decisions as a collaboration and avoid unnecessary repetition of effort. We see consensus decision making and good documentation as keys to achieving this goal.

Large-scale computing efforts are common in nuclear and high-energy physics, and there are several standard components in all of them. High-bandwidth data acquisition and network capability, mass storage, sophisticated reconstruction algorithms leading to high CPU requirements, data volume reduction schemes, generic and experiment-specific software analysis tools, detailed simulation software, and calibration and run parameter management, are all areas that need to be addressed. In this section we present our ideas on the aspects of

the problem directly related to software development. There is a separate effort at JLab to characterize and cost the hardware computing infrastructure necessary to support the entire JLab 12-GeV program.

The `CLAS12` software system is being developed around a *Service-Oriented Architecture* over a distributed network. Details of the architecture will be given in the following sections. Core functions of reconstruction, simulation, and analysis are packaged into discrete units or *services*, distributed over a network, and loosely coupled and combined to develop analysis applications. Communication is achieved by passing data between services, and coordinated through a central process.

Within the high-energy and nuclear physics community, there is currently an expanding suite of services globally available. The *OpenScienceGrid* (OSG) project [329] is a consortium of about 80 National Laboratories, Universities, and Institutions working together to provide a national computing infrastructure for science. The consortium is funded by the National Science Foundation and the U.S. Department of Energy's Office of Science. An example of distributed computing over the OSG is given by Fermilab's D0 experiment [330]. Another example is the *Large Hadron Collider (LHC) Computing Grid Project* [331, 332], being developed for the various LHC experiments.

11.2 Service-Oriented Architecture

A software service is a specialized application with these primary characteristics:

- It does one task or a small set of closely related tasks extremely well;
- It is reliably available over a network, either the internet or an intranet;
- It has an interface that utilizes standard data exchange, often (but not limited to) documents formatted using the Extensible Markup Language (XML);
- The description of the interface is also available on the network and through a URL. This description, typically an XML document, is viewed as a contract. Enhancements to the service might extend the contract, but they should not summarily deprecate an existing interface.

An architecture developed using services is called a Service-Oriented Architecture (SOA). Complex applications, usually called *clients*, are built by piping services together. A given SOA will support any number of clients. The transport might be the standard in industry, based on the Simple Object Access Protocol (SOAP), or it may be based on a more specialized messaging system, such as the Java Messaging Service (JMS).

The potential advantages of an SOA include:

- **Modularity**. While modularity has been a buzz-word for software developers for decades, it is clear that SOAs elevate the concept beyond what has been achieved up to now. While individual applications have been developed that are modular, what is meant in that case is that blocks of the code that are linked into the final executable are replaceable with no effect on the bulk of the application. Nevertheless, such modules generally require a shared object model and binary compatibility. Services require neither. The modularity achieved by services in an SOA extends beyond functional decomposition. Services require no object model or binary compatibility, since all the interaction occurs through implementation agnostic interfaces.

- **Shared Code**. Services are necessarily shared, common resources. A service to extract detector geometry will perform the same function, in the same way, for all clients. While correctness is not guaranteed, consistency is.

- **Interoperability**. Related to the high level of modularity, inter-operability refers to the fact that services can be written (in principle) in any language and run on any machine. Additional inter-operability is achieved by providing well-tested legacy codes with a communication layer (a wrapper) that talks to the service backbone. In this manner, old code can be used without expensive refactoring.

- **Maintainability**. Smaller code modules, as opposed to huge monolithic applications, are manifestly easier to maintain. They also are more robust against the loss of a primary developer to retirement or another job. It is far easier to dig into a thousand line service than a hundred thousand line application.

- **Deployment**. In an SOA, services and clients are replaced, often (though not necessarily) without announcement. That is because, as mentioned, the exposed interface is

viewed as inviolate contract, but the implementation is not. Changing a service implementation does not require a code redistribution or a recompilation on the part of any other code.

- **Loose Coupling**. This advantage refers to the fact that clients are unaware of the implementation details of the service. As such, the chance of unintended consequences resulting from tight coupling (shared access to memory and objects) is effectively eliminated. Interaction is not through shared objects or memory, but only through interfaces. It is vital, in an SOA, that only interfaces are exposed to the clients. Furthermore, these interfaces exchange atomic data by value, not reference.

- **Extensibility** SOAs are extensible in a unique way: once a useful set of services is provided, developers can create applications that are unanticipated by the service architects. Indeed, the unanticipated application is considered a litmus test of a successful SOA. In the `CLAS12` physics environment, we will create basic services with the goal of providing what is necessary for analysis, visualization, and simulation as we see it today, but those same services might be combined more effectively than we imagine.

There are several potential disadvantages of SOAs. For example, communicating using XML or with a messaging system is platform agnostic only when exchanging ASCII (or Unicode) data. Encoding binary data in Unicode is potentially time consuming and bandwidth intensive. To mitigate this problem, the architecture should, in certain cases, ship metadata instead of large amounts of binary data. That is, it should transmit a description of or instructions for accessing large data files rather than the data itself.

While almost all modern computer languages readily adapt to life in an SOA, FORTRAN is the one language that is problematic. For example, the state of the art in FORTRAN XML parsers is lagging behind other languages. How much legacy and new FORTRAN code will be written for `CLAS12` is an open question. Nevertheless, the software group will have to provide extra support for incorporating FORTRAN services and especially clients.

The Service-Oriented Architecture has reached maturity in industry and government. Many successful commercial applications, such as Amazon, are built on publicly accessible services. Many government agencies, such as the Department of Defense, have been pushing their contractors to modify legacy codes to live in a service-oriented environment. The `CLAS12`

software group is confident that we can leverage and adapt what has already been proven in the commercial and government realms for the software needs of the CLAS12 collaboration.

11.3 CLaRa

11.3.1 Introduction

The goal of the ClaRa project is to develop a framework that can be applied to a wide range of physics data processing applications for the CLAS12 experiments. The framework shall cover all stages of the physics data processing, including physics and detector simulation, high-level software triggers, reconstruction programs, physics analysis programs, visualization, etc.. A schematic overview of the ClaRa framework is shown in Fig. 11.1.

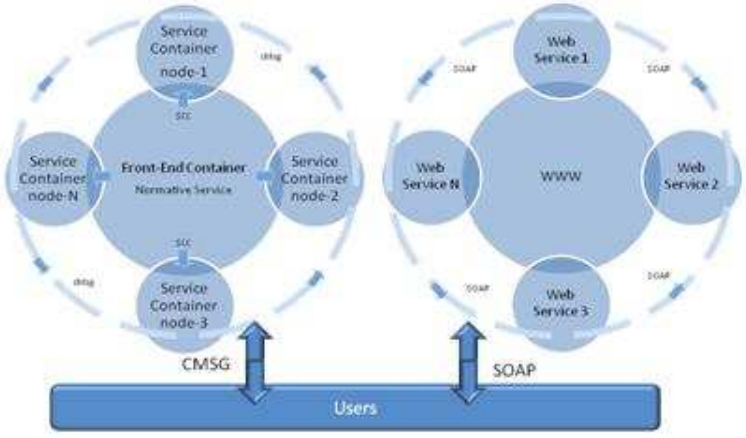

Figure 11.1: ClaRa network distributed service platform. SCC: Service Communication Channel. cMsg: Publish-Subscribe messaging protocol. SOAP: Simple object access protocol.

11.3.2 The Problem Statement

Physics data processing application development is a collaborative process. On one hand, it involves computer scientists developing framework and basic software components, while on the other hand, it calls for physicists to develop and implement the specific algorithms needed for simulation, reconstruction, calibration, etc. In addition, there will also be a physicist developing the data analysis programs to produce the final physics results. The quality of the physics results depends on the number of end-user physicists that are performing and/or cross-

checking the physics data processing stages. The unprecedented scale and complexity of the physics computing environment requires substantial software engineering skills from the end-user physicist. As a result, we have a reduced number of qualified data processing physicists, resulting in a poor physics outcome. The CLAS12 computing environment must keep up with fast-growing computing technologies. Taking into account the long lifetime of the physics data processing applications, we must organize software in a way that permits including or discarding some of the software technologies in an easy way, without major reorganization and/or redesign.

Physics Data Processing Environment

We have categorized three groups of people working with the framework. This categorization is not intended to be exclusive and it is a categorization of interaction rather than of people, since many people will belong to several groups.

- **A. Framework developers:** These people are responsible for the design, implementation, and maintenance of the framework itself.
- **B. Physics application software developers:** This group of people will be required to have strong computing skills and more knowledge of the framework than what is required by the average physicist user.
- **C. Framework users:** These people are primarily interested in getting physics results. Using human machine interfaces they compose desired physics data processing applications and produce histograms, statistical distributions, etc.

Our goal is to widen group C and make this group less dependent on the support of the A and B groups.

Design Requirements

- The framework shall be simple to use and easy to learn.
- The framework should be customizable to be able to adapt to the different data processing tasks.

- The framework shall provide context-sensitive help and assistance, with many real-world physics data processing application examples.
- The framework shall provide ready-to-use modules, encapsulating essential functionalities of the physics data processing system.
- The modules shall be reusable and easily replaceable.
- Physics data processing application design and implementation shall require a few or no programming skills.
- Neither a specific computing environment nor compiling shall be necessary to build and run physics data processing applications.
- The framework shall provide a graphical environment for physics data processing application development.
- The framework shall be network distributed and shall have temporal continuity.
- The new system shall provide web access to the framework for remote configuration and execution of the data processing applications. The necessary security considerations must be addressed.

11.3.3 SOA

ClaRa identifies the physics data processing application as a composite application. A composite application is an application that is both assembled and orchestrated. An assembly is a process of combining together many different pieces into a workable unit, and an orchestration is making sure that those pieces work together collaboratively with one another to solve the given problem in a given scenario. Composite applications are known to be more efficient, robust, and flexible. Composites of the software application known as software services are more specialized, easily maintainable, and easily replaceable and modifiable. Therefore software applications, composed of software services are extremely flexible, robust, and adaptable to address different data processing needs. The SOA provides the foundation for creating, deploying, maintaining, and governing the software services. The ClaRa framework is the implementation of the SOA architecture.

Design Strategies

The ClaRa framework provides guidelines, policies, and approaches for how physics data processing services are designed, deployed, and managed. ClaRa services communicate with each other through message passing. The framework supports two distinct messaging protocols and transports: cMsg over TCP/IP and SOAP over HTTP. The services, using cMsg proprietary publish-subscribe messaging protocol are designed to compose performance critical applications, and do not require special security considerations.

Classification of the Services

ClaRa design guidelines are based on adopted design strategic decisions. In order to optimize service communications and service clustering, ClaRa suggests separation between algorithm and data services. For example *cluster finder* is an example of the algorithmic service and *hits in the calorimeter* is a data service. ClaRa further categorizes data services into three categories: event, detector, and statistical data services. Also standard data exchange format is used between services. EVIO data format is used for data exchange between services. ClaRa supports flexible segmentation of the data processing application. In the very coarse level of segmentation, a service is not different then a large monolithic software application. In this case the ClaRa framework plays the role of a process manager and controller. Fig. 11.2 illustrates an example of a tracking application service composition.

Performance Measurements

Integration and coordination in real-time data and information from network-distributed services will clearly carry performance penalties. It is also obvious that poor decomposition of the physics data processing application in terms of granularity can largely affect composed application performance.

11.3.4 Web Services

ClaRa web services are developed using J2EE (Java Enterprise Edition) JAX WS 2.0. Currently all the ClaRa cMsg services written in Java are also deployed as a ClaRa Web Service. The ClaRa Web Services platform makes `CLAS12` services programmatically accessible over standard Internet protocols.

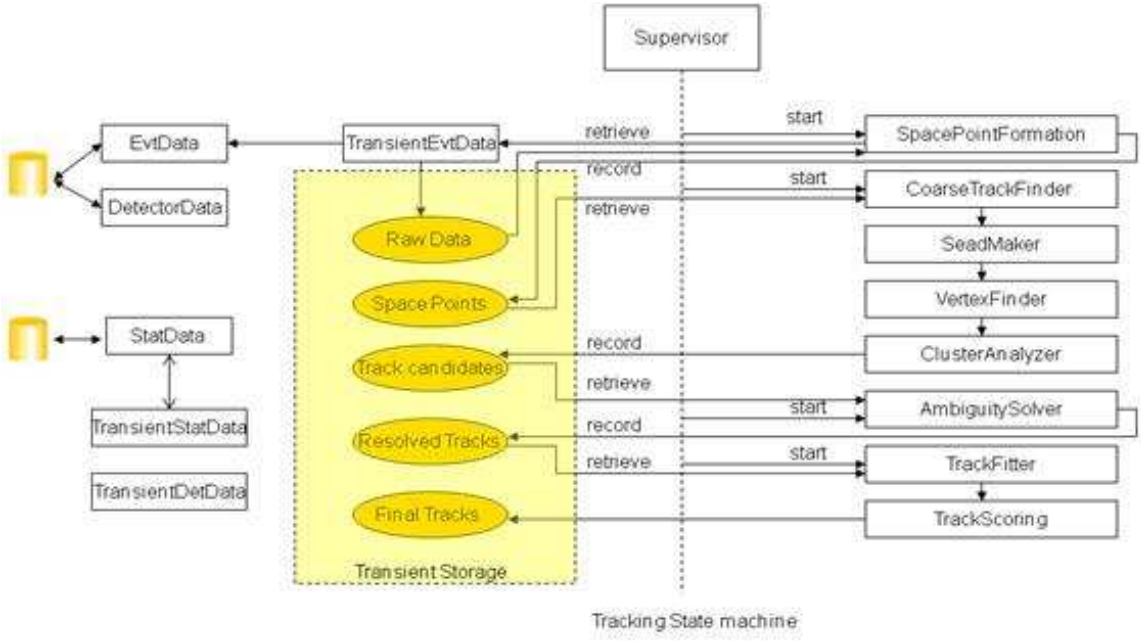

Figure 11.2: Service decomposition of a hypothetical tracking application. Ovals represent in-memory data storage and rectangles represent services. Supervisor is the service that orchestrates the tracking application.

11.4 Services

11.4.1 Authentication

Services, by their nature, are accessible to remote clients. While the ultimate security policy for `CLAS12` has not been addressed, the software group recognizes that some form of user authentication will be required. The authentication service will allow other services to ask whether or not a given user is authorized to receive the information requested.

There are number of ways to implement such a service, including some powerful but platform-specific solutions, such as the authentication suite provided by Microsoft .NET. Again, the loose coupling provide by a Service-Oriented Architecture allows us to define the authentication interface contract even before we decide on an implementation, and it allows us to replace implementations to meet growing needs to address unforeseen security concerns.

So we plan to start with an authentication service that will accept a username and password, and return an integer value for the user's access level. (We may only ever need a no access/full access determination.) The first implementation of the service will just return a

value indicating full access for all requests. That will allow other services to build in their authentication request. From there we will move to an actual implantation, perhaps one using an LDAP or MySQL server that stores username, passwords, and access levels. That may prove sufficient, but if not, we can always migrate to an even more secure authentication scheme without breaking the framework.

11.4.2 Detector Geometry

The geometry service is an example of the Detector Data Service. This is the front-end of the `CLAS12` geometry data, encapsulating data access and data management details from the service consumers. All the ClaRa algorithm services, including simulation, reconstruction, alignment, etc., access the geometry service using standard service communication protocols, provided by the framework. Currently geometry information is stored in the MySQL database, but in the future we might consider changing the geometry data storage technology (for example XML), however all of this will be fully transparent to the geometry service consumers.

11.4.3 Event Display

The single event display in the `CLAS12` framework will be both a service consumer (a client) and a service provider. Implementing the event display as a service consumer provides all the benefits discussed in the section on Service-Oriented Architecture. Additionally, it allows us to use the thin-client model favored by modern software architects. Thin clients, sometimes called smart clients, split their application code between data models and processing, performed as much as possible in a different thread, process or CPU, and visualization. This shrinks the pure visualization code, allowing it to be deployed remotely or updated frequently without incurring a huge download penalty. The most familiar and successful model is probably Google Earth. A thin client is downloaded and runs quickly, but complicated imagery processing is performed remotely.

A Service-Oriented Architecture is one way to implement thin clients. As much as possible, without hampering performance, no visualization processing, such as acquiring detector geometry, is performed by a service and the thin client obtains the geometry by sending a request.

In the case of the event display (see Fig. 11.3), the client will use a variety of services, such

as geometry, magnetic field, event streaming, file system access, run metadata, and analysis. It will also be a service provider through a display service. One service it will provide will include simple pictures of random online events so that remote users, for diagnostic purposes, can see pictures of recent events. Another more sophisticated service will be to answer a request for an image of a specific event viewed in a certain way, such as zoomed in on Region 1 in Sector 3.

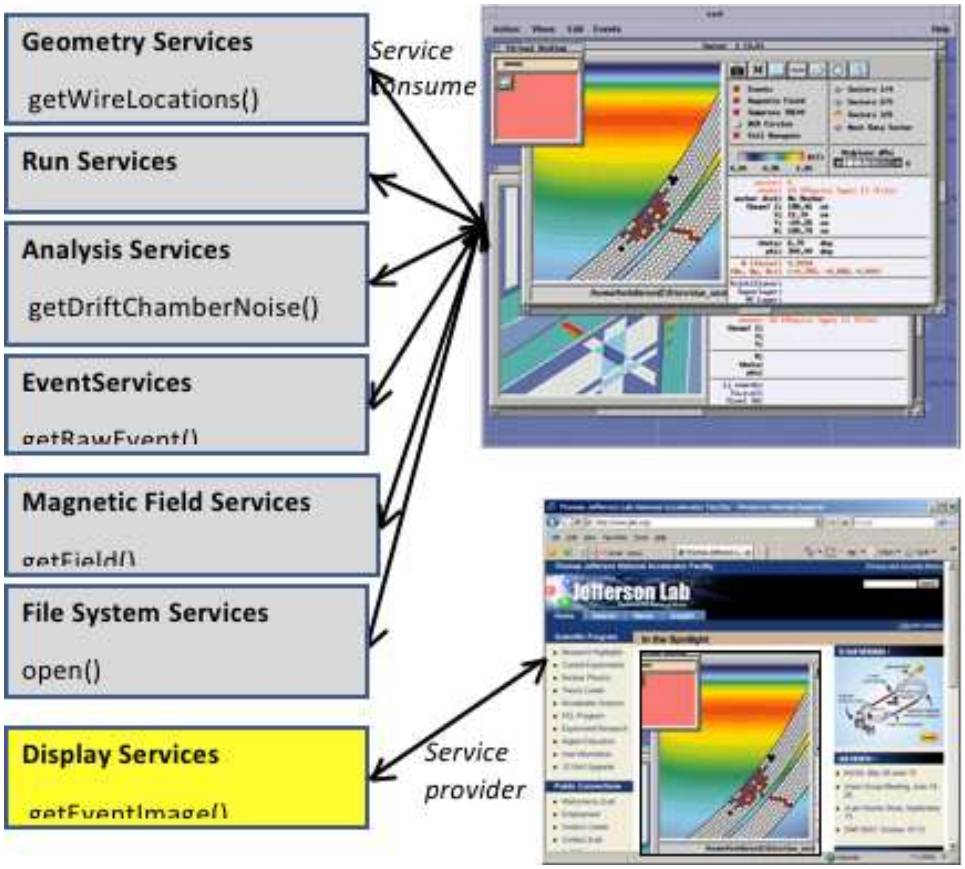

Figure 11.3: The event display will consume a number of `CLAS12` services. It will also provide a display service.

Another feature of the event display is that it will employ a plug-in architecture based on the reflection capabilities of the JAVA language. This will provide a simple yet powerful extendibility feature for users who would like to use the event display to visualize and debug their new analysis and simulation code. Reflection is a way that JAVA applications can examine all the classes in their path. The event display will look for all classes that inherit from a specific abstract base class. Once found, the application will create an object from that class and then provide a set of services for the object, such as notifying it that a new

event has arrived.

In this scheme, neither recompilation or even restart of the event display is required. The developer extending the event display creates the class, drops it into the path, and the class will be plugged-in to the application. If the plug-in proves of general use, it can be placed in the path of the shared event display (e.g., the run in the counting house) and all users will have access. However, if it is found to be an undesirable feature, the class file can simply be deleted. All of this adding and removing of features will occur with no changes to the code or recompilation of the base event display.

11.4.4 Data and Algorithm Services

In addition to our purpose to produce a Service-Oriented Architecture based design, we have decided to separate data services from algorithm services. An algorithm service, in general, will accept and process an output data object from a data service and will then produce a new data object.

Basic Types of Data Services

One of our main design choices is to separate data services dealing with the data objects that are resident on the disk from the data services that manipulate the data objects in memory. An objective that we would like to achieve is to make algorithm services independent of the technology we use for data object persistency. This will allow replacing outdated persistency technology in the future without affecting user-produced algorithm services. By separating persistent and transient data services we also hope to achieve a higher level of optimization by targeting inherently different optimization criteria for persistent and transient data storages. For example, regarding the data objects on the disk, one should invest more effort to optimize I/O performance, data size, avoid multiple I/O requests, etc. On the other hand, for the transient data in the memory, we should achieve highly optimized execution performance, APIs, and usage simplicity.

We foresee three major categories of data objects:

- Event data, such as raw data, simulated data, reconstructed data, etc.
- Detector data, describing a detector apparatus in order to interpret the event data.

Examples of the detector data are geometry data, calibration data, alignment data, slow controls data, etc.

- Statistical data (histograms, n-tuples, etc.)

Specific data services are provided for each of these data categories (see Fig. 11.4).

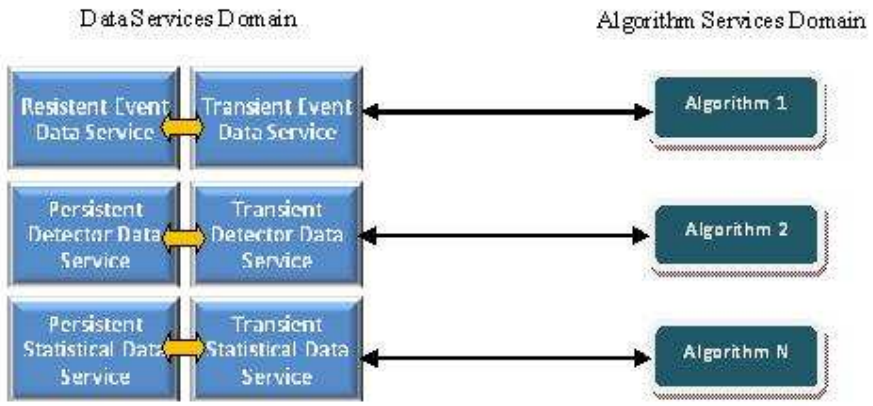

Figure 11.4: Different data services in the ClaRa framework. Algorithm services deal with transient data services only.

11.4.5 Magnetic Field

The magnetic field service is implemented in c++ with extensive use of the standard library's map construct. The entire field map is divided into individual maps corresponding to various magnets such as the solenoid and main torus. In addition, it has methods to get the magnetic field at a certain point, check for consistency within the map, and interpolate values inside the defined grid spacing.

Each map can be tailored to the field it holds. For instance, the main torus is defined in cylindrical coordinates, with $\phi \in [0, \frac{\pi}{6}]$. The class holding the main torus map then has an algorithm to calculate the field at any point $\phi \in [0, 2\pi]$. However, this is only good for ideal fields. For measured fields, the class can be easily extended to handle a case where the field is known precisely in the entire region. Furthermore, the dimensions and coordinates of the map's position and field need not be same. Inside the solenoid field for instance, the position is stored in (r,ϕ), while the magnetic field is stored in $(x,\ y,\ z)$.

A separate *mother* class is responsible for loading in and storing the maps from a database or file. This class is aware of the volumes of the individual maps and sums the fields where appropriate.

The final layer on this system is the magnetic field ClaRa service. This is where the mother class is initialized and held in memory. Several mother classes can be held; i.e. one for the ideal fields, one for the measured fields, and one mix of these two. The service registers itself with the ClaRa system and can provide the various field maps in several formats depending on the consumer's preference. As an example, the service can be polled for an entire map or for an individual position.

11.5 Simulation

There are two different, though overlapping, areas in our current simulation effort. One is focused on validating design decisions for the upgraded detector, the other on building a modern simulation system that can be used for the life of the `CLAS12` program. The former has two components: (1) a parametric Monte Carlo that can estimate the resolution for charged particle tracking and (2) a full GEANT3 system that depends on the code base that has been developed for the current `CLAS` detector, modified to reflect the new design, including reconstruction. The latter is an entirely new GEANT4-based, object-oriented design.

11.5.1 Parametric Monte Carlo

One of the fundamental algorithmic challenges in the design of `CLAS12` is the problem of track reconstruction in a non-uniform magnetic field. Not only does the torus produce an inhomogeneous field in the tracking volume, but charged particles emerging from the solenoid must be tracked as they traverse the fringe field of that magnet. Since no analytic form for the particle trajectories exist, they must be calculated by "swimming" the particles numerically through a map of the magnetic field. Track fitting then becomes very expensive in terms of CPU time. One way to finesse the problem is to linearize it by parameterizing the trajectory as small deviations from a reference trajectory. The reference trajectory must come from a "swim", but subsequent "trial" trajectories, with different starting parameters (momentum, direction), can be computed by a simple matrix inversion. Position resolution is put in at a set of idealized detector planes. It is also possible to incorporate multiple Coulomb scattering

in this model. This technique has already been used to estimate momentum resolution for CLAS12. Results appear in other sections of this document. The method cannot give information on some things, such as the effect of accidentals, track reconstruction efficiency or confusion due to overlapping tracks.

11.5.2 CLAS Software with the CLAS12 Geometry

The current CLAS system consists of over half a million lines of FORTRAN, c, and c++ code contained in about 2,500 source code files. It represents a large investment by the CLAS collaboration over many years. CLAS, with its toroidal magnetic field, also presents the difficulty of tracking in an inhomogeneous field and that problem has been solved in this body of code. Recently, the geometry of crucial detector elements was changed to reflect the CLAS12 design, both in simulation and in reconstruction. The resulting system can now do a full GEANT3-based simulation and reconstruction of CLAS12 events, in particular charged particle tracking in the forward drift chambers. Studies using this system have been carried out to verify momentum resolution results from the parametric Monte Carlo and to estimate the effect of accidental Møller scattering background on track reconstruction. More of the details of the detector subsystems and beam line components of the upgraded configuration are being added to extend the range of these and similar studies.

11.5.3 GEANT4 Object-Oriented Detector Simulation

The GEANT4 simulation software for CLAS12 is called gemc (GEant4 MonteCarlo). The parameters that define the simulation (i.e. geometry, sensitivity, magnetic fields, output banks, etc.) are stored in an external database and used at run-time in STL (c++ Standard Template Library) objects. The database currently in use is the MySQL database. Other options (e.g. XML) are also available for consideration.

Geometry

The GEANT4 volumes are defined as follows:

- Shapes, dimensions. Boolean operations of shapes.
- Material, Magnetic Field, Visual attributes, Identity, Sensitivity and Hit Process.

- Placement(s) in space: position, rotation, copy number.

These parameters are stored in MySQL tables, one table per detector (i.e. HTCC, EC, DC, etc.). At run time, gemc reads an XML file that specifies which detector to include in the simulation, including possible tilts and displacements from the original positions.

CLAS12 Geometry Implementation

Particular attention is paid in reproducing in gemc the design of each detector with as much accuracy and as many details as reasonably achievable. In Fig. 11.5 the SVT GEANT4 representation is shown, while in Fig. 11.6 is shown the GEANT4 implementation of the various central detectors.

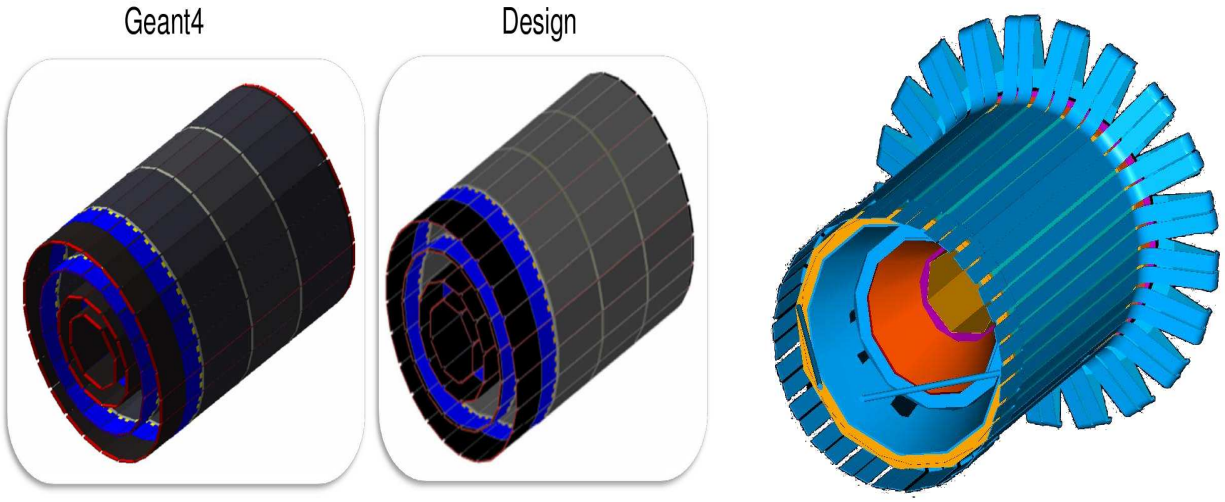

Figure 11.5: The Silicon Vertex Tracker in GEANT4. (Left) The gemc BST, (middle) the CAD model BST, and (right) the complete gemc implementation of the BST+FST.

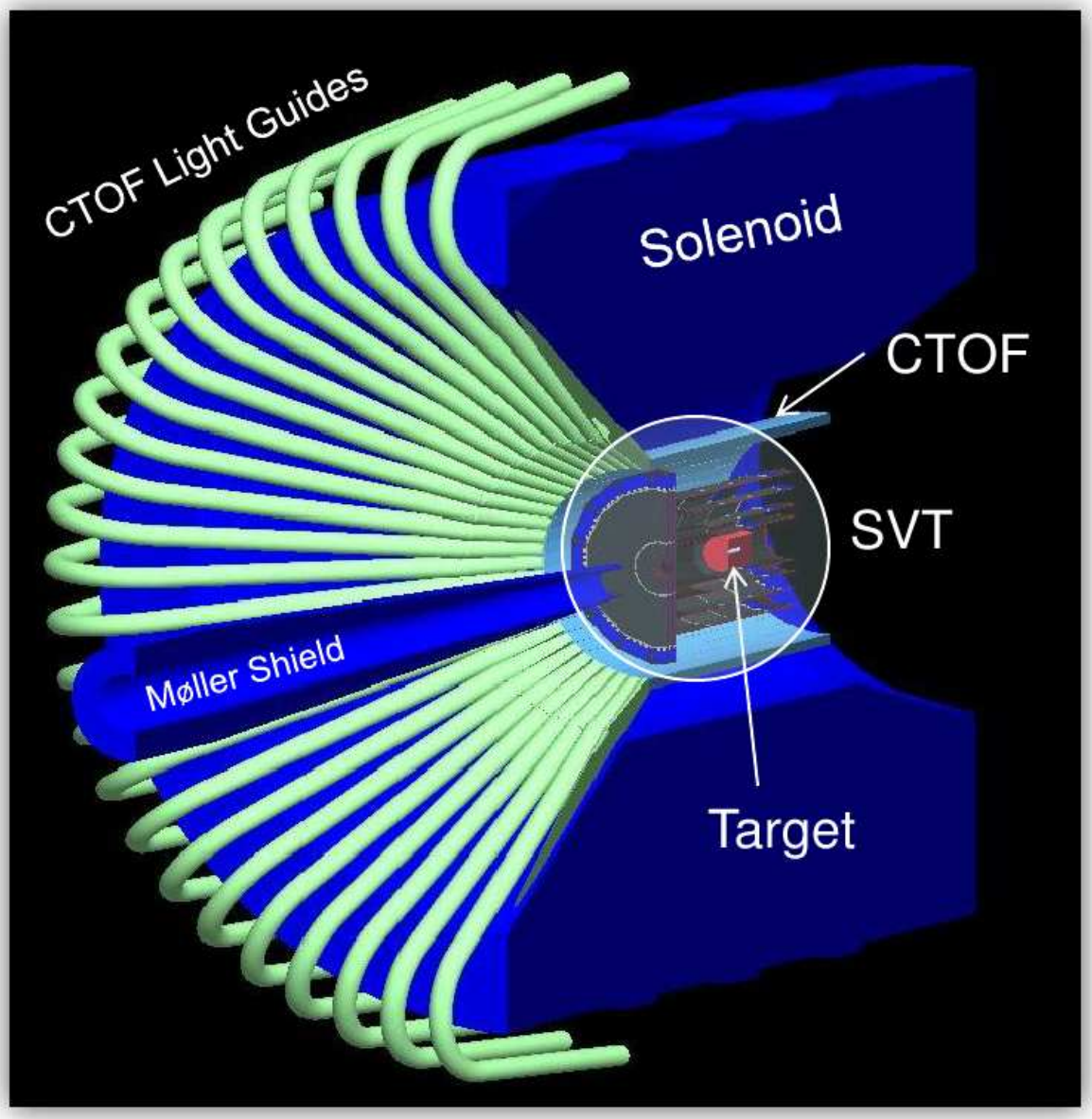

Figure 11.6: The CLAS12 Central Detector. The target (white) is at the CLAS12 center, surrounded by the SVT (which includes both the BST and FST) (red). The CTOF paddles (cyan) are connected to light guides (light green) that wrap around the solenoid (blue). The Møller shield is also visible (blue).

Generator

In `gemc` there are two ways to define the primary generator:

1) `gemc internal generator`: with this method the user defines the primary particle type, momentum range, and vertex range.

2) `external input file`: with this method the user defines the format of the input file and the file name.

The various file formats are registered in `gemc` by a *factory method*, which allows derivation of new formats from the `gemc` c++ pure virtual methods defined for the input, and to choose the desired format at run-time.

In addition to the primary particles, an additional *luminosity beam* can be defined to add realistic backgrounds to the simulation. The user defines the beam particle type, the number of beam particles per event, and the time structure of the beam.

Hit Definition

The `gemc` hit definition is illustrated in Fig. 11.7. A `Time Window` (TW) is associated with each sensitive detector. In the same detector element, tracks within the TW constitute one hit, while tracks separated in time by more than the TW form two separate hits.

Hit Process Factory

Each detector has a custom Hit Process Routine (HPR) associated with it. The `gemc` HPR pure virtual method is used to derive all the detector routines, and all HPRs are registered at run-time by a factory method.

The input to all HPRs is a `gemc hit`. This stores, for each step in the hit, the following information:

- Hit Position (global coordinates);
- Hit Position (relative to the volume in which the step occurs);
- Deposited energy;
- Time of the hit;

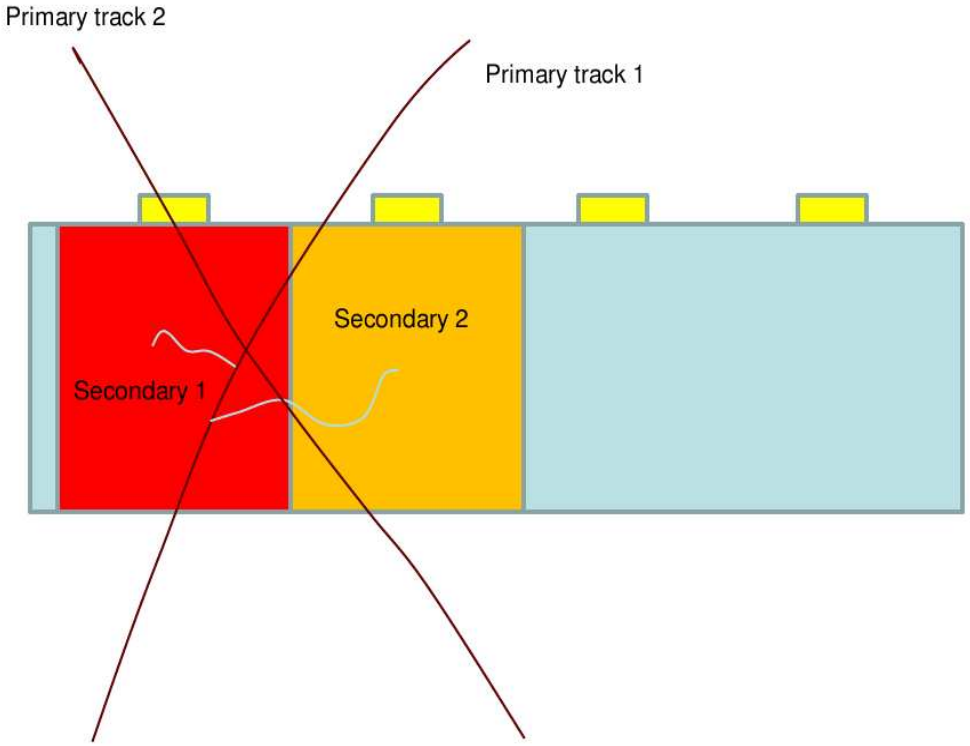

Figure 11.7: Hit definition illustration: In the picture two different detector elements are shown in different colors (red and orange). All tracks within the same TW and the same cell constitute one hit for that cell. If any track has enough time separation from an existing hit, it will form another, separate hit.

- Momentum of the track;
- Energy of the track;
- Primary vertex of track;
- Particle ID;
- G4Track ID;
- Identity;
- Detector hit;
- Mother particle ID;

- Mother G4Track ID;
- Mother primary vertex of track;
- Energy threshold of the sensitive detector.

Each HPR processes the `gemc` hit and produces STL vectors of double (raw information) and integers (digitized informations). Each vector corresponds to a MySQL entry in the bank table corresponding to the HPR.

Elements Identity

In order to correctly identify and process the correct detector element at run time, a class `identifier` is used. The following scenarios can happen:

1) For detectors where each element corresponds to a unique volume, the identifier remains unchanged.
2) For detectors where each element corresponds to a unique volume that is copied, the identifier copy number is determined at run time.
3) For detectors where different elements correspond to the same volume, the identifier is processed at run-time by the identifier method of the Hit Process Routines described above. For example, in the Drift Chamber implementation the single cells are not GEANT4 volumes (due to the fact that there are too many of them). The sensitive volumes are instead layers of gas. At run-time, the cell is identified by the HPR based on the track position in each layer.

Output

The file formats for the simulation output stream are registered in `gemc` by a factory method. New files types can be derived from the c++ pure virtual methods defined in `gemc`. The main registered formats, selectable at run-time, are:

- txt: readable from any editor or shell. Bank names, variables are printed out.

- EVIO: this is the format used by the CODA system, and unanimously chosen to be the default format for the output stream. Banks and variables are identified by integers (tag and num) defined in the MySQL tables.

The EVIO output can be viewed with the utility evio2xml, that outputs events in XML format.

Doxygen Documentation

The c++ code is documented with doxygen. The documentation can be found at:

`http://clasweb.jlab.org/clas12/gemc_doxygen`

11.5.4 The CLAS12 Fast Monte Carlo

Detailed detector simulation and reconstruction of physics events in CLAS12, based on GEANT4, is very CPU intensive and hence time consuming due to the high energy and multiplicity of the Monte-Carlo events and the complexity of the detectors. A dynamically configurable package for fast Monte-Carlo simulation and reconstruction (FASTMC) has been developed for CLAS12 to allow fast studies of effects of detector resolutions and acceptances on various samples of Monte-Carlo events. Each step of the chain – simulation and track reconstruction – has been replaced by modules that parameterize the acceptance and responses of the different detector components.

The FASTMC package uses a configuration file provided by the user, which has all relevant information, including the resolutions and acceptances for different particles and kinematics. The initial set of parameters was derived from calculations and are getting updated with new simulation studies from GEANT4 CLAS12 simulations. Sets of parameters were defined for the central and forward detectors of CLAS12 and for inbending (torus current positive, so electrons will bend in toward the beam axis) and outbending conditions. Two subroutines were called in the FASTMC package subsequently to provide information on acceptance, along with momentum and angular smearing of tracks in CLAS12.

CLAS12 Acceptance

The parameters defining the acceptance of events are listed in the configuration file. The computed acceptance of $ep \to e\pi X$ events is shown in Fig. 11.8.

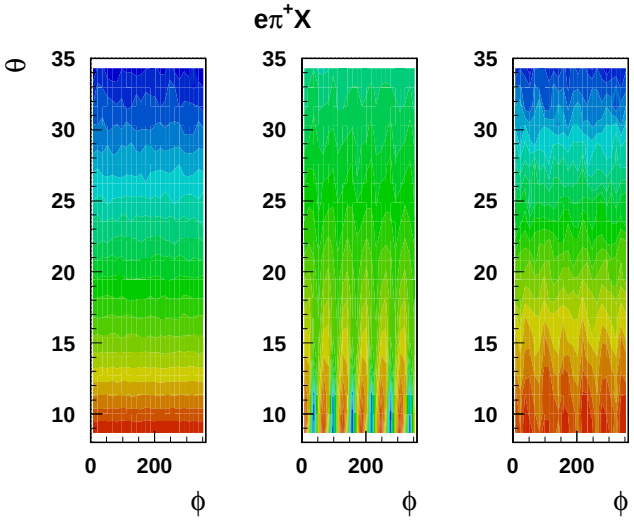

Figure 11.8: CLAS12 acceptances for generated DIS electrons (left), reconstructed electrons (center), and reconstructed π^+ (right).

11.5.5 CLAS12 Momentum and Angular Smearing

The parameters defining the smearing of particle angles and momenta are listed in the configuration file. The resolutions are calculated using simple parameterizations obtained from the GEANT4 simulation for momentum, polar, and azimuthal angles using:

$$\sigma_p = \frac{T_{max}}{T}\sqrt{(\sigma_1^p \cdot p)^2 + \left(\frac{\sigma_2^p}{\beta}\right)^2} \tag{11.1}$$

where,

$$\sigma^p_{[1/2]} = \sigma^1_{[1/2]} + \sigma^2_{[1/2]} \cdot \theta + \sigma^3_{[1/2]} \cdot \theta^2, \tag{11.2}$$

$$\sigma_\theta = \sqrt{\sigma^2_{1\theta} + (\sigma_{2\theta}/p/\beta)^2}\,\sin^2\theta, \tag{11.3}$$

$$\sigma_\phi = \sqrt{\sigma^2_{1\phi} + (\sigma_{2\phi}/p/\beta)^2}. \tag{11.4}$$

The smearing due to energy loss and multiple scattering of particles in the central detector is shown in Fig. 11.9.

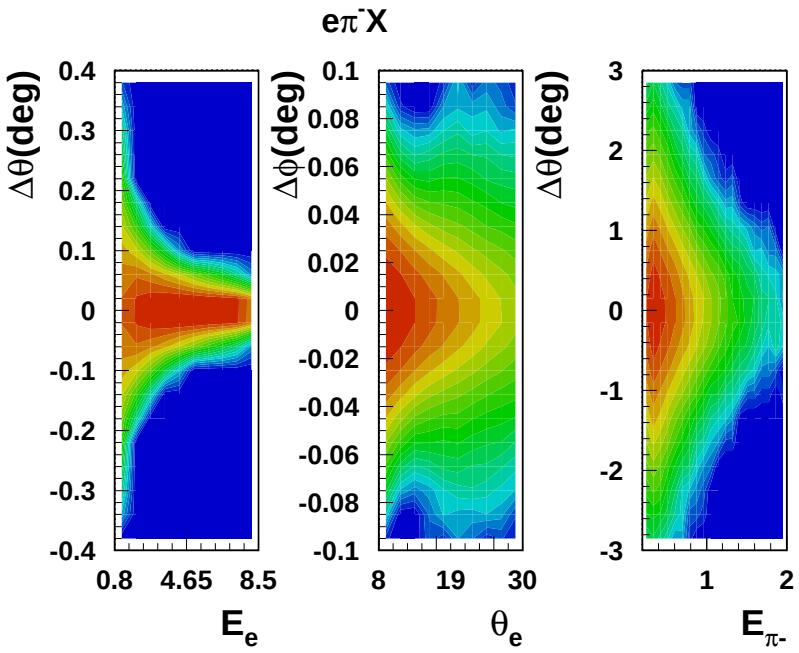

Figure 11.9: Resolutions of electron polar (left) and azimuthal (center) angles in the forward detector and π^- in the central detector (right).

FASTMC allows study of the effects of detector resolutions and smearing on various physics observables. The missing mass resolution of the reaction $ep \rightarrow e\pi X$ is shown in Fig. 11.10. The distribution of events from Λ and Σ decays as a function of the angle between planes containing the Λ and the K are shown in Fig. 11.11. Fig. 11.12 shows the W distribution for a two pion production reaction calculated from the electron momentum and using detected pions in the forward and central detectors.

11.6 Event Reconstruction

The main goal of the event reconstruction program is to provide track parameters and particle identification on an event basis, to any physics analysis. These events will in practice either come from real data or from the Monte Carlo simulation. The reconstruction program should also be able to perform specific tasks, like sending hits and corresponding fit results to the event display service. The program is currently developed in c, but will eventually be coded in c++, with an object oriented structure. Even if the tracking techniques (track finding

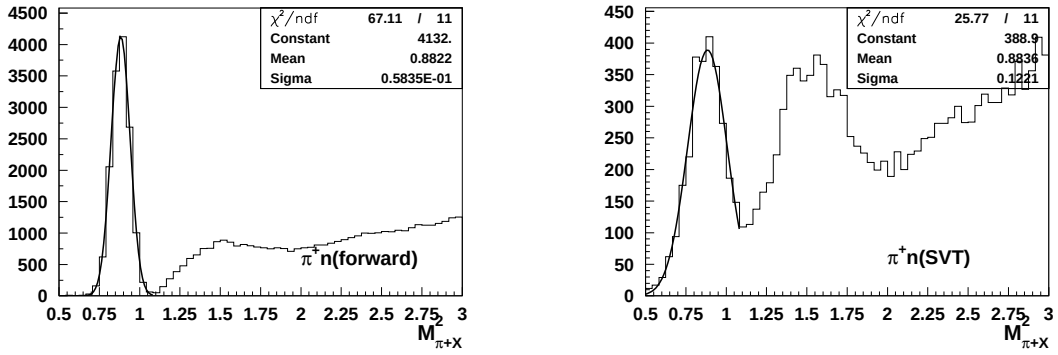

Figure 11.10: Missing mass resolution for $ep \to e'\pi X$ for forward (left) and large angle π^+ (right) events.

and track fitting) can be used in a detector-independent form, their implementation will be adapted to the geometry of the CLAS12 spectrometer, and therefore split in two parts:

Central Tracking: this part provides the reconstruction of particles detected in the Silicon Vertex Tracker, located inside the high magnetic field of the solenoid. Due to the approximate ϕ symmetry of this region, we implemented a Kalman Filter algorithm using cylindrical coordinates. A track finding procedure has also been developed to separate real tracks from the background.

Forward Tracking: particles produced at small angles are detected in two different subsystems, the Forward Vertex Tracker and the Drift Chambers. A key issue of the tracking program is to provide an algorithm that will efficiently match track segments found in these detectors, in the presence of background. As for the central part, we also implemented a Kalman Filter algorithm.

The last task of the tracking program will be to link tracks found in these two regions, that will include a vertex fitting algorithm, thus providing a full event reconstruction. Different outputs (not only the structure, but also the contents) will be produced, depending on the incoming request.

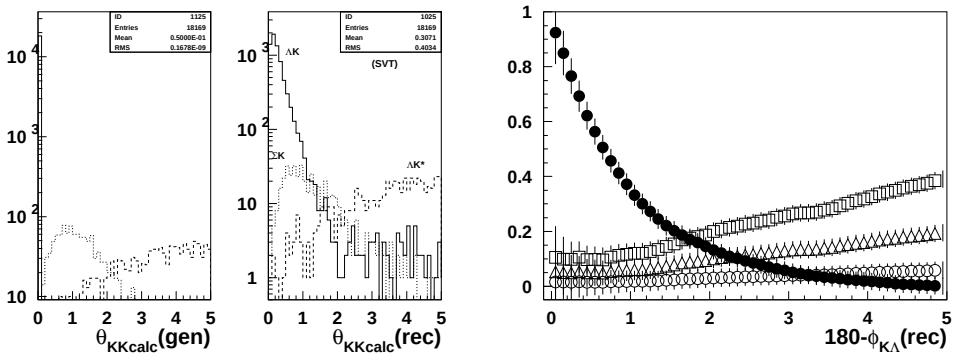

Figure 11.11: Angle between the Λ and the K for different processes for generated (left) and reconstructed (middle) distributions. The right panel shows the corresponding efficiencies (circles) as a function of a cut on that angle and the corresponding contamination (triangles).

11.7 On-Line Software

During the actual data-taking periods of CLAS12, it is of course expected that there will be full construction of a *significant* fraction of the acquired data. Such analysis insures that the data is of expected quality, and permits monitoring of the individual detectors from a different perspective than just hardware readout, such as wire profiles, ADC spectra, etc.. Experimenters should expect they should also be able to monitor the performance of the CLAS12 detector by examining the specific events and physics parameters under study. This capability will require *full* event reconstruction.

In addition, some reconstruction analysis can be utilized as a Level-3 trigger to filter unwanted events from the data stream, thus minimizing storage, bandwidth, and other precious resources.

The entire suite of services will be available to the online and data acquisition system, either directly as network available resources, or as shared code.

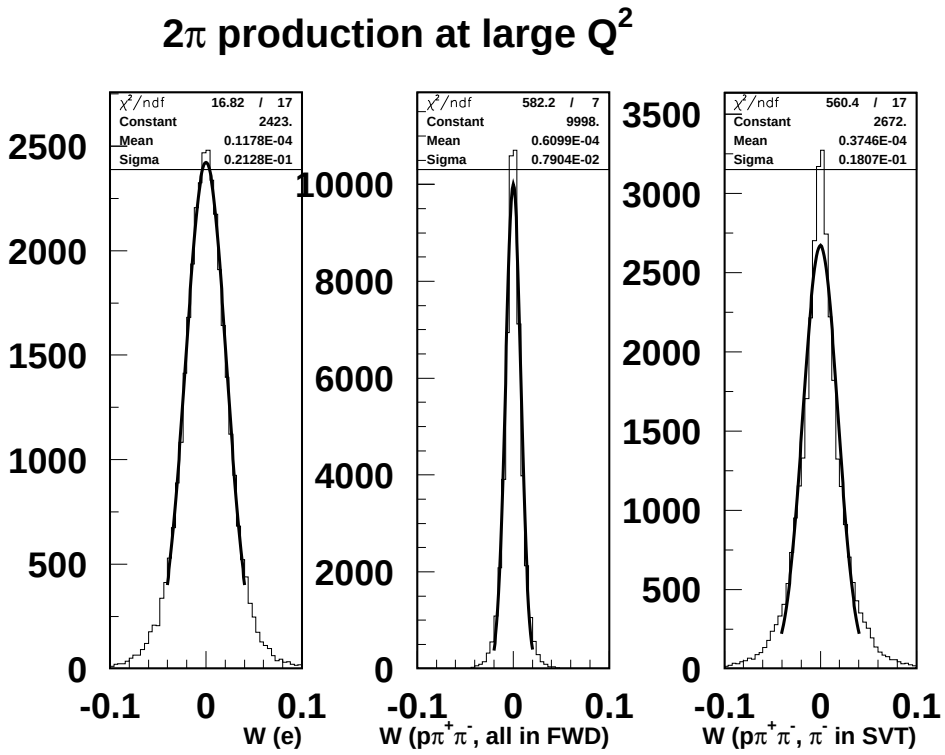

Figure 11.12: W distributions for exclusive two pion processes in CLAS12 from FASTMC. W computed from the electron (left), the detected pions in the forward detectors (middle), and the detected pions in the central detectors (right).

11.8 Code Development and Distribution

11.8.1 Code Management

For CLAS12, we have elected to use the widely adopted and free (open source) subversion revision control system. Subversion is the open source software community's replacement for cvs. It has many of the same features and employs the same no-lockout paradigm. (That is, conflicts are resolved through merging rather than avoided through code locks – the latter generally found to be too draconian and a hindrance to productivity.) In addition, subversion plug-ins are available for the popular integrated development environments, such as the widely used eclipse. This allows one to check in, check out, track changes, and merge differences with mouse-clicks in a development environment rather than through a command line.

In CLAS, all users, whether or not they were developers, accessed the repository, downloaded code, and built scripts. They then tried, with mixed results, to build the complex packages. We have abandoned that approach. In CLAS12, we have decided to implement a three-tiered code distribution system. The first level will be access to the subversion repository. Only developers will access code in this manner. The second level will be code releases, in the form of archives, and intelligent build scripts that do not rely on environment variables. In CLAS, the user wanting to use an application accessed the repository and downloaded the latest code, which may have included bugs checked in the night before. In CLAS12 the user will go to a web page and download a specific, tested released. A third tier of release, for limited systems (probably only for whatever Linux system JLab is supporting) is to distribute binaries. This in an area in which we expect and have already obtained substantive student involvement.

11.8.2 Code Release

The consensus in the software group is to base our software process on what is known in the software community as agile programming. Part of agile programming is a rapid release schedule based on development cycles called sprints. The exact frequency has not yet been determined, but the canonical sprint duration is one month: two weeks of development and two weeks of testing and bug fixing. So every month a new version of all software is released, typically with modest changes from the previous release. Functionality is to advance incrementally, as opposed to infrequent but massively different updates.

11.8.3 Software Tracking

The software group recognized that complicated software development is aided by requirements, task, and bug tracking. To this end, Christopher Newport University has deployed a web-based commercial package called Gemini for the CLAS12 effort. Gemini will allow us to enter projects corresponding to the main development efforts, such as gemc for the GEANT4 simulation. Then resources (developers) are assigned to the project. The time development will match the code release sprint cycles. For the next cycle, the new tasks will be entered, as well as the bugs that have to be fixed. Developers will enter estimates regarding the time it will take to complete the tasks and fix the bugs. Project managers can see if the estimated time fits with the cycle duration, if not they can adjust accordingly by postponing some tasks

or adding new tasks. Developers can log their time to a task or bug so as to develop better intuition for estimating. The subversion revision control system can be set up so that any code checked in must have a comment that ties it, by ID to a task or bug in Gemini.

11.9 Quality Assurance

The Service-Oriented Architecture is composed of many integrated services loosely connected. The usual interaction between the consumer of a service and the supplier of the service is not direct: generally there will be several processes and a network in between. As a result, during an extended development process, there becomes a strong possibility of errors invading the code, rendering it either unusable or incorrect. Quality assurance of developing projects then becomes a major concern.

The program being proposed is *extensive* suite checks to assure that every major release is thoroughly checked prior to being made available to the CLAS12 Collaboration. In addition, at any level the individual code developer will be able to check *any* version against the standard suite.

The suite of reconstruction standards will include three types of data. The first is *pure* simulation, that is Monte Carlo generated data through the CLAS12 detector *without* any detector resolution included. Reconstruction of this data set should return *exactly* what was input; any deviation is suspect and cause for special consideration. The next set of standard data will be a persistent Monte Carlo data set *with* full simulation, whose results should remain consistent with input parameters. Finally, varied sets of actual data, fully testing as completely as possible all aspects of the reconstruction software, will be utilized to track the code development. Of course, in all data types, performance in terms of compute resources and storage will also be tracked. Databases of performance results will be maintained as a service for comparison.

11.10 Computing Resources

Based primarily on experience from the 6 GeV CLAS computing usage, estimates have been made for computing resources required from 2012 through turn-on in 2015 and through the year 2017. These estimates are summarized in Table 11.1.

Year	2012	2013	2014	2015	2016	2017
Simulation						
CPU	5.7E4	5.7E4	5.7E4	5.7E4	5.7E4	5.7E4
Petabytes	2	5	7	5	5	5
DAQ						
Petabytes	0	0	0	2.2	2.4	2.5
Calibration						
CPU						
Reconstruction						
CPU	0	0	0	7.8E3	8.4E3	9.1E3
Petabytes	2	5	7	12	12	13

Table 11.1: `CLAS12` computing resources.

Chapter 12

Commissioning the Experimental Equipment

12.1 Checkout & Quality Assurance Before Detector Installation

12.1.1 Objectives

In general, the objectives of the CLAS12 detector checkout before beam is delivered to Hall B are to eliminate dysfunctional or weak components in the detector system that are instrumental for the overall operation of the individual detector systems and can be spotted without using the electron beam. This will include the following aspects of the detector systems.

After completion of the systems checkout without beam, the overall functioning of the CLAS12 components after installation will have been established.

- Checkout of the cable routing schemes of the signal readout without high voltages or low voltages applied to the detectors. For the drift chamber system, this will be carried out with digital signals injected channel-by-channel into the front-end electronics. Similarly, cable routing of the electromagnetic calorimeters (PCAL, EC), the forward and central time-of-flight (FTOF, CTOF) arrays, the Čerenkov counters (LTCC, HTCC), and the silicon vertex tracker (SVT), will be checked. This procedure will weed out false signal cablings and faulty signal connections.

- The high voltage (HV) system of the drift chambers will be tested by reading out electronic noise in the drift chambers when the high voltage has been applied. This will be done in a "self-triggering" mode, where the discriminator thresholds of the front-end electronics are set to sufficiently low values to allow electronics noise to pass the threshold. This procedure allows checking that all channels are properly supplied with the voltage required to operate the preamplifier and amplifier-discriminator boards (ADBs). Similarly, the HV distribution to the photomultiplier tube (PMT) based detectors (PCAL, EC, HTCC, LTCC, FTOF, CTOF) will be checked by turning the HV supplied to individual channels ON and OFF and observing the appearance and disappearance of noise and cosmic ray signals induced in the scintillators coupled to the PMTs.

- Low Voltage: The functionality of the low voltage (LV) distribution to the front-end electronics will be tested by turning the supplies to clusters of channels ON and OFF and observing the appearance and disappearance of related channels in the occupancy plots. This will be accomplished by using the `CLAS12` data acquisition system run in a free-running mode.

- Slow Controls: The slow controls procedures to adjust the critical parameters of the equipment will be checked out once the full system has been installed in the experimental hall. It will include checkout of all systems controlled by EPICS.

- Trigger and Data Acquisition: Part of the `CLAS12` online system (Trigger and DAQ), as well as the response of the new FTOF and PCAL detectors will be checked without using beam. Cosmic rays will be used to form a trigger from the existing EC and TOF scintillator arrays to determine the response of the new FTOF and PCAL detectors. This will allow a complete checkout and calibration of the two new detector systems that are part of the `CLAS12` forward detector system.

- Laser Calibration TOF: The forward TOF system will be instrumented with a laser-based calibration system. A fast laser pulse will be injected into the center of each TOF paddle, and the response of the scintillator measured at both ends. This allows rapid checkout of the functionality of all FTOF paddles, and will provide accurate timing calibration and time-walk corrections for the PMT-discriminator-TDC chain.

- PCAL, EC, and FTOF systems: Checkout and calibration will proceed with cosmic

rays. The three detector systems are supported together on the forward carriage. After mounting the three detector systems in one of the six sector, the detector packages can be conveniently tested together using cosmic rays. The procedure will be similar to what is currently using in CLAS for calibrating the EC and TOF systems. A trigger will be setup that uses the stereo readout of the inner and outer parts of the EC to form a trigger that selects cosmic rays pointing toward specific regions of the PCAL and FTOF. The analysis of such events allows a detailed mapping of the responses of these detectors across their entire active areas.

- Cosmic ray calibration of the drift chamber systems: The reconstruction efficiency of the DC system can be mapped out using a cosmic ray trigger made by a coincidence of two test scintillation counters oriented such as to sample tracks passing through the DC system and are oriented towards the target region. Efficiency of single DC layers (1 out of 36) or of a single superlayer (1 out of 6) can be mapped by excluding the layer (or superlayer) to be tested from the fit, and measuring the hit probability in that same region by projecting the reconstructed track into that particular region.

- Single photon calibration for HTCC/LTCC: The standard procedure for calibrating the low threshold Gas Čerenkov counter (LTCC) response has been to use the single photo-electron "noise" signal and adjust the PMT HV to equalize the output signal. This technique uses a self-triggering procedure that allows calibrating all 216 channels simultaneously. For the HTCC, a similar procedure will be used. To check the sensitivity of the HTCC PMTs to the fringe field of the solenoid magnet, the calibration will be repeated with the magnetic field ramped up in steps of 1/10 of the maximum field. The (possibly shifted) single photo-electron peak will be recorded, and then the HV will be adjusted to restore the no-field peak position.

- CTOF cosmic ray calibration: After complete assembly and integration into the Solenoid magnet, a single small scintillation start counter will be placed in the center of the CTOF barrel for triggering. A signal in the start counter and a hit in one of the CTOF scintillators, which indicates passage of a cosmic ray muon, will be used to calibrate the CTOF scintillators on the opposite side of the CTOF barrel. The Solenoid will then be powered up in steps of 1/10 of maximum current, and the response of the CTOF PMTs will be measured.

- SVT (barrel part BST) cosmic ray calibration: After complete assembly and installation of the central detector system, cosmic ray triggers by the additional start counter in the CTOF barrel will be used to measure the efficiency of the SVT response and the track reconstruction, first with straight tracks without magnetic field, and then with the Solenoid magnet ramped up to 1/2 and full fields to test the accuracy of track reconstruction in the barrel part. For this the track will be reconstructed in the 8 SVT layers in the upper hemisphere, and checked against the track parameters reconstructed in the 8 SVT layers of the lower hemisphere. Agreement within multiple scattering effects is expected.

- Solenoid and Torus magnet checkout: The Solenoid magnet checkout in Hall B will occur after the initial quality assurance test and field mapping outside of the Hall. It will consist of ramping the field to a moderate level to ensure integrity of the magnet after transport to the Hall, and the functionality of the cryogenics interfaces and controls and of the power supply. The Torus magnet will be assembled in Hall B by the vendor from pre-fabricated components. After assembly, the magnet will be interfaced with the cryogenic system in the hall, cooled down, and ramped up. A magnet quench will be initiated to verify the quench detection and protection system. This will be part of the vendor's responsibility. Once the magnet is accepted and in its final location, magnetic field tests will be carried out to determine deviations from the ideal symmetry.

12.2 Checkout with Beam

12.2.1 Objectives

In general, the objectives of the Hall B and CLAS12 commissioning procedure are to achieve reliable beam transport through thin and extended targets to the beam dump, to verify the optics design of the CLAS12 Torus and Solenoid magnets, and to determine the alignment and operational performance of the CLAS12 detector systems using beam interactions. Operation of the CLAS12 detector system in the presence of magnetic fields, and in conjunction with the trigger and data acquisition system and other ancillary systems will be studied as well.

After completion of the commissioning, the functionality of the Hall B instrumentation, including the beam line, the CLAS12 superconducting Torus and Solenoid magnetic field dis-

tribution, all CLAS12 detectors, the trigger and data acquisition systems, as well as the CLAS12 online software will have been verified.

12.2.2 Beam Line Operation

- Optimize the beam transport through the hall and CLAS12 to the Faraday cup (FC) and/or the beam dump at various beam currents. Determine the temperature rise of the FC for beam currents of 5, 10, 15, 20, 30, and 50 nA, and 6.6, 8.8, and 11 GeV beam energies.
- Verify the accuracy, stability, and reproducibility of the beam monitors.
- Verify beam parameters such as spot size and angle dispersion using the beam position monitors.
- Establish background levels from the beam dump and/or Faraday cup for optimized beam parameters. Develop optimal shielding conditions of the tunnel at various running conditions.
- Calibrate the current integrator (Faraday cup) at various beam energies and beam currents.

12.2.3 CLAS12 Operation

- Study the performance of the CLAS12 detector systems, as well as the trigger and data acquisition system at different beam/target conditions. This includes the measurement of rates in the various detector systems, the FTOF, the HTCC, the PCAL, and the R1, R2, and R3 drift chamber systems in all six CLAS12 sectors. This will be done at different levels of the solenoid field (50%, 75%, 100%), and at different levels of the Torus current (25%, 50%, 75%, 100%).
- Verify the detector alignments, especially the 3 regions of drift chambers, by operating CLAS12 without magnetic fields (both Solenoid and Torus magnets will be OFF) and at very low beam currents (<0.1 nA) to avoid the intense Møller background. Using thin targets will provide a point-like source of charged tracks emerging from the nominal CLAS12 center.

- Calibrate the various CLAS detector systems using beam interactions in a thin target and with various field settings in the CLAS12 Torus and Solenoid magnets. This includes establishment of trigger and detection efficiencies of the various detection systems.
- Measure the timing resolution of the FTOF and CTOF systems using the RF beam structure for accurate information on the start time of charged particles.
- Checkout the CLAS12 calibration and online reconstruction software.
- Study drift chambers occupancies as a function of beam current and test the online reconstruction efficiencies.
- Determine the LTCC and HTCC efficiencies with high-energy electrons identified by large energy deposition in the EC and PCAL.
- Measure the rates of the FTOF and CTOF detectors for different beam currents and different target materials, and determine possible saturation effects.

Chapter 13

Collaboration Responsibilities

13.1 Technical Participation of Research Groups to the Hall B 12-GeV Upgrade

This section lists the responsibilities and technical participation of the outside laboratory and University group to the Hall B 12-GeV Upgrade. Table 13.1 provides a summary of these contributions.

♢ Argonne National Laboratory

The Argonne National Laboratory Medium Energy group is actively involved in this proposal, as well as in the color transparency proposal using CLAS12. Among CLAS12 baseline equipment, the group intends to take responsibility for the design, prototyping, construction, and testing of the high threshold Čerenkov counter. Three research staff and two engineers are likely to work at least part time on this project in the next few years. Funding for the group is from DOE. Additional sources of funding will be sought as appropriate. Beyond the baseline equipment, the group is also interested in exploring the possibility of building a RICH detector for CLAS12.

♢ Arizona State University

The Arizona State University group is actively involved in this proposal. The ASU group is planning to contribute to the development of the CLAS12 software and hardware with regard

to the slow controls system. One professor, two research professors, and several graduate and undergraduate students are likely to work at least part time on this project in the next few years. ASU is also planning to recruit undergraduate students who can contribute.

♢ University of Connecticut

The University of Connecticut (UConn) group is actively involved in this proposal using CLAS12 baseline equipment. Among the CLAS12 baseline equipment, the UConn group is sharing the responsibility for the design, prototyping, construction, and testing of the high threshold Čerenkov counter (HTCC). One faculty member (Kyungseon Joo), one post-doc, and four graduate students are already, or will be, working on this project. The University of Connecticut Research Foundation (UCRF) already funded $32,000 for the equipment purchase for the HTCC prototyping project. UConn is also providing a clean room facility for this project and providing funding for half a post-doc and half a graduate student for the next two years to work on this effort. The group is currently funded by the DOE. Additional sources of funding will be sought as appropriate. Beyond the baseline equipment, the group is also deeply involved in software planning and development for CLAS12. The group was recently awarded a DOE SBIR/STTR Phase I grant with a software company, CyberConnect EZ, to develop a software framework to archive a large-scale nuclear physics experiment data base.

♢ DAPNIA/SPhN-Saclay, France

The DAPNIA/SPhN-Saclay group is actively involved in this proposal. Among CLAS12 baseline equipment, the group intends to take responsibility for the design, prototyping, construction, and testing of the central tracker (both the cylindrical part and the forward part). The group has started working on an option based on cylindrical Micromegas detectors. Provided this is shown to work as designed, the group anticipates that this option will be examined in comparison with the Silicon Vertex Tracker toward the end of 2007 or the beginning of 2008. Four research staff members and four technicians/engineers are likely to work at least part time on this project in the next few years. Funding for the group is from CEA-France. Additional sources of funding (ANR-France, European Union 7th PCRD) will be sought as appropriate. In case the Micromegas option is not suitable, or not selected for valid reasons, the group would study other technical participation in the CLAS12 baseline equipment. Beyond

the baseline equipment, the group is also interested in exploring neutral particle detection (mostly neutrons) in the central detector of CLAS12, in the so far empty space between the CTOF scintillators and the solenoid cryostat.

♢ Fairfield University

Fairfield University is actively involved in the DVCS proposal, as well as other CLAS12 proposals. The FU group is planning to contribute to the development of the CLAS12 software, such as the GEANT4 simulation effort. FU is also planning to recruit undergraduate students who can work on hardware projects over the summer at JLab or in collaboration with other groups.

♢ Florida International University

The Florida International University group is actively involved in this proposal. The FIU group will take responsibility of the beamline devices, detectors, readout electronics, targets, and software associated with the Hall B Møller polarimeter. FIU is also planning to recruit graduate and undergraduate students who can work on this project.

♢ Hampton University

Hampton University (HU) is actively involved in this proposal, as well as in the original BONUS experiment. The HU group will continue to support development, augmentation, and use of the BONUS target and detector system for CLAS12. The HU nuclear experimental suite consists of over 1,400 square feet of lab space with an electronic lab station, mechanical lab station, computer/graphic processing bay, and a dedicated radiation hot lab. The physics department, furthermore, has a 1,300 square foot class-10,000 clean room for component preparation and module construction. Research support for the Hampton University nuclear experimental group comes predominantly from the NSF.

♢ University of Glasgow, United Kingdom

The Glasgow group plans to contribute to the design, prototyping, construction, and testing of the following CLAS12 baseline equipment: the silicon vertex tracker electronic readout

system, data acquisition, GRID computing, and the photon beamline. Beyond the baseline equipment, the group is also interested in building a RICH detector for kaon identification in CLAS12. Seven faculty members and research staff of four technicians/engineers are likely to work at least part time on this project in the next few years. Funding for the group is from the UK Engineering and Physical Sciences Research Council, EPSRC. Additional sources of funding will be sought as appropriate.

♢ Idaho State University

The Idaho State University group is actively involved in this proposal. Among CLAS12 baseline equipment, the group intends to take responsibility for the design, prototyping, construction, and testing of the Region 3 Drift Chambers. Three faculty, an engineer, and several students are likely to work at least part time on this project in the next few years. ISU has also provided significant high bay laboratory space with clean room capabilities for this project. Detector prototype testing will utilize the existing Idaho Accelerator Center and related infrastructure. The group will seek other sources of funding as appropriate.

♢ Institute for Theoretical and Experimental Physics

The ITEP group is actively involved in this proposal and in the CLAS12 upgrade. The ITEP team is responsible for the design, prototyping, construction, and testing of the superconducting magnets (torus and solenoid), the tracking system, and the high threshold Čerenkov counter (HTCC). Oleg Pogorelko is serving as a coordinator for the magnet design. Alex Vlassov is doing the Monte Carlo program for the Čerenkov counter, and Sergey Kuleshov will participate in the tracking system design and will improve the parameters of the Inner Calorimeter. Nikolay Pivnyuk and Ivan Bedlinsky are committed to significant contributions in the development of the CLAS12 software.

♢ James Madison University

The James Madison University group is actively involved in this proposal. Among CLAS12 baseline equipment, the group intends to be involved as a major contributor with the design, prototyping, construction, and testing of the pre-shower calorimeter. Laboratory space is

currently being set up at the university for the testing of photomultiplier tubes and fibers. The group is supported by a grant from the NSF and has a strong undergraduate research component.

♢ Kyungpook National University, Republic of Korea

The Kyungpook National University group has been actively participating in the CLAS collaboration. The group has been contributing to the laser calibration of the TOF system and playing a central role in developing the prototype for the 12-GeV central TOF detector. The group is committed to design, construct, test, and maintain the 12-GeV CTOF detector. The group also intends to participate in data analysis.

♢ Moscow State University

The Moscow State University Group (MSU) is actively involved in development of CLAS12 base equipment needed for proposed experiments. In particular, the MSU group will participate in development of the simulation (GEANT4) and reconstruction software, and the trigger and data acquisition. The MSU group takes responsibility for the maintenance and development of the special database needed for N^* studies in coupled-channel analyses. This project will be developed jointly with Hall B and EBAC. MSU personnel will also participate in the development of the pre-shower calorimeter, the HTCC, and the drift chambers under supervision of the Hall B staff. At least 4 staff scientists and 5 graduate students will be involved in base equipment development.

♢ University of New Hampshire

The University of New Hampshire Nuclear Physics group is committed to significant contributions in the development of the CLAS12 software. Maurik Holtrop is currently chair of the CLAS12 GEANT4 simulation group and has a post-doc contributing to the effort as well. Since currently the main software efforts for CLAS12 are in the area of simulation, the UNH group is part of and contributing to the general CLAS12 software group. Current manpower commitments to this effort are 0.15 FTE of a faculty and 0.4 FTE of one post-doc. They expect to increase this effort as their CLAS activities wind down and their CLAS12 activities pick up.

They plan on attracting some talented undergraduate students to this project. Among the CLAS12 baseline equipment, the group intends to take responsibility for the design, prototyping, construction, and testing of the silicon vertex detector and perhaps the inner detector's silicon tracking detectors. Faculty member Maurik Holtrop is likely to work at least part time on this project in the next few years and is likely to be joined by Jim Connel, a cosmic ray experimentalist with a background in nuclear physics, who is very interested in joining the vertex detector project. He has considerable experience with silicon detectors for space observations. Funding for the group is from DOE and additional sources of funding will be sought for this project to bring aboard Prof. Connel. If funded they would like to attract a post-doc, a graduate student, and one or two undergraduate students to this project. Beyond the baseline equipment, the group is also interested in exploring an extended inner calorimeter for CLAS12.

♢ Norfolk State University

Norfolk State University is actively involved in this proposal using CLAS12. Among CLAS12 baseline equipment, the group intends to make important contributions to the prototyping, construction, and testing of the pre-shower calorimeter. Two faculty members and several students are likely to work at least part time on this project in the next few years. Funding for the group is from NSF. Additional sources of funding will be sought as appropriate.

♢ Ohio University

Ohio University is actively involved in this proposal using CLAS12. Among CLAS12 baseline equipment, the group intends to make important contributions to the prototyping, construction, and testing of the pre-shower calorimeter. One faculty member and a graduate student are likely to work at least part time on this project in the next few years. Funding for the group is from NSF. Additional sources of funding will be sought as appropriate.

♢ Old Dominion University

The Old Dominion University group is actively involved in this proposal, as well as several other proposals using CLAS12. Among CLAS12 baseline equipment, the group intends to take

responsibility for the design, prototyping, construction, and testing of the Region 1 Drift Chamber. Five faculty (including one research faculty) and one technician are likely to work at least part time on this project in the next few years. Funding for the group is from DOE and from the university (75% of research faculty salary + one regular faculty summer salary + 50% of the technician). ODU has also provided 6,000 square feet of high bay laboratory space with clean room capabilities for this project. The group will seek other sources of funding as appropriate. Gail Dodge is the chair of the CLAS12 Steering Committee and the user coordinator for the CLAS12 tracking technical working group. Beyond the baseline equipment, the group is also interested in exploring improvements to the BONUS detector and a future RICH detector for CLAS12.

♢ Rensselaer Polytechnic Institute

The RPI group is actively involved in this proposal using the CLAS12 base equipment. Paul Stoler is a member of the CLAS12 Steering Committee. Among the CLAS12 baseline equipment, the RPI group is involved in the design, prototyping, construction, and testing of the high threshold Čerenkov counter (HTCC) and the modification of the low threshold Čerenkov counter (LTCC). Currently, Paul Stoler is serving as a coordinator of the HTCC and LTCC groups involved in the effort. Research scientist Valery Kubarovsky is designing and building the apparatus for testing the prototype components. Two undergraduates are spending the summer at JLab working on prototype mirror fabrication and computer-aided optics design and simulation. The group will continue to be fully involved as needed. The group is currently funded by NSF and RPI. Additional sources of funding will be sought as appropriate.

♢ University of Richmond

The University of Richmond group is actively involved in this proposal using CLAS12. Among CLAS12 baseline equipment, the group intends to take responsibility for the design, prototyping, development, and testing of software for event simulation and reconstruction. One faculty member along with 2-3 undergraduates each year are likely to work at least part time on this project in the next few years. The group has a 100-CPU computing cluster solely for nuclear physics supported by a linux-trained, technical staff member. The cluster was funded by NSF and the University. The University also supports routine travel to JLab and undergraduate

summer stipends. Funding for the group is from DOE. Additional sources of funding will be sought as appropriate.

♢ University of South Carolina

The University of South Carolina group is actively involved in this proposal using CLAS12 base equipment. Ralf Gothe is a member of the CLAS12 Steering Committee. Among the CLAS12 baseline equipment, the USC group has taken responsibility for the design, prototyping, construction, and testing of the forward time-of-flight detector. Ralf Gothe is currently heading FTOF technical working group. Three USC faculty members (R. Gothe, S. Strauch, and D. Tedeschi), one post-doc, three graduate students, and two undergraduate students are already working on this project. The USC nuclear physics group is committed to carry out this project and will continue to be fully involved as needed. The group is currently funded by NSF. USC is providing a detector assembly hall for the duration of the project and has funded $60,000 for the initial infrastructure needs. Additional sources of funding will be sought as appropriate. Beyond the baseline equipment, the group has also been deeply involved in software planning and development for CLAS12.

♢ Temple University

The Temple University group has one faculty member (Z.-E. Meziani), a post-doc, a research associate, and several graduate students. The major source of funding for the group is DOE, however, the research associate is only paid half by DOE the other half of his salary is provided by the University. The intended contribution is 1 FTE-year for the Čerenkov counter installation and commissioning, as well as the analysis of the experiment.

♢ University of Virginia

The University of Virginia Polarized Target Group is actively involved in this proposal, as well as other proposals using CLAS12. The group's contribution to the CLAS12 baseline equipment will be the design, construction, and testing of the longitudinally polarized target discussed in this proposal. The target will use a horizontal ^{4}He evaporation refrigerator with a conventional design and similar to ones built and operated at JLab in the past. The refrigerator will be

constructed in the Physics Department workshop; the workshop staff have experience with building such devices. Testing will be done in our lab where all the necessary infrastructure is on hand. Two research professors (75% of salary from UVA, 17% from DOE), two post-docs, and two graduate students, all supported by DOE, will spend their time as needed on this project. Other funding will be pursued as necessary. Outside the base equipment considerations, one member of the group (DGC) has started working with Oxford Instruments on a design for an optimized transverse target magnet to be used for transverse polarization measurements.

♢ Virginia Polytechnic Institute and State University

Virginia Tech is actively involved in this proposal. The VT group is planning to contribute to the development of the CLAS12 software, such as the GEANT4 simulation effort.

♢ The College of William and Mary

The College of William and Mary group is actively involved in this proposal, as well as several other proposals using CLAS12. Among CLAS12 baseline equipment, the group is committed to building part of the forward tracking system, but the exact tasks have not yet been determined. At least one faculty member, two graduate students, half a post-doc and several undergraduates are likely to work at least part time on this project in the next few years. Funding for the group is from the DOE and from the NSF. Additional funding will be sought for building the base equipment. Facilities at William and Mary include a clean room suitable for drift-chamber construction, and, on the time scale of a few years, ample space for detector construction and testing.

♢ The Yerevan Physics Institute

The Yerevan Physics Institute group is actively involved in this proposal, as well as several other proposals using CLAS12. Among CLAS12 baseline equipment, the group is participating in the upgrade of the Electromagnetic Calorimeter. This includes designing, prototyping, constructing, calibrating, and commissioning the EC preshower detector (under the supervision of S. Stepanyan). It also includes writing and implementing the EC Preshower software

package. Three faculty or staff members and several graduate students are likely to work at least part time on this project in the next few years.

Institution	Commitment to CLAS12
Argonne National Laboratory	High Threshold Čerenkov
Arizona State University	Slow Controls
University of Connecticut	High Threshold Čerenkov University Infrastructure
DAPNIA/SPhN-Saclay, France	Central Tracker
Fairfield University	Software Development
Florida International University	Møller Polarimeter
University of Glasgow, United Kingdom	SVT readout, DAQ, GRID Computing
Hampton University	BONUS Detector
Idaho State University	Region 3 Drift Chambers University Infrastructure
Institute for Theoretical and Experimental Physics	SC Magnets: Torus and Solenoid Software development, Inner Calorimeter
James Madison University	Preshower Calorimeter
Kyungpook National University, Korea	Central TOF, Laser Calibration System
Moscow State University	Software Development, DAQ
University of New Hampshire	SVT, Software development
Norfolk State University	Preshower Calorimeter
Ohio University	Preshower Calorimeter
Old Dominion University	Region 1 Drift Chambers University Infrastructure
Rensselaer Polytechnic Institute	High Threshold Čerenkov Modification to the Low Threshold Čerenkov
University of Richmond	Software development
University of South Carolina	Forward TOF System University Infrastructure
Temple University	High Threshold Čerenkov
The College of William and Mary	Drift Chambers
University of Virginia	Polarized Target
Virginia Tech	Software Development
Yerevan Physics Institute	Preshower

Table 13.1: Summary table of the contributions of research groups to the CLAS12 upgrade project.

Bibliography

[1] R.W. Mcallister and R. Hofstadter, Phys. Rev. **102**, 851 (1956).

[2] E.D. Bloom *et al.*, Phys. Rev. Lett. **23**, 930 (1969).

[3] M. Breidenbach *et al.*, Phys. Rev. Lett. **23**, 935 (1969).

[4] M. Gell-Mann, Phys. Lett. **8**, 214 (1964).

[5] G. Zweig, CERN-TH-412, (1964).

[6] B. Fillipone and X. Ji, Adv. in Nucl. Phys. **20**, 1 2001.

[7] D. Müller *et al.*, Fortschr. Phys. **42**, 101 (1994).

[8] X. Ji, Phys. Rev. Lett. **78**, 610 (1997).

[9] X. Ji, Phys. Rev. D **55**, 7114 (1997).

[10] A.V. Radyushkin, Phys. Lett. B **380**, 417 (1996).

[11] A.V. Radyushkin, Phys. Rev. D **56**, 5524 (1997).

[12] M. Burkardt, hep-ph/0206269, (2002).

[13] A. Belitsky and D. Mueller, Nucl. Phys. A **711**, 118 (2002).

[14] X.D. Ji, Phys. Rev. D **55**, 7114 (1997).

[15] X.D. Ji, Phys. Rev. Lett. **78**, 610 (1997).

[16] A.V. Belitsky, D. Mueller, and A. Kirchner, Nucl. Phys. B **629**, 323 (2002).

[17] A. Airapetian *et al. (HERMES Collaboration)*, Phys. Rev. Lett. **87**, 182001 (2001).

[18] S. Stepanyan *et al. (CLAS Collaboration)*, Phys. Rev. Lett. **87**, 182002 (2001).

[19] V. Burkert *et al. (CLAS Collaboration)*, JLab Experiment E01-113, (2001).

[20] P. Bertin *et al. (Hall A Collaboration)*, JLab Experiment E00-110, (2000).

[21] S. Chen *et al. (CLAS Collaboration)*, hep-ex/0605012, (2006).

[22] A. Airapetian *et al. (HERMES Collaboration)*, hep-ex/0605108, (2006).

[23] S. Chekanov *et al. (ZEUS Collaboration)*, Phys. Lett. B **573**, 46 (2003).

[24] C. Adloff *et al. (H1 Collaboration)*, Phys. Lett. B **517**, 47 (2001).

[25] M. Vanderhaeghen, P.A.M. Guichon, and M. Guidal, Phys. Rev. D **60**, 094017 (1999).

[26] HERMES collaboration, in preparation.

[27] J. Dreschler *(HERMES Collaboration)*, AIP Conf. Proc. PANIC **842**, 375 (2005).

[28] A.V. Belitsky, AIP Conf. Proc. **698**, 607 (2004).

[29] J.C. Collins, L. Frankfurt, and M. Strikman, Phys. Rev. D **56**, 2982 (1997).

[30] H. Fenker *et al.*, JLab Experiment E03-12, (2003).

[31] X. Zheng *et al. (HallA Collaboration)*, Phys. Rev. C **70**, 065207 (2004).

[32] K.V. Dharmawardane *et al. (CLAS Collaboration)*, Phys. Lett. B **641**, 11 (2006).

[33] S. Kuhlmann *et al.*, Phys. Lett. B **476**, 291 (2000).

[34] S. Kuhn *et al.*, JLab experiment E12-06-113, (2006).

[35] The Longitudinal Spin Structure of the Nucleon, JLab experiment E12-06-109, (2006).

[36] E. Leader, A.V. Sidorov, and D.B. Stamenov, Phys. Rev. D **73**, 034023 (2006).

[37] R. Fatemi *et al. (CLAS Collaboration)*, Phys. Rev. Lett. **91**, 222002 (2003).

[38] J. Yun *et al. (CLAS Collaboration)*, Phys. Rev. C **67**, 055204 (2003).

[39] J.P. Chen, A. Deur, and Z.E. Meziani, Mod. Phys. Lett. A **20**, 2745 (2005).

[40] J.D. Bjorken, Phys. Rev. **148**, 1467 (1966).

[41] S.D. Drell and A.C. Hearn, Phys. Rev. Lett. **16**, 908 (1966).

[42] S.B. Gerasimov, Sov. J. Nucl. Phys. **2**, 430 (1966).

[43] X.D. Ji and J. Osborne, J. Phys. G **27**, 127 (2001).

[44] A. Airapetian *et al. (HERMES Collaboration)*, Eur. Phys. J. C **26**, 527 (2003).

[45] K. Abe *et al. (E143 Collaboration)*, Phys. Rev. D **58**, 112003 (1998).

[46] P.L. Anthony *et al. (E155 Collaboration)*, Phys. Lett. B **493**, 19 (2000).

[47] V.D. Burkert and B.L. Ioffe, Phys. Lett. B **296**, 223 (1992).

[48] V.D. Burkert and B.L. Ioffe, J. Exp. Theor. Phys. **78**, 619 (1994).

[49] E. Thomas and N. Bianchi, Nucl. Phys. Proc. Suppl. **82**, 256 (2000).

[50] A. Deur *et al.*, Phys. Rev. Lett. **93**, 212001 (2004).

[51] K. Helbing, Talk at GDH04 conference, (2004).

[52] SLAC E159, www.slac.stanford.edu/exp/e159/prop.pdf.

[53] S. Simula and M. Osipenko, Nucl. Phys. B **675**, 289 (2003).

[54] S. Bethke, α_S 2002 High-Energy Physics Int'l Conference in Quantum Chromodynamics, Montpellier (France) (2002).

[55] I. Niculescu *et al.*, Phys. Rev. Lett. **85**, 1186 (2000).

[56] M.E. Christy *et al. (E94-110 Collaboration).*

[57] E.D. Bloom and F.J. Gilman, Phys. Rev. Lett. **25**, 1140 (1970).

[58] E.D. Bloom and F.J. Gilman, Phys. Rev. D **4**, 2901 (1971).

[59] A. De Rujula, H. Georgi, and H.D. Politzer, Ann. Phys. **103**, 315 (1977).

[60] N. Isgur *et al.*, Phys. Rev. D **64**, 054005 (2001).

[61] M. Amarian *et al.*, Phys. Rev. Lett. **92**, 022301 (2004).

[62] P. Solvigon, Contribution to the proceedings of the First Workshop on Quark-Hadron Duality and the Transition to pQCD, A. Fantoni, S. Luiti, and O. Rondon ed., World Scientific (2006).

[63] P.E. Bosted *et al. (CLAS Collaboration)*, Phys. Rev. C **75**, 035203 (2007).

[64] J. Ashman *et al.*, Phys. Lett. B **206**, 364 (1988).

[65] D. Adams *et al. (SMC Collaboration)*, Phys. Rev. D **56**, 5330 (1997).

[66] P.L. Anthony *et al. (E155 Collaboration)*, Phys. Lett. B **458**, 529 (1999).

[67] K. Ackerstaff *et al. (HERMES Collaboration)*, Phys. Lett. B **464**, 123 (1999).

[68] A. Airapetian *et al. (HERMES Collaboration)*, Phys. Rev. D **71**, 012003 (2005).

[69] S.J. Brodsky, D.S. Hwang, and I. Schmidt, Phys. Lett. B **530**, 99 (2002).

[70] J.C. Collins, Phys. Lett. B **536**, 43 (2002).

[71] X. Ji and F. Yuan, Phys. Lett. B **543**, 66 (2002).

[72] A.V. Belitsky, X. Ji, and F. Yuan, Nucl. Phys. B **656**, 165 (2003).

[73] D. Boer, P.J. Mulders, and F. Pijlman, Nucl. Phys. B **667**, 201 (2003).

[74] X. Ji, J. Ma and F. Yuan, Phys. Rev. D **71**, 034005 (2005).

[75] J.C. Collins and A. Metz, Phys. Rev. Lett. **93**, 252001 (2004).

[76] X.d. Ji, J.P. Ma, and F. Yuan, Nucl. Phys. B **652**, 383 (2003).

[77] D.W. Sivers, Phys. Rev. D **43**, 261 (1991).

[78] M. Anselmino and F. Murgia, Phys. Lett. B **442**, 470 (1998).

[79] S.J. Brodsky, D.S. Hwang, and I. Schmidt, Nucl. Phys. B **642**, 344 (2002).

[80] M. Burkardt, Phys. Rev. D **72**, 094020 (2005).

[81] M. Gockeler *et al.*, Nucl. Phys. Proc. Suppl. **153**, 146 (2006).

[82] M. Gockeler *et al.*, hep-lat/0612032, (2006).

[83] J.C. Collins, Nucl. Phys. B **396**, 161 (1993).

[84] A.V. Efremov, K. Goeke, and P. Schweitzer, Phys. Rev. D **67**, 114014 (2003).

[85] A. Afanasev and C.E. Carlson, hep-ph/0308163, (2003).

[86] F. Yuan, Phys. Lett. B **589**, 28 (2004).

[87] A. Metz and M. Schlegel, Eur. Phys. J. A **22**, 489 (2004).

[88] A. Airapetian *et al. (HERMES Collaboration)*, Phys. Rev. Lett. **84**, 4047 (2000).

[89] A. Airapetian *(HERMES Collaboration)*, hep-ex/0612059, (2006).

[90] H. Avakian *et al. (CLAS Collaboration)*, Phys. Rev. D **69**, 112004 (2004).

[91] Conceptual Design Report (CDR) for The Science and Experimental Equipment for The 12 GeV Upgrade of CEBAF, Prepared for the DOE Science Review, April 6–8, 2005).

[92] A. Airapetian *et al. (HERMES Collaboration)*, Phys. Rev. Lett. **94**, 012002 (2005).

[93] V.Y. Alexakhin *et al. (COMPASS Collaboration)*, Phys. Rev. Lett. **94**, 202002 (2005).

[94] J.P. Ralston and D.E. Soper, Nucl. Phys. B **152**, 109 (1979).

[95] R.L. Jaffe and X.D. Ji, Nucl. Phys. B **375**, 527 (1992).

[96] P.J. Mulders and R.D. Tangerman, Nucl. Phys. B **461**, 197 (1996).

[97] A. Kotzinian, Nucl. Phys. B **441**, 234 (1995).

[98] A.M. Kotzinian and P.J. Mulders, Phys. Rev. D **54**, 1229 (1996).

[99] E. Leader, A.V. Sidorov, and D.B. Stamenov, Phys. Lett. B **462**, 189 (1999).

[100] H.C. Kim, M.V. Polyakov, and K. Goeke, Phys. Lett. B **387**, 577 (1996).

[101] R.D. Tangerman and P.J. Mulders, Phys. Rev. D **51**, 3357 (1995).

[102] H. Avakian *et al.*, AIP Conf. Proc. **792**, 945 (2005).

[103] A. Afanasev, C.E. Carlson, and C. Wahlquist, Phys. Lett. B **398**, 393 (1997).

[104] D. Boer and P.J. Mulders, Phys. Rev. D **57**, 5780 (1998).

[105] K.A. Oganesian *et al.*, Eur. Phys. J. C **5**, 681 (1998).

[106] L.P. Gamberg, G.R. Goldstein, and K.A. Oganessyan, Phys. Rev. D **67**, 071504 (2003).

[107] V. Barone, Z. Lu, and B.Q. Ma, Phys. Lett. B **632**, 277 (2006).

[108] S. Falciano *et al. (NA10 Collaboration)*, Z. Phys. C **31**, 513 (1986).

[109] J.S. Conway *et al.*, Phys. Rev. D **39**, 92 (1989).

[110] Z. Lu and B.Q. Ma, Phys. Rev. D **70**, 094044 (2004).

[111] Z. Lu and B.Q. Ma, Phys. Lett. B **615**, 200 (2005).

[112] R. Jakob, P.J. Mulders, and J. Rodrigues, Nucl. Phys. A **626**, 937 (1997).

[113] A. Bacchetta, A. Schaefer and J.J. Yang, Phys. Lett. B **578**, 109 (2004).

[114] ZEUS, J. Breitweg *et al. (ZEUS Collaboration)*, Phys. Lett. B **481**, 213 (2000).

[115] A. Bacchetta *et al.*, Phys. Rev. D **65**, 094021 (2002).

[116] A.M. Kotzinian *et al.*, hep-ph/9908466, (1999).

[117] Belle, K. Abe *et al. (Belle Collaboration)*, Phys. Rev. Lett. **96**, 232002 (2006).

[118] A. Airapetian *et al.,(HERMES Collaboration)*, Phys. Rev. D **64**, 097101 (2001).

[119] M. Anselmino *et al.*, hep-ph/0701006, (2007).

[120] A.V. Efremov *et al.*, Phys. Lett. B **612**, 233 (2005).

[121] A. Kotzinian, B. Parsamyan and A. Prokudin, Phys. Rev. D **73**, 114017 (2006).

[122] M. Anselmino *et al.*, Phys. Rev. D **74**, 074015 (2006).

[123] S.J. Brodsky and S.D. Drell, Phys. Rev. D **22**, 2236 (1980).

[124] S.J. Brodsky, M. Burkardt, and I. Schmidt, Nucl. Phys. B **441**, 197 (1995).

[125] M. Gluck *et al.*, Phys. Rev. D **53**, 4775 (1996).

[126] S. Kretzer, E. Leader, and E. Christova, Eur. Phys. J. C **22**, 269 (2001).

[127] A.V. Efremov, K. Goeke, and P. Schweitzer, Czech. J. Phys. **55**, A189 (2005).

[128] K. Goeke *et al.*, Phys. Lett. B **567**, 27 (2003).

[129] K. Goeke, A. Metz and M. Schlegel, Phys. Lett. B **618**, 90 (2005).

[130] J. Levelt and P.J. Mulders, Phys. Lett. B **338**, 357 (1994).

[131] X. Ji *et al.*, Phys. Rev. D **73**, 094017 (2006).

[132] D. Boer, Nucl. Phys. B **603**, 195 (2001).

[133] R.L. Jaffe, Int. J. Mod. Phys. A **18**, 1141 (2003).

[134] V. Del Duca, S.J. Brodsky, and P. Hoyer, Phys. Rev. D **46**, 931 (1992).

[135] B.Z. Kopeliovich *et al.*, Nucl. Phys. A **740**, 211 (2004).

[136] X. Guo and X.N. Wang, Phys. Rev. Lett. **85**, 3591 (2000).

[137] S.J. Brodsky and A.H. Mueller, Phys. Lett. B **206**, 685 (1988).

[138] W. Brooks, Fizika B **13**, 321 (2006).

[139] K. Hafidi, nucl-ex/0609005, (2006).

[140] M.B. Johnson *et al.*, hep-ph/0606126, (2006).

[141] M.B. Johnson *et al.*, Phys. Rev. C **65**, 025203 (2002).

[142] M. Riordan and W. Zajc, Sci. Amer. **294**, 34A (2006).

[143] J. Adams *et al.*, Nucl. Phys. A **757**, 102 (2005).

[144] R. Baier *et al.*, Phys. Lett. B **345**, 277 (1995).

[145] L.D. Landau and I. Pomeranchuk, Dokl. Akad. Nauk Ser. Fiz. **92**, 735 (1953).

[146] L.D. Landau and I. Pomeranchuk, Dokl. Akad. Nauk Ser. Fiz. **92**, 535 (1953).

[147] A.B. Migdal, Phys. Rev. **103**, 1811 (1956).

[148] H. Liu, K. Rajagopal, and U.A. Wiedemann, hep-ph/0605178, (2006).

[149] J.M. Maldacena, Adv. Theor. Math. Phys. **2**, 231 (1998).

[150] E. Witten, Adv. Theor. Math. Phys. **2**, 505 (1998).

[151] S.S. Gubser, I.R. Klebanov, and M.A. Polyakov, Phys. Lett. B **428**, 105 (1998).

[152] R. Baier *et al.*, Nucl. Phys. A **715**, 209 (2003).

[153] R. Baier *et al.*, hep-ph/0310274, (2003).

[154] B. Blattel *et al.*, Phys. Rev. Lett. **70**, 896 (1993).

[155] E.M. Aitala *et al.*, Phys. Rev. Lett. **86**, 4773 (2001).

[156] G. Bertsch *et al.*, Phys. Rev. Lett. **47**, 297 (1981).

[157] L.L. Frankfurt, G.A. Miller, and M. Strikman, Phys. Lett. B **304**, 1 (1993).

[158] L.L. Frankfurt, G.A. Miller, and M. Strikman, Found. of Phys. **30**, 533 (2000).

[159] G. Garino *et al.*, Phys. Rev. C **45**, 780 (1992).

[160] N.C.R. Makins *et al.*, Phys. Rev. Lett. **72**, 1986 (1986).

[161] T.G. O'Neill *et al.*, Phys. Lett. **351**, 87 (1995).

[162] K. Garrow *et al.*, Phys. Rev. C **66**, 044613 (2002).

[163] A.S. Carroll *et al.*, Phys. Rev. Lett. **61**, 1698 (1998).

[164] Y. Mardor *et al.*, Phys. Rev. Lett. **81**, 5085 (1998).

[165] A. Leskanov *et al.*, Phys. Rev. Lett. **87**, 212301 (2001).

[166] J.P. Ralston and B. Pire, Phys. Rev. Lett. **61**, 1823 (1998).

[167] M.R. Adams *et al.*, Phys. Rev. Lett. **74**, 1525 (1995).

[168] A. Airapetian *et al.*, Phys. Rev. Lett. **90**, 052501 (2003).

[169] B. Kopeliovich *et al.*, Phys. Rev. C **65**, 035201 (2002).

[170] K. Ackerstaff *et al.*, Phys. Rev. Lett. **82**, 3025 (1999).

[171] K. Hafidi, Jlab experiment E02-110, 2002.

[172] A. Airapetian *et al.*, *(HERMES Collaboration)*, Phys. Lett. B **577**, 37 (2003).

[173] X.N. Wang, Nucl. Phys. A **750**, 98 (2005).

[174] F.A. Arleo, Eur. Phys. J. C **30**, 213 (2003).

[175] K. Gallmeister and U. Mosel, nucl-th/0701064v2, (2007).

[176] C.E. Carlson and K.E. Lassila, Phys. Rev. C **51**, 364 (1995).

[177] W. Melnitchouk and A.W. Thomas, Phys. Lett. B **377**, 11 (1996).

[178] L.L. Frankfurt and M.I. Strikman, Phys. Rep. **76**, 217 (1981).

[179] L.L. Frankfurt and M.I. Strikman, Nucl. Phys. B **250**, 1585 (1998).

[180] S.E. Kuhn *et al.*, JLab experiment E94-102, 1994.

[181] K.S. Egiyan *et al. (CLAS Collaboration)*, Phys. Rev. Lett. **96**, 082501 (2006).

[182] J. Arrington, *"Inclusive Electron Scattering From Nuclei at $x > 1$ and High Q^2"*, Ph.D. thesis, California Institute of Technology, 2006.

[183] X. Lopez *et al. (FOPI Collaboration)*, Phys. Rev. C **75**, 011901 (2007).

[184] I. Cloet, W. Bentz, and A.W. Thomas, Phys. Lett. B **642**, 210 (2006).

[185] M. Ripani *et al. (CLAS Collaboration)*, Phys. Rev. Lett. **91**, 022002 (2003).

[186] S. Stepanyan *et al. (CLAS Collaboration)*, Phys. Rev. Lett. **91**, 25001 (2003).

[187] V. Kubarovsky *et al. (CLAS Collaboration)*, Phys. Rev. Lett. **92**, 032001 (2004).

[188] R. Thompson *et al. (CLAS Collaboration)*, Phys. Rev. Lett. **86**, 1702 (2001).

[189] J.W.C. McNabb *et al. (CLAS Collaboration)*, Phys. Rev. C **69**, 042201R (2004).

[190] J.W. Price *et al. (CLAS Collaboration)*, Phys. Rev. C **71**, 058201 (2005).

[191] L. Guo *et al. (CLAS Collaboration)*, submitted to Phys. Rev. C, nucl-ex/0702027, (2007).

[192] P. Ambrozewicz *et al. (CLAS Collaboration)*, Phys. Rev. C **75**, 045203 (2007).

[193] N. Dombey, Rev. Mod. Phys. **41**, 236 (1969).

[194] C. Morningstar, AIP Conf. Proc. **698**, 530 (2003).

[195] N. Mathur *et al.*, Phys. Lett. B **605**, 137 (2005).

[196] S.P. Barrow *et al. (CLAS Collaboration)*, Phys. Rev. C **64**, 044601 (2001).

[197] N. Isgur and J. Paton, Phys. Rev. D **31**, 2910 (1985).

[198] N. Isgur, R. Kokoski, and J. Paton, Phys. Rev. Lett. **54**, 869 (1985).

[199] S. Stepanyan *et al.*, JLab experiment E07-009, 2007.

[200] G.S. Adams, C.W. Salgado, and D.P. Weygand, JLab experiment E01-017, 2001.

[201] V. Burkert and T-S.H. Lee, Int. J. Mod. Phys. E **13**, 1035 (2004).

[202] K. Joo *et al. (CLAS Collaboration)*, Phys. Rev. Lett. **88**, 122001 (2002).

[203] T. Sato, T-S.H. Lee, and T. Nakamura, nucl-th/0411013, (2004).

[204] M. Bhagwat, Phys. Rev. C **68**, 015203 (2003).

[205] P. Bowman, hep-lat/0209129, (2002).

[206] T. Takahashi and H. Suganuma, Phys. Rev. D **70**, 074506 (2004).

[207] Review of Particle Physics, Phys. Lett. B **592**, 1 (2004).

[208] S. Basak *et al. (LHP Collaboration)*, hep-lat/0409082, (2004).

[209] S. Basak *et al. (LHP Collaboration)*, Nucl. Phys. Proc. Suppl. **129**, 209 (2004).

[210] R. Edwards *et al. (LHP Collaboration)*, Nucl. Phys. Proc. Suppl. **129**, 236 (2004).

[211] R. Gothe *et al.*, JLab experiment E04-010, 2004.

[212] R. Hofstadter and R.W. McAllister, Phys. Rev. **98**, 183 (1955).

[213] Science Review of the Proposed 12 GeV CEBAF Upgrade for the Thomas Jefferson National Accelerator Facility, April 6-8, 2005, U.S. Department of Energy Office of Nuclear Physics, 2005.

[214] G.P. Lepage and S.J. Brodsky, Phys. Rev. D **22**, 2157 (1980).

[215] M.K. Jones *et al.*, Phys. Rev. Lett. **84**, 1398 (2000).

[216] O. Gayou *et al.*, Phys. Rev. Lett. **88**, 092301 (2002).

[217] S. Platchkov *et al.*, Nucl. Phys. A **510**, 740 (1990).

[218] N. Isgur, G. Karl and D.W.L. Sprung, Phys. Rev. D **23**, 163 (1981).

[219] A.W. Thomas, Adv. Nucl. Phys. **13**, 1 (1984).

[220] The Lattice Hadron Physics Collaboration, *"Nuclear Theory with Lattice QCD: A Proposal to use Lattice QCD to Understand the Structure and Interactions of Hadrons"*, submitted to the U.S. Dept. of Energy, March 2000.

[221] P.E. Bosted, Phys. Rev. C **51**, 409 (1995).

[222] C.E. Hyde-Wright and K. deJager, Ann. Rev. Nucl. Part. Sci. **54**, 217 (2004).

[223] X. Ji, J. Phys. G **24**, 1181 (1998).

[224] E.D. Bloom and F.J. Gilman, Phys. Rev. Lett. **16**, 1140 (1970).

[225] A. de Rújula, H. Georgi and H.D. Politzer, Ann. Phys. **103**, 315 (1975).

[226] X. Ji and P. Unrau, Phys. Rev. D **52**, 72 (1995).

[227] X. Ji and W. Melnitchouk, Phys. Rev. D **56**, 1 (1997).

[228] S.D. Drell and T.M. Yan, Phys. Rev. Lett. **24**, 181 (1970).

[229] G.B. West, Phys. Rev. Lett. **24**, 1206 (1970).

[230] W. Melnitchouk, Phys. Rev. Lett. **86**, 35 (2001).

[231] C.E. Carlson and N.C. Mukhopadhyay, Phys. Rev. D **58**, 094029 (1998).

[232] W. Melnitchouk, R. Ent, and C. Keppel, Phys. Rept. **406**, 127 (2005).

[233] D.G. Richards *et al.*, J. Phys. Conf. Ser. **9**, 238 (2005).

[234] W. Melnitchouk *et al.*, Phys. Rev. D **67**, 114506 (2003).

[235] T. Burch *et al.*, Phys. Rev. D **70**, 054502 (2004).

[236] C. Alexandrou *et al.*, Phys. Rev. D **69**, 114506 (2004).

[237] C. Alexandrou *et al.*, hep-lat/0409122, (2004).

[238] H. Ichie *et al.*, hep-lat/0212024, (2002).

[239] T.T. Takahashi and H. Suganuma, Phys. Rev. D **70**, 074506 (2004).

[240] I.G. Aznauryan and K. Oganessyan, Phys. Lett. B **249**, 309 (1990).

[241] S. Capstick and B.D. Keister, Phys. Rev. D **51**, 3598 (1995).

[242] M. Aiello, M.M. Giannini and E. Santopinto, J. Phys. G **24**, 753 (1998).

[243] A. Holl, C.D. Roberts and S.V. Wright, nucl-th/0601071, (2006).

[244] D. Merten *et al.*, Eur. Phys. J. A **14**, 477 (2002).

[245] V.D. Burkert, Prog. Part. Nucl. Phys. **55**, 108 (2005).

[246] A. Matsuyama, T. Sato and T-S.H. Lee, nucl-th/0608051, (2006).

[247] S.J. Brodsky, hep-ph/0412101, (2004).

[248] L. Del Debbio *et al.*, Nucl. Phys. Proc. Suppl. **83**, 235 (2000).

[249] M. Burkardt and S. Dalley, Prog. Part. Nucl. Phys. **48**, 317 (2002).

[250] H.C. Pauli and S.J. Brodsky, Phys. Rev. D **32**, 2001 (1985).

[251] PAC32 report, http://www.jlab.org/exp_prog/PACpage/PAC32/PAC32_report.pdf, 2007.

[252] W. Brooks *et al.*, JLab experiment E94-017, 1994.

[253] S. Jeschonnek, private communication.

[254] H. Arenhoevel, private communication.

[255] J.D. Lachniet, *"A High Precision Measurement of the Neutron Magnetic Form Factor Using the CLAS Detector"*, Ph.D. thesis, Carnegie Mellon University, 2005.

[256] S. Rock *et al.*, Phys. Rev. Lett. **49**, 1139 (1982).

[257] V.I. Mokeev, Talk at N*2005 Workshop, November 4-6 2005, Newport News, VA, edited by S. Capstick, V. Crede and P. Eugenio, p.47, World Scientific, 2005.

[258] V.I. Mokeev *et al.*, PAC30 CLAS proposal PR12-06-116, *"Nucleon Resonance Studies with CLAS12 in the Transition from Soft to Partonic Physics"*, http://www.jlab.org/exp_prog/proposals/06prop.html.

[259] I.G. Aznauryan, Phys. Rev. C **68**, 065204 (2003).

[260] I.G. Aznauryan, Phys. Rev. C **67**, 015209 (2003).

[261] V.D. Burkert *et al.*, Phys. Atom. Nucl. **67**, 1940 (2004).

[262] I.G. Aznauryan *et al.*, Phys. Rev. C **72**, 045201 (2005).

[263] Pre-Conceptual Design Report the Science and Experimental Equipment for the 12 GeV Upgrade of CEBAF, see www.jlab.org/12GeV/collaboration.html.

[264] FASTMC is a fast parametric Monte Carlo of `CLAS12`; the code and documentation are contained in CVS under 12GeV/fastmc.

[265] PAC30 report, http://www.jlab.org/exp_prog/PACpage/PAC30/PAC30_report.pdf, 2006.

[266] A. Yegneswaran *et al.*, *"Proposal to Study a Section of the Silicon Vertex Tracker Envisioned for CLAS12"*, CLAS-Note 2004-042, (2004).

[267] M.A. Antonioli *et al.*, *"Two Possible Configurations of the Silicon Vertex Tracker"*, CLAS-Note 2006-21, (2006).

[268] M. Halappanavar *et al.*, *"Silicon Vertex Tracker's Simulation Status"*, CLAS-Note 2004-13, (2004).

[269] A.V. Vlassov *et al.*, *"Background Study for the Central Detector Planned for the 12 GeV Upgrade of CLAS"*, CLAS-Note 2006-20, (2006).

[270] B. Eng *et al.*, *"Simulation of the SVX4 ASICs Performance"*, CLAS-Note 2006-13, (2004).

[271] B. Eng *et al.*, *"Dead Time Due to the Frequency of Reset and Restore Operations of the SVX4 ASICs"*, CLAS-Note 2006-24, (2006).

[272] P. Bonneau *et al.*, *"A New Type of Single Board Computer for Detectors"*, CLAS-Note 2004-04, (2004).

[273] T. Chinwanawich *et al.*, *"Status Report on the Prototyping of Silicon Vertex Tracker"*, CLAS-Note 2004-029, (2004).

[274] Hall B Instrumentation Group, *"Silicon Vertex Tracker's Prototype Progress"*, CLAS-Note 2005-009, (2005).

[275] M.A. Antonioli *et al.*, *"FY05 R&D on the SVT Data Acquisition System"*, CLAS-Note 2005-016, (2005).

[276] M.A. Antonioli *et al.*, *"FY05 R&D on the SVT High Voltage Control Program"*, CLAS-Note 2005-017, (2005).

[277] M.A. Antonioli *et al.*, *"FY05 R&D on the SVT Low Voltage Control Program"*, CLAS-Note 2005-018, (2005).

[278] M.A. Antonioli *et al.*, *"SVT's R&D Annual Report FY05"*, CLAS-Note 2005-020, (2005).

[279] M.A. Antonioli *et al.*, *"SVT R&D for FY06"*, CLAS-Note 2005-019, (2005).

[280] P. Bonneau *et al.*, *"FY06 R&D Status Report"*, CLAS-Note 2006-010, (2006).

[281] M.D. Mestayer *et al.*, Nucl. Inst. and Meth. A **449**, 81 (2000).

[282] B.A. Mecking *et al.*, Nucl. Inst. Meth. A **503**, 513 (2003).

[283] R.L. Ford and W.R. Nelson, The EGS code system: Computer program for the Monte Carlo simulation of electromagnetic cascade showers, SLAC-210 (1978).

[284] B.A. Mecking, The MOMRES package is used as an input to FASTMC and is a program to estimate the momentum and angle resolution given a table of material thicknesses, position resolution, and integral magnetic field. The program is in CVS under 12GeV/momres.

[285] R. Fruhwirth, Nucl. Inst. and Meth. A **262**, 444 (1987).

[286] G. Welch and G. Bishop, *An Introduction to the Kalman Filter*, University of North Carolina Technical Report TR 95-041, (2004).

[287] A. Yegneswaran *et al.*, *Manufacturing, Assembly, and Alignment Requirements for the Silicon Vertex Tracker*, CLAS-Note 2008-009, (2008).

[288] H. Avakian, General event generator. The program is under CVS control in the repository at 12GeV/fastmc/clasev.

[289] E.S.Smith *et al.*, Nucl. Instr. and Meth. A **432**, 265 (1999).

[290] V. Baturin *et al.*, Nucl. Instr. and Meth. A **562**, 327 (2006).

[291] V.N. Batourine *et al.*, *"Measurements of PMT time resolution at Kyungpook National University"*, CLAS-Note 2004-16, (2004); V.N. Batourine *et al.*, *"Studies of time resolution of the Burle 85001 micro-channel plate photo-multipliers in comparison with standard PMTs"*, CLAS-Note 2004-39, (2004).

[292] V.N. Batourine *et al.*, *"Status Report on the studies at Kyungpook National University in 2005"*, CLAS-Note 2005-3, (2005).

[293] F.Barbosa *et al.*, *"Status and further steps towards the CLAS12 start-counter"*, CLAS-Note 2006-011, (2006).

[294] V.Kuznetsov, *"Time resolution of fine mesh PMTs with cosmic rays"*, to be submitted as CLAS-Note, (2007).

[295] Gordon Mutchler and Y. Sharabian, *"Wrapping Tests and Monte Carlo evaluation of a new Highly Segmented CLAS Start Counter"*, CLAS-Note 2005-004, (2005).

[296] F.Barbosa and V.Popov, *"The assembly of MCP PM Burle85011 with the on-board preamplifier"*, to be submitted as CLAS-Note, (2007).

[297] H. Kichimi *et al.*, Nucl. Inst. and Meth. A **325**, 451 (1993).

[298] J.Va'vra, "Photon detectors", SLAC, Japan 2005.

[299] M. Bonesini *et al.*, Nucl. Inst. and Meth. A **567**, 200 (2006).

[300] M. Foucher, M. Herndon, and H. Jawahery, Nucl. Inst. and Meth. A **374**, 57 (1996).

[301] G. Cecchet, "Timing counter status", CSNI, Assisi 2004.

[302] B. Dolgoshein, "Large area Silicon Photomultiplier: Performance and Applications", 4th ICNDP, Beaune-2005.

[303] Alfred Q.R. Baron., "Avalanche Diodes (APD) Detectors: Introduction and Recent Advances", Harima RIKEN & Spring-8/JASRI, International Symposium on the Development of Detectors for Particle, Astro-Particle, and Synchrotron Radiation Experiments, SLAC, Stanford, April 2006.

[304] S. Taylor *et al.*, Nucl. Inst. and Meth. A **462**, 484 (2001).

[305] E. Smith *et al.*, Nucl. Inst. and Meth. A **432**, 265 (1999).

[306] Y.D. Kim *et al.*, Nucl. Inst. and Meth. A **372**, 431 (1996).

[307] E. Chen *et al.*, hep-ex/9606007, (1996).

[308] For the forward-angle counters (15-cm wide) of the present `CLAS` TOF we have λ=134 cm + $0.36L$ and λ=430 cm for the large-angle scintillators (22-cm wide), σ_0=0.062 ns, σ_1=2.1 ns, σ_P=0.0118 ns/cm, and N_{pe}=1043.

[309] E.S. Smith and R. Jacobs, *"Photomultiplier Tests for the CLAS TOF"*, CLAS-Note 91-003, 1991.

[310] M. Amarian *et al.*, Nucl. Inst. and Meth. **A 460**, 239 (2001),

[311] N. Dashyan and S. Stepanyan, *"GEANT simulations of the CLAS12 pre-shower calorimeter"*, CLAS-Note 2007-001, (2007).

[312] K. Whitlow, N. Dashyan and S. Stepanyan, *"The CLAS12 pre-shower performance studies"*, CLAS-Note 2007-002, (2007).

[313] Ph. Rosier, Preliminary Finite Element Analysis of the Preshower Calorimeter for the CLAS12.

[314] N. Dashyan and S. Stepanyan, *"Improved Reconstruction Algorithm for the CLAS Forward Calorimeter"*, CLAS-Note 2006-016, (2006).

[315] MINOS Far detector, arXiv:hep-ex/0507018 (2005).

[316] FNAL Extruder http://www.nicadd.niu.edu/research/extruder.

[317] M. Amarian *et al.*, *"The Characteristics of Yerevan High Transparency Scintillators"*, CLAS-Note 1992-012, (1992).

[318] K. Giovanetti and A. Stavola, Fiber adapters for pre-shower tests (JMU).

[319] V. Burkert *et al.*, *"Light Readout System for the Electromagnetic Shower Calorimeter of the CEBAF Large Acceptance Spectrometer"*, CLAS-Note 1992-008, (1992).

[320] S. Pozdnyakov, *"Study of Flash ADCs as a new electronics for CLAS"*, CLAS-Note 2006-023, (2006).

[321] C. Smith, to be submitted as CLAS-Note, (2007).

[322] K. Mikhailov *et al.*, *"On-line trigger study for CLAS12"*, CLAS-Note 2007-009, (2007).

[323] CODA DAQ System.

[324] N. Akopov *et al.*, Nucl. Inst. and Meth. A **479**, 511 (2002).

[325] C. Fabjan, *"Techniques and Concepts in High Energy Physics III"*, Plenum Pub., T. Ferbel ed., (1985).

[326] R. Wigmans, *"Calorimetry"*, Oxford Science Pub., (2000).

[327] M. Antonelli *et al.*, Nucl. Inst. and Meth. A **409**, 558 (1996).

[328] D.W. Hertzog *et al.*, Nucl. Inst. and Meth. A **294**, 446 (1990).

[329] Open Science Grid, http://www.opensciencegrid.org.

[330] B. Abbott *et al.*, *"D-Zero data-intensive computing on the Open Science Grid"*, Fermilab Report fermilab-pub-07-462-cd, 2007.

[331] J. Beringer, *"Physics analysis at LHC: A wish list for grid computing (V1.2)"*, CERN Report CERN-LCGAPP-2003-09, 2003.

[332] A. Sciaba, *"The LHC Computing Grid"*, 4th International Workshop on Frontier Science, Milan, Biococca, Italy, 12-17 Sep. 2005.